ON THE EFFECTS OF CIRCULAR BOLT PATTERNS ON THE BEHAVIOR OF THE EXTENDED END-PLATE CONNECTIONS

by

ROOZBEH KIAMANESH

Presented to the Faculty of the Graduate School of

The University of Texas at Arlington in Partial Fulfillment

of the Requirements

for the Degree of

DOCTOR OF PHILOSOPHY

THE UNIVERSITY OF TEXAS AT ARLINGTON

August 2011

ACKNOWLEDGMENTS

I would like to express my gratitude to Dr. Ali Abolmaali for serving as my Committee Chairman. His patience, teaching, and encouragement during the course of my graduate study will always be remembered. Appreciations are also extended to Dr. Simon Chao, Dr. Frank Lu, Dr. Joe Lundy, Dr. John Matthys, and Dr. Guillermo Ramirez for serving on my committee. Laboratory work was made easier with the appreciated help of Jorge Fortza. Thanks to my colleagues and friends Dr. Tri Le, Dr. Anapoung Kararam, Mohammad Razavi, and Ruth Bribiesca, who donated their time and energy to this research.

The love and support of my parents Dr. Alireza Kiamanesh and Jahandokht Jahangiri Ghajar was the driving force behind the completion of this dissertation.

April 1, 2011

ABSTRACT

ON THE EFFECTS OF CIRCULAR BOLT PATTERNS ON BEHAVIOR OF THE EXTENDED END-PLATE CONNECTIONS

Roozbeh Kiamanesh, PhD

The University of Texas at Arlington, 2011

Supervising Professor: Ali Abolmmali

This study is a pioneer in introducing the circular bolt pattern configuration in extended end-plate steel connections. Discovering the static and cyclic behavior of such connections is at the forefront of this research study. To accomplish this goal, full-scale experimental testing complemented with three dimensional non-linear finite element analysis was conducted.

Due to the similarity between the behavior of T-Stubs under tension, and tension flange of the extended end-plate connection, experimental study was conducted on several T-Stub connections to study the effect of the bolt pattern configuration on the ductility, bolt force distribution, flange deformation, and overall performance of the connection. The specimens were fabricated in the laboratory and the bolts were strain gauged to monitor the bolt force during testing. This experimental study was coupled with nonlinear finite element modeling for further validation of the FEM results.

Three-dimensional non-linear finite element models were developed for each case using the corresponding geometric values. The steel plates were modeled with 8-noded linear brick, reduced integration, and hourglass control element. Six-noded linear triangular prism elements were used to model the bolts, bolt head, nuts, and the washers. The combined hardening plasticity algorithm was used in order to model the behavior of the Grade-50 hot-rolled steel

elements during monotonic and cyclic loading. Isotropic hardening was used to model the material properties for the high strength steel bolts. Small sliding surface-to-surface contact algorithm was considered for all the contacts. The welds were modeled by a tie-contact algorithm. The frictional surfaces accompanied by tangential forces were modeled by a tangential-contact algorithm. The contact surfaces between the end-plate and column were modeled by the frictional contact using the penalty method.

One hundred eighty two numerical models with circular and square bolt patterns were developed and analyzed by using the developed FEM. A comprehensive test matrix was used to investigate the effectiveness of the various geometric parameters on the overall behavior of the connections. The parametric study included seven bolt diameters, six values of end-plate thickness, three beam sizes, and two different bolt pattern configurations based on the most commonly used range of variables. The numerical results of the connections with circular bolt pattern were compared with that of the connections with traditional square bolt pattern. Also, the effects of these parameters on the moment-rotation characteristics and energy dissipation of the connection were investigated.

To simulate the hysteresis behavior of the connection (i.e. energy dissipation), four parameter tri-linear hysteresis models were used to fit the outer loops of the moment-rotation hysteresis loops obtained from the FEM experiments. Comprehensive regression analyses were conducted to obtain equations for dependent variables (tri-linear model parameters) in terms of independent geometric variables.)

The results of this study show that the circular bolt pattern can enhance the moment capacity, reduce pinching, and ultimately increase energy dissipation of the connections depending on their geometric parameters.

TABLE OF CONTENTS

ACKNOWLEDGMENTS iii

ABSTRACT iv

LIST OF ILLUSTRATIONS x

LIST OF TABLES i

Chapter Page

1. INTRODUCTION 1

1.1 General 1

1.2 Research Objectives 4

2. BACKGROUND REVIEW 7

2.1 General 7

2.2 End-Plate Design 7

2.3 Bolt Design 12

2.4 Finite Element Analysis Of End-Plate Moment Connections 14

2.5 T-Stubs Design 16

3. EXPERIMENTAL INVESTIGATION 22

3.1 Introduction 22

3.2 T-Stub Testing Program 22

3.2.1 Bolt Pattern Configuration 23

3.2.2 Test Specimen 24

3.2.3 Bolt Instrumentation 25

3.2.3.1 Flat Strain-Gauge, Omega SG/LY11 27

3.2.3.1.1 Wiring Precautions 27

3.2.3.1.2 Surface Preparation 28
3.2.3.1.3 Coating And Protection 28
3.2.3.1.4 Verification 29
3.2.3.2 Cylindrical Strain-Gauge, MLT-BL2 30
3.2.3.2.1 Bolt Preparation 31
3.2.3.2.2 Strain-Gauge Installation 31
3.2.3.2.3 Verification 31
3.2.4 Test Setup 32
3.2.5 Testing Procedure 33
3.2.6 Test Results 34
3.3 Beam-Column Connection 36
3.3.1 Extended End-Plate Connection 36
3.3.2 Top-And-Seat Connection 37
3.3.3 Bolted/Bolted Double Web Angle Connection 38
3.3.4 Welded/Bolted Double Web Angle Connection 39
3.3.5 Flush End-Plate Connection 40
3.3.6 Experimental Testing 41
4. FINITE ELEMENT MODELING AND VALIDATION 45
4.1 Introduction 45
4.2 Finite Element Modeling 45
4.3 Material Modeling 47
4.4 Contact Modeling 48
4.5 Comparison Of Numerical And Experimental Results 51
4.5.1 T-Stub 51
4.5.1.1 Specimen TS-L 51
4.5.1.2 Specimen TS-S 53
4.5.1.3 Specimen TS-C 54

4.5.2 Beam-Column Connection 56
4.5.2.1 Extended End-Plate Connection 57
4.5.2.2 Top-And-Seat Angle Connection 58
4.5.2.3 Bolted/Bolted Double Web Angle Connection 60
4.5.2.4 Welded-bolted Double Web Angle Connection 62
4.5.2.5 Flush End-Plate Connection 64
5. DEVELOPMENT OF HYSTERESIS MATHEMATICAL MODELS 66
5.1 Introduction 66
5.2 Selection Of Test Cases 66
5.3 Finite Element Modeling 70
5.4 Hysteresis Characteristics 73
5.5 Finite Element Results 77
5.6 Development Of Hysteresis Model Equation 91
5.6.1 Basis Of Hysteresis Development 91
5.6.2 Basis Of Regression Analysis 93
5.6.3 Equations Of Hysteresis Behavior 96
6. DISCUSSION OF THE RESULTS 108
6.1 Introduction 108
6.2 Results And Discussions 109
6.3 Energy Dissipation 111
6.4 Bolt Force Variation Under Monotonic Loading 116
6.5 Bolt-Force Variation Under Cyclic Loading 126
6.6 Effect Of The End-Plate Deformation 133
7. SUMMARY, CONCLUSION, AND RECOMMENDATIONS 139
7.1 Summary 139
7.2 Conclusion: 140
7.3 Recommendations 141

APPENDIX 143
A. APPLIED TORGUE VERSUS PRE-TENSIONING BOLT FORCE 143
B. TEST MATRIX 145
C. HYSTERESIS OF THE MODELS WITH SQUARE BOLT PATTERN 149
D. HYSTERESIS OF THE MODELS WITH CIRCULAR BOLT PATTERN 183
E. COMPARISSON OF THE MODELS WITH CIRCULAR AND SQUARE BOLT PATTERN 215
F. NON-LINIEAR REGRESSION ANALYSIS 245
REFERENCES 263
BIOGRAGHICAL INFORMATION 270

LIST OF ILLUSTRATIONS

Figure Page

1-1 Failure Modes For A Bolted End-Plate Connection.(a) Thin, (b) Intermediate, And (c) Thick 2

1-2 Typical Extended End-Plate Connection With Circular Bolt Pattern Configuration 5

2-1 End-Plate Connection Decomposition According To Eurocode-3 [7] 17

2-2 Free-Body Diagram Of A T-Stubs Connection. 19

2-3 Tension Angle Free-Body Diagram 20

3-1 Bolt Pattern Configurations, (a) Line, (b) Square, And (c) Circular. 23

3-2 Final Product Of The TS-L Specimen 24

3-3 Final Product Of The TS-S Specimen 25

3-4 Final Product Of The TS-C Specimen 25

3-5 Deformed Shape Of The T-Stubs With Line Bolt Pattern (κ_i Is Curvature In Direction i) 26

3-6 Deformed Shape Of The T-Stubs With Circulare Bolt Pattern (κ_i, And κ_j Are Curvature In Direction i, And j Respectively) 27

3-7 The Instrumented Bolt 28

3-8 Schematic Drawing Of The Test Setup Used To Verify The Functionality Of The Strain Gauges 30

3-9 Test Setup Used To Verify The Functionality Of The Strain Gauges. 30

3-10 Schematic Of The MLT-BL2 Strain Gauge 31

3-11 T-Stubs Test Setup With Line Bolt Pattern 32

3-12 T-Stubs Test Setup With Square Bolt Pattern 33

3-13 T-Stubs Test Setup With Circular Bolt Pattern 33

3-14 Applied Force Vs. Flange Separation Response Of The T-Stubs With Various Bolt Pattern Configuration 36

3-15 Configuration Of Extended End-Plate Test Specimen 37

3-16 Configuration Of Extended End-Plate Test Specimen 38

3-17 Configuration Of Bolted/Bolted Double Web Angle Connection Test Specimen 39

3-18 Configuration Of Welded/Bolted Double Web Angle Connection Test Specimen 40

3-19 Configuration Of Flush End-Plate Test Specimen 41

3-20 Typical configuration of the beam column connection test setup 43

4-1 A Typical Bolt Mesh 47

4-2 Stress-Strain Relationship For High Strength Bolts 47

4-3 Contacts In Typical Extended End-Plate Connection; (a) Friction Contact, Between The End-Plate And Face Of The Column, And Between The Bolt-Head And End-Plate, (b) Frictionless Contact, Between The Bolt-Shank And Bolt-Hole, And (c) Tie Contact, Between The Bolt-Head And Internal Face Of The Column Flange 50

4-4 Finite Element Model Of TS-L Specimen 51

4-5 Applied Force Versus Flange Separation Response For TS-L Specimen 52

4-6 Bolt Force History In TS-L Specimen 52

4-7 Finite Element Model Of TS-S Specimen 53

4-8 Applied Force Versus Flange Separation Response For TS-S Specimen 53

4-9 Bolt Force History In TS-S Specimen 54

4-10 Finite Element Model Of TS-C Specimen 55

4-11 Applied Force Versus Flange Separation Response For TS-C Specimen 55

4-12 Bolt Force History In TS-C Specimen 56

4-13 Extended End-Plate Finite Element Model, And Mesh Properties. 57

4-14 Comparison Of The Hysteresis Of The FEM And Experimental Results Of The Extended End-Plate Connections. 58

4-15 Top-And-Seat Angle Connection Finite Element Model, And Mesh Properties. 59

4-16 Comparison Of The Hysteresis Of The FEM And Experimental Results Of The Top-And-Seat Angle Connection. 59

4-17 Failure Of Bolts In The Extended End-Plate Connection 60

4-18 Bolted/Bolted Double Web Angle Connection Finite Element Model, And Mesh Properties. 61

4-19 Comparison Of The Hysteresis Of The FEM And Experimental Results Of The Bolted/Bolted Double Web Angle Connection. 61

4-20 Deformation Of The Bolt-Holes From Round To Oval Due To Excessive Elongation In Bolted/Bolted Double Web Angle Connection 62

4-21 Welded/Bolted Double Web Angle Finite Element Model, And Mesh Properties. 63

4-22 Comparison Of The Hysteresis Of The FEM And Experimental Results Of The Welded/Bolted Double Web Angle Connection. 63

4-23 Failure Of The Angle Due To Excessive Elongation In Welded/Bolted Double Web Angle Connection 64

4-24 Flush End-Plate Connection Finite Element Model, And Mesh Properties. 65

4-25 Comparison Of The Hysteresis Of The FEM And Experimental Results Of The Flush End-Plate Connections. 65

5-1 Detail Of The End-Plate, (a) Proposed Circular Bolt Pattern, (b) Rectangular Bolt Pattern 68

5-2 The Detail Of The Parameters 70

5-3 Finite Element Model Of The Extended End-Plate Connection With Circular Bolt Pattern Configuration. 71

5-4 Cyclic Loading History, FEMA 350. 73

5-5 Schematic Drawing Of The End-Plate Rotation. 74

5-6 Tri-Linear Hysteresis Behavior Of The Models With “End-Plate Behavior” 76

5-7 Tri-Linear Hysteresis Behavior Of The Models With “Bolt Behavior” 77

5-8 Flowchart For Simulation Of The Hysteresis Behavior Of The Extended End-Plate Connections. 92

5-9 Comparison Of The Predicted Vs. Actual Moment Capacity Of The Connection At Yield With ±5% Error Envelope For The Category-1 Connections With Circular Bolt Pattern 98

5-10 Comparison Of The Predicted Vs. Actual Initial Stiffness Of The Connection With ±5% Error Envelope For The Category-1 Connections With Circular Bolt Pattern 98

5-11 Comparison Of The Predicted Vs. Actual Post-Yield Stiffness Of The Connection With ±5% Error Envelope For The Category-1 Connections With Circular Bolt Pattern 99

5-12 Comparison Of The Predicted Vs. Actual Ultimate Rotation Capacity Of The Connection With ±5% Error Envelope For The Category-1 Connections With Circular Bolt Pattern 99

5-13 Comparison Of The Predicted Vs. Actual Moment Capacity Of The Connection At Yield With ±5% Error Envelope For The Category-2 Connections With Circular Bolt Pattern 100

5-14 Comparison Of The Predicted vs. Actual Initial Stiffness Of The Connection With ±5% Error Envelope For The Category-2 Connections With Circular Bolt Pattern 101

5-15 Comparison Of The Predicted Vs. Actual Post-Yield Stiffness Of The Connection With ±5% Error Envelope For The Category-2 Connections With Circular Bolt Pattern 101

5-16 Comparison Of The Predicted vs. Actual Ultimate Rotation Capacity Of The Connection With ±5% Error Envelope For The Category-2 Connections With Circular Bolt Pattern 102

5-17 Comparison Of The Predicted Vs. Actual Moment Capacity Of The Connection At Yield With ±5% Error Envelope For The Category-1 Connections With Square Bolt Pattern 103

5-18 Comparison Of The Predicted Vs. Actual Initial Stiffness Of The Connection With ±5% Error Envelope For The Category-1 Connections With Square Bolt Pattern 103

5-19 Comparison Of The Predicted Vs. Actual Post-Yield Stiffness Of The Connection With ±5% Error Envelope For The Category-1 Connections With Square Bolt Pattern 104

5-20 Comparison Of The Predicted Vs. Actual Ultimate Rotation Capacity Of The Connection With ±5% Error Envelope For The Category-1 Connections With Square Bolt Pattern 104

5-21 Comparison Of The Predicted Vs. Actual Moment Capacity Of The Connection At Yield With ±5% Error Envelope For The Category-2 Connections With Square Bolt Pattern 105

5-22 Comparison Of The Predicted Vs. Actual Initial Stiffness Of The Connection With ±5% Error Envelope For The Category-2 Connections With Square Bolt Pattern 106

5-23 Comparison Of The Predicted Vs. Actual Post-Yield Stiffness Of The Connection With ±5% Error Envelope For The Category-2 Connections With Square Bolt Pattern 106

5-24 Comparison Of The Predicted Vs. Actual Ultimate Rotation Capacity Of The Connection With ±5% Error Envelope For The Category-2 Connections With Square Bolt Pattern 107

6-1 Comparison Of The Hysteresis Of The Connections With Circular And Square Bolt Pattern, Bd=1¼ in. 113

6-2 Comparison Of The Hysteresis Of The Connections With Circular And Square Bolt Pattern, B_d=¾ in. 114

6-3 Comparison Of The Hysteresis Of The Connections With Circular And Square Bolt Pattern, B_d=½ in. 115

6-4 Comparison Of The Bolt Forces During Monotonic Loading 118

6-5 Comparison Of The Bolt Forces During Monotonic Loading 119

6-6 Comparison Of The Bolt Forces During Monotonic Loading 120

6-7 Comparison Of The Bolt Forces During Monotonic Loading 121

6-8 Comparison Of The Bolt Forces During Monotonic Loading 122

6-9 Comparison Of The Bolt Forces During Monotonic Loading 123

6-10 End-Plate Deformation Of (a) Tp1-Bd1¼-d30-CIR And (b) Tp1-Bd1¼-d30-SQR 124

6-11 End-Plate Out Of Plain Deformation Contour Of (a) Tp1-Bd1¼-d30-CIR And (b) Tp1-Bd1¼-d30-SQR 125

6-12 Comparison Of The Bolt Forces During Cyclic Loading, And Corresponding Story Drift. 127

6-13 Comparison Of The Bolt Forces During Cyclic Loading, And Corresponding Story Drift. 128

6-14 Comparison Of The Bolt Forces During Cyclic Loading, And Corresponding Story Drift.. 129

6-15 Comparison Of The Bolt Forces During Cyclic Loading, And Corresponding Story Drift.. 130

6-16 Comparison Of The Bolt Forces During Cyclic Loading, And Corresponding Story Drift.. 131

6-17 Comparison Of The Bolt Forces During Cyclic Loading, And Corresponding Story Drift. 132

6-18 End-Plate Deformation Of (a) Tp½-Bd1-d24-CIR And (b) Tp½-Bd1-d24-SQR 135

6-19 End-Plate Deformation Of (a) T_p¾-B_d1-d24-CIR And (b) T_p¾-B_d1-d24-SQR 135

6-20 End-Plate Deformation Of (a) T_p118-B_d1-d24-CIR And (b) T_p118-B_d1-d24-SQR 136

6-21 End-Plate Deformation Of (a) T_p1½-B_d1-d24-CIR And (b) T_p1½-B_d1-d24-SQR 136

6-22 End-Plate Out Of Plain Deformation Contour Of (a) Tp¾-Bd1-d24-CIR And (b) Tp¾-Bd1-d24-SQR 138

6-23 End-Plate Out Of Plain Deformation Contour Of (a) Tp1½-Bd1-d24-CIR And (b) Tp1½-Bd1-d24-SQR 138

LIST OF TABLES

Table Page

3-1 T-Stubs Test Matrix 23

3-2 The Results Summary Of The Monotonic Testing On T-Stubs 35

3-3 Definitions And Geometric Values Of The Extended End-Plate Specimen 37

3-4 Definitions And Geometric Values Of The Top-and-Seat Specimen 38

3-5 Definitions And Geometric Values Of The Bolted/Bolted Double Web Angle Connection 39

3-6 Definitions And Geometric Values Of The Welded/Bolted Double Web Angle Connection 40

3-7 Definitions And Geometric Values Of The Flush End-Plate Specimen 41

4-1 The Mesh Size Distribution In The Bolts 46

4-2 Material Properties 48

5-1 Range Of Element Thickness And Designated Symbols 67

5-2 The Angular Coordinate For Each Bolt 69

5-3 Parametric Value Of The Moment And Rotation Of The Points On The Hysteresis Model Of The Connections With “End-Plate Behavior” 76

5-4 Parametric Value Of The Moment And Rotation Of The Points On The Hysteresis Model Of The Connections With “*Bolt Behavior*” 77

5-5 Numerical Results Of The Models With Circular Bolt Pattern 79

5-6 Numerical Results Of The Models With Square Bolt Pattern 83

5-7 Summary Of The Results And Percentage Variation 87

6-1 Types And Details Of The Sampled Specimens And Relative Energy Dissipation 109

6-2 Energy Dissipation Percentage Variation Between The Connection With Circular And Square Bolt Pattern With d=30in 110

6-3 Energy Dissipation Percentage Variation Between The Connection With Circular And Square Bolt Pattern With d=24in 110

6-4 Energy Dissipation Percentage Variation Between The Connection With Circular And Square Bolt Pattern With d=36in 110

6-5 Energy Dissipation And Their Persentaige Variation. 133

CHAPTER 1

INTRODUCTION

1.1 General

Among the moment resisting bolted connections, the extended end-plate connections with approximately 90% compatibility with the available beam sections are the most popular types of the bolted connections, AISC [1]. Moment resisting bolted connections exhibits a behavior ranging from fully-restraint (rigid) to partially restraint (semi-rigid) depending on their type and geometric parameters. Although numerous studies have been conducted on the behavior of these connections, limited attention has been drawn toward the configuration of the bolt patterns, end-plate deformation, and their effect on the bolt-force distribution and overall connection performance.

The investigations to evaluate bolt-forces in the connections date back to 1960s with contributions from Douty and McGuire [2], Kato and McGuire [3], and Nair et al. [4]. These investigations were conducted on T-Stubs to evaluate the bolt-forces including the effects of the prying force generated near the edge of the end-plate. Kennedy et al. [5][6] were pioneers in developing a design procedure for determining the bolt forces in the flush, extended, stiffened, and unstiffened end-plate moment connections. Their design procedure introduced three stages of flange behavior based on the end-plate thickness condition; thin, intermediate, and thick. The three main failure modes for end-plate bolted connection are adopted in Eurocode-3 [7], and AISC Design Guide-16 [8]. Figure 1-1 illustrates the three modes of plate behavior for each thickness condition.

Mode-1: plastic hinges form at the bolt-line and at the beam web, Figure 1-1(a).

Mode-2: plastic hinges form at the beam web followed by yielding of the bolts Figure 1-1(b); and

Mode-3: yielding of the bolts only while the end-plate remains elastic Figure 1-1(c).

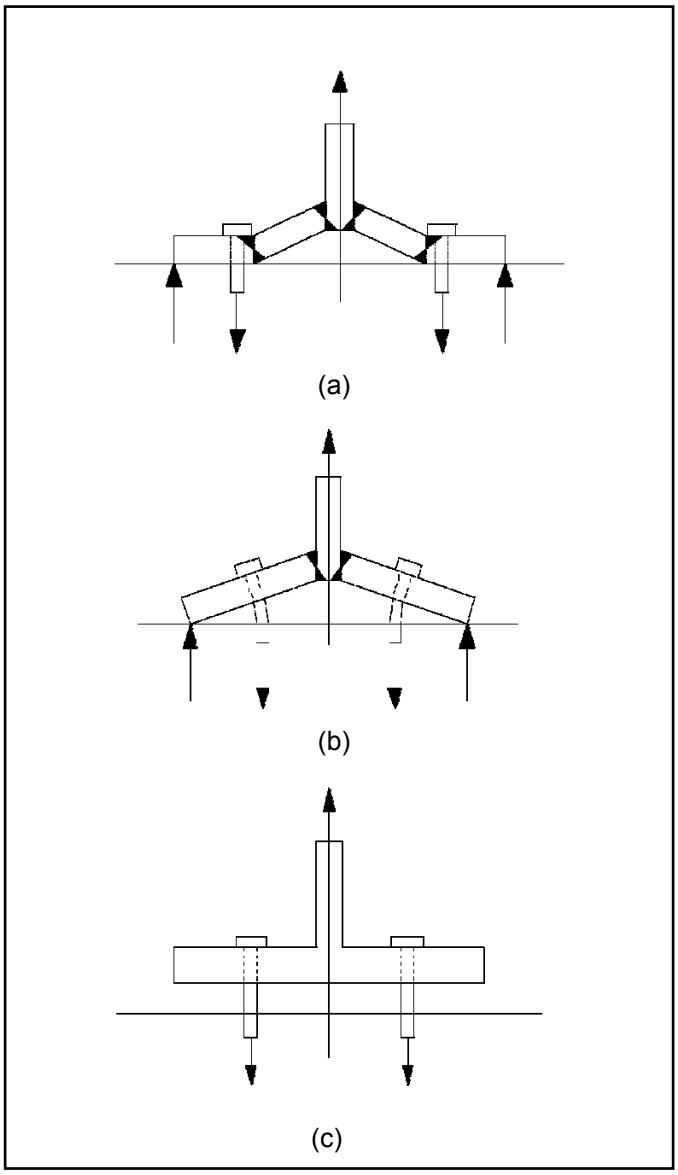

Figure 1-1 Failure Modes For A Bolted End-Plate Connection.(a) Thin, (b) Intermediate, And (c) Thick

Mode-1 has high ductility, but the connection with this failure mode is expected to possess low moment resistance and stiffness characteristic. To the contrary, Mode-3 tends to possess a high level of moment resistance with a brittle failure mechanism. In Mode-2, the joint can resist an intermediate level of moment, while remaining reasonably ductile [6].

Due to the low accuracy in predicting the prying forces in the intermediate case, a series of research studies were carried out by Srouji et al. [9], Hendrick et al. [10], and Morrison et al. [11][12] to adjust the location and magnitude of the prying forces and to improve the accuracy of the distribution of the bolt-

forces in a given bolt row. Borgsmiller [13] introduced a simplified version of the Kennedy et al. [5] method with only two stages of plate behavior; thick plate with no prying force, and thin plate behavior with maximum prying force. The threshold between thin and thick plate behavior was established as the point in which prying force was negligible. Therefore, the intermediate stage introduced by Kennedy et al. [5] was ignored. Consequently, this design philosophy was adopted by the AISC Design Guide-16 [8] with the assumption that the column and end-plate are relatively stiff and remain elastic, and bolts are not subjected to noticeable prying forces. These models have been used for many years as a design philosophy to design a steel moment resisting bolted connections.

On January 17, 1994, the Northridge earthquake became a turning point for the design philosophy of the steel connections. This earthquake caused many unexpected failures on numerous fully-welded beam-to-column connections. More than 150 welded steel moment frame structures sustained brittle fractures in their welded moment connections, which demonstrated in no uncertain terms the vulnerability of welded connections to seismic loading. This earthquake event initiated a series of new research studies to investigate the true behavior of steel moment resisting connections subjected to cyclic loading. The premature brittle failure of welded connections was also noticed in the 1995 Hyogo-ken Nanbu (Kobe) earthquake. To address this vital issue, the U.S. Federal Emergency Management Agency (FEMA) initiated a 5-year program to develop and verify reliable and cost-effective methods for the inspection, evaluation, repair, rehabilitation, design, and construction of steel moment frame structures. This program was managed and administrated by the joint venture between **S**tructural Engineers Association of California, the **A**pplied Technology Council, and the **C**alifornia Universities for Research in Earthquake Engineering (SAC). This research is commonly known as the SAC Steel Project. SAC was divided into two phases. The initial phase focused on determining the cause of the fully welded connection failures, and the second phase of the research focused on finding alternative connections which can sustain seismic loading. This investigation included experimental testing and numerical modeling to determine suitable welded connection or bolted connection with an end-plate for use in seismic force resisting moment frame. Among the important tasks identified by FEMA/SAC Phase II, the connection performance and system (frame) performance under earthquake loads were most

noticeable. Among those, Asteneh-asl [14], Adey et al. [15], Meng and Murray [16][17], and Boorse [18] conducted experimental investigation, and Bursi and Jaspart [19][20], and Mays [21] performed a finite element analysis to study the performance of the moment resisting bolted connections. Murray [22] studied the end-plate behavior and bolt force distribution in both flush and extended end-plate connections by using finite element analyses. This study indicated that in the eight-bolted extended end-plate connections, four near bolts are fully effective, while the far four bolts are effective approximately up to 70% of their tensile strength. Based on this study, only 6.8 out of eight bolts are considered effective in the design of end-plate connections. Thus, the AISC design manual [23] conservatively adopted six effective bolts for these connections.

In general, the ultimate moment capacity is the main focus in designing moment resisting connections. Particularly, in seismic regions a balance between strength, stiffness, and ductility is at the forefront of design philosophies. To ensure ductility, it is necessary that a yielding mechanism fully develops before brittle failure occurs. Since fracture of the bolts will result in sudden loss of strength and stiffness, it is common design practice to increase the bolt resistance to be greater than the other failure modes in the connection, AISC [8].

1.2 Research Objectives

Despite the large number of research studies conducted on the behavior of the moment resisting bolted connections, most efforts have been concentrated on the behavior of the end-plate and bolts. To the author knowledge no studies have been conducted on the effect of the configuration of the bolt pattern on overall connection behavior. The focus of this research is to investigate the behavior of the extended end-plate bolted connections with unconventional circular bolt pattern configuration. A circular bolt pattern configuration is proposed as an alternative bolt pattern for the extended end-plate moment connection. Figure 1-2 shows a typical extended end-plate connection used in this research. The results of this study show that circular bolt pattern may improve and enhance the overall behavior of the connection depending on their geometric parameters.

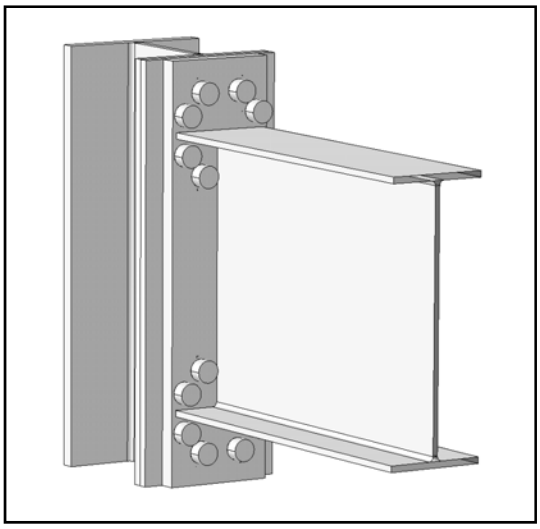

Figure 1-2 Typical Extended End-Plate Connection With Circular Bolt Pattern Configuration

Uneven distribution of the bolt-forces in the connection bolts causes high stress concentration on the bolts closer to the beam flange which results in an early yielding of these bolts. The pinching phenomenon is due to the reduction in pre-tensioning force in the connection because of the yielding of the bolts or fracture in the end-plate. The elongation of the bolts significantly reduces the pre-tensioning force in bolts which leads to strength reduction of the connection in the subsequent loading cycle during cyclic loading. In addition, pinching may occur if early yielding of the end-plate takes place before the bolts are fully loaded. The end-plate thickness vs. bolt diameter ratio is an indicator of connection performance which will be addressed and discussed in this research.

Based on experimental and numerical investigations, the proposed circular bolt pattern configuration in the steel bolted connections results in a more uniform distribution of the forces in the bolts. This prevents early yielding of the bolts in the connection during loading which consequently reduces the pinching effect.

The objectives of this research are divided into the following primary goals:

1- To reduce and redistribute bolt-forces in the moment resisting bolted connection by changing the bolt pattern configuration. Due to unique deformation characteristics of the end-plate in the connections with a circular bolt pattern, the far bolt can engage and experience load in an earlier stage of loading when it is compared with the connections with a square bolt pattern. This

phenomenon will decrease the bolt-force in the bolts closer to the beam-flange and increase the bolt-forces in the bolts far from the beam-flange, which consequently increases the ultimate loading capacity of the connection.

2- To enhance connection energy dissipation by reducing the pinching phenomenon in the cyclic hysteresis behavior of the bolted beam to column connection. Using the circular bolt pattern configuration reduces the bolt-forces in the bolts closer to beam flange, which delay their yielding. Thus, connections with a circular bolt pattern sustain pre-tension forces for longer duration. This means that pinching may be reduced or delayed in connections with a circular bolt pattern when compared with those with a square bolt pattern.

3- To develop a prediction equation for strength, stiffness, and other related parameters, which predict the moment-rotation hysteresis behavior of the connection with circular and square bolts patterns. These parameters are commonly defined by the yield moment, the yielding rotation, the ultimate moment capacity, and the ultimate rotation.

4- To develop a unified multi-linear hysteresis method to predict the hysteresis behavior of the extended end-plate connections under cyclic loading for any given geometry.

5- To compare the energy dissipation variation between connections with circular and square bolt patterns. This is accomplished by comparing the area under the hysteresis outer-loops of each model, which be defines their energy dissipation characteristics.

6- To conduct a detailed investigation with regard to the end-plate and bolt behavior of connections with circular and square bolt patterns with different geometric variables.

CHAPTER 2

BACKGROUND REVIEW

2.1 General

A great deal of research on the behavior and design of the end-plate moment connection has been conducted over the past several years and are available in the literature. In this chapter, a brief review of the background literatures are organized and presented in four sections: end-plate design, bolt design, and finite element analysis of end plate moment connection. In addition, a separate section is designated to review the numerical and experimental studies conducted on the behavior of the T-Stubs. To the author knowledge no studies have been conducted on the effect of the bolt pattern configuration on overall connection performance. Therefore, no literature was found to support the idea that was the driving force of this research. In this literature review, the author attempts to gather the general information that was implemented in this research.

2.2 End-Plate Design

Much researches has been conducted since the early 1950s to develop a refined design procedure for both flush and extended end-plate connections. The earlier design methods were based on the static forces and simplified assumptions were made to consider the prying action in the connection. These methods in general resulted in a thick end-plate and large diameter bolts. Many of the recent studies are based on the yield line theory, the finite element method, and the finite element method together with regression analysis to develop equations suitable for design use.

Early experimental studies were done on bolted rigid connections by Douty and McGuire [2] (1963). They investigated the increase in bolt tensile forces caused by prying effects in the end-plate of eight ASTM A7 W16x36 beams and compared theoretical and experimental results. They reported a significant increase in bolt tension when a thinner end-plate was used. Semi-empirical equations were developed to predict the prying force ratio.

Douty and McGuire [3] (1965) conducted full-scale testing on 27 T-Stubs specimens and seven extended end-plate moment resisting connections. The prying force induced by the tension flange force at the edge of the specimen was studied for both types of connections. Since the extent of the results was not adequate to develop a design procedure for end-plate connection, the bolt forces were assumed to be related to a linear strain model assuming a rigid end-plate, i.e. the prying forces were neglected.

Grundy et al. [24] conducted two experimental tests on the extended end-plate connections. They used two rows of four bolts (eight total) to design an end-plate and bolt system that provides a moment capacity greater than the plastic moment capacity of the beam being connected. They concluded that the end-plate bolted connections are prone to non-ductile failure, whether the end-plate is “thick” or “thin”, and regardless of the available theory used in design. A detailed procedure for the design of the beam to column connection is elaborated in the paper. In this approach, the bolt forces were subjected to a 20 percent increase in the direct force to account for the prying action.

Srouji et al. [9] conducted an experimental study on the two-bolt and four-bolt flush end-plate connections. They noted that the strength yield-line analysis accurately predicts the strength of the end-plate, and the modified Kennedy [5] method can adequately predict the bolt forces for the flush end-plate. Also it was noted that with a few discrepancies, the strength of the end-plates tested by Krishnamurthy [25] can adequately be predicted by using strength yield-line theory.

Morrison et al. [11][12] conducted a series of analytical studies to develop a design method for multiple row extended end-plate and four-bolt extended stiffened end-plate connection. The numerical results of the multiple row, extended end-plate connections were compared against the six beam-to-column experimental testing with the beam depth ranging from 30 in. to 62 in. In addition, four-bolt extended stiffened end-plate connections were tested to verify the numerical results. The beam depths of 16 in., 20 in., and 24 in. were used in this part of the study. The design method developed for the connections consists of finding the thickness of the end-plate based on strength. This thickness is then determined to act as a thick, thin, or intermediate plate depending on the loading situation. The prying force, if present, and consequently the bolt forces are then determined using the method developed by Kennedy and Hafez [6].

Kennedy and Hafez [6] investigated the moment-rotation capacity of eight end-plate connections that are designed to transfer shear. The purpose of this research was to establish an analytical method to predict the behavior of the connection up to, at least, the point where the end rotation causes the bottom flange of the beam to touch the flange of the column. The developed numerical method had good agreement (less than 11 percent error) with experimental data for a practical range of end-plate thicknesses, gage distance between bolt holes, and connection depth.

Aggarwal and Coates [26] conducted tests on fifteen four-bolt extended un-stiffened end-plate moment connections. Eight specimens were tested monotonically while the other seven were subjected to cyclic loading. It was shown that the Australian and British standards design procedure produce conservative end-plate and bolt strength for the test loading. In addition, the results of their research reveal that the margin of safety for the end-plate to beam flange welds dramatically decreased from the static test to the dynamic loading.

Murray [22] presented an overview of the past literature and design methods for both flush and extended end-plate configuration, including exterior columns limit state. This design procedure also includes the design method for eight-tension-bolt, stiffened moment end-plates that are capable of resisting the full moment capacity of most available hot-rolled beam shapes. Design procedures, based on analytical and experimental research in the United State were presented in AISC/ASD design manual [27].

Murray [28] presented an overview of the design procedure for the four-bolt un-stiffened, four-bolt wide un-stiffened and eight-bolt extended stiffened end-plate moment connection. The end-plate design procedures were based on the work of Krishnamurthy [25], Ghassemieh et al. [29], and Murray and Kukreti [30].

Ghobareh et al. [31][32] studied the performance of a series of experimental tests on the end-plate connections under cyclic loading. They concluded that properly designed, detailed and fabricated extended end-plate connections can be considered suitable for moment resisting frames in areas of high seismic intensity. In addition, they did not recommend the use of an un-stiffened column at the connection in the high seismic zone regions.

Tsai and Popov [33] performed three tests on large-size beams with end-plate moment connections to column flanges under severe cyclic loading. They concluded that the end-plate extended stiffener and stronger bolts can significantly improve the behavior of the end-plate connections under large cyclic loading. The extended end-plate moment connections can be designed properly to achieve the full plastic moment capacity of the beam when it is subjected to cyclic loading. They also pointed out that the effect of prying force is reduced significantly by the use of an end-plate extended (rib) stiffener.

Chasten et al. [34] conducted seven tests on large extended unstiffened end-plate connection with eight bolts placed in two rows across the end-plate at the tension flange (four bolts wide). In this study, the end-plate connections were designed to resist 50-70% of the beam plastic moment capacity. Both snug and fully tensioned bolts were used in the testing. At least one connection failed by bolt fracture, weld fracture, or plate shear fraction. The experimental results led to concerns for bolt prying forces and end-plate shear forces. Finite element analysis was used to predict the bolt forces and to predict the magnitude and location of the prying forces. In the model, the column flange was assumed to be a rigid surface, and there were no stiffeners between the column flanges. Their report does not address the moment-rotation behavior of the tested connections. The analytical results were compared with experimentally measured forces and reasonable agreement was found. In addition, simple design rules that complement the existing procedures are presented.

Graham [35] reviewed existing design methods and recommended a limit-state design method for the design of rigid beam-to-unstiffened column extended end-plate connections.

Borgsmiller [13] and Adey et al. [15] concluded extensive experimental investigations on 15 cyclically loaded extended end-plate connections to evaluate the significance of certain design parameters. The results of this study conclude that the medium-size beam connections are more ductile than larger beam connections, and the use of relaxed bolt configurations improves the energy dissipation as well as the connection ductility. In addition, these authors proposed that the application of the end-plate stiffener (rib) increased the connection flexural strength, yielding rotation, as well as energy dissipation capacity.

Yorgun et al. [36] performed two full-scale tests to investigate the effect of gaps between the end-plate of the column and the flange of the column when the extended end-plate connection was subjected

to cyclic loading. It was concluded that an end-plate connection with a gap provided by placing an I-Shaped element showed better performance than the standard connection.

Broderick and Thomson [37] compared the performance of eight beam-to-column with flush end-plate under monotonic and cyclic loading conditions, with the design employed by Eurocode [7]. The comparison showed the mode of failure was usually predicted accurately, but a tendency to overestimate joint stiffness and underestimate joint moment capacity.

Sumner and Murray [38] performed six multiple row extended end-plate connection tests to investigate the validity of the current design procedure for gravity, wind and low seismic loading. In addition, the tests investigated the effects of standard and large inner pitch distances and the connections utilized both A325 and 490 bolts. Good correlation between experimental and analytical results was observed.

Sumner and Murray [39] investigated extended end-plate connections with four high strength bolts per row instead of the traditional two-bolts per row. The eight-bolt extended, four bolts wide and three rows extended, and four-bolt wide end-plate moment connections were investigated. Seven end-plate connection tests were performed and a modified design procedure, similar to the procedure presented by Borgsmiller [13] was proposed. It was concluded that the modified design procedure conservatively predicts the strength of the two connections configuration.

Murray and Shoemaker [8] presented a guideline for the design and analysis of the flush and extended and-plate moment connections. The guide included provisions for the design of four flush and five extended end-plate connection configurations. The design provisions are limited to connections subjected to gravity, wind and low-seismic forces; moderate and high seismic applications are not included. A unified design procedure, based on the simplified methods presented by Borgsmiller [13] was employed. It is based on yield line analysis for the determination of the end-plate thickness and the modified Kennedy [5] method for determination of the bolt forces. A stiffness criterion for flush end-plate moment connections was also included in this procedure.

Sumner [40] investigated the performance of eleven cyclically loaded extended end-plate bolted connection. The experimental results demonstrate that a properly designed and detailed extended end-

plate moment connection can be use in seismic force resisting moment frames. He suggested a strong column, strong connection and weak beam design philosophy should be utilized. He presented a unified method for the design of eight extended end-plate moment connection configuration subjected to cyclic/seismic loading. The design procedure used yield line theory to predict the end-plate and column flange strength. The bolt forces are determined using the simplified method developed by Brogsmiller [13]. Results of ninety end-plate moment connection tests used to evaluate the unified design method. Good correlation with the experimental results was obtained using the unified design method.

Shi et al. [41][42] studied eight full-scale structural steel beam-to-column end-plate moment connection under earthquake loading in order to investigate the influences on the connection moment capacity, rotational stiffness, rotational capacity and hysteretic curves. He concluded the end-plate connection extended on both sides can improved the strength, joint rotational stiffness, ductility and energy dissipation capacity required for use in seismic force moment resisting frames. The results indicate that the energy dissipation capacity of the connections with flush end-plate degrades significantly due to the pinching phenomena in the hysteretic loop. These connections are not recommended to use in seismic steel frames.

2.3 Bolt Design

There has been a great deal of research conducted on the behavior of the bolts utilizes within steel moment resisting bolted connections. When bolted T-stubs or end-plate connections are subjected to tension, prying forces develop, resulting in an increase of the bolt force beyond the magnitude that might be expected from the applied external tension. Since the force increase within the bolt due to the prying action might be considerable, this important issue needs to be address accordingly in the design procedures. Investigating the prying force and predicting the possible prying forces induce within the end-plate was the primary focus of many of the past studies. Prying force is a function of end-plate and column flange thickness, as well as the bolt diameter. Many researchers proposed the method to predict the point of action of the prying force. The majority of the bolt-force prediction methods were developed using an analogy between the end-plate connection and an equivalent T-Stubs in tension.

Douty and McGuire [2][3] conducted and early studies on the performance of the T-Stubs to evaluate the force increase in the high strength bolts because of prying action. In this study, they only considered the cases with two rows of bolts in the T-Stubs flanges, not the four rows.

Kato and McGuire [43] investigated the performance of the high strength bolted T-Stub flange to column connections up to the point of failure. The effect of the flange thickness, and the bolt diameter on the performance of the connection was evaluated. The focus of their study was on the behavior of the bolts that yields before the separation of the connected parts and the interrelation between the strength of the bolt and the flange plate. They developed a design method to evaluate the prying force in the connection. The results of the proposed designed method showed a good agreement with the test results.

Agerskov [44][45] proposed an approximate theory to calculate the resulting bolt forces due to prying. They consider the effect of spacing between the two rows of bolts, in addition to the normal forces in the bolt due to bending, and shear stresses induced in the bolt during loading. These parameters have been neglected in previous proposed analytical methods [3][43][4]. In the proposed method of analysis, the shear stresses were taken into account by introducing the Von Mises' yield criterion. Fisher and Struik [46] introduced a comprehensive review of the previous cited design methods in their design guide.

Fleischman et al. [47] studied the effect of partially (snug-tight) and fully pre-tensioned bolts on the performance of the top-and-seat-angle and extended end-plate connections. They concluded that the snug-tight connection for multiple bolt rows behaved similar at moderate loads, and ultimate strength was the same for either cases. Snug –tight connections actually behaved stiffer during the course of reversal loading.

Ghobarah et al. [31] investigated the performance of five cyclically loaded four-bolt extended end-plate connections, and ascertained the effect of bolt pre-tensioning force on the overall performance of the connection. Their results show a significant degradation of the bolt pre-tensioning force with repeated load cycle. To ensure that the bolts do not fail and do not lose their pre-tensioning forces significantly

during moderate earthquake excitation, they recommended that the bolts be designed to sustain a force corresponding to 1.3 times a plastic moment capacity, M_p, of the beam.

Bahaari and Sherbourn [48] studied the end-plate and column flange interaction by altering the bolt positioning. They concluded an alternative to the two rows, eight-bolt connection, and they suggested a hybrid configuration which one four-bolt row is located above the top flange, and two rows of two-bolt are under the beam flange.

Murray et al. [49] performed eleven experimental tests representing six different connection configurations. The main focus of their study was to investigate the behavior of extended end-plate moment connections with snug-tight bolts subjected to cyclic wind loading. The analytical predictions had a good agreement with an experimental result. It was concluded that the end-plate moment connection with snug-tight bolts slightly reduces the stiffness when compared with the fully pre-tensioned end-plate connections.

2.4 Finite Element Analysis Of End-Plate Moment Connections

Finite element investigations on the behavior of the steel bolted connections are started as early as 1976. The majority of the early studies were focused on the correlation of the results from the 2-D models with actual 3D specimen. Computation capability, time dependency of old computers in addition to the substantially high cost of creating and running the 3-D model was the main reason that early research was conducted in 2-D model. With the advancement of the computer technology, very sophisticated 3-D models are capable of being run without a substantial penalty in computation time or cost. Nevertheless, in spite of all these difficulties and complexities, a large number of advanced finite element studies have been conducted on the extended end-plate connection to estimate the stiffness, strength, and ductility of the connection for a large variety of connection geometry.

Krishnamurty et al. [50][51][52] was a pioneer to develop a finite element method for the analysis of end-plate connections. This study was greatly limited by the technology of the time. An exhaustive analytical study of four-bolt, un-stiffened, extended end-plates, in addition to a series of intensive experimental investigation, leads to the development of the design procedure presented in the 3rd

edition of AISC steel design manual [53]. They utilized a 2-D constant strain triangle element and a 3-D eight-node brick element to determine adequate correlation between the results. The finite element models were analyzed under bolt pre-tension, half service load, and full service load. The results from the 2-D model were used to find the correlation between the 3-D models and to predict the overall behavior of the connection. According to this research, because of the time involved in programming, as well as computational time it was not feasible to conduct a 3-D analysis on the end-plate connections using the technology of the time.

To obtain a reasonable results from the finite element analysis, Krishnamurty et al. [50][51][52] made several simplifying assumptions. The 3-D models were developed based on a constant strain triangle and eight-node subparametric brick elements. Bolt heads were omitted, and the bolts were assumed to have a rectangular shank with similar cross section as rounded bolts. No “contact element” algorithm was used to model the contacts or constrains. The bolts were assumed to be in tension and the effective square area of the compression flange was assumed to be compressed against the column flange. Some seven correlation-factors between the 2-D and 3-D models were introduced using the results obtained from the numerical analysis.

Kukreti et al. [54] presented the results of their investigation conducted on the behavior of the stiffened moment end-plate with two rows of bolts inside and outside the beam tension flange. Finite element was used to model the tension flange. For simplification, the tension flange and the end-pate at the tension flange was assumed to have similar behavior as a stiffened T-Stub (tee-hanger). They also conducted a parametric analysis to develop an empirical equation to predict the behavior of the end-plate connections.

Kukreti et al. [55] utilized the finite element modeling to develop an equation to characterize the behavior of the extended stiffened end-plate connections that can be used for predicting the heavier of the beams used in steel building frames. The regression analysis performed on the data collected leads to an equation which predicts the end-plate strength, end-plate stiffness, and the bolt forces. The design methodology was outlined using the prediction equations. The results obtained from the prediction equation were validated by the experimental results.

Gebbeken et al.[56] used the finite element analysis to study the behavior of the four-bolt un-stiffened end-plate connection. He suggested that the quality of the results from the 2-D models and 3-D models depends on the finite element model chosen. The 3-D finite element models were recommended for general modeling while the 2-D models were advised only for special investigation. This Study also emphasized on modeling the non-linear material behavior and the contact between the end-plate and column flange or the adjacent end-plate.

Bahari and Sherbourne [57] developed an analytical method to predict the moment-rotation relationship for the steel bolted end-plate connection, using a commercially available finite element code ANSYS. The effect of the end-plate and column flange thickness on the moment-rotation relationship was studied using various design approaches. They recommended the 3-D finite element models to be used for general analytical formulation to predict the behavior of the bolted connections.

Bahaari and Sherbourne [58][59] extend their investigation on the performance of the bolted connections to the four bolt stiffened and un-stiffened extended end-plate connected to an un-stiffened column flange using high strength pre-stressed bolts. They emphasized on the significance of end-plate and column flange interaction.

Bahaari and Sherbourne (1999)[48] studied the behavior of the three large capacity, extended end-plate connection with snug-tight and fully pretension bolts using finite element 3D model. They concluded that the behavior of these connections can be satisfactorily simulated using plate, bricks and truss elements. The results compared well with experimental data in terms of both strength and stiffness.

Maggi et al. [60] performed a parametric study on the behavior of the extended end-plate bolted connection and the interaction between the bolts and the end-plate using finite element tools. They considered material non-linearity, geometrical discontinuity, and large displacements. The comparisons between numerical and experimental data showed a satisfactory agreement; also, the models successfully predicted the failure associated with the connection.

2.5 T-Stubs Design

Due to the similarity between the behaviors of the T-Stubs and the tension flange of the end-plate bolted connection, many past researchers used T-Stubs to simplify the behavior of the connection.

Figure 2-1 illustrated the tension flange of the connection which is compared by T-Stubs. The prying forces developed in the connection bolt due to the deformation of the flange were the main focus of majority of these studies. In this section, quick review over the studies conducted on the behavior of the T-Stubs is presented.

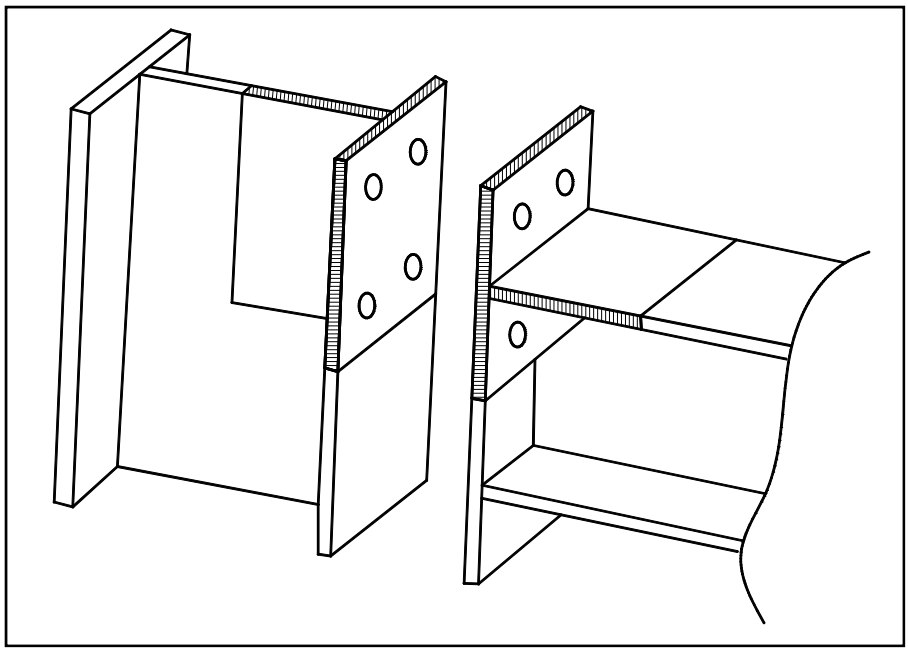

Figure 2-1 End-Plate Connection Decomposition According To Eurocode-3 [7]

The distribution of the bolt forces and the resulting responses of the bolt group in the T-Stubs connection is a function of many parameters including bolt diameter and pretension, the gage and pitch, number of bolt rows flexibility of the detailed element, contact surface condition, etc. Fleischman et al. [61] discussed the effect of the tension, bending, and prying forces in the overall behavior of the T-Stub connection. Although the bolts are implemented to transfer the tensile force through the elements in the structures, this tensile force may be amplified by prying action. However, the bending of the bolt induces an additional bending force to the bolt shank, which is increasing the tensile force in the bolt. In beam-to-column connection, a lateral component of shear is also act on the bolt. However, in many cases, the shear in the connection is assumed to be carried by friction in the compression portion of the connection. The summery of their findings is presented in this section,

Tension, when components of the connection are bolted, the bolt pretension will affect the overall response to external tensile loading; however, the ultimate strength is unaffected [62]. Until the external

load overcomes the pretension forces, the assemblage of the bolts and connected plies acts as one, resulting in an overall increase in stiffness. After pretension is overcome (plate separation), the bolt forces are simply equal to the external load, regardless of the original magnitude of the bolt pretension[61].

Prying Action, bolt groups in tension are susceptible to prying action. The applied tensile load *T* must be transfer through the connection, two rows of bolts presented in Figure 2-2. The bending moment developed in the connection flange must be resisted by the point load $Q=f(M_b)$ at the edge of the flange. This force developed due the bending of the flange is called prying force. If can be seen from the Figure 2-2, that the bolt forces in the connection will include force component from both the applied load and additional forces due to prying action. For *n* bolts acting to resist the applied load *T*, the following is obtained:

$$\sum_{i=1}^{n} B = T + Q$$

Since the prying forces are a function of M_b, their magnitude depends on an interaction of the flexural rigidity of the flange and the connector's pretension as discussed in the following paragraphs[61].

Flexural Rigidity – If the T-Stubs flange is significantly rigid, the bending deformation and consequently resulting flange moments will be minimal. However, if the flange is relatively flexible, the bending deformation of the flange will induce significantly large moment, thus the value of M_b will be trivial.

Pretension – In the pretension connections, the flange separation occurs when the applied force overcome the pretension forces. Since the development of M_b requires the flange separation, the value of M_b will remain insignificant while the flange remains un-deformed. Therefore, Assuming the T-Stubs flange is flexible; lowering the pretension will result in prying action at a lower value of the external load. Test results show that initial clamping force does not influence the magnitude of prying forces at the ultimate loading condition [62].

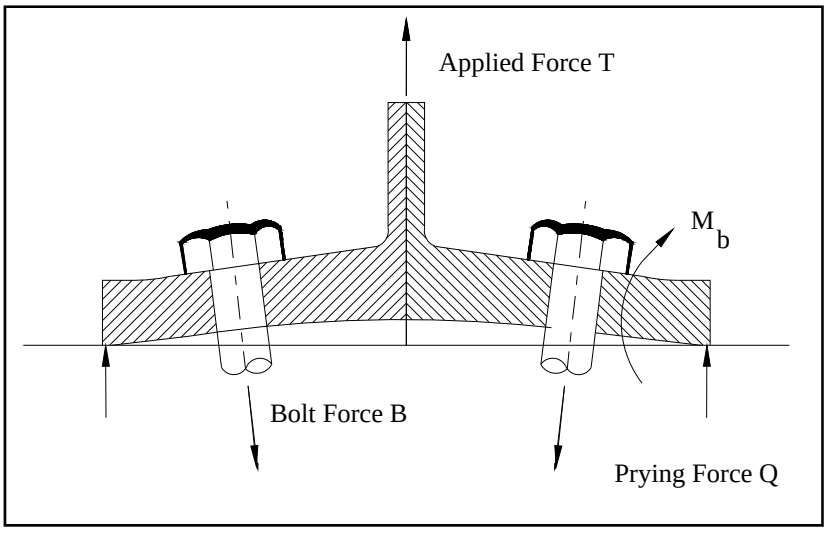

Figure 2-2 Free-Body Diagram Of A T-Stubs Connection.

Bending – The bending relation will be developed for the cases of a tension angle within a connection; a similar relationship can be derived for other connections. Figure 2-3 shows the free-body diagram of the angle member. As the applied force *T* works to overcome the contact forces at the bolt line, a moment initiates which tends to increase the contact force (prying) at the far side of the bolt line and decreases contact on the near side. The bolt pretension gradually overcome as the contact surface recedes. In addition to the tensile force *T* and the prying force *Q*, moment M_a from the angle curvature and a proportion (α) of the total connection shear V_{conn} exist. The details of these analyses are presented in research paper by Fleischman et al. [61].

Nair et al. [4] conducted 27 full-scale experimental tests to investigate the effect of the prying forces on the overall behavior of the T-Stubs. The four-bolted T-Stubs were tested under both static and fatigue loading. The static testing was involved loading the specimens to the failure and monitoring the applied force versus the elongation of the bolts. While the dynamic loading involved loading the specimens cyclically through up to 3-million cycles or fracture. They concluded that the capacity of the connection could reduce substantially due to the prying forces and fatigue strength of the bolts in the connections. Using the geometry and the thickness of the T-Stubs, they introduced and empirical relation between the flange forces and prying forces, which was recommended to used while designing the connection bolt forces.

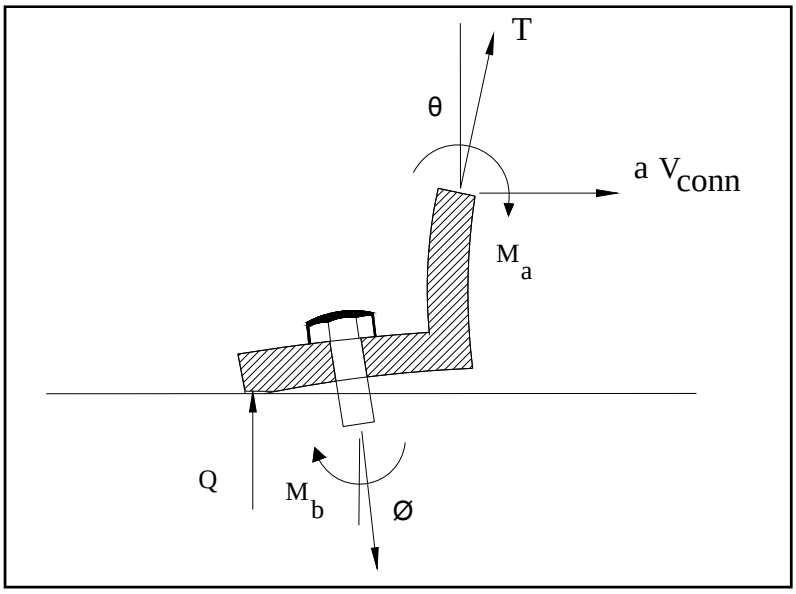

Figure 2-3 Tension Angle Free-Body Diagram

Kennedy et al. [5][6]was a pioneer to develop a unified method for predicting the additional bolt forces due to the prying action in the T-Stubs connection. They assumed that a T-Stubs or a bolted end-plate goes through three stages of behavior as it is shown in Figure 1-1. The summery of these three stages of behavior is presented in Chapter-1. They presented equations which identifies the thin and thick plate limits based on the geometric properties of the connection, yield stress value of the plate, and applied flange force. Ultimately, the prying forces in the bolts are calculated for each type of plate behavior determined.

The European structure code [7] introduces the philosophy of the component-based design methods. In this procedure, the connection is divided into several basic T-stubs and the behavior of an isolated T-stub is related to its actual position in the connection. Figure 2-1 illustrates the decomposition of the end-plate into basic T-stubs.

Piluso and Rizzano [63] studied the behavior of the 28 T-stubs with two high strength bolts. The scope of their research was to extend the design method so called component approach presented in Eurocode 3 [7] and develop a numerical method for modeling and analyzing the T-stubs under monotonic and cyclic loading. The displacement control load was applied to the specimens with both constant and increasing amplitude. Using the experimental results, semi-analytical models for predicting the cyclic behavior of the T-stubs were developed starting from the geometrical and mechanical

properties of the specimens. The degree of accuracy of the proposed models showed a good agreement with the experimental results in terms of energy dissipation capacity.

CHAPTER 3

EXPERIMENTAL INVESTIGATION

3.1 Introduction

The details of the experimental study conducted in this research are presented in this chapter. A description of the test specimens, test setup, testing procedure, and test results are provided for each specimen. The initial investigation was conducted on three T-Stub connections to study the effect of the bolt pattern configuration on the ductility, bolt force distribution, and overall performance of the connection. The results obtained from T-Stubs test specimens were also used for FEM models verification. Initially, the T-Stub with different bolt pattern configuration were loaded monotonically. The details of this experimental study are elaborated in detail in Chapter-4. Also, the details of five experimental studies conducted by Abolmaali et al. [64][65] are presented in this chapter. The experimental results obtained from these experimental investigations are used to verify the results obtained from the numerical analysis presented in Chapter-4.

3.2 T-Stub Testing Program

Due to similarity between the behavior of the T-Stubs under tension, and tension flange of the extended end-plate connection, numerical T-Stub models were used in the first phase of this study to create reasonable benchmarks for further investigations. Several bolt pattern configurations were proposed and finite element models were developed and analyzed with various bolt size, plate thickness, pitch sizes (P_f), and gage lengths (g). The scope of this phase of the study was to study the potential performance enhancement of the T-Stubs due to various bolt pattern configuration. The compression of the numerical results obtained from finite element analysis revealed that the circular bolt had the most impact on the tensile capacity of the T-Stubs connections.

3.2.1 Bolt Pattern Configuration

Several bolt patterns were selected and a testing matrix was developed. The bolt pattern was selected from regular geometric shapes to simplify the design as well as fabrication process. Figure 3-1 illustrated the regular geometric shapes that were proposed and tested in this study.

`

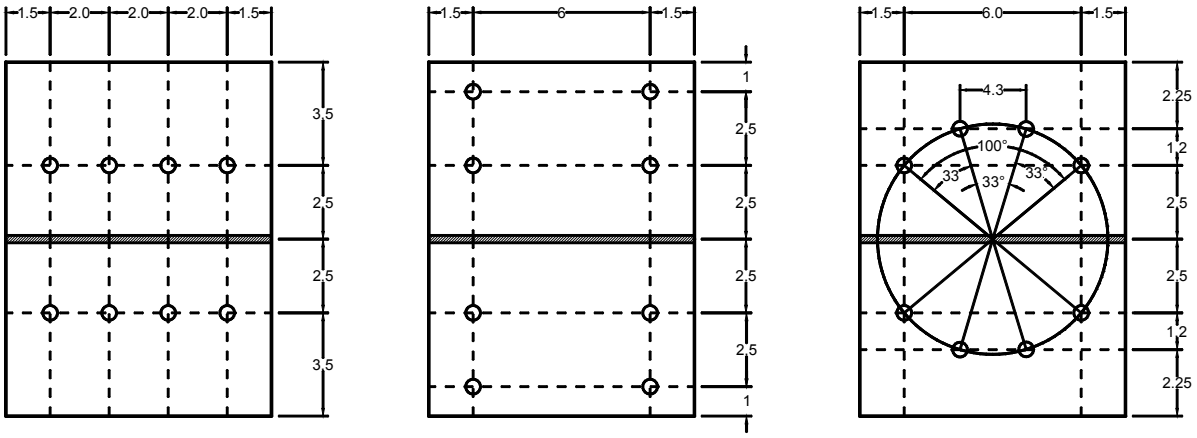

(a) (b) (c)

Figure 3-1 Bolt Pattern Configurations, (a) Line, (b) Square, And (c) Circular.
(All Units Are In Inches)

Figure 3-1(a) shows the bolt pattern configuration in which all the bolts are located at the same distance with respect to the stem. The designation name "*Line*" is assigned to this bolt configuration. Figure 3-1(b) shows the connection with the traditional square bolt pattern. This pattern has been widely used in the industry with various gage, and pitch spacing. Figure 3-1(c) illustrates the proposed circular bolt pattern. The designated name for each test is tabulated in Table 3-1.

Table 3-1 T-Stubs Test Matrix

Specimen ID	Bolt Diameter	Bolt Pattern
TS-L	½ "	*Line*
TS-S		*Square*
TS-C		*Circular*

To validate the numerical results obtained from the finite element analysis, three models with different bolt pattern configurations were selected and tested experimentally, and the results were

compared with results collected from finite element models. The detail and results of this study are elaborated in detail in the following sections.

3.2.2 Test Specimen

The experimental investigation was conducted on three T-Stubs as part of this study. The W12x72 hot-rolled beam was cut into half through the mid-height of the web and flanges were positioned against each other to form the T-Stubs. Grade 50 beam and ½ in. diameter ASTM A325 bolts with 125-ksi ultimate strength were used during this investigation. The tensile force was applied monotonically and the specimens were loaded to their ultimate failure.

To fabricate the specimens, the exact positions of the bolt-holes were marked by pointer and the bolt-holes were drilled using the drill-press. The contact surface was washed by soap and brushed by electric wire-brush to meet the Class-C surface specified in AISC design manual [1]. Finally, the specimens were coated by white-wash to simplify the visual observation of the yield patterns. Figure 3-3, and

Figure 3-4 illustrate the final product of the TS-L, TS-S, and TS-C specimens prior to testing, respectively.

Figure 3-2 Final Product Of The TS-L Specimen

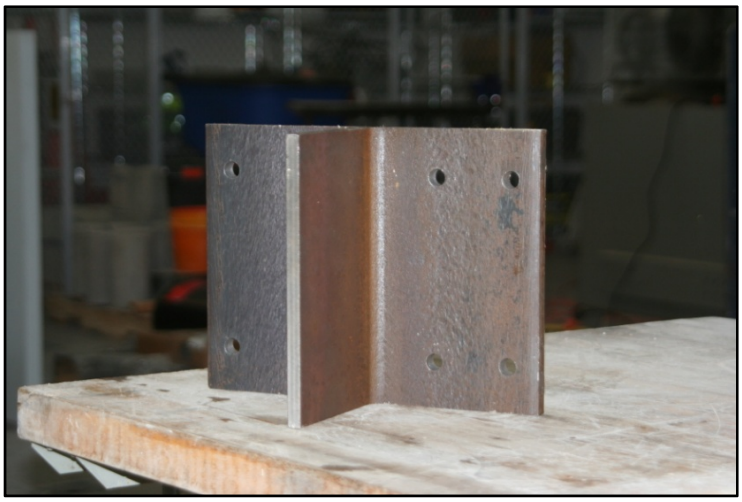

Figure 3-3 Final Product Of The TS-S Specimen

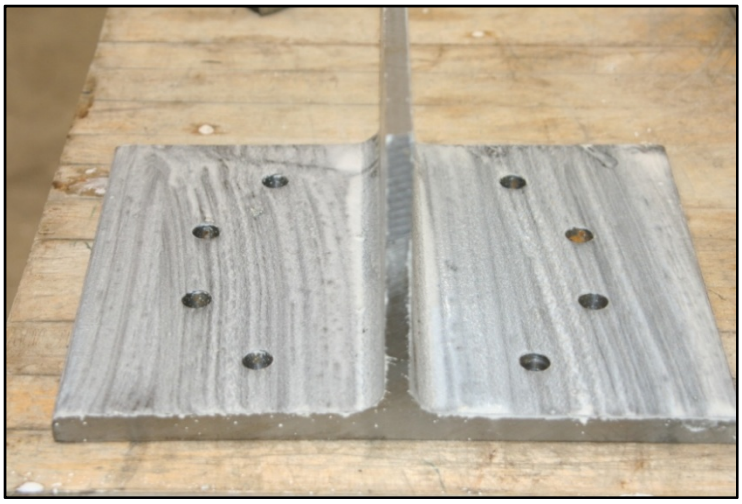

Figure 3-4 Final Product Of The TS-C Specimen

3.2.3 Bolt Instrumentation

Two types of strain gauges were used in this research; Omega SG/LY11 and MLT-BL2. Two Omega SG/LY11 were installed on the opposite face of the bolt shank to measure the variation of the strain due to bending of the bolt. To minimize the strain variation, the bolts were placed such that the strain gauges were perpendicular to the stem. The results obtained from this type of strain gauge were satisfactory for a *TS-L* and *TS-S* specimens when they were compared with finite element results. This is due to single curvature of the flange when a line or square bolt pattern was used. Figure 3-5 shows the deformed shape of the T-Stubs with a line bolt pattern. The arrow presented in this figure shows the single curvature of the flange during loading.

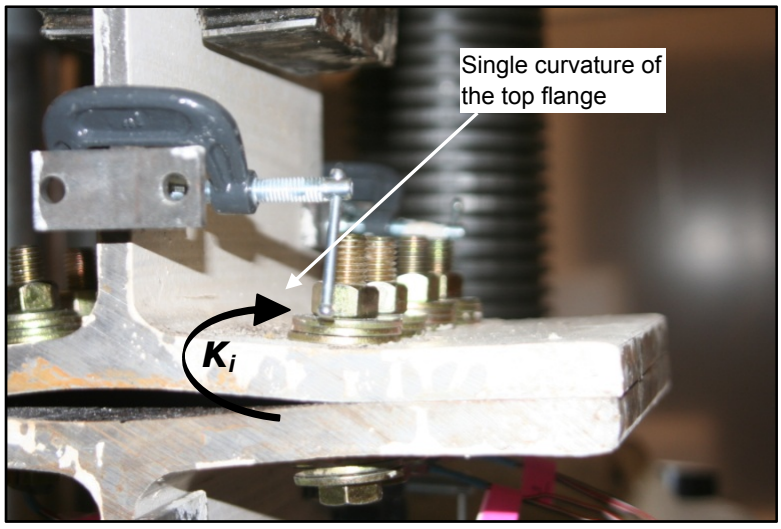

Figure 3-5 Deformed Shape Of The T-Stubs With Line Bolt Pattern (K_i Is Curvature In Direction i)

The deformed shape of the T-Stub with the circular bolt pattern is presented in Figure 3-6. This figure shows that the flange of the specimen with a circular bolt pattern deforms in two orthogonal directions, which causes the double curvature of the flange. This double curvature of the flange causes the bolt to bend in two directions. The phenomenon is in contrast with the bolts of the T-Stubs in the line and square bolt patterns, where the bolts only bend in one direction. It was mentioned that in order to improve the accuracy of the strain gauge results, the bolts instrumented with Omega SG/LY11 were placed in such a ways to measure the minimum and maximum strain at the surface of the bolt shank. However, due to double curvature of bolts in the T-Stubs with a circular bolt pattern, placing the bolt in a position that precisely measures the minimum and maximum strain of the bolt-shank seemed to be impossible. Therefore, the results obtained from the Omega SG/LY11 for T-Stubs with circular bolt pattern were not adequate.

To overcome this situation, the MLT-BL2 strain gauge was used to measure the bolt stress in the TS-C specimen. This strain gauge is placed precisely at the center of the bolt shank (See Figure 3-10). It is noteworthy to mention that the elongation at the center line of the bolt measured by MLT-BL2 is measuring the true elongation of the bolt-shank independent of strain variation due to the plate curvature and is a better representation of the axial force in the bolt. The installation procedure of the strain gauges used in this research is elaborated in detail in the following sections.

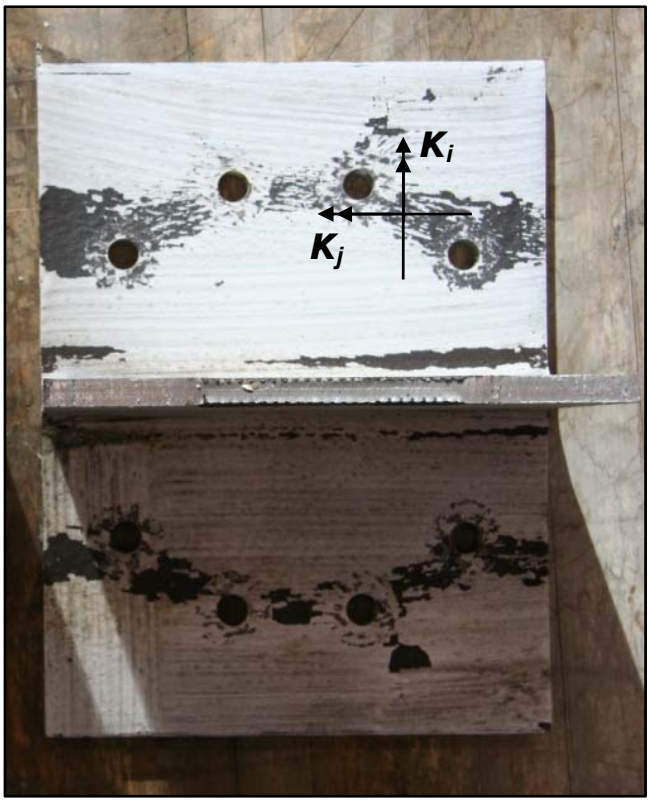

Figure 3-6 Deformed Shape Of The T-Stubs With Circulare Bolt Pattern (κ_i, And κ_j Are Curvature In Direction ***i***, And ***j*** Respectively)

3.2.3.1 Flat Strain-Gauge, Omega SG/LY11

To measure the forces in the bolts, the strain gauges were installed onto the bolt shank. Since the bolt shank is in contact with the bolt hole during the test, special provisions were made to protect the strain gauges and their wiring during testing. These provisions are elaborated in details in the following section. In addition, the strain gauges are highly sensitive to the curvature of the surface, which becomes more critical as bolts with relatively small diameters are used, because of the higher curvature of the bolt shank. Several methods were proposed and tested to find the most effective way to instrument the bolts with the strain gauge. The following steps are proposed by the author to improve the accuracy of the results while decreasing the chance of the damaging the strain gauges.

3.2.3.1.1 Wiring Precautions

The strain gauge wires were protected from any physical damage and/or static arching between the wires and the bolt-hole. This task is achieved by creating a fine longitudinal cut in the bolt

head. Two varnished copper wires were soldered carefully to the strain gauge terminals and the wires were passed through the cut created in the bolt head, see Figure 3-7(a)

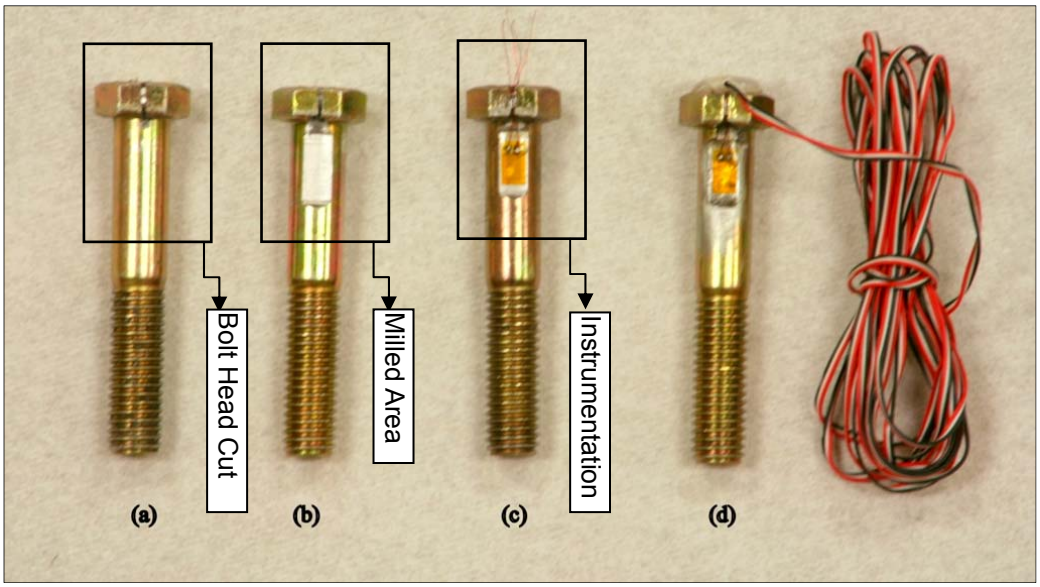

Figure 3-7 The Instrumented Bolt

3.2.3.1.2 Surface Preparation

A proper implementation of the strain gauge is a tedious exercise. The strain gauges should be carefully installed, wired, and should be tested with the upmost precaution. This task becomes more critical when the strain gauge is installed in the 1/16 in. space between the bolt shank and bolt-hole. To reduce the possibility of damage to the strain gauges, the bolt shank was milled flat to create a sufficient surface for installation of the strain gauges. This effort ensured a flat surface for the installation of the strain gauges as well as minimizing the chance of the strain gauge and its wiring to be in contact with the bolt-hole. Figure 3-7(b) shows a modified bolt with a flat surface.

The Vishay [66] strain gauge installation handout is followed carefully during the strain gauge installation procedure. Figure 3-7(c) illustrates the instrumented bolt with strain gauge and wiring.

3.2.3.1.3 Coating And Protection

The wires were glued to the specimen to minimize the risk of damage. A thin layer of *Vishay coating-A* epoxy was used to cover the strain gauge and its terminals. This elastic epoxy protects the

strain gauge from potential damage during installation and testing, as well as reducing the risk of static arching. Figure 3-7(d) shows the instrumented bolt with wiring and coating.

The strain variation on the opposite surfaces of the bolt due to the curvature reduces the accuracy of the data obtained from the strain gauges. To eliminate this error, two strain gauges were installed symmetrically on opposite sides of the bolt shank. The alignment of the two strain gauges was arrenged to be perpendicular to the T-Stub stems or beam flanges during tightening of the bolts. Thus, the maximum and minimum strain at the body of the bolt-shank was measured. The reported axial force in the bolt was calculated by taking the average of the two strain gauges' measured values.

3.2.3.1.4 Verification

In spite of precautions taken during the installation of the strain gauges, some of the strain gauges failed during preliminary testing. These failures were due to inadequate bond between the strain gauge and the bolt and/or damage to the wiring during the installation or the testing procedure. To ensure adequate bond between the strain gauge and the bolt, each bolt was tested individually using the test setup shown in

Figure 3-8 and Figure 3-9. Each bolt was pulled monotonically up to 50% of its yield strength, and the forces obtained from the strain gauge were compared with the reading from the load cell. This procedure ensures the proper bond between the strain gauge and the bolt, and verifies the functionality of the strain gauges during the test.

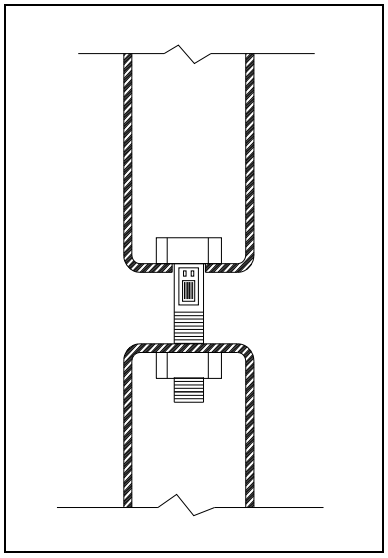

Figure 3-8 Schematic Drawing Of The Test Setup Used To Verify The Functionality Of The Strain Gauges

Figure 3-9 Test Setup Used To Verify The Functionality Of The Strain Gauges.

3.2.3.2 Cylindrical Strain-Gauge, MLT-BL2

The specific and installation procedure of the MLT-BL2 is discussed in this section.

3.2.3.2.1 Bolt Preparation

This strain gauge is designed to be installed at the center of the bolt shank, as is shown in Figure 3-10. A high-speed milling machine with high strength carbon drill bit was used to drill the bolt-hole required for installation of the MLT-BL2 strain gauge. The in. (3 mm) bolt-hole with the depth of 1.25 in. (32 mm) was drilled at the center of the bolt shank through the bolt-head. Cooling agent was used during drilling to prevent the damage to the drill bit. The specimens were washed in soapy water using an ultrasound shaker to remove any grease or contamination in the bolt-hole.

3.2.3.2.2 Strain-Gauge Installation

The installation procedure of MLT-BL2 stain gauge was easy, fast, and reliable. The 1/16 in. (2 mm) wide strain gauge was purchased prewired and coated. Vishay AE-10 adhesive was prepared carefully following the recommended procedure provided in the instruction manual. The adhesive was injected in the bolt-hole using a syringe. The bolt-hole was over filled to remove any possible air bubble. Then, the strain gauge was inserted carefully through the hole and secured for 15 min. The specimens were kept at room temperature for 24 hours to allow for proper curing.

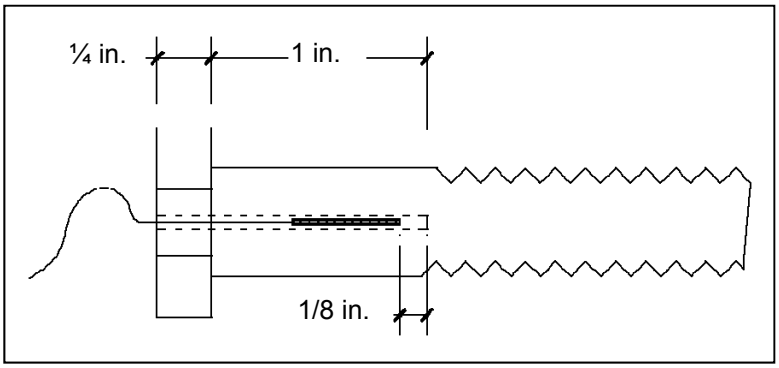

Figure 3-10 Schematic Of The MLT-BL2 Strain Gauge

3.2.3.2.3 Verification

To ensure a proper installation, each bolt was pulled monotonically to 50% of its yield stress and the bolt force obtained from the strain gauge was compared with the load recorded by the load cell. This procedure was similar to the bolt force validation presented for Omega SG/LY11 strain gauge.

3.2.4 Test Setup

The 400K compression/tension testing machine was used to apply a monotonic load to the T-Stubs. All bolts were pretensioned to 70% of the ultimate strength (proof load) [1]. It is a common practice to relate the bolt-force due to pre-tensioning, F_i, to a quantity that is easier to measure such as the applied torque, *T*. The required torque was calculated to be $100lb.ft$ for a ½ in. diameter bolt. The detail calculations to find a required applied torque are provided in Appendix-A. To verify the pre-tensioning force in the bolts, the applied bolt force by wrench was compared by the data collected from the strain gauges. The results revealed that the agreement between these two data set was satisfactory.

The specimens were covered with whitewash to permit better observation of the yielding within the specimen. Two LVDT with $\pm 0.25\ in.$ stroke were installed on both sides of the specimen aligned with the stem of the T-Stubs to measure the separation of the flanges during the test.

Figure 3-11, Figure 3-12, and Figure 3-13 show the locations of the LVDTs and the T-Stubs test setup used for specimens TS-L, TS-S and TS-C, respectively. The instruments were calibrated prior to the testing and connected to *Vishay* data acquisition system. The data was recorded using a PC-based data acquisition system with the rate of two data points per second (2 Hz).

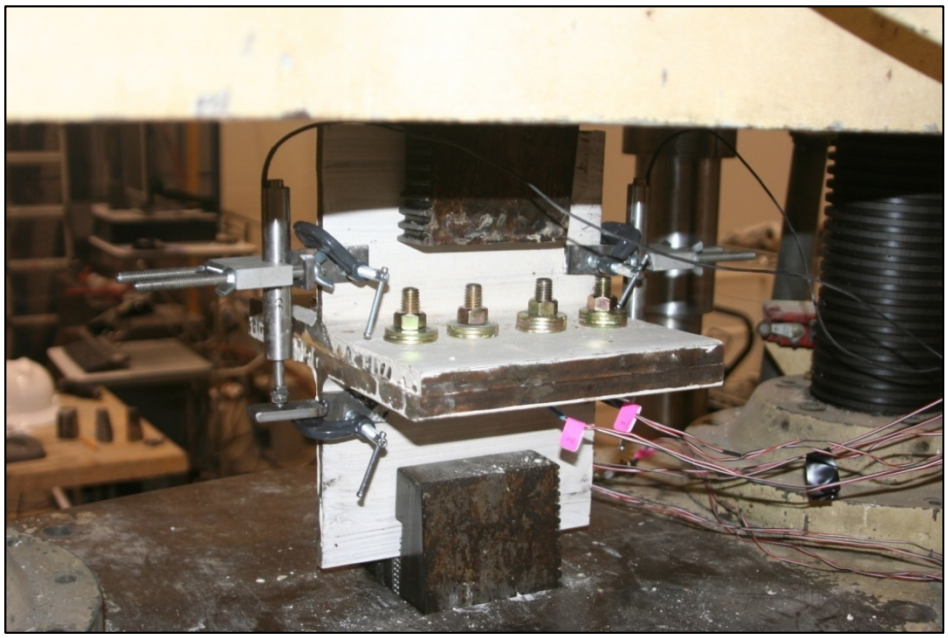

Figure 3-11 T-Stubs Test Setup With Line Bolt Pattern

Figure 3-12 T-Stubs Test Setup With Square Bolt Pattern

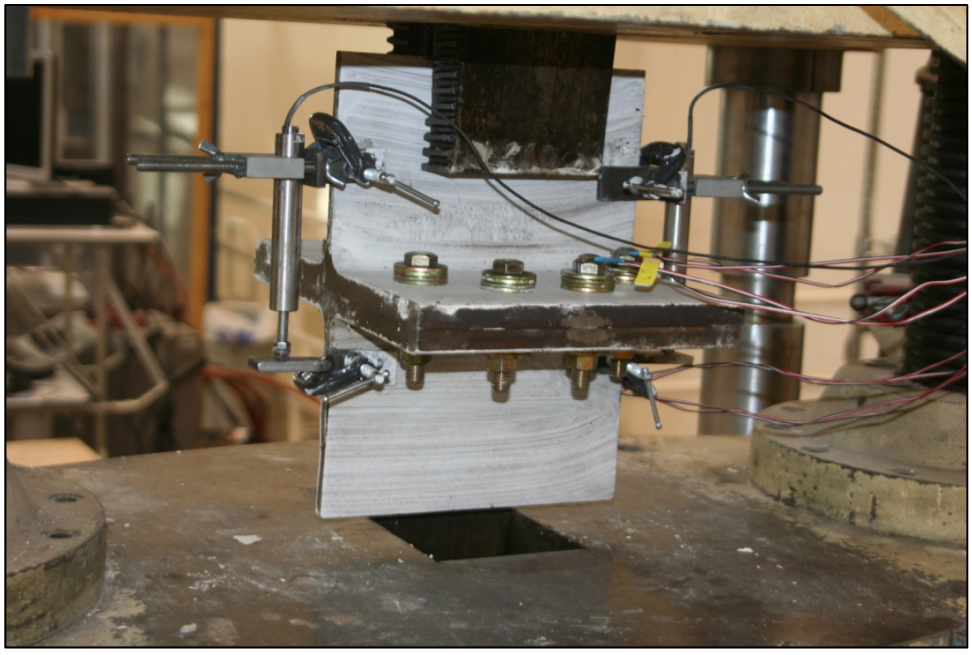

Figure 3-13 T-Stubs Test Setup With Circular Bolt Pattern

3.2.5 Testing Procedure

The same test procedure was used for all three T-Stub specimens. The stems of the T-Stubs were placed and secured by the jaws of the compression/tension machine before the bolts were assembled.

The instrumented bolts were connected to the data acquisition system and the shunt of the *Wetson-Bridge* was zeroed and calibrated while the bolts were in a relaxed state. The LVDTs and load cell were connected to the data acquisition system and all the readings were set to zero. The bolts were then tightened, using a calibrated torque-wrench to the proof load specified by the LRFD design manual [1]. A cross-pattern tightening sequence was used. The bolts were pre-tensioned in two steps to prevent the damage to the bolts and the instrumentation. The two pieces of the T-Stubs were pulled together in the first step of bolt tightening, and the proof load was applied on the second step.

A monotonic load was applied on to the specimen at approximately $5\text{kips}/\text{min}$. The specimens were loaded to failure. The observations were documented and the photographs were taken while the test was in progress.

3.2.6 Test Results

As mentioned before, the main scope of this experimental study was to investigate the behavior of the T-Stubs under various bolt pattern configuration. In addition, the data collected in this section was used to validate the results of the numerical models in Chapter-4.

Table 3-2 shows the summary of the test results. The tensile yield forces presented in this table are determined by using a bi-linear curve fit of the T-Stubs data. In addition, the flange separations versus the applied force for three specimens are presented and compared in Figure 3-14. The first line represents the initial stiffness of the T-Stubs and the second line represents the post-yield stiffness. The intersection of the two lines is considered as the yielding tensile force; thus, the corresponding flange separation is recorded as flange separation at yield (Δ_y). The ultimate tensile force (P_u) is the maximum tensile force resisted by the specimen, and the maximum flange separation was reported as Δ_u in this table.

Table 3-2 The Results Summary Of The Monotonic Testing On T-Stubs

Specimen	Yielding Tensile Force Py kips (kN)	Plate Separation Δ_y in (mm)	Ultimate Tensile Force P_u Kips (kN)	Plate separation Δ_u in (mm)
TS-L	110 (490)	0.035 (0.89)	132 (590)	0.316 (8.02)
TS-S	87 (390)	0.05 (1.27)	92 (410)	0.141 (3.58)
TS-C	95 (420)	0.04 (1.01)	101 (450)	0.154 (3.91)

Figure 3-14 shows the applied force versus the flange separation for the T-Stubs with three various bolt pattern configuration. Close examination of the results presented in this figure and Table 3-2 reveals that the specimen with *Line* bolt pattern configuration has the best performance between the tested specimens. This specimen has higher yielding point and almost two times the ductility of the specimens with a circular or a square bolt pattern configuration. These results show that the specimen with a circular bolt pattern has higher yielding (9% increase) and ultimate capacity (10% increase), but similar ductility when compared with the specimen with a square bolt pattern. It is noteworthy to mention that the connection with the line bolt pattern has the best performance; however fabrication of the connection with line bolt pattern is not always feasible due to geometric constrains in placing more than two bolts per row especially for connections which require larger bolt diameters. The AISC design guide [8] introduces various design procedure for connection with both line and square bolt pattern with different geometric characteristics.

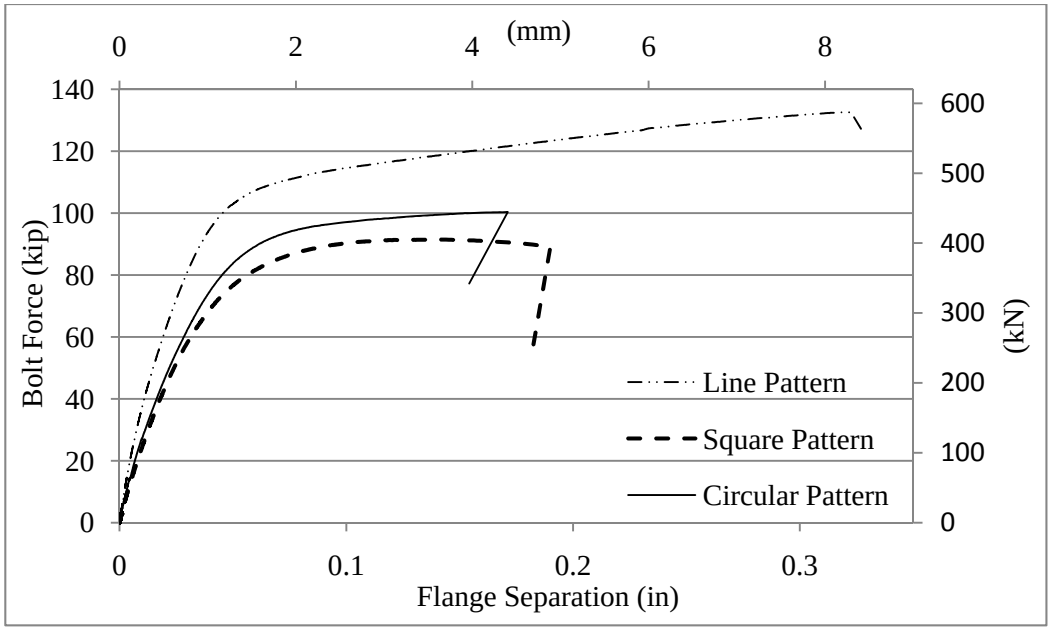

Figure 3-14 Applied Force Vs. Flange Separation Response Of The T-Stubs With Various Bolt Pattern Configuration

3.3 Beam-Column Connection

For further verification of the numerical results obtained from the finite element models on the extended end-plate connections with circular and square bolt patterns presented in Chapter-5, it was important to validate the numerical results against the results obtained from full-scale connection experimental testing. To achieve this goal, the experimental results of five bolted beam-column connections with various connection details were selected and the corresponding finite element models were developed. These results were used to validate the numerical results in Chapter-4.

In this chapter, a summary of the experimental work of ***a***) extended end-plate connection, ***b***) top-and-seat angle connection, ***c***) welded/bolted double web angle, ***d***) bolded/bolted double web angle connections, and ***e***) flush end-plate connections conducted by Abolmaali et al. [64][65] is presented. The results of these studies are used in Chapter-4 to validate the results obtained from the numerical analysis.

3.3.1 Extended End-Plate Connection

A W16x67 hot-rolled beam with length of 70 in. (180 cm) was connected to a W14x159 column with length of 80 in. (200 cm). The size of the end-pate was 10½ x 22½ in.^{2} (27 x 57 cm^2) with the thickness

of ½ in. (13 mm). The geometric parameters describing the configuration of the extended end-plate connection are shown in Figure 3-15. The definition of the geometric parameters used in Figure 3-15 and the corresponding geometric parameter of each variable are tabulated in Table 3-3.

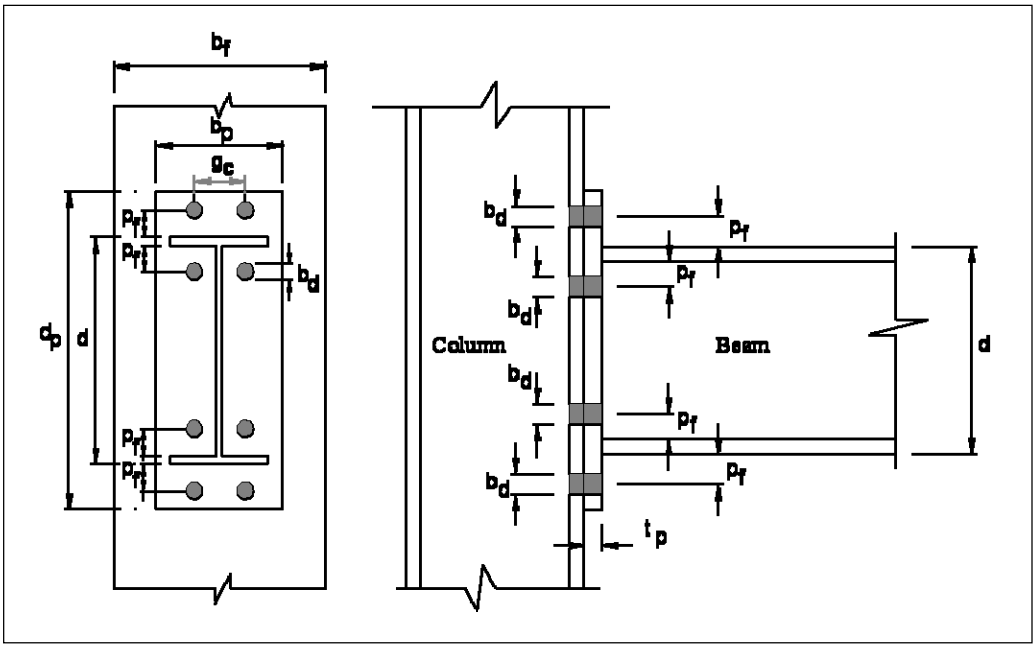

Figure 3-15 Configuration Of Extended End-Plate Test Specimen

Table 3-3 Definitions And Geometric Values Of The Extended End-Plate Specimen

Variable	Definition	Value in. (mm)
b_p	End-plate width	10 (254)
d_p	End-plate depth	22 ½ (572)
t_p	End-plate thickness	½ (13)
b_d	Bolt diameter	7/8 (22)
p_f	Flange pitch, the distance from top of the flange to first row of bolts	1 3/8 (35)
g_c	Column bolt gauge	4½ (114)
d	Beam depth	16 5/16 (414)
b_f	Column flange width	15 7/8 (401)

3.3.2 Top-And-Seat Connection

A W16x67 hot-rolled beam with length of 70 in. (180 cm) was connected to a W14x159 column with length of 80 in. (200 cm). Two 10.2 in. (260 mm) L6x6x¾ hot-rolled angles were used to connect the beam to the column. As shown, one leg of angle is connected to the beam flange by two rows of bolts, and the other leg is connected to the column flange by one row of bolts. The geometric parameters

describing the configuration of the top-and-seat connection are shown in Figure 3-16. The definition of the geometric parameters used in Figure 3-16 and the corresponding geometric values of each parameter are tabulated in Table 3-4.

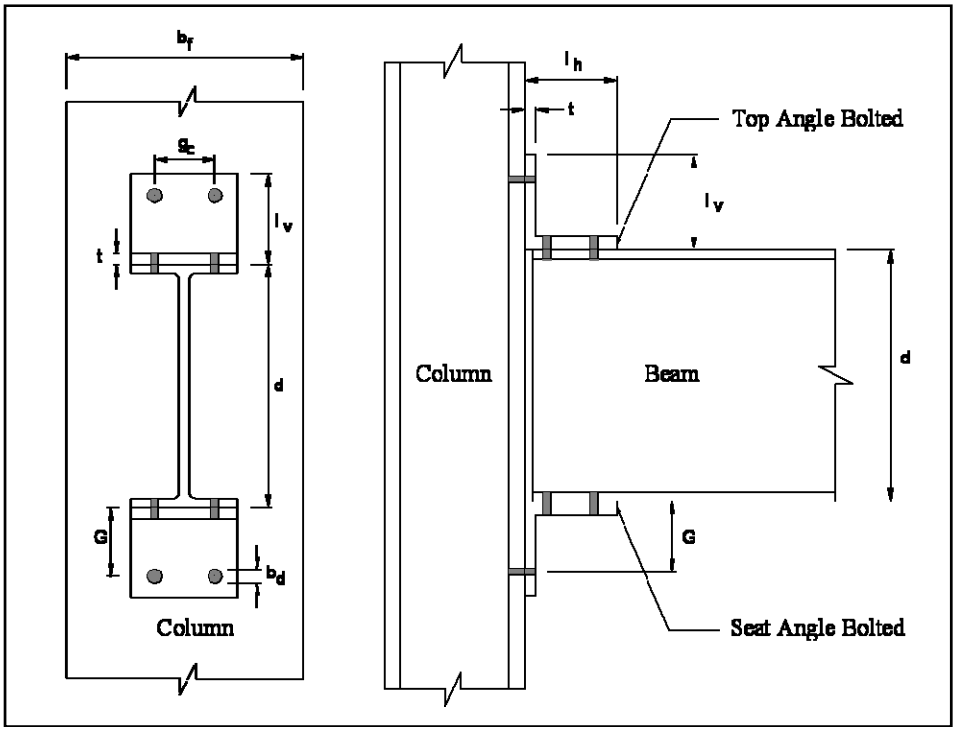

Figure 3-16 Configuration Of Extended End-Plate Test Specimen

Table 3-4 Definitions And Geometric Values Of The Top-and-Seat Specimen

Variable	Definition	Value in. (mm)
l_h	Length of horizontal angle legs	6 (152)
l_v	Length of vertical angle leg	6 (152)
t	Angle thickness	¾ (19)
b_d	Bolt diameter	7/8 (22)
G	Distance from the heel of the angle to the column bolt row	2½ (64)
g_c	Column bolt gauge	4 (102)
d	Beam depth	16 (406)
b_f	Column flange width	15 7/8 (401)

3.3.3 Bolted/Bolted Double Web Angle Connection

A W24x104 hot-rolled beam with length of 70 in. (180 cm) was connected to a W14x159 column with length of 80 in. (200 cm). Two 15 in. (380 mm) L5x5x¾ hot-rolled angles were used to connect the beam to the column. As shown, one leg of angle is connected to the beam web using five ¾ in. high strength

bolts, and the other leg is connected to the column flange by one row of bolts. The geometric Parameters describing the configuration of the bolted/bolted double web angle connection are shown in Figure 3-17. The definition of the geometric parameters used in this figure and the corresponding geometric values of each parameter are tabulated in Table 3-5.

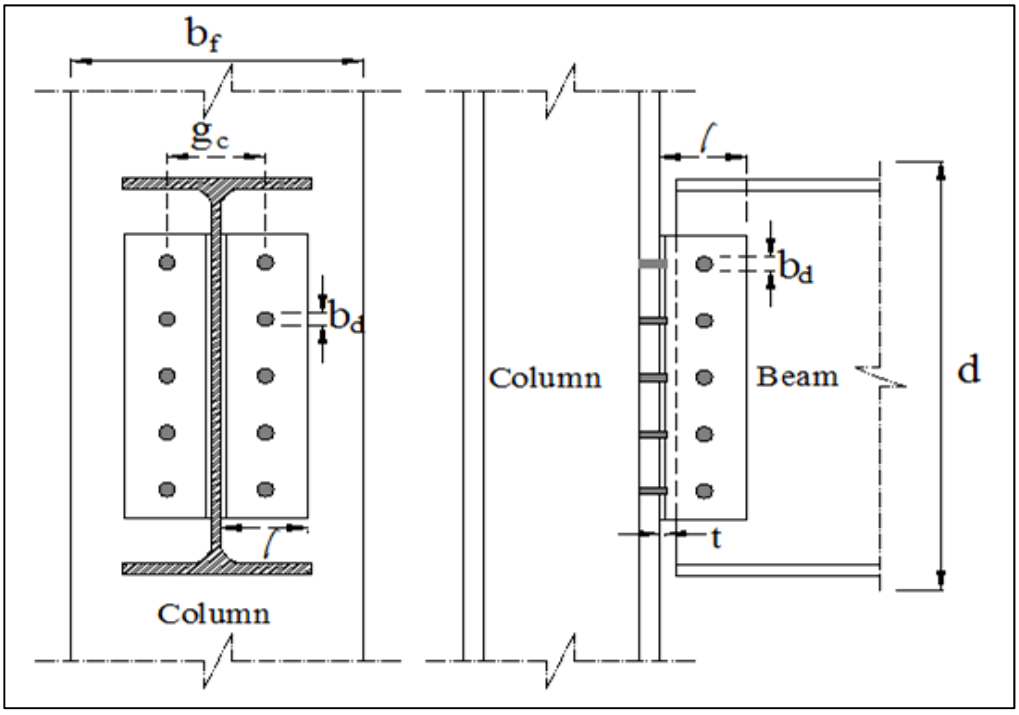

Figure 3-17 Configuration Of Bolted/Bolted Double Web Angle Connection Test Specimen

Table 3-5 Definitions And Geometric Values Of The Bolted/Bolted Double Web Angle Connection

Variable	Definition	Value in. (mm)
l	Length of horizontal angle legs	5 (127)
t	Angle thickness	¾ (19)
N	Number of Bolts	4 (4)
b_d	Bolt diameter	¾ (19)
g_c	Column bolt gauge	4 ½ (114)
d	Beam depth	24 (610)

3.3.4 Welded/Bolted Double Web Angle Connection

A W24x104 hot-rolled beam with length of 70 in. (180 cm) was connected to a W14x159 column with length of 80 in (200 cm). Two 15 in. (380 mm) L5x5x¾ hot-rolled angles were used to connect the beam to the column. As shown, one leg of angle is welded to the beam web, and the other leg is bolted to the

column flange by one row of ¾ in. diameter high strength A-325 bolts. The geometric parameters describing the configuration of the welded/bolted double web angle connections are shown in

Figure 3-18. The definition of the geometric parameters used in this figure and the corresponding geometric values of each parameter are tabulated in Table 3-6.

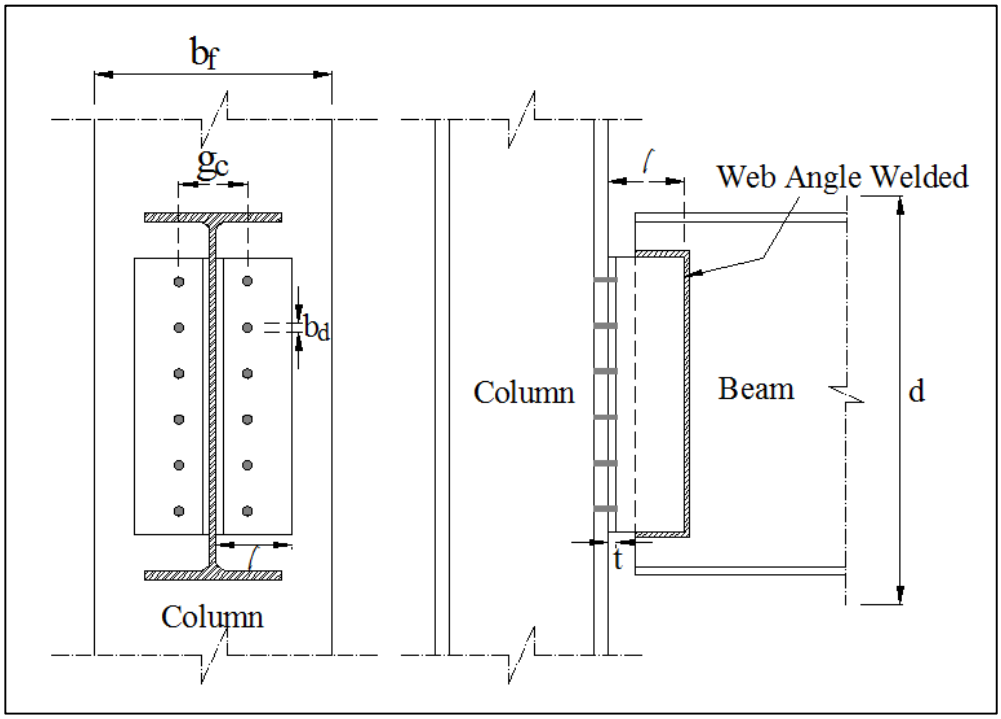

Figure 3-18 Configuration Of Welded/Bolted Double Web Angle Connection Test Specimen

Table 3-6 Definitions And Geometric Values Of The Welded/Bolted Double Web Angle Connection

Variable	Definition	Value in. (mm)
l	Length of horizontal angle legs	5 (127)
t	Angle thickness	¾ (19)
b_d	Bolt diameter	¾ (19)
N	Number of Bolts	4 (4)
g_c	Column bolt gauge	5 ½ (140)
d	Beam depth	24 (610)

3.3.5 Flush End-Plate Connection

A W18x46 hot-rolled beam with length of 70 in. (180 cm) was connected to a W14x159 column with length of 80 in. (200 cm). The size of the end-pate was 6 x 18 in^2 (15.2 x 45.7 cm^2) with the thickness of 3/8 in. (9.5 mm). The geometric parameters describing the configuration of the flush end-plate

connection are shown in Figure 3-19. The definition of the geometric parameter used in this figure and the corresponding geometric parameter of each variable are tabulated in Table 3-7.

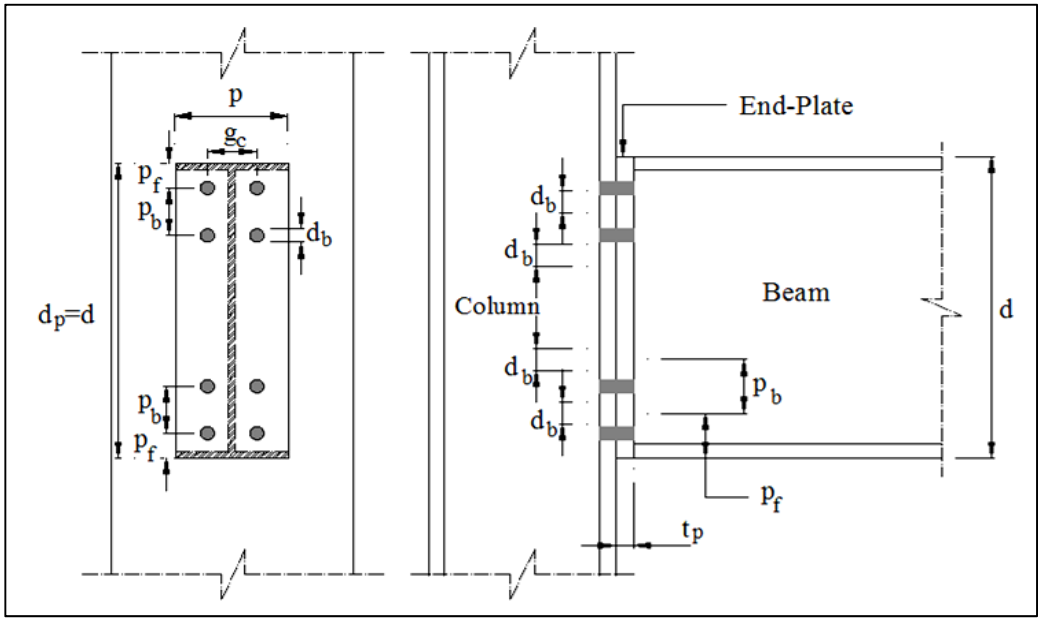

Figure 3-19 Configuration Of Flush End-Plate Test Specimen

Table 3-7 Definitions And Geometric Values Of The Flush End-Plate Specimen

Variable	Definition	Value in (mm)
b_p	End-plate width	6 (152)
d_p	End-plate depth	18 (457)
t_p	End-plate thickness	3/8 (22)
b_d	Bolt diameter	¾ (19)
p_f	Flange pitch, the distance from top of the flange to first row of bolts	1 5/8 (41)
p_b	Flange pitch, the distance from top of the flange to first row of bolts	3 (76)
g_c	Column bolt gauge	3 (76)

3.3.6 Experimental Testing

The basic configuration of the test setup used to test the extended end-plate connection and the top-and-seat angle connection is shown in Figure 3-20, which consisted of: (1) an actuator to apply the force; (2) a test beam connected to a test column; and (3) the test reaction frame. The entire reaction frame was bolted to the laboratory floor, and the column of the test specimen was connected to the column of the reaction frame. Lateral braces were provided at the beam end connected to the actuator swivel to

prevent out-of-plane buckling of the test specimen. The basic configuration of the test setup used for both connections is shown in Figure 3-20.

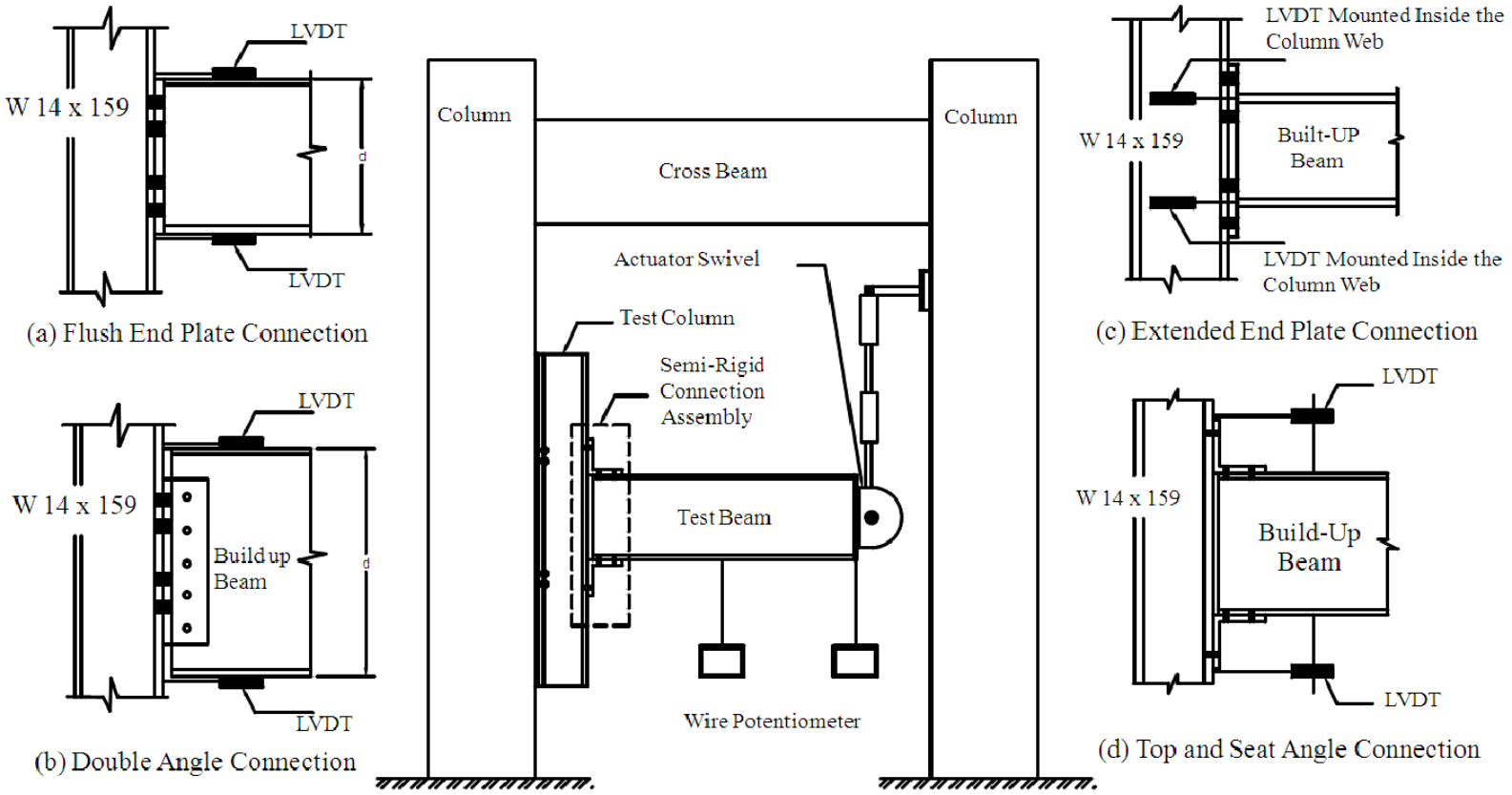

Figure 3-20 Typical Configuration Of The Beam Column Connection Test Setup

Figure 3-20(c) shows the test instrumentation and setup for the extended end-plate connection. The instrumentation consisted of two displacement transducers to measure the relative connection rotation. The displacement transducers were mounted in the column web to reach the centerlines of the top and bottom beam flanges by drilling two holes from the back of the column flange; see Figure 3-20(c). Also, two wire potentiometers were used to measure the displacements at two separate points along the beam span. In addition, a load cell and displacement transducers were installed in the actuator to measure the cyclic load applied to the beam-end and the actuator stroke (displacement), respectively.

Figure 3-20(d) shows the test instrumentation and setup for the top-and-seat angle connection. The displacement transducers were placed directly above and below the outer edge of top-and-seat angle respectively. Two displacement transducers were installed along the length of the beam. Also, similar load cell was used to measure the applied cyclic load to the beam-end.

The relative displacements measured by the two displacement transducers, divided by the vertical distance between their tips, was defined to be the local rotation of the connection. The global rotation of the connection was calculated by dividing the vertical displacement recorded by each wire potentiometer by the distance of the wire potentiometer from the face of the specimen column flange. Hence, the connection rotation at every load level was measured in three independent ways. The moment applied to the connection was calculated by multiplying the force recorded by the actuator load cell times the distance from the center of the actuator to the face of the column.

CHAPTER 4

FINITE ELEMENT MODELING AND VALIDATION

4.1 Introduction

Nonlinear 3-D finite element models were developed to simulate the response of the T-Stubs and beam-column connections under static and cyclic displacement control loading. The results obtained from the numerical analyses were compared with the results collected from the experimental testing to verify the accuracy of the numerical results. The details of finite element modeling are presented in this chapter.

4.2 Finite Element Modeling

In this study, the steel plates were modeled with 8-node linear brick, reduced integration, and hourglass control element (bricks C3D8R). The 6-noded linear triangular prism element (C3D6) was used to model the bolts, bolt head, nuts, and the washers. These elements were proven efficient in many past studies, although the accuracy of the results decreases in case of excessive deformation. Initially, the models were seeded using ½ in (12 mm) spacing, and then the mesh was refined on critical locations to the required size. In the beam-column models, the size of the mesh was gradually increased up to 6 in. (15.2 cm) at the regions with significantly low strain. The option “seed by number” provided in ABAQUS 6-10.1 was used for simplicity and consistency. The details by the sizes and locations of the meshes of the bolts are presented in Table 4-1.

Based on the results of the study conducted by Bursi and Jaspart [19][20] the number of the layers of mesh in the modeling of the steel bolted connection can significantly affect the accuracy of the numerical results. The models were meshed in one, two and three layers and the results were compared with experimental values for convergence requirements. The best results were obtained from the models with an 8-noded reduced integration, as it was recommended by Zienkiewics [67].

Table 4-1 The Mesh Size Distribution In The Bolts

Element	Line Number	Number of Seeds	Schematic
Washer	W1	20	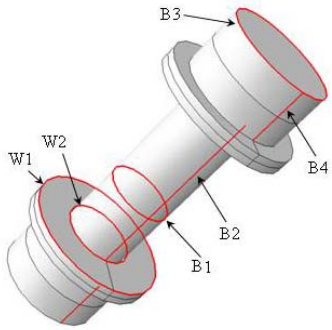
	W2	15	
Bolt	B1	15	
	B2	10	
	B3	15	
	B4	4	

A typical meshed bolt is presented in Figure 4-1. The element type C3D6 was used for both the bolt-head and the bolt-shank. The nuts were modeled similar to the bolt-head while the extended length of the bolt beyond each nut was ignored. The nut and the bolt-head were considered as a single body with bolt shank. The threaded part of the bolt shank was ignored and the bolt shank was replaced with a cylinder with a nominal diameter of the bolt. Washers were placed on both ends of the bolt (nut and bolt-head) to simulate the actual experimental specimen. The length of the bolt was set equal to the actual bolt length for each specimen. The pre-tensioning bolt-force was modeled by applying an initial displacement to two parallel surfaces in the bolt-shank, using bolt-force with adjustments length function of the ABAQUS 6-10.1. The value of the initial displacement was adjusted by trial and error to achieve a sufficient pre-tensioning bolt-force as specified by AISC design manual [53]. The bolts were pre-tensioned in the first step load and the displacement control loads were applied to the specimen during the next steps.

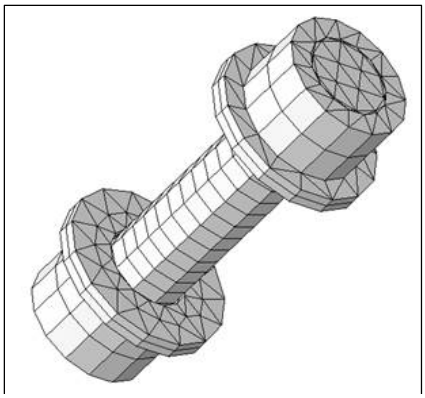

Figure 4-1 A Typical Bolt Mesh

4.3 Material Modeling

The combined hardening plasticity model was used in order to model the material behavior during the cyclic loading. The parameters suggested by Kiamanesh et al. [68] and Ghobadi et al. [69] for combined strain hardening of Grade-50 hot-rolled steel were selected in the analysis algorithm. Isotropic hardening was used to model the material properties of the high strength steel bolts with a material constitutive law as shown in Figure 4-2.

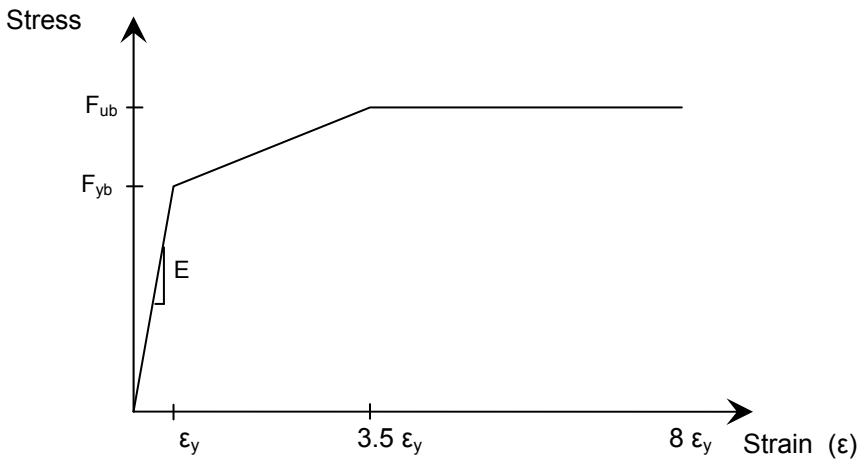

Figure 4-2 Stress-Strain Relationship For High Strength Bolts.

The algorithm used for the combined hardening of the low-carbon material in ABAQUS 6.10-1 [70] is based on the study conducted by Doghri et al. [71], which is capable of performing both kinematic and isotropic hardening. The kinematic hardening parameters “C” and “γ” are defined as the initial hardening

modulus and the rate at which the hardening modulus increases with increasing plastic strain, respectively.

The isotropic hardening behavior of the material is modeled with exponential law. The parameters "Q_∞" and "b" are defined as the maximum increase in the plastic range and the rate at which the maximum size is reached when plastic strain develops, respectively. The values of the combined strain hardening parameters used in this research are tabulated in Table 4-2. A Young's modulus of $E=30\times10^3$ ksi (210 GPa) and a Poisson's ratio of $\upsilon=0.3$ were used to define the elastic response of the material with $R_yF_y=55$ ksi (385 MPa), where R_y is the ratio of the expected yield stress to the specified minimum yield stress F_y [72].

Table 4-2 Material Properties

Parameter	Value
C ksi (MPa)	2030 (14000)
γ	140
Q_∞ ksi (MPa)	261 (1800)
b	0.26

4.4 Contact Modeling

The numerical results are highly sensitive to the contact properties between the components of the model. In the bolted connections, the forces are transferred through friction and due to clamping action between the members caused by pre-tensioning of the bolts.

Small sliding surface-to-surface was considered for all the contacts. The welds were assumed to be rigid and modeled by a tie-contact algorithm. The frictional surfaces accompanied by tangential force were modeled by a tangential-contact algorithm as shown in Figure 4-3(a). The surface contact between the end-plate and column was modeled by frictional contact using penalty stiffness with the penalty value of 0.3. The surfaces with normal force were modeled using the Augmented Lagrangian Formulation (ALF) [70]. The augmented Lagrange approach is used for contact modeling based on monitoring the gaps between pairs of nodes. A constraint is inserted when the gap between two nodes (on opposite surfaces) becomes zero or negative. The tangential contact between the bolt-hole and the bolt shank was considered to be frictionless, see Figure 4-3(b). Also, hard contact was used for the connection between bolt-head/nuts to the end-plate/column flange as it is shown in Figure 4-3(c). It was mentioned before that

the contacts between the bolt and the end-plate and column flange serves as a boundary condition. Excessive elongation of the bolts during the loading reduces the pre-tension force, which consequently reduced the boundary, degree of freedom, to zero. Using the hard contact on the column side of the bolt will assure a constant contact, boundary condition, between the bolts and other element and eliminates the numerical errors.

Master surfaces of the contacts pair represent the surface of column flange, T-stubs flange, bolt-head, bolt-shank, washer. The slave surface is defined as the surface interfacing with the master surface. The master surface in general should have finer mesh. The automated “find contact pair” option of ABAQUS 6-10.1 is used to define the contacts and constrains. This function is a build in commend in ABAQUS software which find all the contact pairs based in the manually defined criteria by the operator and assigns the master/slave surface automatically.

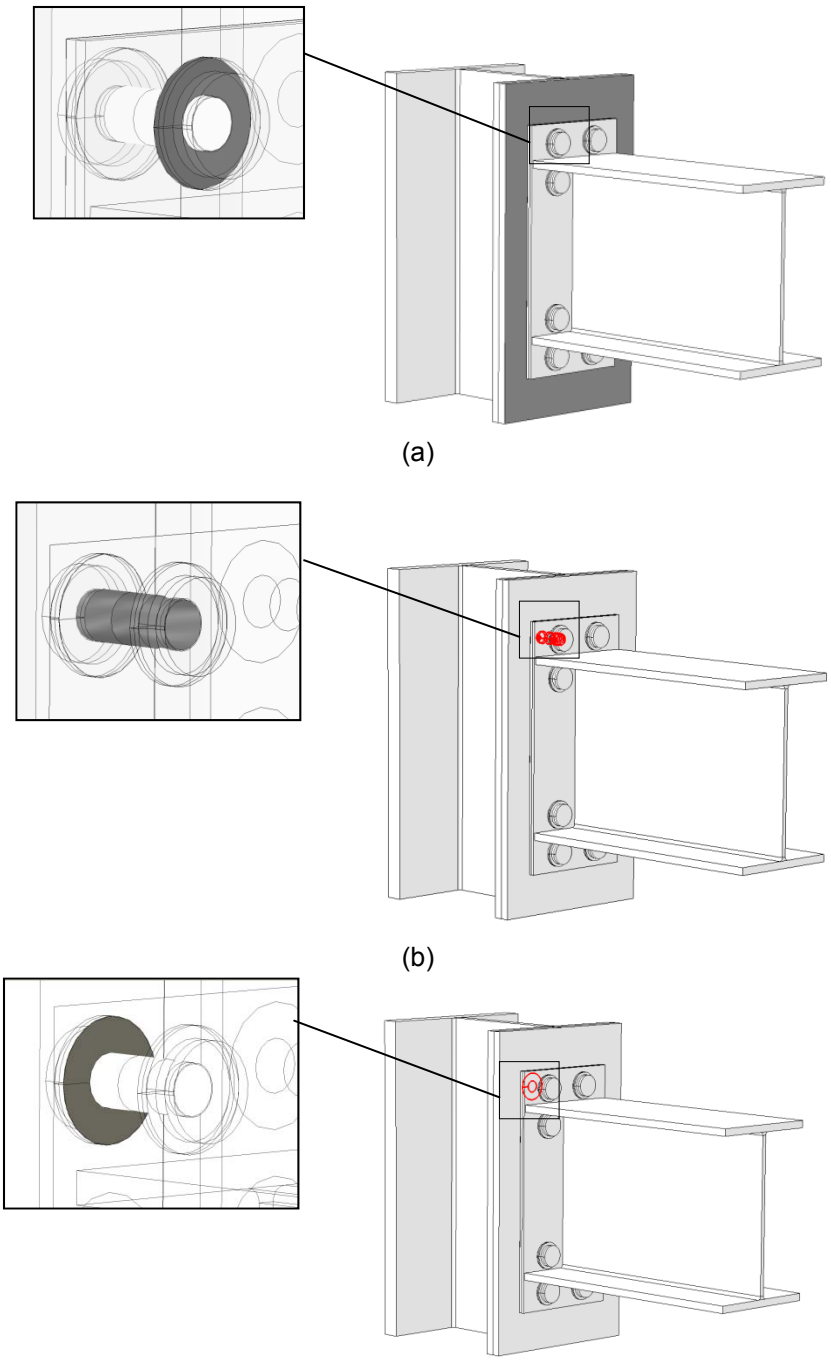

Figure 4-3 Contacts In Typical Extended End-Plate Connection; (a) Friction Contact, Between The End-Plate And Face Of The Column, And Between The Bolt-Head And End-Plate, (b) Frictionless Contact, Between The Bolt-Shank And Bolt-Hole, And (c) Tie Contact, Between The Bolt-Head And Internal Face Of The Column Flange

4.5 Comparison Of Numerical And Experimental Results

4.5.1 T-Stub

The details of the numerical models for the T-Stubs are similar to the specimens explained in Chapter-3. These finite elements models are subjected to displacement control monotonic loading, and the results are compared with those of experimental tests.

4.5.1.1 Specimen TS-L

The finite element model of the TS-L specimen is presented in Figure 4-4. The applied load versus flange separation obtained from the experimental and numerical analysis for the Model TS-L is presented in Figure 4-5. These results show a close agreement between the experimental and numerical results. The finite element model predicts the initial stiffness and the yielding point accurately.

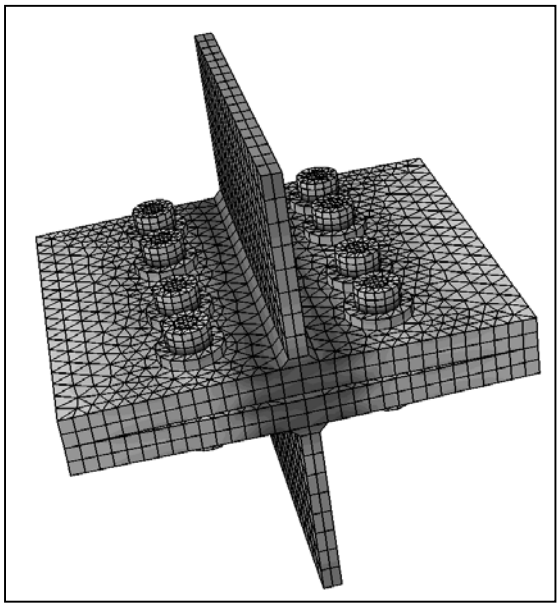

Figure 4-4 Finite Element Model Of TS-L Specimen

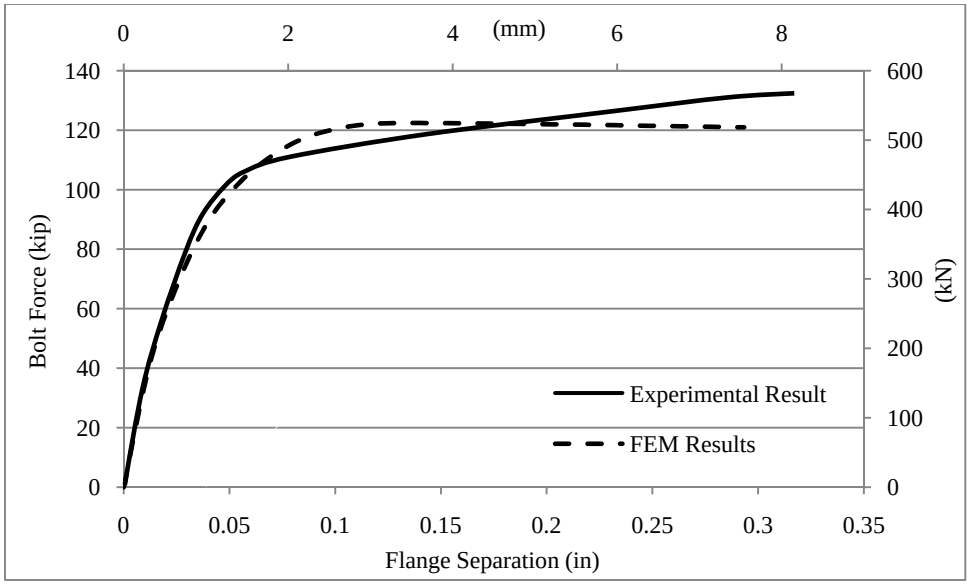

Figure 4-5 Applied Force Versus Flange Separation Response For TS-L Specimen

The bolt force history of the Model TS-L is illustrated in

Figure 4-6. Because of the geometry of the bolt patterns, it was expected that all the bolts exercise a similar level of stress during each loading step. This phenomenon is observed in both experimental and numerical results. Good correlation between the experimental and analytical results is observed.

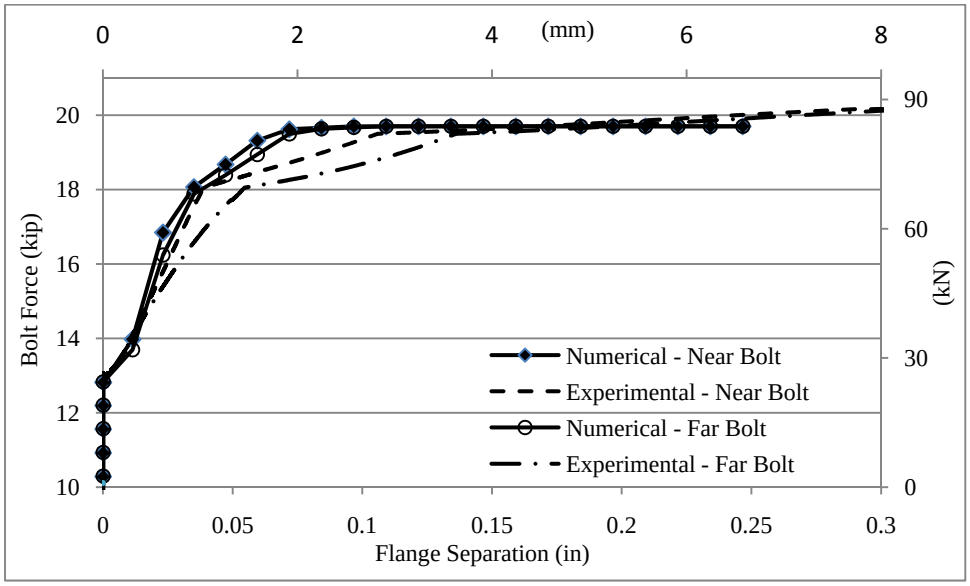

Figure 4-6 Bolt Force History In TS-L Specimen

4.5.1.2 Specimen TS-S

Figure 4-8 shows a deformed TS-S model prior to loading. The flange separation of the T-Stub with square bolt pattern versus applied load for both experimental and analytical models are illustrated in Figure 4-8. The results show a close agreement between the experimental and numerical results.

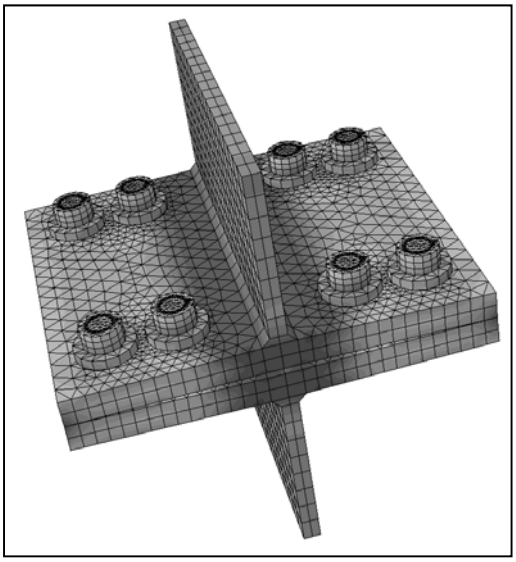

Figure 4-7 Finite Element Model Of TS-S Specimen

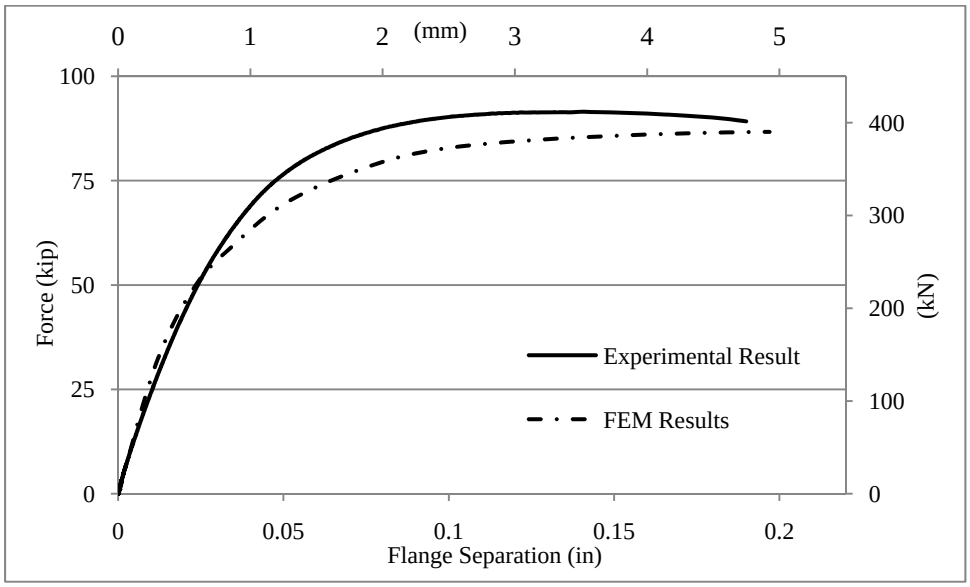

Figure 4-8 Applied Force Versus Flange Separation Response For TS-S Specimen

The bolt force history of the specimen TS-S specimen is illustrated in Figure 4-9. The bolt forces obtained from the numerical analysis has a close agreement with the results obtained from experiment.

It can be seen from the results presented in Figure 4-9 that the near bolts start taking load at a very early stage of loading. However, it can be seen from this figure that the far bolts do not take the load for flange separation less than 0.05 in. (1 mm). It should noted that the bolt force in the near bolts increases in a higher rate than the far bolts.

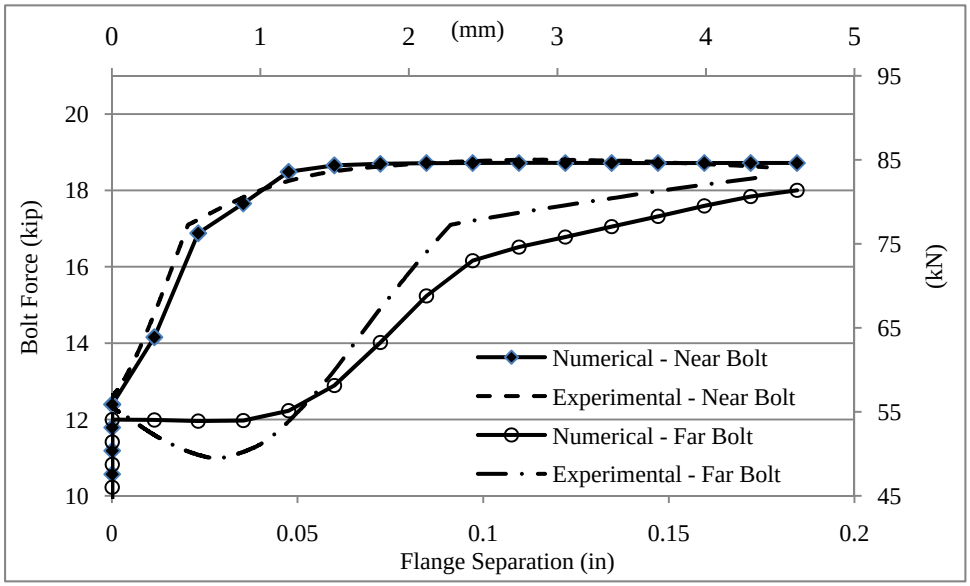

Figure 4-9 Bolt Force History In TS-S Specimen

4.5.1.3 Specimen TS-C

The finite element model of the TS-C specimen is presented in Figure 4-10. Also, the results obtained from the FE model and the experimental study conducted on the T-Stubs with a circular bolt pattern are presented in Figure 4-11. An examination of these results shows a close agreement with the data collection during the testing.

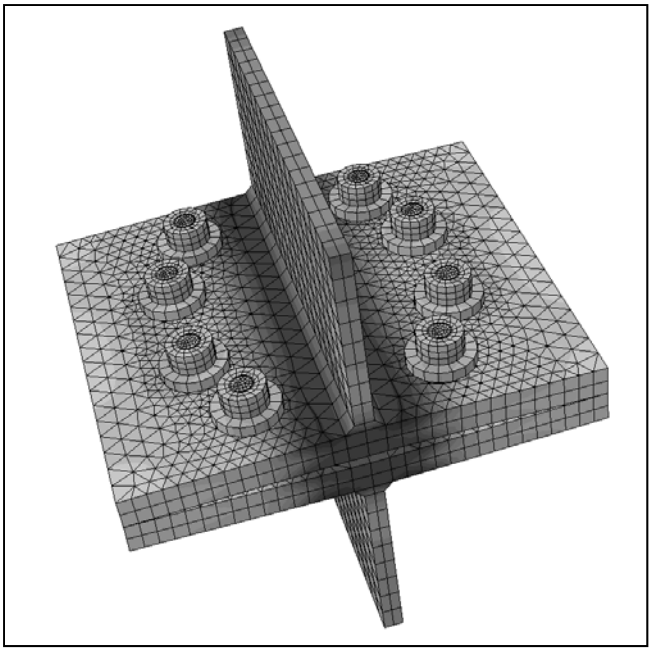

Figure 4-10 Finite Element Model Of TS-C Specimen

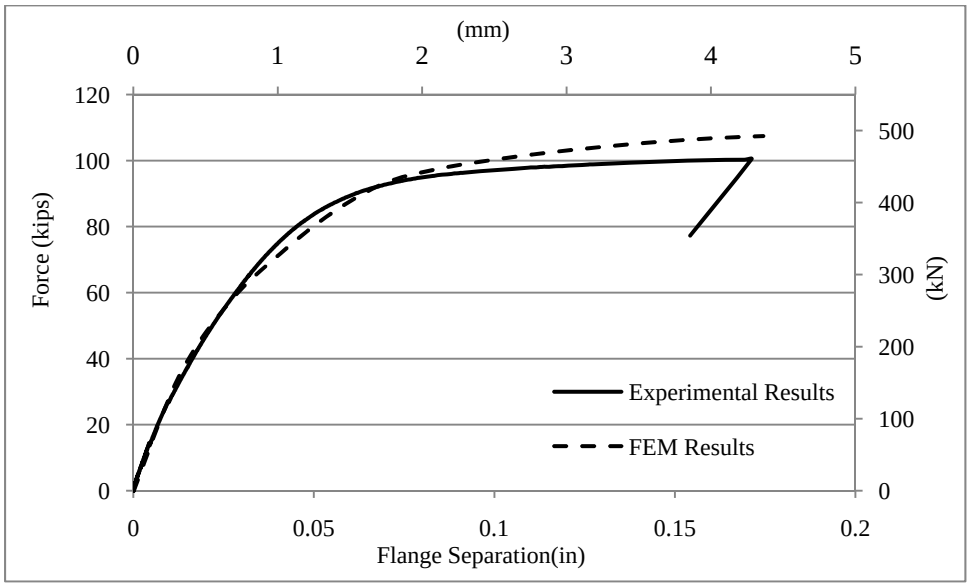

Figure 4-11 Applied Force Versus Flange Separation Response For TS-C Specimen

The bolt force history of the T-Stub with a circular bolt pattern is illustrated in Figure 4-12. These results show that the bolt forces obtained from the numerical analysis have a close agreement with the results obtained from experiment.

The bolt force behavior observed in the connection with circular bolt pattern is similar to the connection with square bolt pattern. It can be seen from Figure 4-12 that the near bolts start taking load at

a very early stage of loading with higher gradient, while the bolt force in the far bolt with a small delay increases with smaller rate. It should be noted that this delay 0.01 in. (0.2 mm) is much smaller than the delay in the connection with square bolt pattern (0.05 in. see Figure 4-9).

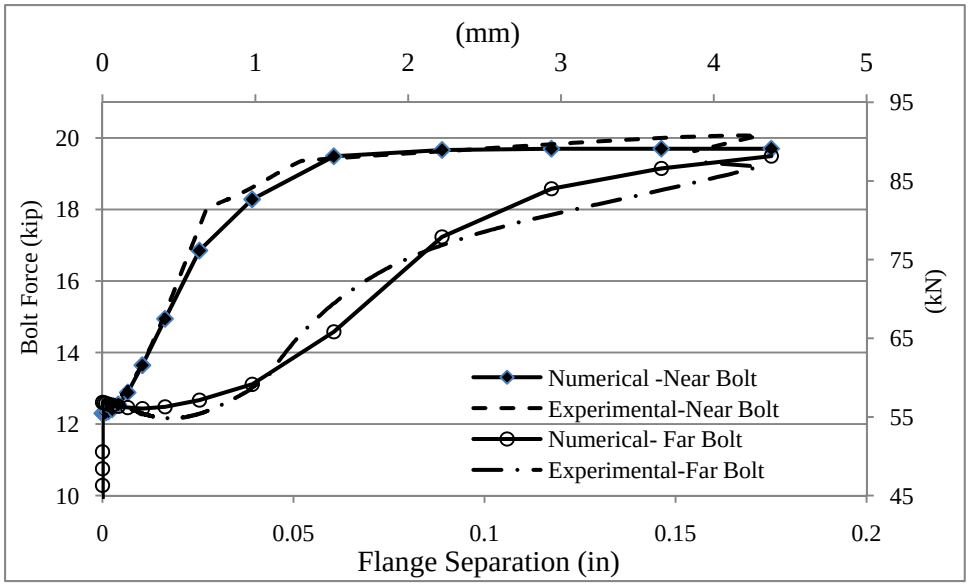

Figure 4-12 Bolt Force History In TS-C Specimen

4.5.2 Beam-Column Connection

The numerical results obtained for the finite element analysis are compared against the data collected during the experimental testing of several full-scale connections in order to validate the numerical results obtained from the finite element analysis. The details of the finite element models developed in this study are based on the experimental testing conducted by Abolmaali et al. [64][65] on the following connections: ***i***) extended end-plate connection, ***ii***) top-and-seat connection, ***iii***) bolted/bolted double web angle, ***iv***) welded/bolted double web angle connections, and ***v***) blush end-plate connections.

During the numerical model development, the beam and column sizes and other geometric parameters of full connection models were kept identical to the geometry of the specimens used during the experimental testing as it is presented in Chapte-3. The comparison of the results and discussions for each connection are presented in the following sections.

4.5.2.1 Extended End-Plate Connection

A 3-D finite element model of the extended end-plate connection is presented in Figure 4-13. A W16x67 hot-rolled cantilever beam is connected to a W14x159 column using an extended end-pate and eight high strength slip-critical bolts. The cyclic displacement loading was applied at the tip of the beam. The details of the finite element model were discussed in Chapter-3.

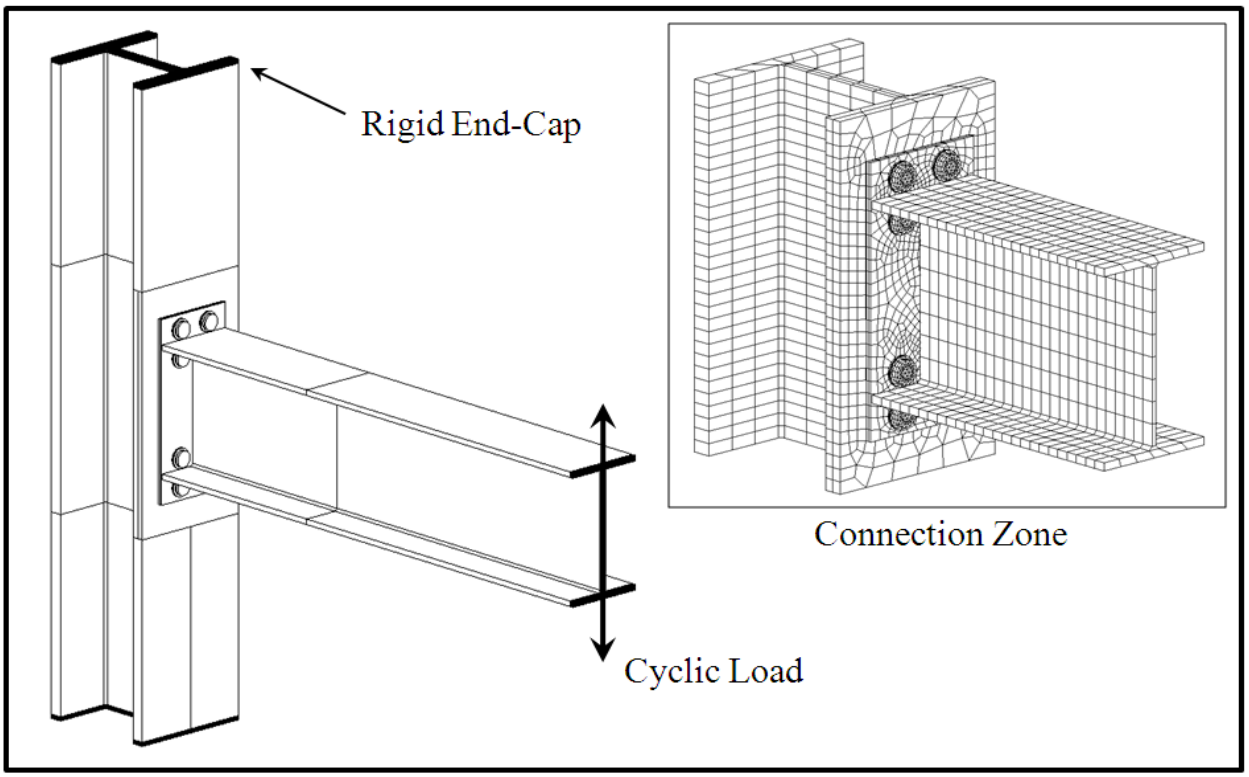

Figure 4-13 Extended End-Plate Finite Element Model, And Mesh Properties.

Figure 4-14 shows the comparison of the FEM moment rotation hysteresis with the experimental results. This figure shows that the FEM algorithm closely predicts the hysteresis loops of the experimental data, which confirms the accuracy of the coupled nonlinear algorithm complemented by proper cyclic plasticity formulation.

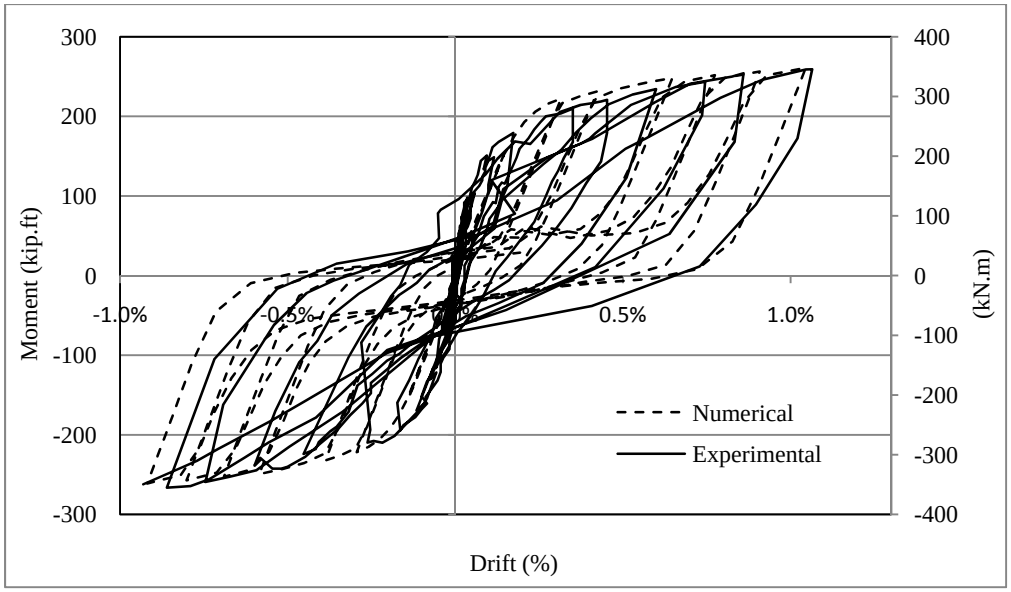

Figure 4-14 Comparison Of The Hysteresis Of The FEM And Experimental Results Of The Extended End-Plate Connections.

4.5.2.2 Top-And-Seat Angle Connection

To model the behavior of the top-and-seat connection under cyclic loading, a hot-rolled W16x67 cantilever beam is connection to a hot-rolled W14x159 column using two 6 inches in L5x5x¾ angles. The dimensions and the material properties of the elements were discusses in detail in Chapter-3. Figure 4-15 shows a 3-D finite element of the top-and-seat angle connection developed in this study. The hysteresis results illustrated in Figure 4-16 shows a good correlation between the moment-curvature curves obtained from experimental testing and finite element analysis. It should be noted that no pinching was observed during the experimental testing and the numerical model predicted the behavior accurately.

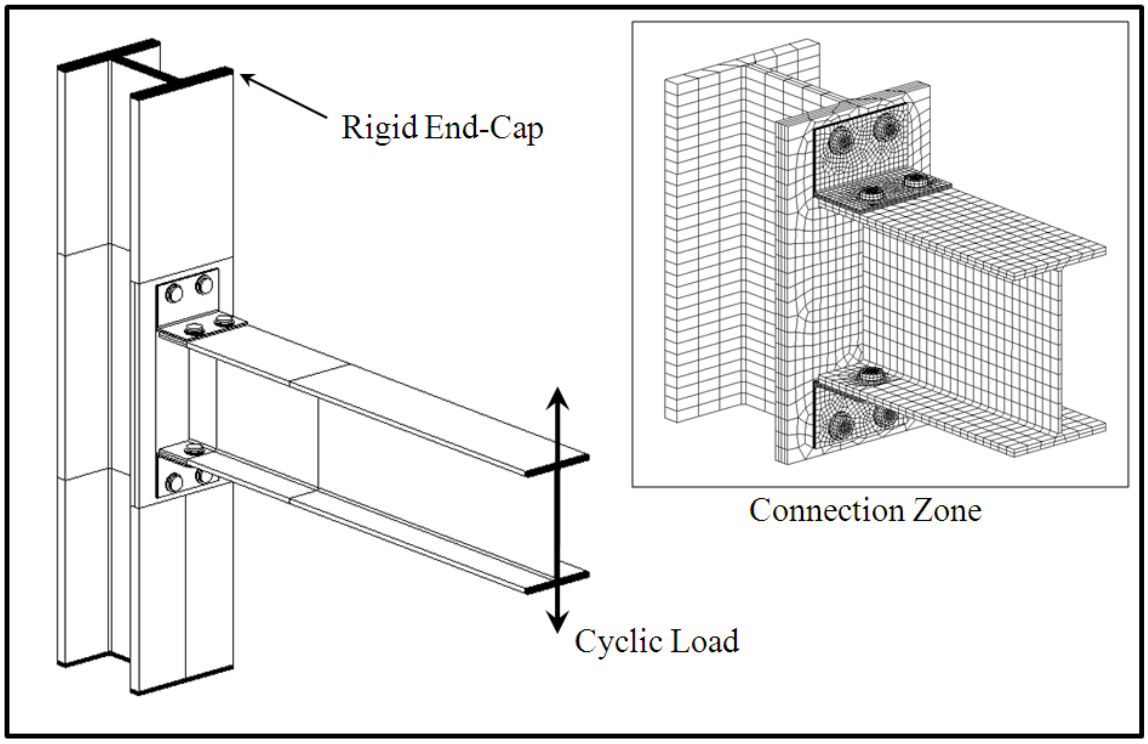

Figure 4-15 Top-And-Seat Angle Connection Finite Element Model, And Mesh Properties.

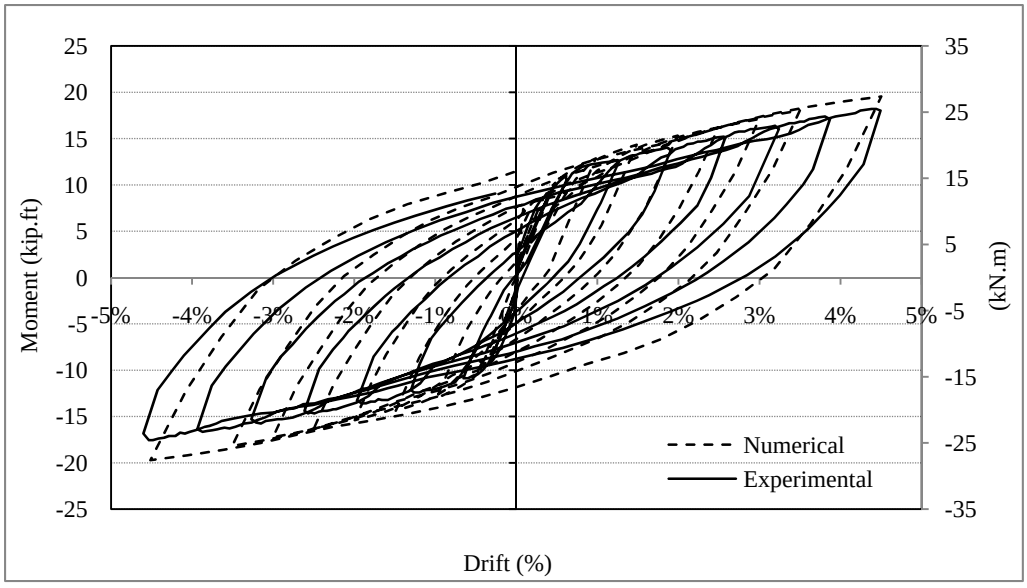

Figure 4-16 Comparison Of The Hysteresis Of The FEM And Experimental Results Of The Top-And-Seat Angle Connection.

Experimental data showed that the bolt-failure was the failure mode for this connection which is also confirmed in this study as shown in Figure 4-17.

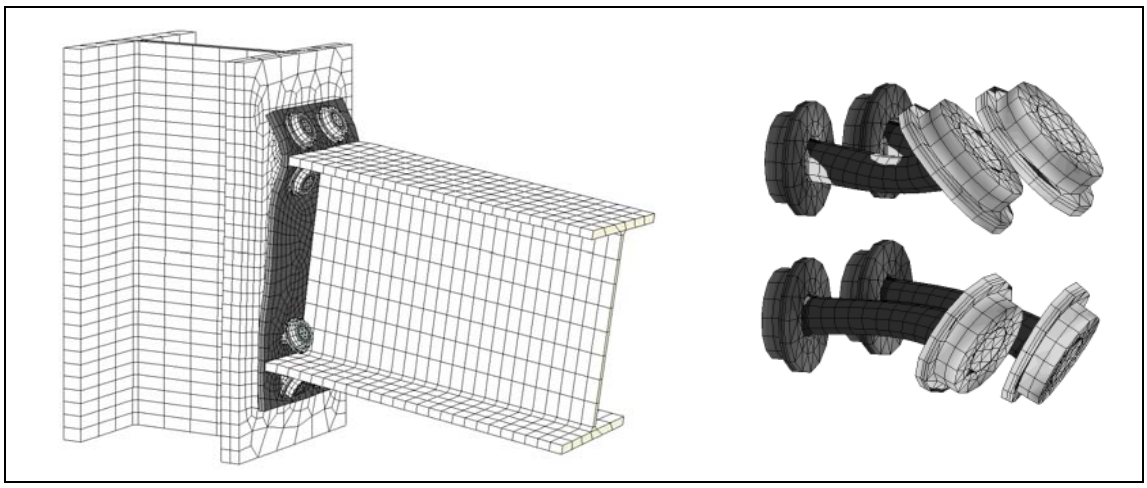

Figure 4-17 Failure Of Bolts In The Extended End-Plate Connection

4.5.2.3 Bolted/Bolted Double Web Angle Connection

To model the behavior of the bolted/bolted double web angle connection under cyclic loading, a hot-rolled W24x104 cantilever beam was connection to a hot-rolled W14x159 column. This test specimen was bolted to both the beam web and the column flange using two 15 in. L5x5x¾ on both side of the web, as shown in Figure 4-18. The dimensions and the material properties of the elements were discussed in detail in Chapter-3. This finite element model is validated with the experimental results. Figure 4-19 shows a 3-D finite element model of the bolted/bolted double web angle connection. The hysteresis results illustrated in Figure 4-19 shows a good correlation between the moment-curvature hysteresis obtained from the experimental testing and finite element analysis.

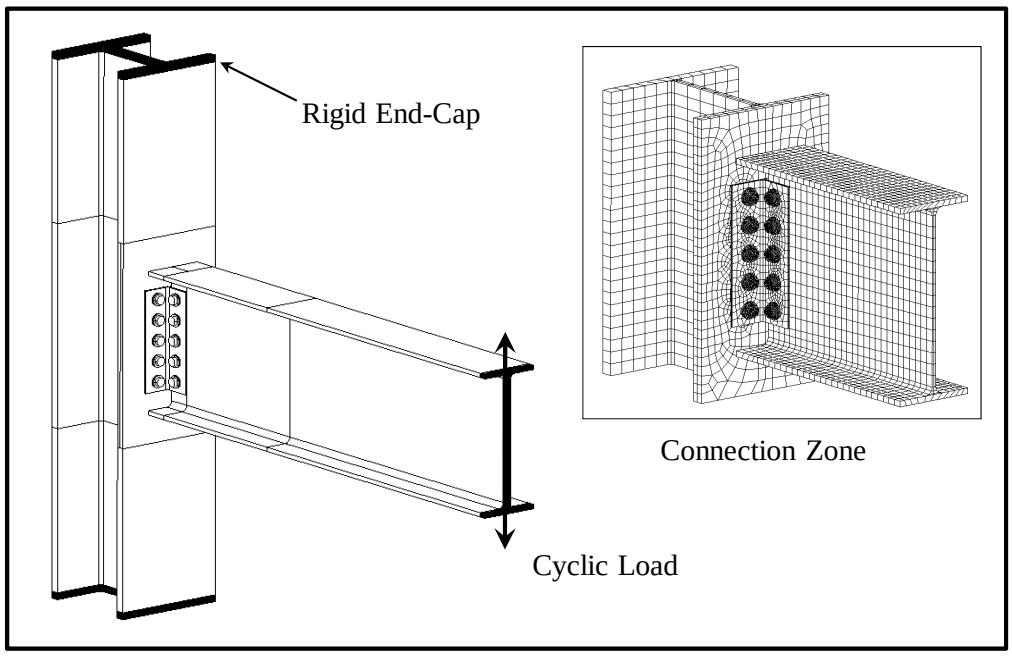

Figure 4-18 Bolted/Bolted Double Web Angle Connection Finite Element Model, And Mesh Properties.

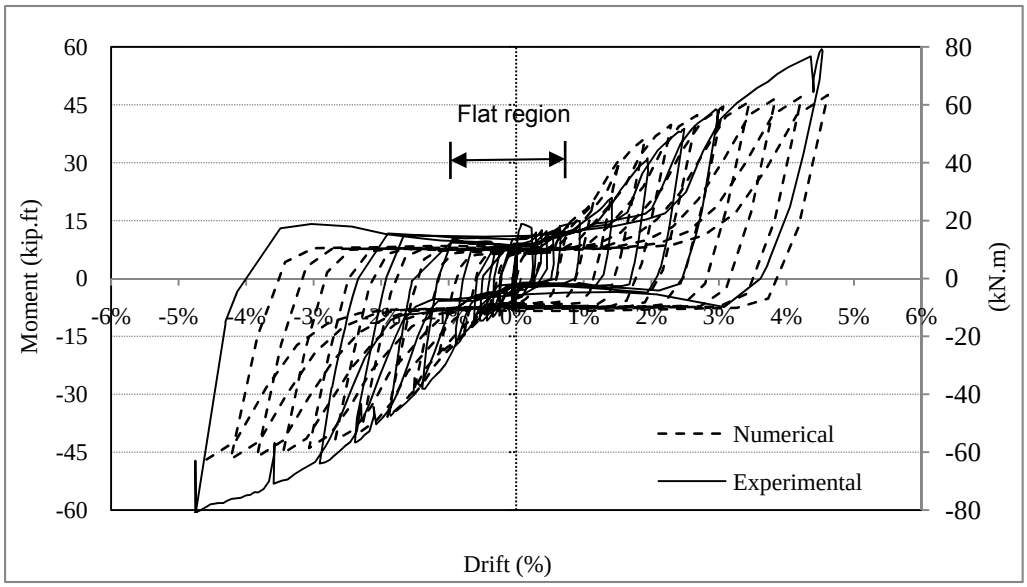

Figure 4-19 Comparison Of The Hysteresis Of The FEM And Experimental Results Of The Bolted/Bolted Double Web Angle Connection.

It is interesting to note that the flat region formed in the hysteresis of the bolted/bolted double web angle connection is identically predicted by the FEM algorithm. The flat region presented in Figure 4-19 is due to the elongation of the beam web's bolt-holes and the bearing failure which causes a change in

geometrical configuration of bolt holes from circular to oval shape. This assists the bolts to move freely in the bolt-holes during loading or load reversal during cyclic action. The connection zone of the beam-web of this connection is presented in Figure 4-20. This figure shows the FEM prediction of the bearing failure during cyclic loading of these connections. The plastic deformation of the beam web at the vicinity of the bolts that comply the results obtained from the experimental tests is shown in this figure.

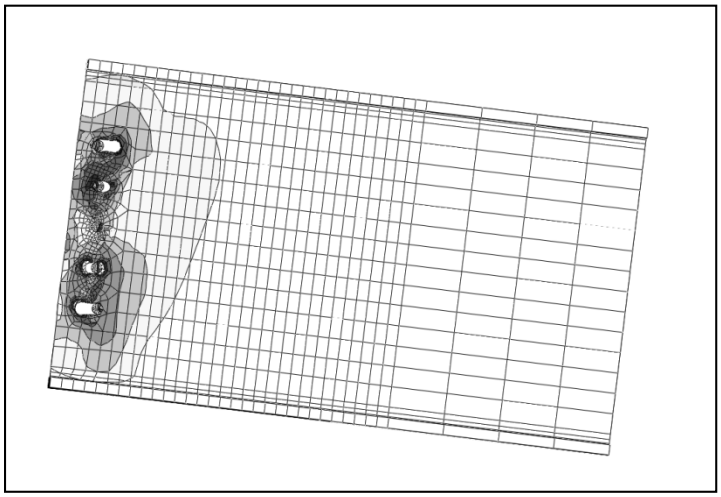

Figure 4-20 Deformation Of The Bolt-Holes From Round To Oval Due To Excessive Elongation In Bolted/Bolted Double Web Angle Connection .

4.5.2.4 Welded-bolted Double Web Angle Connection

A 3-D finite element model of the welded-bolted double web angle connection is presented in Figure 4-21. A W24x104 hot-rolled cantilever beam is connected to a W14x159 column using two 15 in. L5x5x¾ angle on both side of the web. The angles are welded to the beam-web and bolted to the column flange using eight ¾. in diameter high strength slip-critical bolts. A cyclic displacement control load is applied at the tip of the beam. The details of the finite element model were discussed in Chapter-3.

Figure 4-22 shows the comparison of the experimental and FEM moment rotation hysteresis loop for this connection. This figure show a capability of the FEM in predicting the experimental results. Particularly, the loading and unloading values and hysteresis stiffness are identically predicted.

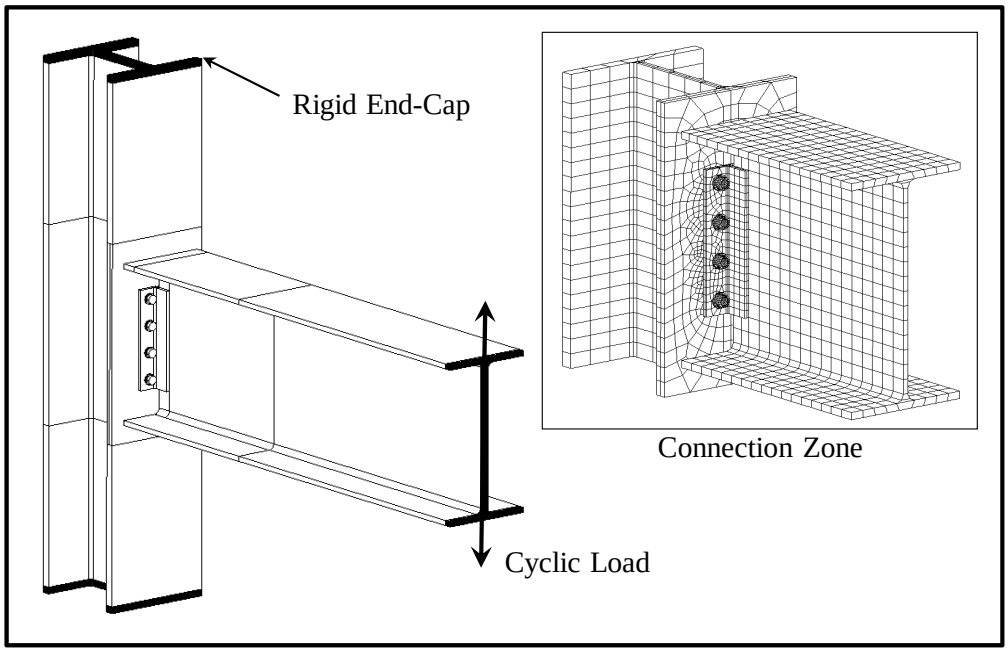

Figure 4-21 Welded/Bolted Double Web Angle Finite Element Model, And Mesh Properties.

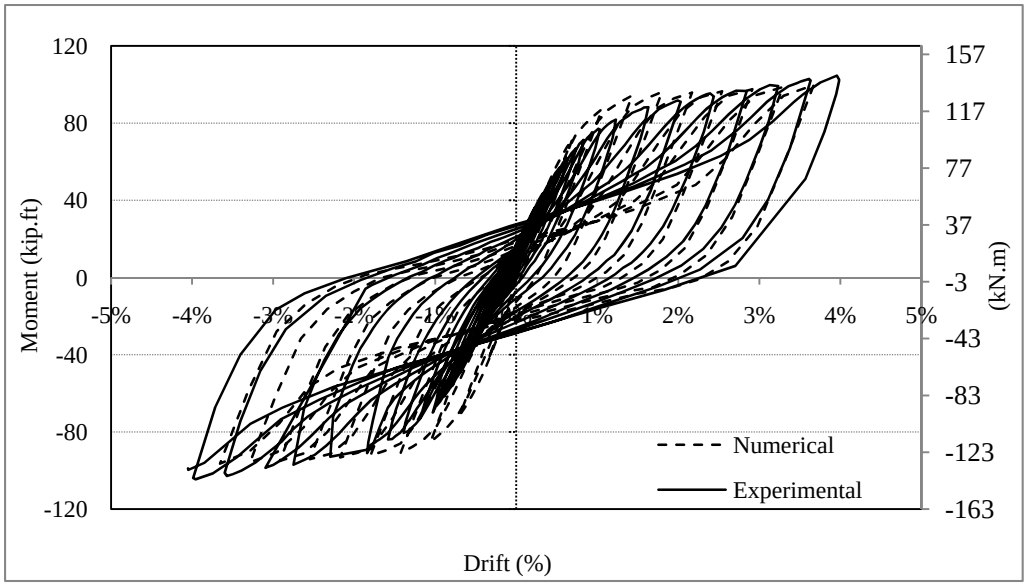

Figure 4-22 Comparison Of The Hysteresis Of The FEM And Experimental Results Of The Welded/Bolted Double Web Angle Connection.

Experimental results indicated that this connection failed due to excessive yielding of the angles. Same failure mode was predicted by the finite element models developed in this research.

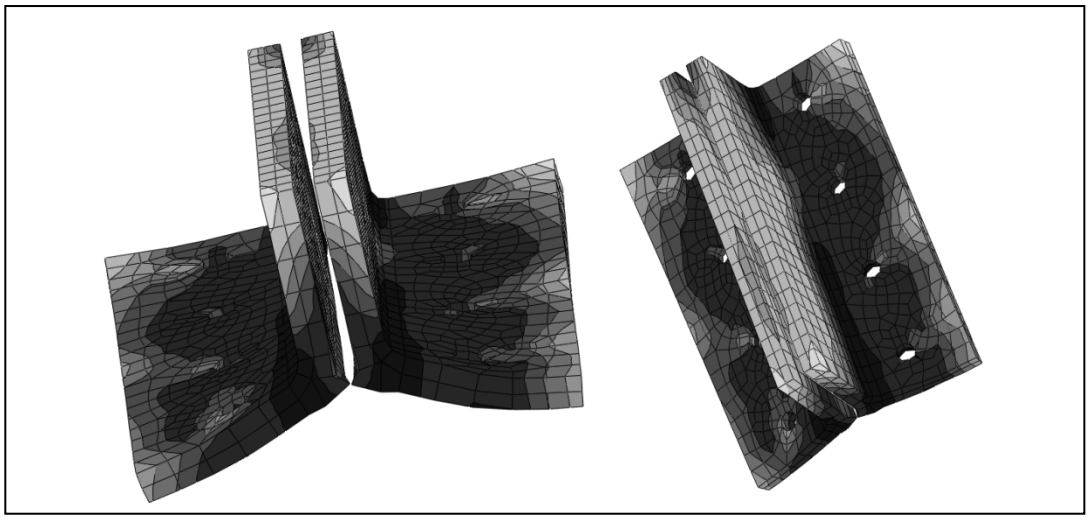

Figure 4-23 Failure Of The Angle Due To Excessive Elongation In Welded/Bolted Double Web Angle Connection

4.5.2.5 Flush End-Plate Connection

A 3-D finite element model of the flush end-plate connection is presented in Figure 4-24. A W18x46 hot-rolled cantilever beam is connected to a W14x159 column using a $^{3}/_{8}$ in. flush end-pate and eight ¾ in. high strength bolts. The cyclic displacement control load was applied to the tip of the beam. The details of the finite element model were discussed in Chapter-3.

Figure 4-25 shows the comparison of the hysteresis behavior of experimental versus FEM analysis. For this particular test, the governing mode of failure was bolt fracture. This was also detected during the FEM analysis in which the ultimate bolt strain was reached at approximately the same drift value.

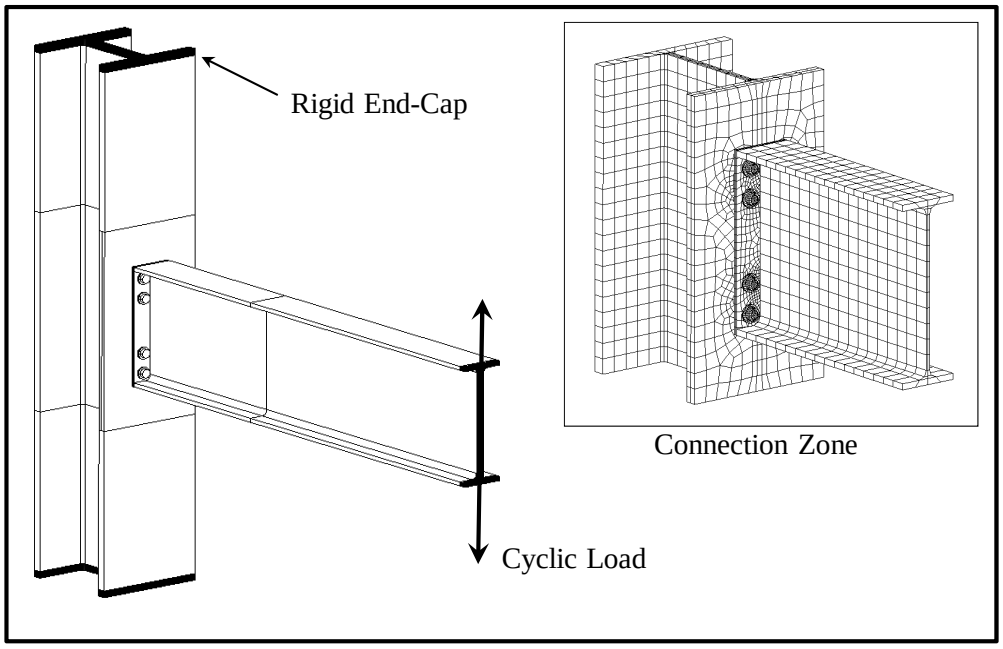

Figure 4-24 Flush End-Plate Connection Finite Element Model, And Mesh Properties.

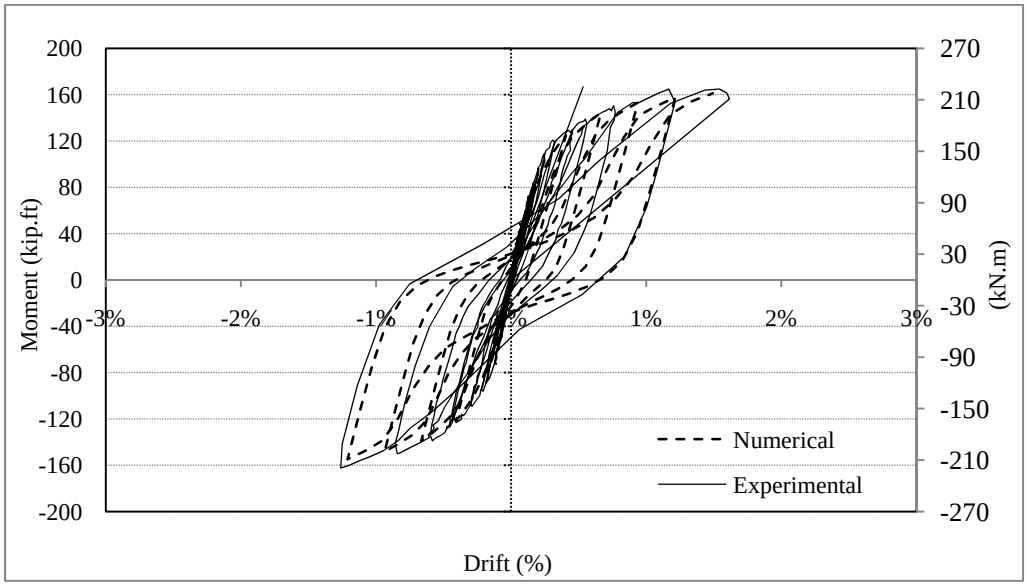

Figure 4-25 Comparison Of The Hysteresis Of The FEM And Experimental Results Of The Flush End-Plate Connections.

CHAPTER 5

DEVELOPMENT OF HYSTERESIS MATHEMATICAL MODELS

5.1 Introduction

The details of the finite element models used for validation of the numerical models were presented in the previous chapter. In this chapter, the test matrix used and the results of finite element analysis obtained from this parametric study are discussed. To simulate the tri-linear moment-rotation hysteresis behavior of the connection observed during testing, four parameters are required. These parameters are selected as the moment capacity of the connection at yield (M_y), the initial stiffness of the connection (E), the post yielding stiffness of the connection (E_t), and the maximum rotation of the end-plate at the fracture of the bolt (θ_f). These parameters can be used to calculate the value of the moment capacity of the connection at fracture (M_f), and the rotation of the end-plate at yield (θ_y). These parameters for the models with circular and square bolt pattern are presented and compared in this chapter. Finally, non-linear regression was used to develop questions for parameters defining connections hysteresis moment-rotation behavior.

5.2 Selection Of Test Cases

The focus of this study is to understand the behavior of the extended end-plate connections with circular bolt pattern and compare their behavior with the behavior of the connections with traditional square bolt pattern. To achieve this goal, parametric studies were conducted on one hundred and eighty two models with circular and square bolt pattern configurations and the results were compared. The values of the bolt-diameter, end-plate thickness, and beam sizes were varied in order to investigate the effect of each component on the connection performance. The values of bolt-diameter, bd, used were $1/2$, $5/8$, $3/4$, 1, $1\,1/8$ and $1\,1/4$ in (127, 159, 190, 254, 285, and 317 mm), while the thickness values of the end-plate, tp, were $1/2$, $5/8$, $3/4$, 1, $1\,1/8$, $1\,1/4$, and $1\,1/2$ in (127, 159, 190, 100, 285, 317, and 381 mm). The test matrix was modified several time throughout the research to eliminate the

repetitive results as well as accelerating the progress of the research. The range and the definition of each parameter are presented in Table 5-1. Parametric study was conducted for all possible combinations of t_p and b_d on the models with 30 in. nominal beam depth. The size of the test matrix was reduced to 40% for models with different nominal beam depth to accelerate the speed of the research. The details of the test matrix are provided in Appendix-B. The designated name for the models is a combination of the end-plate thickness, bolt diameter, nominal beam depth, and bolt pattern configuration. For example, the model designation of Tp1½-bd¾-d24-Cir indicates a model with $1\ 1/2$ in. (381 mm) end-plate, ¾ in. (190 mm) bolt diameter, with nominal beam depth of 24 in. (612 mm), and with circular bolt pattern configuration.

Table 5-1 Range Of Element Thickness And Designated Symbols.

Element	Symbol	Range in (mm)
Beam Depth	d	24(61.2), 30(75.5), 36(90.4)
Plate Thickness	T_p	½(13), 5/8(16), ¾ (19),1.0(25), 1-1/8(28), 1-¼(32), 1-½(38)
Bolt Diameter	b_d	½(13), 5/8(16), ¾ (19),1.0(25), 1-1/8(28), 1-¼(32)
Bolt Pattern		Cir, Sqr

A W14x193 hot-rolled column with length of 130 in. (330 cm) was used for each of the models. To isolate the connection behavior for the column rotation and column-flange deformation the thickness of the column flange was increased to 2.1 in. (53 mm). Sixteen high strength bolts, as shown in Figure 5-1, were used to connect a 70 in. beam (180 cm), and an extended end-plate to the column.

Traditionally, the bolt-holes in the end-plate are placed in several rows parallel to the beam flange cross section and with equal gauge spacing. In the proposed circular bolt pattern configuration, the bolts are placed in a circular pattern with the center at the intersection of the beam-flange and beam-web as shown in Figure 5-1(a). This corresponds to moving the bolts in Rows-2 and 3 horizontally to the edge of the end-plate. The edge distance from the edge of the plate to the center of the bolt was kept to be larger than the minimum required spacing by the AISC [1]. Thus, bolts on Rows-1 and 4 (far bolts) were relocated relative to bolts on Rows-2 and 3 (near bolts) to complete the formation of the circular pattern.

The schematic comparison of the proposed and conventional rectangular bolt patterns is also presented in Figure 5-1. Using this method, the bolts in Row-4 (Bolts-4) are placed at a distance closer to the beam web, which increased the load bearing capacity of the bolts in Row-1 and Row-4. Also it can be seen from Figure 5-1 that in the proposed bolt pattern configuration, the bolt in Row-4 are located closer to the beam web, which attracts more load to this bolt.

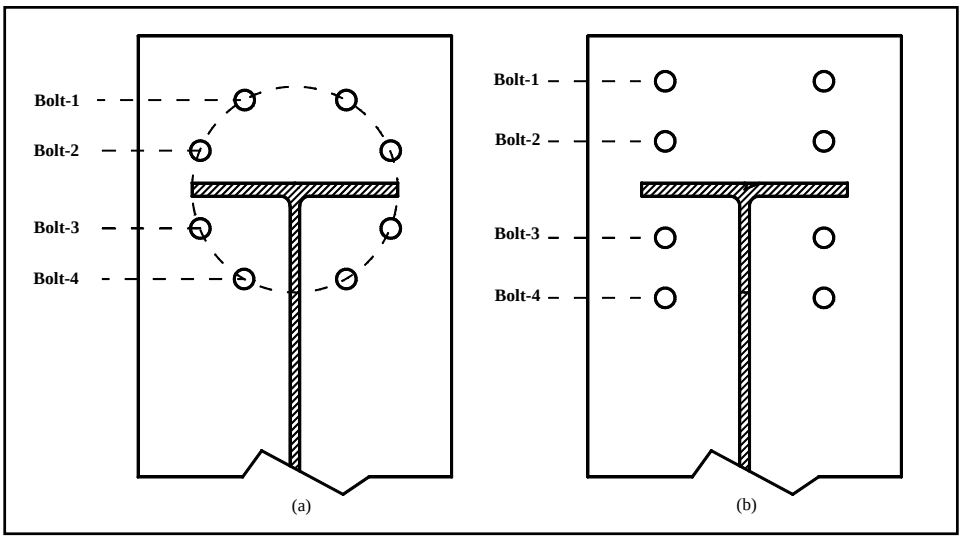

Figure 5-1 Detail Of The End-Plate, (a) Proposed Circular Bolt Pattern, (b) Rectangular Bolt Pattern

To find a location of the bolts in the connections with circular bolt pattern a group of equations is developed. These equations are developed such that the position of the bolt-holes for any connection with different geometric values can be located. The results of these equations are pronounced in Cartesian system with the origin located at the intersection of the beam-flange and beam-web. The radius of the bolt configuration is selected as one half of the flange width (½b_f). The location of each bolt can be calculated using the following equations;

$$\text{Location of each bolt} = \begin{cases} x = r \times \sin(\emptyset) \\ y = r \times \cos(\emptyset) \end{cases}$$

Where;

$r = \frac{b_f}{2}$, and

$b_f =$ width of the beam flange

the corresponding angular coordinate , Ø, for each bolt is tabulated in Table 5-2;

Table 5-2 The Angular Coordinate For Each Bolt

Bolt	Angle
Bolt-1	$\emptyset = Arcsin(\frac{2P_{fo} + t_f}{b_f})$
Bolt-2	$\emptyset = Arcsin\left(\frac{2P_{fo} + t_f}{b_f}\right) + \theta$
Bolt-3	$\emptyset = \pi - Arcsin\left(\frac{2P_{fo} + t_f}{b_f}\right) - \theta$
Bolt-4	$\emptyset = \pi - Arcsin\left(\frac{2P_{fo} + t_f}{b_f}\right)$
Bolt-5	$\emptyset = \pi + Arcsin\left(\frac{2P_{fo} + t_f}{b_f}\right)$
Bolt-6	$\emptyset = \pi + Arcsin\left(\frac{2P_{fo} + t_f}{b_f}\right) + \theta$
Bolt-7	$\emptyset = -Arcsin\left(\frac{2P_{fo} + t_f}{b_f}\right) - \theta$
Bolt-8	$\emptyset = -Arcsin\left(\frac{2P_{fo} + t_f}{b_f}\right)$

Where;

P_{fo} = the $distance\ from\ the\ edge\ of\ the\ flange\ to\ the\ center\ of\ the\ near\ bolt$

$t_f = beam\ flange\ thickness$, and

$\theta = the\ angular\ spaceing\ between\ the\ near\ and\ far\ bolt.$

These parameters and position of each bolt are illustrated in Figure 5-2.

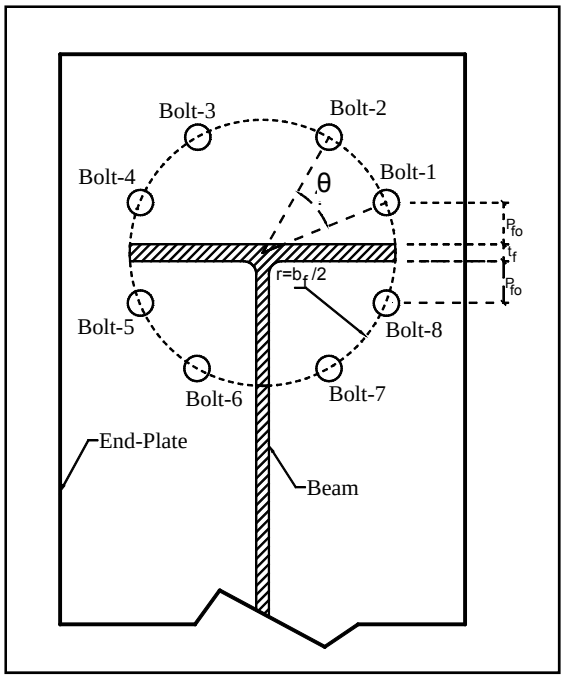

Figure 5-2 The Detail Of The Parameters

5.3 Finite Element Modeling

The details of the finite element models used in this study are very similar to the models presented in Chapter-4. ABAQUS 6.10-1, was used to develop and analyze the finite element models of the extended end-plate connection with both circular and square bolt pattern configurations. Due to the symmetry of the beam-column connection only half of the connection was modeled. Figure 5-3 shows a typical extended end-plate connection with circular bolt pattern configuration.

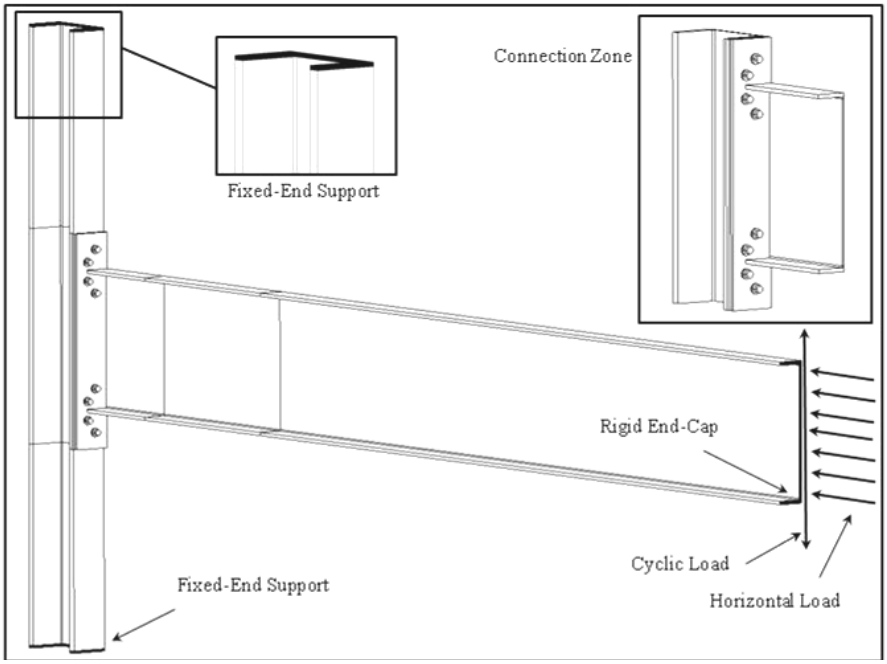

Figure 5-3 Finite Element Model Of The Extended End-Plate Connection With Circular Bolt Pattern Configuration.

The focus of this research is to study effect of the circular bolt pattern configuration on the hysteresis behavior of the extended end-plate connection with various beam size, bolt diameter, and end-plate thickness. To eliminate the effects of the column flange thickness on the overall behavior of the connection, the column was selected to have thick flange thickness (2.1 in. (53 mm)) when compared with the connection end-plate thickness.

Large elongation of the bolts especially in the cases with small bolt diameter causes the complete separation of the end-plate at the face of the column. Since the contact between the end-plate and the face of the column acts as a boundary condition for the beam, the lack of contact between these two surfaces reduces the degrees of freedom of the beam and eventually force this value to zero. This phenomenon slows down and ultimately stops the convergence process of the model due to the numerical error. To assure a constant contact between the end-plate and the face of the column, a small (0.1 kip) horizontal load was applied at the tip of the beam. This load gently pushes the beam end-plate against the face of the column and provides the necessary contact (support) to avoid the numerical error. The location of the applied forces and boundary conditions are illustrated in detail in Figure 5-3.

The analyses were conducted by applying the increasing cyclic variable amplitude displacement at the tip of the beam. The cyclic displacement amplitude followed the loading protocol in the AISC Seismic Provisions [73], which is identical to the SAC loading protocol, and FEMA [74]. The loading protocol composed of the following steps was incorporated in ABAQUS:

- Step 1: 6 cycles with peak drift angle of 0.00375 rad
- Step 2: 6 cycles with peak drift angle of 0.005 rad
- Step 3: 6 cycles with peak drift angle of 0.0075 rad
- Step 4: 4 cycles with peak drift angle of 0.01 rad
- Step 5: 2 cycles with peak drift angle of 0.015 rad
- Step 6: 2 cycles with peak drift angle of 0.02 rad
- Step 7: 2 cycles with peak drift angle of 0.03 rad
- Step 8 and further steps will be repeated with the drift angle of 0.01 rad for each 2 cycles until the beam or connection zone reaches inelastic mode.

The loading protocol is shown in

Figure 5-4. The tip displacement corresponding to a story drift ratio of 0.01 rad was 2.4 in. (60 mm). A rigid part (un-deformable mesh region) was attached to the tip of the beam to simulate a rigid beam end-cap which distribute the load caused by the cyclic displacement control evenly at the tip of the beam (Figure 5-3). Similarly, two rigid parts was attached at both ends of the column to distribute the support reaction forces evenly at the tip of the column (see Figure 5-3).

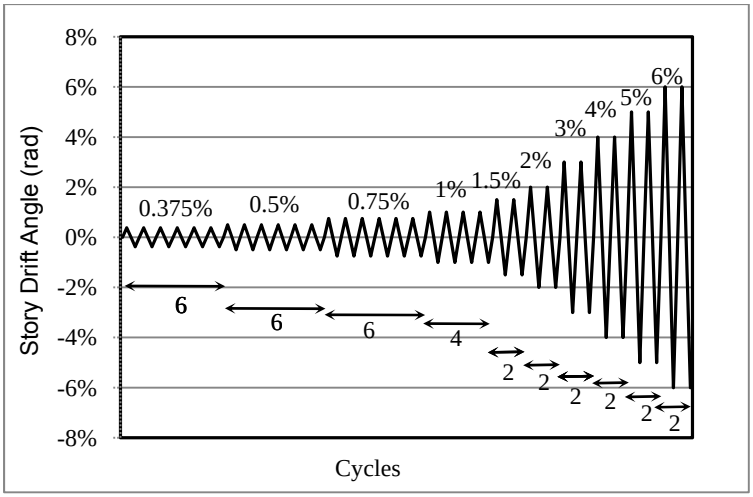

Figure 5-4 Cyclic Loading History, FEMA 350.

5.4 Hysteresis Characteristics

The numerical results obtained from finite element analysis are presented and discussed in this section. The applied moment versus the end-plate rotation of each model with square and circular bolt pattern configuration are presented in Appendix-C and Appendix-D, respectively. The applied moment was calculated by multiplying the applied load at the tip of the beam by the distance from the point of the load to the face of the column. The end-plate rotation was calculated by using the following equation;

$$\theta = \frac{\Delta_T - \Delta_B}{d}$$

where;

Δ_T = out of plane deformation of the end-plate at the location of the beam top-flange

Δ_B = out of plane deformation of the end-plate at the location of the beam bottom-flange, and

d = beam depth

Figure 5-5 shows the schematic drawing of the end-plate rotation and corresponding parameters.

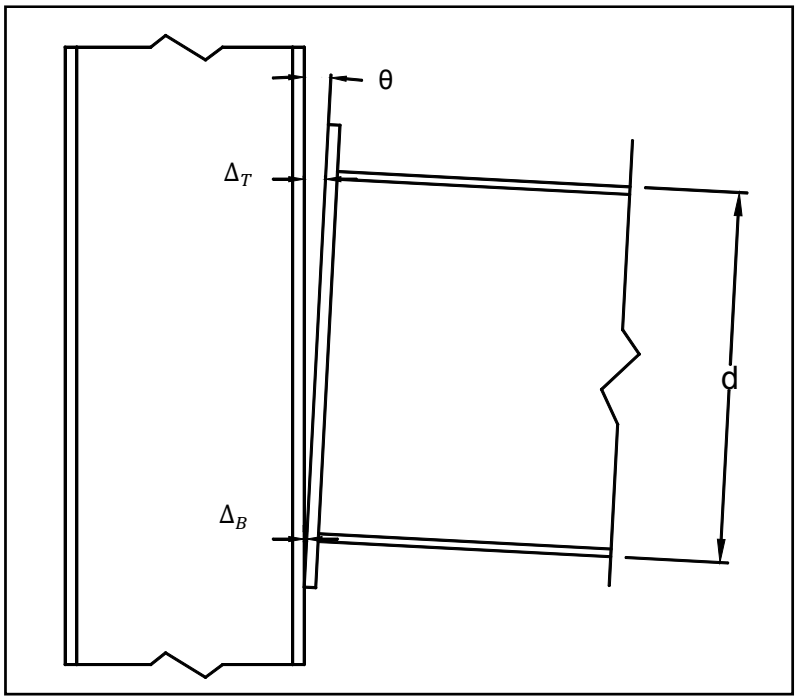

Figure 5-5 Schematic Drawing Of The End-Plate Rotation

Yield moment of the connection, M_y, is defined as the point that the non-linear behavior of the connection is initiated. This point is determined by using bi-linear curve fit on the moment-rotation hysteresis of the models. The initial stiffness of the connection is defined as corresponding stiffness of the connection before the yield, which is calculated by, $E = {M_y}/{\theta_y}$. The post yield stiffness of the connection is calculated by following equation;

$$E_t = \frac{M_f - M_y}{\theta_f - \theta_y}$$

where;

M_f = ultimate moment capacity of the connection at failure, and

θ_f = ultimate rotation capacity of the connection,

The hysteresis results presented in Appendix-C and Appendix-D show that the hysteresis behavior of the models can be classified into two separate categories. In the models with relatively large bolt diameter, the non-linear behavior and consequently pinching is due to plastic deformation of the end-plate

or the beam. This category of the hysteresis is called "*End-Plate Behavior*" by the author. The tri-linear hysteresis model of "*End-Plate Behavior*" category is presented in Figure 5-6.

The second category is the models with relatively small bolt diameter. Due to an early and large deformation of the bolts in these models, the hysteresis behaviors of these connections are largely governed by the overall behavior of the bolts in the connections. Therefore, this category of the hysteresis behavior is called "*Bolt Behavior.*" The tri-linear hysteresis model of the "*Bolt Behavior*" category is presented in Figure 5-7.

Visual observation of the hysteresis results of the models shows that the threshold between the two hysteresis behavior of the "*End-Plate Behavior.*" and "*Bolt Behavior*" is the bolt diameter of ¾ in. The models with bolt diameter equal of smaller than ¾ in. undergo a large bolt elongation and present "*Bolt Behavior*", while the models with bolt diameter larger than ¾ in. present "*End-Plate Behavior*".

To simulate the hysteresis behavior of the connections, four essential parameters were determined for each model using the results collected from the finite element analysis. These parameters are; the moment capacity of the connection at yield (M_y), the initial stiffness (E), the post yielding stiffness (E_t), and the maximum rotation of the end-plate at the failure (θ_f). Figures 5-6 and 5-7 show the schematic drawing of the tri-linear hysteresis model and the corresponding parameters for connections with "*End-Plate Behavior*" and "*Bolt Behavior*" respectively.

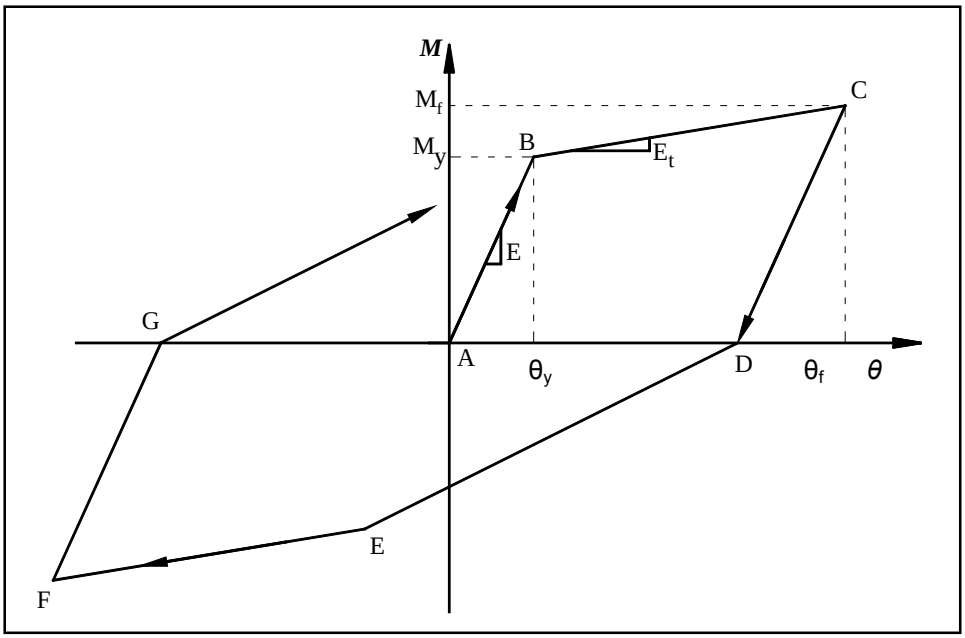

Figure 5-6 Tri-Linear Hysteresis Behavior Of The Models With “End-Plate Behavior”

Pass $\overline{ABCDEFGB}$ in Figure 5-6 shows an outer hysteresis envelope of the models with “*End-Plate Behavior.*” The parametric value of the moment and rotation for each point of the hysteresis is calculated using the four basic parameters and are presented in Table 5-3.

Table 5-3 Parametric Value Of The Moment And Rotation Of The Points On The Hysteresis Model Of The Connections With “End-Plate Behavior”

Point	Moment (M)	Rotation (θ)
A	0	0
B	M_y	θ_y
C	$M_y + E_t.(\theta_f-\theta_y)$	θ_f
D	0	$\theta_f - [M_y + E_t.(\theta_f-\theta_y)]/ E_t$
E	$-M_y$	$-\theta_y$
F	$-[M_y - E_t.(\theta_f-\theta_y)]$	$-[\theta_f - [M_y + E_t.(\theta_f-\theta_y)]/ E_t]$
B	M_y	θ_y

Pass $\overline{ABCDAEFGA}$ in Figure 5-7 shows an outer hysteresis envelope of the models with “*Bolt Behavior.*” The parametric value of the moment and rotation for each point of the hysteresis is calculated using four basic parameters and are presented in Table 5-4.

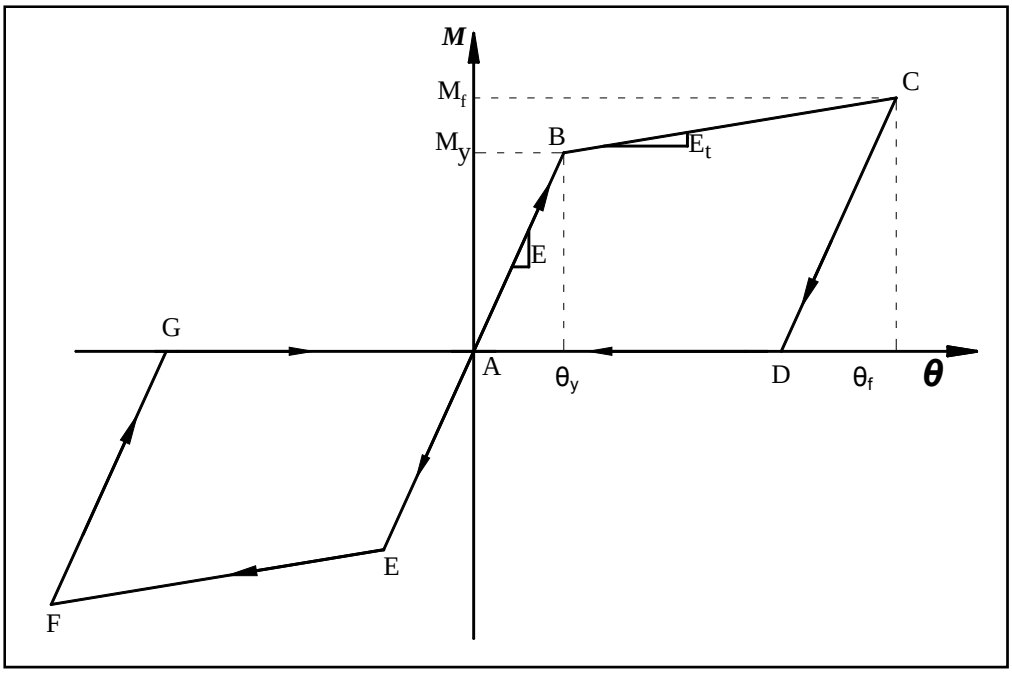

Figure 5-7 Tri-Linear Hysteresis Behavior Of The Models With “Bolt Behavior”

Table 5-4 Parametric Value Of The Moment And Rotation Of The Points On The Hysteresis Model Of The Connections With “*Bolt Behavior*”

Point	Moment (M)	Rotation (θ)
A	0	0
B	M_y	θ_y
C	$M_y + E_t.(\theta_f-\theta_y)$	θ_f
D	0	$\theta_f - [M_y + E_t.(\theta_f-\theta_y)]/ E_t$
A	0	0
E	$- M_y$	$- \theta_y$
F	$-[M_y + E_t.(\theta_f-\theta_y)]$	$- \theta_f$
G	0	$-[\theta_f - [M_y + E_t.(\theta_f-\theta_y)]/ E_t]$
A	0	0

5.5 Finite Element Results

The designated name, label of geometric parameters, and hysteresis characteristic values for models with circular and square bolt pattern configuration are summarized in Tables 5-5, and 5-6 respectively.

The hysteresis results obtained from finite element analysis for the models with square and circular bolt pattern are presented in Appendix-C and Appendix-D respectively. Tri-linear model were used to

simulate the hysteresis characteristic of each model. The simulated tri-linear model for each connection is also presented in these Appendixes.

To simplify the investigation of the bolt pattern configuration affect on the hysteresis behavior and energy dissipation of the connection, the results and their percentage variation are presented in Table 5-7. Close examination of the results shows that the circular bolt pattern will enhance the moment capacity, initial and post-yield stiffness of the connection. In addition, these results show that the models with circular bolt pattern present higher ductility when they are compared with the models with square bolt pattern. The results will be discussed in detail in chapter 6.

Table 5-5 Numerical Results Of The Models With Circular Bolt Pattern

	Name	Category	Independent Variables					Dependent Variables					
			Tp (in)	bd (in)	d (in)	S (in^3)	Z (in^3)	M_v (kip.ft)	θ_v 10^{-3}	E_v (ksi)	M_f (kip.ft)	θ_f 10^{-3}	E_t (ksi)
1	Tp1½-bd½-d30 -Cir	1	1½	½	30	269	312	450	3	150000	455	4.47	3238
2	Tp1½-bd5/8-d30 -Cir	1	1½	5/8	30	269	312	650	3.8	171053	664	6.24	5823
3	Tp1½-bd¾-d30 -Cir	1	1½	¾	30	269	312	830	4.5	184444	860	8.42	7615
4	Tp1½-bd1-d30 -Cir	1	1½	1	30	269	312	1170	5.1	229412	1273	10.74	18201
5	Tp1½-bd1 1/8-d30 -Cir	1	1½	1 1/8	30	269	312	1190	5.5	216364	1434	14.58	26885
6	Tp1½-bd1¼-d30 -Cir	1	1½	1¼	30	269	312	1320	5	264000	1739	17.11	34568
7	Tp1¼-bd½-d30 -Cir	1	1¼	½	30	269	312	430	3	143333	434	4.05	3420
8	Tp1¼- bd5/8-d30 -Cir	1	1¼	5/8	30	269	312	630	4.2	150000	638	5.75	5176
9	Tp1¼- bd¾-d30 -Cir	1	1¼	¾	30	269	312	780	5	156000	796	7.36	7001
10	Tp1¼-bd1-d30 -Cir	1	1¼	1	30	269	312	1080	6	180000	1159	12.20	12806
11	Tp1¼-bd1 1/8-d30 -Cir	1	1¼	1 1/8	30	269	312	1130	5.8	194828	1274	14.69	16175
12	Tp1¼-bd1¼-d30 -Cir	2	1¼	1¼	30	269	312	1300	6.2	209677	1454	18.74	12273
13	Tp1 1/8-bd½-d30 -Cir	1	1 1/8	½	30	269	312	430	3.5	122857	435	4.77	3719
14	Tp1 1/8- bd5/8-d30 -Cir	1	1 1/8	5/8	30	269	312	600	4.1	146341	607	5.76	4520
15	Tp1 1/8- bd¾-d30 -Cir	1	1 1/8	¾	30	269	312	750	5	150000	769	7.59	7490
16	Tp1 1/8-bd1-d30 -Cir	1	1 1/8	1	30	269	312	1020	6	170000	1083	11.29	11853
17	Tp1 1/8-bd1 1/8-d30 -Cir	2	1 1/8	1 1/8	30	269	312	1090	6.5	167692	1196	14.90	12596
18	Tp1 1/8-bd1¼-d30 -Cir	2	1 1/8	1¼	30	269	312	1180	6.5	181538	1340	20.36	11562
19	Tp1-bd½-d30 -Cir	1	1	½	30	269	312	430	3.5	122857	434	4.76	3564
20	Tp1- bd5/8-d30 -Cir	1	1	5/8	30	269	312	600	4.5	133333	608	6.16	4559
21	Tp1- bd¾-d30 -Cir	1	1	¾	30	269	312	750	5.5	136364	765	7.74	6814
22	Tp1-bd1-d30 -Cir	2	1	1	30	269	312	1040	7	148571	1101	14.26	8401
23	Tp1-bd1 1/8-d30 -Cir	2	1	1 1/8	30	269	312	1050	6.5	161538	1154	16.36	10506
24	Tp1-bd1¼-d30 -Cir	2	1	1¼	30	269	312	1100	6.5	169231	1304	21.88	13248

Table 5-5 Continued

	Name	Category	Independent Variables					Dependent Variables					
			Tp (in)	bd (in)	d (in)	S (in^3)	Z (in^3)	M_v (kip.ft)	θ_v 10^{-3}	E_v (ksi)	M_f (kip.ft)	θ_f 10^{-3}	E_t (ksi)
25	Tp¾-bd½-d30 -Cir	1	¾	½	30	269	312	370	4	92500	373	5.03	3077
26	Tp¾- bd5/8-d30 -Cir	1	¾	5/8	30	269	312	530	5	106000	538	6.74	4465
27	Tp¾- bd¾-d30 -Cir	2	¾	¾	30	269	312	670	6	111667	681	8.10	5038
28	Tp¾-bd1-d30 -Cir	2	¾	1	30	269	312	750	6.2	120968	808	12.88	8712
29	Tp¾-bd1 1/8-d30 -Cir	2	¾	1 1/8	30	269	312	800	6.2	129032	910	16.20	11008
30	Tp¾-bd1¼-d30 -Cir	2	¾	1¼	30	269	312	850	6.5	130769	1029	21.22	12143
31	Tp5/8-bd½-d30 -Cir	1	5/8	½	30	269	312	380	4.5	84444	384	5.75	3251
32	Tp5/8- bd5/8-d30 -Cir	2	5/8	5/8	30	269	312	500	5.2	96154	504	6.41	3391
33	Tp5/8- bd¾-d30 -Cir	2	5/8	¾	30	269	312	550	5.7	96491	563	8.30	4872
34	Tp5/8-bd1-d30 -Cir	2	5/8	1	30	269	312	630	6	105000	694	14.57	7419
35	Tp5/8-bd1 1/8-d30 -Cir	2	5/8	1 1/8	30	269	312	640	6	106667	728	15.54	9218
36	Tp5/8-bd1¼-d30 -Cir	2	5/8	1¼	30	269	312	650	6	108333	822	20.91	11533
37	Tp½-bd½-d30 -Cir	2	½	½	30	269	312	300	4.1	73171	303	5.00	2922
38	Tp½- bd5/8-d30 -Cir	2	½	5/8	30	269	312	330	4.2	78571	337	5.72	4384
39	Tp½- bd¾-d30 -Cir	2	½	¾	30	269	312	370	4.7	78723	385	7.69	4957
40	Tp½-bd1-d30 -Cir	2	½	1	30	269	312	450	5.1	88235	503	12.53	7144
41	Tp½-bd1 1/8-d30 -Cir	2	½	1 1/8	30	269	312	470	5	94000	566	14.99	9601
42	Tp½-bd1¼-d30 -Cir	2	½	1¼	30	269	312	500	5.4	92593	661	19.68	11288
43	Tp1½-bd½-d24 -Cir	1	1½	½	24	258	289	420	2.8	150000	421	3.00	3512
44	Tp1½- bd5/8-d24 -Cir	1	1½	5/8	24	258	289	560	3.5	160000	561	3.80	4651
45	Tp1½- bd¾-d24 -Cir	1	1½	¾	24	258	289	780	4.2	185714	783	4.60	6682
46	Tp1½-bd1-d24 -Cir	1	1½	1	24	258	289	1000	4.5	222222	1052	7.20	19331
47	Tp1½-bd1 1/8-d24 -Cir	1	1½	1 1/8	24	258	289	1150	4.9	234694	1277	10.00	24881
48	Tp1½-bd1¼-d24 -Cir	1	1½	1¼	24	258	289	1320	5.2	253846	1596	12.30	38897

Table 5-5 Continued

	Name	Category	Independent Variables					Dependent Variables					
			T_p (in)	b_d (in)	d (in)	S (in^3)	Z (in^3)	M_v (kip.ft)	θ_v 10^{-3}	E_v (ksi)	M_f (kip.ft)	θ_f 10^{-3}	E_t (ksi)
49	Tp1 1/8-bd½-d24 -Cir	1	1 1/8	½	24	258	289	430	3.5	122857	431	3.60	5037
50	Tp1 1/8- bd 5/8-d24 -Cir	1	1 1/8	5/8	24	258	289	550	4	137500	551	4.30	3812
51	Tp1 1/8- bd¾-d24 -Cir	1	1 1/8	¾	24	258	289	770	4.8	160417	772	5.10	7457
52	Tp1 1/8-bd1-d24 -Cir	1	1 1/8	1	24	258	289	1000	5.4	185185	1035	8.30	11978
53	Tp1 1/8-bd1 1/8-d24 -Cir	2	1 1/8	1 1/8	24	258	289	1090	6.3	173016	1189	13.60	13587
54	Tp1 1/8-bd1¼-d24 -Cir	2	1 1/8	1¼	24	258	289	1140	6.5	175385	1542	15.00	47345
55	Tp¾-bd½-d24 -Cir	1	¾	½	24	258	289	370	3.7	100000	371	3.90	3784
56	Tp¾- bd 5/8-d24 -Cir	1	¾	5/8	24	258	289	490	4.5	108889	491	4.70	4051
57	Tp¾- bd¾-d24 -Cir	2	¾	¾	24	258	289	600	5.3	113208	604	6.10	4413
58	Tp¾-bd1-d24 -Cir	2	¾	1	24	258	289	650	5.3	122642	692	9.50	9948
59	Tp¾-bd1 1/8-d24 -Cir	2	¾	1 1/8	24	258	289	700	6	116667	778	13.00	11193
60	Tp¾-bd1¼-d24 -Cir	2	¾	1¼	24	258	289	800	6.1	131148	928	18.30	10495
61	Tp½-bd½-d24 -Cir	2	½	½	24	258	289	300	4	75000	300	4.20	2482
62	Tp½- bd 5/8-d24 -Cir	2	½	5/8	24	258	289	340	4.6	73913	341	4.80	3133
63	Tp½- bd¾-d24 -Cir	2	½	¾	24	258	289	390	5	78000	394	6.10	3893
64	Tp½-bd1-d24 -Cir	2	½	1	24	258	289	400	4.5	88889	450	11.00	7726
65	Tp½-bd1 1/8-d24 -Cir	2	½	1 1/8	24	258	289	420	5	84000	503	14.00	9201
66	Tp½-bd1¼-d24 -Cir	2	½	1¼	24	258	289	450	5	90000	594	18.20	10891
67	Tp1½-bd½-d36 -Cir	1	1½	½	36	439	509	590	2.7	218519	591	2.90	2911
68	Tp1½- bd 5/8-d36 -Cir	1	1½	5/8	36	439	509	800	3.5	228571	805	4.58	4524
69	Tp1½- bd¾-d36 -Cir	1	1½	¾	36	439	509	1050	4.1	256098	1067	5.83	10101
70	Tp1½-bd1-d36 -Cir	1	1½	1	36	439	509	1630	6	271667	1665	8.54	13766
71	Tp1½-bd1 1/8-d36 -Cir	1	1½	1 1/8	36	439	509	1750	6	291667	1881	11.80	22615
72	Tp1½-bd1¼-d36 -Cir	1	1½	1¼	36	439	509	1850	6	308333	2065	14.10	26603

Table 5-5 Continued

	Name	Category	Independent Variables					Dependent Variables					
			T_p (in)	b_d (in)	d (in)	S (in^3)	Z (in^3)	M_v (kip.ft)	θ_v 10^{-3}	E_v (ksi)	M_f (kip.ft)	θ_f 10^{-3}	E_t (ksi)
73	Tp1 1/8-bd½-d36 -Cir	1	1 1/8	½	36	439	509	560	3.2	175000	560	3.30	3590
74	Tp1 1/8- bd 5/8-d36 -Cir	1	1 1/8	5/8	36	439	509	750	4	187500	755	4.80	6758
75	Tp1 1/8- bd¾-d36 -Cir	1	1 1/8	¾	36	439	509	1050	4.8	218750	1059	6.20	6747
76	Tp1 1/8-bd1-d36 -Cir	1	1 1/8	1	36	439	509	1490	6.5	229231	1528	9.50	12625
77	Tp1 1/8-bd1 1/8-d36 -Cir	2	1 1/8	1 1/8	36	439	509	1600	6	266667	1681	11.00	16203
78	Tp1 1/8-bd1¼-d36 -Cir	2	1 1/8	1¼	36	439	509	1650	6	275000	1789	13.50	18493
79	Tp¾-bd½-d36 -Cir	1	¾	½	36	439	509	530	4	132500	531	4.20	3888
80	Tp¾- bd 5/8-d36 -Cir	1	¾	5/8	36	439	509	750	4.9	153061	750	5.00	4958
81	Tp¾- bd¾-d36 -Cir	2	¾	¾	36	439	509	870	4.5	193333	911	6.20	24344
82	Tp¾-bd1-d36 -Cir	2	¾	1	36	439	509	980	5.1	192157	1022	9.00	10696
83	Tp¾-bd1 1/8-d36 -Cir	2	¾	1 1/8	36	439	509	1100	5.6	196429	1179	11.90	12560
84	Tp¾-bd1¼-d36 -Cir	2	¾	1¼	36	439	509	1180	5.8	203448	1296	15.20	12308
85	Tp½-bd½-d36 -Cir	2	½	½	36	439	509	480	4	120000	482	4.20	11270
86	Tp½- bd 5/8-d36 -Cir	2	½	5/8	36	439	509	500	4	125000	516	4.40	40978
87	Tp½- bd¾-d36 -Cir	2	½	¾	36	439	509	510	4.3	118605	522	6.10	6437
88	Tp½-bd1-d36 -Cir	2	½	1	36	439	509	580	4	145000	625	9.20	8624
89	Tp½-bd1 1/8-d36 -Cir	2	½	1 1/8	36	439	509	600	4	150000	711	13.30	11949
90	Tp½-bd1¼-d36 -Cir	2	½	1¼	36	439	509	640	4	160000	852	18.30	14829

Table 5-6 Numerical Results Of The Models With Square Bolt Pattern

	Name	Category	Independent Variables					Dependent Variables					
			T_p (in)	b_d (in)	d (in)	S (in^3)	Z (in^3)	M_v (kip.ft)	θ_v 10^{-3}	E_v (ksi)	M_f (kip.ft)	θ_f 10^{-3}	E_t (ksi)
1	Tp1½-bd½-d30 -Sqr	1	1½	½	30	269	312	430	3.0	143333	431	3.5	2264
2	Tp1½- bd5/8-d30 -Sqr	1	1½	5/8	30	269	312	630	4.0	157500	633	4.7	4674
3	Tp1½- bd¾-d30 -Sqr	1	1½	¾	30	269	312	800	4.8	166667	812	6.5	6833
4	Tp1½-bd1-d30 -Sqr	1	1½	1	30	269	312	1050	5.6	187500	1084	8.0	14152
5	Tp1½-bd1 1/8-d30 -Sqr	1	1½	1 1/8	30	269	312	1100	5.8	189655	1202	11.8	16924
6	Tp1½-bd1¼-d30 -Sqr	1	1½	1¼	30	269	312	1270	5.7	222807	1423	14.0	18434
7	Tp1¼-bd½-d30 -Sqr	1	1¼	½	30	269	312	420	3.1	135484	421	3.4	2469
8	Tp1¼- bd5/8-d30 -Sqr	1	1¼	5/8	30	269	312	600	4.4	136364	602	4.9	4342
9	Tp1¼- bd¾-d30 -Sqr	1	1¼	¾	30	269	312	730	5.2	140385	734	5.8	6804
10	Tp1¼-bd1-d30 -Sqr	1	1¼	1	30	269	312	1040	6.1	170492	1081	9.7	11360
11	Tp1¼-bd1 1/8-d30 -Sqr	1	1¼	1 1/8	30	269	312	1100	6.0	183333	1178	12.0	12960
12	Tp1¼-bd1¼-d30 -Sqr	2	1¼	1¼	30	269	312	1250	6.7	186567	1344	16.0	10152
13	Tp1 1/8-bd½-d30 -Sqr	1	1 1/8	½	30	269	312	420	3.6	116667	421	4.1	2648
14	Tp1 1/8- bd5/8-d30 -Sqr	1	1 1/8	5/8	30	269	312	580	4.3	134884	583	4.9	4337
15	Tp1 1/8- bd¾-d30 -Sqr	1	1 1/8	¾	30	269	312	720	5.1	141176	725	5.8	6559
16	Tp1 1/8-bd1-d30 -Sqr	1	1 1/8	1	30	269	312	1000	6.1	163934	1024	8.9	8603
17	Tp1 1/8-bd1 1/8-d30 -Sqr	2	1 1/8	1 1/8	30	269	312	1050	6.6	159091	1109	12.4	10161
18	Tp1 1/8-bd1¼-d30 -Sqr	2	1 1/8	1¼	30	269	312	1130	6.7	168657	1239	17.8	9812
19	Tp1-bd½-d30 -Sqr	1	1	½	30	269	312	420	3.5	120000	421	4.1	1787
20	Tp1- bd5/8-d30 -Sqr	1	1	5/8	30	269	312	580	4.6	126087	581	5.1	2982
21	Tp1- bd¾-d30 -Sqr	1	1	¾	30	269	312	730	5.7	128070	734	6.5	5018
22	Tp1-bd1-d30 -Sqr	2	1	1	30	269	312	900	6.7	134328	944	12.0	8214
23	Tp1-bd1 1/8-d30 -Sqr	2	1	1 1/8	30	269	312	1030	6.7	153731	1090	14.0	8244
24	Tp1-bd1¼-d30 -Sqr	2	1	1¼	30	269	312	1050	6.7	156716	1173	19.3	9743

Table 5-6 Continued

	Name	Category	Independent Variables					Dependent Variables					
			T_p (in)	b_d (in)	d (in)	S (in^3)	Z (in^3)	M_y (kip.ft)	θ_y 10^{-3}	E_y (ksi)	M_f (kip.ft)	θ_f 10^{-3}	E_t (ksi)
25	Tp¾-bd½-d30 -Sqr	1	¾	½	30	269	312	350	3.8	92105	351	4.3	2394
26	Tp¾- bd5/8-d30 -Sqr	1	¾	5/8	30	269	312	500	5.1	98039	503	5.8	3619
27	Tp¾- bd¾-d30 -Sqr	2	¾	¾	30	269	312	600	6.0	100000	603	6.6	4967
28	Tp¾-bd1-d30 -Sqr	2	¾	1	30	269	312	730	6.2	117742	766	11.0	7416
29	Tp¾-bd1 1/8-d30 -Sqr	2	¾	1 1/8	30	269	312	780	6.3	123810	847	14.1	8561
30	Tp¾-bd1¼-d30 -Sqr	2	¾	1¼	30	269	312	840	6.6	127273	956	19.0	9338
31	Tp5/8-bd½-d30 -Sqr	1	5/8	½	30	269	312	330	4.1	80488	332	4.9	2473
32	Tp5/8- bd5/8-d30 -Sqr	2	5/8	5/8	30	269	312	430	4.9	87755	431	5.3	3317
33	Tp5/8- bd¾-d30 -Sqr	2	5/8	¾	30	269	312	520	5.9	88136	525	7.0	4386
34	Tp5/8-bd1-d30 -Sqr	2	5/8	1	30	269	312	610	6.1	100000	656	13.0	6596
35	Tp5/8bd1 1/8-d30 -Sqr	2	5/8	1 1/8	30	269	312	630	6.2	101613	694	13.8	8403
36	Tp5/8-bd1¼-d30 -Sqr	2	5/8	1¼	30	269	312	630	6.1	103279	769	19.0	10804
37	Tp½-bd½-d30 -Sqr	2	½	½	30	269	312	280	4.2	66667	280	4.4	2312
38	Tp½- bd5/8-d30 -Sqr	2	½	5/8	30	269	312	310	4.3	72093	312	4.8	3793
39	Tp½- bd¾-d30 -Sqr	2	½	¾	30	269	312	360	5.0	72000	368	6.7	4875
40	Tp½-bd1-d30 -Sqr	2	½	1	30	269	312	440	5.1	86275	481	11.2	6705
41	Tp½-bd1 1/8-d30 -Sqr	2	½	1 1/8	30	269	312	460	5.2	88462	531	13.5	8571
42	Tp½-bd1¼-d30 -Sqr	2	½	1¼	30	269	312	500	5.5	90909	625	18.0	9993
43	Tp1½-bd½-d24 -Sqr	1	1½	½	24	258	289	390	2.8	139286	390	2.9	2587
44	Tp1½- bd5/8-d24 -Sqr	1	1½	5/8	24	258	289	520	3.6	144444	521	3.8	4111
45	Tp1½- bd¾-d24-Sqr	1	1½	¾	24	258	289	700	4.5	155556	700	4.6	6274
46	Tp1½-bd1-d24-Sqr	1	1½	1	24	258	289	940	5.7	164912	950	6.5	13096
47	Tp1½-bd1 1/8-d24 -Sqr	1	1½	1 1/8	24	258	289	1000	5.3	188679	1046	7.6	19457
48	Tp1½-bd1¼-d24 -Sqr	1	1½	1¼	24	258	289	1120	6.3	177778	1176	9.7	16580

Table 5-6 Continued

	Name	Category	Independent Variables					Dependent Variables					
			T_p (in)	b_d (in)	d (in)	S (in^3)	Z (in^3)	M_y (kip.ft)	θ_y 10^{-3}	E_y (ksi)	M_f (kip.ft)	θ_f 10^{-3}	E_t (ksi)
49	Tp1¼-bd½-d24 -Sqr	1	1¼	½	24	258	289	350	2.8	125000	350	2.9	3169
50	Tp1¼- bd5/8-d24 -Sqr	1	1¼	5/8	24	258	289	480	3.5	137143	481	3.7	4775
51	Tp1¼- bd¾-d24 -Sqr	1	1¼	¾	24	258	289	650	4.8	135417	658	6.0	6351
52	Tp1¼-bd1-d24 -Sqr	1	1¼	1	24	258	289	900	5.6	160714	915	7.0	10430
53	Tp1¼-bd1 1/8-d24 -Sqr	1	1¼	1 1/8	24	258	289	1000	6.2	161290	1028	9.5	8641
54	Tp1¼-bd1¼-d24 -Sqr	2	1¼	1¼	24	258	289	1110	6.5	170769	1209	11.2	21286
55	Tp1 1/8-bd½-d24 -Sqr	1	1 1/8	½	24	258	289	350	2.9	120690	351	3.1	3048
56	Tp1 1/8- bd5/8-d24 -Sqr	1	1 1/8	5/8	24	258	289	530	3.9	136598	531	4.1	2764
57	Tp1 1/8- bd¾-d24 -Sqr	1	1 1/8	¾	24	258	289	650	4.8	135417	652	5.2	4644
58	Tp1 1/8-bd1-d24 -Sqr	1	1 1/8	1	24	258	289	800	5.5	145455	807	6.1	10625
59	Tp1 1/8-bd1 1/8-d24 -Sqr	2	1 1/8	1 1/8	24	258	289	980	6.0	163333	1036	11.4	10441
60	Tp1 1/8-bd1¼-d24 -Sqr	2	1 1/8	1¼	24	258	289	1000	6.4	156250	1072	12.6	11522
61	Tp¾-bd½-d24 -Sqr	1	¾	½	24	258	289	320	3.3	96970	320	3.4	1353
62	Tp¾- bd5/8-d24 -Sqr	1	¾	5/8	24	258	289	400	3.8	105263	401	4.0	3093
63	Tp¾- bd¾-d24 -Sqr	2	¾	¾	24	258	289	500	4.5	111111	503	5.3	4026
64	Tp¾-bd1-d24 -Sqr	2	¾	1	24	258	289	610	5.0	122000	631	8.1	6847
65	Tp¾-bd1 1/8-d24 -Sqr	2	¾	1 1/8	24	258	289	640	5.5	116364	689	11.5	8204
66	Tp¾-bd1¼-d24 -Sqr	2	¾	1¼	24	258	289	750	5.8	129310	834	16.6	7756
67	Tp½-bd½-d24 -Sqr	2	½	½	24	258	289						
68	Tp½- bd5/8-d24 -Sqr	2	½	5/8	24	258	289	300	4.1	73171	301	4.3	2660
69	Tp½- bd¾-d24 -Sqr	2	½	¾	24	258	289	350	4.5	77778	352	5.3	2934
70	Tp½-bd1-d24 -Sqr	2	½	1	24	258	289	390	4.5	86667	420	10.1	5410
71	Tp½-bd1 1/8-d24 -Sqr	2	½	1 1/8	24	258	289	410	4.9	83673	462	13.1	6364
72	Tp½-bd1¼-d24 -Sqr	2	½	1¼	24	258	289	440	5.0	88000	531	17.2	7471

Table 5-6 Continued

	Name	Category	Independent Variables					Dependent Variables					
			T_p (in)	b_d (in)	d (in)	S (in^3)	Z (in^3)	M_v (kip.ft)	θ_v 10^{-3}	E_v (ksi)	M_f (kip.ft)	θ_f 10^{-3}	E_f (ksi)
49	Tp1¼-bd½-d24 -Sqr	1	1¼	½	24	258	289	350	2.8	125000	350	2.9	3169
50	Tp1¼- bd5/8-d24 -Sqr	1	1¼	5/8	24	258	289	480	3.5	137143	481	3.7	4775
51	Tp1¼- bd¾-d24 -Sqr	1	1¼	¾	24	258	289	650	4.8	135417	658	6.0	6351
52	Tp1¼-bd1-d24 -Sqr	1	1¼	1	24	258	289	900	5.6	160714	915	7.0	10430
53	Tp1¼-bd1 1/8-d24 -Sqr	1	1¼	1 1/8	24	258	289	1000	6.2	161290	1028	9.5	8641
54	Tp1¼-bd1¼-d24 -Sqr	2	1¼	1¼	24	258	289	1110	6.5	170769	1209	11.2	21286
55	Tp1 1/8-bd½-d24 -Sqr	1	1 1/8	½	24	258	289	350	2.9	120690	351	3.1	3048
56	Tp1 1/8- bd5/8-d24 -Sqr	1	1 1/8	5/8	24	258	289	530	3.9	136598	531	4.1	2764
57	Tp1 1/8- bd¾-d24 -Sqr	1	1 1/8	¾	24	258	289	650	4.8	135417	652	5.2	4644
58	Tp1 1/8-bd1-d24 -Sqr	1	1 1/8	1	24	258	289	800	5.5	145455	807	6.1	10625
59	Tp1 1/8-bd1 1/8-d24 -Sqr	2	1 1/8	1 1/8	24	258	289	980	6.0	163333	1036	11.4	10441
60	Tp1 1/8-bd1¼-d24 -Sqr	2	1 1/8	1¼	24	258	289	1000	6.4	156250	1072	12.6	11522
61	Tp¾-bd½-d24 -Sqr	1	¾	½	24	258	289	320	3.3	96970	320	3.4	1353
62	Tp¾- bd5/8-d24 -Sqr	1	¾	5/8	24	258	289	400	3.8	105263	401	4.0	3093
63	Tp¾- bd¾-d24 -Sqr	2	¾	¾	24	258	289	500	4.5	111111	503	5.3	4026
64	Tp¾-bd1-d24 -Sqr	2	¾	1	24	258	289	610	5.0	122000	631	8.1	6847
65	Tp¾-bd1 1/8-d24 -Sqr	2	¾	1 1/8	24	258	289	640	5.5	116364	689	11.5	8204
66	Tp¾-bd1¼-d24 -Sqr	2	¾	1¼	24	258	289	750	5.8	129310	834	16.6	7756
67	Tp½-bd½-d24 -Sqr	2	½	½	24	258	289						
68	Tp½- bd5/8-d24 -Sqr	2	½	5/8	24	258	289	300	4.1	73171	301	4.3	2660
69	Tp½- bd¾-d24 -Sqr	2	½	¾	24	258	289	350	4.5	77778	352	5.3	2934
70	Tp½-bd1-d24 -Sqr	2	½	1	24	258	289	390	4.5	86667	420	10.1	5410
71	Tp½-bd1 1/8-d24 -Sqr	2	½	1 1/8	24	258	289	410	4.9	83673	462	13.1	6364
72	Tp½-bd1¼-d24 -Sqr	2	½	1¼	24	258	289	440	5.0	88000	531	17.2	7471

Table 5-7 Summary Of The Results And Percentage Variation

	Name	M_y (kip.ft)			E_y (ksi)			E_t (ksi)			θ_f 10^{-3}			Energy Dissipation (kip.in)		
		Cir	Sqr	% variation	Cir	Sqr	% variation	Cir	Sqr	% variation	Cir	Sqr	% variation	Cir	Sqr	% variation
1	Tp1½-bd½-d30	450	430	4.7	150000	143333	4.7	3238	2264	43.0	4.47	3.50	27.8	15.68	6.06	159.0
2	Tp1½-bd$^5/_8$-d30	650	630	3.2	171053	157500	8.6	5823	4674	24.6	6.24	4.70	32.8	36.40	12.24	197.4
3	Tp1½-bd¾-d30	830	800	3.8	184444	166667	10.7	7615	6833	11.4	8.42	6.50	29.6	72.48	36.01	101.3
4	Tp1½-bd1-d30	1170	1050	11.4	229412	187500	22.4	18201	14152	28.6	10.74	8.00	34.3	168.91	70.65	139.1
5	Tp1½-bd1$^1/_8$-d30	1190	1100	8.2	216364	189655	14.1	22363	16924	32.1	14.58	11.80	23.5	276.34	185.88	48.7
6	Tp1½-bd1¼-d30	1320	1270	3.9	264000	222807	18.5	29808	18434	61.7	17.11	14.00	22.2	417.69	301.72	38.4
7	Tp1¼-bd½-d30	430	420	2.4	143333	135484	5.8	3420	2469	38.5	4.05	3.40	19.2	10.95	3.61	203.6
8	Tp1¼- bd$^5/_8$-d30	630	600	5.0	150000	136364	10.0	5176	4342	19.2	5.75	4.90	17.4	23.36	8.44	176.9
9	Tp1¼- bd¾-d30	780	730	6.8	156000	140385	11.1	7585	6804	11.5	7.36	5.80	26.8	42.68	12.11	252.3
10	Tp1¼-bd1-d30	1080	1040	3.8	180000	170492	5.6	12806	11360	12.7	12.20	9.70	25.8	171.99	106.21	61.9
11	Tp1¼-bd1$^1/_8$-d30	1130	1100	2.7	194828	183333	6.3	16175	12960	24.8	14.69	12.00	22.4	259.20	188.34	37.6
12	Tp1¼-bd1¼-d30	1300	1250	4.0	209677	186567	12.4	12273	10152	20.9	18.74	16.00	17.1	430.75	338.08	27.4
13	Tp1$^1/_8$-bd½-d30	430	420	2.4	122857	116667	5.3	3719	2648	40.5	4.77	4.10	16.3	13.10	5.92	121.4
14	Tp1$^1/_8$- bd$^5/_8$-d30	600	580	3.4	146341	134884	8.5	4520	4337	4.2	5.76	4.90	17.5	23.66	9.72	143.4
15	Tp1$^1/_8$- bd¾-d30	750	720	4.2	150000	141176	6.3	7490	6559	14.2	7.59	5.80	30.9	44.77	13.89	222.3
16	Tp1$^1/_8$-bd1-d30	1020	1000	2.0	170000	163934	3.7	11853	8603	37.8	11.29	8.90	26.9	138.33	80.23	72.4
17	Tp1$^1/_8$-bd1$^1/_8$-d30	1090	1050	3.8	167692	159091	5.4	12596	10161	24.0	14.90	12.40	20.2	236.08	174.23	35.5
18	Tp1$^1/_8$-bd1¼-d30	1180	1130	4.4	181538	168657	7.6	11562	9812	17.8	20.36	17.80	14.4	432.02	365.78	18.1
19	Tp1-bd½-d30	430	420	2.4	122857	120000	2.4	3564	1787	99.4	4.76	4.10	16.1	13.02	7.10	83.5
20	Tp1- bd$^5/_8$-d30	600	580	3.4	133333	126087	5.7	4559	2982	52.9	6.16	5.10	20.8	23.80	8.23	189.2
21	Tp1- bd¾-d30	750	730	2.7	136364	128070	6.5	6814	5018	35.8	7.74	6.50	19.2	39.46	16.20	143.6
22	Tp1-bd1-d30	1040	900	15.6	148571	134328	10.6	8401	8993	6.6	14.26	12.00	18.8	196.03	136.52	43.6
23	Tp1-bd1$^1/_8$-d30	1050	1030	1.9	161538	153731	5.1	10506	8244	27.4	16.36	14.00	16.9	270.03	217.63	24.1
24	Tp1-bd1¼-d30	1100	1050	4.8	169231	156716	8.0	13248	9743	36.0	21.88	19.30	13.3	446.90	386.73	15.6

Table 5-7 Continued

	Name	M_y (kip.ft)			E_y (ksi)			E_t (ksi)			θ_f 10^{-3}			Energy Dissipation (kip.in)		
		Cir	Sqr	% variation	Cir	Sqr	% variation	Cir	Sqr	% variation	Cir	Sqr	% variation	Cir	Sqr	% variation
25	Tp¾-bd½-d30	370	350	5.7	92500	92105	0.4	3077	2394	28.5	5.03	4.30	16.9	9.28	4.93	88.4
26	Tp¾- bd$^5/_8$-d30	530	500	6.0	106000	98039	8.1	4465	3619	23.4	6.74	5.80	16.2	21.95	9.74	125.4
27	Tp¾- bd¾-d30	670	600	11.7	111667	100000	11.7	5038	4967	1.4	8.10	6.60	22.7	33.41	9.98	234.6
28	Tp¾-bd1-d30	750	730	2.7	120968	117742	2.7	8712	7416	17.5	12.88	11.00	17.0	128.68	100.10	28.5
29	Tp¾-bd1$^1/_8$-d30	800	780	2.6	129032	123810	4.2	11008	8561	28.6	16.20	14.10	14.9	206.54	174.75	18.2
30	Tp¾-bd1¼-d30	850	840	1.2	130769	127273	2.7	12143	9338	30.0	21.22	19.00	11.7	327.94	302.86	8.3
31	Tp$^5/_8$-bd½-d30	380	330	15.2	84444	80488	4.9	3251	2473	31.5	5.75	4.90	17.4	11.54	7.29	58.3
32	Tp$^5/_8$- bd$^5/_8$-d30	500	430	16.3	96154	87755	9.6	3391	3317	2.2	6.41	5.30	20.9	14.80	4.85	205.2
33	Tp$^5/_8$- bd¾-d30	550	520	5.8	96491	88136	9.5	4872	4386	11.1	8.30	7.00	18.5	33.22	15.54	113.8
34	Tp$^5/_8$-bd1-d30	630	610	3.3	105000	100000	5.0	7419	6596	12.5	14.57	13.00	12.1	140.07	120.87	15.9
35	Tp$^5/_8$-bd1$^1/_8$-d30	640	630	1.6	106667	101613	5.0	9218	8403	9.7	15.54	13.80	12.6	157.50	136.21	15.6
36	Tp$^5/_8$-bd1¼-d30	650	630	3.2	108333	103279	4.9	11533	10804	6.8	20.91	19.00	10.0	254.36	234.40	8.5
37	Tp½-bd½-d30	300	280	7.1	73171	66667	9.8	2444	2312	5.7	5.00	4.40	13.7	6.68	2.00	234.1
38	Tp½- bd$^5/_8$-d30	330	310	6.5	78571	72093	9.0	4186	3793	10.4	5.72	4.80	19.1	11.80	4.27	176.5
39	Tp½- bd¾-d30	370	360	2.8	78723	72000	9.3	4957	4875	1.7	7.69	6.67	15.3	24.90	15.61	59.5
40	Tp½-bd1-d30	450	440	2.3	88235	86275	2.3	7144	6705	6.5	12.53	11.20	11.9	86.24	76.56	12.6
41	Tp½-bd1$^1/_8$-d30	470	460	2.2	94000	88462	6.3	9601	8571	12.0	14.99	13.47	11.3	121.63	108.36	12.2
42	Tp½-bd1¼-d30	510	500	2.0	94444	90909	3.9	11065	9993	10.7	19.68	18.00	9.3	191.50	180.79	5.9
43	Tp1½-bd½-d24	420	390	7.7	150000	139285	7.7	2763	2587	6.8	3.00	2.90	3.4	2.18	1.35	61.9
44	Tp1½- bd$^5/_8$-d24	560	520	7.7	160000	144444	10.8	4479	4111	8.9	3.80	3.80	0.0	4.3	2.98	44.2
45	Tp1½- bd¾-d24	780	700	11.4	185714	155556	19.4	6349	6373	1.2	4.60	4.50	1.1	7.92	4.73	67.5
46	Tp1½-bd1-d24	950	940	1.1	211111	164912	28.0	16563	13096	26.5	7.20	6.50	10.8	180.83	106.06	70.5
47	Tp1½-bd1$^1/_8$-d24	1090	1000	9.0	222449	188679	17.9	21525	19457	10.6	10.00	7.64	30.8	205.12	125.69	63.2
48	Tp1½-bd1¼-d24	1200	1120	7.1	181818	177778	2.3	20810	16580	25.5	12.30	9.70	26.7	212.52	132.66	60.2

Table 5-7 Continued

	Name	M_y (kip.ft)			E_y (ksi)			E_t (ksi)			θ_f 10^{-3}			Energy Dissipation (kip.in)		
		Cir	Sqr	% variation	Cir	Sqr	% variation	Cir	Sqr	% variation	Cir	Sqr	% variation	Cir	Sqr	% variation
49	Tp1 1/8-bd½-d24	430	350	22.9	122857	120690	1.8	3966	3048	30.1	3.80	3.10	22.6	3.29	2.01	64.0
50	Tp1 1/8- bd 5/8-d24	550	530	3.8	137500	136597	0.7	4236	2763	53.3	4.30	4.10	4.8	4.22	3.37	25.4
51	Tp1 1/8- bd¾-d24	770	650	18.5	160417	135417	18.5	6864	4644	47.8	5.40	5.20	3.8	11.54	7.35	56.9
52	Tp1 1/8-bd1-d24	1000	800	25.0	166667	145455	14.6	11359	10625	6.9	8.30	6.14	35.2	120.50	66.67	80.7
53	Tp1 1/8-bd1 1/8-d24	1040	980	6.1	165079	163333	1.1	10639	10440	1.9	13.60	11.35	19.8	196.55	150.05	31.0
54	Tp1 1/8-bd1¼-d24	1100	1000	10.0	157143	156250	0.6	30998	11522	169.0	15.00	12.62	18.9	205.06	176.99	15.9
55	Tp¾-bd½-d24	370	320	15.6	100000	96970	3.1	2960	1353	118.7	3.90	3.40	14.7	1.91	0.94	103.5
56	Tp¾- bd 5/8-d24	490	400	22.5	108889	105263	3.4	3779	3093	22.2	4.70	4.00	17.5	2.52	2.29	9.9
57	Tp¾- bd¾-d24	600	500	20.0	113208	111111	1.9	4413	4026	9.6	6.10	5.3	15.1	11.95	11.03	8.4
58	Tp¾-bd1-d24	650	610	6.6	122642	122000	0.5	7719	6847	12.7	9.50	8.09	17.4	70.22	54.06	29.9
59	Tp¾-bd1 1/8-d24	700	640	9.4	116667	116364	0.3	9109	8204	11.0	13.00	11.49	13.2	125.67	109.56	14.7
60	Tp¾-bd1¼-d24	800	750	6.7	131148	129310	1.4	8081	7755	4.2	18.30	16.57	10.4	257.44	236.24	9.0
61	Tp½-bd½-d24	300			75000			2176			4.20			1.55		
62	Tp½- bd 5/8-d24	340	300	13.3	73913	73170	1.0	2846	2659	7.0	4.80	4.70	11.6	1.74	1.71	1.9
63	Tp½- bd¾-d24	390	350	11.4	78000	77777	0.3	3035	2934	3.4	6.10	5.26	16.0	10.52	10.07	4.4
64	Tp½-bd1-d24	400	390	2.6	88889	86667	2.6	6037	5410	11.6	11.00	10.13	8.5	67.57	63.42	6.5
65	Tp½-bd1 1/8-d24	420	410	2.4	84000	83673	0.4	7165	6364	12.6	14.00	13.09	6.9	98.13	97.04	1.1
66	Tp½-bd1¼-d24	450	440	2.3	90000	88000	2.3	8476	7471	13.5	18.20	17.23	5.6	157.32	157.91	0.4
67	Tp1½-bd½-d36	590			218519			3993			2.90			3.06		
68	Tp1½- bd 5/8-d36	800	750	6.7	228571	214286	6.7	6287	6270	0.3	4.58	3.80	20.5	21.01	10.39	102.2
69	Tp1½- bd¾-d36	1050	1030	1.9	256098	245238	4.4	12415	9679	28.3	5.83	4.90	19.0	42.53	19.87	114.1
70	Tp1½-bd1-d36	1630	1520	7.2	271667	271428	0.1	16969	15747	7.8	8.54	6.70	27.5	105.73	47.43	122.9
71	Tp1½-bd1 1/8-d36	1750	1650	6.1	291667	279661	4.3	28022	20828	34.5	11.80	8.02	47.2	255.39	97.76	161.2
72	Tp1½-bd1¼-d36	1850	1700	8.8	308333	293103	5.2	33180	22843	45.3	14.10	10.10	39.6	378.54	206.04	83.7

Table 5-7 Continued

	Name	M_y (kip.ft)			E_y (ksi)			E_t (ksi)			θ_f 10^{-3}			Energy Dissipation (kip.in)		
		Cir	Sqr	% variation	Cir	Sqr	% variation	Cir	Sqr	% variation	Cir	Sqr	% variation	Cir	Sqr	% variation
73	Tp1 1/8-bd½-d36	560	540	3.7	175000	174193	0.5	4377	4273	2.4	3.30	3.20	3.12	1.46	1.56	6.7
74	Tp1 1/8- bd 5/8-d36	750	740	1.4	187500	185000	1.4	6964	6607	5.4	4.80	4.30	11.62	14.80	6.28	135.5
75	Tp1 1/8- bd¾-d36	1050	1000	5.0	218750	208333	5.0	8271	8207	0.8	6.20	5.30	17.0	35.54	13.99	154.0
76	Tp1 1/8-bd1-d36	1490	1350	10.4	229231	228814	0.2	15563	11230	38.6	9.50	6.80	39.7	113.67	34.75	227.1
77	Tp1 1/8-bd1 1/8-d36	1600	1400	14.3	266667	254545	4.8	19972	14987	33.3	11.00	7.54	45.9	203.98	81.20	151.2
78	Tp1 1/8-bd1¼-d36	1650	1500	10.0	275000	250000	10.0	22849	15922	43.5	13.50	11.00	22.7	316.97	214.40	47.8
79	Tp¾-bd½-d36	530	490	8.2	132500	128947	2.8	3542	3537	43.5	4.30	4.10	4.8	4.39	4.19	4.7
80	Tp¾- bd 5/8-d36	750	650	15.4	151162	144737	1.3	4958	4804	0.1	5.50	4.80	14.5	11.36	9.13	24.3
81	Tp¾- bd¾-d36	870	700	24.3	193333	184211	5.0	24344	8101	200.5	6.20	4.32	43.6	32.57	10.03	224.8
82	Tp¾-bd1-d36	980	870	12.6	192157	189130	1.6	13071	12376	5.6	9.00	6.88	30.8	97.84	56.23	74.0
83	Tp¾-bd1 1/8-d36	1100	980	12.2	196429	192157	2.2	15387	11387	35.1	11.90	9.52	25.0	177.52	124.36	42.7
84	Tp¾-bd1¼-d36	1180	1000	18.0	203448	200000	1.7	15036	13300	13.0	15.20	12.65	20.2	288.42	221.44	30.2
85	Tp½-bd½-d36	480			120000			11270			4.20			2.32		
86	Tp½- bd 5/8-d36	500			125000			40978			4.40			3.59		
87	Tp½- bd¾-d36	510	450	13.3	118605	118421	0.2	7863	7636	3.0	6.10	5.00	22.1	21.19	14.07	50.6
88	Tp½-bd1-d36	580	550	5.5	145000	134146	8.1	10487	8416	24.6	9.20	7.95	15.8	77.91	60.64	28.5
89	Tp½-bd1 1/8-d36	600	580	3.4	150000	138095	8.6	14535	10093	44.0	13.30	12.00	10.8	146.28	131.53	11.2
90	Tp½-bd1¼-d36	640	620	3.2	160000	158974	0.6	18101	17710	2.2	18.30	16.92	8.2	248.69	241.78	2.9

5.6 Development Of Hysteresis Model Equation

5.6.1 Basis Of Hysteresis Development

The scope of this section is to summarized the different classifications and methods developed and defined in this research to assist the designer to use a proper set of equations and hysteresis models while predicting the outer envelope hysteresis characteristic and consequently the energy dissipation of the extended end-plate connections. The summery of this section is presented in flowchart format in Figure 5.8 This flowchart also can be implemented in the design software for more sophisticated design procedures in the future.

The “condition” presented in Row-1 of this flowchart, indicated if the hysteresis behavior of the connection with circular or square bolt pattern is been simulated.

Nonlinear regression analyses were performed to develop the dependent parameters required to simulate the hysteresis behavior of the connection. These results are elaborated in detail in Section 5-6-3. To increase the accuracy of the regression analysis and reduce the error in predicting the dependent parameters, the numeric models are divided into two sub-categories based on the relation between the end-plate thickness, and bolt diameter. The definitions of these two categories are also provided in Section 5-6-3. The conditions presented in the Row-2 of the flowchart assist the engineer to use a proper category, Category-1 or Category-2, while simulating the hysteresis behavior of the connection.

Also, as it was presented in Section 5.4, the hysteresis behaviors of the models were divided into two sub-categories; “*End-Plate Behavior*”, and “*Bolt Behavior*”. The threshold between these two hysteresis behavior was defined by the bolt diameter. This condition is implemented in the Row-3 of the flowchart.

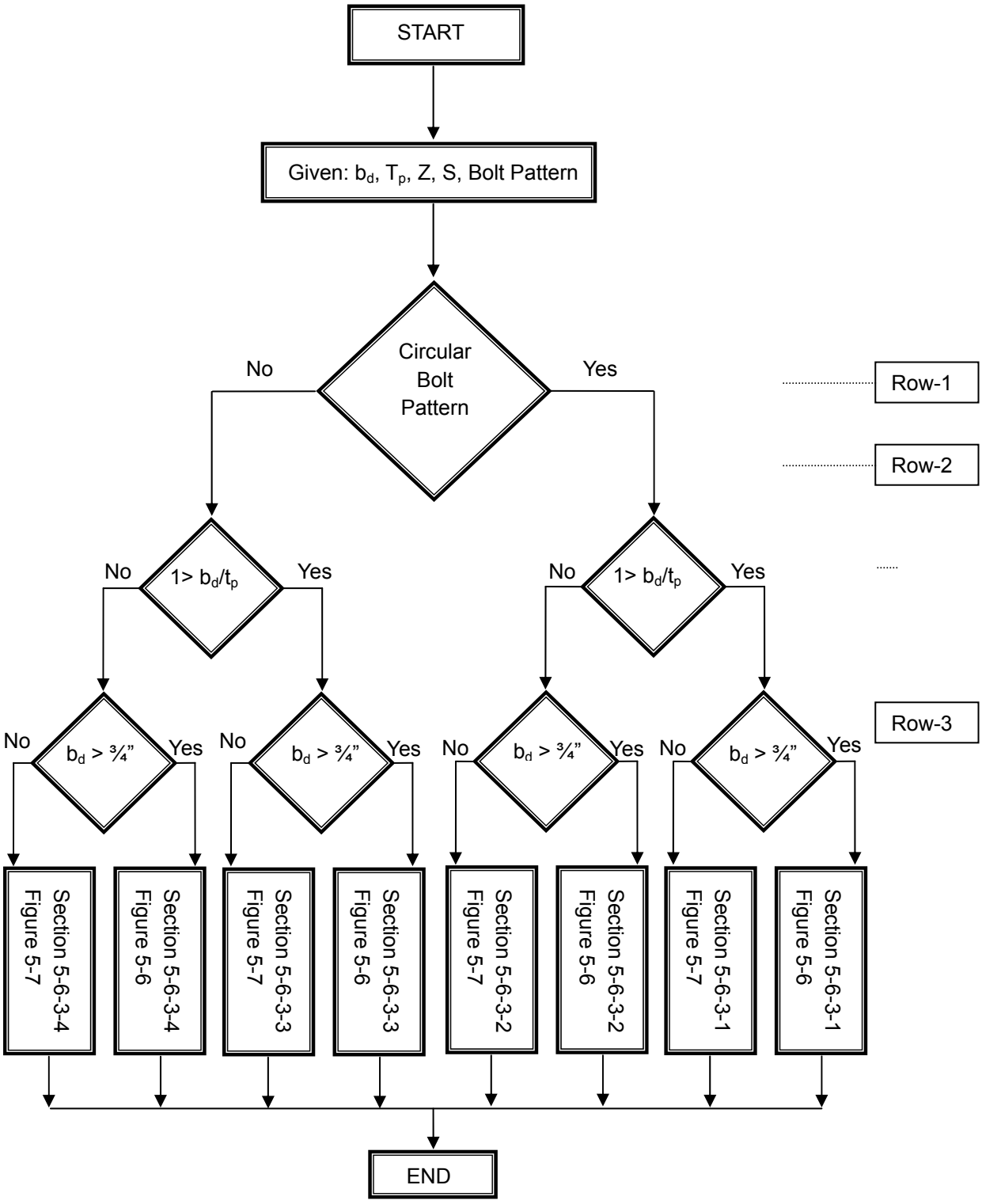

Figure 5-8 Flowchart For Simulation Of The Hysteresis Behavior Of The Extended End-Plate Connections.

5.6.2 Basis Of Regression Analysis

To develop a numerical model for the hysteresis behavior of the extended end-plate connections, the nonlinear regression equations are developed using the data collected from finite element analysis. To model the hysteresis of the connections, it is important to accurately predicting the value of four parameters. These parameters are selected as the moment capacity of the connection at yield (M_y), the initial stiffness of the connection (E), the post yielding stiffness of the connection (E_t), and the maximum rotation of the end-plate at the fracture of the bolt (θ_f). These parameters can be used to calculate the value of the moment capacity of the connection at fracture (M_f), and the rotation of the end-plate at yield (θ_y). These parameters are presented in Figures 5-6 and 5-7.

Non-linear regression analysis was performed to obtain prediction equations for dependent parameters as functions of independent variables. The dependent variables are defined as parameters defining the outer loop of moment-rotation hysteresis model and the independent variables are geometric variables of the connection assembly.

Thus, the dependent variables are:

$$\begin{cases} M_y = f(b_d, t_p, S) \\ E = f(b_d, t_p, S) \\ E_t = f(b_d, t_p, Z) \\ \theta_y = f(b_d, t_p, S, Z) \end{cases} \quad (5.1)$$

Determination of the function *f(x)* is discussed in general terms as follows. Let

$$x = f(X_1, X_2, X_3, \ldots\ldots\ldots\ldots X_n) \quad (5.2)$$

be a function of n independent parameters, intended to fit data collected from a study. A linear (or summation) regression model for the function is written as

$$x = C_0 + C_1X_1 + C_2\ X_2 + C_3X_3 + \ldots\ldots\ldots\ldots\ldots + C_nX_n + C_{12}X_1X_2$$

$$+ C_{23}X_2X_3 + \ldots\ldots\ldots + C_{n1}X_nX_1 + C_{123}X_1X_2X_3 + \ldots\ldots\ldots\ldots$$

$$+ C_{123\ldots\ldots n}(X_1X_2X_3\ldots\ldots\ldots\ldots\ldots\ldots X_n) \quad (5.3)$$

These techniques yield information on the relative significance of not only the main parameters $X_1, X_2, ..., X_n$, but also the interactions between the same parameters $X_1X_2X_3, ..., (X_1X_2...X_n)$. However, in most practical problems, such as the one studied, many of the higher-order interactions may be eliminated on the basis of physical and intuitive considerations. Probable interactions must, however, be included in the model. The behavior of the extended end-plate connection seems to be a simple solution considering the cantilever profile of the member, but there are many more parameters that can be considered in an analytical study and regression analysis. For example, bolt diameter, end-plate thickness, column flange thickness, beam depth, and many other parameters can be contributing in the connection behavior. This possibility makes this type of an analytical study and regression analysis a complex and interesting study, but does not facilitate the complete defining of all the interactions.

If a linear regression model is not found satisfactory, an alternative method is the product regression model of the form:

$$x = C_0 X_1^{C_1} X_2^{C_2} ... X_n^{C_n} \quad (5.4)$$

This nonlinear regression method was used in this project because of the complexity of the interactions involved. This may be reduced to a linear regression model if the logarithms are taken off from both sides as shown below:

$$\ln x = \ln C_0 + C_1 \ln X_1 + C_2 X_2 + ... + C_n \ln X_n \quad (5.5)$$

Denoting the logarithms of the various parameters by prime superscripts, Equation 5.5 becomes:

$$x' = C_0' + C_1 X_1' + C_2 X_2' + ... + C_n X_n' \quad (5.6)$$

This is similar to the first group of terms in Equation 5.3. It should be noted that in Equation 5.6, product terms of the form X_1', X_2', X_3', etc., do not occur, so no interactions are present.

In this study, the coefficient C_0' and the exponents $C_1, C_2, ..., C_n$ in Equation 5.5 are determined by multiple regression analysis, so as to obtain the best least square fit to the data. With this method, the best fit regression equation is taken as the one which minimizes the sum of the squares of the deviations of the data points from the equation fit to the data. To demonstrate the basic principles, say that the value

of the dependent variable predicted from the best fit equation is x_i', for any particular set of values, $X_{li}', X_{2i}', X_{3i}', ..., X_{ni}'$, while it is measured (or directly determined) that the value is $\bar{X}_i$. Deviation of the predicted value from the measured value is given by:

$$\bar{x}_i - x_i' = \bar{x}_i - \left(C_0' + C_1 x_{1i}' + C_2 x_{2i}' + ... + C_n x_{ni}'\right) \quad (5.7)$$

The sum of the squares, S for m number of data is given by:

$$S = \sum_{i=1}^{m} \left(\bar{x}_i' - x_i'\right)^2 \quad (5.8)$$

The unknown coefficients $C_0', C_1, C_2, ..., C_n$ are determined by minimizing the quality S with respect to each coefficient; in other words, by setting it equal to zero, as shown below.

$$\frac{\partial S}{\partial C_0'} = \frac{\partial S}{\partial C_1} = \frac{\partial S}{\partial C_2} = ... = \frac{\partial S}{\partial C_n} = 0 \quad (5.9)$$

This will result in $(n+1)$ linear simultaneous equations from which the coefficients $C_0', C_1, C_2, ..., C_n$ can be determined. To determine C_0, the anti-logarithm of C_0' must be found.

A "goodness of fit" of the prediction equation is a comparison of S, the sum of the squares, and the deviations for the constant term C_0 above. The constant term model is:

$$S = C_0' \quad (5.10)$$

and the sum of the squares of this model can be written as

$$S_0 = \sum_{i=1}^{m} \left(\bar{x}_i' - x_0'\right)^2 \quad (5.11)$$

in which x_0' is the mean. The difference between S_0 and S is called as the "sum of squares due to regression" and the ratio $\frac{(S_0 - S)}{S_0}$ is called as the "coefficient of multiple determination," R^2 which can also be written:

$$R^2 = 1 - \frac{S}{S_0} \quad (5.12)$$

A value of $R^2 = 1$ implies that S is zero and the regression prediction equation passes through all the data points. A value of $R^2 = 0.90$ means that 90 % of the sum of squares of the deviations of the observed (or directly determined) $\overline{x}_i'$ values about their x_0' can be explained by the prediction equation obtained.

In the parametric study conducted, all the cases considered had the independent parameters inputted into the finite element computer program, ABAQUS, and the output was the response of the dependent variables. The coefficient of multiple determination value R^2 was the unique criterion used to measure the accuracy of the prediction equations to characterize the hysteresis behavior of the connection.

5.6.3 Equations Of Hysteresis Behavior

The nonlinear regression analysis was used to derive a set of equations to model the hysteresis behavior of the connections with circular bolt pattern configuration. To increase the accuracy of the regression analysis and reduce the error in the prediction of the dependent variables, the numeric models are divided into two sub-categories as below,

Category-1: Models with an end-plate thickness greater than the bolt diameter, $t_p/b_d > 1$,

Categoty-2: Models with an end-plate thickness smaller than the bolt diameter, $t_p/b_d \leq 1$.

The categories of each connection are indicated in Tables 5-5 and 5-6 for models with circular and square bolt pattern, respectively.

The empirical equation for four parameters M_y, E, E_t, and θ_f was developed by conducting the non-linear regression analyses. This is accomplished by multiplication of the undetermined powers for all the geometric parameters. It simply implies that the changes in these geometric parameters are independent to each other thus, they are independent variables. The aforementioned empirical equations for the M_y, E, E_t, and θ_f of the connections with circular bolt pattern are presented in Equations 5-13 through 5-20. Also the empirical equations for these dependent parameters for the connections with square bolt pattern configuration are presented in Equations 5.21 through 5.28.

5-6-3-1 The prediction equations for Category-1 connections with circular bolt pattern, $\boldsymbol{t_p/b_d} > 1$:

The prediction equations for the Category-1 connections with circular bolt pattern configuration are presented in this section;

The prediction equation for moment capacity of the connection at yield, M_y, with R^2= 0.99 is;

$$M_y = e^{3.38012}.t_p{}^{0.19041}.A_b{}^{0.61254}.S^{0.65610} \quad (5\text{-}13)$$

The prediction equation for the initial stiffness of the connection, E, with R^2= 0.98 is;

$$E = e^{8.56929}.t_p{}^{0.66707}.A_b{}^{021273}.S^{0.60448} \quad (5\text{-}14)$$

The prediction equation for the post yield stiffness of the connection, E_t, with R^2= 0.98 is;

$$E_t = e^{6.85939}.t_p{}^{0.26963}.A_b{}^{1.07114}.Z^{0.50453} \quad (5\text{-}15)$$

The prediction equation for maximum rotation at fracture, θ_f, with R^2= 0.98 is;

$$\theta_f = e^{-2.99938}.t_p{}^{-0.2706}.A_b{}^{0.73699}.S^{-11.509}.Z^{11.0069} \quad (5\text{-}16)$$

The summery of the statistical parameters of the nonlinear regression analysis are presented in Appendix-F.

The predicted moment capacity of connection, M_y, versus the actual moment capacity is presented in Figure 5-9. Also the ±5% error envelope is presented in this figure. The results presented in this figure shows that the predicted values have close agreement with the actual values collected from finite element analysis.

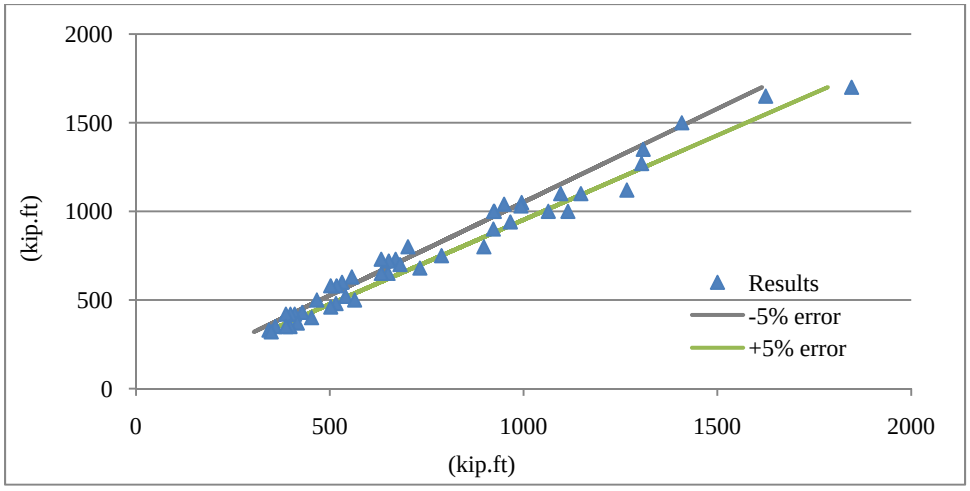

Figure 5-9 Comparison Of The Predicted Vs. Actual Moment Capacity Of The Connection At Yield With ±5% Error Envelope For The Category-1 Connections With Circular Bolt Pattern

Figure 5-10 shows the predicted initial stiffness of the connections versus the actual initial stiffness of the connection. The results presented in this figure show a close agreement between the predicted and actual initial stiffness of the connection.

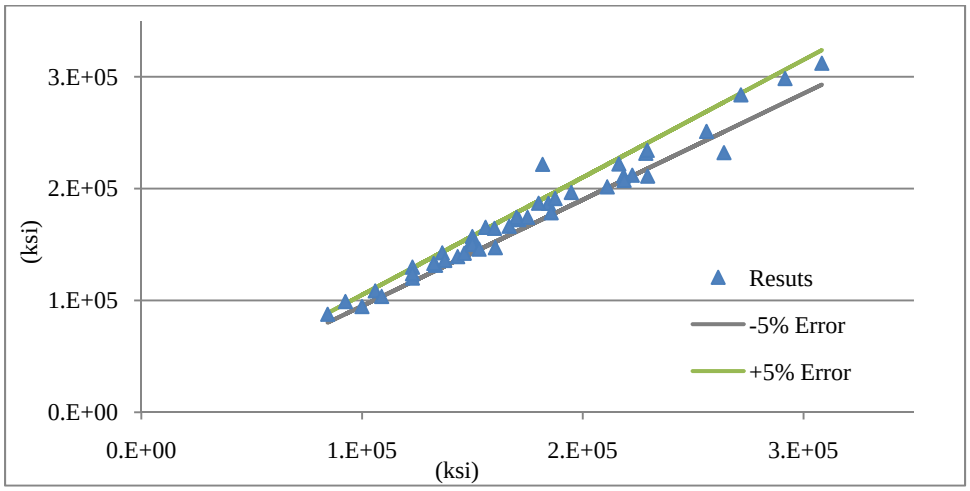

Figure 5-10 Comparison Of The Predicted Vs. Actual Initial Stiffness Of The Connection With ±5% Error Envelope For The Category-1 Connections With Circular Bolt Pattern

The predicted post-yield stiffness of the connections versus the results obtained from the finite element analysis are presented in Figure 5-11. These results show a close agreement between these predicted and actual values.

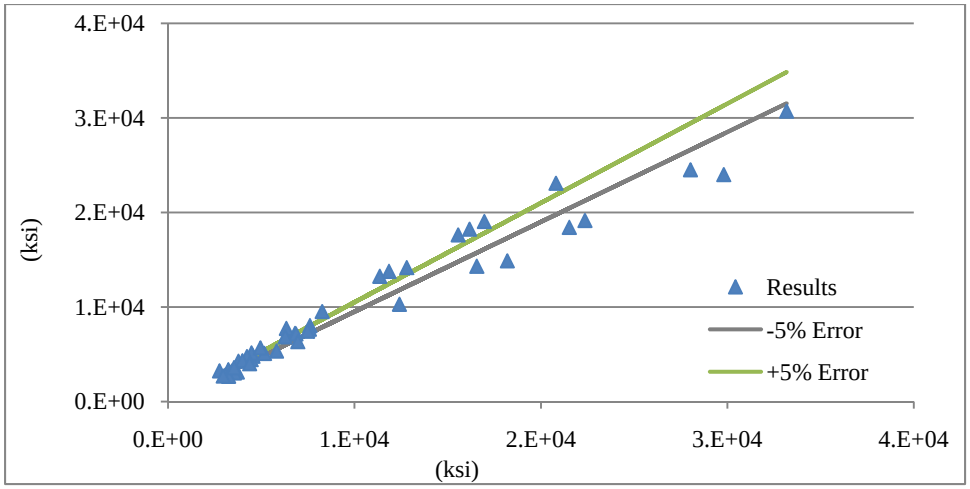

Figure 5-11 Comparison Of The Predicted Vs. Actual Post-Yield Stiffness Of The Connection With ±5% Error Envelope For The Category-1 Connections With Circular Bolt Pattern

The results presented in Figure 5-12 show the predicted ultimate rotation capacity of the connection versus the actual rotation capacity of the connection at failure. A close examination of these results reveals that majority of data point fall in between ±5% error envelope, which shows close agreements between the predicted and calculated values.

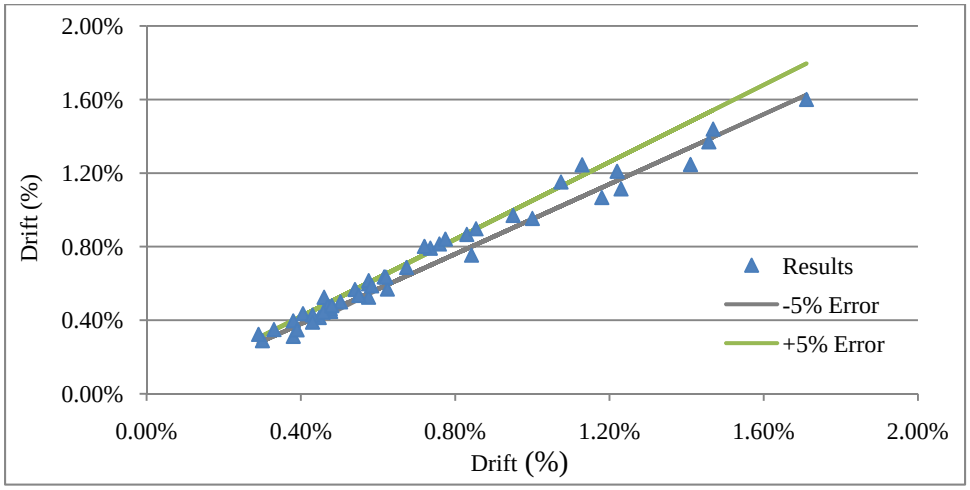

Figure 5-12 Comparison Of The Predicted Vs. Actual Ultimate Rotation Capacity Of The Connection With ±5% Error Envelope For The Category-1 Connections With Circular Bolt Pattern

5.6.3.2 The prediction equations for Category-2 connections with circular bolt pattern, $\boldsymbol{t_p/b_d \leq 1}$:

The prediction equations for the Category-2 connections with circular bolt pattern configuration are presented in this section;

The prediction equation for moment capacity of the connection at yield, M_y, with R^2= 0.99 is;

$$M_y = e^{3.19037}.t_p{}^{1.14643}.A_b{}^{0.22106}.S^{0.66963} \quad (5\text{-}17)$$

The prediction equation for the initial stiffness of the connection, E, with R^2= 0.99 is;

$$E = e^{6.71341}.t_p{}^{0.78200}.A_b{}^{0.12852}.S^{0.91723} \quad (5\text{-}18)$$

The prediction equation for the post yield stiffness of the connection, E_t, with R^2= 0.982 is;

$$E_t = e^{1.67455}.t_p{}^{0.29148}.A_b{}^{0.78567}.Z^{1.32145} \quad (5\text{-}19)$$

The prediction equation for maximum rotation at fracture, θ_f, with R^2= 0.98 is;

$$\theta_f = e^{-1.51032}.t_p{}^{-0.0500}.A_b{}^{0.89251}.S^{-7.62079}.Z^{6.97083} \quad (5\text{-}20)$$

The summery of the statistical parameters of the nonlinear regression analysis are presented in Appendix-F.

Figure 5-13shows the ±5% error envelope of the predicted moment capacity of the connection at yield versus the actual moment capacity at yield. The results presented in this figure show a close agreement between the predicted values and the results obtained from finite element analysis.

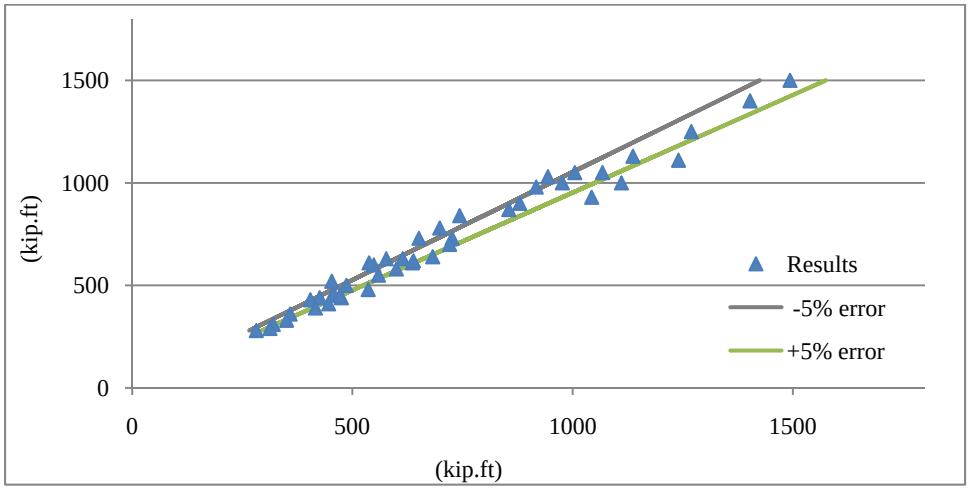

Figure 5-13 Comparison Of The Predicted Vs. Actual Moment Capacity Of The Connection At Yield With ±5% Error Envelope For The Category-2 Connections With Circular Bolt Pattern

Figure 5-14 shows the predicted initial stiffness of the connections versus the calculated initial stiffness of the connection. The results presented in this figure show a close agreement between the predicted and calculated initial stiffness of the connection.

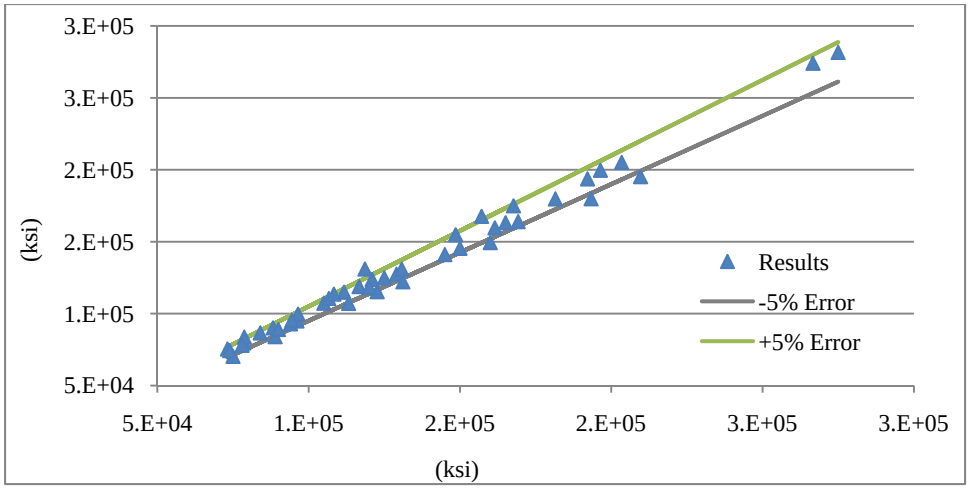

Figure 5-14 Comparison Of The Predicted vs. Actual Initial Stiffness Of The Connection With ±5% Error Envelope For The Category-2 Connections With Circular Bolt Pattern

The predicted post-yield stiffness of the connections versus the results obtained from the finite element analysis is presented in Figure 5-15. These results show a close agreement between these predicted and actual values.

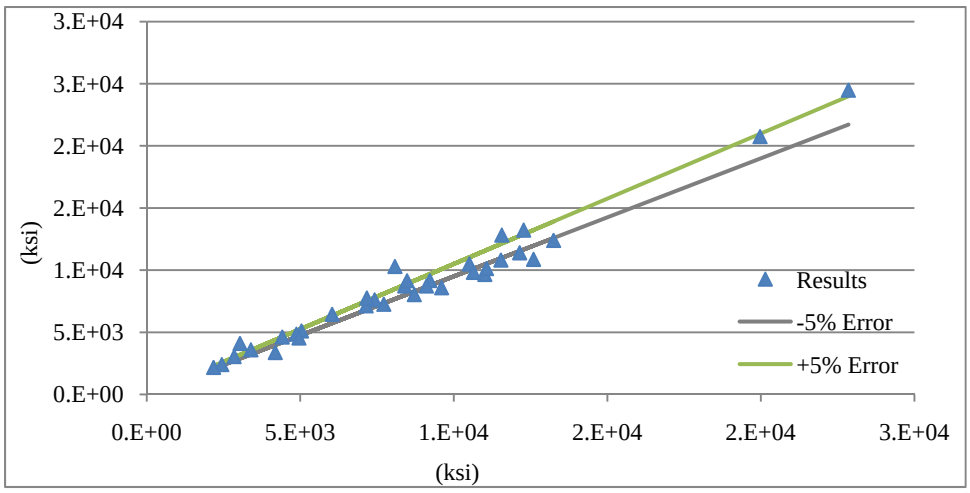

Figure 5-15 Comparison Of The Predicted Vs. Actual Post-Yield Stiffness Of The Connection With ±5% Error Envelope For The Category-2 Connections With Circular Bolt Pattern

The results presented in Figure 5-16 show the predicted ultimate rotation capacity of the connection versus the ultimate rotation capacity of the connection at failure. A close examination of these results reveals that majority of data point fall in between ±5% error envelope, which shows close agreements between the predicted and calculated values.

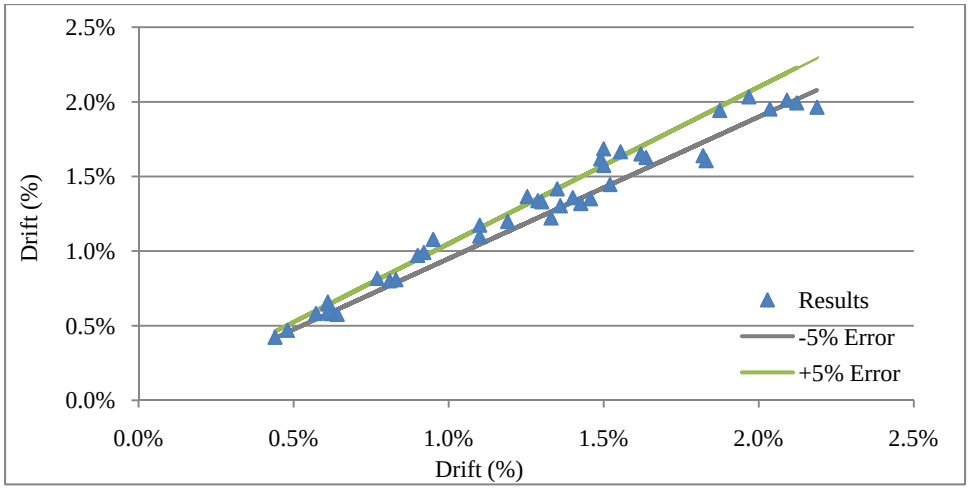

Figure 5-16 Comparison Of The Predicted vs. Actual Ultimate Rotation Capacity Of The Connection With ±5% Error Envelope For The Category-2 Connections With Circular Bolt Pattern

5.6.3.3 The prediction equations for Category-1 connections with square bolt pattern, $\boldsymbol{t_p/b_d} > 1$:

The prediction equations for the Category-1 connections with square bolt pattern configuration are presented in this section;

The prediction equation for moment capacity of the connection at yield, M_y, with R^2= 0.98 is;

$$M_y = e^{2.97855}.t_p{}^{0.25499}.A_b{}^{0.60680}.S^{0.70912} \quad (5\text{-}21)$$

The prediction equation for the initial stiffness of the connection, E, with R^2= 0.98 is;

$$E = e^{7.60584}.t_p{}^{0.55080}.A_b{}^{0.18993}.S^{0.77405} \quad (5\text{-}22)$$

The prediction equation for the post yield stiffness of the connection, E_t, with R^2= 0.98 is;

$$E_t = e^{7.76466}.t_p{}^{0.57849}.A_b{}^{0.19009}.Z^{0.72848} \quad (5\text{-}23)$$

The prediction equation for maximum rotation at fracture, θ_f, with R^2= 0.98 is;

$$\theta_f = e^{-2.76931}.t_p{}^{-0.23269}.A_b{}^{0.65754}.S^{-8.54407}.Z^{8.02903} \quad (5\text{-}24)$$

The summery of the statistical parameters of the nonlinear regression analysis are presented in Appendix-F.

Figure 5-17 shows the ±5% error envelope of the predicted moment capacity of the connection at yield versus the calculated moment capacity. The results presented in this figure show a close agreement between the predicted values and the results obtained from finite element analysis.

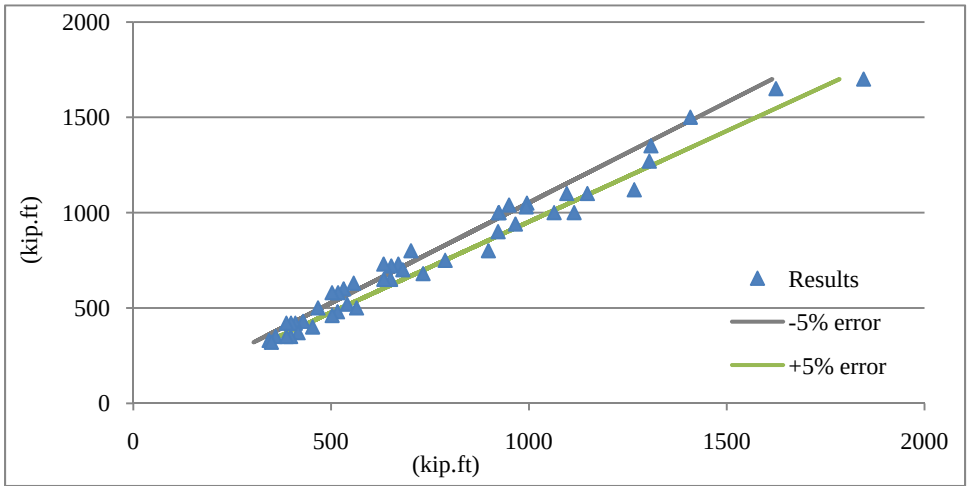

Figure 5-17 Comparison Of The Predicted Vs. Actual Moment Capacity Of The Connection At Yield With ±5% Error Envelope For The Category-1 Connections With Square Bolt Pattern

Figure 5-18 shows the predicted initial stiffness of the connections versus the actual initial stiffness of the connection. The results presented in this figure show a close agreement between the predicted and calculated initial stiffness of the connection.

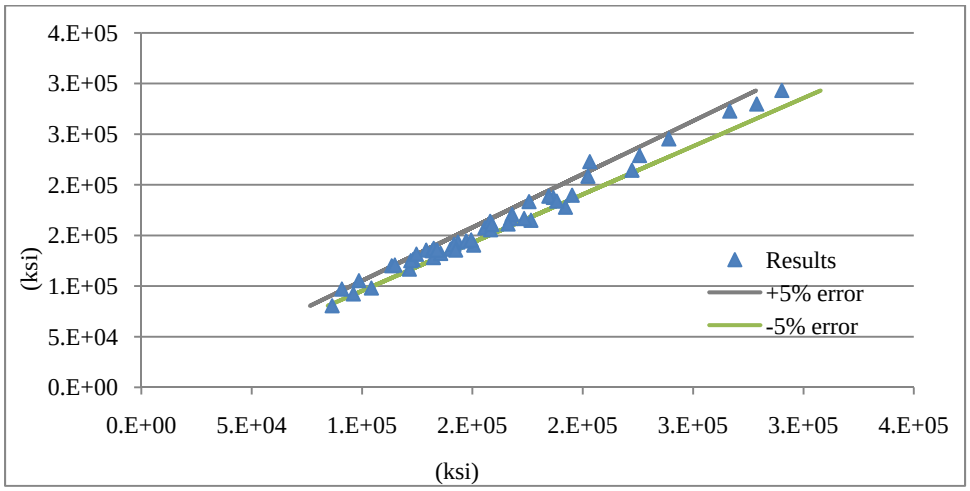

Figure 5-18 Comparison Of The Predicted Vs. Actual Initial Stiffness Of The Connection With ±5% Error Envelope For The Category-1 Connections With Square Bolt Pattern

The predicted post-yield stiffness of the connections versus the results obtained from the finite element analysis are presented in Figure 5-19. These results show a close agreement between these predicted and actual values.

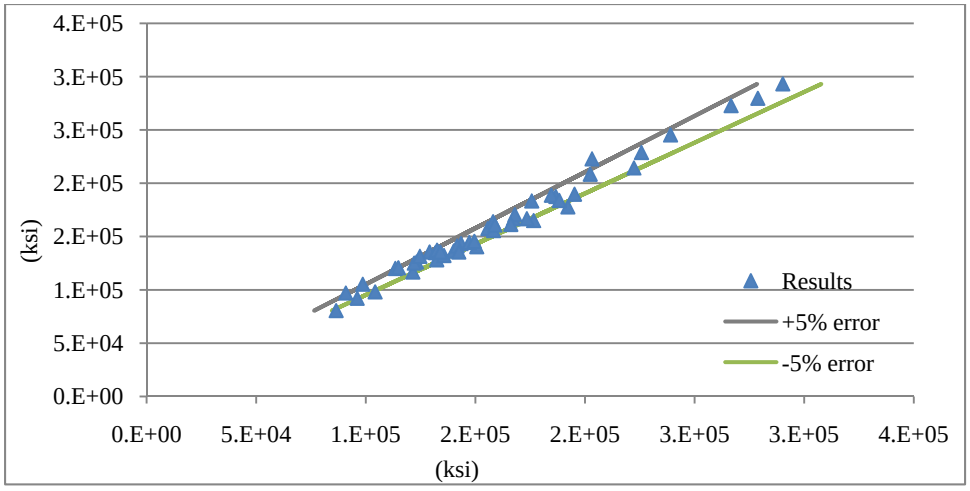

Figure 5-19 Comparison Of The Predicted Vs. Actual Post-Yield Stiffness Of The Connection With ±5% Error Envelope For The Category-1 Connections With Square Bolt Pattern

Figure 5-20 shows the predicted ultimate rotation capacity of the connection versus the rotation capacity of the connection at failure. A close examination of these results reveals that majority of data point fall in between ±5% error envelope, which shows close agreements between the predicted and calculated values.

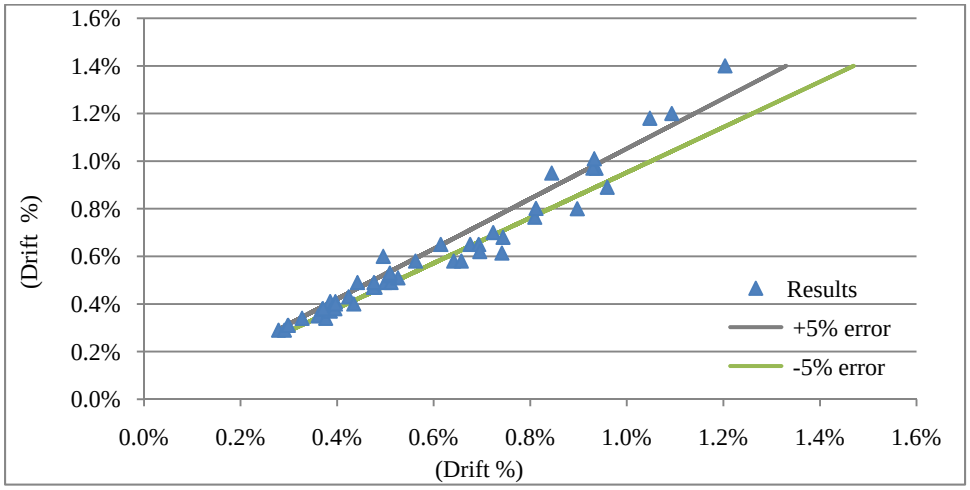

Figure 5-20 Comparison Of The Predicted Vs. Actual Ultimate Rotation Capacity Of The Connection With ±5% Error Envelope For The Category-1 Connections With Square Bolt Pattern

5.6.3.4 The prediction equations for Category-2 connections with square bolt pattern, $\boldsymbol{t_p/b_d \leq 1}$:

The prediction equations for the Category-2 connections with square bolt pattern configuration are presented in this section;

The prediction equation for moment capacity of the connection at yield, M_y, with R^2= 0.98 is;

$$M_y = e^{3.73532}.t_p{}^{1.04753}.A_b{}^{0.29760}.S^{0.55703} \quad (5\text{-}25)$$

The prediction equation for the initial stiffness of the connection, E, with R^2= 0.99 is;

$$E = e^{6.61301}.t_p{}^{0.74872}.A_b{}^{0.16026}.S^{0.94787} \quad (5\text{-}26)$$

The prediction equation for the post yield stiffness of the connection, E_t, with R^2= 0.97 is;

$$E_t = e^{4.22877}.t_p{}^{0.29322}.A_b{}^{0.66655}.Z^{0.85181} \quad (5\text{-}27)$$

The prediction equation for maximum rotation at fracture, θ_f, with R^2= 0.98 is;

$$\theta_f = e^{-0.58470}.t_p{}^{-0.20309}.A_b{}^{0.94784}.S^{-8.74824}.Z^{7.87893} \quad (5\text{-}28)$$

The summery of the statistical parameters of the nonlinear regression analysis are presented in Appendix-F.

Figure 5-21 shows the ±5% error envelope of the predicted moment capacity of the connection at yield versus the actual moment capacity. The results presented in this figure show a close agreement between the predicted values and the results obtained from finite element analysis.

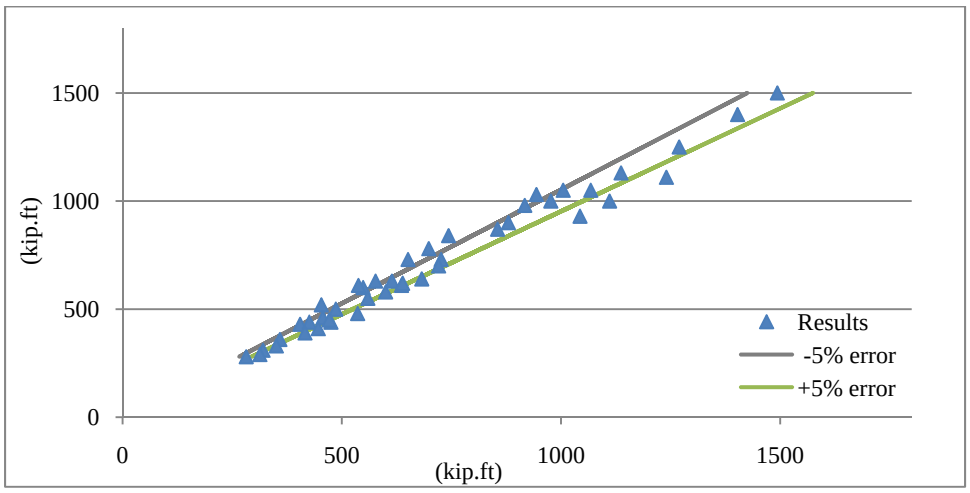

Figure 5-21 Comparison Of The Predicted Vs. Actual Moment Capacity Of The Connection At Yield With ±5% Error Envelope For The Category-2 Connections With Square Bolt Pattern

Figure 5-22 shows the predicted initial stiffness of the connections versus the actual initial stiffness of the connection. The results presented in this figure show a close agreement between the predicted and calculated initial stiffness of the connection.

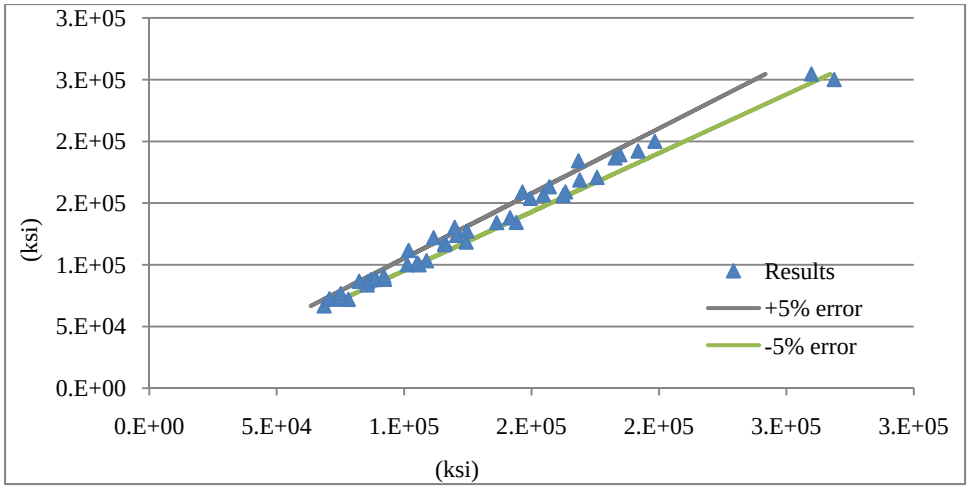

Figure 5-22 Comparison Of The Predicted Vs. Actual Initial Stiffness Of The Connection With ±5% Error Envelope For The Category-2 Connections With Square Bolt Pattern

The predicted post-yield stiffness of the connections versus the results obtained from the finite element analysis are presented in Figure 5-23. These results show a close agreement between these predicted and actual values.

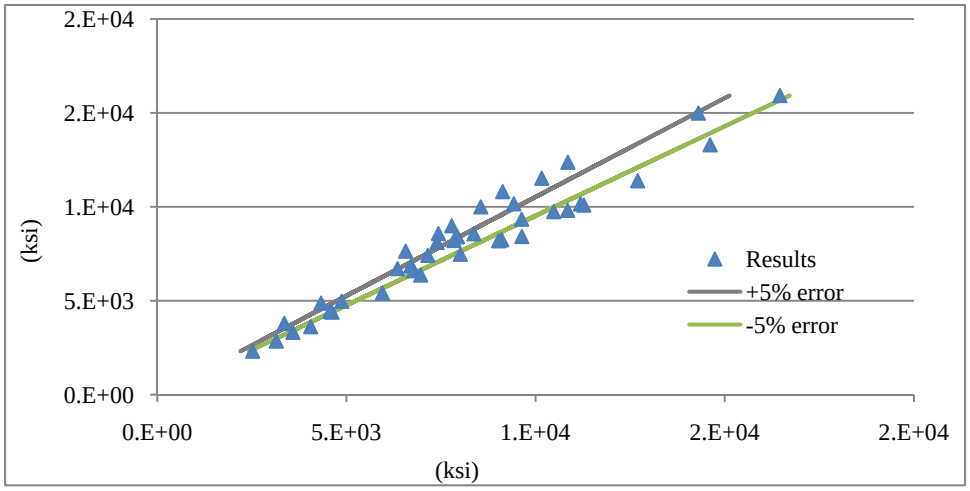

Figure 5-23 Comparison Of The Predicted Vs. Actual Post-Yield Stiffness Of The Connection With ±5% Error Envelope For The Category-2 Connections With Square Bolt Pattern

The results presented in Figure 5-24 shows the predicted ultimate rotation capacity of the connection versus the rotation capacity of the connection at failure. A close examination of these results reveals that majority of data point fall in between ±5% error envelope, which shows close agreements between the predicted and calculated values.

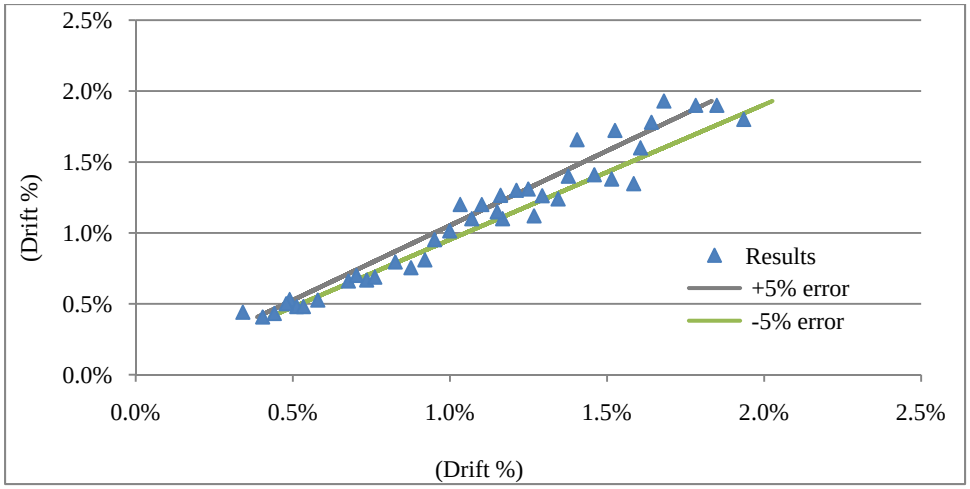

Figure 5-24 Comparison Of The Predicted Vs. Actual Ultimate Rotation Capacity Of The Connection With ±5% Error Envelope For The Category-2 Connections With Square Bolt Pattern

CHAPTER 6

DISCUSSION OF THE RESULTS

6.1 Introduction

A parametric study was conducted to identify the effects of the connection geometric parameters on the performance of connections with circular bolt pattern. More than one hundred and eighty finite element models of eight bolt extended end-plate connections with various end-plate thicknesses and bolt diameters including both square and circular pattern are analyzed under cyclic loading. Since studying the behavior of each model, 182 models, and the compression of the results are a time consuming and ineffective task, the researcher decided to carefully sample the models and only discuss the behavior of these models. These models are sampled such that their behavior best represent the overall behavior of the entire test matrix. Sixteen models from the connections with 30 in. nominal beam depth are selected and the results were discussed. Similar behavior was observed when the results of the models with 24 in. and 36 in. were studied. The discussions of these results are provided in this chapter. The details of the sampled specimens are shown in Table 6-1.

Also for a better representation of the bolt forces and their variation in the connections with circular and square bolt pattern, the selected models are subjected to monotonic loading to the failure. The discussion of these results and the effect of the circular bolt pattern on the bolt force variation in the connection are discussed in details in this chapter.

Table 6-1 Types And Details Of The Sampled Specimens And Relative Energy Dissipation

Model Name	θ_f^* 10^{-3}	Energy Dis. kip.ft.rad	Energy Dis. Variation
T_p½-B_d1¼-SQR	18.00	180.79	5.9%
T_p½-B_d1¼-CIR	19.68	191.50	
T_p1-B_d1¼-SQR	19.30	386.73	15.6%
T_p1-B_d1¼-CIR	21.88	446.90	
T_p1½-B_d1¼-SQR	14.00	301.72	38.4
T_p1½-B_d1¼-CIR	17.11	417.69	
T_p¾-B_d¾SQR	6.60	9.98	234.6%
T_p¾-B_d¾-CIR	8.10	33.41	
T_p1½-B_d¾SQR	4.50	36.01	101.3%
T_p1½-B_d¾-CIR	4.60	72.48	
T_p½-B_d½-SQR	4.40	2.00	234.1%
T_p½-B_d½-CIR	5.00	6.68	
T_p1-B_d½-SQR	4.10	7.10	83.5%
T_p1-B_d½-CIR	4.76	13.02	
T_p1½-B_d½-SQR	3.50	6.06	159.0%
T_p1½-B_d½-CIR	4.47	15.68	

* The analysis was terminated when ultimate strain was reached.

6.2 Results And Discussions

The results and energy dissipation percentage variation between the connection with circular and square bolt pattern are tabulated in Figure 5-7. To simplify the compression between the energy dissipations, and study the effectiveness of geometric parameters on the energy dissipation characteristics of the connection, these results are rearranged in respect to the nominal beam depth and presented in Table 6-2, Table 6-3, and Table 6-4. Also the critical connections with the most affect on the energy dissipation are highlighted in these tables. These results show that the increase in of the energy dissipation of the connection is a function of both the end-plate thickness and the bolt diameter. Close examination of the results and the deformed shape of the connections reveal that the energy dissipation increase in the connections with large bolt diameter is due to the unique end-plate deformation, while this energy dissipation increase in the connections with smaller bolt diameter is due to larger ductility of the connection which significantly increases the area under the moment-rotation curve. These results will discuss in details in this chapter.

Table 6-2 Energy Dissipation Percentage Variation Between The Connection With Circular And Square Bolt Pattern With d=30in

d=30 in		B_d (in)					
		1/2	5/8	3/4	1.0	1-1/8	1-1/4
T_p (in)	1/2	234.1	176.5	59.5	12.6	12.2	5.9
	5/8	58.3	205.2	113.8	15.9	15.6	8.5
	3/4	88.4	125.4	234.6	28.5	18.2	8.3
	1.0	83.5	189.2	143.6	43.6	24.1	15.6
	1-1/8	121.4	143.4	222.3	72.4	35.5	18.1
	1-1/4	203.6	176.9	252.3	61.9	37.6	27.4
	1-1/2	159.0	197.4	101.3	139.1	48.7	38.4

Table 6-3 Energy Dissipation Percentage Variation Between The Connection With Circular And Square Bolt Pattern With d=24in

d=24 in		B_d (in)					
		1/2	5/8	3/4	1.0	1-1/8	1-1/4
T_p (in)	1/2		1.9	4.4	6.5	1.1	0.4
	3/4	103.5	9.9	8.4	29.9	14.7	9.0
	1-1/8	64.0	25.4	56.9	80.7	31.0	15.9
	1-1/2	61.9	44.2	67.5	70.5	63.2	60.2

Table 6-4 Energy Dissipation Percentage Variation Between The Connection With Circular And Square Bolt Pattern With d=36in

d=36 in		B_d (in)					
		1/2	5/8	3/4	1.0	1-1/8	1-1/4
T_p (in)	1/2			50.6	28.5	11.2	2.9
	3/4	4.7	24.3	224.8	74.0	42.7	30.2
	1-1/8	6.7	135.5	154.0	227.1	151.2	47.8
	1-1/2		102.2	114.1	122.9	161.2	83.7

6.3 Energy Dissipation

It should be noted that the hysteresis loops presented in this chapter for each connection was obtained for the applied moment versus the story drift. It is in contract with the results presented in Appendix-C, D and E, which the rotation of the end-plate was used. The Models Tp½-Bd1¼-d30, and T_p½-B_d½-d30 with both circular and square bolt pattern were subjected to localized excessive yielding of the end-plate at 2% loading stage, while early fracture of the bolts were notices at 2.5% story drift in the connections with ½ in. bolt diameter. However, for the sake of comparison the hysteresis results of these models are reported up to 4% story drift. These steps were taken to simplify the compression of the hysteresis loops and the results.

The results presented in Table 6-2, Table 6-3, and Table 6-4 show the increase in the energy dissipation of each connection when the circular bolt pattern configuration was used. The percentage variations of the energy dissipation between square and circular pattern are also provided in this table. The hysteresis plots of the models with square and circular bolt patterns subjected to the cyclic displacement control of Figure 5-4 are illustrated in Figure 6-1, Figure 6-2, and Figure 6-3 .

The effect of varying the end-plate thickness on the hysteresis behavior of the connections by keeping the same bolt diameter is compared in Figure 6-1, Figure 6-2, and Figure 6-3, for bolt diameters of 1¼, ¾, and ½ respectively. Figure 6-1(a) shows that in the model with square bolt pattern pinching started at an early stage of loading, and the maximum moment resistance of the connection did not exceed 760 kip.ft (1030 kN.m). While, the same connection with circular bolt pattern has limited pinching, and the connection exhibits greater moment and energy dissipation capacities with 5.9% increase in energy dissipation when it is compared with its counterpart model with square bolt pattern (Table 6-1).

These figures show that only the models with relatively large bolt diameter and end-plate thickness (T_p1-B_d1¼-d30, Figure 6-1(b) and T_p1½-B_d1¼-d30, Figure 6-1(c)) reached the ultimate moment capacity of the beam which was Mp=1,573 kip.ft (2130 kN.m),(refer to Figure 6-1(b and c)). Model T_p1½-B_d¾, with thick end-plate and relatively smaller bolt diameter, b_d=¾ in., reached only 50% of the ultimate capacity of the beam (790 kip.ft (1070 kN.m)) as it is shown in Figure 6-2(b). Models T_p1-B_d1¼-d30 and T_p1½-B_d1¼-d30 with square bolt pattern undergo pinching during loads corresponding to 3% and 4% drift,

respectively. While in similar models with circular bolt pattern, pinching started in Model T_p1-B_d1¼-d30 at a load corresponding to 4% drift (see Figure 6-1(b)), and no evidence of pinching was observed in Model T_p1½-B_d1¼-d30 (see Figure 6-1(c)).

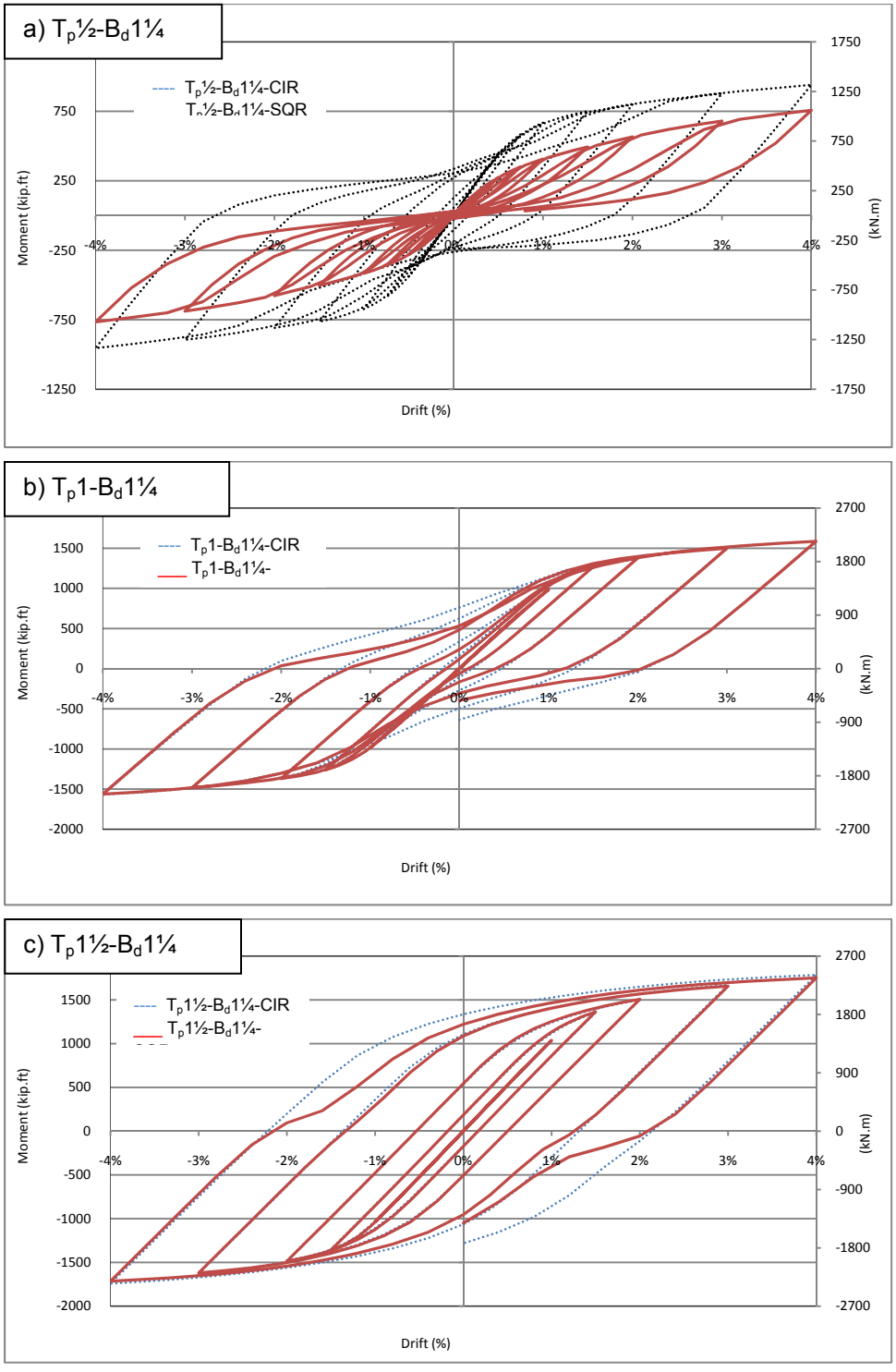

Figure 6-1 Comparison Of The Hysteresis Of The Connections With Circular And Square Bolt Pattern, Bd=1¼ in.

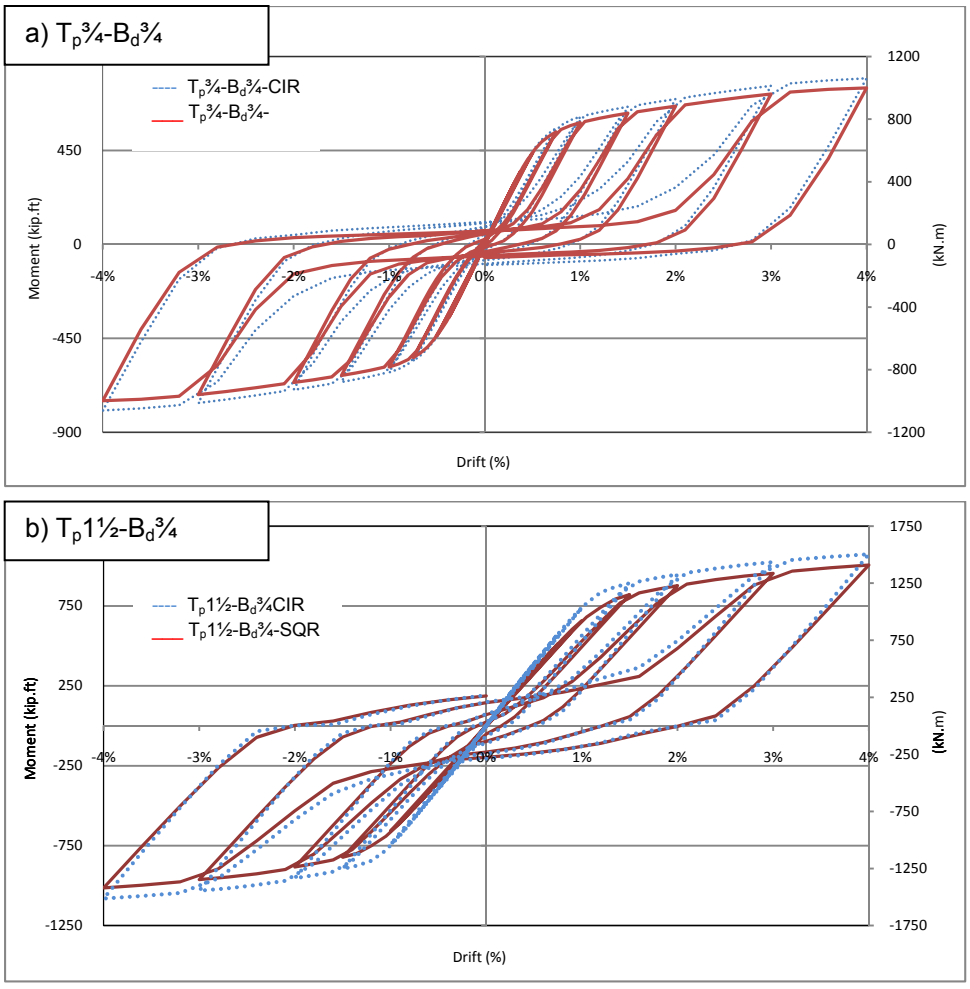

Figure 6-2 Comparison Of The Hysteresis Of The Connections With Circular And Square Bolt Pattern, B_d=¾ in.

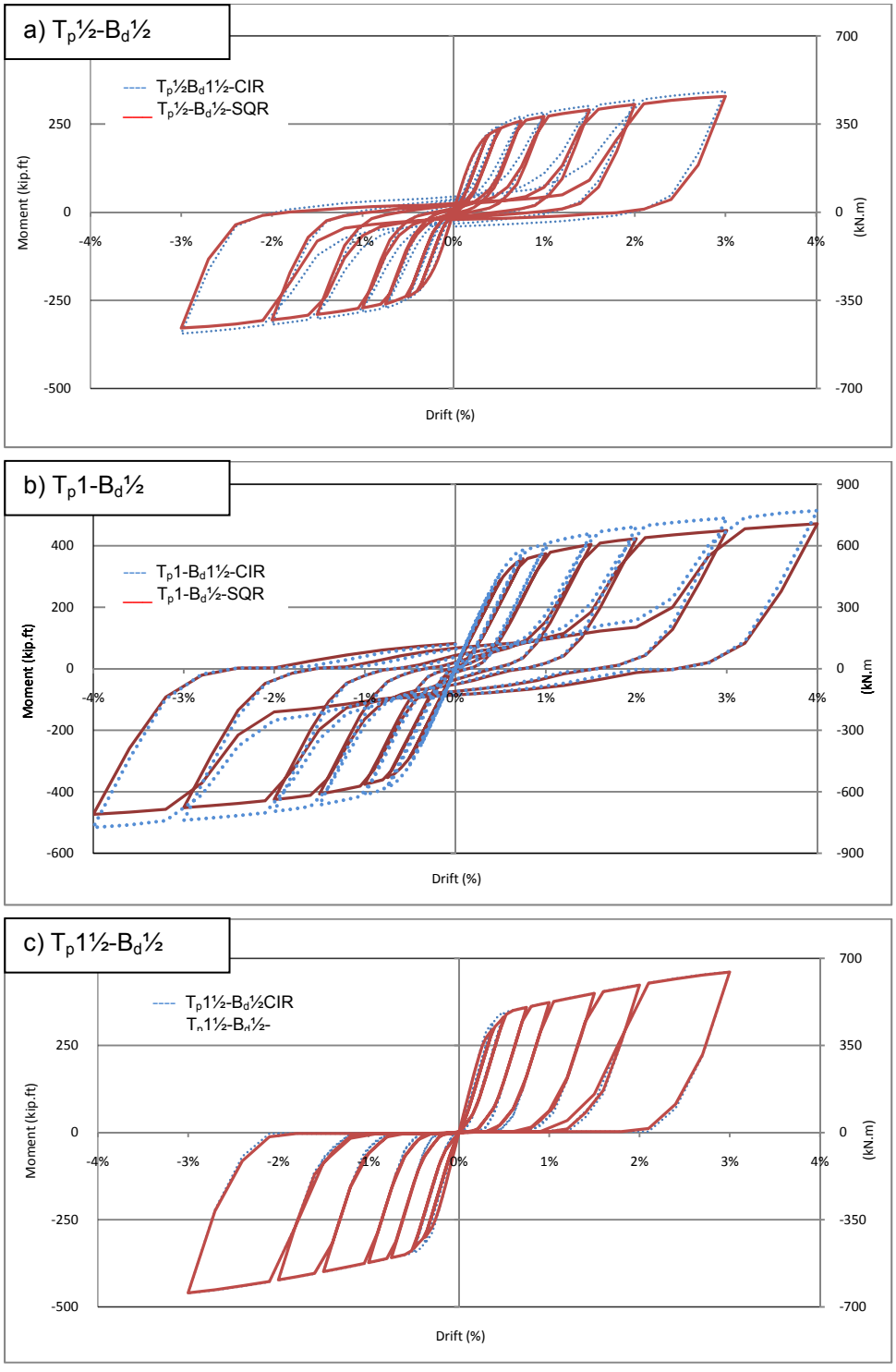

Figure 6-3 Comparison Of The Hysteresis Of The Connections With Circular And Square Bolt Pattern, B_d=½ in.

Models T_p1½-B_d½-d30, T_p1-B_d½-d30, and T_p½-B_d½-d30 (Figure 6-3 (a, b and c)) have the smallest bolt diameter between the models studied in this research. It can be seen that these models undergo pinching during an early stage of loading and exhibit small moment carrying capacity. The comparison of the results of the Models T_p¾-B_d¾-d30, Figure 6-2(a), and T_p1½-B_d½-d30, Figure 6-3(a), presented indicates that the Models T_p¾-B_d¾-d30 and T_p½-B_d½-d30 with similar end-plate thickness to bolt diameter ration, $\frac{T_p}{B_d} = 1$, have similar hysteresis characteristics. Also, using the circular bolt pattern slightly enhances the energy dissipation of the connection more than 235% (see Table 6-2). Also the results presented in Table 5-7 shows that the maximum energy dissipation observed was for Model T_p1½-B_d¾-d30, with the value of 252.3%. Thus, the effectiveness of the circular bolt pattern is observed in connections with relatively thick and-plate and large bolt diameter.

6.4 Bolt Force Variation Under Monotonic Loading

To future investigate the effectiveness of the circular bolt pattern, the bolt-force history and the deformed shape of the end-plates under monotonic loading are investigated. The effects of the end-plate thickness on the bolt force distribution in the circular and square bolt pattern are compared in Figure 6-4 through Figure 6-9. These figures show that in the connections with circular bolt pattern far bolts (Bolts-4) engage to carry the load for all end-plate thickness sizes more effectively than square bolt pattern. Indeed, Figure 6-4(a), Figure 6-5(a), and Figure 6-6(a) show that the far bolts (Bolts-4) carry the same amount of load as near bolts (Bolts-2 and Bolts-3) which are located closer to the beam flange. It is interesting to note that as the end-plate thickness increases, near bolts become more effective. For example, in connection T_p1½-B_d1¼-d30-CIR, Figure 6-6(a), Bolts-4 take more load than Bolts-2 and Bolts-3, when the circular bolt pattern is employed.

Furthermore, Model T_p1-B_d1¼-d30-SQR,Figure 6-5(b), shows that far bolts (Bolts-1) carry no forces when beam is loaded to less than 1.6% drift. While, in its counterpart connection with circular bolt pattern, T_p1-B_d1¼-d30-CIR, Figure 6-4(a), Bolts-1 engage in resisting load at 0.7% drift. Similar behavior is observed in connection T_p1½-B_d1¼-d30-SQR, Figure 6-6(b), with square bolt pattern in which Bolts-1 start resisting the load at approximately 2.1% drift while Bolts-1 in the same connection with circular

pattern, T_p1½-B_d1¼-d30-CIR, Figure 6-6(a), engage at 0.8% drift. Similar behavior was also observed in the far bolts, Bolts-4.

In Figure 6-4(a) with end-plate thickness (t_p=½ in. (13 mm)), Bolts-1 hardly embroils in taking the applied flange force, while in Figure 6-5(a) (t_p=1 in (25 mm)) Bolts-1 engagement in load carrying capacity is pronounced. Finally, in Figure 6-6(a) (t_p=1½ in (38 mm)) far bolts carry similar loads as near bolts with circular bolt pattern.

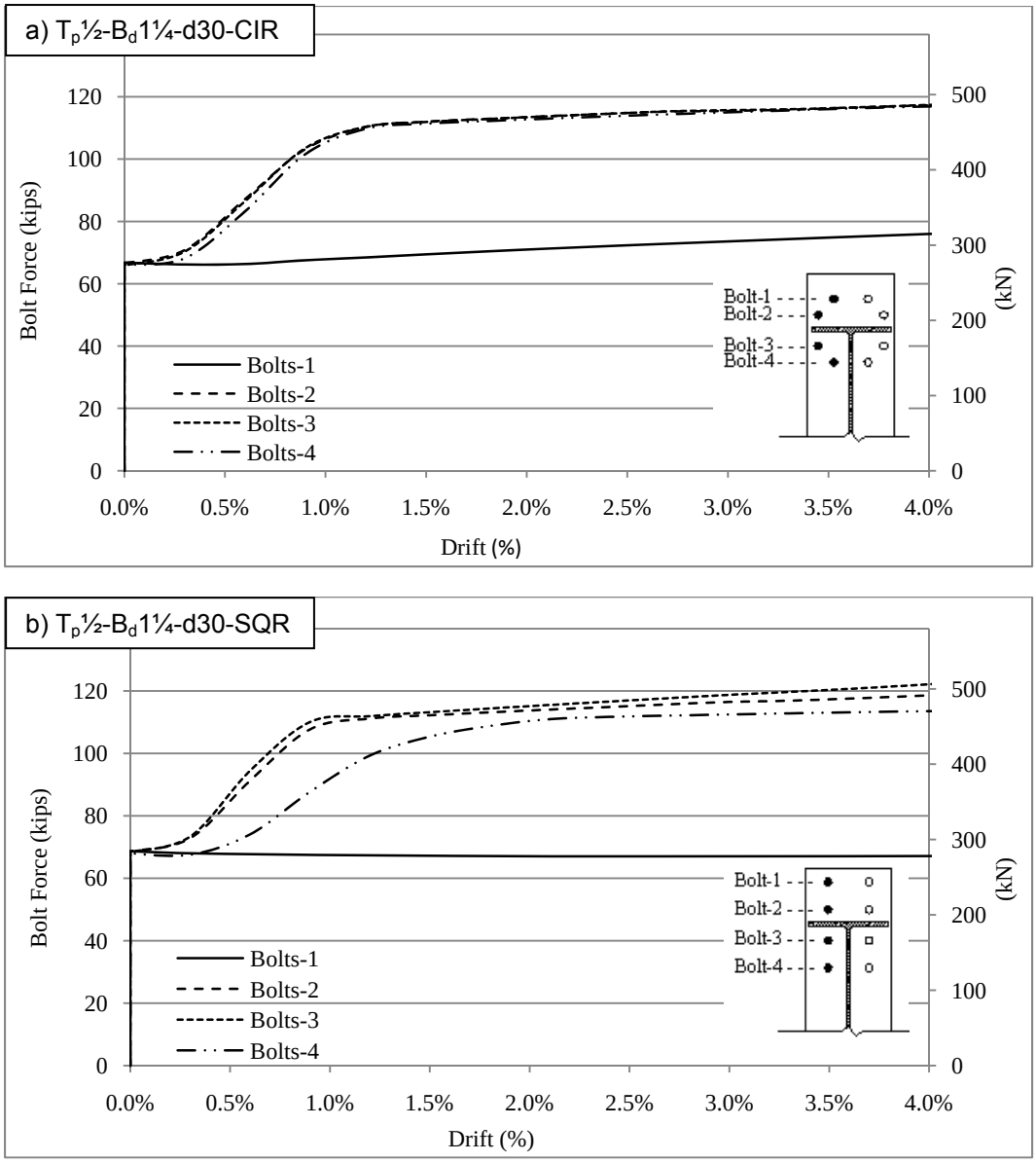

Figure 6-4 Comparison Of The Bolt Forces During Monotonic Loading

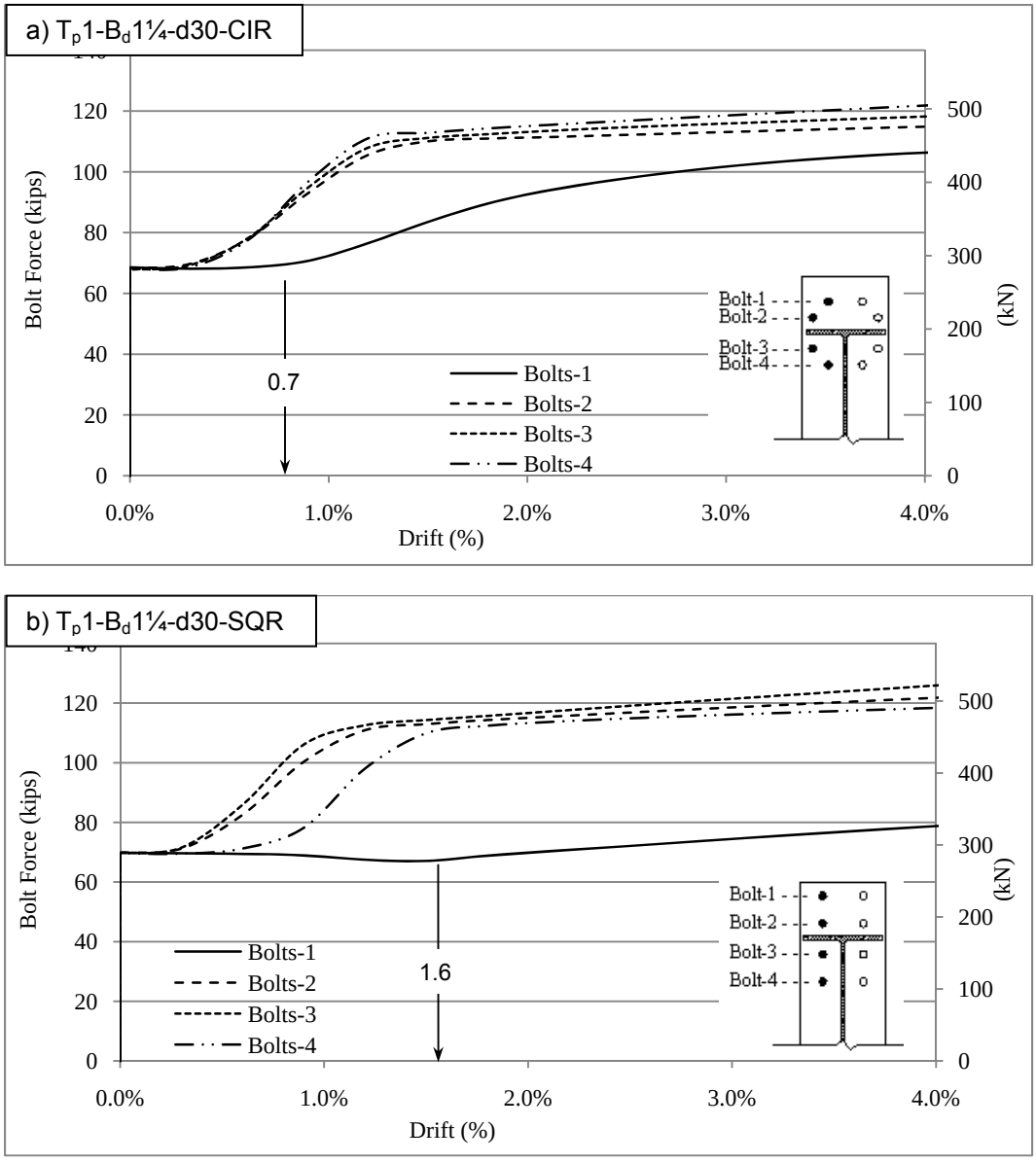

Figure 6-5 Comparison Of The Bolt Forces During Monotonic Loading

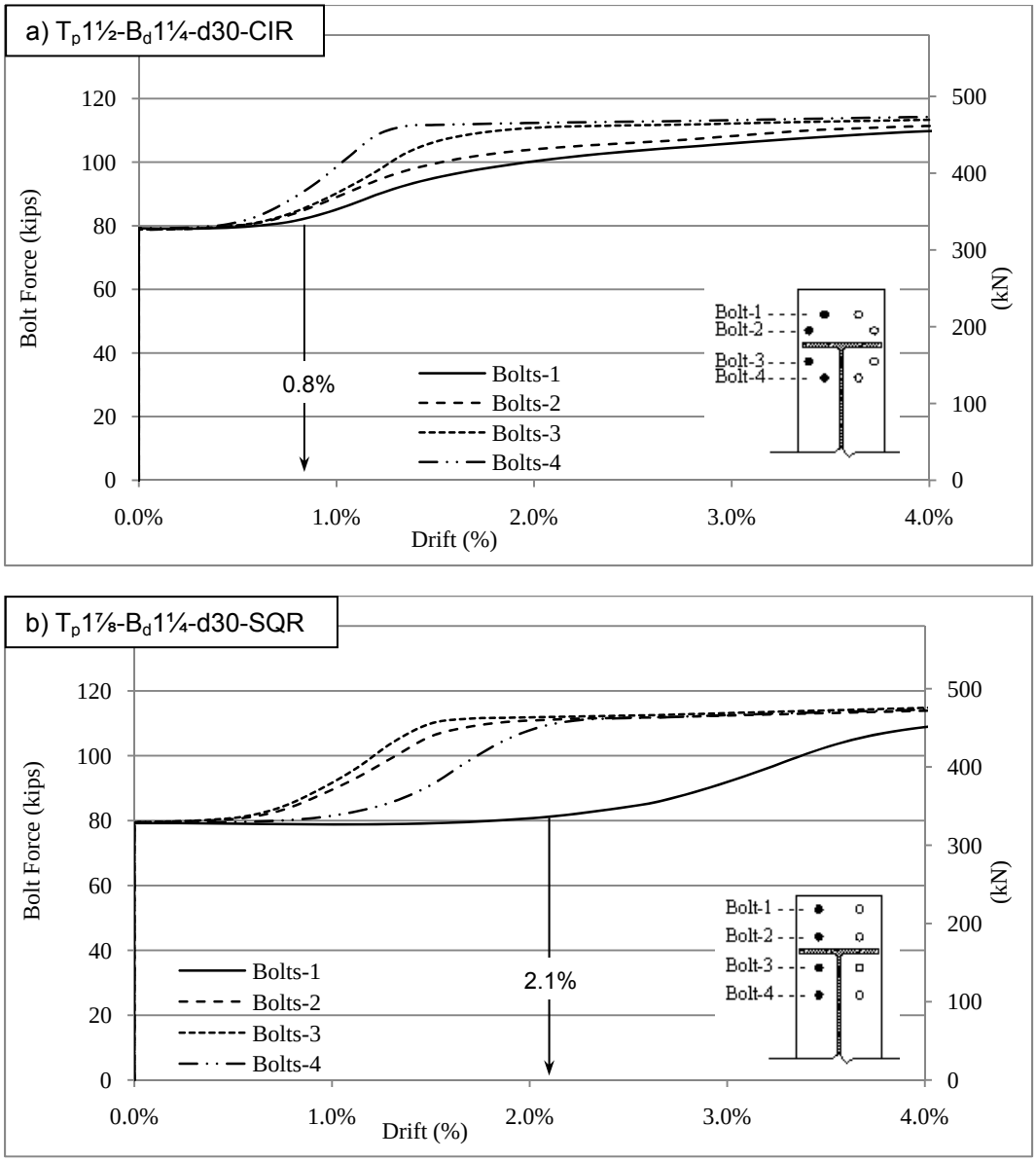

Figure 6-6 Comparison Of The Bolt Forces During Monotonic Loading

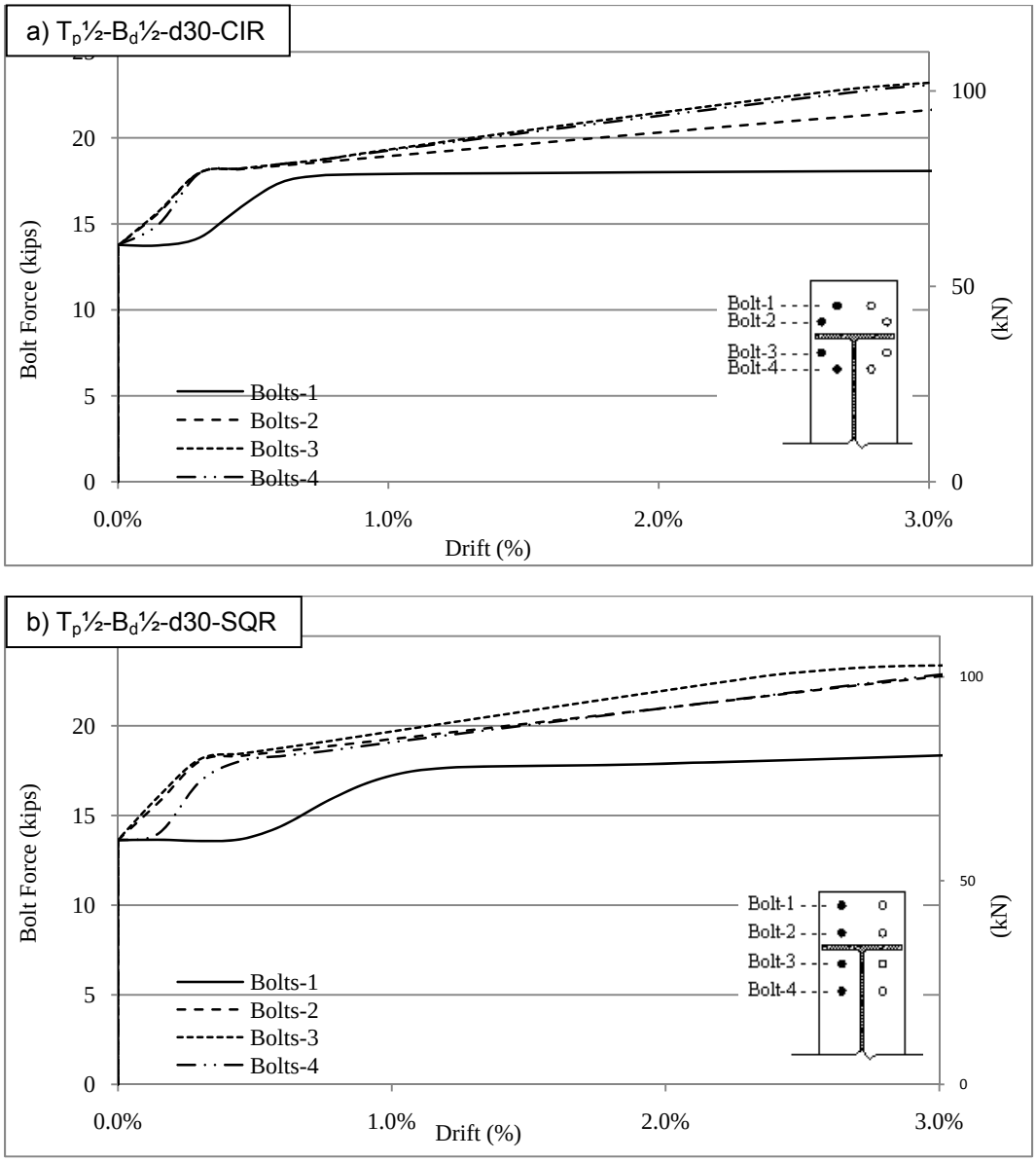

Figure 6-7 Comparison Of The Bolt Forces During Monotonic Loading

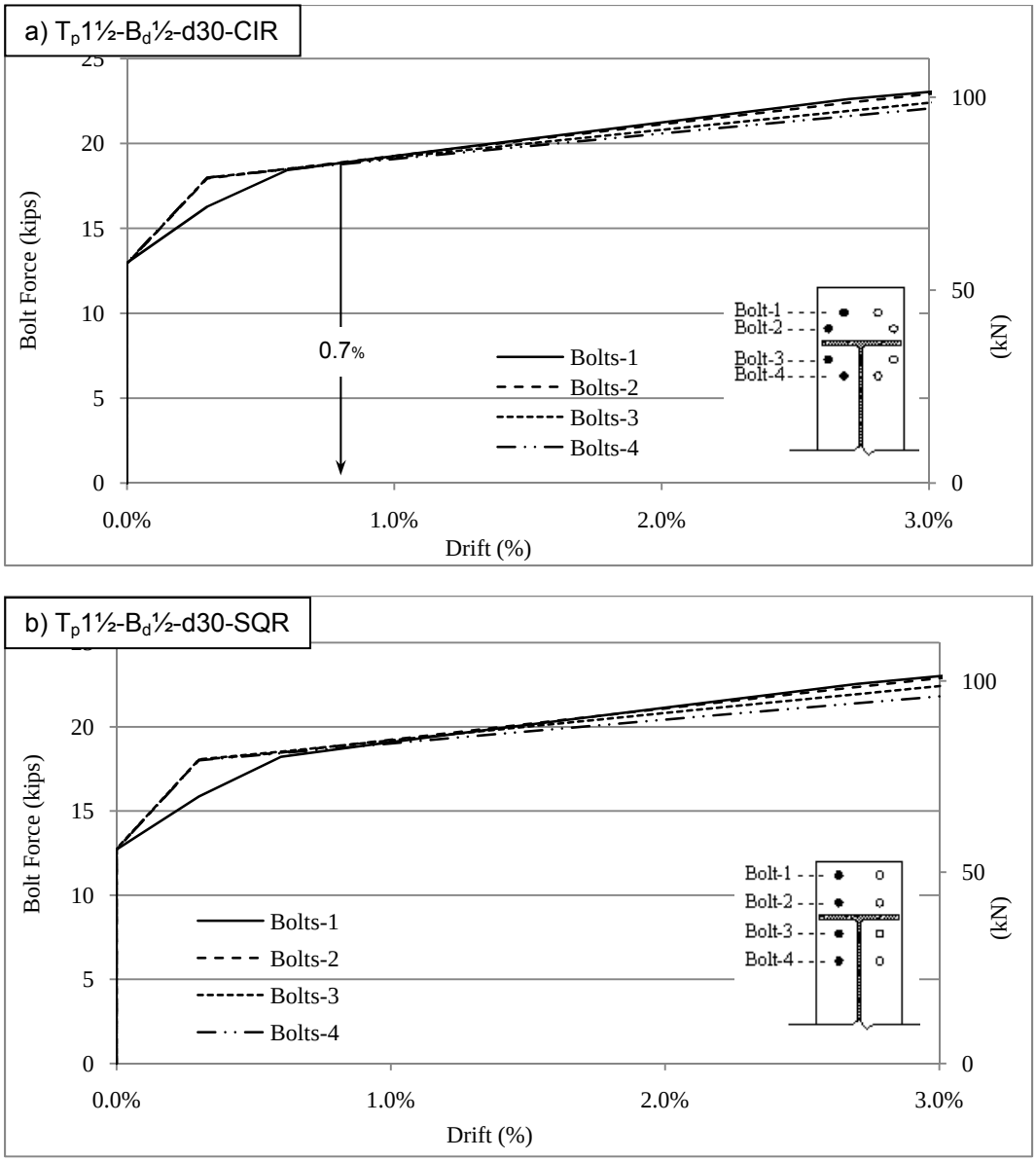

Figure 6-8 Comparison Of The Bolt Forces During Monotonic Loading

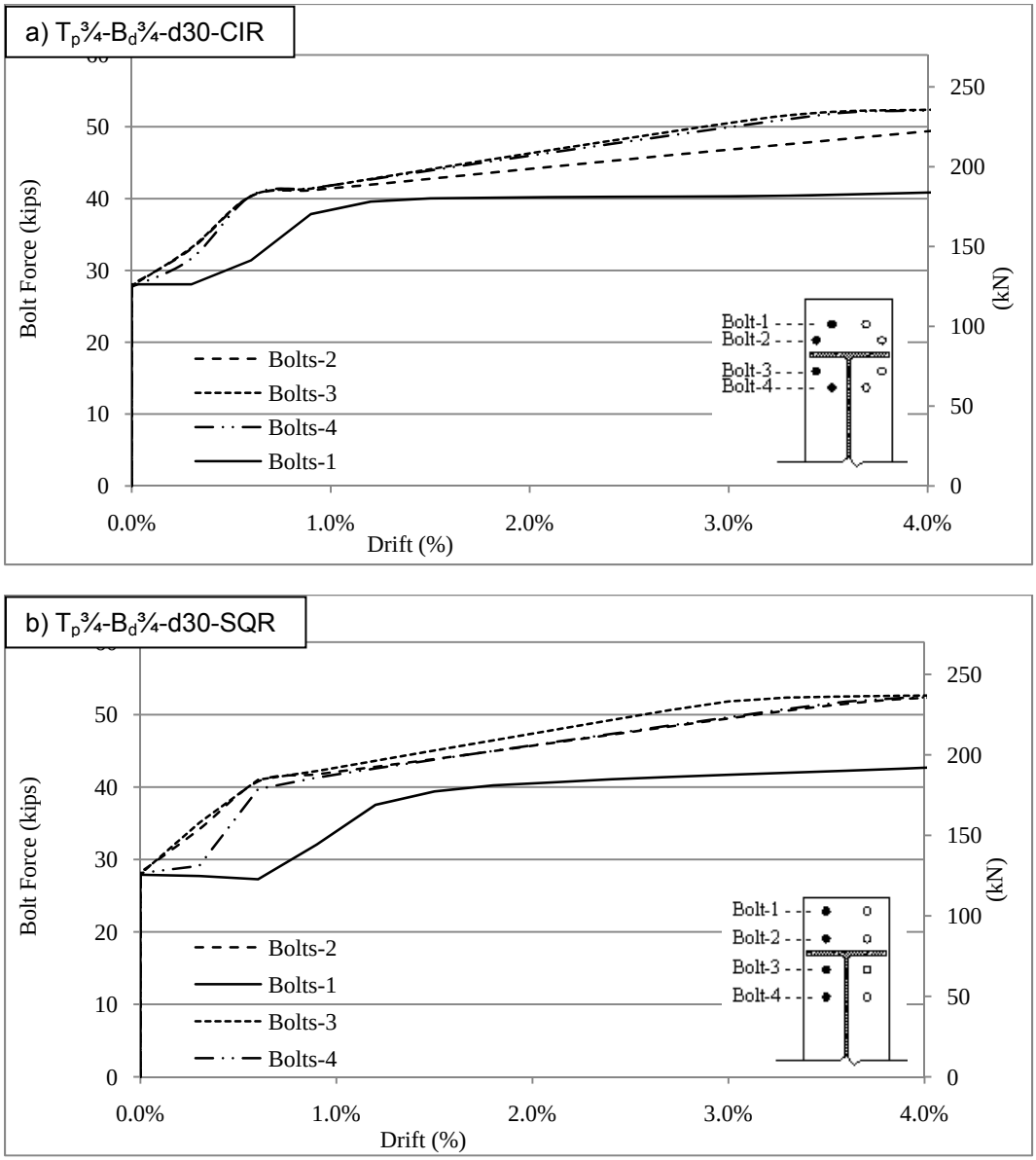

Figure 6-9 Comparison Of The Bolt Forces During Monotonic Loading

This phenomenon is attributed to the unique coupled interactive deformation of the end-plate and bolt when circular bolt pattern is used. To illustrate this, the magnified deformed configurations of the finite element models of both circular and square bolt patterns for the T_p1-B_d1¼-d30 connection with a medium end-plate thickness (i.e. 1 in (25 mm)) are shown in Figure 6-10(a and b). By visual inspection, it can be seen that near bolts undergo more deformation compared with far bolts in the connection with square bolt pattern (Figure 6-10(b)). Indeed, the end-plate at the locations of near bolts (Bolts-2 and Bolt-3) has separated from the column flange with visible gap. In contrast, the deformed shape of the connection with circular bolt pattern (Figure 6-10(a)) shows less deformation, at the location of near bolts (Bolts-2 and Bolt-3), at the same load level with the end-plate being mostly intact with the column flange at the locations of the near bolts.

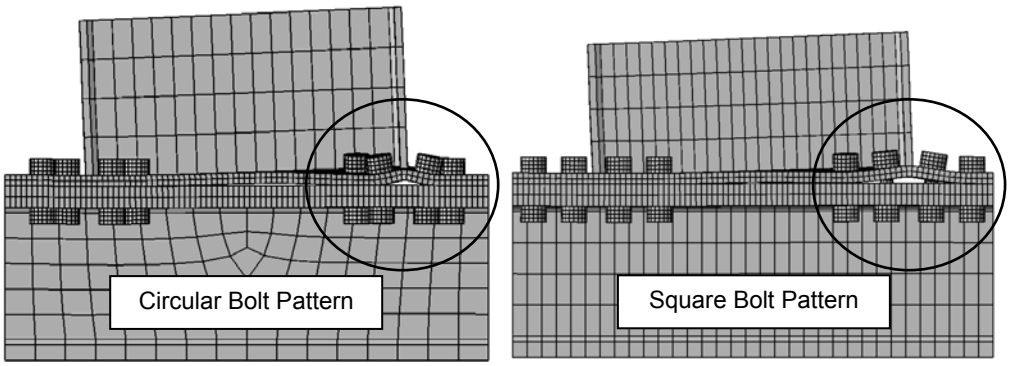

Figure 6-10 End-Plate Deformation Of (a) Tp1-Bd1¼-d30-CIR And (b) Tp1-Bd1¼-d30-SQR

To further verify the above analogy, the contour lines of out of plane deformation of the end-plate from the FE analysis are shown in Figure 6-11(a and b) for circular and square bolt patterns, respectively. These contour lines show that the out of plane end-plate deformation at the location of near bolts (Bolts-3) is distinctly different from that of the far bolt (Bolts-4) for the square bolt pattern of Figure 6-11(b), (i.e. 0.4 in versus 0.2 in). However, the examination of the contour lines for circular bolt pattern (Figure 6-11(a)) indicates that the out of plane deformation at the locations of the Bolts-3 and Bolts-4 share the same contour lines. For example, contour lines of 0.3 in and 0.4 in (7 mm and 10 mm) pass through both the near and far bolts.

In general, the end-plate contour lines at locations of the near and far bolts are more condensed for the connections with circular bolt pattern and, thus, end-plate deforms more uniformly at the locations of the near and far bolts.

Finally, Figure 6-7(a) through Figure 6-8(a) present cases in which the effects of circular bolt pattern are minimal, in which relatively small bolt diameter is used (B_d=½ in (13 mm)). For particular cases in which the ratios of plate thickness to bolt diameter are unity ($\frac{T_p}{B_d} = 1.0$) as shown in Figure 6-7(a) and Figure 6-9(a), albeit the advantages of the circular pattern over square pattern are observed, but they are minimal. For the special cases, with small bolt diameter and large plate thickness (Figure 6-8(a) and (b)), the circular bolt pattern has no effect.

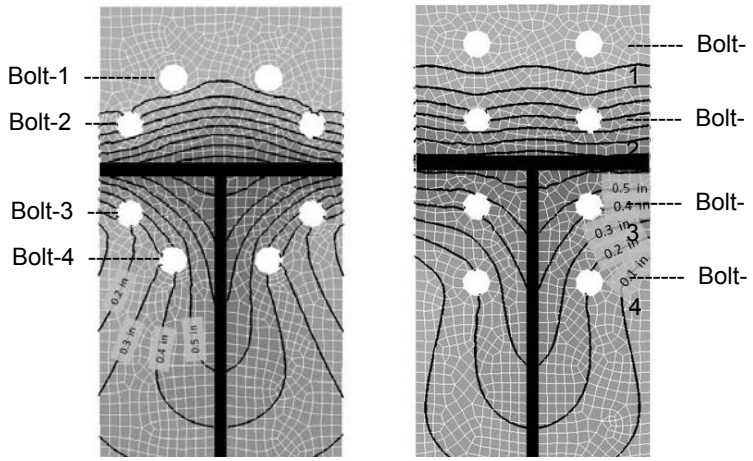

Figure 6-11 End-Plate Out Of Plain Deformation Contour Of (a) Tp1-Bd1¼-d30-CIR And (b) Tp1-Bd1¼-d30-SQR

6.5 Bolt-Force Variation Under Cyclic Loading

The bolt force history of Model Tp½-Bd1¼-d30 is presented in Figure 6-12 (a and b). These results show that in the models with relatively thin end-plate and large bolt diameter the effect of circular bolt pattern is minimal. Also, it should be noted that the bolts in this model are not yielded, while the model undergo major pinching (see Figure 6-1(a)). This behavior is due to the excessive bending of the relatively thin end-plate.

A close examination of the bolt forces of Model T_p1-B_d1¼-d30-SQR presented in Figure 6-13(b) show that two of the near bolts (Bolts-2 and Bolts-3) are yielded at the end of the 1.5% story drift and far bolts (Bolts-4) are fully yielded at the end of the 2% story drift. While in the same model with circular bolt pattern (see Figure 6-13(a)), it takes 3% drift to fully yield the near bolts and lose the pre-tensioning force while the far bolts (Bolts-4) are still maintaining a portion of their pre-tensioning force. It should be noted that in the Model Tp1-Bd1¼, far bolts (Bolt-1) takes no force in the connection with square bolt pattern, while the same bolts engage in taking additional load at the early stage of loading, and they lose their pre-tensioning force during 2% story drift (compare Figure 6-13(a), and Figure 6-13(b)).

Similar behavior was observed when the bolt forces of the Model T_p1½-B_d1¼-d30 were examined. Bolts-2, Bolts-3, and Bolts-4 are completely yielded with square bolt pattern, while Bolts-1, Bolts-2 and Bolts-3 are maintaining a sufficient amount of the pre-tensioning force in circular bolt pattern (compare Figure 6-14(a), and Figure 6-14(b)).

The same behavior was also observed when the bolt force history of the Model T_p¾-B_d¾-d30 with circular and square bolt patterns were compared; see Figure 6-17(a and b). The circular bolt pattern delays the yielding of the bolts and increases the bolt force in far bolt (Bolts-1).

The bolt-force history of the Models T_p½-B_d½-d30 and T_p1½-B_d½-d30 are presented in Figure 6-14(a and b) and Figure 6-15(a and b). These models with small bolt diameter are prone to yielding of the bolts during early stage of loading. Thus, the entire bolts are fully yielded after the connection is subjected to the first cyclic load.

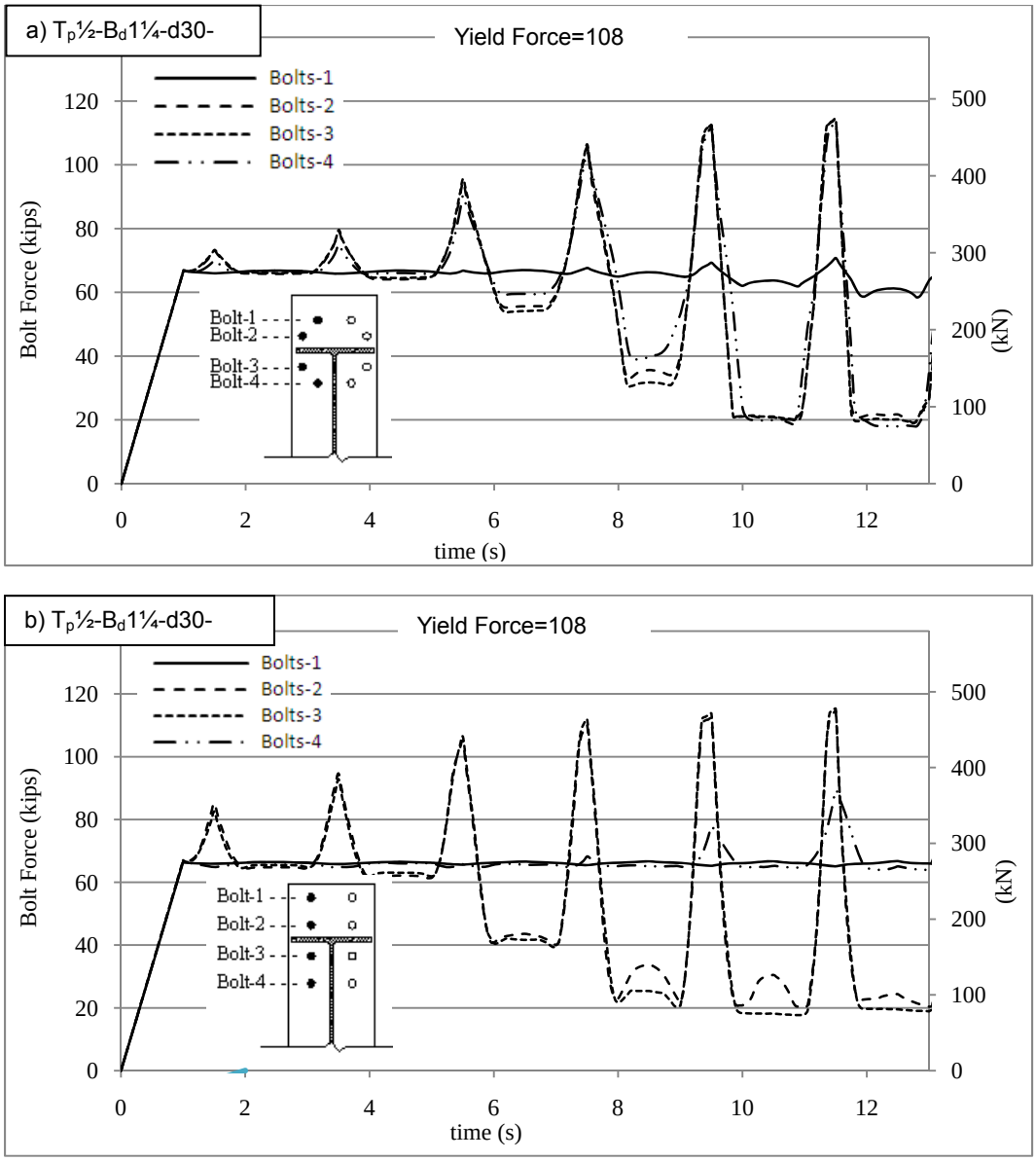

Figure 6-12 Comparison Of The Bolt Forces During Cyclic Loading, And Corresponding Story Drift.

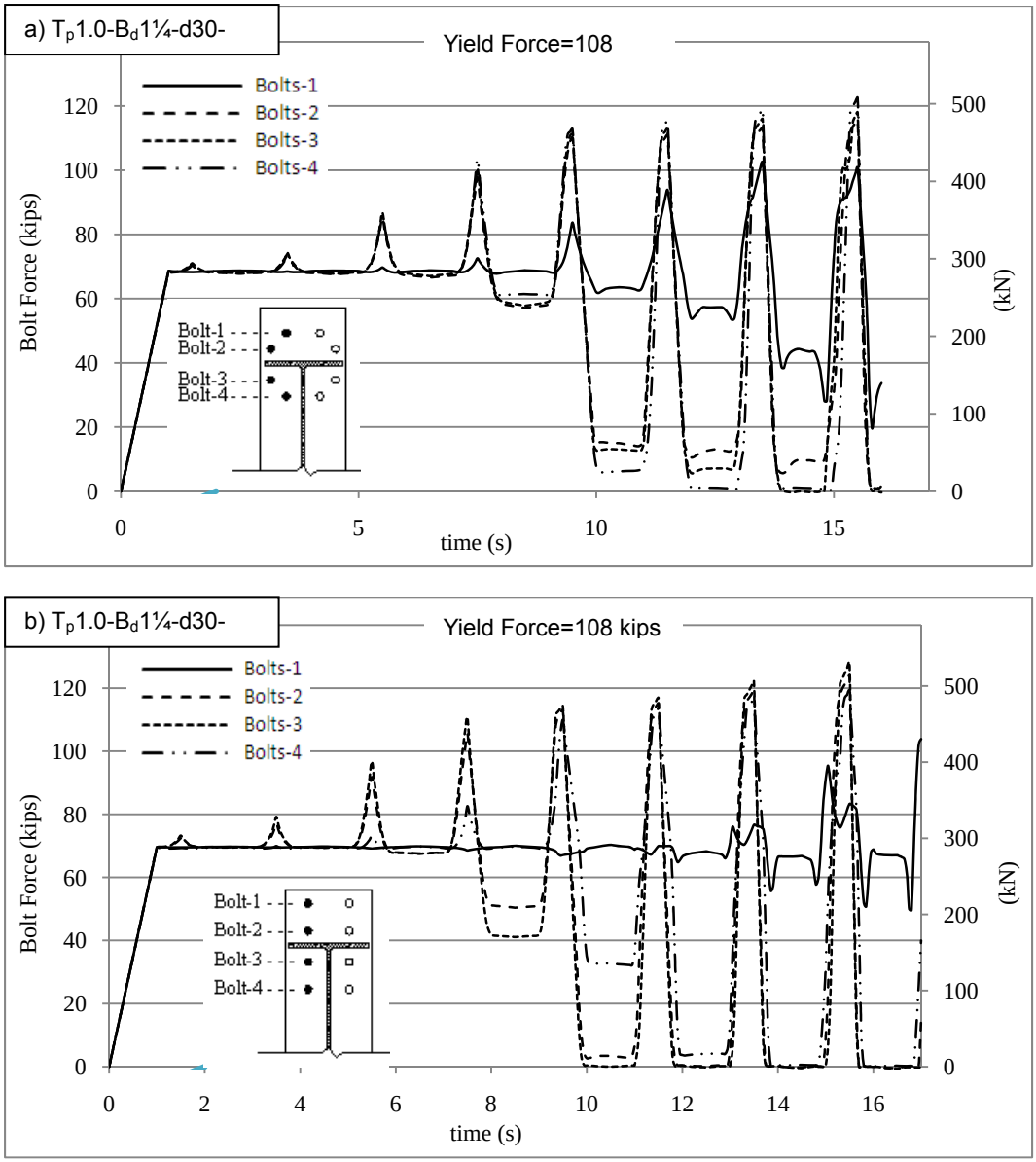

Figure 6-13 Comparison Of The Bolt Forces During Cyclic Loading, And Corresponding Story Drift.

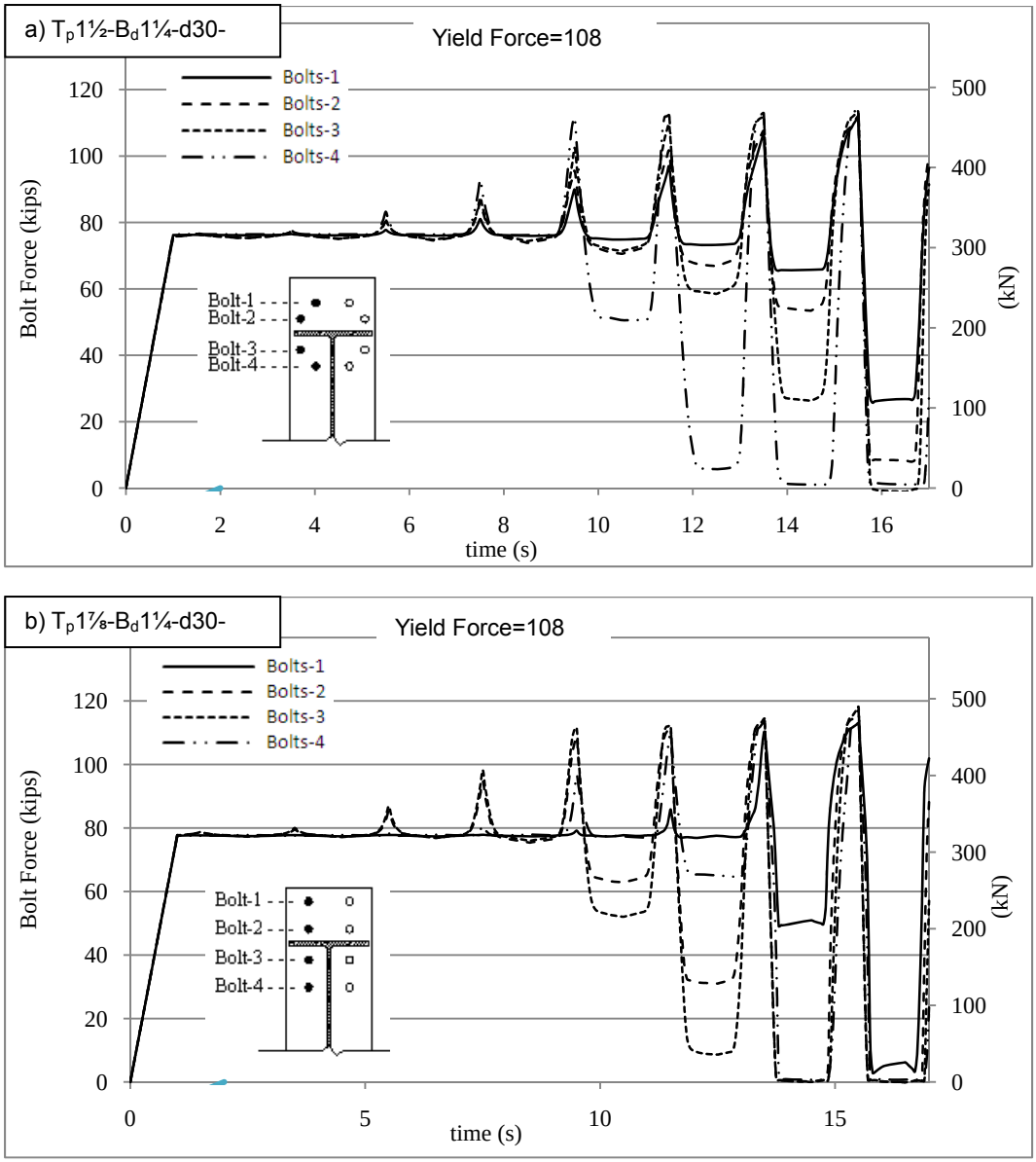

Figure 6-14 Comparison Of The Bolt Forces During Cyclic Loading, And Corresponding Story Drift..

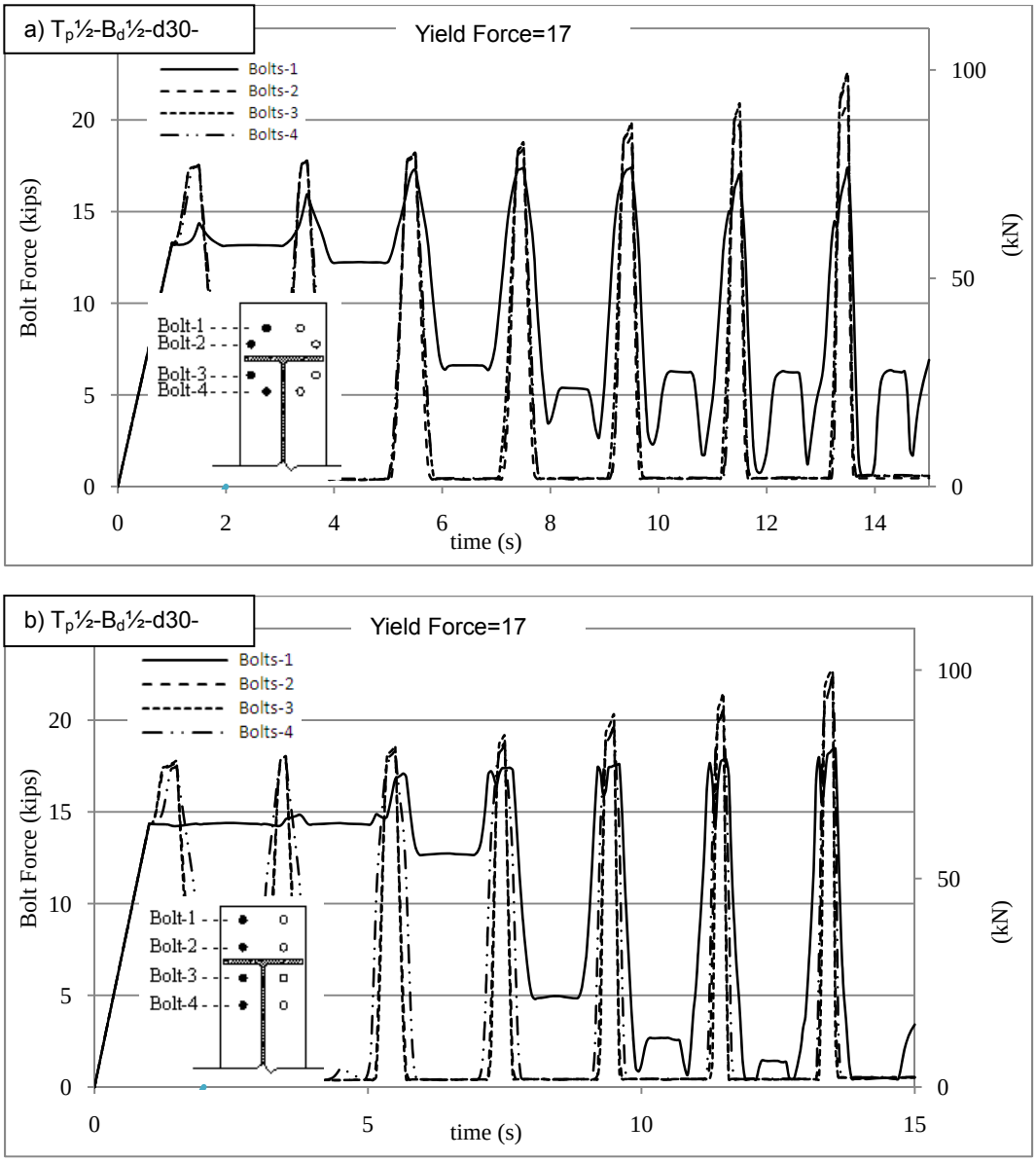

Figure 6-15 Comparison Of The Bolt Forces During Cyclic Loading, And Corresponding Story Drift..

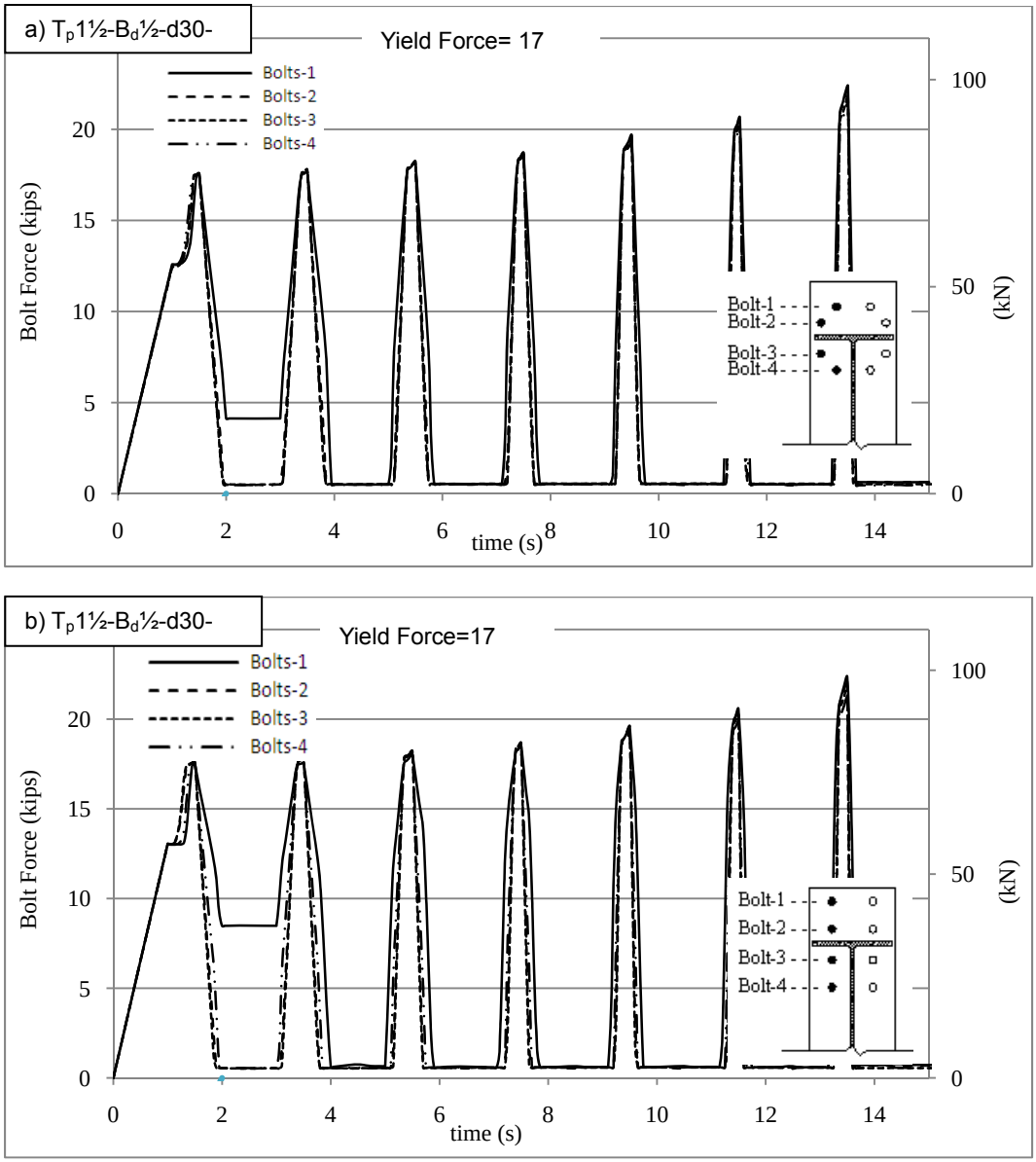

Figure 6-16 Comparison Of The Bolt Forces During Cyclic Loading, And Corresponding Story Drift..

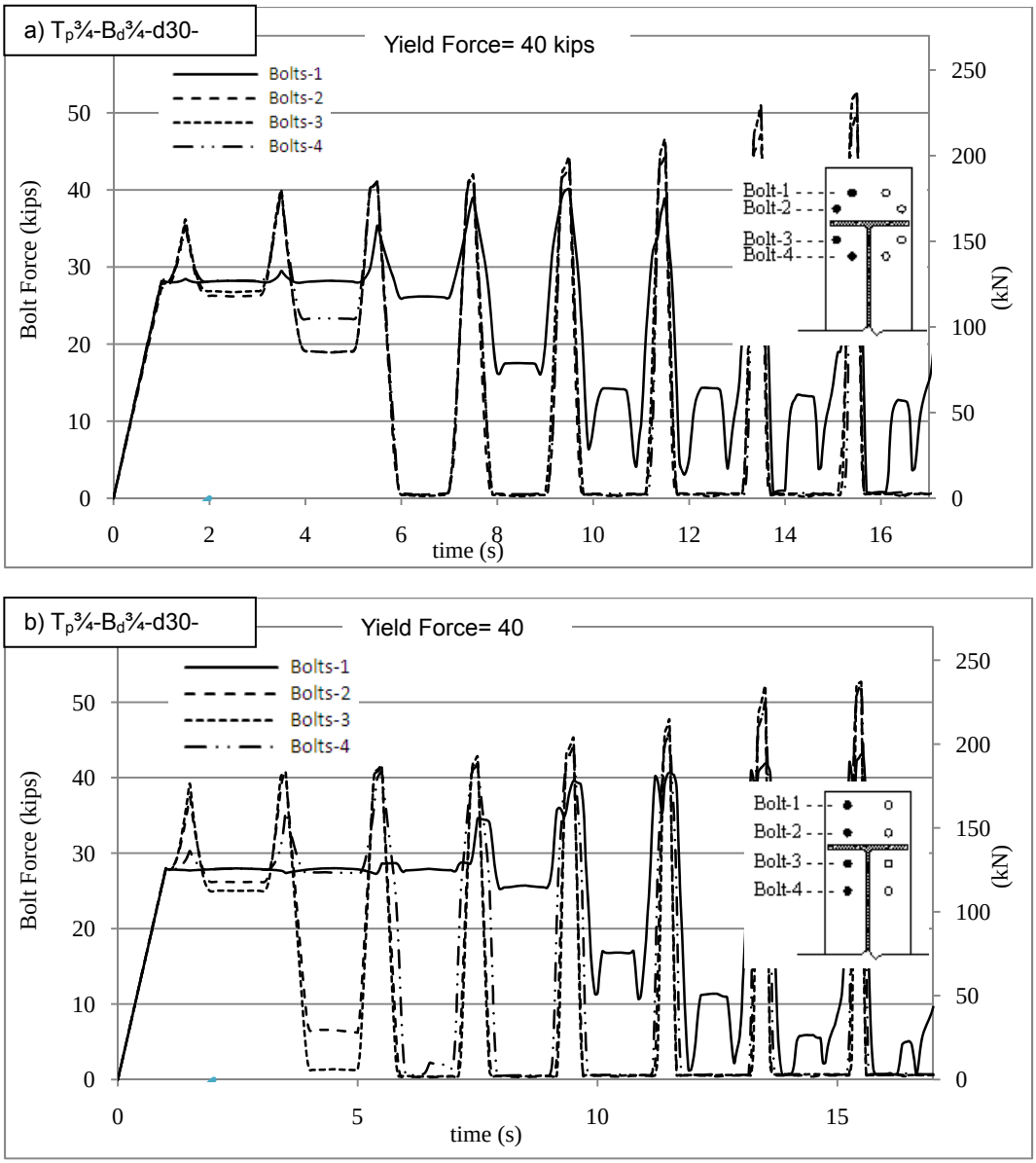

Figure 6-17 Comparison Of The Bolt Forces During Cyclic Loading, And Corresponding Story Drift.

6.6 Effect Of The End-Plate Deformation

To future investigate the effectiveness of the circular bolt pattern the relation between the changes in energy dissipation of the connection and the deformed shape of the end-plate are investigated. Four models with relatively large bolt diameter, 1 in., were selected from the models with 24 in. nominal beam depth and the results were compared. The models with large bolt diameter were selected so that the behavior of the bolts has minimum effect on the overall behavior of the connection. The end-plate deformation of the Models Tp½-Bd1-d24, Tp¾-Bd1-d24, Tp$1\frac{1}{8}$-Bd1-d24, and Tp1½-Bd1-d24 are presented in pair for circular and square bolt pattern in

(b)

Figure 6-18 through Figure 6-21, respectively. To simplify the investigation of the end-plate deformation affect on the hysteresis behavior and energy dissipation of each connection and their percentage variation are presented in Table 6-5.

Table 6-5 Energy Dissipation And Their Persentaige Variation.

Model Name	Energy Dissipation kip.ft.rad		Energy Dissipation Variation %
	SQR Pattern	CIR Pattern	
T_p½-B_d1-24	67.57	63.42	6.5
T_p¾-B_d1-d24	70.22	54.06	29.9
$T_p1\frac{1}{8}$-B_d1-d24	120.50	66.67	80.7
T_p1½-B_d1-d24	180.83	106.05	70.5

The results presented in this table shows that between the models with one inch bolt diameter, the Model $T_p1\frac{1}{8}$-B_d1-d24-Cir with 80.7% variation, has the most increase of the energy dissipation when it is subjected to cyclic loading. These results show that using the circular bolt pattern has limited influence of the connections with thin end-plate, see Model Tp½-Bd1-24 with 6.5%. Also, it can be concluded from these results that the effect of using the circular bolt pattern on the energy dissipation of the connection increases as the end-plate thickness is increasing.

As it was mentioned before, this phenomenon is attributed to the unique coupled interactive deformation of the end-plate and bolt when circular bolt pattern is used. To illustrate this, the deformed

configurations of the finite element models of both circular and square bolt patterns of the models with similar bolt diameter and various end-plate thicknesses are presented in pair and compared in this section; see Figure 6-18 through Figure 6-21.

The end-plate deformations of the Model T_p½-B_d1-d24 with both circular and square bolt pattern are presented in Figure 6-18(a) and Figure 6-18 (b), respectively. These figures show no significant different between the end-plate deformation of the connections with circular or square bolt pattern. Compression of these two figures reveal that due to the small thickness of the end-plate, majority of the rotation and deformation occur in the end-plate and the loads are been absorbed by only the close bolts, Bolt-2 and Bolt-3, while the far bolts remain mostly un-touched.

The end-plate deformations of the Model Tp½-Bd1-d24 with both circular and square bolt pattern are presented in Figure 6-19(a) and Figure 6-19(b). Using circular bolt pattern on these connections enhances the energy dissipation of the connection by 29.9%, see Table 6-5. Studying the end-plate deformation of these connections shows that the connection with circular bolt pattern has a smaller end-plate separation while the evidence of elongation in Bolt-4 of the model with circular bolt pattern is more pronounce when it is compared with the model with square bolt pattern, compare Figure 6-19(a) and Figure 6-19(b).

The end-plate deformations of the Models Tp1$^1/_8$-Bd1-d24 and Tp1½-Bd1-d24 with 80.7% and 70.5% energy dissipation variation are presented in Figure 6-20 and Figure 6-21 respectively. By visual inspection, it can be seen that near bolts undergo more deformation compared with far bolts in the connection with square bolt pattern, compare Figure 6-20(b) and Figure 6-21(b). Indeed, the end-plate at the locations of near bolts (Bolts-2 and Bolt-3) has separated from the column flange with visible gap. In contrast, the deformed shape of the connection with circular bolt pattern Figure 6-20(b), and Figure 6-21(a) shows less deformation, at the location of near bolts (Bolts-2 and Bolt-3), at the same load level with the end-plate being mostly intact with the column flange at the locations of the near bolts.

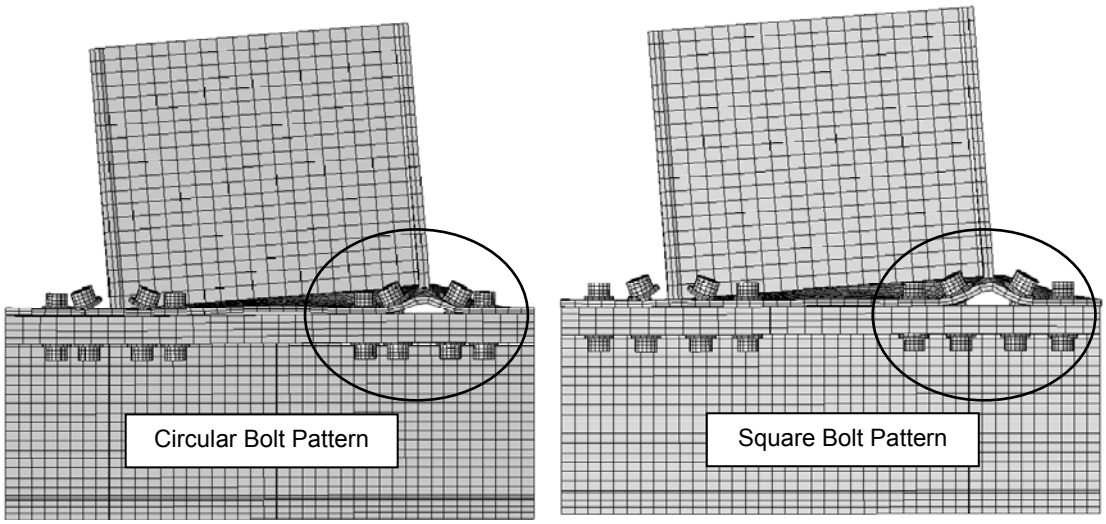

(a) (b)

Figure 6-18 End-Plate Deformation Of (a) Tp½-Bd1-d24-CIR And (b) Tp½-Bd1-d24-SQR

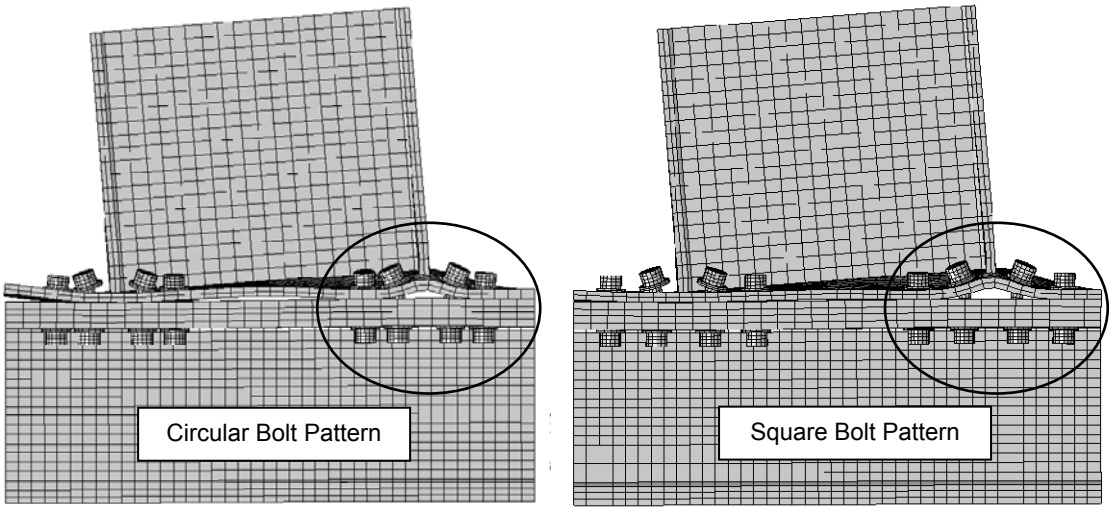

(a) (b)

Figure 6-19 End-Plate Deformation Of (a) T_p¾-B_d1-d24-CIR And (b) T_p¾-B_d1-d24-SQR

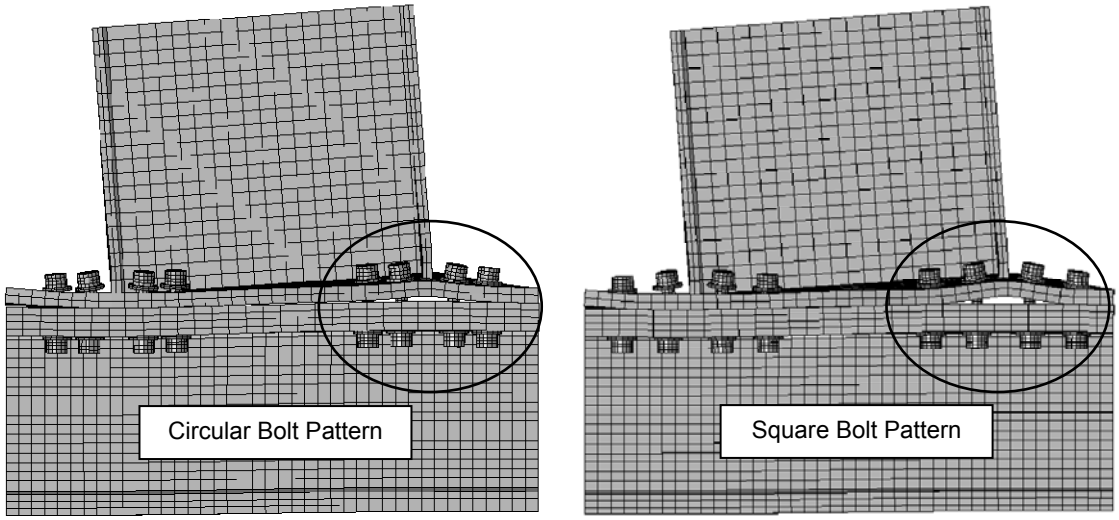

(a) (b)

Figure 6-20 End-Plate Deformation Of (a) $T_p1\frac{1}{8}$-B_d1-d24-CIR And (b) $T_p1\frac{1}{8}$-B_d1-d24-SQR

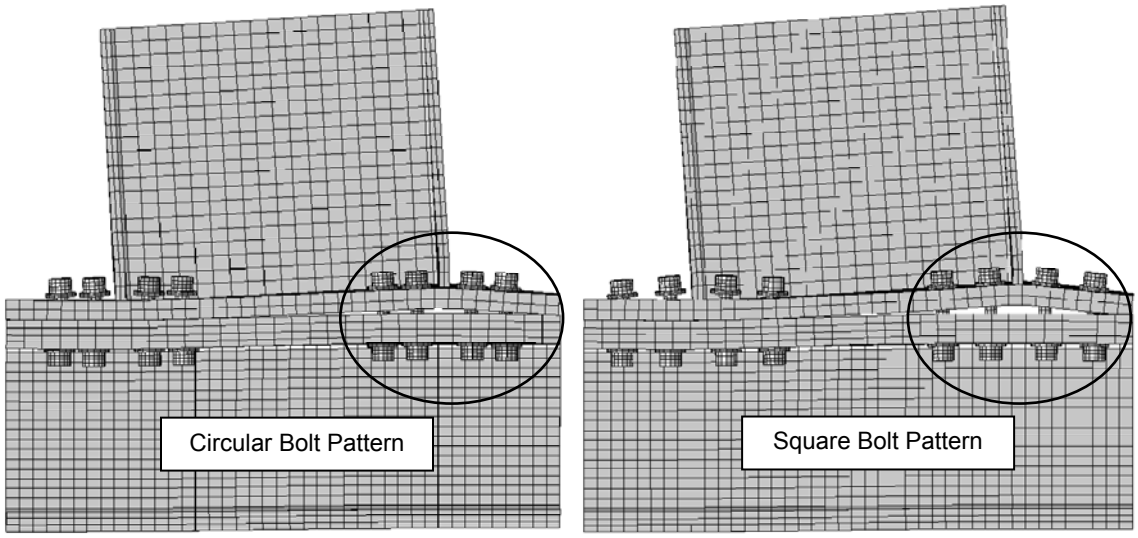

(a) (b)

Figure 6-21 End-Plate Deformation Of (a) T_p1½-B_d1-d24-CIR And (b) T_p1½-B_d1-d24-SQR

To further verify the above analogy, the contour lines of out of plane deformation of the end-plate from the FE analysis of the Models T_p¾-B_d1-d24 and T_p1½-B_d1-d24 for both circular and square bolt patterns are shown in Figure 6-22 and Figure 6-23, respectively.

The contour lines presented in Figure 6-22 show that the out of plane end-plate deformation at the location of near bolts (Bolts-1) is distinctly different from that of the far bolt (Bolts-2) for the model with square bolt pattern presented in Figure 6-22(b), (i.e. 0.6 in versus 0.1 in). However, the examination of the contour lines for circular bolt pattern (Figure 6-22(a)) indicates that the out of plane deformation at the locations of the Bolts-1 and Bolts-2 show and smaller variation. For example, contour lines of 0.4 passed through Bolt-2 while counter line 0.1 passes through Bolt-1. Is can be seen from the results presented in this figures that the Bolt-3 and Bolt-4 undergoing similar out of plain deformation, 0.3 in, in the connection with circular however, in the connection with square bolt pattern the Bolt-3 with 0.6 in. out of plain deformation encounter larger elongation than Bolt-4 with 0.1 in. out of plain deformation.

Same analogy can be used to explain the hysteresis behavior of the Model $T_p1½$-B_d1-d24. The out of plain end-plate deformation of this model for both circular and square bolt pattern is presented in Figure 6-23. The contour lines presented in Figure 6-23(b) show that the end-plate out of plane deformation at the location of near bolts (Bolts-2) is distinctly different from that of the far bolt (Bolts-1) for the square bolt pattern of Figure 6-23(b), (i.e. 0.5 in versus 0.25 in). However, the examination of the contour lines for circular bolt pattern (Figure 6-23(a)) indicates that the out of plane deformation at the locations of the Bolts-1 and Bolts-2 show and smaller variation. For example, contour lines of 0.4 passed through Bolt-2 while counter line 0.3 passes through Bolt-1.

Using the results presented in this section, it can be concluded that the end-plate contour lines at locations of the near and far bolts are more condensed for the connections with circular bolt pattern and, thus, end-plate deforms more uniformly at the locations of the near and far bolts.

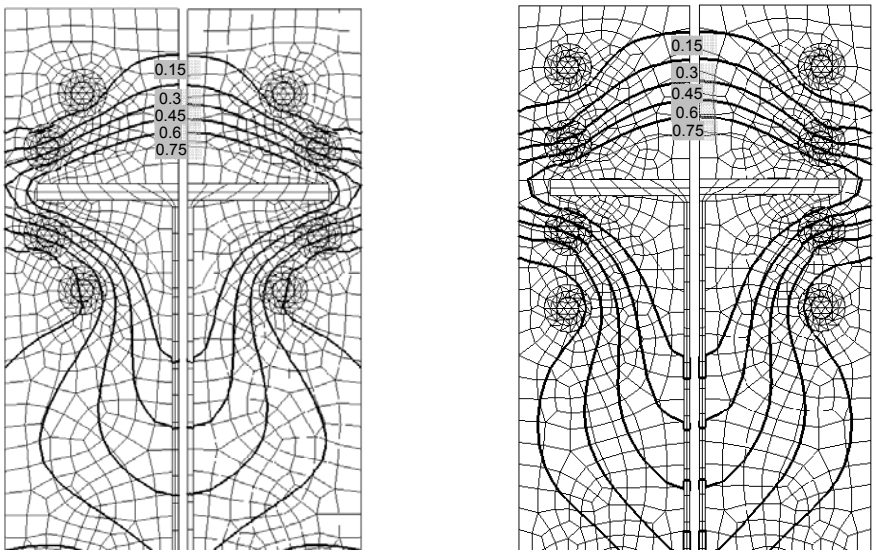

(a) (b)

Figure 6-22 End-Plate Out Of Plain Deformation Contour Of (a) Tp¾-Bd1-d24-CIR And (b) Tp¾-Bd1-d24-SQR

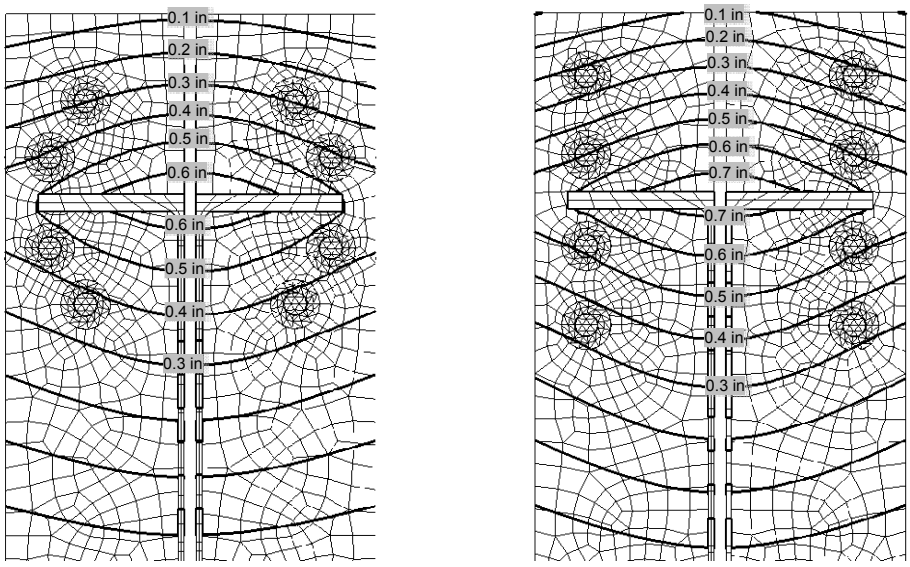

(a) (b)

Figure 6-23 End-Plate Out Of Plain Deformation Contour Of (a) Tp1½-Bd1-d24-CIR And (b) Tp1½-Bd1-d24-SQR

CHAPTER 7

SUMMARY, CONCLUSION, AND RECOMMENDATIONS

7.1 Summary

The behaviors of the extended end-plate connections with both circular and square bolt pattern configuration under static and cyclic loads are investigated. One hundred eighty two three-dimensional nonlinear finite element models were developed and analyzed by using Abaqus 6.10-1 finite element software. A comprehensive test matrix was developed to investigate the effectiveness of various geometric parameters on the overall behavior of the connections. The parametric study conducted in this research included seven bolt diameters, six end-plate thicknesses, three beam sizes, and two different bolt pattern configurations bases on most commonly used range of variables .

The combined hardening plasticity model was used in order to model the behavior of the Grade-50 hot-rolled steel elements during the monotonic and cyclic loading. Isotropic hardening was used to model the material properties of the high strength steel bolts.

Small sliding surface-to-surface was considered for all the contacts. The welds were assumed to be rigid and modeled by tie-contact algorithm. The frictional surfaces accompanied by tangential force were modeled by tangential-contact algorithm. The surface contact between the end-plate and column was modeled by frictional contact using penalty stiffness.

To validate the numerical results obtained from the finite element analysis, the results obtained from three full-scale experimental T-Stubs tests and five semi-rigid connections tests were collected. The numerical models for each specimen was developed using the corresponding geometric and material values. A close agreement between the numerical results and the experimental results were reported.

The regression analysis was conducted on the numerical results obtained from the finite element analysis and the equations were developed to predict and model the hysteresis behavior of the extended end-plate connections. The dependant variables i.e. moment capacity of the connection at yield ($M_{y)}$,

initial stiffness of the connection (E), post yield stiffness of the connection (E_t), and maximum rotation at fracture (θ_f) for each connection were calculated using an independent geometric values: i.e. bolt diameter (b_d), end-plate thickness (t_p), elastic section modules (S), and plastic section modules (Z). Using these results, the predicted hysteresis for each model was created and the area under the curve that represents the energy dissipation of the connection was calculated.

Extensive investigations with regard to the behavior of both circular and square bolt pattern were conducted. This included but not limited to comparison of the effect of bolt diameter and end-plate thickness on moment-rotation curves and hysteresis loops of the connections with both circular and square bolt pattern. The end-plate deformation and yield line pattern for both connection types were compared.

7.2 Conclusion:

- The results of this study show that the circular bolt pattern delays the pinching, improves the connection strength, and enhances the energy dissipation for certain connection parameters. This phenomenon is due to a better distribution of the bolt-forces in the connection which reduces the early yielding of the bolts.
- The circular bolt pattern was shown to be highly effective in eliminating hysteresis pinching in connections with relatively large bolt diameter and end-plate thickness.
- In connections with circular bolt pattern with relatively large bolt diameter, as the plate thickness increases, the effectiveness of the far bolts in carrying the flange force becomes more pronounced. It was shown that in connections with large bolt diameters and plate thickness, all the four bolts carry approximately the same load when circular bolt pattern was used. Particularly, the far bolts closer to the region of beam web fully contribute in load carrying capacity of the connection.
- This study shows that for relatively small bolt diameter and end-plate thickness, the benefits of circular bolt pattern are minimal. This effect is insignificant for connections with relatively large plate thickness and small bolt diameter.
- It is concluded the unique deformation of the end-plate in connections with circular bolt patterns plays the main role in the overall behavior of the connection. Close examination of the end-plate

deformed shape contour lines showed that the end-plate contour lines at locations of the near and far bolts are more condensed, closer to each other, for the connections with circular bolt pattern, thus the end-plate deforms more uniformly at the locations of the near and far bolts. This results in a more uniform distribution of the bolt force between the bolts in the connection.

- Tri-linear hysteresis model was used to simulate the behavior of the connection. To predict the hysteresis characteristics of the connection the hysteresis behavior was divided into two categories: "*End-Plate Behavior*" and "*Bolt Behavior.*" The proposed tri-linear hysteresis models are different from what are commonly found in the literature. The proposed models promise a better prediction of the hysteresis characteristics of the connection and reduce the degree of un-conservativeness.
- The tri-linear model equations are developed based on four parameters (i.e., M_y, E, E_t, and θ_f). For each of the above parameters (dependant variables), prediction equation were developed using a non-linear regression analysis. These equations are in term of connection dependent geometric variables (i.e., b_d, t_p, S, and Z).
- The results obtained from the prediction equations were compared by the true value for each connection using corresponding independent geometric variables. This study was conducted on connections with both circular and square bolt pattern separately. The results of this comparison show that majority of the predicted variables fall into ±5 error envelope when they are compared with the true value of the corresponding connection. Therefore, the developed equations proposed as an alternative method to model the hysteresis characteristic of the extended-end-plate connection.
- Using the predicted dependent variables and the proposed hysteresis models introduced in this research the predicted hysteresis for each connection was graphed against the hysteresis results obtained from the finite element models. The comparison of the presented results shows satisfactory agreement between the predicted and true behavior of the connection.

7.3 Recommendations

The parametric study conducted in this research was limited to seven bolt diameters, six end-plate thicknesses, three beam sizes, and two different bolt pattern configurations, while other important factors that affect the overall behavior of the connection was neglected. Further investigation with more

parameters is recommended to study the effect of other parameters on the hysteresis characteristic of the connections.

The tri-linear model with kinematic, isotropic, or combined hardening is commonly used in the design software to simulate the hysteresis characteristic of the connections, which is necessary while analyzing the overall behavior of the moment resisting frames. Implementation of the proposed hysteresis models in the frame analysis of frames systems, particularly; SAC frames subjected to ground base motion with different amplitude and frequencies are highly recommended.

APPENDIX A

APPLIED TORGUE VERSUS PRE-TENSIONING BOLT FORCE

The relation between applied torque, T, and pre-tensioning load is;

$$T = k.F_i.d$$

Where d is the nominal outside diameter of the bolt and k is the correction factor that depends on the material, size, surface friction, and threading of the bolt. For most small to mid size bolts, k is between 0.15 and 0.3. For dry (un-lubricated) mid-size steel bolts the k is approximation k=0.2

Required torque for 0.5 in bolt:

Where;

$$d = 0.5 \text{ in}$$

$$F_i = 12 \text{ kips}$$

$$k = 0.2$$

$$T = 0.2 \times 12 \text{ kips} \times 0.5 \text{ in} = 1200 \text{ lb.in} = 100 \text{ lb.ft}$$

APPENDIX B

TEST MATRIX

Table B-1 Test Matrix Of The Connections With Minimal Beam Depth Of 30 in.

d=30 in		B_d (in)					
		1/2	5/8	3/4	1.0	1-1/8	1-1/4
Tp I(in)	1/2	Tp½-bd½-d30-Cir	Tp½ bd$^{5}/_{8}$ d30 Cir	Tp½-bd¾-d30-Cir	Tp½-bd1-d30-Cir	Tp½ bd1$^{1}/_{8}$ d30 Cir	Tp½-bd1¼-d30-Cir
		Tp½-bd½-d30-Sqr	Tp½-bd$^{5}/_{8}$-d30-Sqr	Tp½-bd¾-d30-Sqr	Tp½-bd1-d30-Sqr	Tp½-bd1$^{1}/_{8}$-d30-Sqr	Tp½-bd1¼-d30-Sqr
	5/8	Tp$^{5}/_{8}$-bd½-c30-Cir	Tp$^{5}/_{8}$-bd$^{5}/_{8}$-d30-Cir	Tp$^{5}/_{8}$-bd¾-d30-Cir	Tp$^{5}/_{8}$-bd1-d30-Cir	Tp$^{5}/_{8}$-bd1$^{1}/_{8}$-d30-Cir	Tp$^{5}/_{8}$-bd1¼-d30-Cir
		Tp$^{5}/_{8}$-bd½-d30-Sqr	Tp$^{5}/_{8}$-bd$^{5}/_{8}$-d30-Scr	Tp$^{5}/_{8}$-bd¾-d30-Sqr	Tp$^{5}/_{8}$-bd1-d30-Sqr	Tp$^{5}/_{8}$-bd1$^{1}/_{8}$-d30-Sqr	Tp$^{5}/_{8}$-bd1¼-d30-Sqr
	3/4	Tp¾-bd½-d30-Cir	Tp¾-bd$^{5}/_{8}$-d30-Cir	Tp¾-bd¾-d30-Cir	Tp¾-bd1-d30-Cir	Tp¾-bd1$^{1}/_{8}$-d30-Cir	Tp¾-bd1¼-d30-Cir
		Tp¾-bd½-d30-Sqr	Tp¾-bd$^{5}/_{0}$-d30-Sqr	Tp¾-bd¾-d30-Sqr	Tp¾-bd1-d30-Sqr	Tp¾-bd1$^{1}/_{0}$-d30-Sqr	Tp¾-bd1¼-d30-Sqr
	1.0	Tp1-bd½-d30-Cir	Tp1-bd$^{5}/_{8}$-d30-Cir	Tp1-bd¾-d30-Cir	Tp1-bd1-d30-Cir	Tp1-bd1$^{1}/_{8}$-d30-Cir	Tp1-bd1¼-d30-Cir
		Tp1-bc½-d30-Sqr	Tp1-bd$^{5}/_{8}$-d30-Sqr	Tp1-bd¾-d30-Sqr	Tp1-bd1-d30-Sqr	Tp1-bc1$^{1}/_{8}$-d30-Sqr	Tp1-bd1¼-d30-Sqr
	1-1/8	Tp1$^{1}/_{8}$-bd½-d30-Cir	Tp1$^{1}/_{8}$-bd$^{5}/_{8}$-d30-Cir	Tp1$^{1}/_{8}$-bd¾-d30-Cir	Tp1$^{1}/_{8}$-bd1-d30-Cir	Tp1$^{1}/_{8}$-bd1$^{1}/_{8}$-d30-Cir	Tp1$^{1}/_{8}$-bd1¼-d30-Cir
		Tp1$^{1}/_{8}$-bd½-d30-Sqr	Tp1$^{1}/_{8}$-bc$^{5}/_{8}$-d30-Sqr	Tp1$^{1}/_{8}$-bd¾-d30-Sqr	Tp1$^{1}/_{8}$-bd1-d30-Sqr	Tp1$^{1}/_{8}$-bd1$^{1}/_{8}$-d30-Sqr	Tp1$^{1}/_{8}$-bd1¼-d30-Sqr
	1-1/4	Tp1¼-bd½-d30-Cir	Tp1¼-bc$^{5}/_{8}$-d30-Cir	Tp1¼-bd¾-d30-Cir	Tp1¼-bd1-d30-Cir	Tp1¼-bd1$^{1}/_{8}$-d30-Cir	Tp1¼-bd1¼-d30-Cir
		Tp1¼-bd½-c30-Sqr	Tp1¼-bd$^{5}/_{8}$-d30-Sqr	Tp1¼-bd¾-d30-Sqr	Tp1¼-bd1-d30-Sqr	Tp1¼-bd1$^{1}/_{8}$-d30-Sqr	Tp1¼-bd1¼-d30-Sqr
	1-1/2	Tp1½-bd½-d30-Cir	Tp1½-bc$^{5}/_{8}$-d30-Cir	Tp1½-bd¾-d30-Cir	Tp1½-bd1-d30-Cir	Tp1½-bd1$^{1}/_{8}$-d30-Cir	Tp1½-bd1¼-d30-Cir
		Tp1½ bd½ c30 Sqr	Tp1½-bd$^{5}/_{8}$-d30-Sqr	Tp1½ bd¾ d30 Sqr	Tp1½ bd1 d30 Sqr	Tp1½-bd1$^{1}/_{8}$-d30-Sqr	Tp1½ bd1¼ d30 Sqr

Table B-2 Test Matrix Of The Connections With Minimal Beam Depth Of 24 in.

d=24 in		B_c (in)					
		1/2	5/8	3/4	1.0	1-1/8	1-1/4
T_p l(in)	1/2	Tp½-bd½-d24-Cir	Tp½-bd⅝-d24-Cir	Tp½-bd¾-d24-Cir	Tp½bd1-d24-Cir	Tp½-bc1⅛-d24-Cir	Tp½-bd1¼-d24-Cir
		Tp½-bd½-d24-Sqr	Tp½-bd⅝-d24-Sqr	Tp½-bd¾-d24-Sqr	Tp½-bd1-d24-Sqr	Tp½-bd1⅛-d24-Sqr	Tp½-bd1¼-d24-Sqr
	5/8						
	3/4	Tp¾-bd½-d24-Cir	Tp¾-bd⅝-d24-Cir	Tp¾-bd¾-d24-Cir	Tp¾-bd1-d24-Cir	Tp¾-bc1⅛-d24-Cir	Tp¾-bd1¼-d24-Cir
		Tp¾-bd½-d24-Sqr	Tp¾-bd⅝-d24-Sqr	Tp¾-bd¾-d24-Sqr	Tp¾-bd1-d24-Sqr	Tp¾-bd1⅛-d24-Sqr	Tp¾-bd1¼-d24-Sqr
	1.0						
	1-1/8	Tp1⅛-bd½-d24-Cir	Tp1⅛-bd⅝-d24-Cir	Tp1⅛-bd¾-d24-Cir	Tp1⅛-bd1-d24-Cir	Tp1⅛-bd1⅛-d24-Cir	Tp1⅛-bd1¼-d24-Cir
		Tp1⅛-bd½-d24-Sqr	Tp1⅛-bd⅝-d24-Sqr	Tp1⅛-bd¾-d24-Sqr	Tp1⅛-bd1-d24-Sqr	Tp1⅛-bd1⅛-d24-Sqr	Tp1⅛-bd1¼-d24-Sqr
	1-1/4						
		Tp1¼-bd½-d24-Sqr	l p1¼-bc⅝-d24-Sqr	Tp1¼-bd¾-d24-Sqr	Tp1¼-bd1-d24-Sqr	l p1¼-bd1⅛-d24-Sqr	Tp1¼-bd1¼-d24-Sqr
	1-1/2	Tp1½-bd½-d24-Cir	Tp1½-bd⅝-d24-Cir	Tp1½-bd¾-d24-Cir	Tp1½-bd1-d24-Cir	Tp1½-bd1⅛-d24-Cir	Tp1½-bd1¼-d24-Cir
		Tp1½-bd½-d24-Sqr	Tp1½-bc⅝-d24-Sqr	Tp1½-bd¾-d24-Sqr	Tp1½-bd1-d24-Sqr	Tp1½-bd1⅛-d24-Sqr	Tp1½-bd1¼-d24-Sqr

Table B-3Test Matrix Of The Connections With Minimal Beam Depth Of 30 in.

d= 36 in		B_d (in)					
		1/2	5/8	3/4	1.0	1-1/8	1-1/4
T_p l(in)	1/2	Tp½-bd½-d36-Cir	Tp½-bd⅝-d36-Cir	Tp½-bd¾-d36-Cir	Tp½-bd1-d36-Cir	Tp½-bd1⅛-d36-Cir	Tp½-bd1¼-d36-Cir
		Tp½-bd½-d36-Sqr	Tp½-bd⅝-d36-Sqr	Tp½-bd¾-d36-Sqr	Tp½-bd1-d36-Sqr	Tp½-bd1⅛-d36-Sqr	Tp½-bd1¼-d36-Sqr
	5/8						
	3/4	Tp¾-bd½-d36-Cir	Tp¾-bd⅝-d36-Cir	Tp¾-bd¾-d36-Cir	Tp¾-bd1-d36-Cir	Tp¾-bd1⅛-d36-Cir	Tp¾-bd1¼-d36-Cir
		Tp¾-bd½-d36-Sqr	Tp¾-bd⅝-d36-Sqr	Tp¾-bd¾-d36-Sqr	Tp¾-bd1-d36-Sqr	Tp¾-bd1⅛-d36-Sqr	Tp¾-bd1¼-d36-Sqr
	1.0						
	1-1/8	Tp1⅛-bd½-d36-Cir	Tp1⅛-bd⅝-d36-Cir	Tp1⅛-bd¾-d36-Cir	Tp1⅛-bd1-d36-Cir	Tp1⅛-bd1⅛-d36-Cir	Tp1⅛-bd1¼-d36-Cir
		Tp1⅛-bd½-d36-Sqr	Tp1⅛-bd⅝-d36-Sqr	Tp1⅛-bd¾-d36-Sqr	Tp1⅛-bd1-d36-Sqr	Tp1⅛-bd1⅛-d36-Sqr	Tp1⅛-bd1¼-d36-Sqr
	1-1/4						
	1-1/2	Tp1½-bd½-d36-Cir	Tp1½-bd⅝-d36-Cir	Tp1½-bd¾-d36-Cir	Tp1½-bd1-d36-Cir	Tp1½-bd1⅛-d36-Cir	Tp1½-bd1¼-d36-Cir
		Tp1½-bd½-d36-Sqr	Tp1½-bd⅝-d36-Sqr	Tp1½-bd¾-d36-Sqr	Tp1½-bd1-d36-Sqr	Tp1½-bd1⅛-d36-Sqr	Tp1½-bd1¼-d36-Sqr

APPENDIX C

HYSTERESIS OF THE MODELS WITH SQUARE BOLT PATTERN

The hysteresis results obtained from finite element analysis for the models with square bolt pattern are presented individually in this Appendix. Tri-linear model were used to simulated hysteresis characteristic of each model. The simulated tri-linear model for each connection is also presented in the graphs. It should be noted that the procedure presented in the flowchart of Figure 5.8 were used to calculate the dependent values required to construct the hysteresis. Comparison of the results show a close agreement between the results obtained from the numerical analysis and the results obtained from the proposed tri-linear simulation.

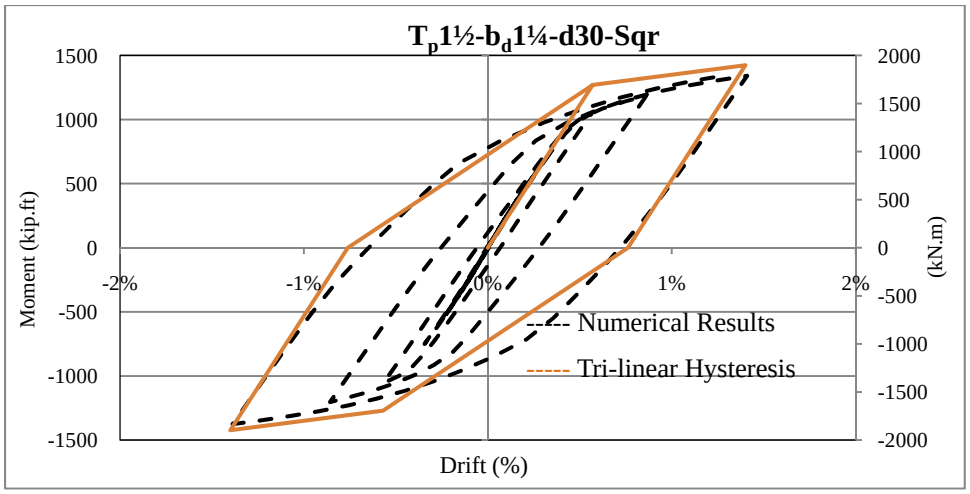

Figure C-1 Comparison Of The Numerical And Simulated Tri-Linear Hysteresis Of The $T_p1½\text{-}b_d1¼$-d30-Sqr Connection

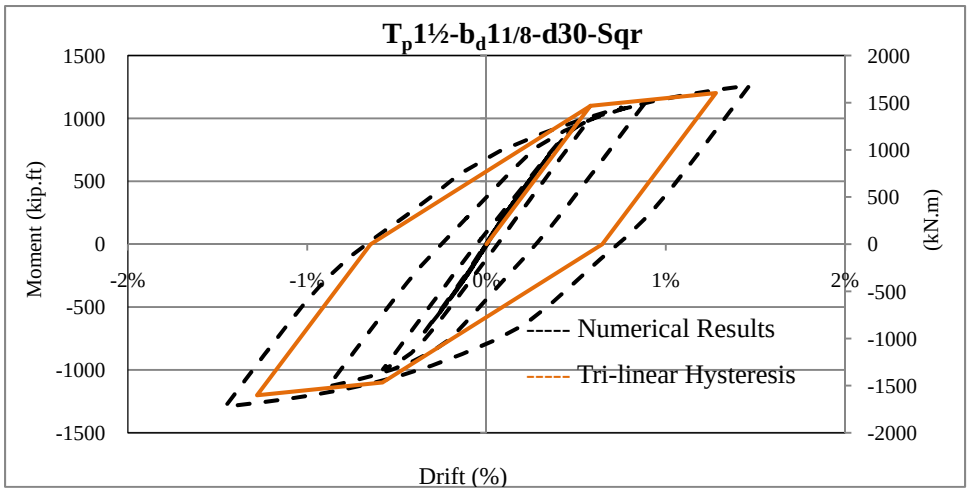

Figure C-2 Comparison Of The Numerical And Simulated Tri-Linear Hysteresis Of The $T_p1½\text{-}b_d11/8$-d30-Sqr Connection

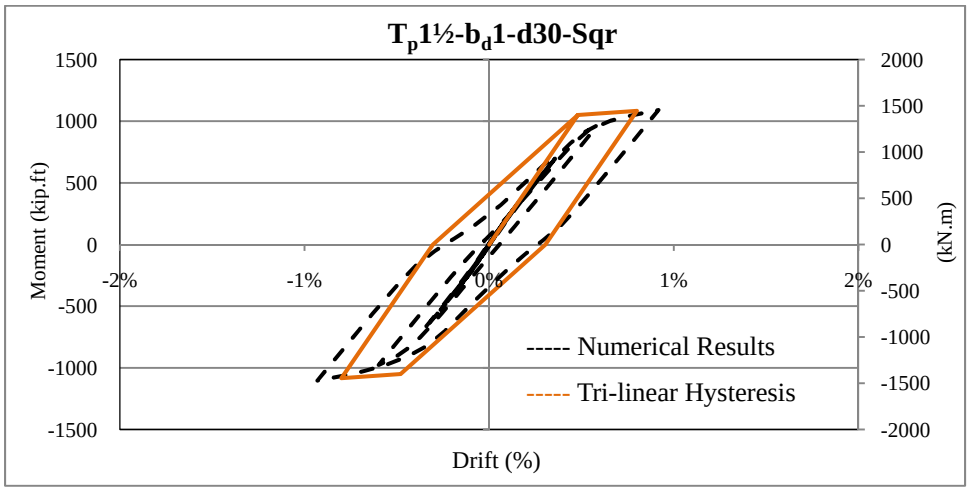

Figure C-3 Comparison Of The Numerical And Simulated Tri-Linear Hysteresis Of The $T_p1½\text{-}b_d1$-d30-Sqr Connection

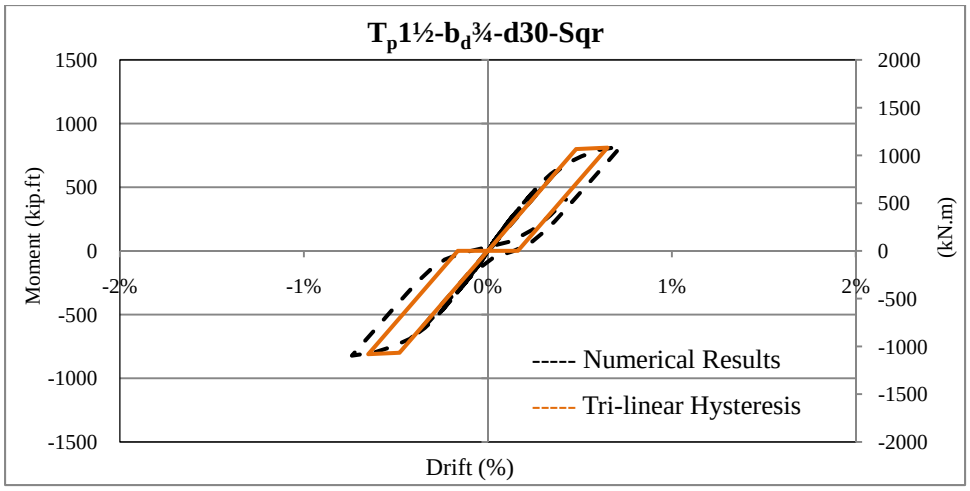

Figure C-4 Comparison Of The Numerical And Simulated Tri-Linear Hysteresis Of The Tp1½-bd¾-d30-Sqr Connection

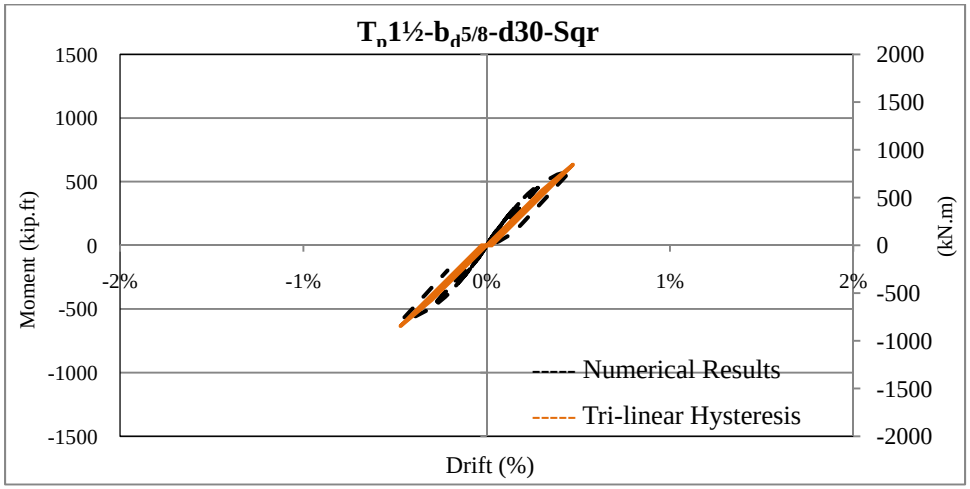

Figure C-5 Comparison Of The Numerical And Simulated Tri-Linear Hysteresis Of The Tp1½-bd5/8-d30-Sqr Connection

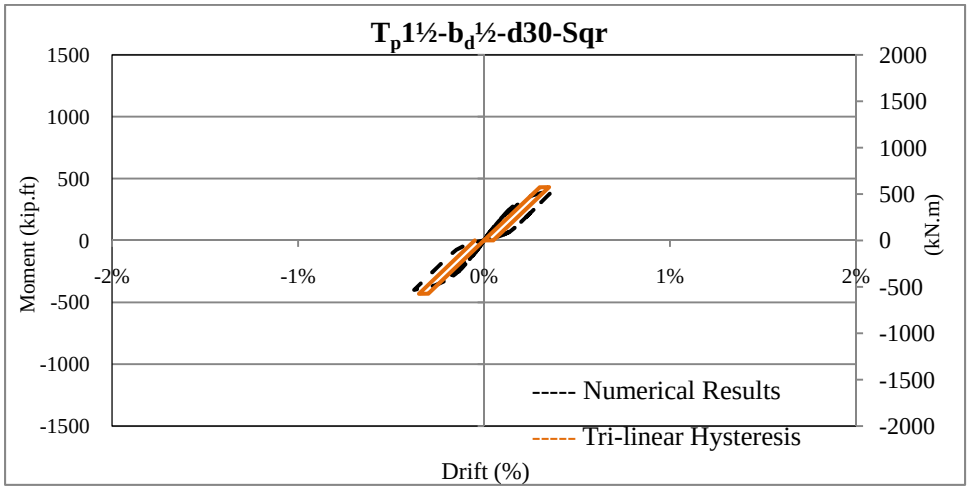

Figure C-6 Comparison Of The Numerical And Simulated Tri-Linear Hysteresis Of The T_p1½-b_d½-d30-Sqr Connection

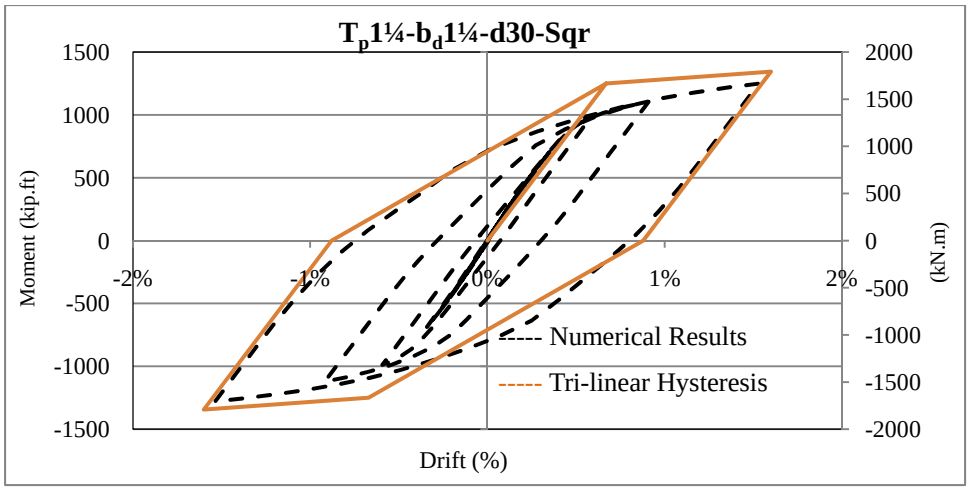

Figure C-7 Comparison Of The Numerical And Simulated Tri-Linear Hysteresis Of The Tp1¼-bd1¼-d30-Sqr Connection

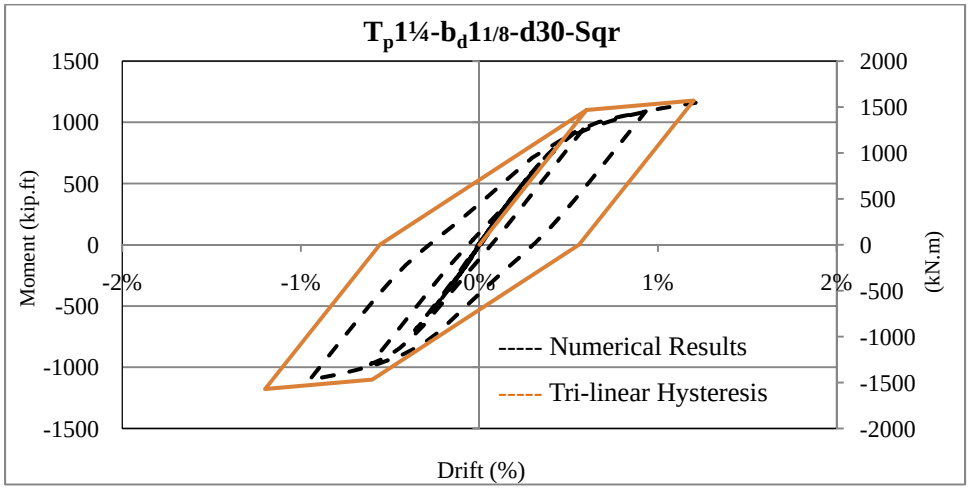

Figure C-8 Comparison Of The Numerical And Simulated Tri-Linear Hysteresis Of The Tp1¼-bd11/8-d30-Sqr Connection

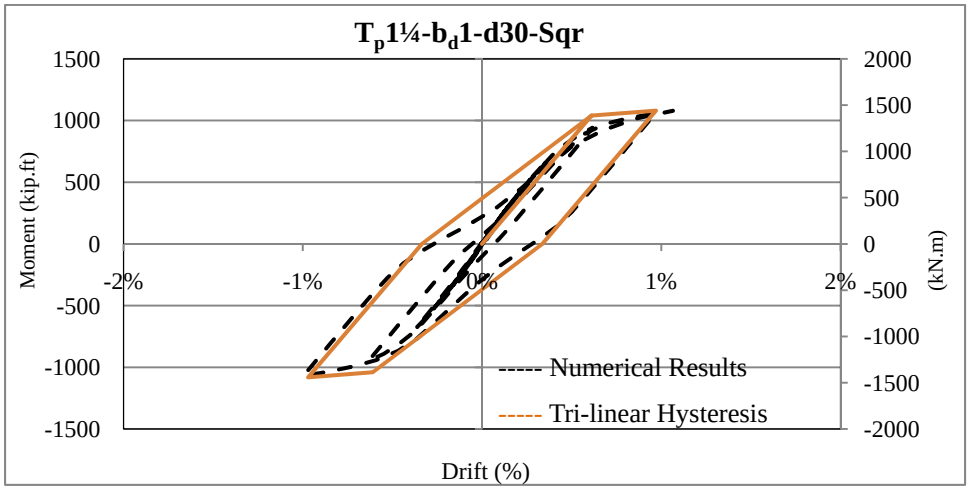

Figure C-9 Comparison Of The Numerical And Simulated Tri-Linear Hysteresis Of The T_p1¼-b_d1-d30-Sqr Connection

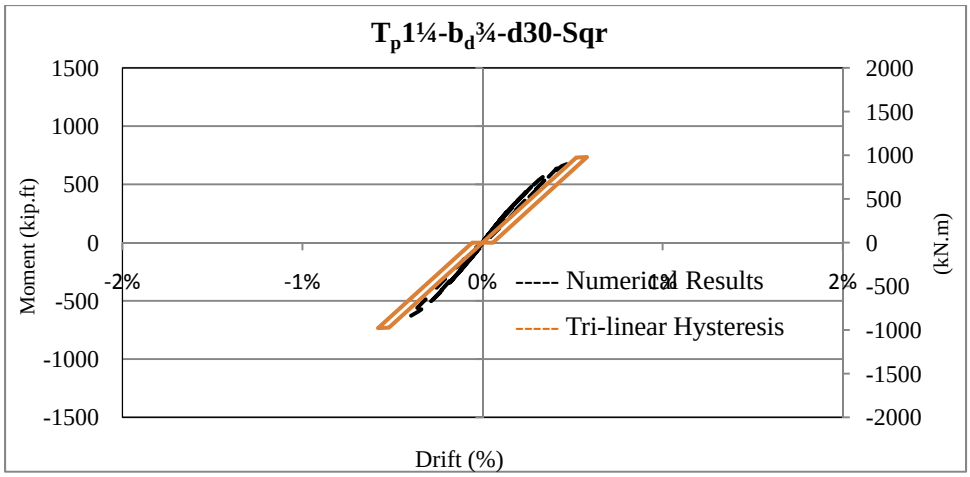

Figure C-10 Comparison Of The Numerical And Simulated Tri-Linear Hysteresis Of The $T_p1¼\text{-}b_d¾\text{-}d30\text{-}Sqr$ Connection

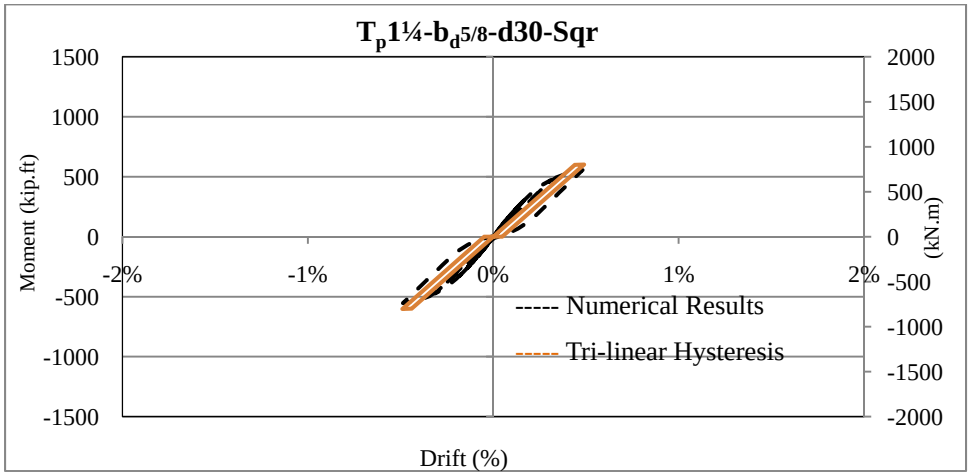

Figure C-11 Comparison Of The Numerical And Simulated Tri-Linear Hysteresis Of The $T_p1¼\text{-}b_d5/8\text{-}d30\text{-}Sqr$ Connection

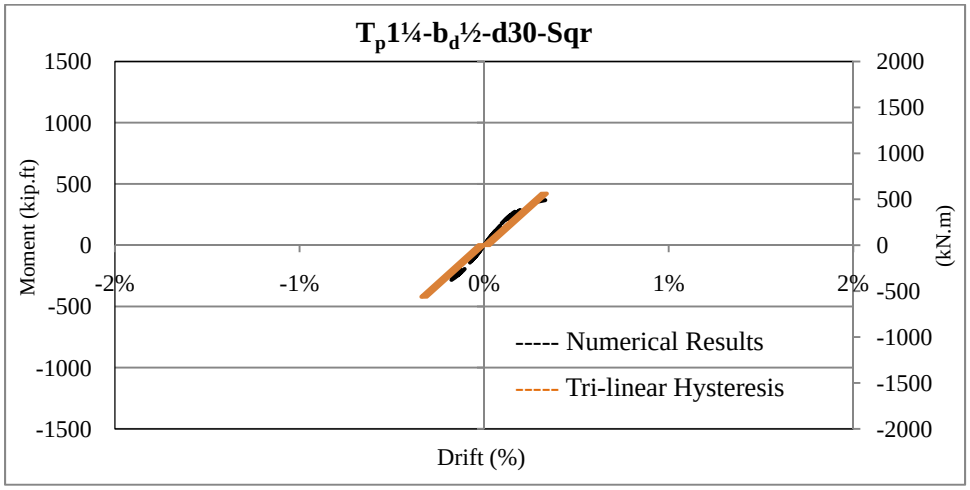

Figure C-12 Comparison Of The Numerical And Simulated Tri-Linear Hysteresis Of The $T_p1¼\text{-}b_d½\text{-}d30\text{-}Sqr$ Connection

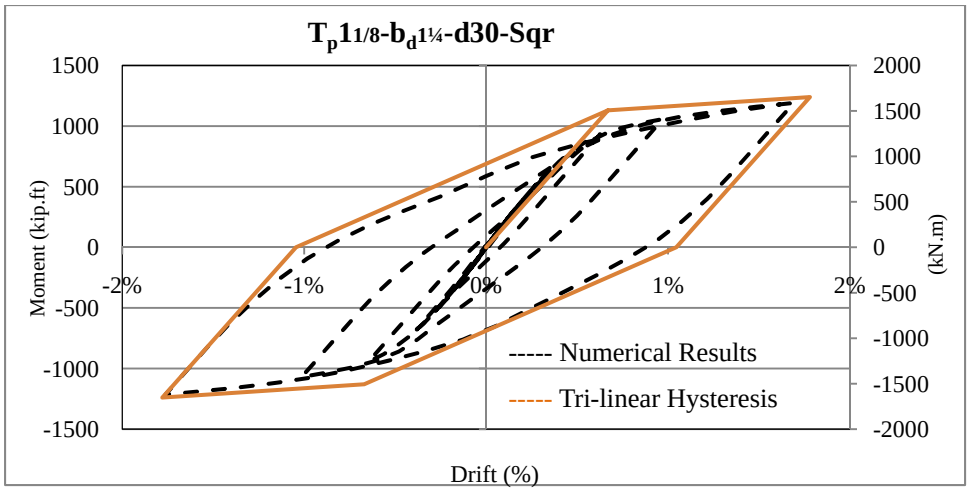

Figure C-13 Comparison Of The Numerical And Simulated Tri-Linear Hysteresis Of The T_p11/8-b_d1¼-d30-Sqr Connection

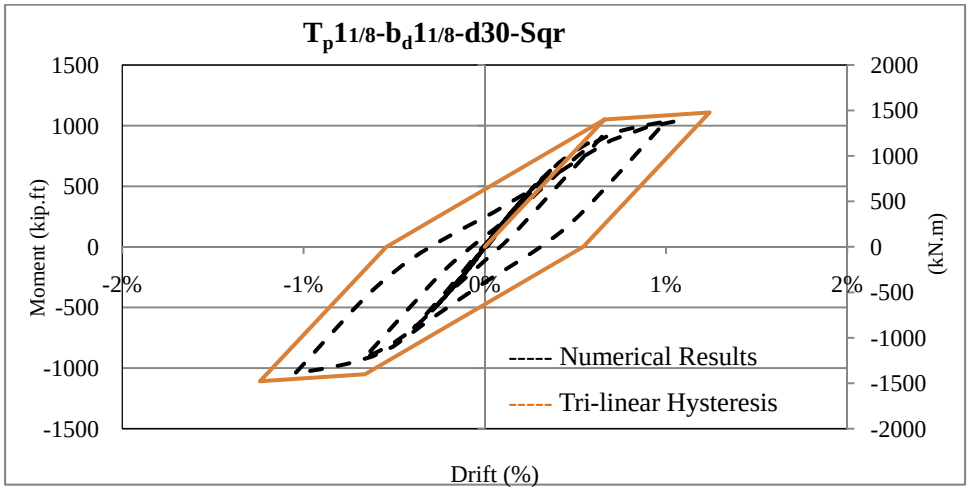

Figure C-14 Comparison Of The Numerical And Simulated Tri-Linear Hysteresis Of The T_p11/8-b_d11/8-d30-Sqr Connection

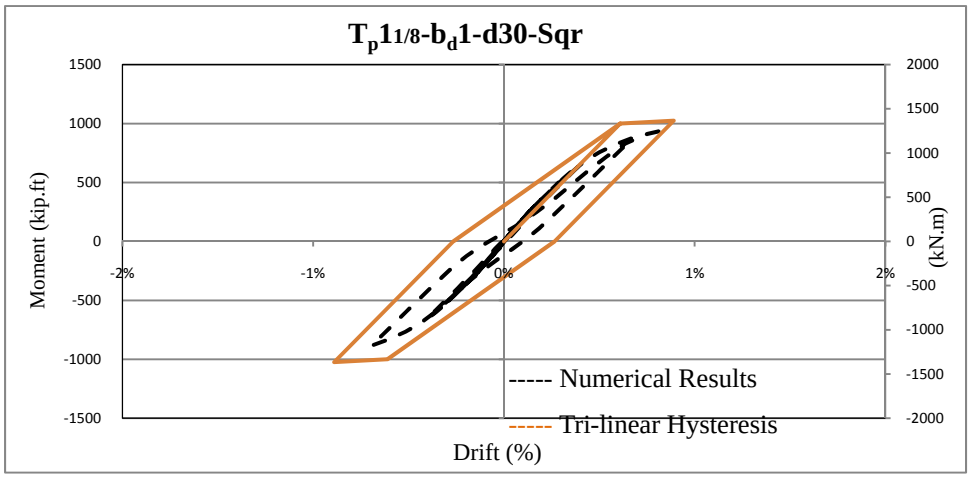

Figure C-15 Comparison Of The Numerical And Simulated Tri-Linear Hysteresis Of The T_p11/8-b_d1-d30-Sqr Connection

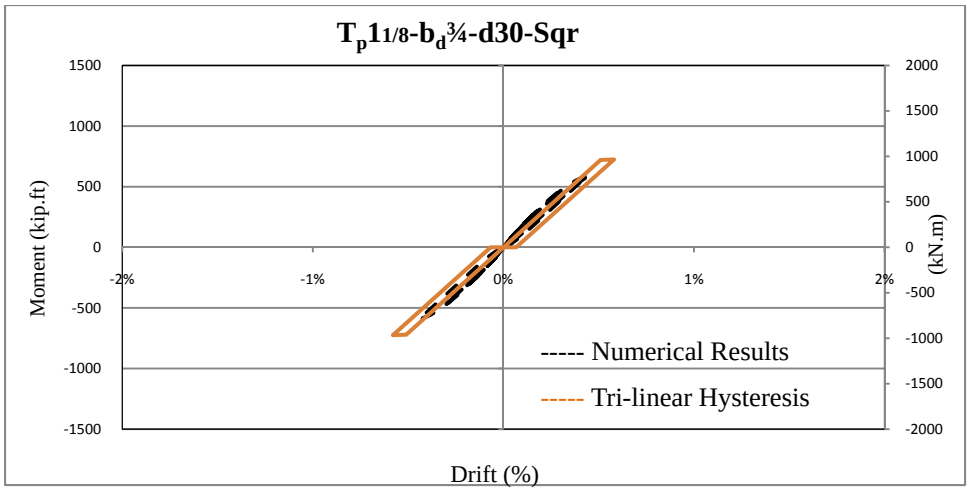

Figure C-16 Comparison Of The Numerical And Simulated Tri-Linear Hysteresis Of The T_p11/8-b_d¾-d30-Sqr Connection

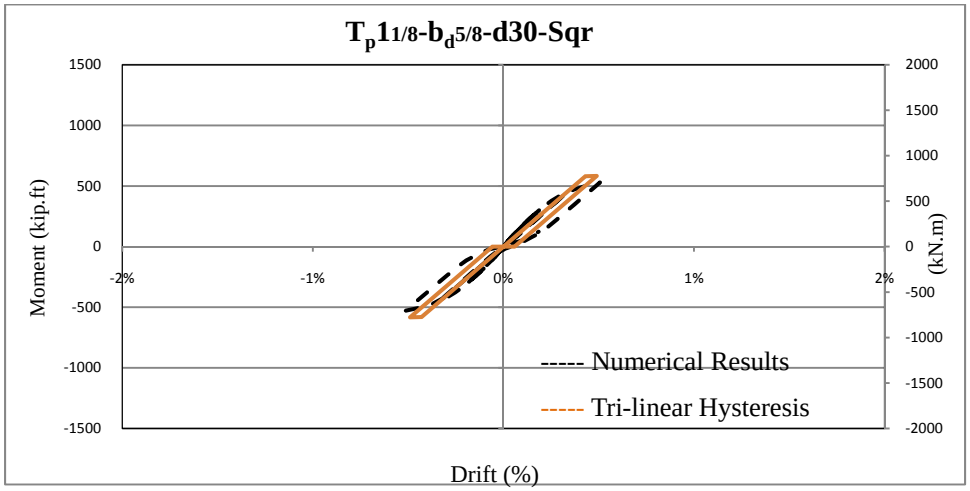

Figure C-17 Comparison Of The Numerical And Simulated Tri-Linear Hysteresis Of The T_p1 1/8-b_d5/8-d30-Sqr Connection

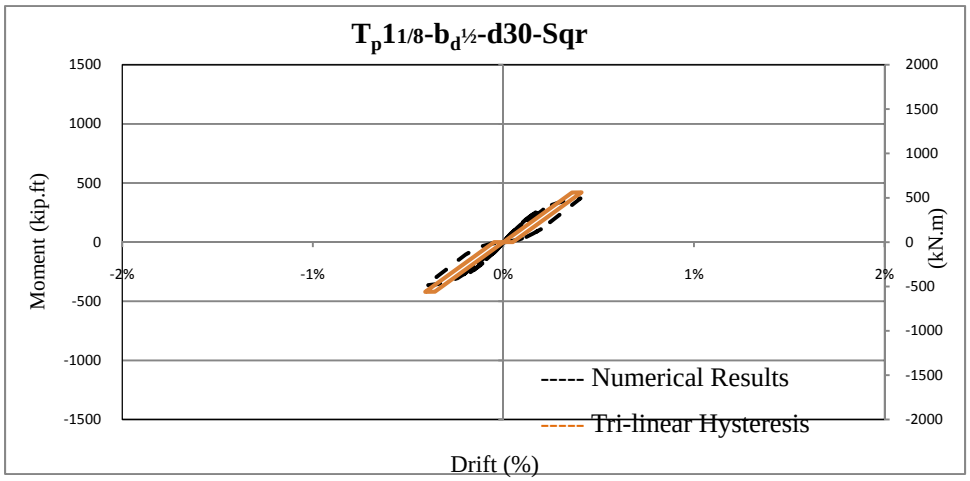

Figure C-18 Comparison Of The Numerical And Simulated Tri-Linear Hysteresis Of The T_p1 1/8-b_d½-d30-Sqr Connection

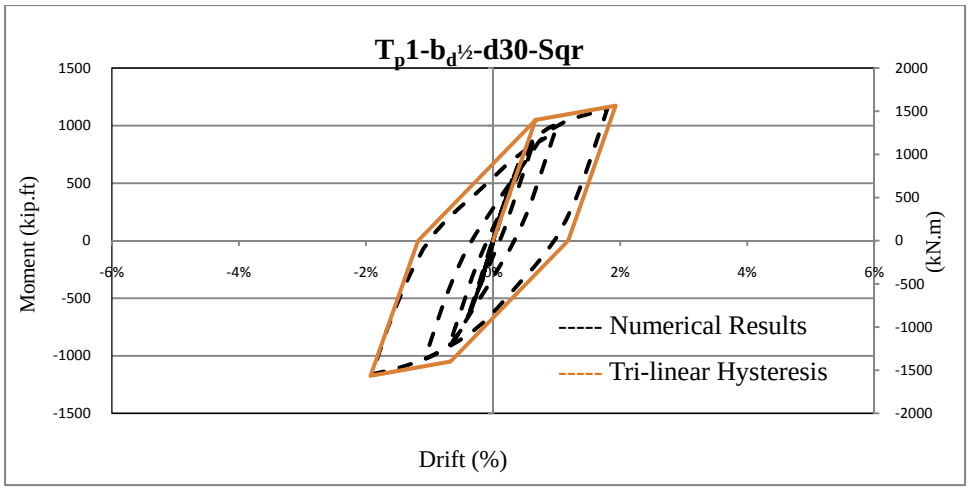

Figure C-19 Comparison Of The Numerical And Simulated Tri-Linear Hysteresis Of The T_p1-b_d½-d30-Sqr Connection

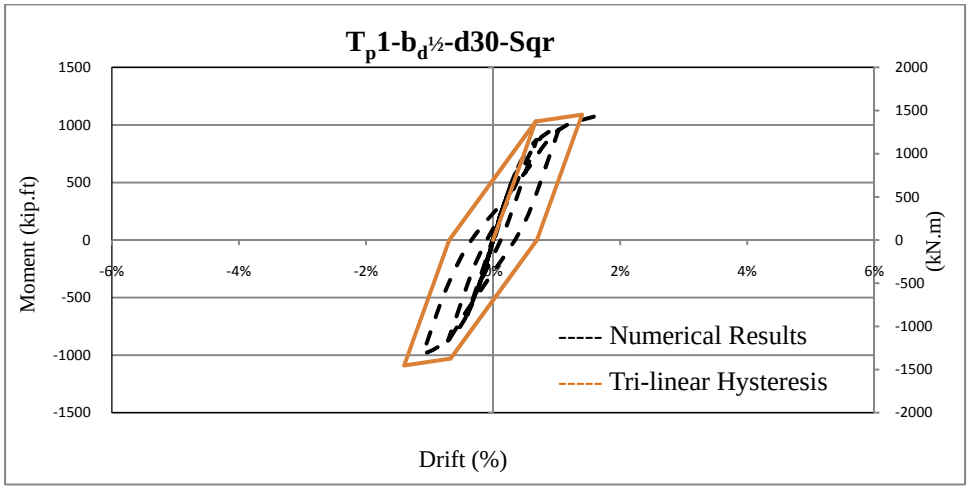

Figure C-20 Comparison Of The Numerical And Simulated Tri-Linear Hysteresis Of The T_p1-b_d½-d30-Sqr Connection

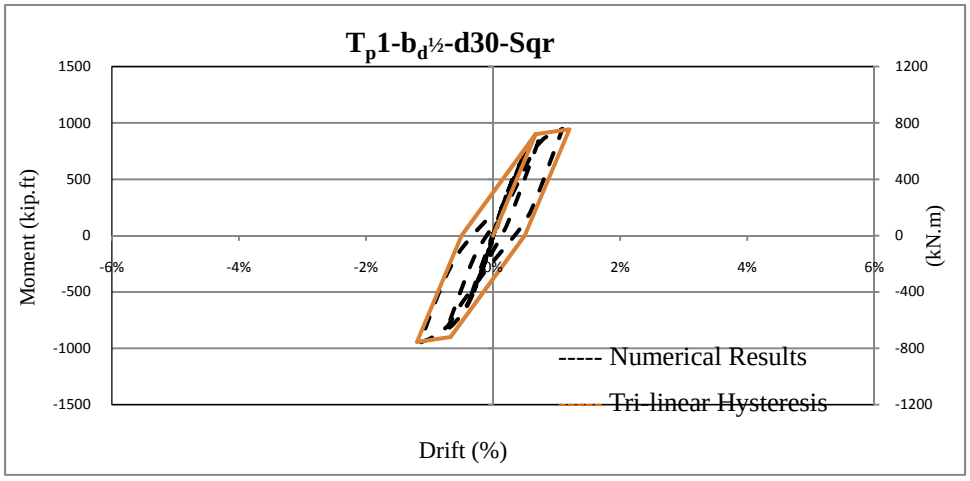

Figure C-21 Comparison Of The Numerical And Simulated Tri-Linear Hysteresis Of The T_p1-b_d½-d30-Sqr Connection

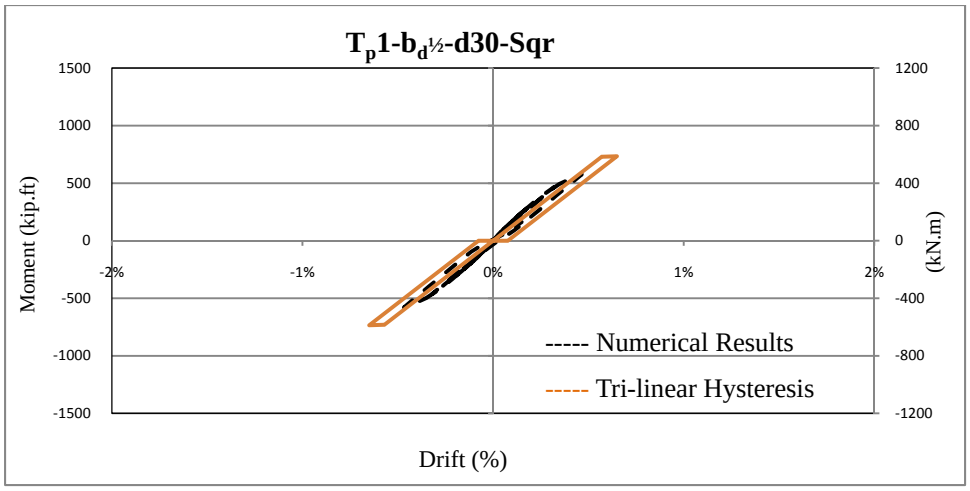

Figure C-22 Comparison Of The Numerical And Simulated Tri-Linear Hysteresis Of The T_p1-b_d½-d30-Sqr Connection

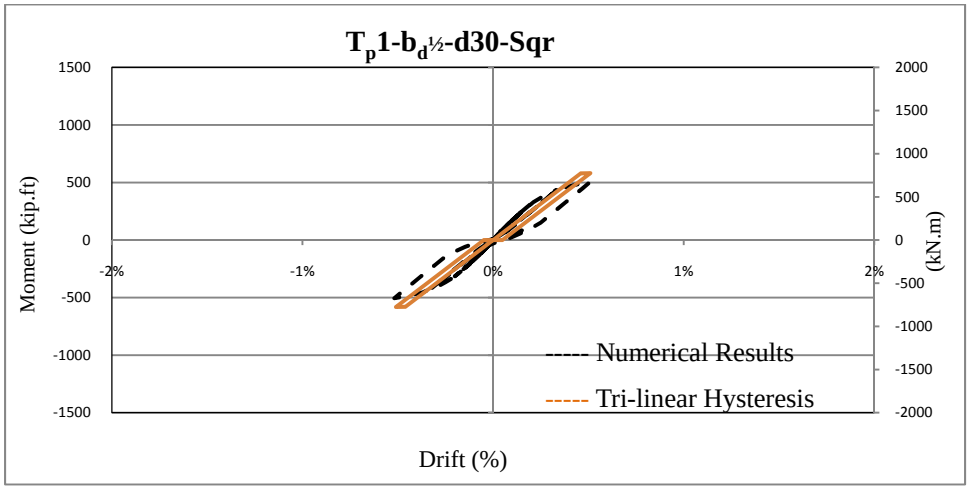

Figure C-23 Comparison Of The Numerical And Simulated Tri-Linear Hysteresis Of The T_p1-b_d½-d30-Sqr Connection

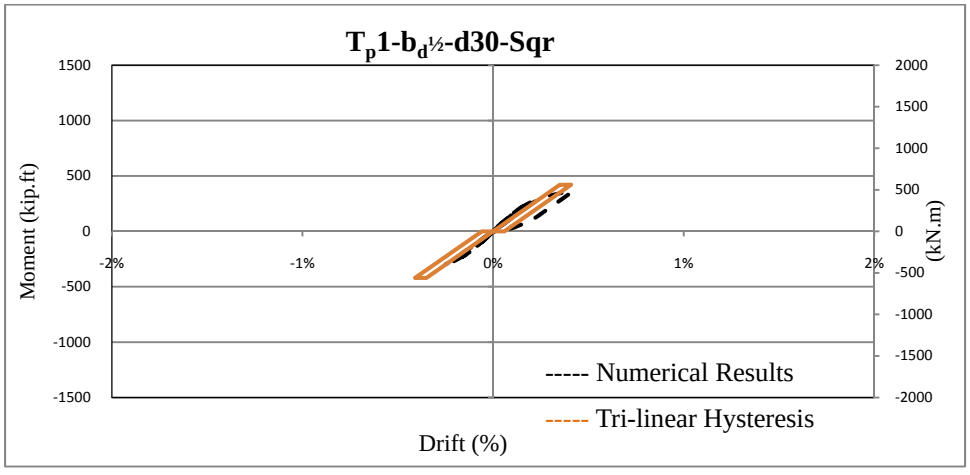

Figure C-24 Comparison Of The Numerical And Simulated Tri-Linear Hysteresis Of The T_p1-b_d½-d30-Sqr Connection

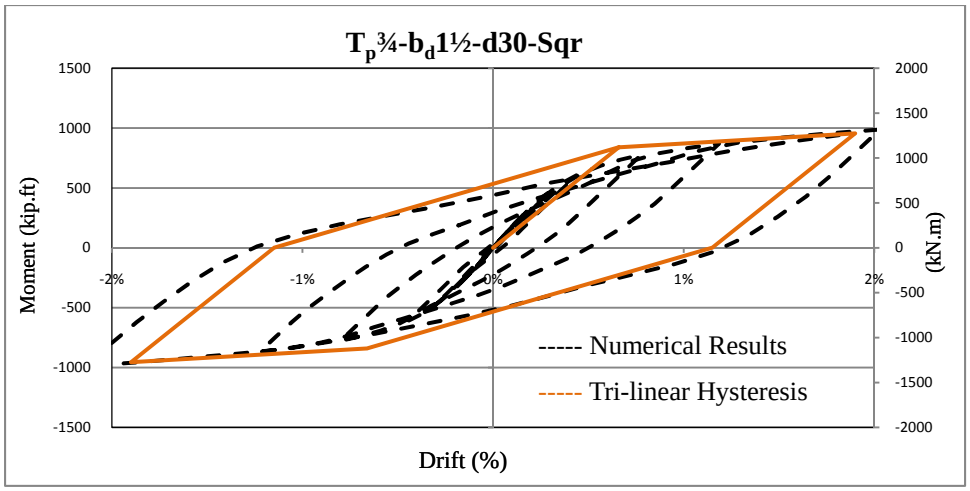

Figure C-25 Comparison Of The Numerical And Simulated Tri-Linear Hysteresis Of The T_p¾-b_d1½-d30-Sqr Connection

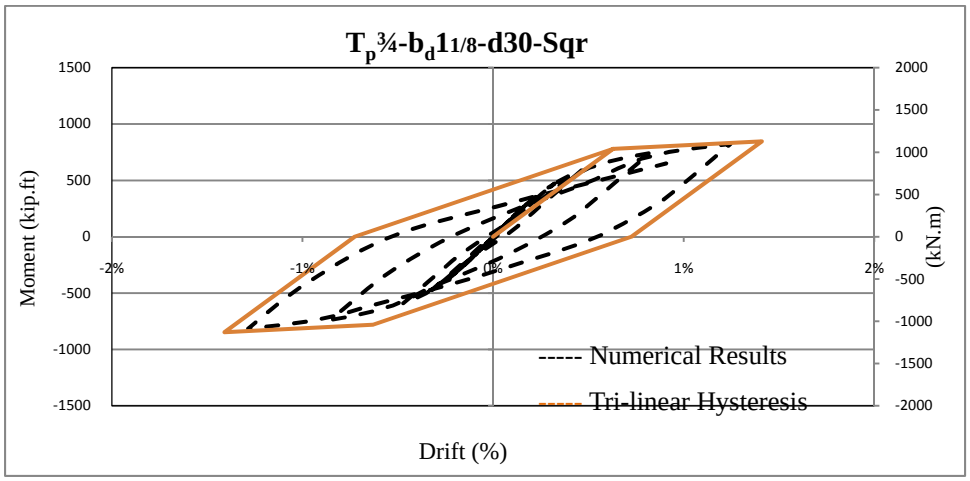

Figure C-26 Comparison Of The Numerical And Simulated Tri-Linear Hysteresis Of The T_p¾-b_d11/8-d30-Sqr Connection

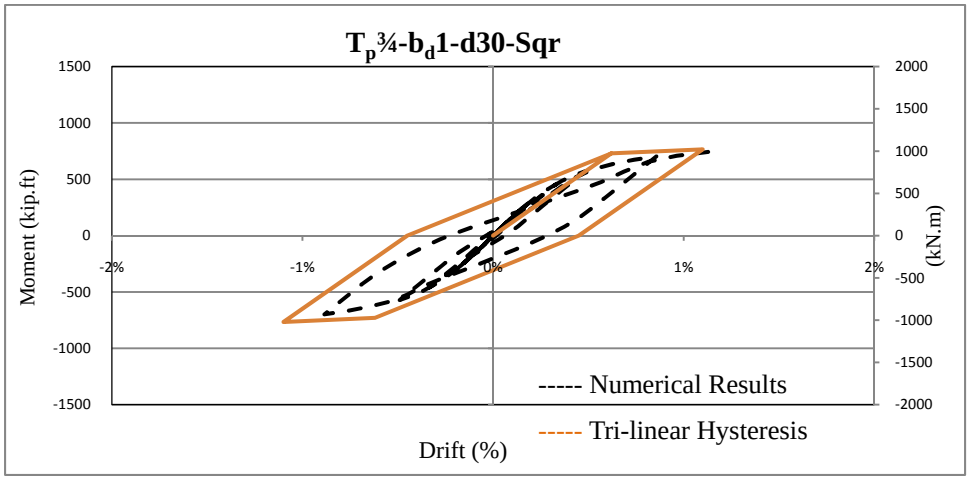

Figure C-27 Comparison Of The Numerical And Simulated Tri-Linear Hysteresis Of The T_p¾-b_d1-d30-Sqr Connection

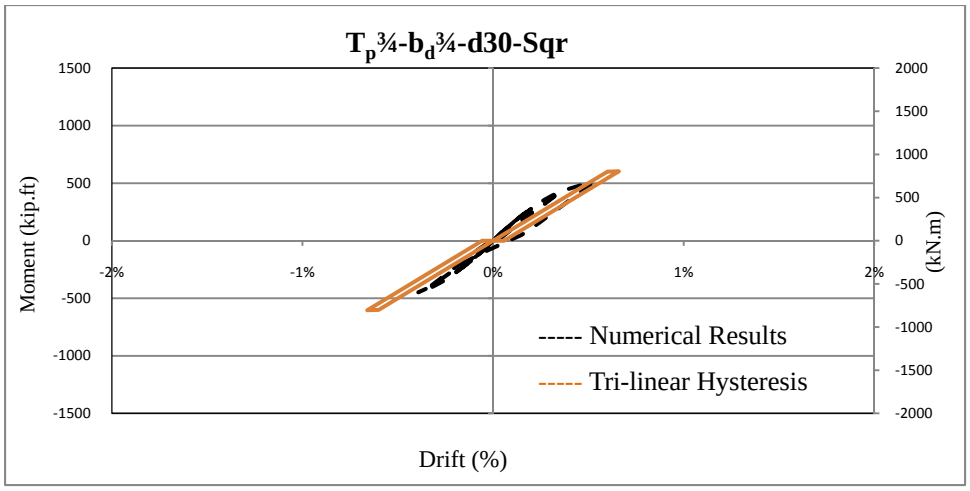

Figure C-28 Comparison Of The Numerical And Simulated Tri-Linear Hysteresis Of The T_p¾-b_d¾-d30-Sqr Connection

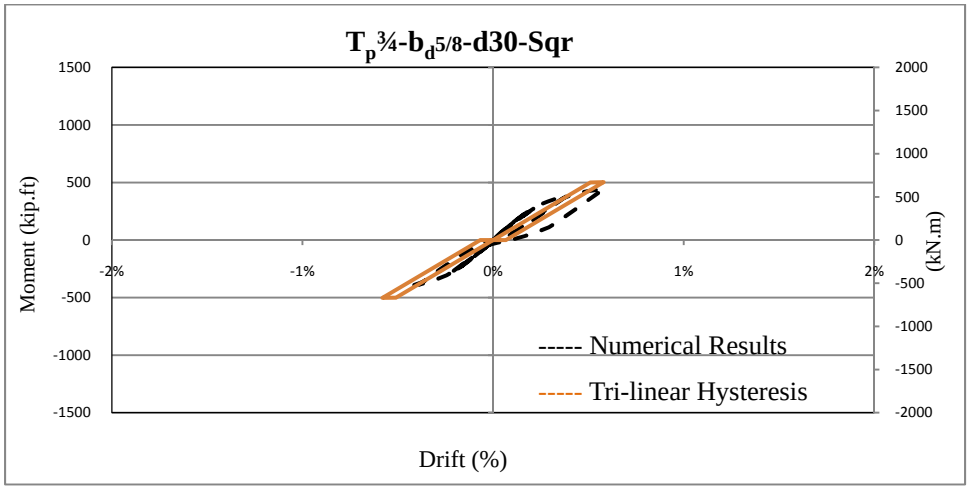

Figure C-29 Comparison Of The Numerical And Simulated Tri-Linear Hysteresis Of The T_p¾-b_d5/8-d30-Sqr Connection

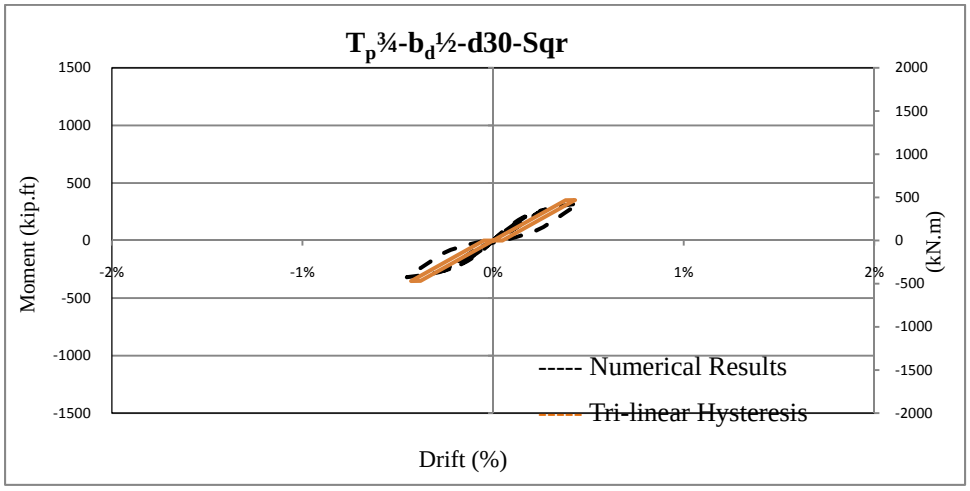

Figure C-30 Comparison Of The Numerical And Simulated Tri-Linear Hysteresis Of The T_p¾-b_d½-d30-Sqr Connection

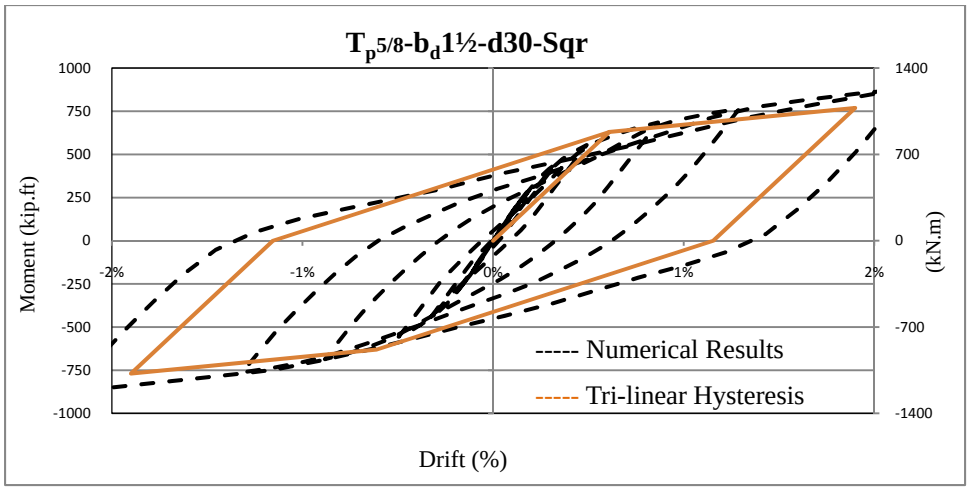

Figure C-31 Comparison Of The Numerical And Simulated Tri-Linear Hysteresis Of The T_p5/8-b_d1½-d30-Sqr Connection

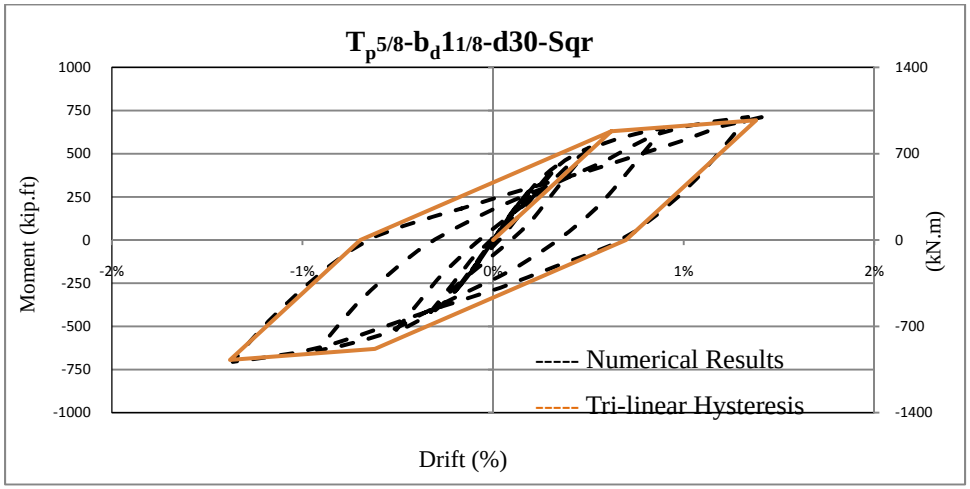

Figure C-32 Comparison Of The Numerical And Simulated Tri-Linear Hysteresis Of The T_p5/8-b_d11/8-d30-Sqr Connection

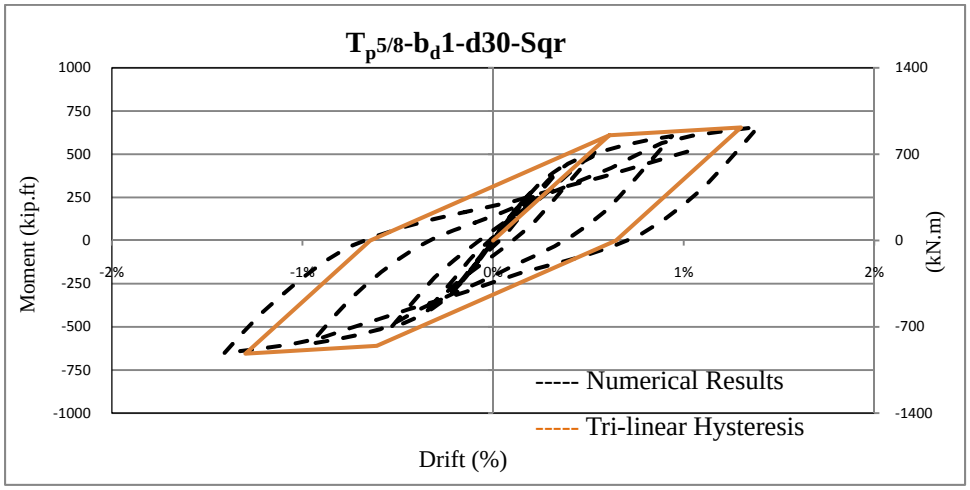

Figure C-33 Comparison Of The Numerical And Simulated Tri-Linear Hysteresis Of The T_p5/8-b_d1-d30-Sqr Connection

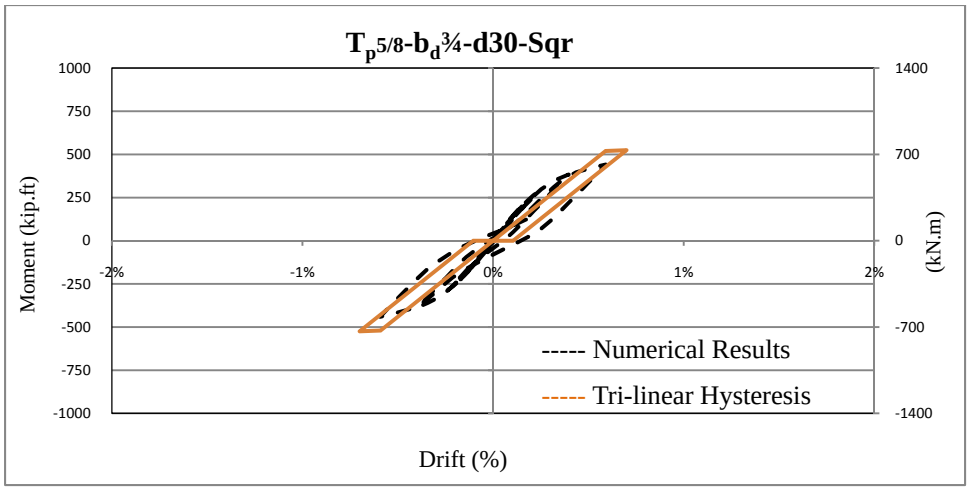

Figure C-34 Comparison Of The Numerical And Simulated Tri-Linear Hysteresis Of The T_p5/8-b_d¾-d30-Sqr Connection

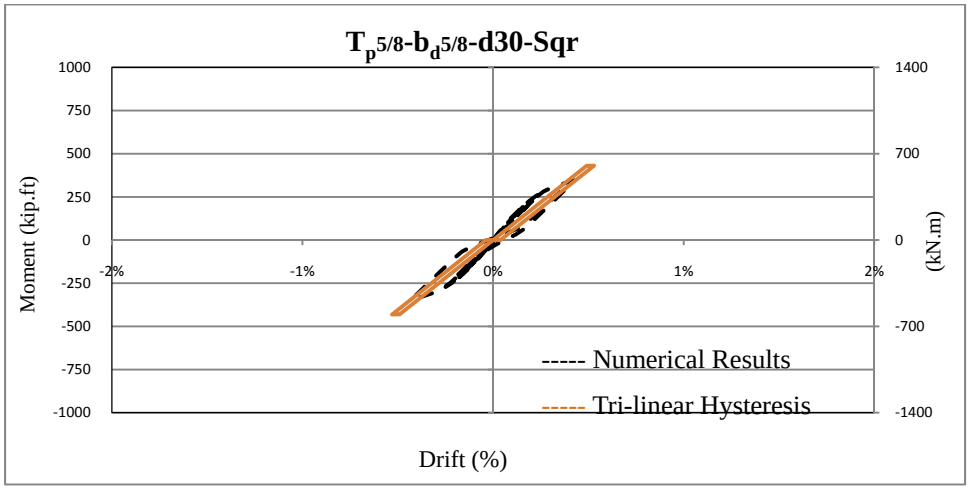

Figure C-35 Comparison Of The Numerical And Simulated Tri-Linear Hysteresis Of The T_p5/8-b_d5/8-d30-Sqr Connection

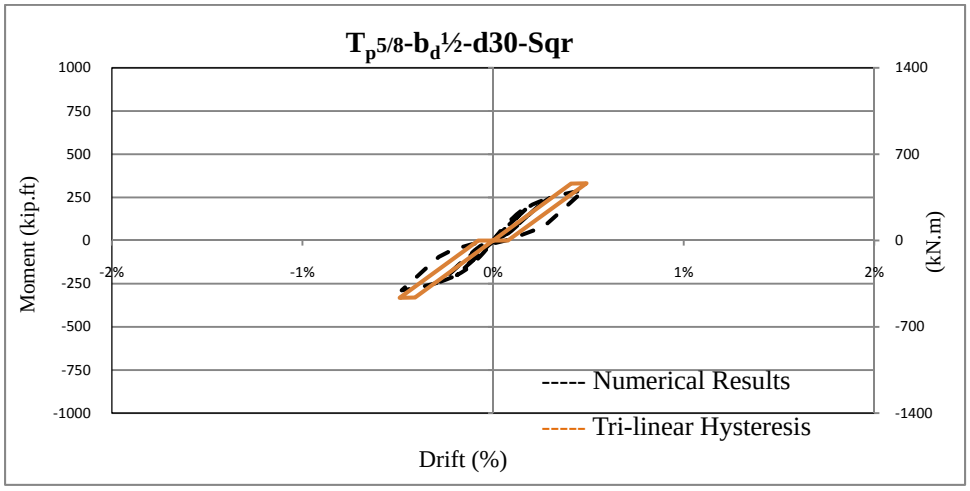

Figure C-36 Comparison Of The Numerical And Simulated Tri-Linear Hysteresis Of The T_p5/8-b_d½-d30-Sqr Connection

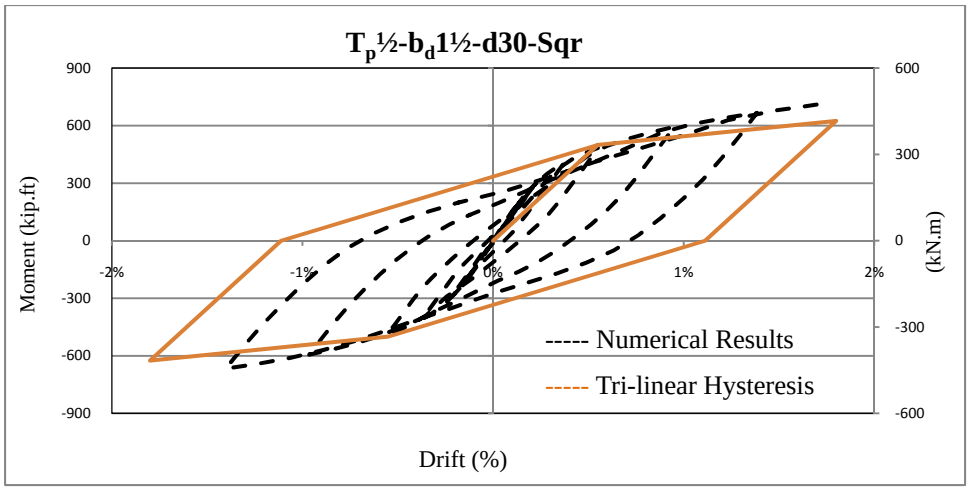

Figure C-37 Comparison Of The Numerical And Simulated Tri-Linear Hysteresis Of The T_p½-b_d1½-d30-Sqr Connection

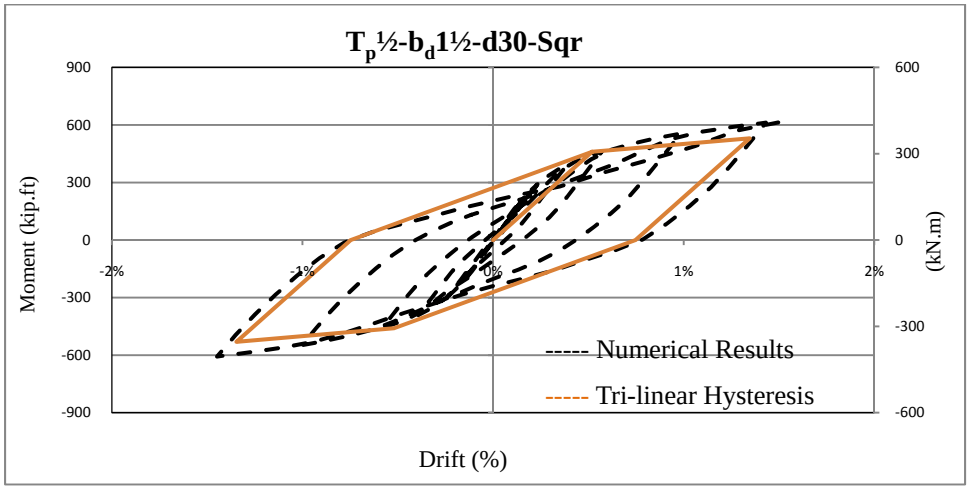

Figure C-38 Comparison Of The Numerical And Simulated Tri-Linear Hysteresis Of The T_p½-b_d1½-d30-Sqr Connection

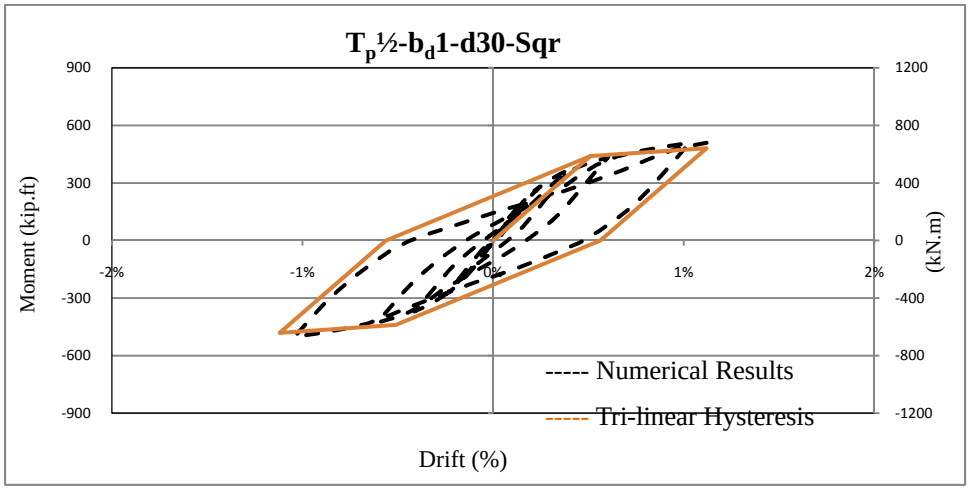

Figure C-39 Comparison Of The Numerical And Simulated Tri-Linear Hysteresis Of The T_p½-b_d1-d30-Sqr Connection

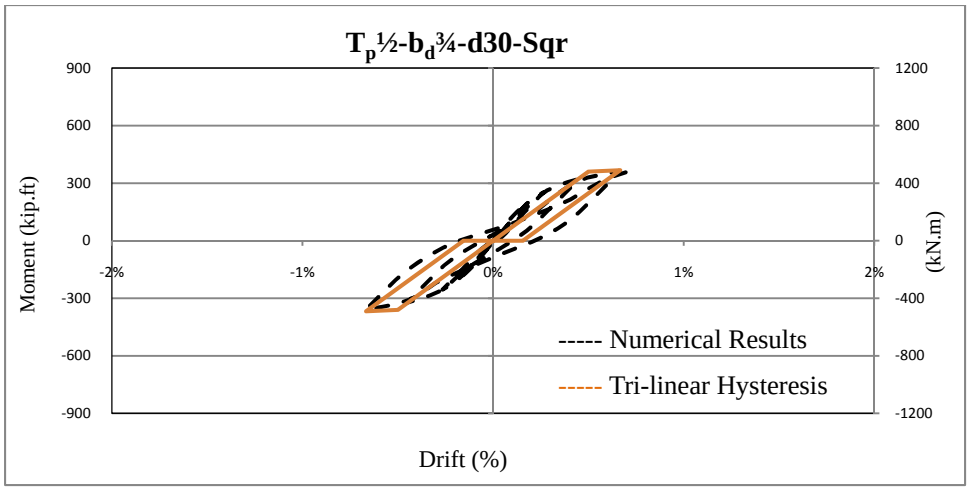

Figure C-40 Comparison Of The Numerical And Simulated Tri-Linear Hysteresis Of The T_p½-b_d¾-d30-Sqr Connection

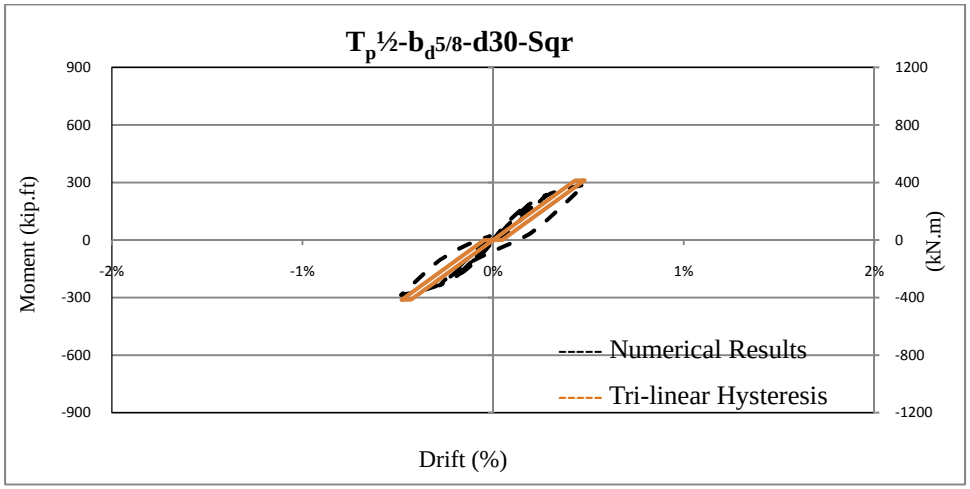

Figure C-41 Comparison Of The Numerical And Simulated Tri-Linear Hysteresis Of The T_p½-b_d5/8-d30-Sqr Connection

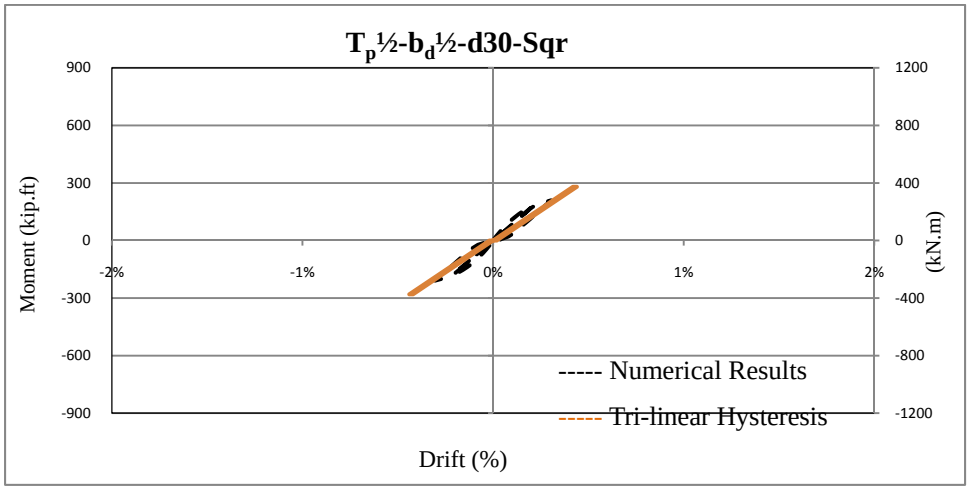

Figure C-42 Comparison Of The Numerical And Simulated Tri-Linear Hysteresis Of The T_p½-b_d½-d30-Sqr Connection

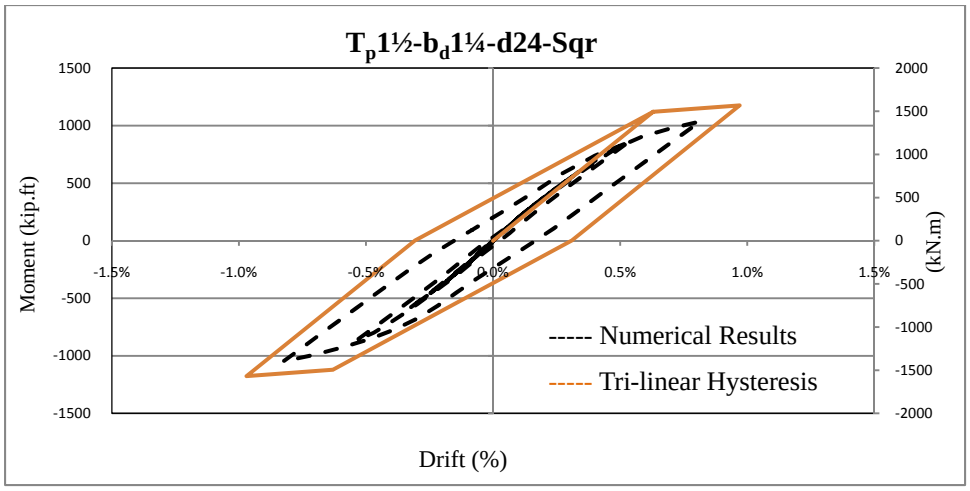

Figure C-43 Comparison Of The Numerical And Simulated Tri-Linear Hysteresis Of The $T_p1½\text{-}b_d1¼\text{-}d24\text{-}Sqr$ Connection

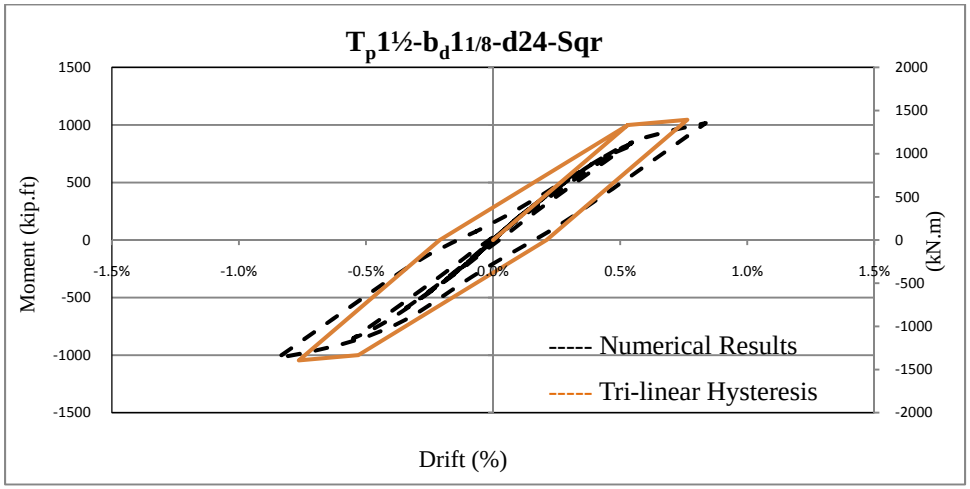

Figure C-44 Comparison Of The Numerical And Simulated Tri-Linear Hysteresis Of The $T_p1½\text{-}b_d11/8\text{-}d24\text{-}Sqr$ Connection

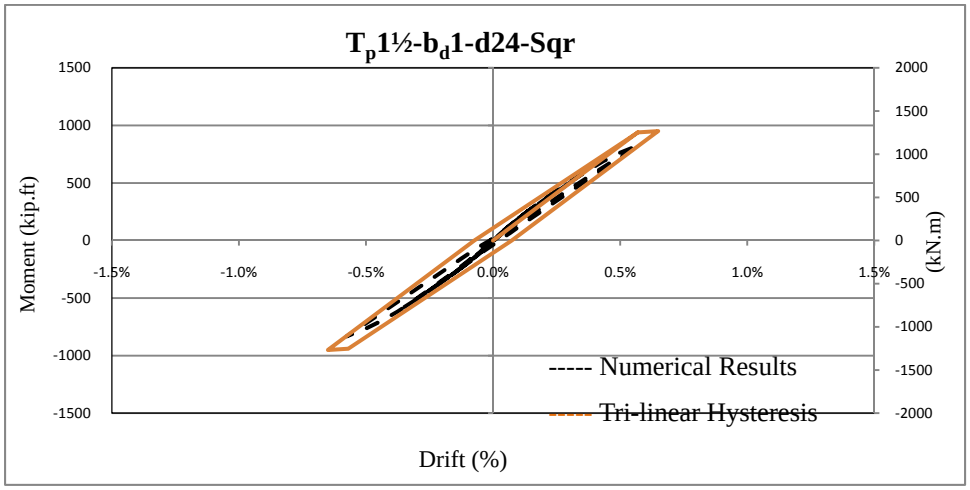

Figure C-45 Comparison Of The Numerical And Simulated Tri-Linear Hysteresis Of The $T_p1½\text{-}b_d1\text{-}d24\text{-}Sqr$ Connection

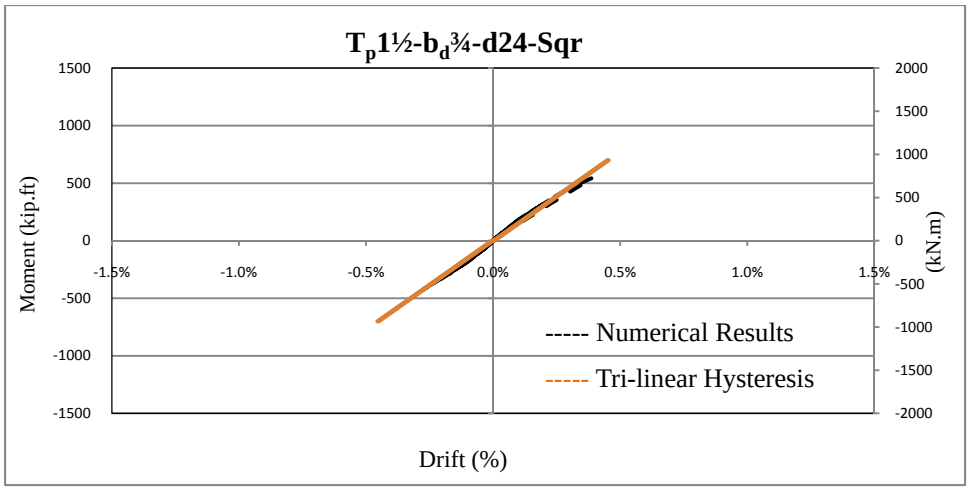

Figure C-46 Comparison Of The Numerical And Simulated Tri-Linear Hysteresis Of The $T_p1½\text{-}b_d¾\text{-}d24\text{-}Sqr$ Connection

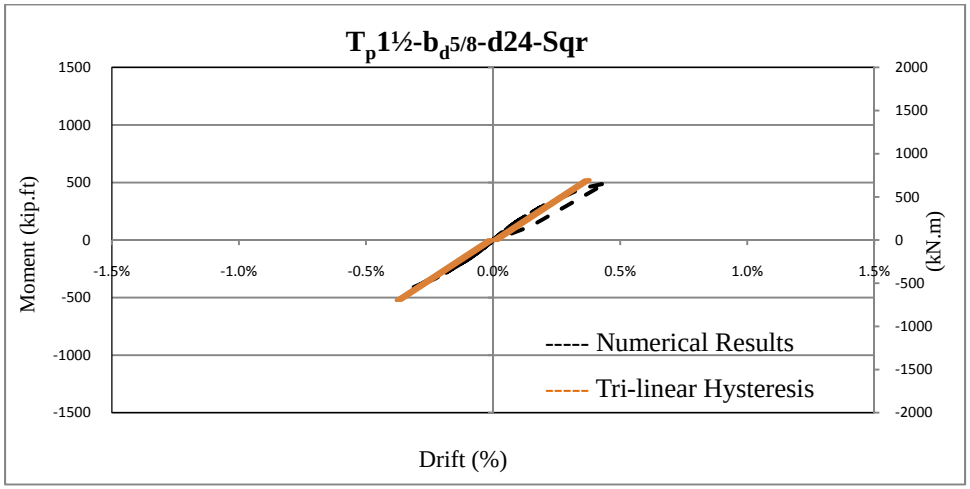

Figure C-47 Comparison Of The Numerical And Simulated Tri-Linear Hysteresis Of The $T_p1½\text{-}b_d5/8\text{-}d24\text{-}Sqr$ Connection

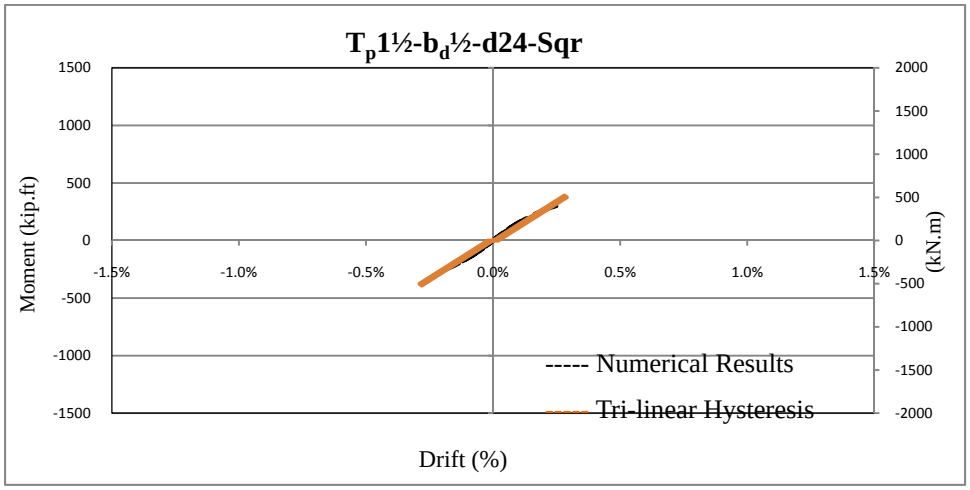

Figure C-48 Comparison Of The Numerical And Simulated Tri-Linear Hysteresis Of The $T_p1½\text{-}b_d½\text{-}d24\text{-}Sqr$ Connection

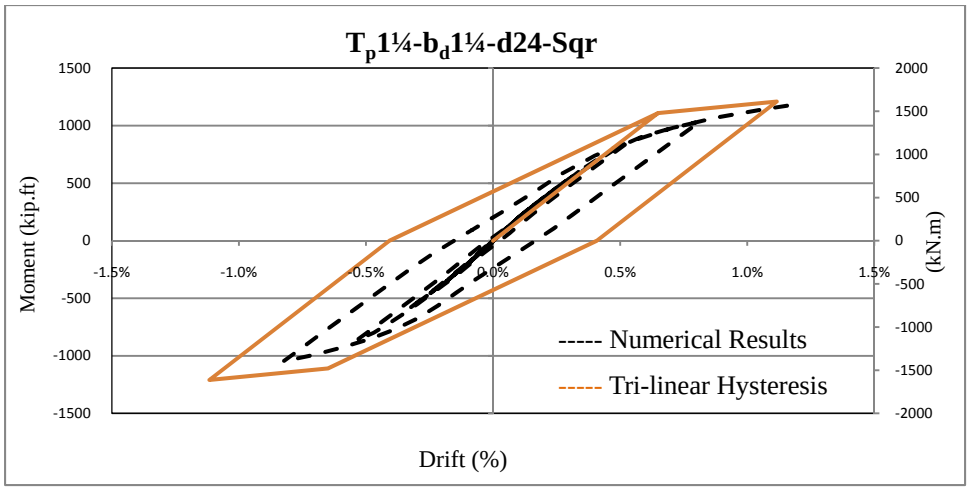

Figure C-49 Comparison Of The Numerical And Simulated Tri-Linear Hysteresis Of The $T_p1¼$-$b_d1¼$-d24-Sqr Connection

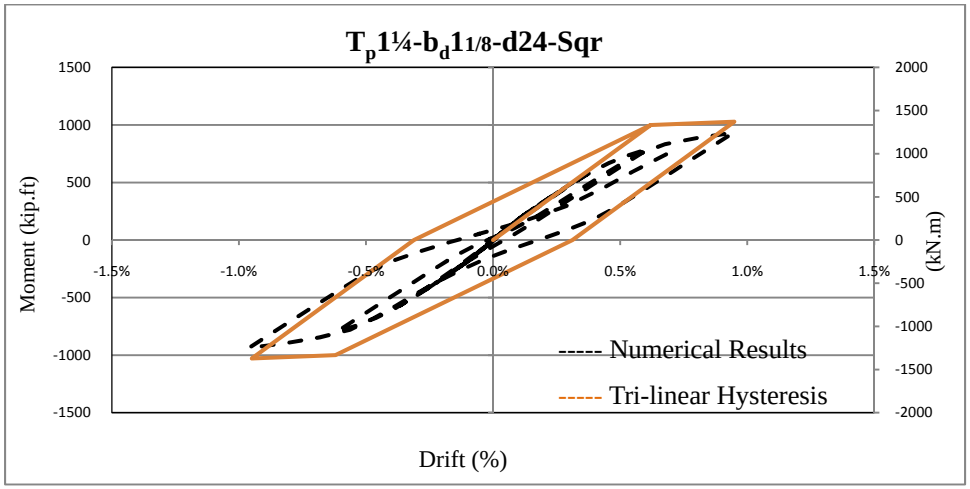

Figure C-50 Comparison Of The Numerical And Simulated Tri-Linear Hysteresis Of The $T_p1¼$-$b_d11/8$-d24-Sqr Connection

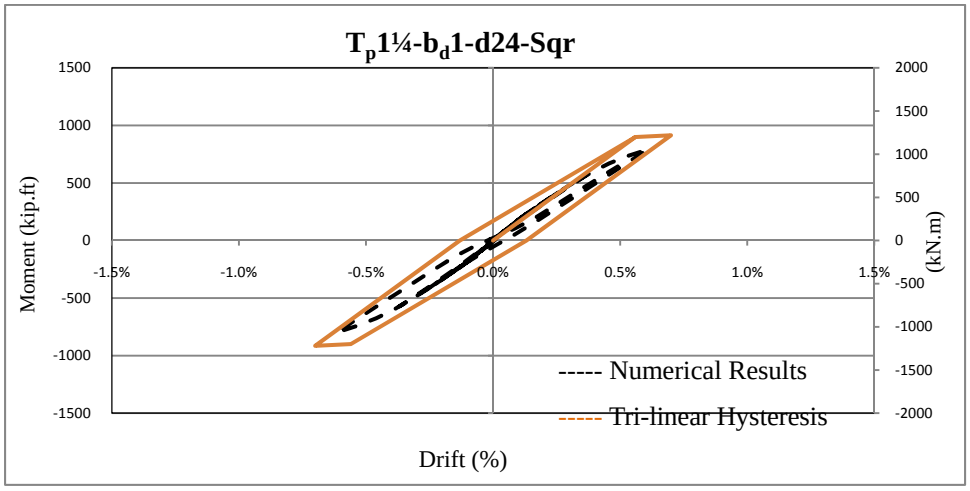

Figure C-51 Comparison Of The Numerical And Simulated Tri-Linear Hysteresis Of The $T_p1¼$-b_d1-d24-Sqr Connection

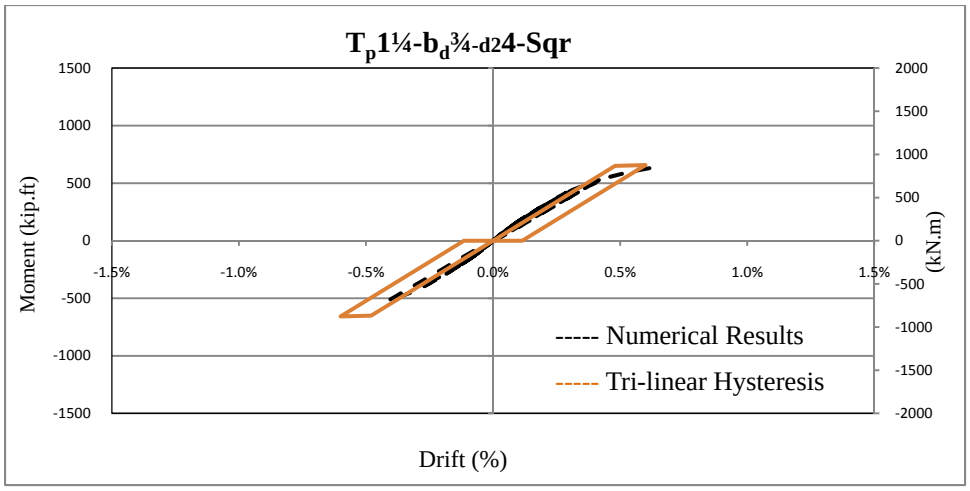

Figure C-52 Comparison Of The Numerical And Simulated Tri-Linear Hysteresis Of The $T_p1¼\text{-}b_d¾\text{-}d24\text{-}Sqr$ Connection

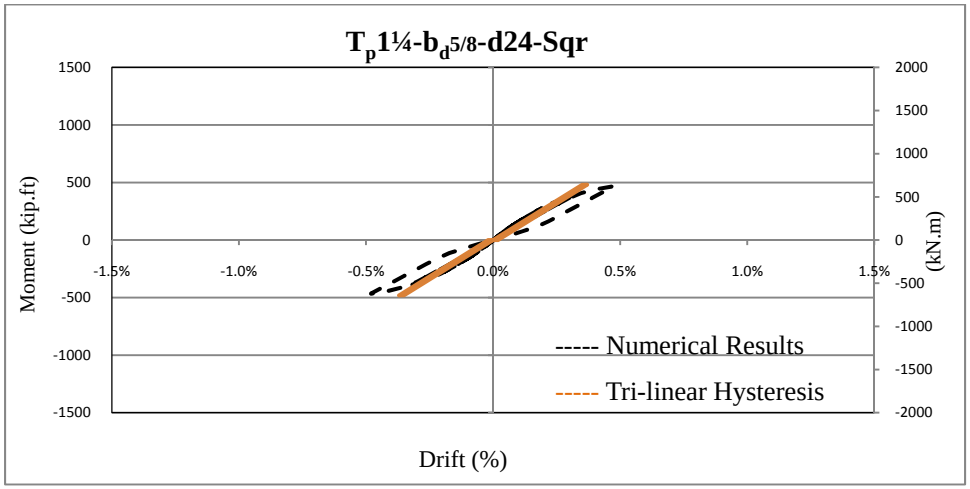

Figure C-53 Comparison Of The Numerical And Simulated Tri-Linear Hysteresis Of The $T_p1¼\text{-}b_d5/8\text{-}d24\text{-}Sqr$ Connection

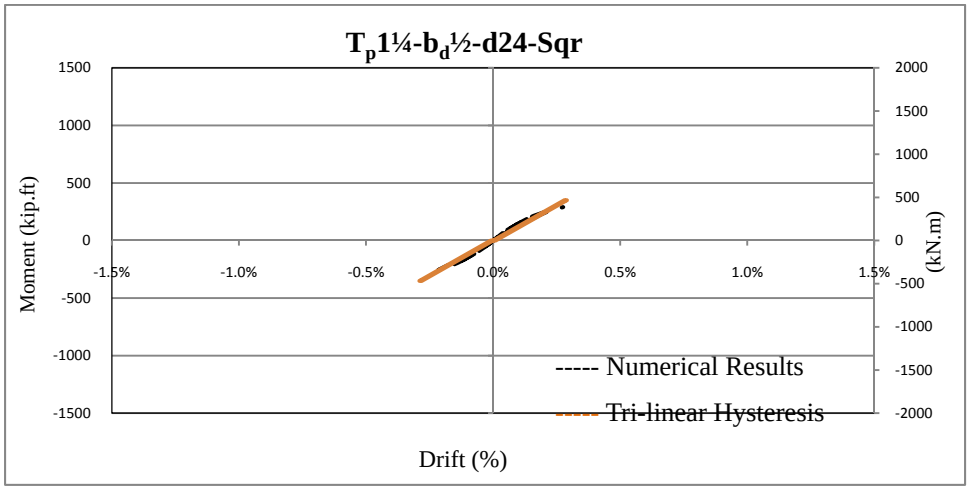

Figure C-54 Comparison Of The Numerical And Simulated Tri-Linear Hysteresis Of The $T_p1¼\text{-}b_d½\text{-}d24\text{-}Sqr$ Connection

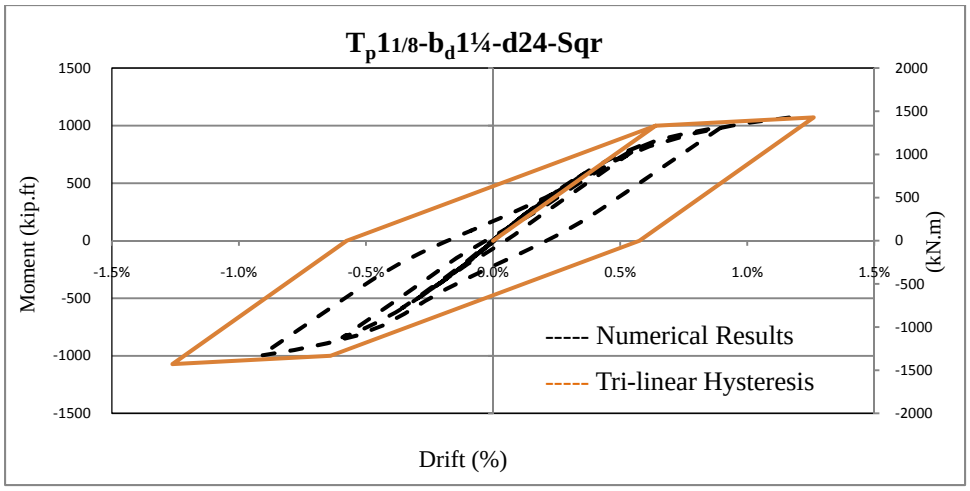

Figure C-55 Comparison Of The Numerical And Simulated Tri-Linear Hysteresis Of The $T_p11/8$-$b_d1¼$-d24-Sqr Connection

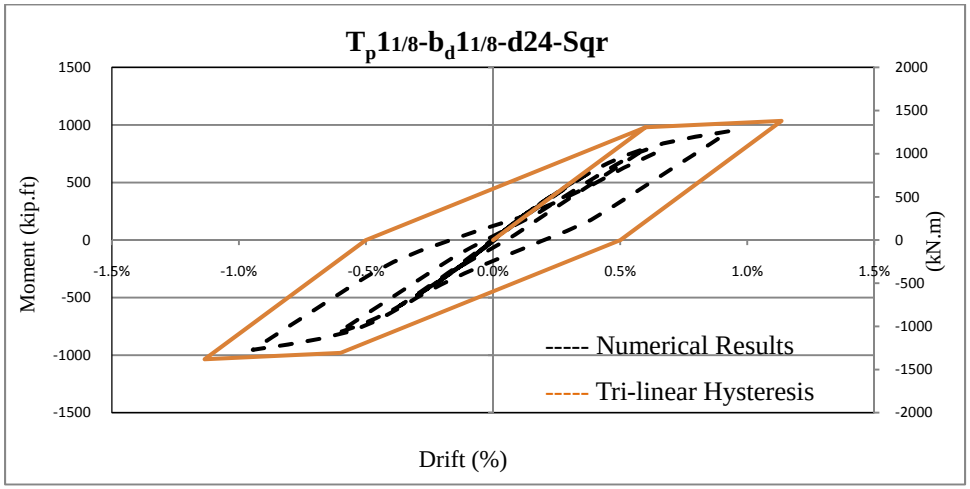

Figure C-56 Comparison Of The Numerical And Simulated Tri-Linear Hysteresis Of The $T_p11/8$-$b_d11/8$-d24-Sqr Connection

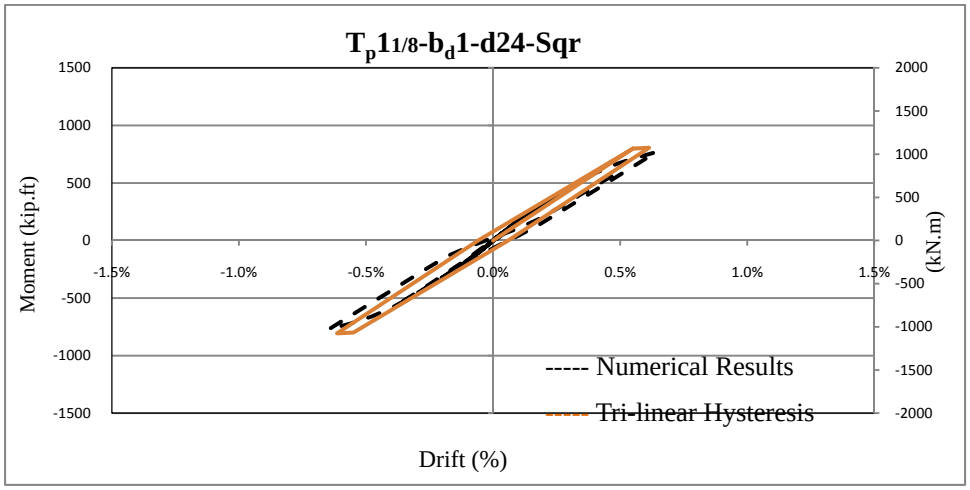

Figure C-57 Comparison Of The Numerical And Simulated Tri-Linear Hysteresis Of The $T_p11/8$-b_d1-d24-Sqr Connection

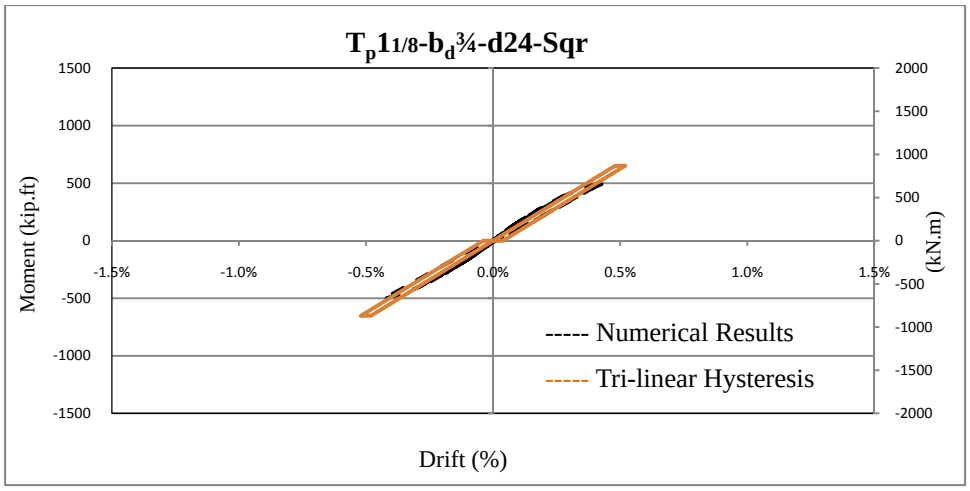

Figure C-58 Comparison Of The Numerical And Simulated Tri-Linear Hysteresis Of The T_p11/8-b_d¾-d24-Sqr Connection

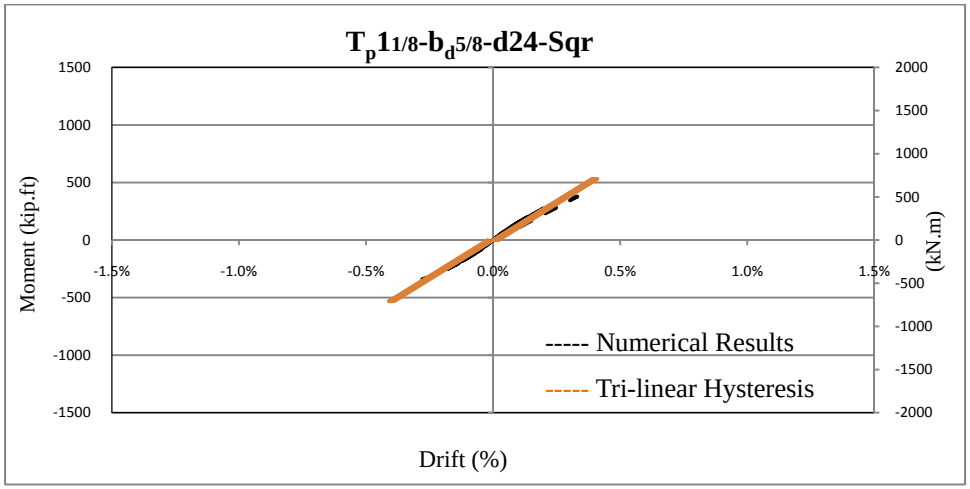

Figure C-59 Comparison Of The Numerical And Simulated Tri-Linear Hysteresis Of The T_p11/8-b_d5/8-d24-Sqr Connection

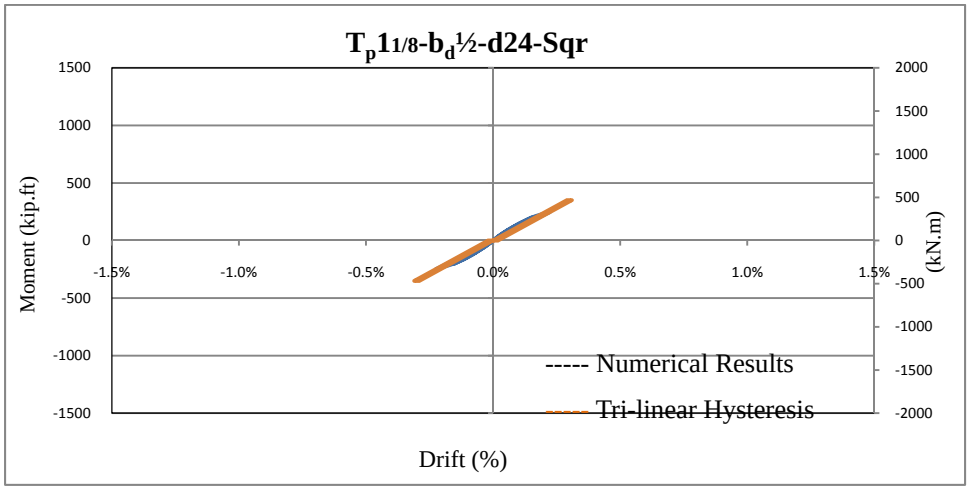

Figure C-60 Comparison Of The Numerical And Simulated Tri-Linear Hysteresis Of The T_p11/8-b_d½-d24-Sqr Connection

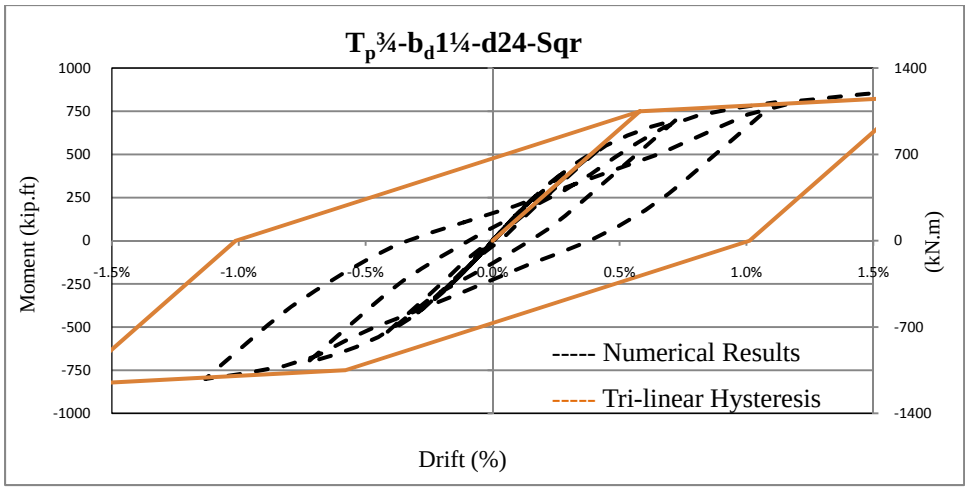

Figure C-61 Comparison Of The Numerical And Simulated Tri-Linear Hysteresis Of The T_p¾-b_d1¼-d24-Sqr Connection

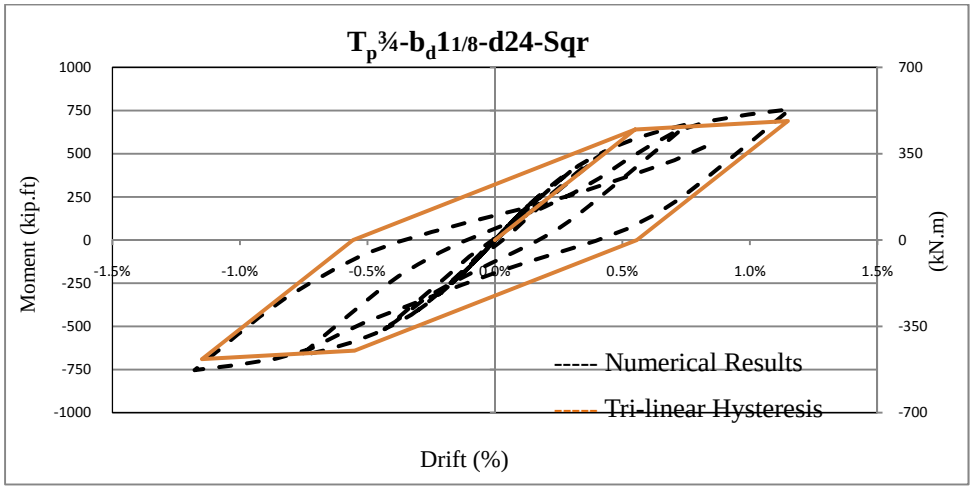

Figure C-62 Comparison Of The Numerical And Simulated Tri-Linear Hysteresis Of The T_p¾-b_d11/8-d24-Sqr Connection

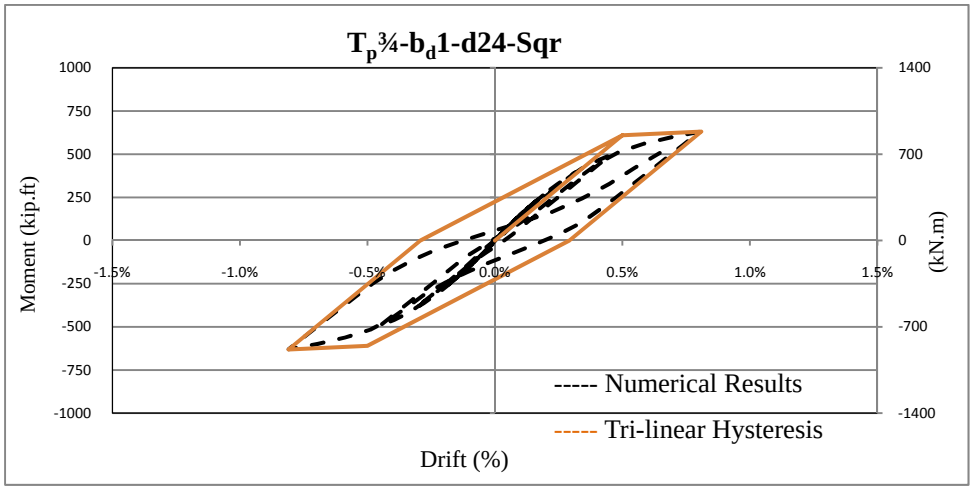

Figure C-63 Comparison Of The Numerical And Simulated Tri-Linear Hysteresis Of The T_p¾-b_d1-d24-Sqr Connection

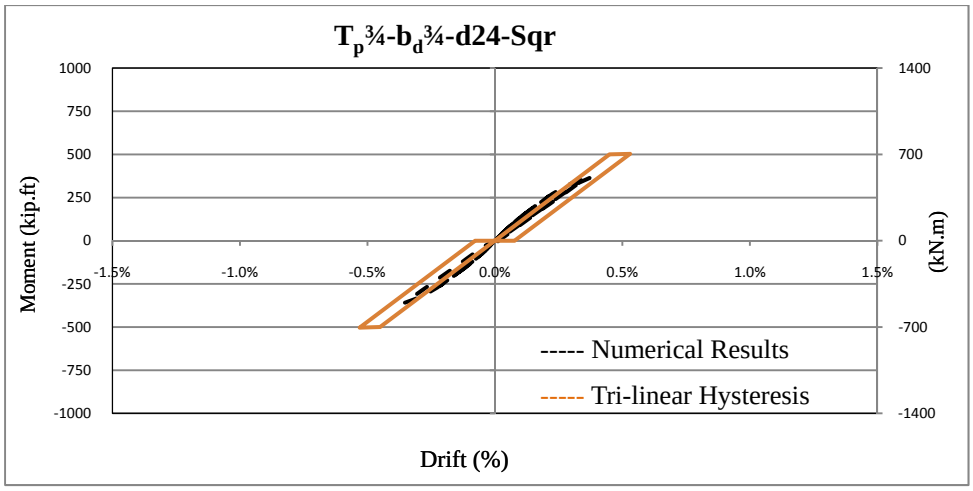

Figure C-64 Comparison Of The Numerical And Simulated Tri-Linear Hysteresis Of The T_p¾-b_d¾-d24-Sqr Connection

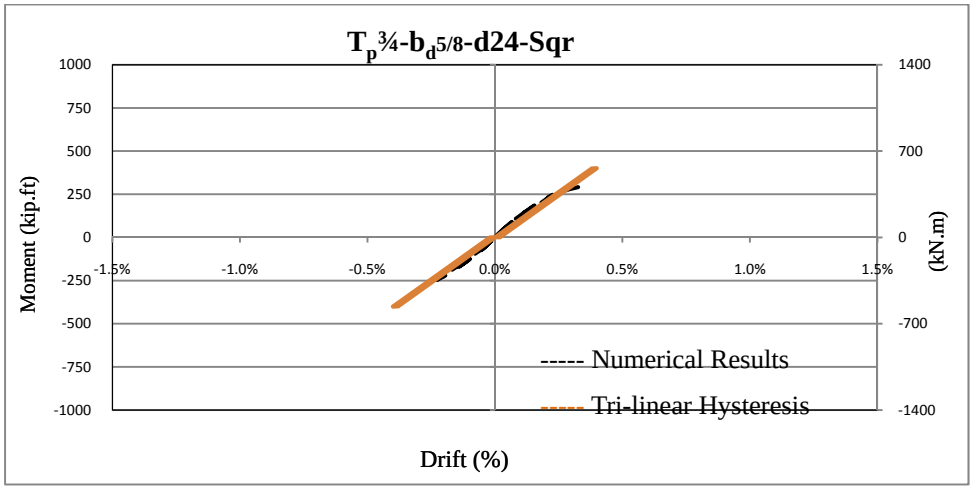

Figure C-65 Comparison Of The Numerical And Simulated Tri-Linear Hysteresis Of The T_p¾-b_d5/8-d24-Sqr Connection

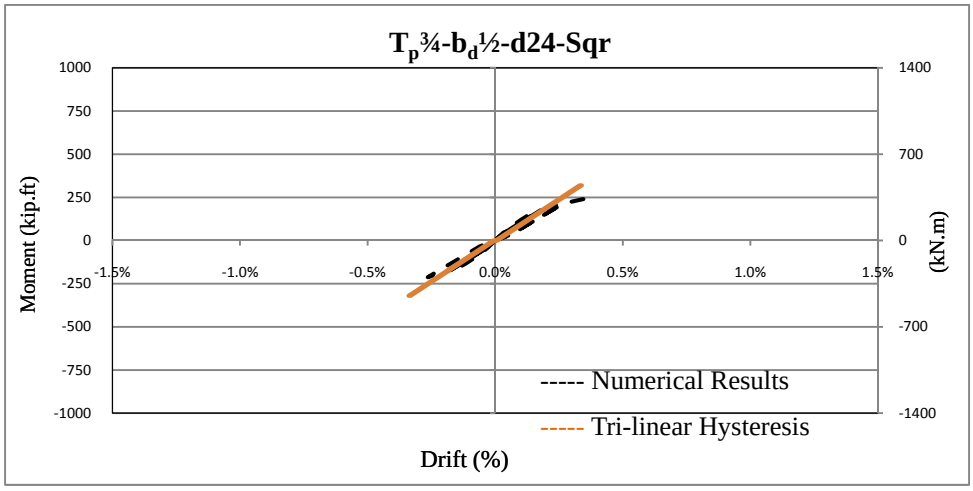

Figure C-66 Comparison Of The Numerical And Simulated Tri-Linear Hysteresis Of The T_p¾-b_d½-d24-Sqr Connection

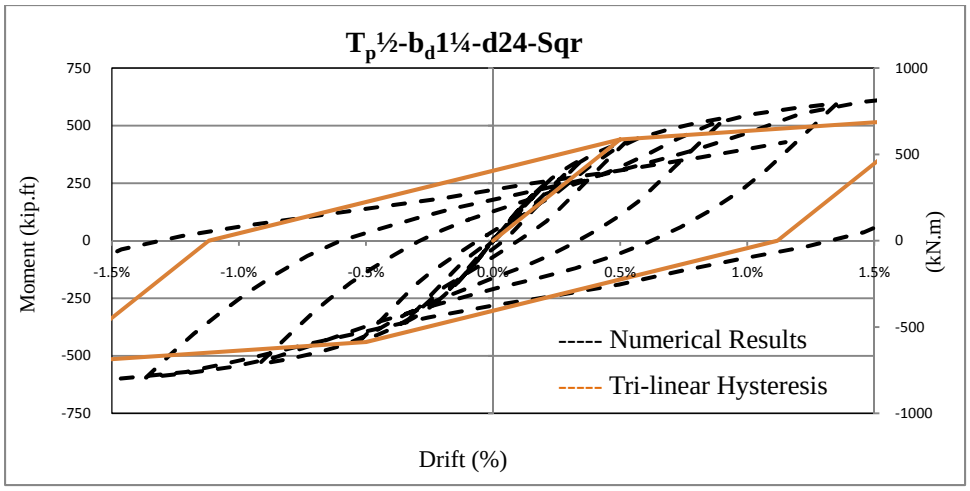

Figure C-67 Comparison Of The Numerical And Simulated Tri-Linear Hysteresis Of The T_p½-b_d1¼-d24-Sqr Connection

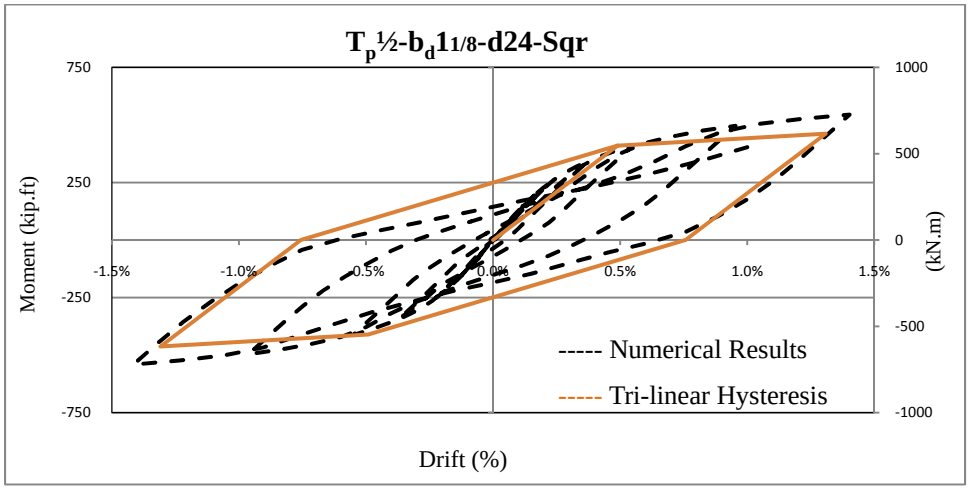

Figure C-68 Comparison Of The Numerical And Simulated Tri-Linear Hysteresis Of The T_p½-b_d11/8-d24-Sqr Connection

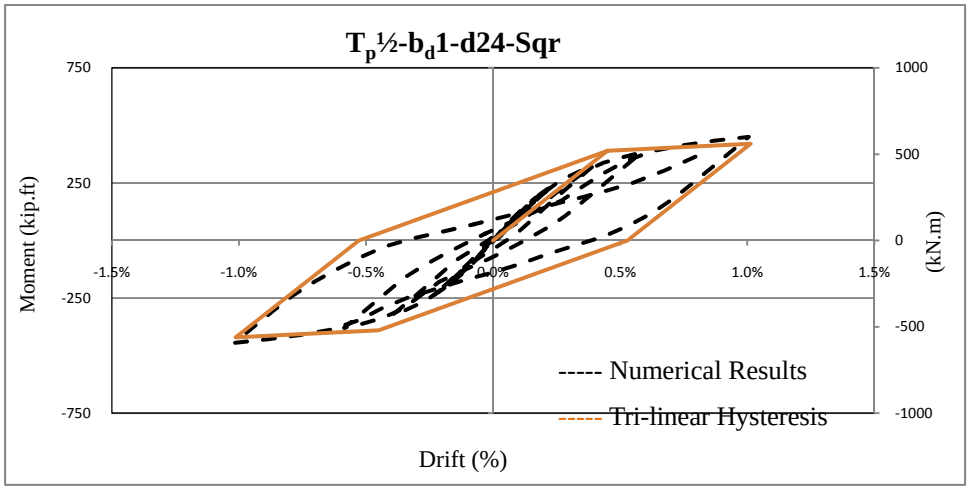

Figure C-69 Comparison Of The Numerical And Simulated Tri-Linear Hysteresis Of The T_p½-b_d1-d24-Sqr Connection

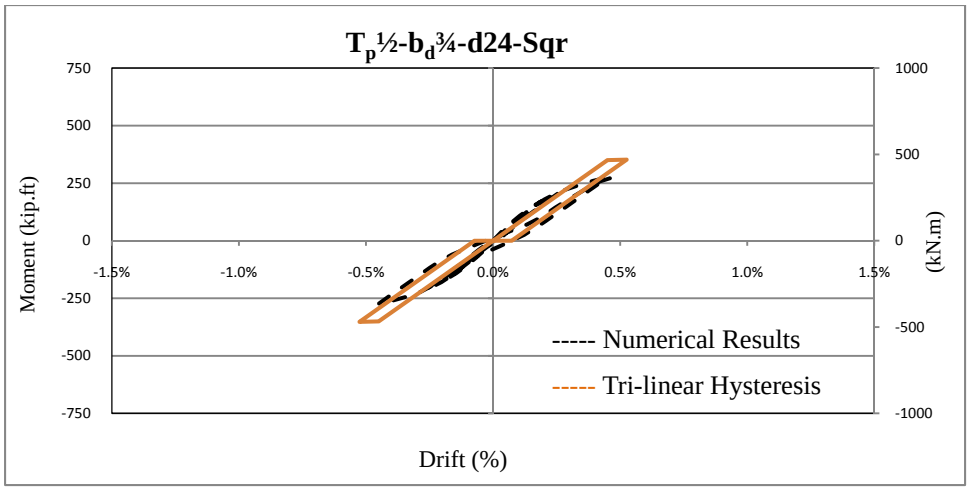

Figure C-70 Comparison Of The Numerical And Simulated Tri-Linear Hysteresis Of The T_p½-b_d¾-d24-Sqr Connection

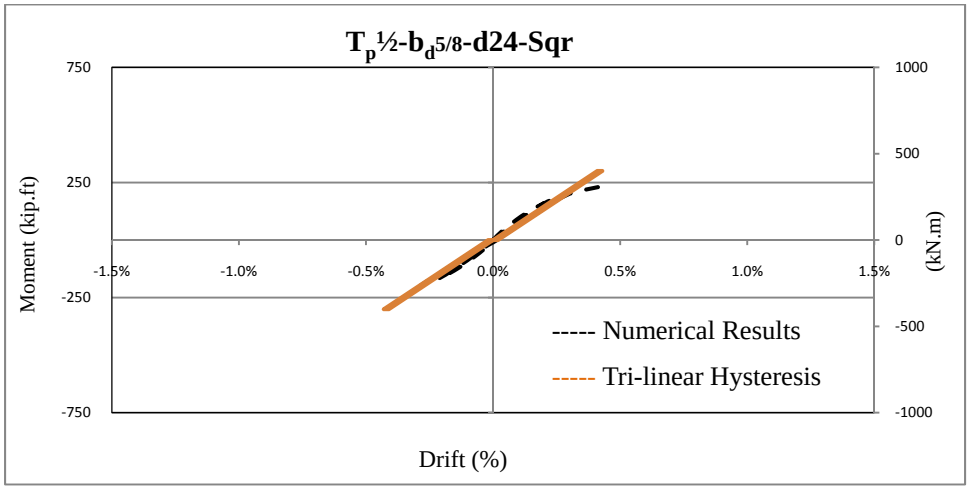

Figure C-71 Comparison Of The Numerical And Simulated Tri-Linear Hysteresis Of The T_p½-b_d5/8-d24-Sqr Connection

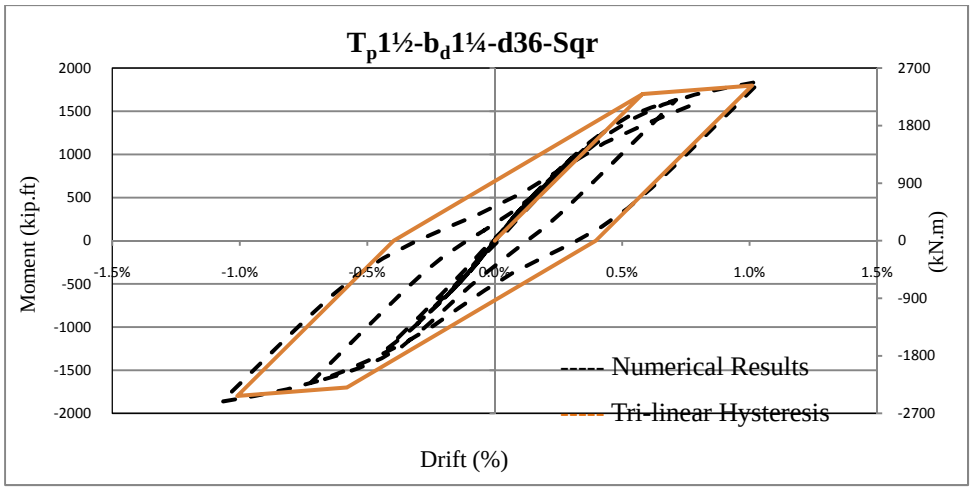

Figure C-72 Comparison Of The Numerical And Simulated Tri-Linear Hysteresis Of The $T_p1½\text{-}b_d1¼$-d36-Sqr Connection

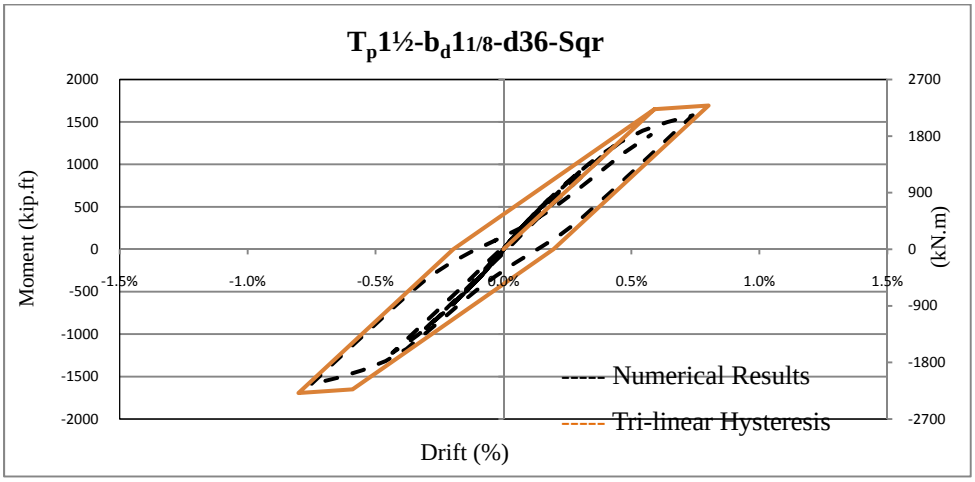

Figure C-73 Comparison Of The Numerical And Simulated Tri-Linear Hysteresis Of The $T_p1½\text{-}b_d11/8$-d36-Sqr Connection

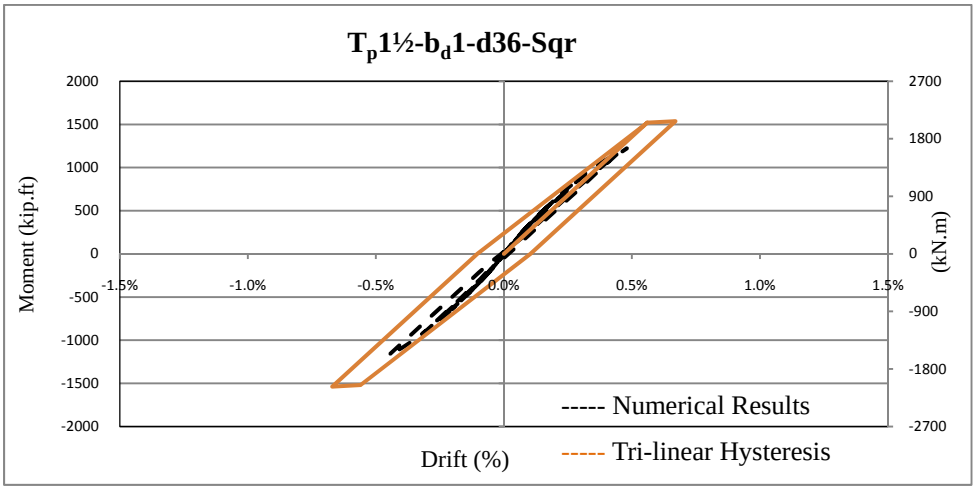

Figure C-74 Comparison Of The Numerical And Simulated Tri-Linear Hysteresis Of The $T_p1½\text{-}b_d1$-d36-Sqr Connection

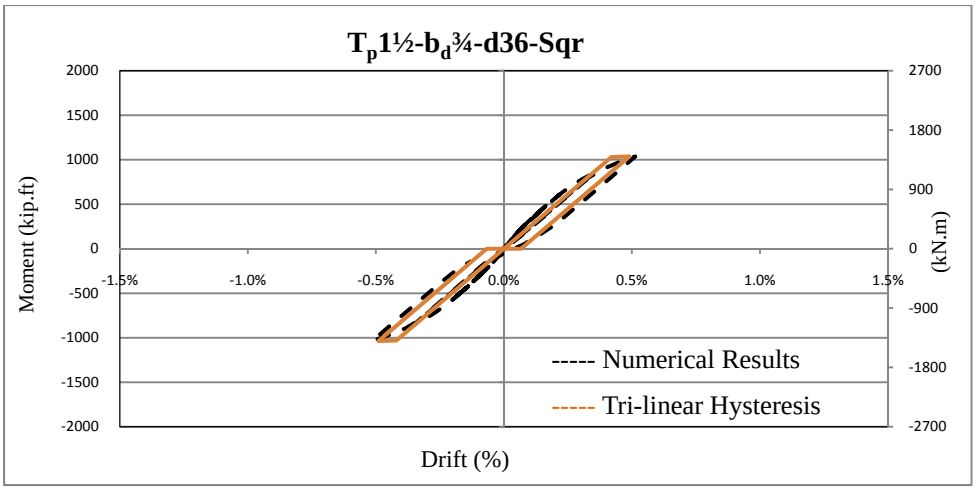

Figure C-75 Comparison Of The Numerical And Simulated Tri-Linear Hysteresis Of The $T_p1½\text{-}b_d¾\text{-}d36\text{-}Sqr$ Connection

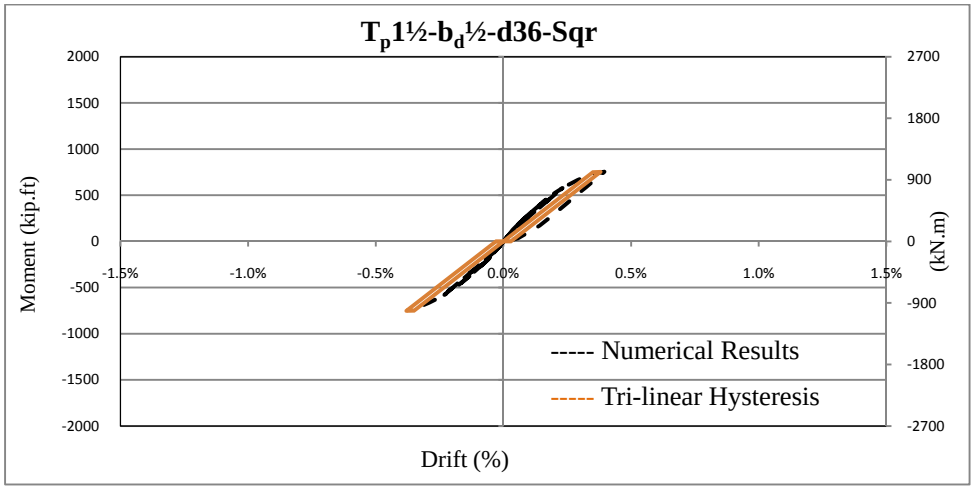

Figure C-76 Comparison Of The Numerical And Simulated Tri-Linear Hysteresis Of The $T_p1½\text{-}b_d½\text{-}d36\text{-}Sqr$ Connection

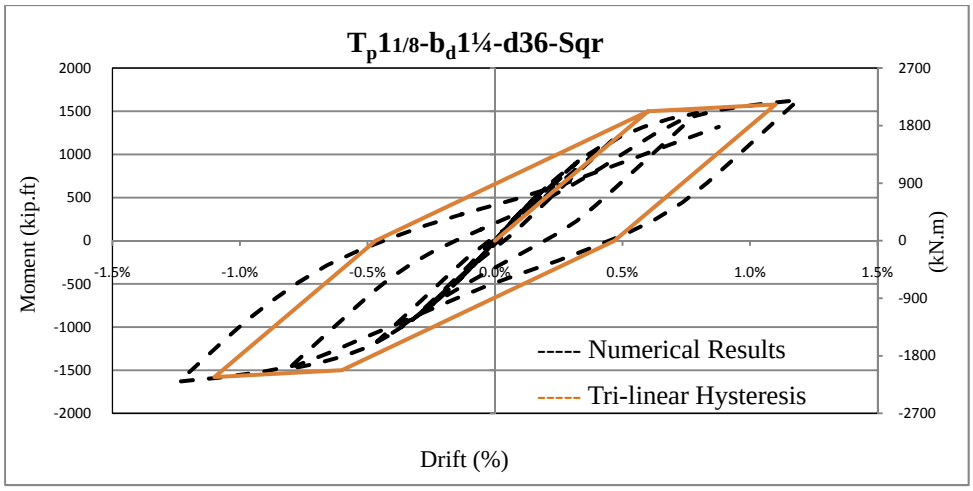

Figure C-77 Comparison Of The Numerical And Simulated Tri-Linear Hysteresis Of The T_p11/8-b_d1¼-d36-Sqr Connection

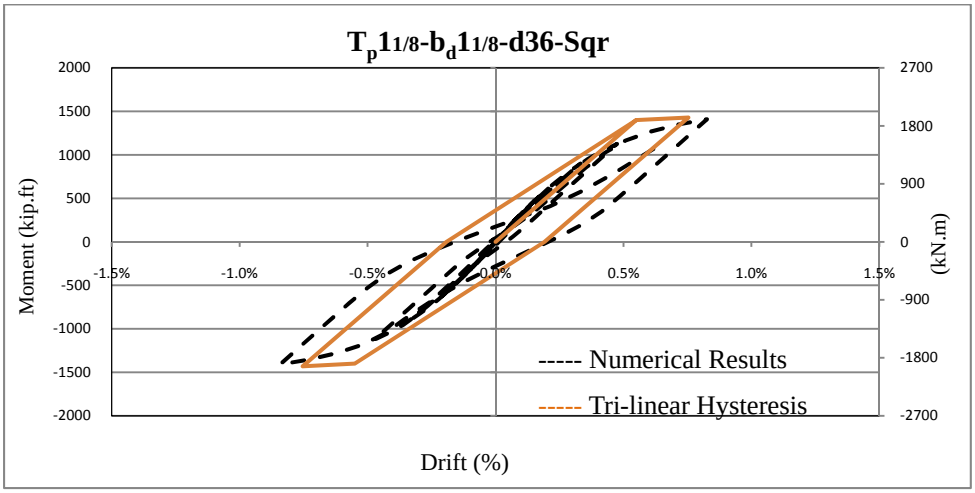

Figure C-78 Comparison Of The Numerical And Simulated Tri-Linear Hysteresis Of The T_p11/8-b_d11/8-d36-Sqr Connection

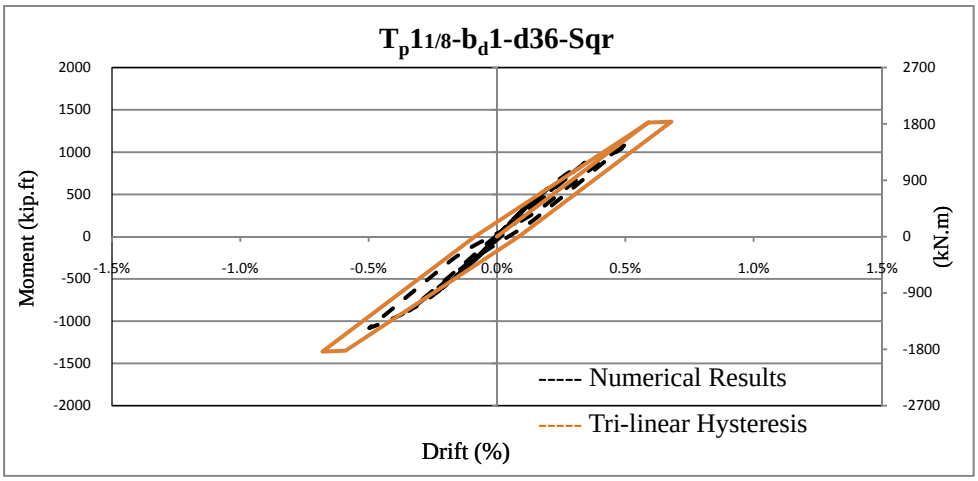

Figure C-79 Comparison Of The Numerical And Simulated Tri-Linear Hysteresis Of The T_p11/8-b_d1-d36-Sqr Connection

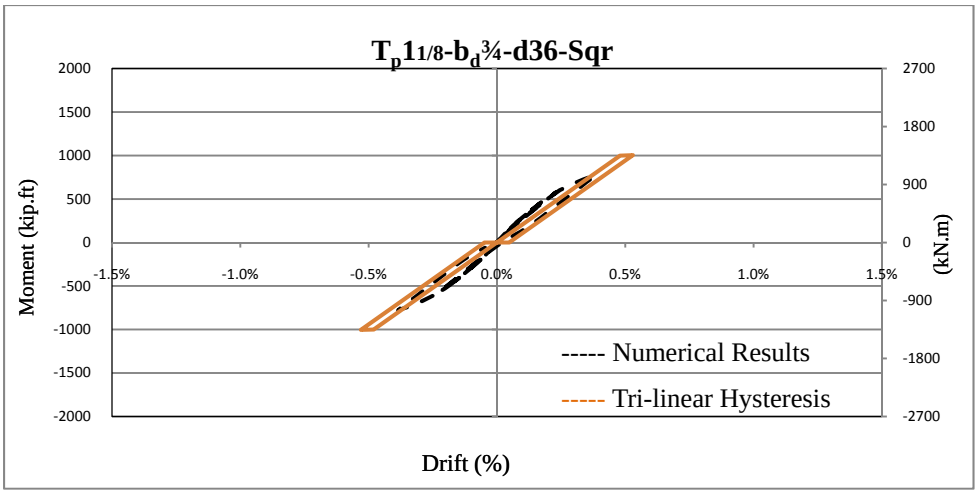

Figure C-80 Comparison Of The Numerical And Simulated Tri-Linear Hysteresis Of The T_p11/8-b_d¾-d36-Sqr Connection

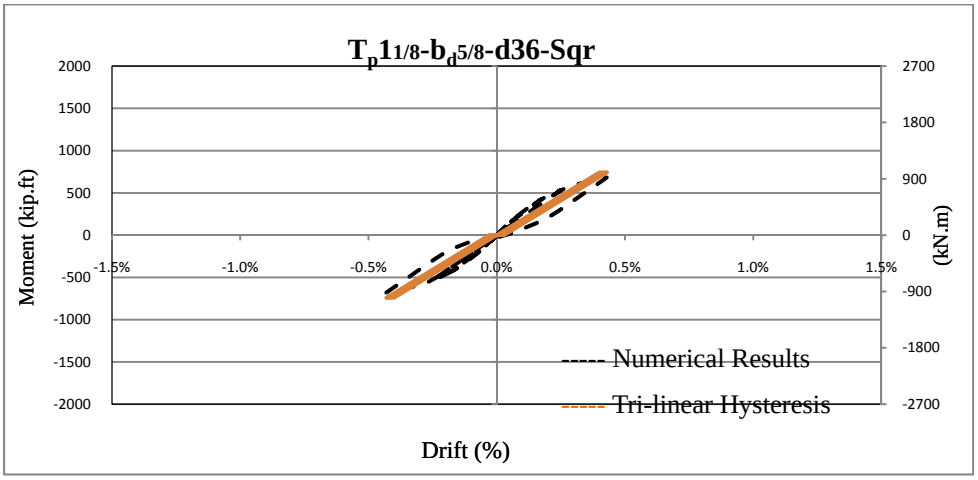

Figure C-81 Comparison Of The Numerical And Simulated Tri-Linear Hysteresis Of The T_p11/8-b_d5/8-d36-Sqr Connection

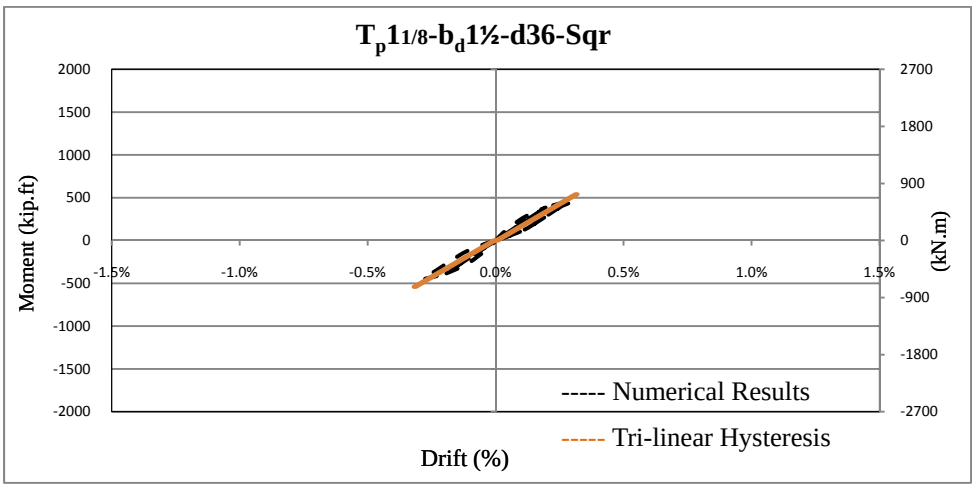

Figure C-82 Comparison Of The Numerical And Simulated Tri-Linear Hysteresis Of The T_p1½-b_d1¼-d24-Sqr Connection

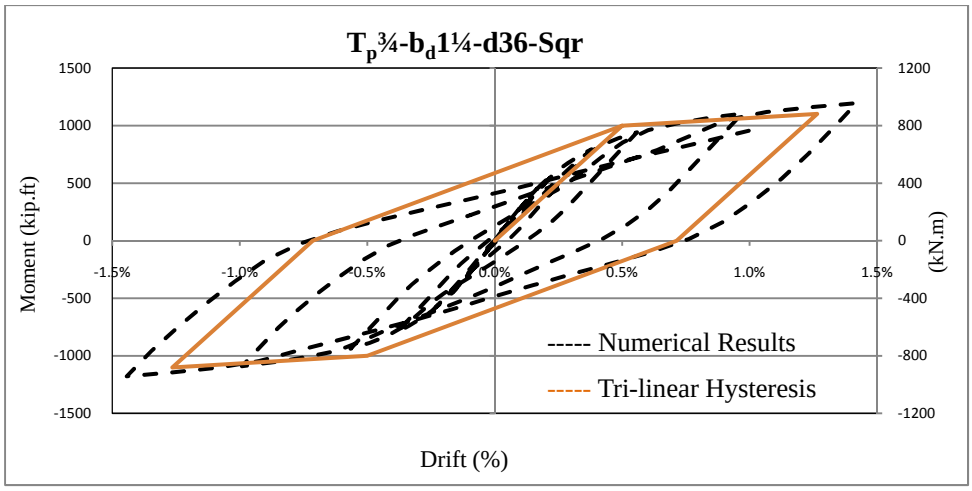

Figure C-83 Comparison Of The Numerical And Simulated Tri-Linear Hysteresis Of The T_p¾-b_d1¼-d36-Sqr Connection

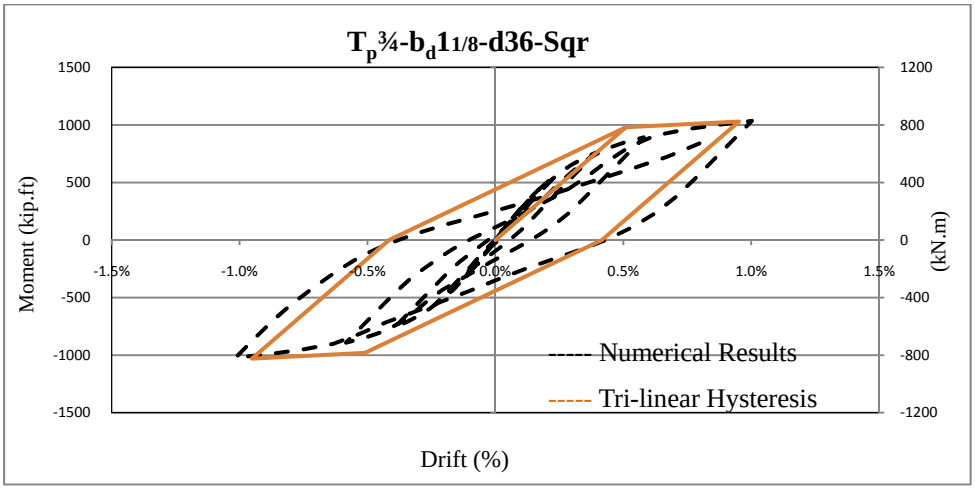

Figure C-84 Comparison Of The Numerical And Simulated Tri-Linear Hysteresis Of The T_p¾-b_d11/8-d36-Sqr Connection

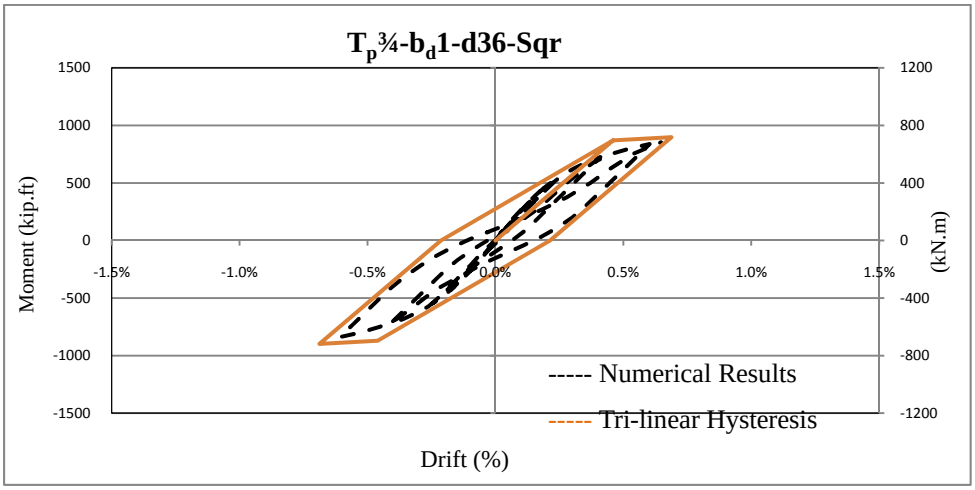

Figure C-85 Comparison Of The Numerical And Simulated Tri-Linear Hysteresis Of The T_p¾-b_d1-d36-Sqr Connection

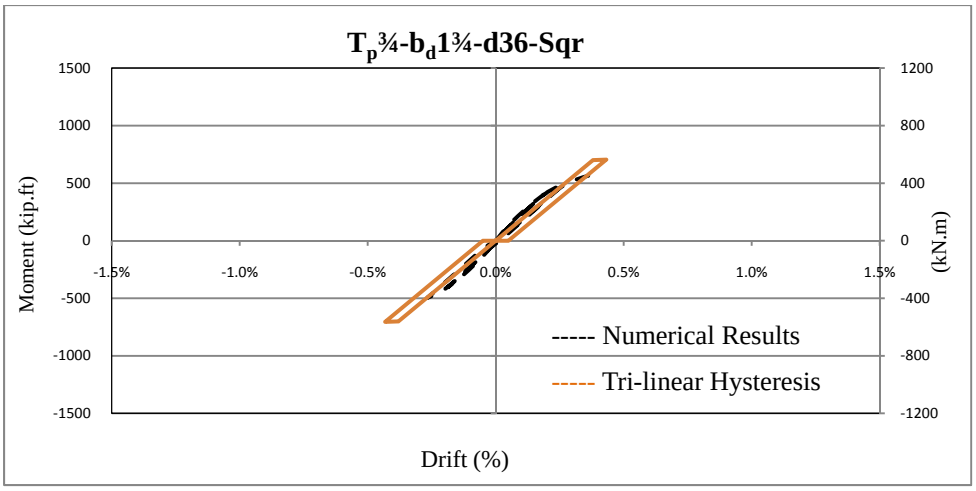

Figure C-86 Comparison Of The Numerical And Simulated Tri-Linear Hysteresis Of The T_p¾-b_d1¾-d36-Sqr Connection

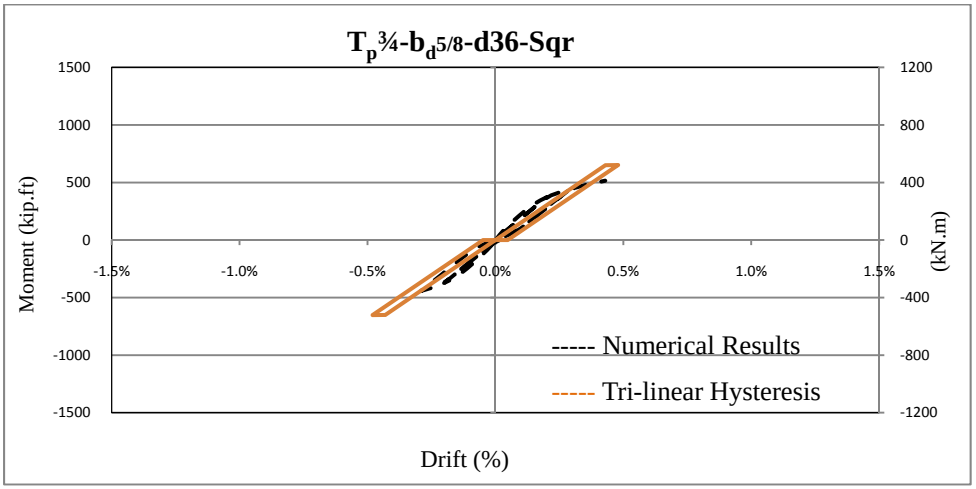

Figure C-87 Comparison Of The Numerical And Simulated Tri-Linear Hysteresis Of The T_p¾-b_d5/8-d36-Sqr Connection

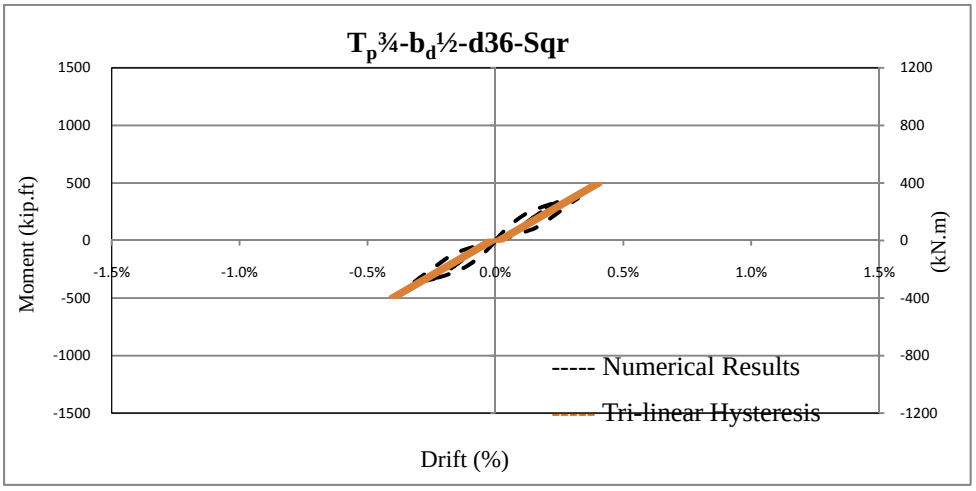

Figure C-88 Comparison Of The Numerical And Simulated Tri-Linear Hysteresis Of The T_p¾-b_d½-d36-Sqr Connection

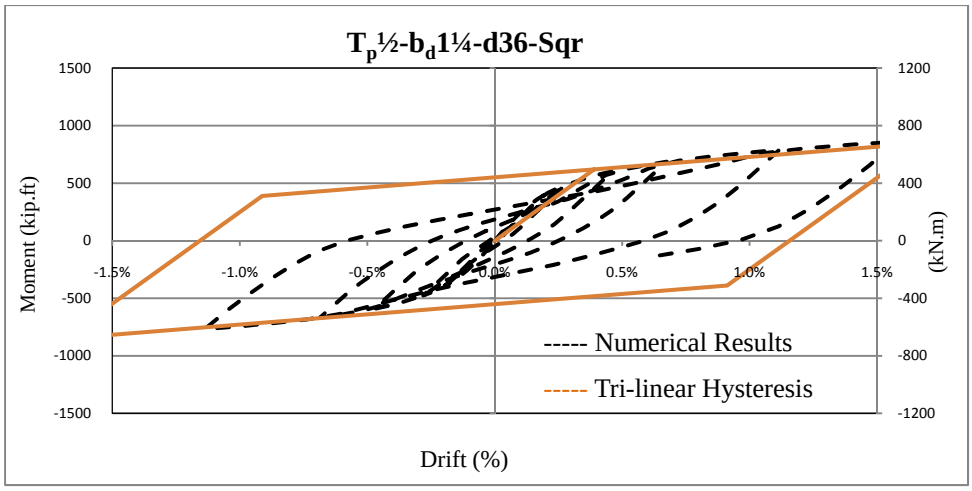

Figure C-89 Comparison Of The Numerical And Simulated Tri-Linear Hysteresis Of The T_p½-b_d1¼-d36-Sqr Connection

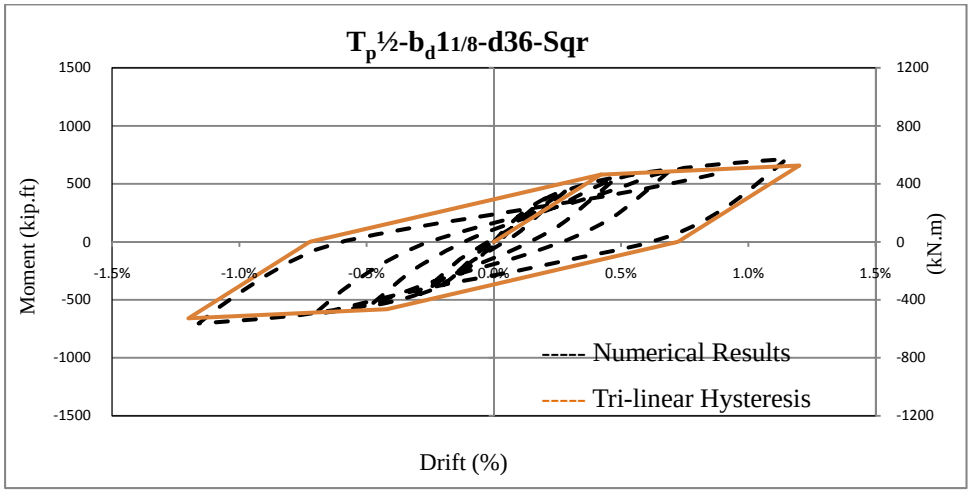

Figure C-90 Comparison Of The Numerical And Simulated Tri-Linear Hysteresis Of The T_p½-b_d11/8-d36-Sqr Connection

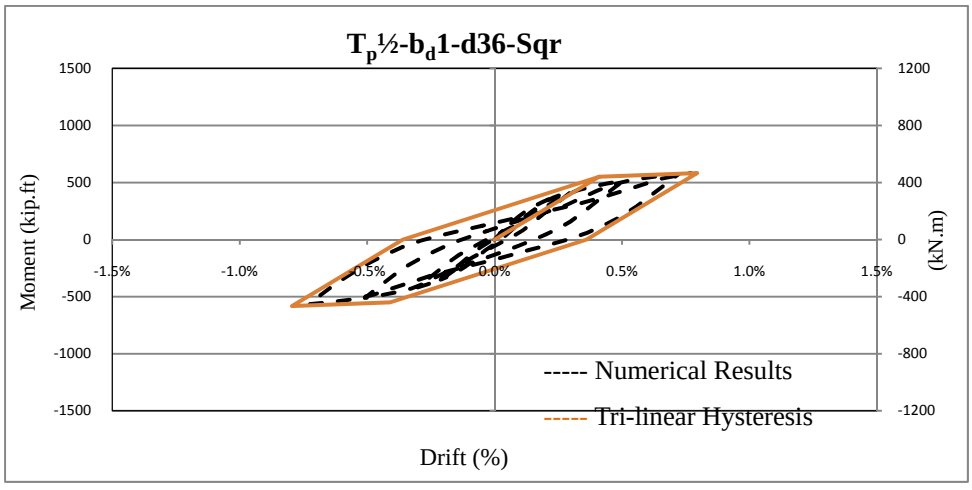

Figure C-91 Comparison Of The Numerical And Simulated Tri-Linear Hysteresis Of The T_p½-b_d1-d36-Sqr Connection

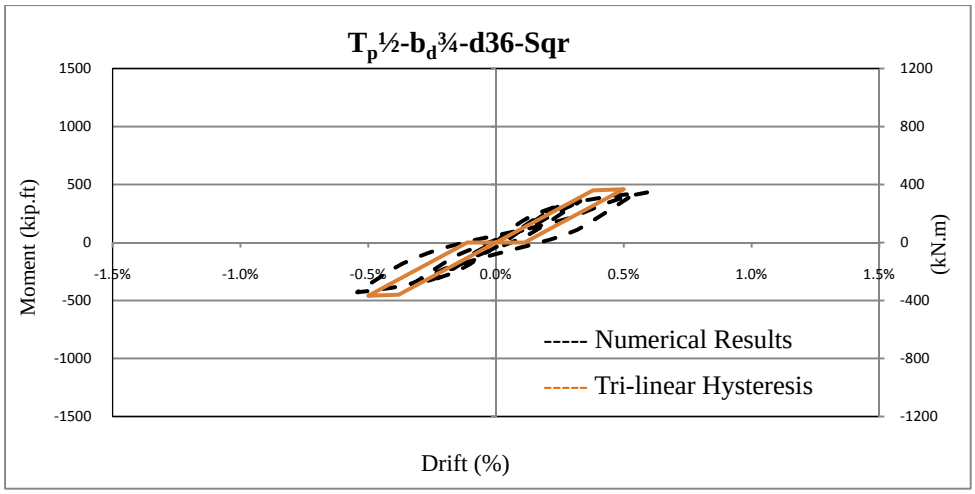

Figure C-92 Comparison Of The Numerical And Simulated Tri-Linear Hysteresis Of The T_p½-b_d¾-d36-Sqr Connection

APPENDIX D

HYSTERESIS OF THE MODELS WITH CIRCULAR BOLT PATTERN

The hysteresis results obtained from finite element analysis for the models with circular bolt pattern are presented individually in this Appendix. Tri-linear model were used to simulated hysteresis characteristic of each model. The simulated tri-linear model for each connection is also presented in the graphs. It should be noted that the procedure presented in the flowchart of Figure 5.8 were used to calculate the dependent values required to construct the hysteresis. Comparison of the results show a close agreement between the results obtained from the numerical analysis and the results obtained from the proposed tri-linear simulation.

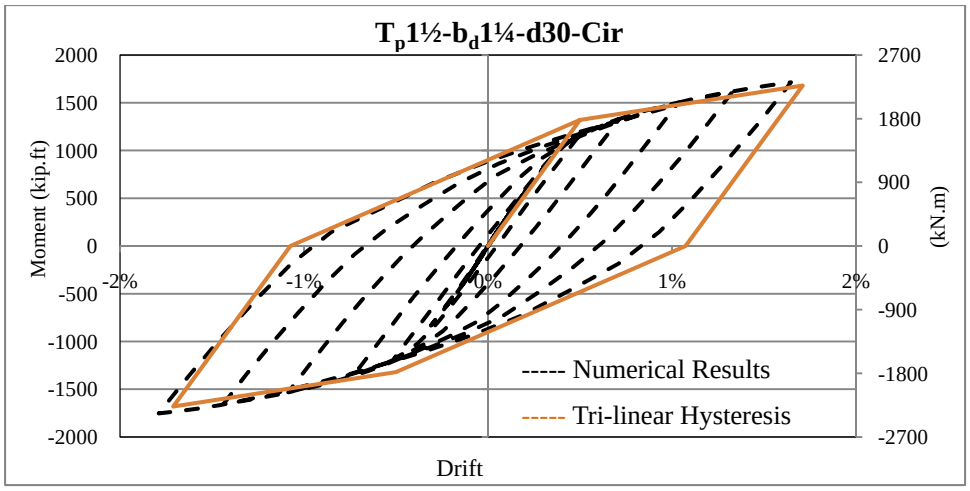

Figure D-1 Comparison Of The Numerical And Simulated Tri-Linear Hysteresis Of The $T_p1½-b_d1¼$-d30-Cir Connection

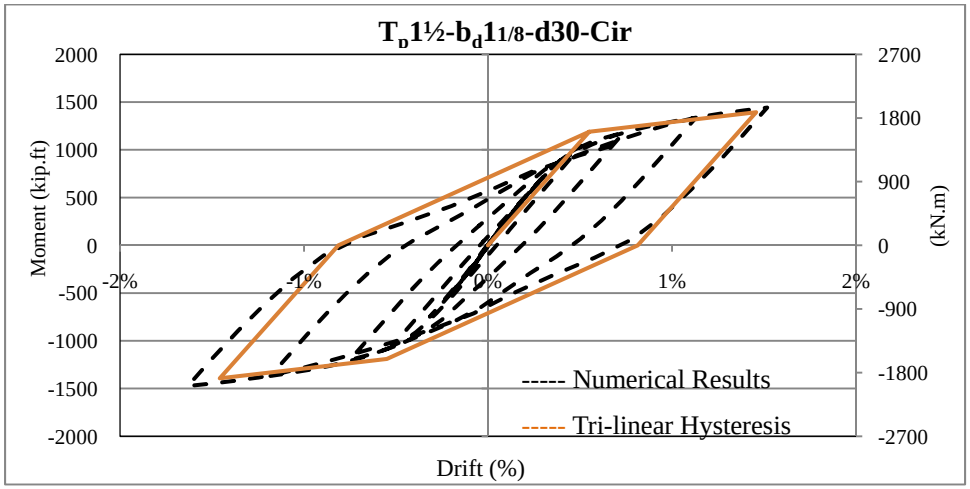

Figure D-2 Comparison Of The Numerical And Simulated Tri-Linear Hysteresis Of The $T_p1½-b_d11/8$-d30-Cir Connection

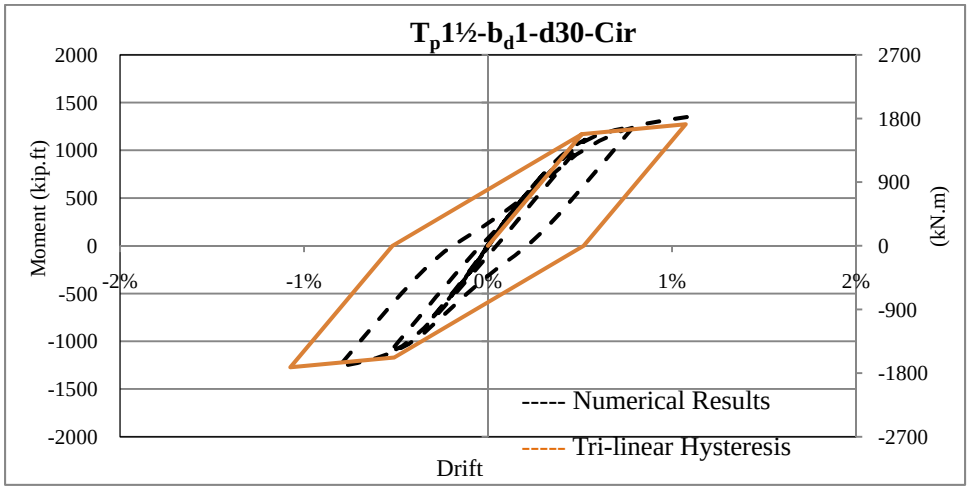

Figure D-3 Comparison Of The Numerical And Simulated Tri-Linear Hysteresis Of The $T_p1½-b_d1$-d30-Cir Connection

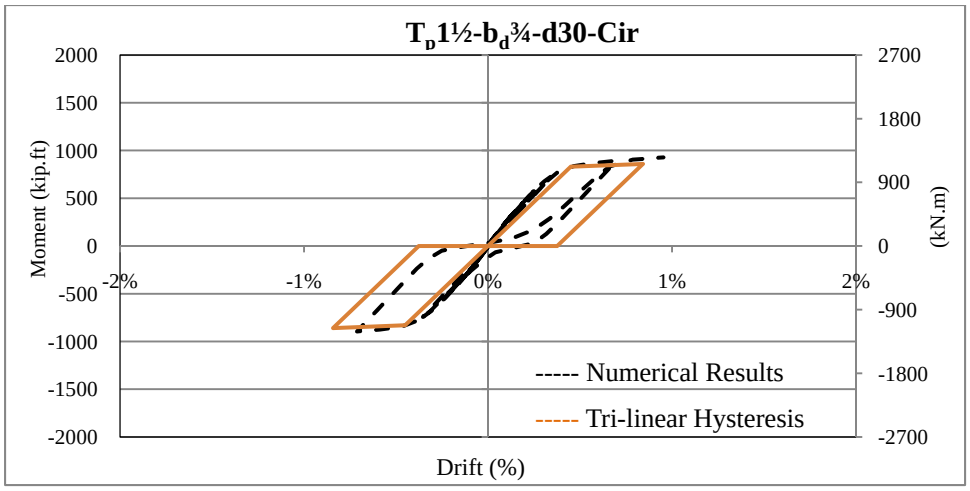

Figure D-4 Comparison Of The Numerical And Simulated Tri-Linear Hysteresis Of The $T_p1½\text{-}b_d¾\text{-}d30\text{-}Cir$ Connection

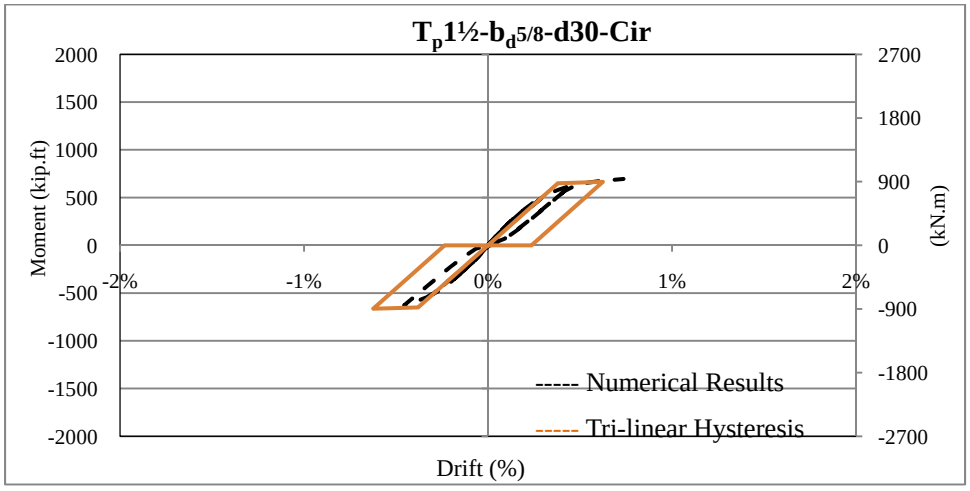

Figure D-5 Comparison Of The Numerical And Simulated Tri-Linear Hysteresis Of The $T_p1½\text{-}b_d5/8\text{-}d30\text{-}Cir$ Connection

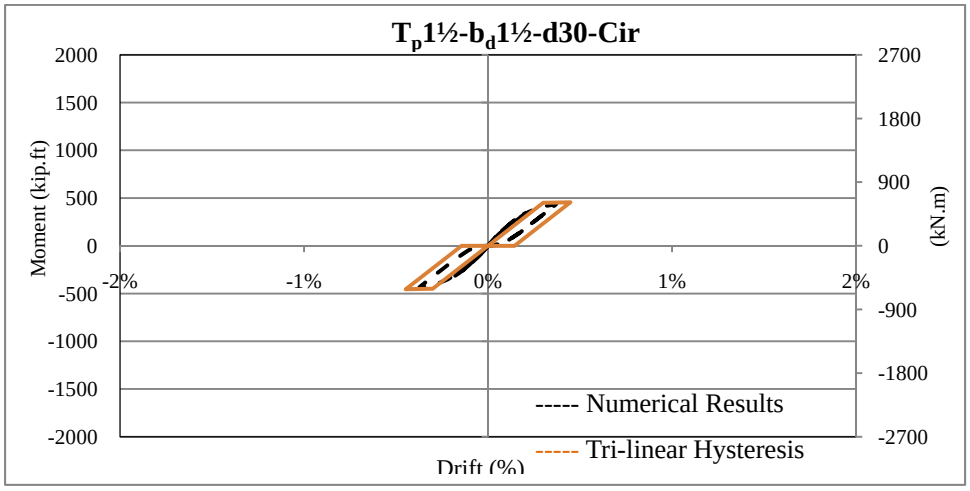

Figure D-6 Comparison Of The Numerical And Simulated Tri-Linear Hysteresis Of The $T_p1½\text{-}b_d1½\text{-}d30\text{-}Cir$ Connection

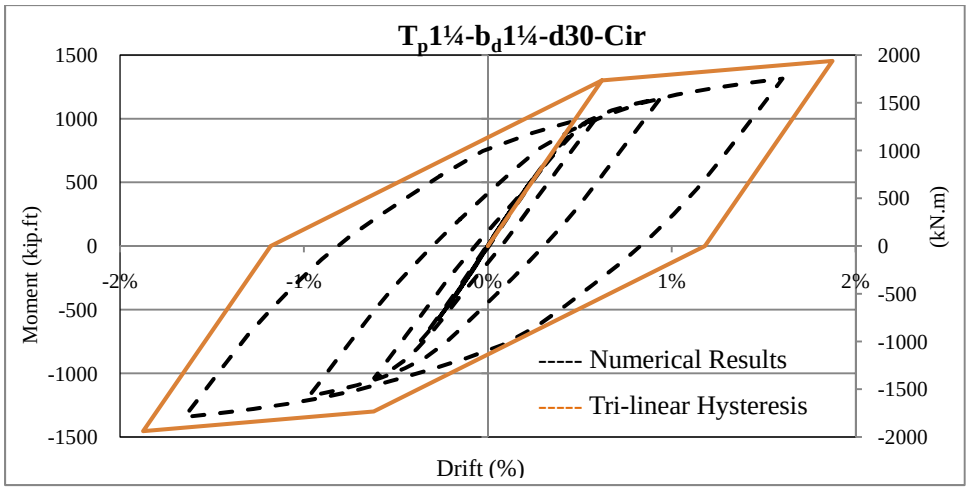

Figure D-7 Comparison Of The Numerical And Simulated Tri-Linear Hysteresis Of The $T_p1¼$-$b_d1¼$-d30-Cir Connection

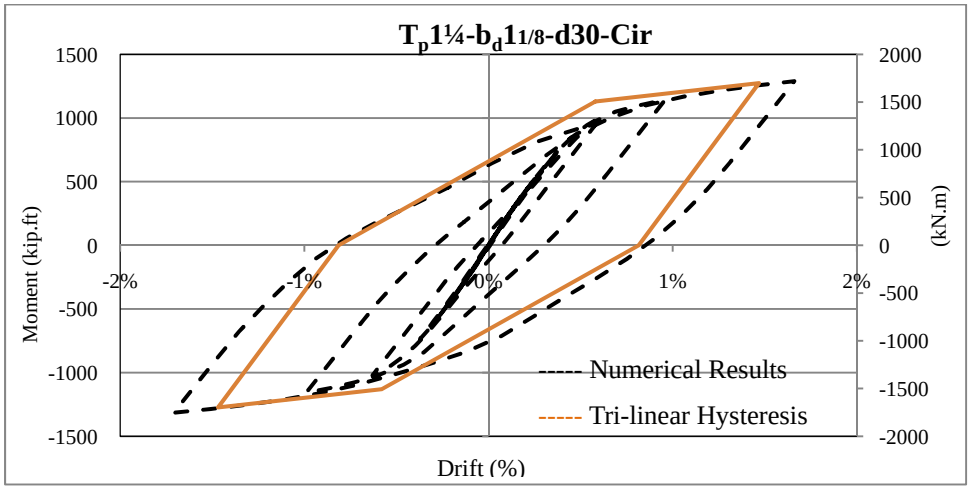

Figure D-8 Comparison Of The Numerical And Simulated Tri-Linear Hysteresis Of The $T_p1¼$-$b_d11/8$-d30-Cir Connection

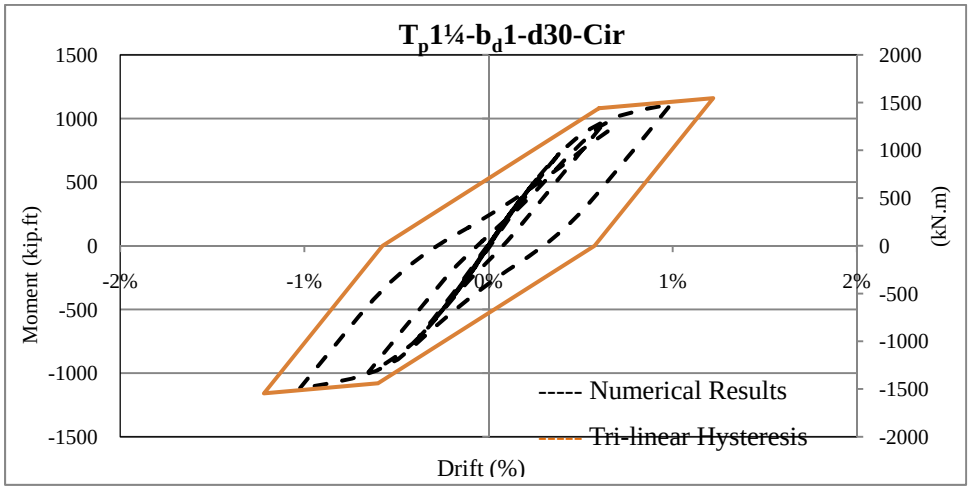

Figure D-9 Comparison Of The Numerical And Simulated Tri-Linear Hysteresis Of The $T_p1¼$-b_d1-d30-Cir Connection

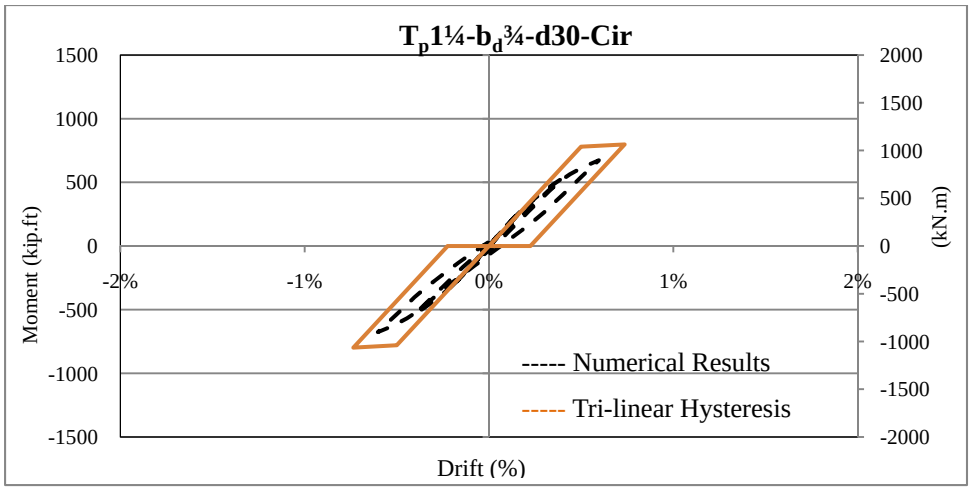

Figure D-10 Comparison Of The Numerical And Simulated Tri-Linear Hysteresis Of The $T_p1¼-b_d¾$-d30-Cir Connection

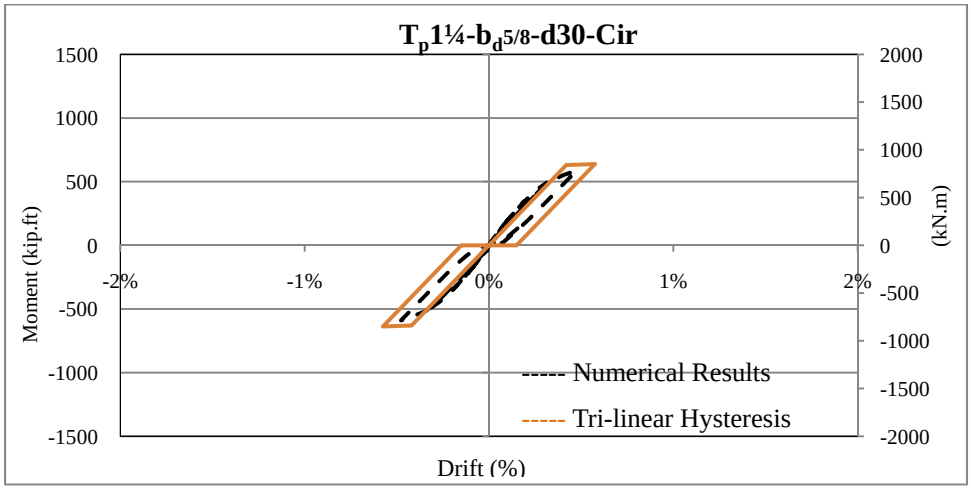

Figure D-11 Comparison Of The Numerical And Simulated Tri-Linear Hysteresis Of The $T_p1¼-b_d5/8$-d30-Cir Connection

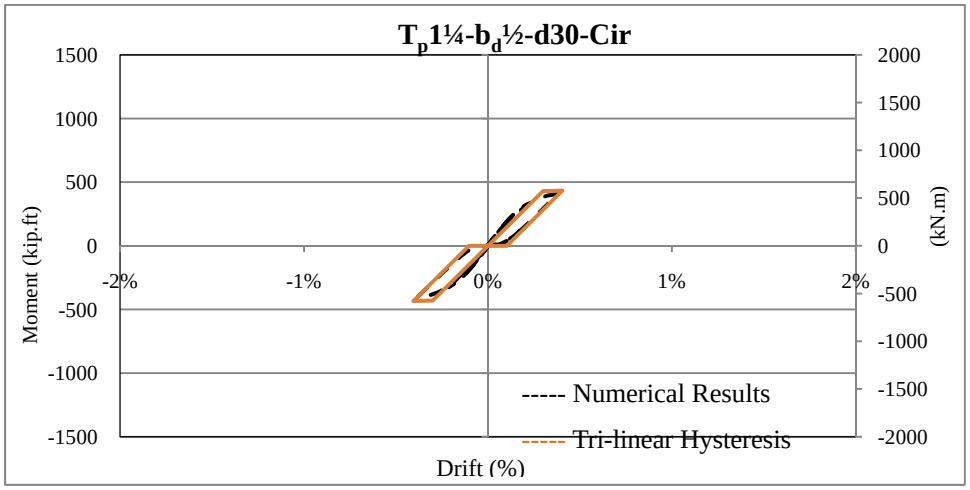

Figure D-12 Comparison Of The Numerical And Simulated Tri-Linear Hysteresis Of The $T_p1¼-b_d½$-d30-Cir Connection

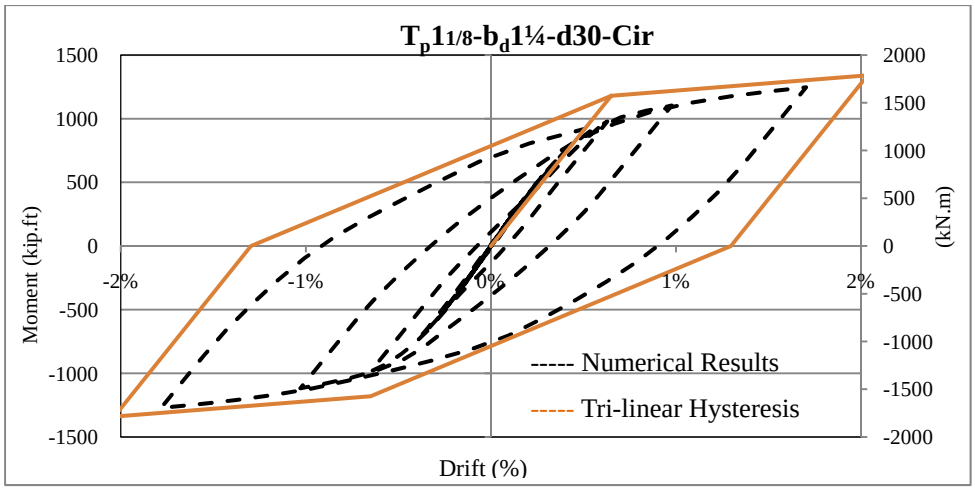

Figure D-13 Comparison Of The Numerical And Simulated Tri-Linear Hysteresis Of The $T_p11/8$-$b_d1¼$-d30-Cir Connection

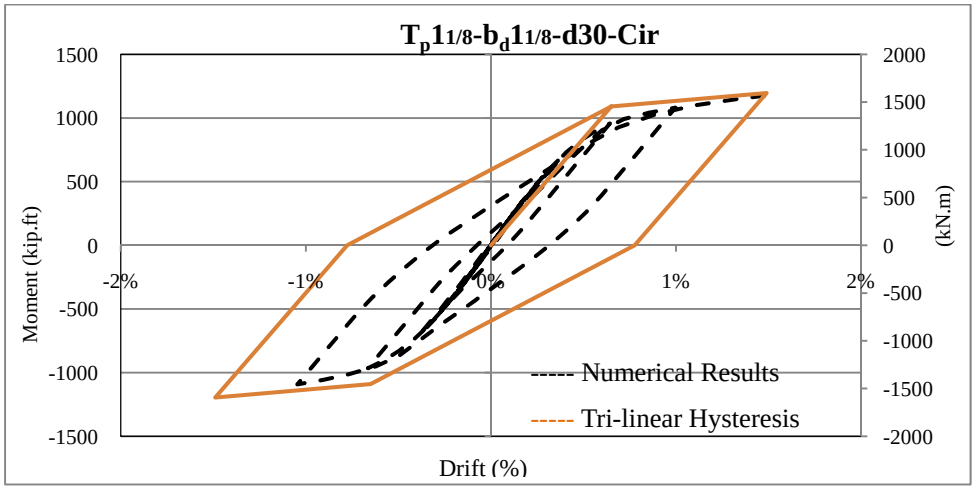

Figure D-14 Comparison Of The Numerical And Simulated Tri-Linear Hysteresis Of The $T_p11/8$-$b_d11/8$-d30-Cir Connection

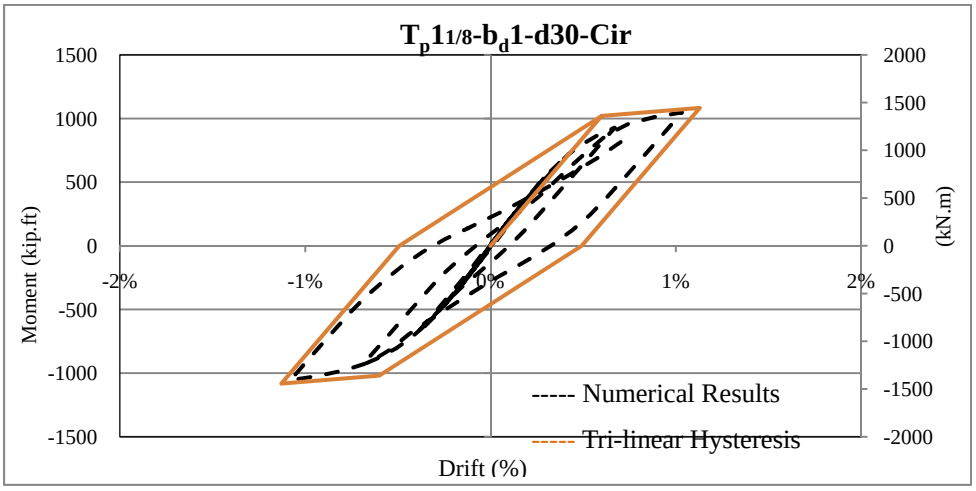

Figure D-15 Comparison Of The Numerical And Simulated Tri-Linear Hysteresis Of The $T_p11/8$-b_d1-d30-Cir Connection

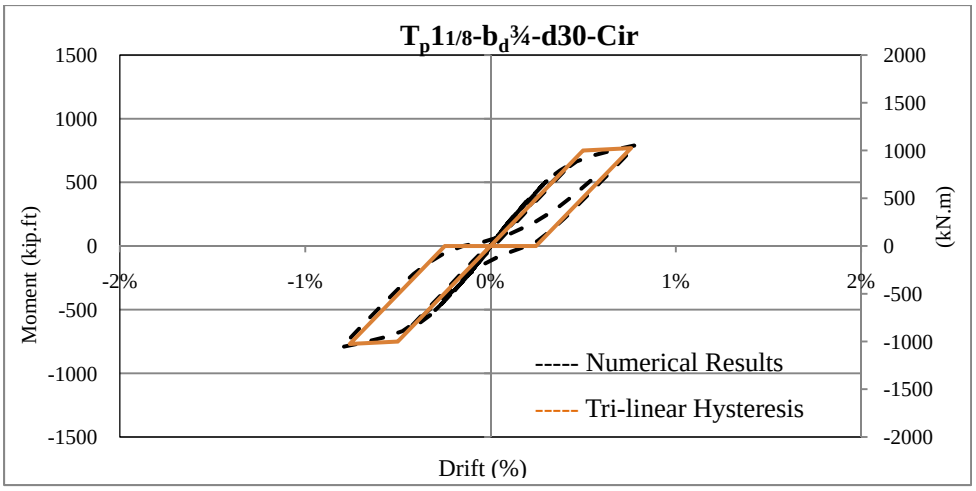

Figure D-16 Comparison Of The Numerical And Simulated Tri-Linear Hysteresis Of The T_p11/8-b_d¾-d30-Cir Connection

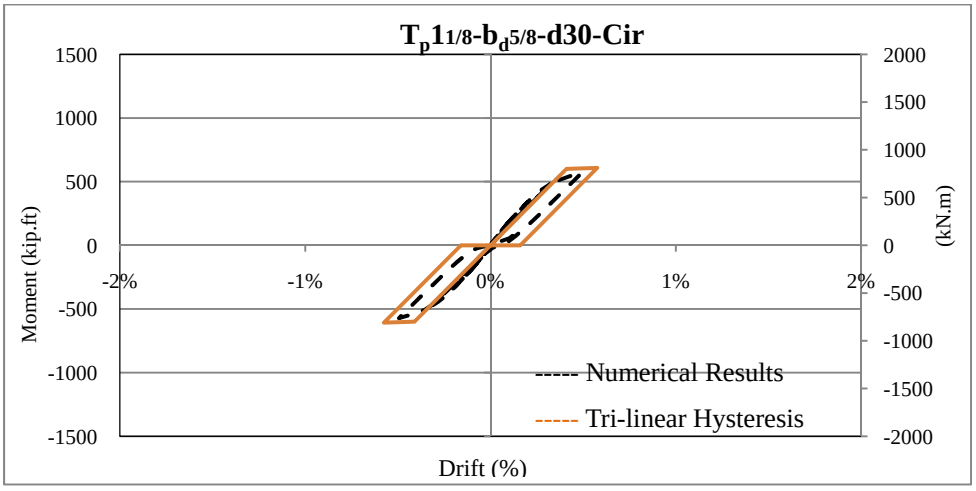

Figure D-17 Comparison Of The Numerical And Simulated Tri-Linear Hysteresis Of The T_p11/8-b_d5/8-d30-Cir Connection

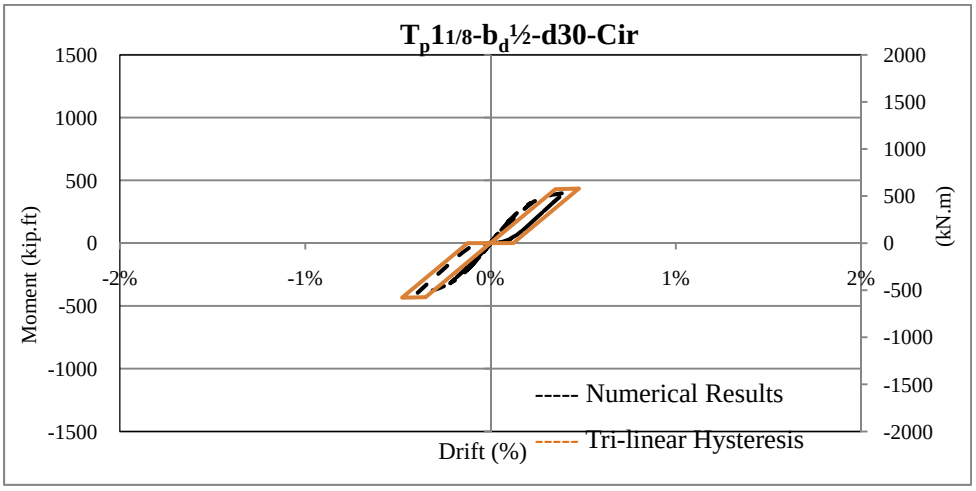

Figure D-18 Comparison Of The Numerical And Simulated Tri-Linear Hysteresis Of The T_p11/8-b_d½-d30-Cir Connection

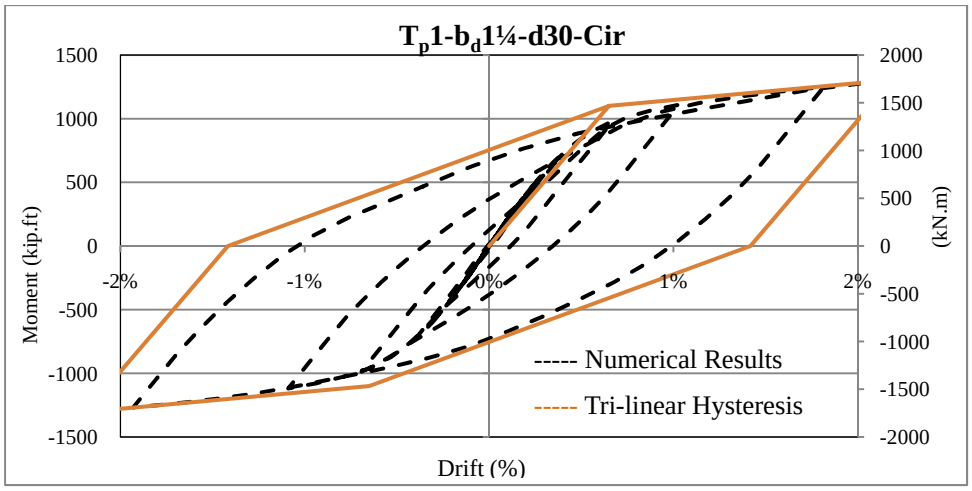

Figure D-19 Comparison Of The Numerical And Simulated Tri-Linear Hysteresis Of The T_p1-$b_d1¼$-d30-Cir Connection

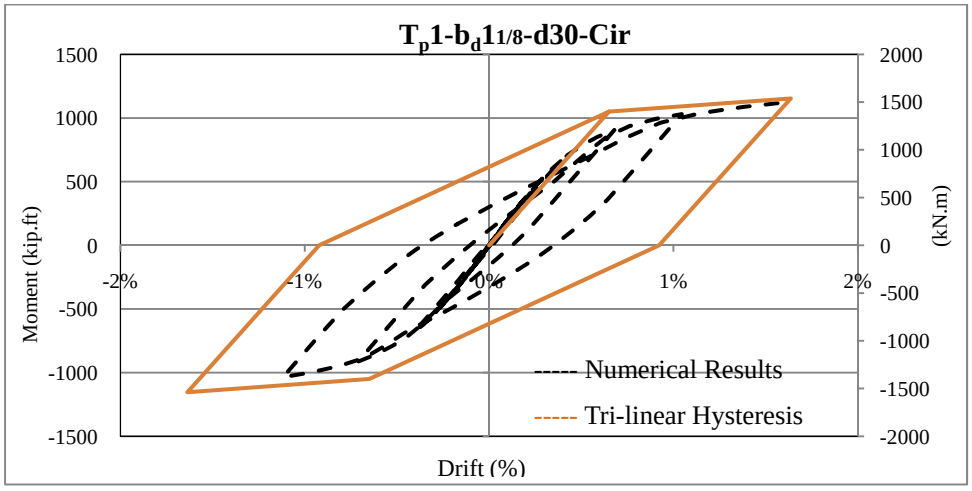

Figure D-20 Comparison Of The Numerical And Simulated Tri-Linear Hysteresis Of The T_p1-b_d11/8-d30-Cir Connection

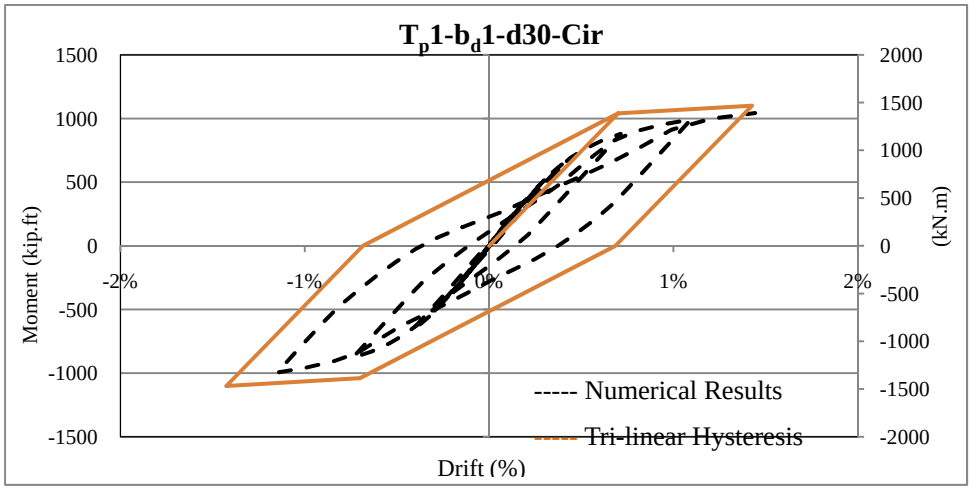

Figure D-21 Comparison Of The Numerical And Simulated Tri-Linear Hysteresis Of The T_p1-b_d1-d30-Cir Connection

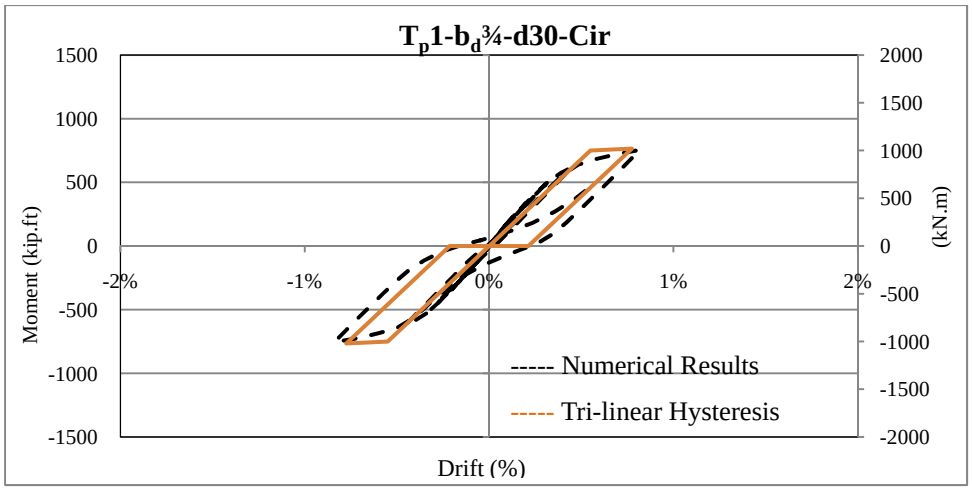

Figure D-22 Comparison Of The Numerical And Simulated Tri-Linear Hysteresis Of The T_p1-b_d¾-d30-Cir Connection

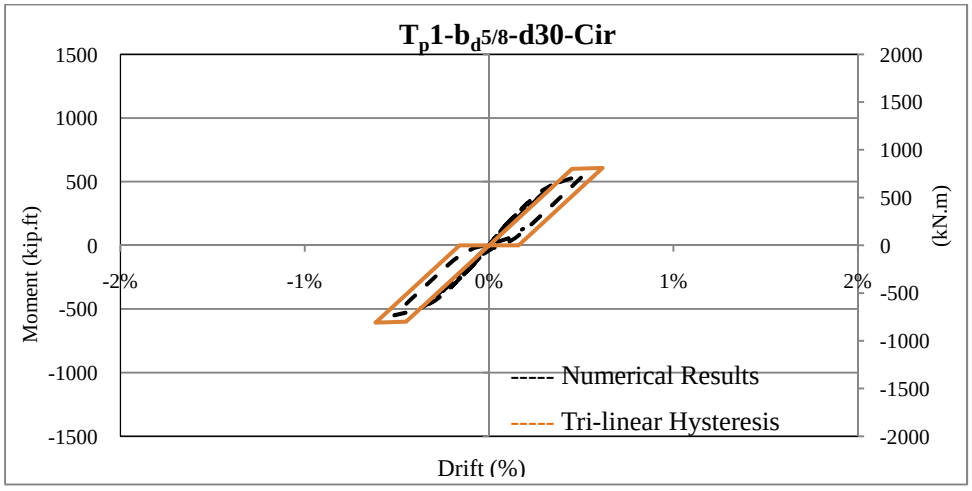

Figure D-23 Comparison Of The Numerical And Simulated Tri-Linear Hysteresis Of The T_p1-b_d5/8-d30-Cir Connection

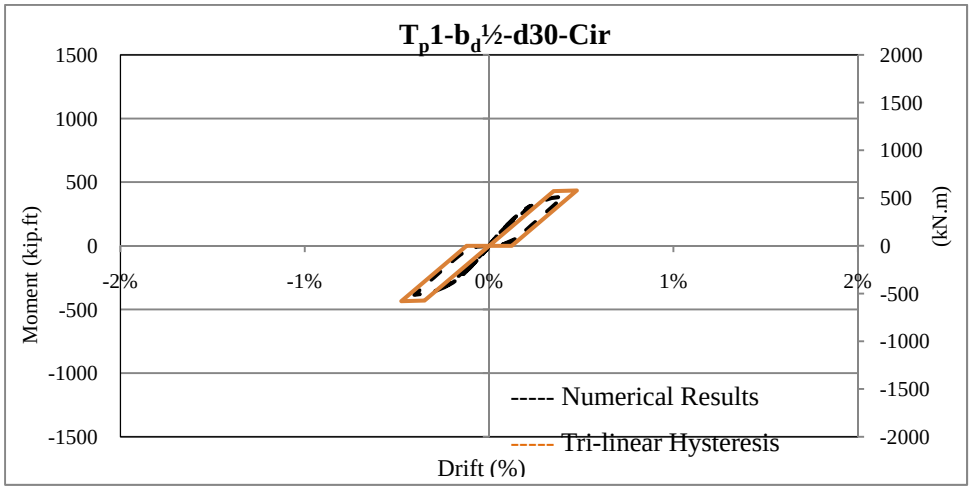

Figure D-24 Comparison Of The Numerical And Simulated Tri-Linear Hysteresis Of The T_p1-b_d½-d30-Cir Connection

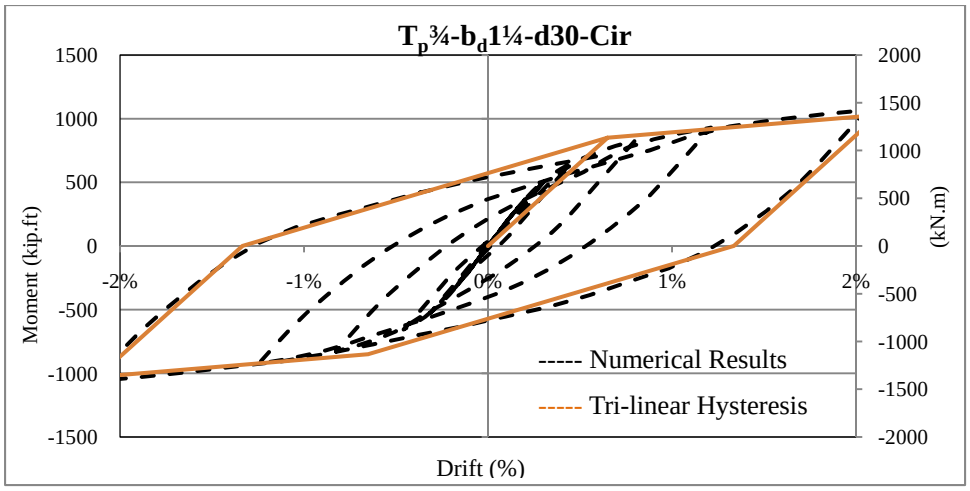

Figure D-25 Comparison Of The Numerical And Simulated Tri-Linear Hysteresis Of The T_p¾-b_d1¼-d30-Cir Connection

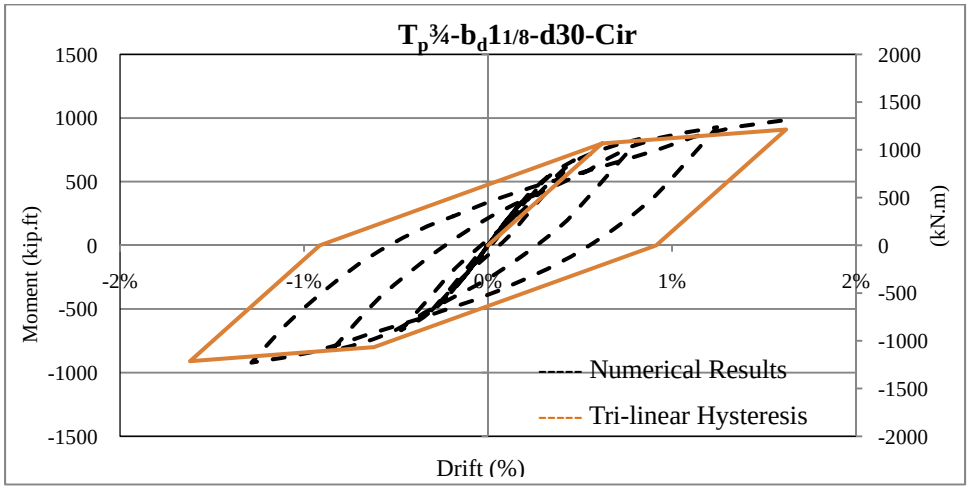

Figure D-26 Comparison Of The Numerical And Simulated Tri-Linear Hysteresis Of The T_p¾-b_d11/8-d30-Cir Connection

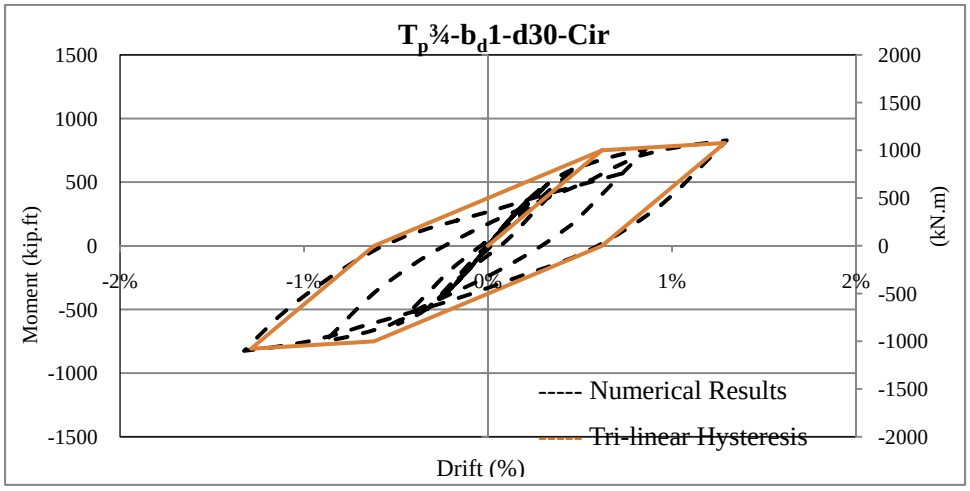

Figure D-27 Comparison Of The Numerical And Simulated Tri-Linear Hysteresis Of The T_p¾-b_d1-d30-Cir Connection

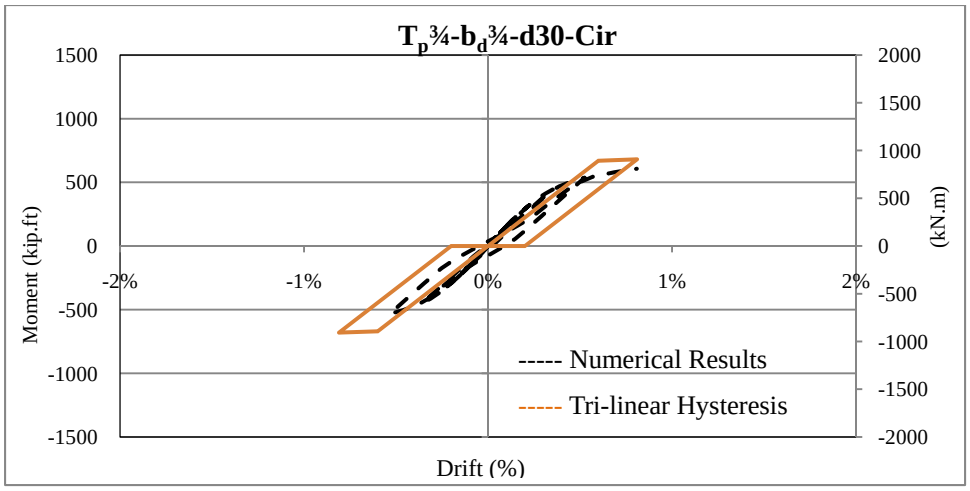

Figure D-28 Comparison Of The Numerical And Simulated Tri-Linear Hysteresis Of The T_p¾-b_d¾-d30-Cir Connection

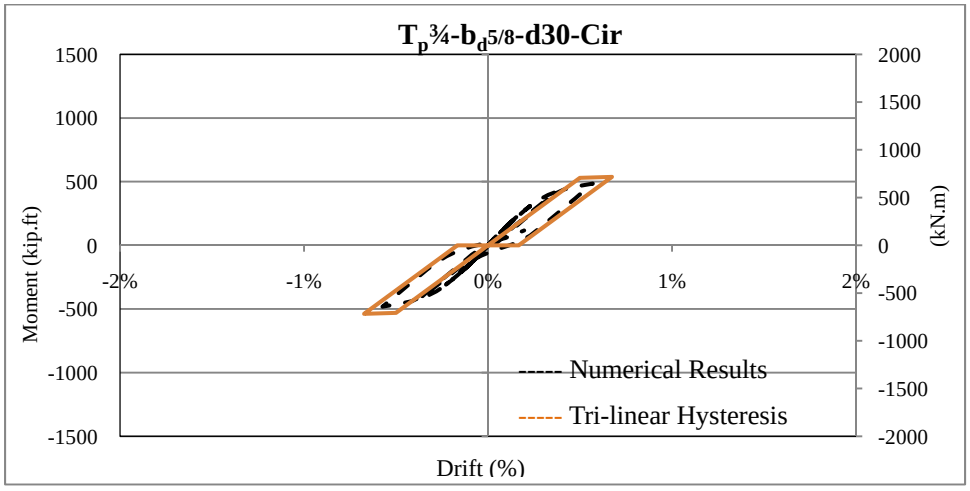

Figure D-29 Comparison Of The Numerical And Simulated Tri-Linear Hysteresis Of The T_p¾-b_d5/8-d30-Cir Connection

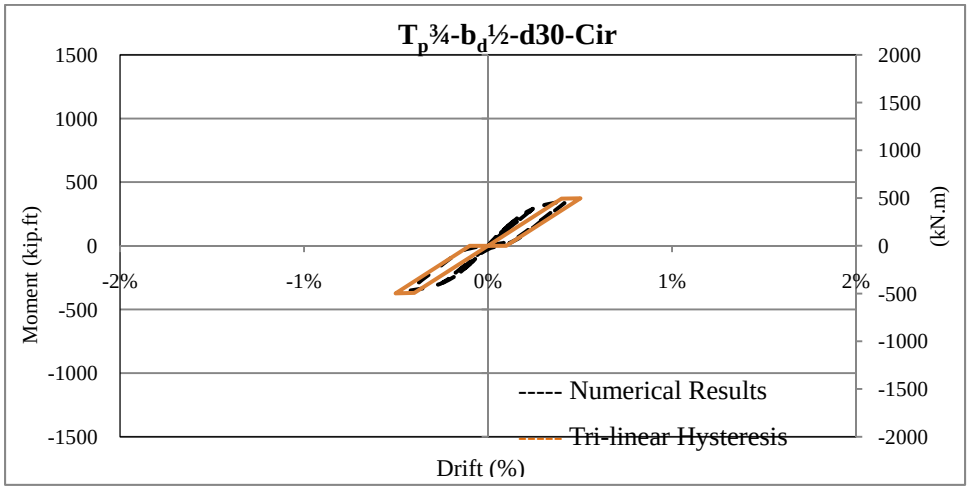

Figure D-30 Comparison Of The Numerical And Simulated Tri-Linear Hysteresis Of The T_p¾-b_d½-d30-Cir Connection

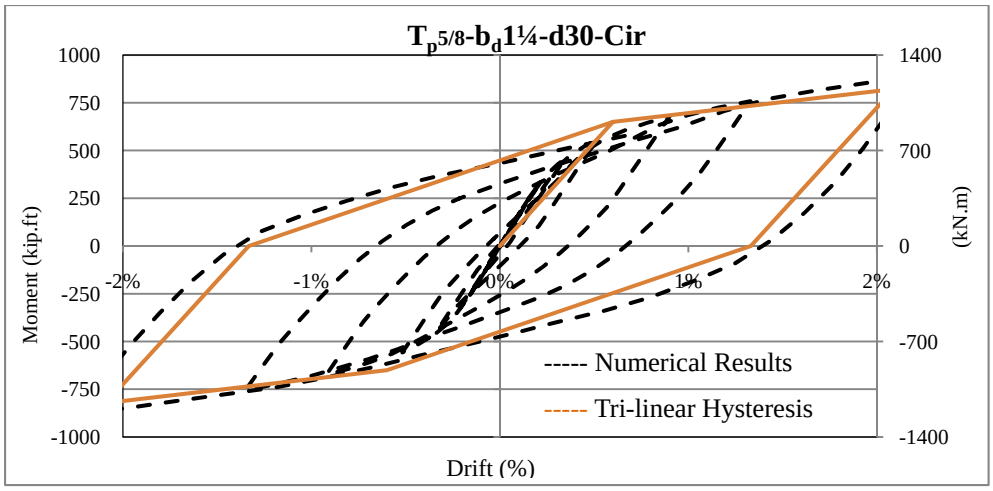

Figure D-31 Comparison Of The Numerical And Simulated Tri-Linear Hysteresis Of The T_p5/8-b_d1¼-d30-Cir Connection

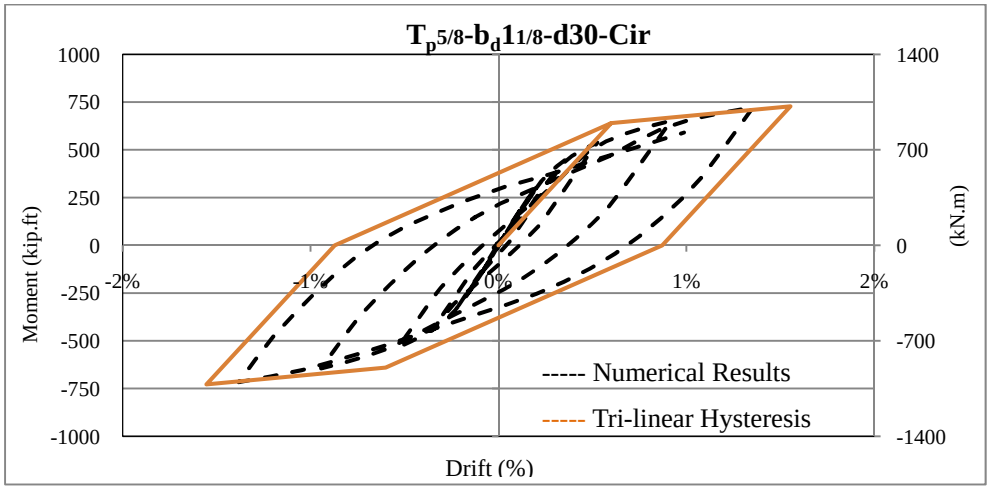

Figure D-32 Comparison Of The Numerical And Simulated Tri-Linear Hysteresis Of The T_p5/8-b_d11/8-d30-Cir Connection

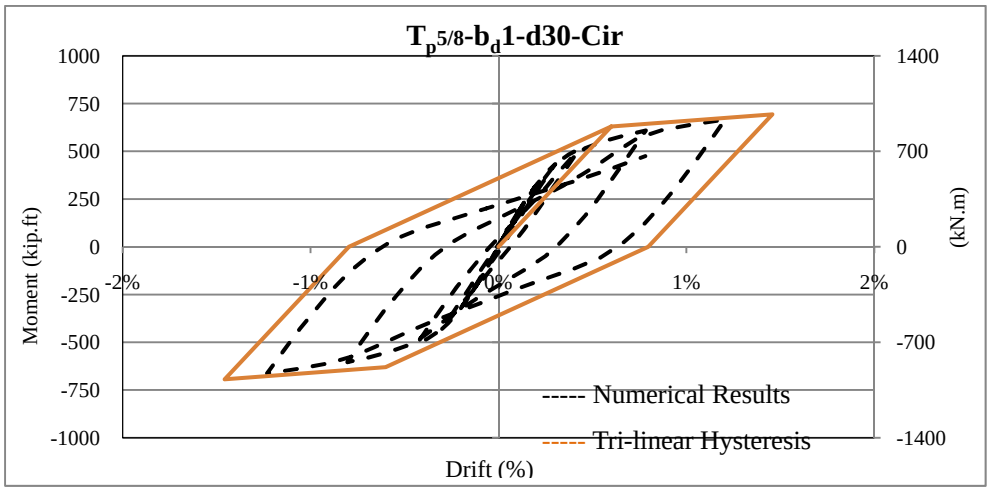

Figure D-33 Comparison Of The Numerical And Simulated Tri-Linear Hysteresis Of The T_p5/8-b_d1-d30-Cir Connection

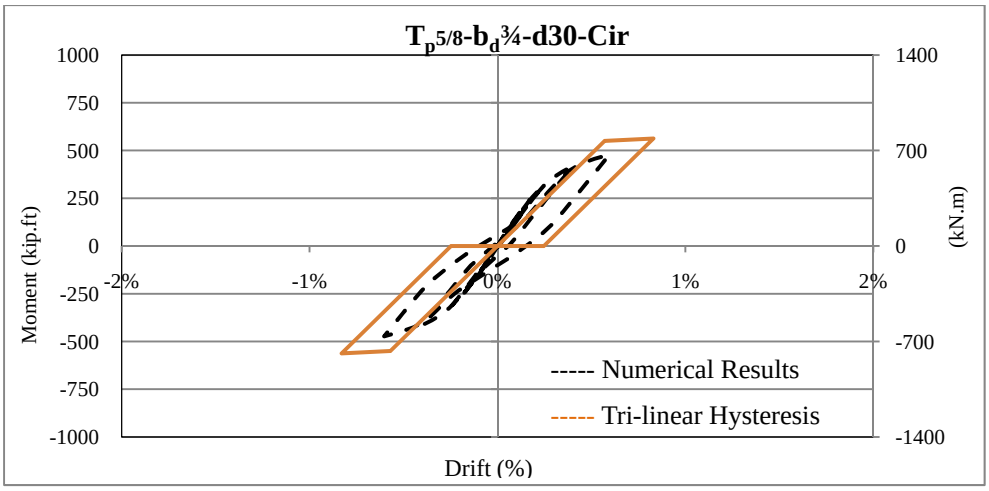

Figure D-34 Comparison Of The Numerical And Simulated Tri-Linear Hysteresis Of The T_p5/8-b_d¾-d30-Cir Connection

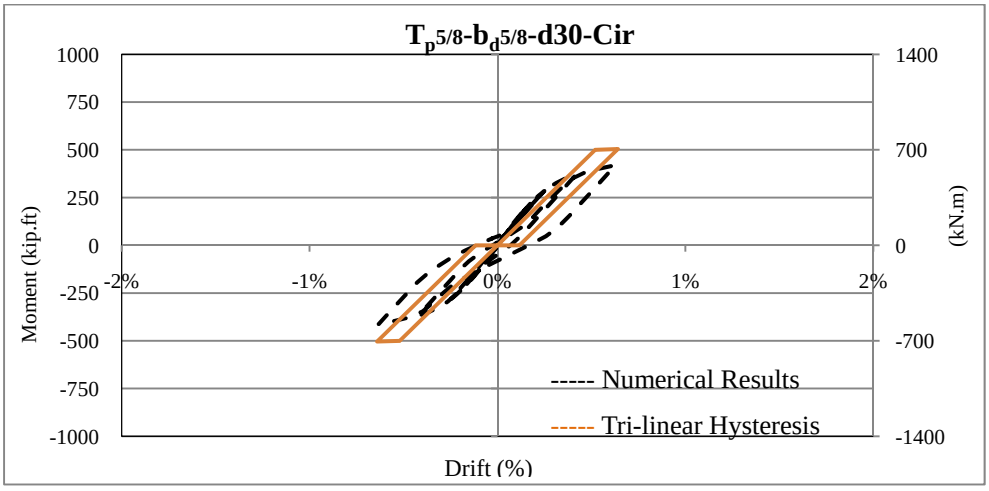

Figure D-35 Comparison Of The Numerical And Simulated Tri-Linear Hysteresis Of The T_p5/8-b_d5/8-d30-Cir Connection

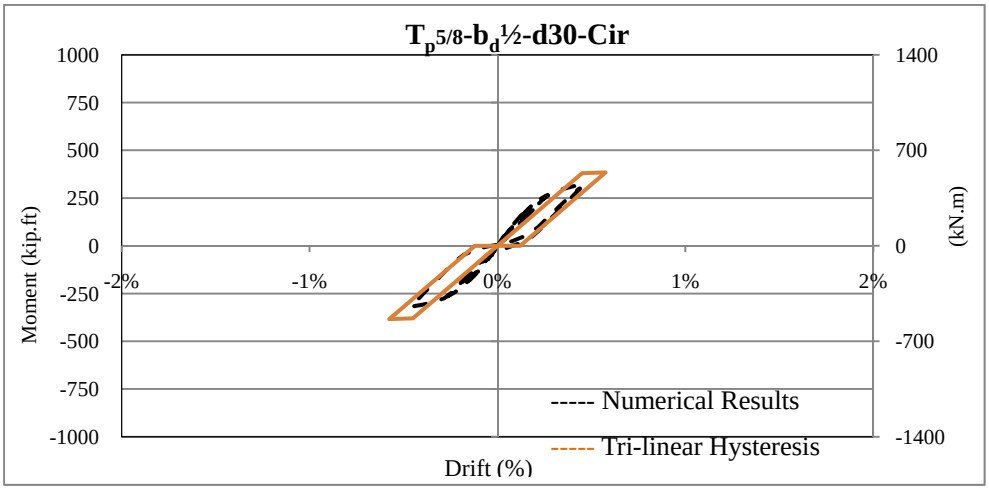

Figure D-36 Comparison Of The Numerical And Simulated Tri-Linear Hysteresis Of The T_p5/8-b_d½-d30-Cir Connection

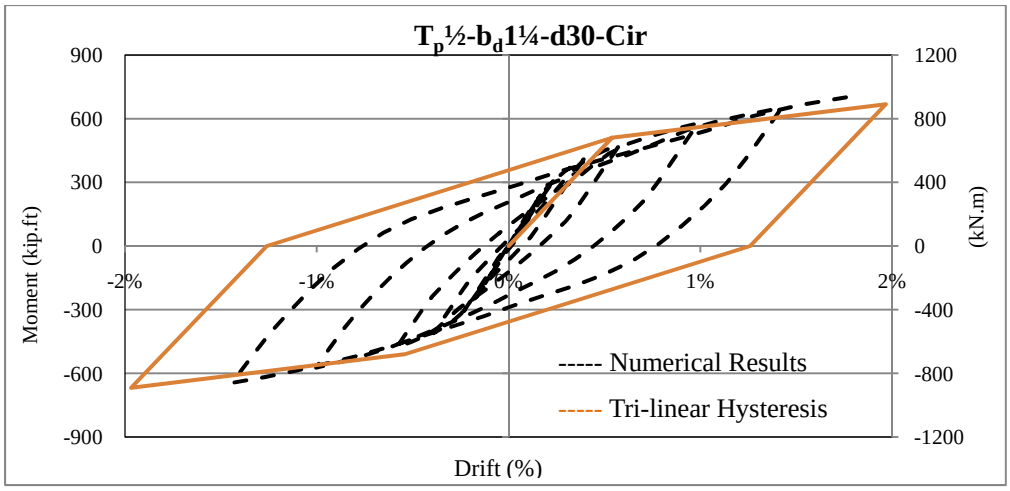

Figure D-37 Comparison Of The Numerical And Simulated Tri-Linear Hysteresis Of The T_p½-b_d1¼-d30-Cir Connection

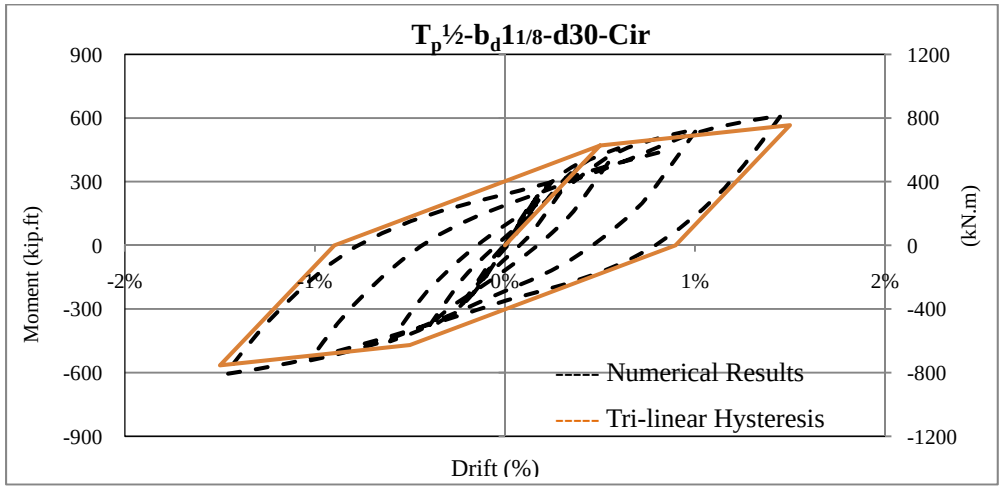

Figure D-38 Comparison Of The Numerical And Simulated Tri-Linear Hysteresis Of The T_p½-b_d11/8-d30-Cir Connection

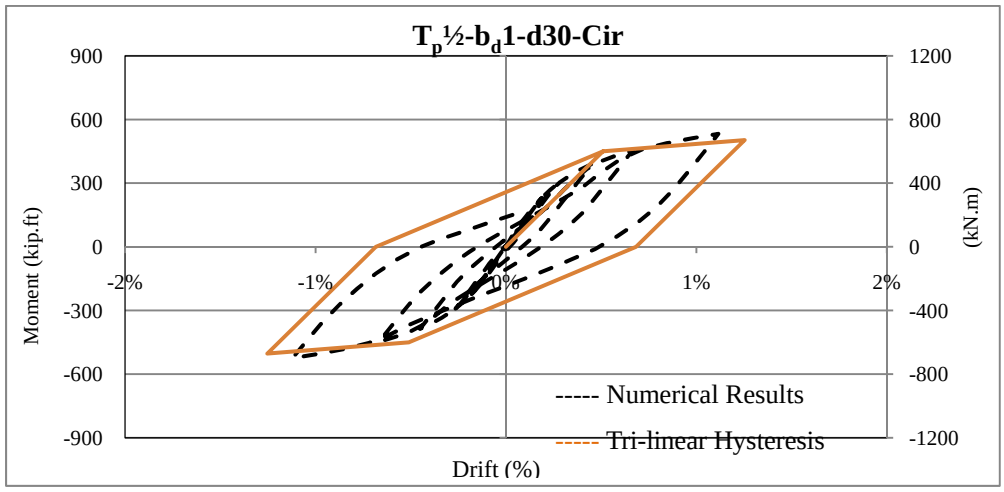

Figure D-39 Comparison Of The Numerical And Simulated Tri-Linear Hysteresis Of The T_p½-b_d1-d30-Cir Connection

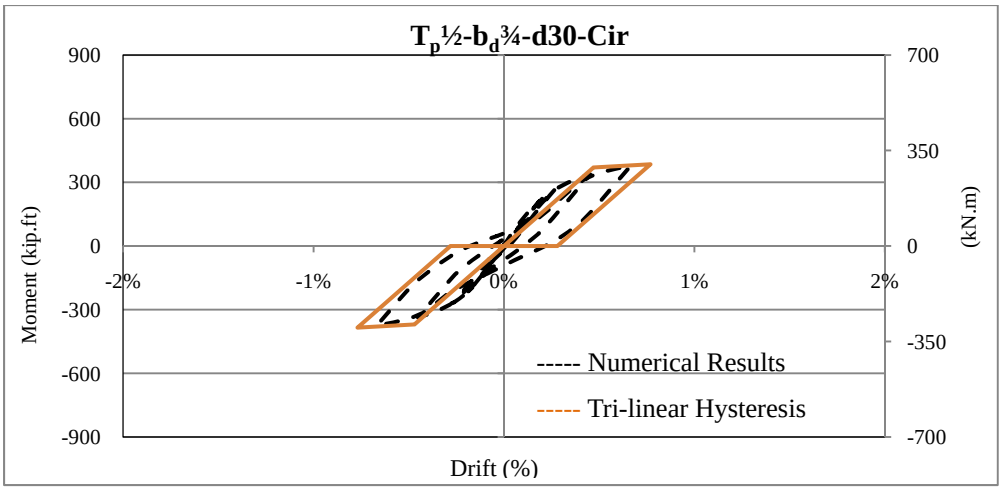

Figure D-40 Comparison Of The Numerical And Simulated Tri-Linear Hysteresis Of The T_p½-b_d¾-d30-Cir Connection

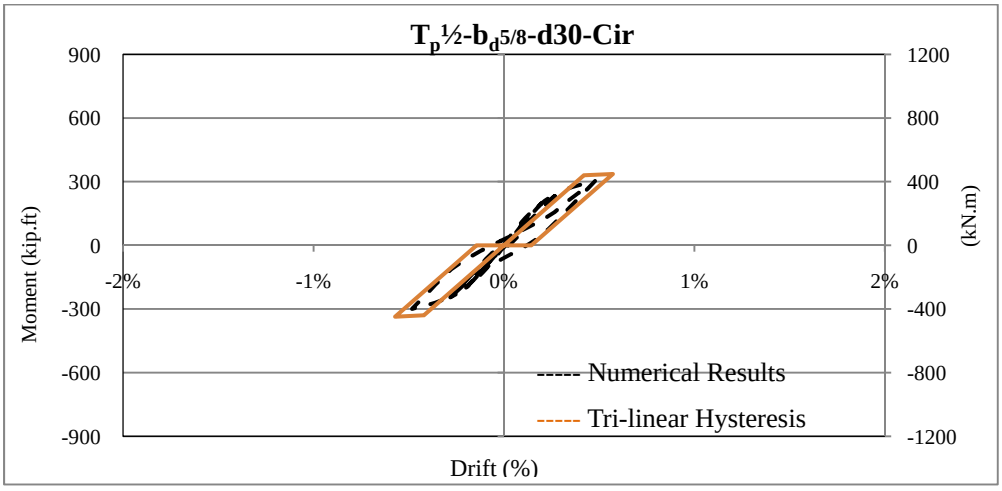

Figure D-41 Comparison Of The Numerical And Simulated Tri-Linear Hysteresis Of The T_p½-b_d5/8-d30-Cir Connection

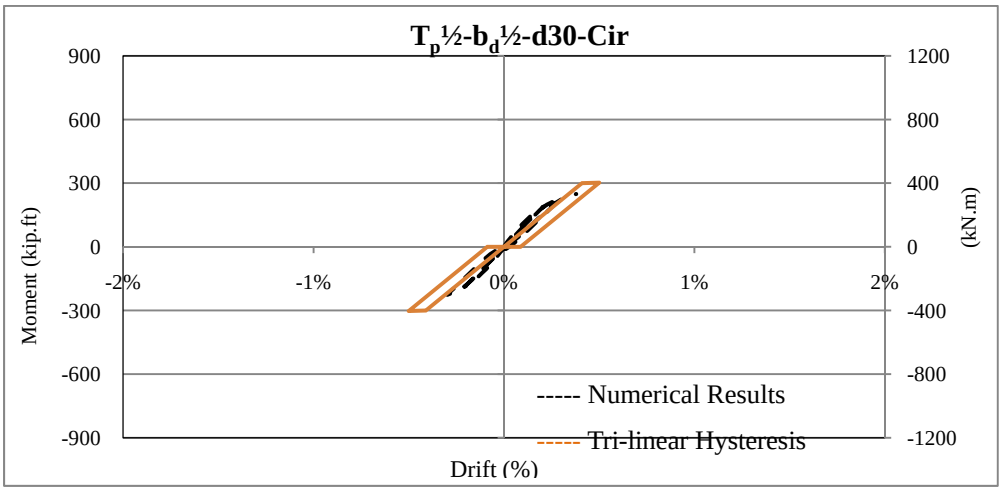

Figure D-42 Comparison Of The Numerical And Simulated Tri-Linear Hysteresis Of The T_p½-b_d½-d30-Cir Connection

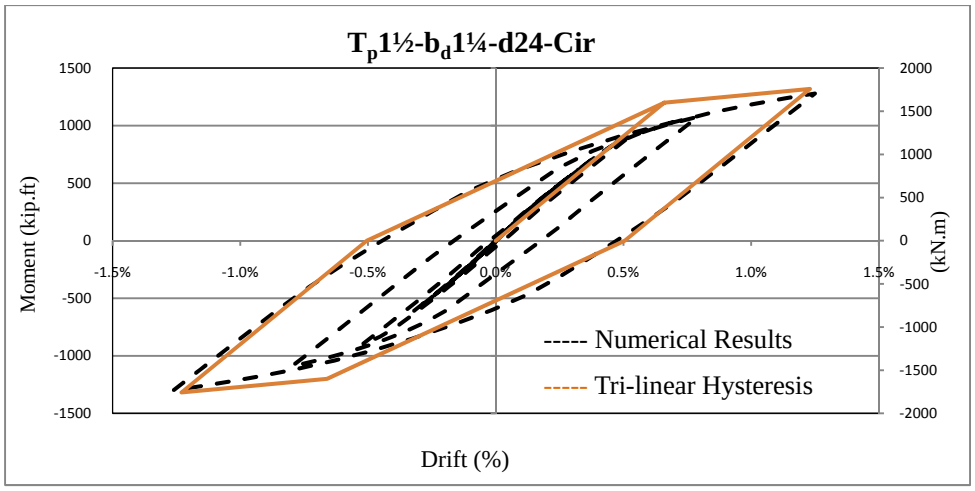

Figure D-43 Comparison Of The Numerical And Simulated Tri-Linear Hysteresis Of The $T_p1½\text{-}b_d1¼$-d24-Cir Connection

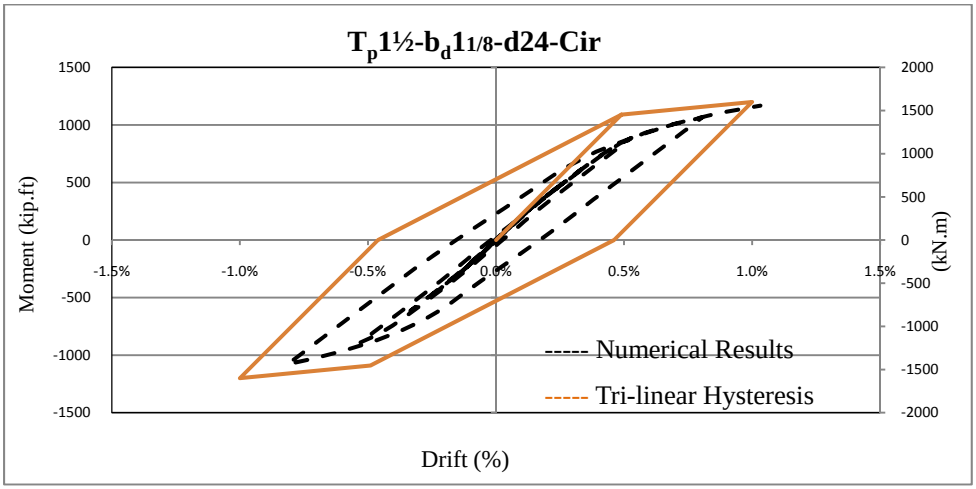

Figure D-44 Comparison Of The Numerical And Simulated Tri-Linear Hysteresis Of The $T_p1½\text{-}b_d11/8$-d24-Cir Connection

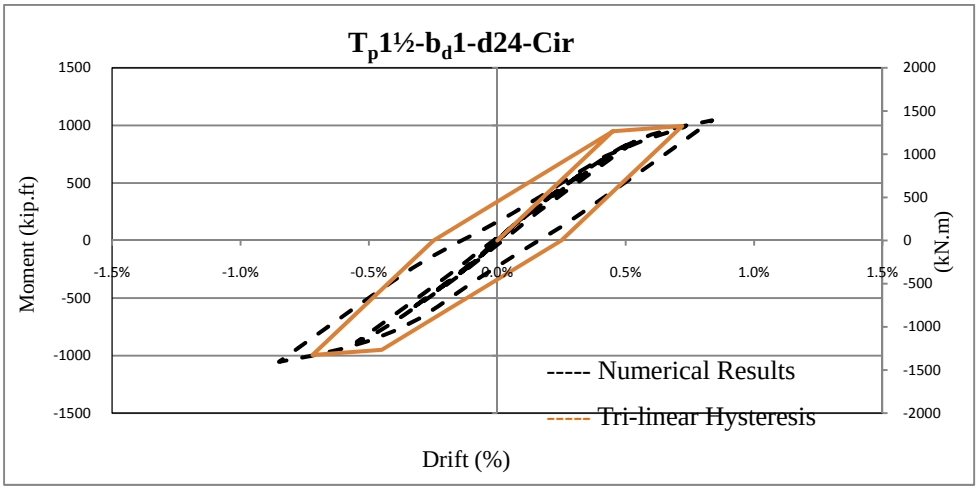

Figure D-45 Comparison Of The Numerical And Simulated Tri-Linear Hysteresis Of The $T_p1½\text{-}b_d1$-d24-Cir Connection

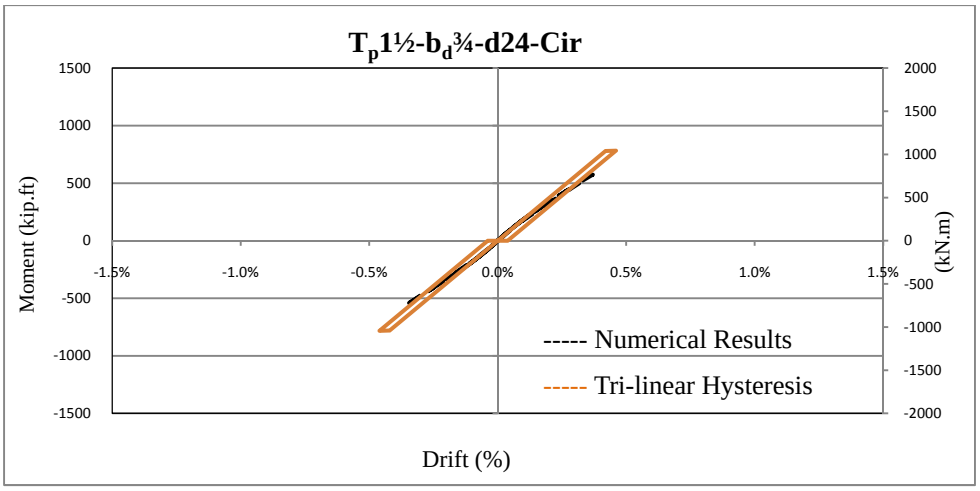

Figure D-46 Comparison Of The Numerical And Simulated Tri-Linear Hysteresis Of The $T_p1½\text{-}b_d1¼$-d30-Cir Connection

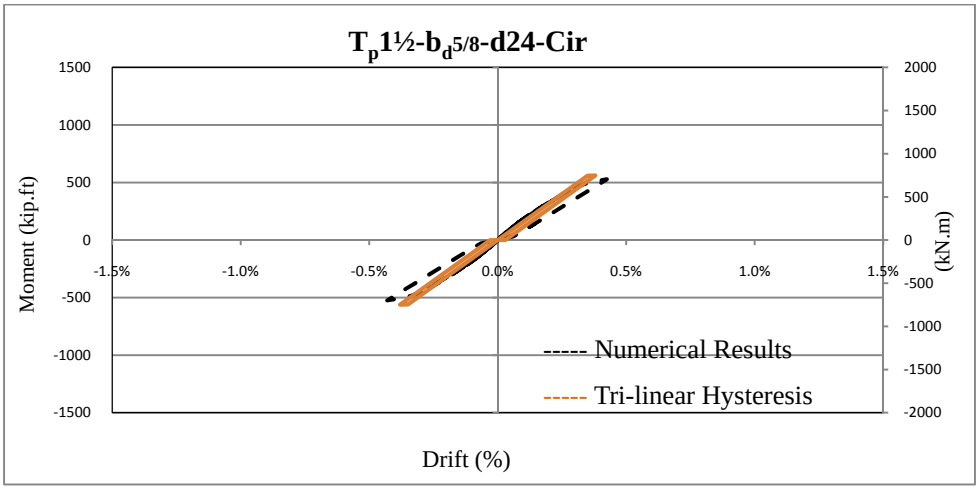

Figure D-47 Comparison Of The Numerical And Simulated Tri-Linear Hysteresis Of The $T_p1½\text{-}b_d5/8$-d24-Cir Connection

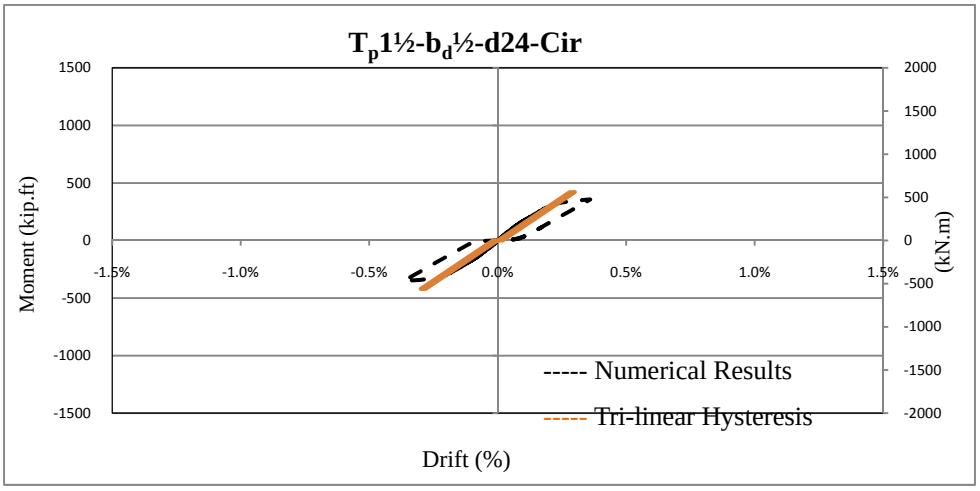

Figure D-48 Comparison Of The Numerical And Simulated Tri-Linear Hysteresis Of The $T_p1½\text{-}b_d½$-d24-Cir Connection

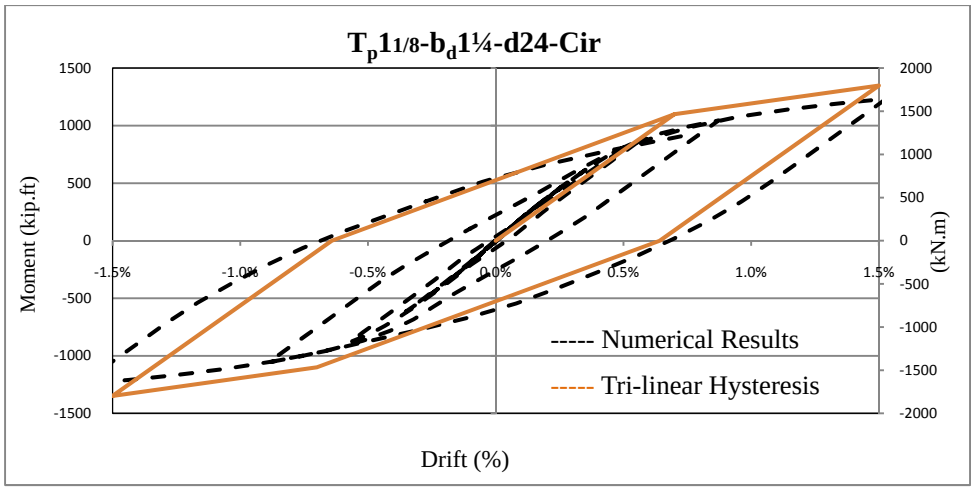

Figure D-49 Comparison Of The Numerical And Simulated Tri-Linear Hysteresis Of The T_p11/8-b_d1¼-d24-Cir Connection

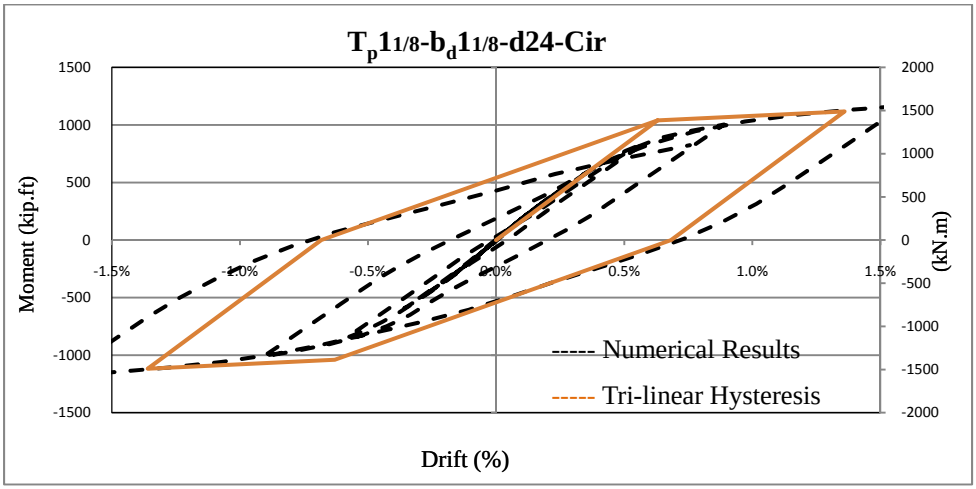

Figure D-50 Comparison Of The Numerical And Simulated Tri-Linear Hysteresis Of The T_p11/8-b_d11/8-d24-Cir Connection

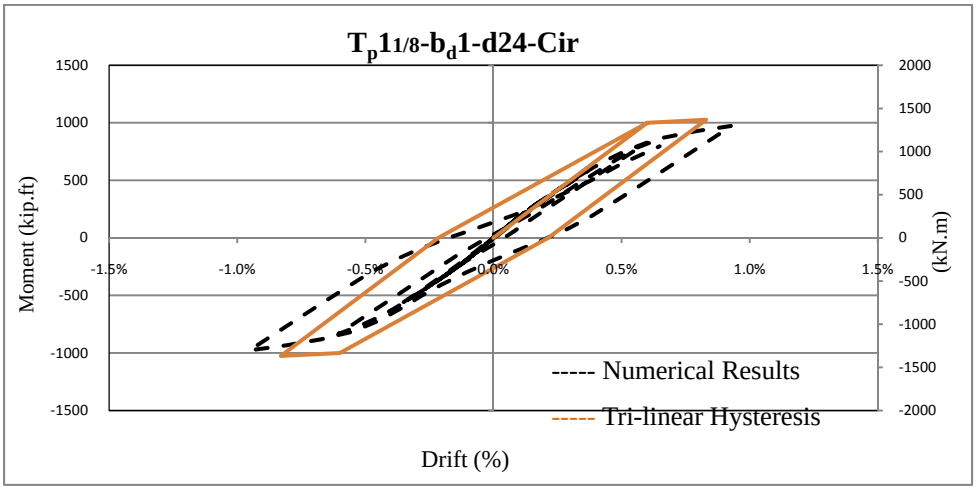

Figure D-51 Comparison Of The Numerical And Simulated Tri-Linear Hysteresis Of The T_p11/8-b_d1-d24-Cir Connection

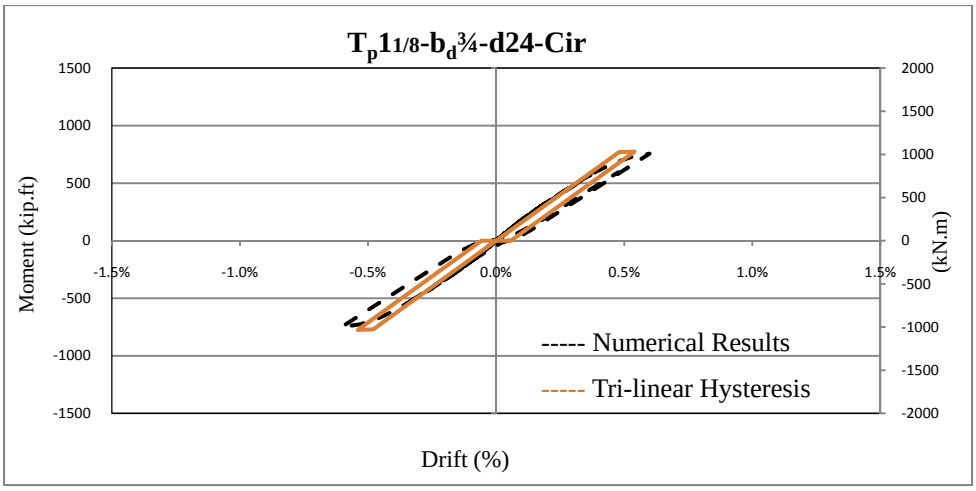

Figure D-52 Comparison Of The Numerical And Simulated Tri-Linear Hysteresis Of The T_p11/8-b_d¾-d24-Cir Connection

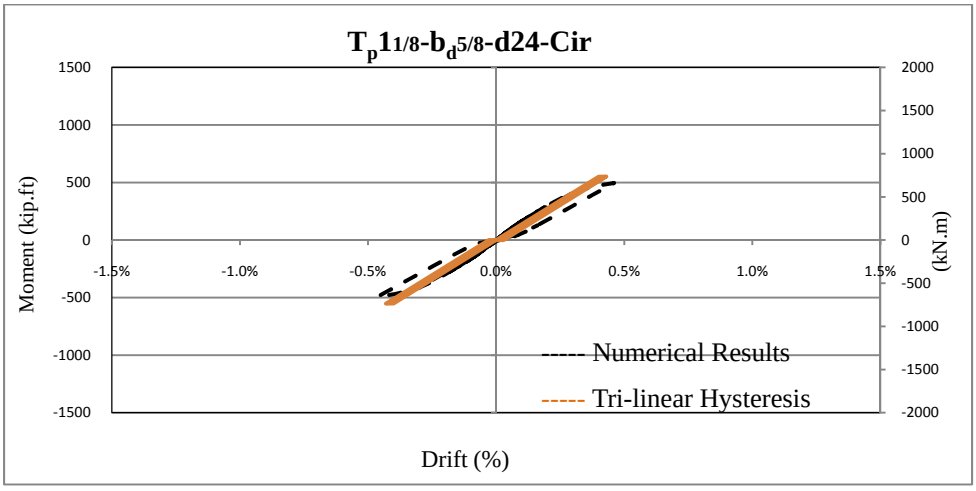

Figure D-53 Comparison Of The Numerical And Simulated Tri-Linear Hysteresis Of The T_p11/8-b_d5/8-d24-Cir Connection

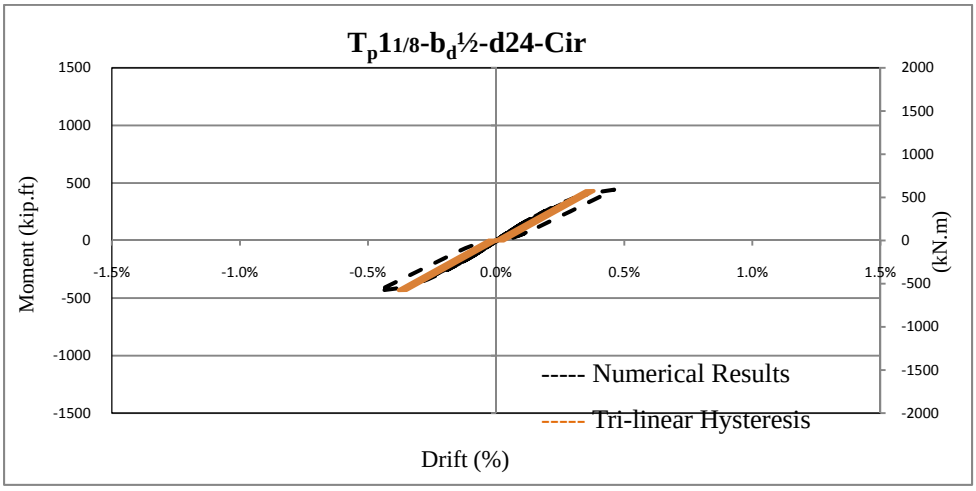

Figure D-54 Comparison Of The Numerical And Simulated Tri-Linear Hysteresis Of The T_p11/8-b_d½-d24-Cir Connection

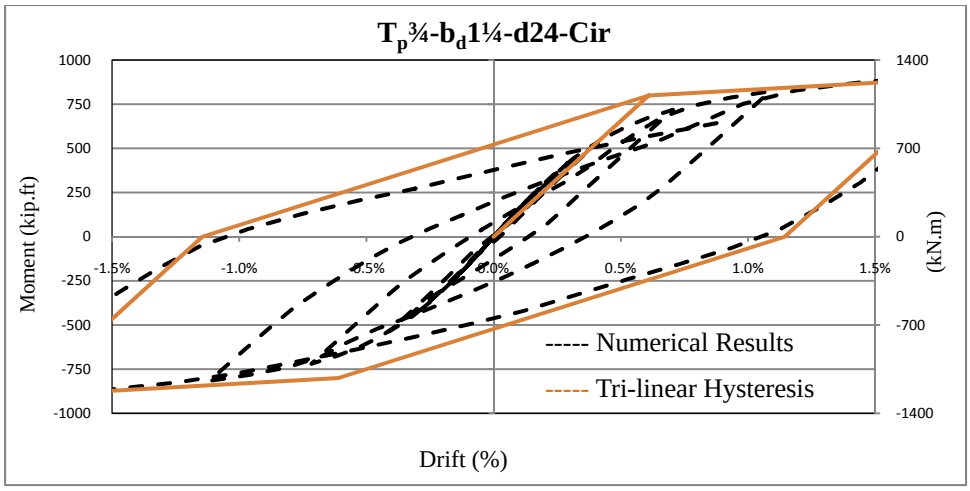

Figure D-55 Comparison Of The Numerical And Simulated Tri-Linear Hysteresis Of The T_p¾-b_d1¼-d24-Cir Connection

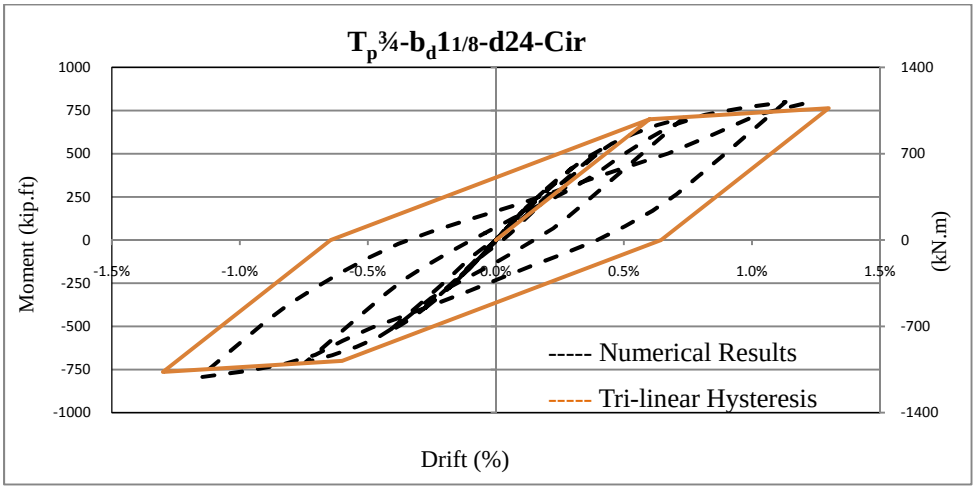

Figure D-56 Comparison Of The Numerical And Simulated Tri-Linear Hysteresis Of The T_p¾-b_d11/8-d24-Cir Connection

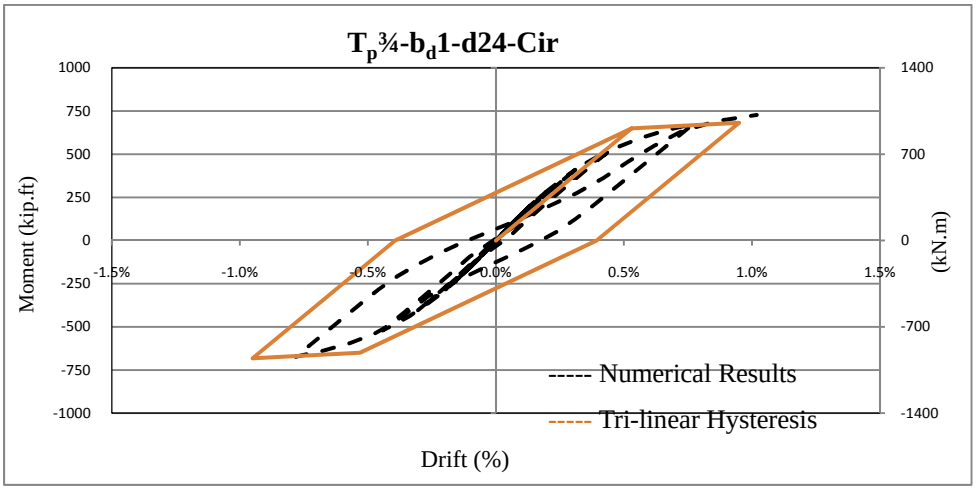

Figure D-57 Comparison Of The Numerical And Simulated Tri-Linear Hysteresis Of The T_p¾-b_d1-d24-Cir Connection

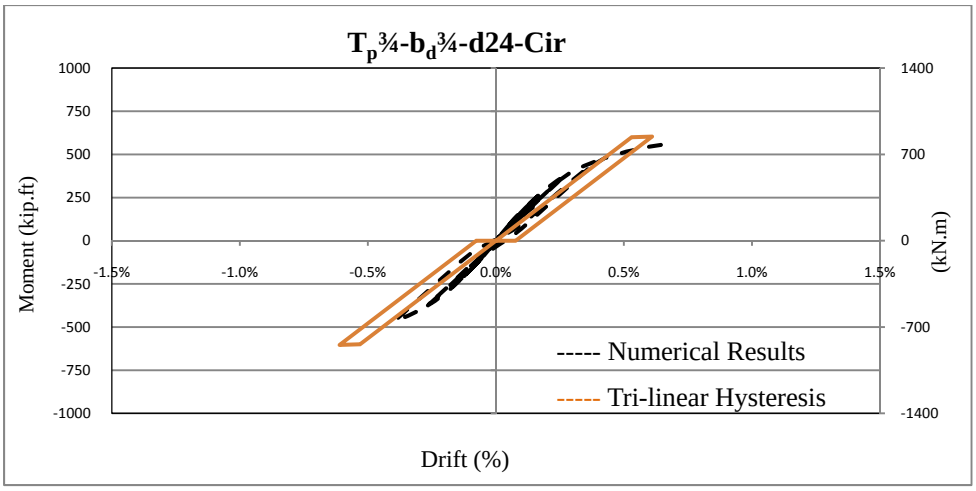

Figure D-58 Comparison Of The Numerical And Simulated Tri-Linear Hysteresis Of The T_p¾-b_d¾-d24-Cir Connection

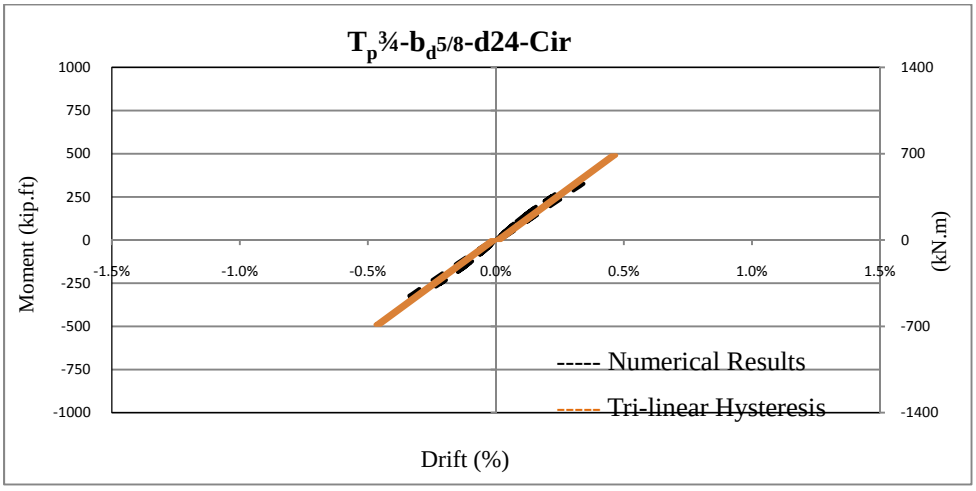

Figure D-59 Comparison Of The Numerical And Simulated Tri-Linear Hysteresis Of The T_p¾-b_d5/8-d24-Cir Connection

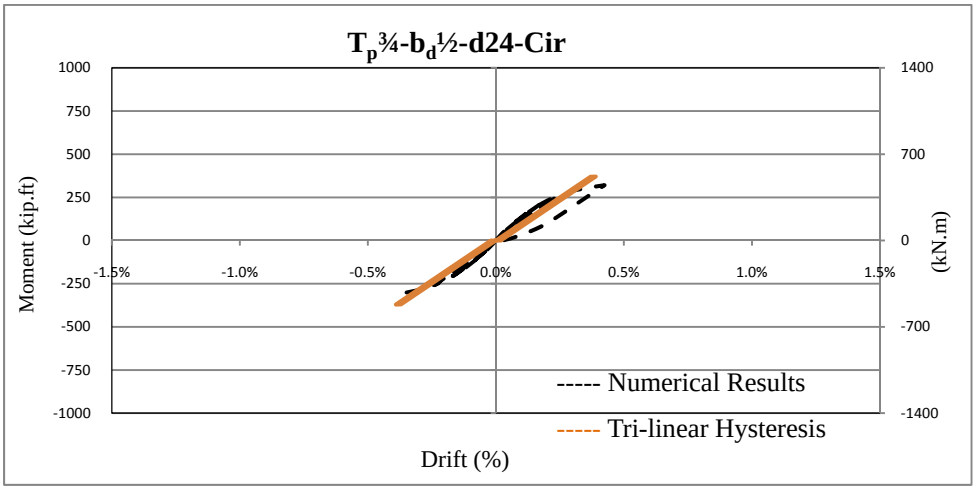

Figure D-60 Comparison Of The Numerical And Simulated Tri-Linear Hysteresis Of The T_p¾-b_d½-d24-Cir Connection

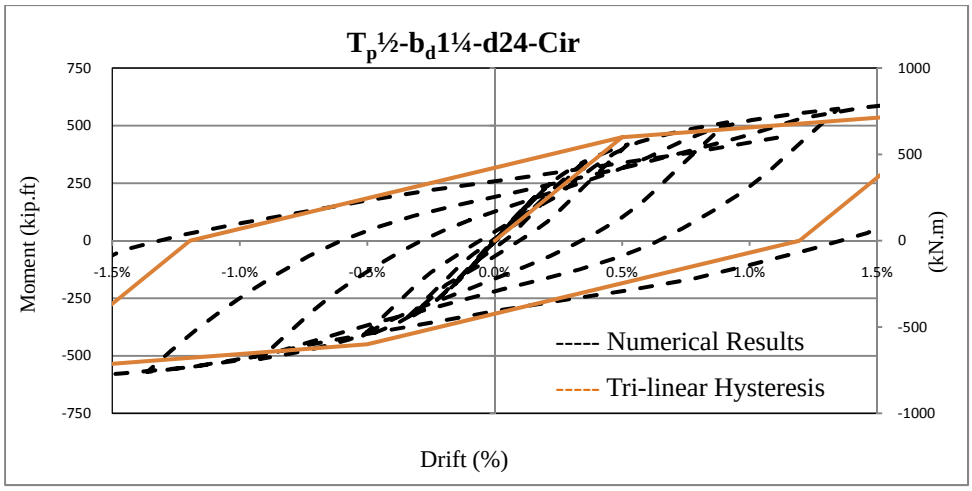

Figure D-61 Comparison Of The Numerical And Simulated Tri-Linear Hysteresis Of The T_p½-b_d1¼-d24-Cir Connection

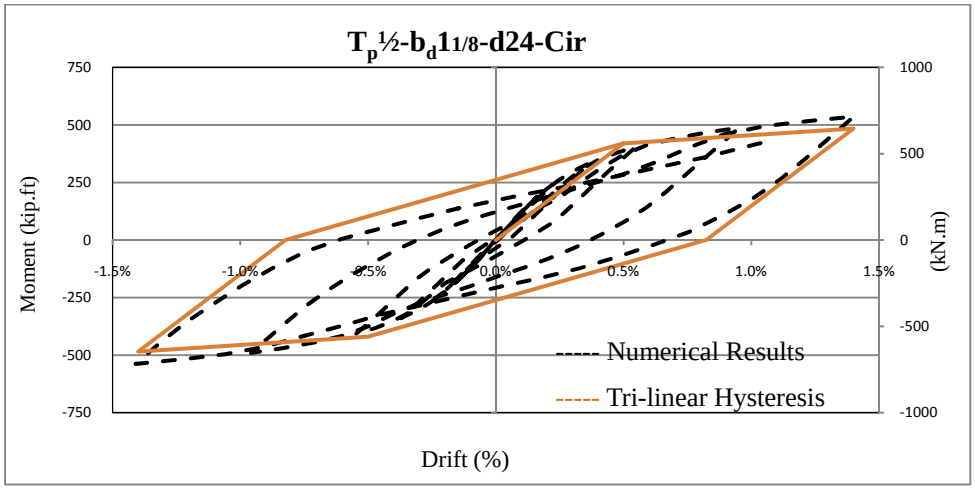

Figure D-62 Comparison Of The Numerical And Simulated Tri-Linear Hysteresis Of The T_p½-b_d11/8-d24-Cir Connection

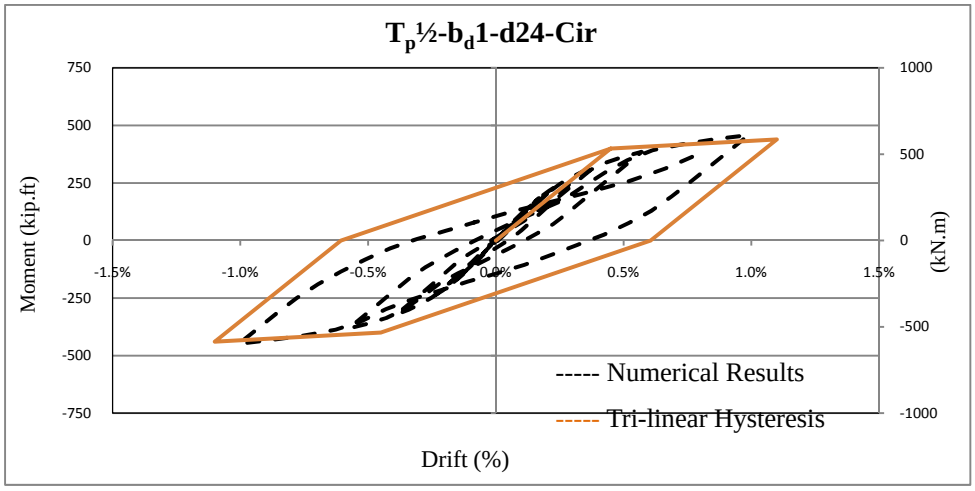

Figure D-63 Comparison Of The Numerical And Simulated Tri-Linear Hysteresis Of The T_p½-b_d1-d24-Cir Connection

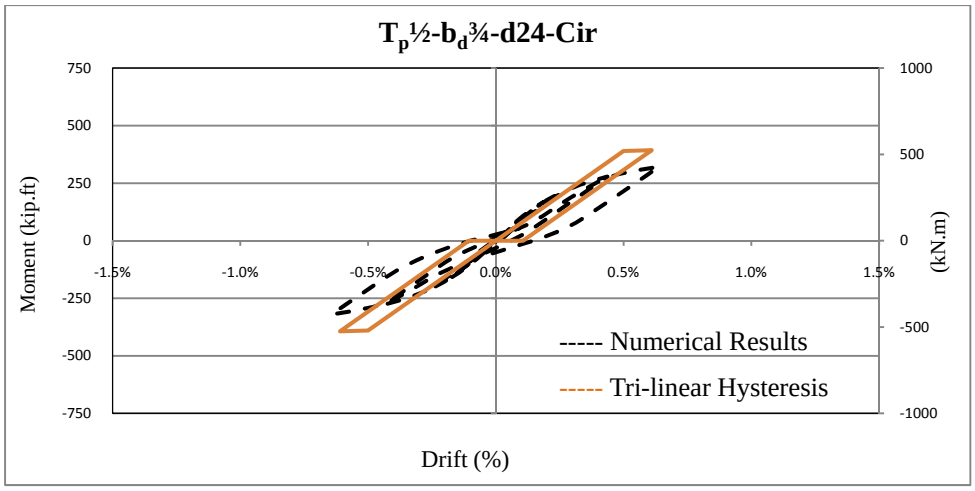

Figure D-64 Comparison Of The Numerical And Simulated Tri-Linear Hysteresis Of The T_p½-b_d¾-d24-Cir Connection

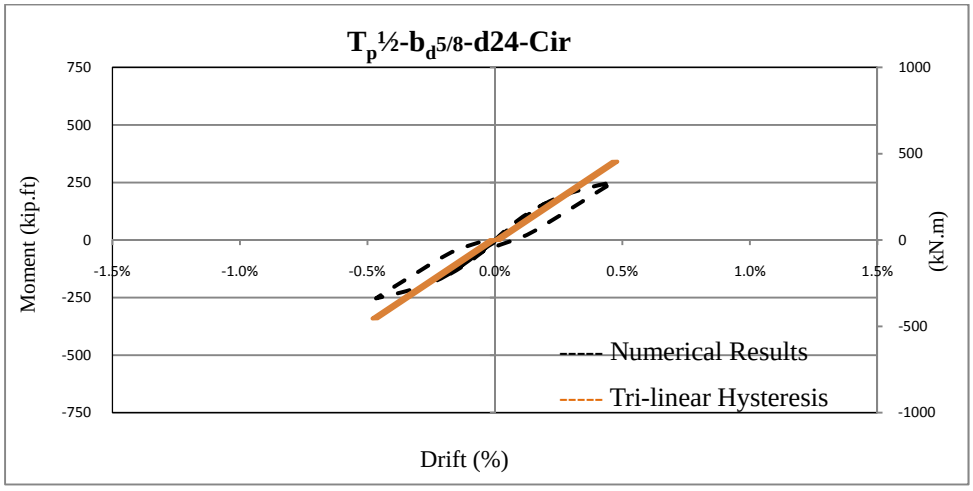

Figure D-65 Comparison Of The Numerical And Simulated Tri-Linear Hysteresis Of The T_p½-b_d5/8-d24-Cir Connection

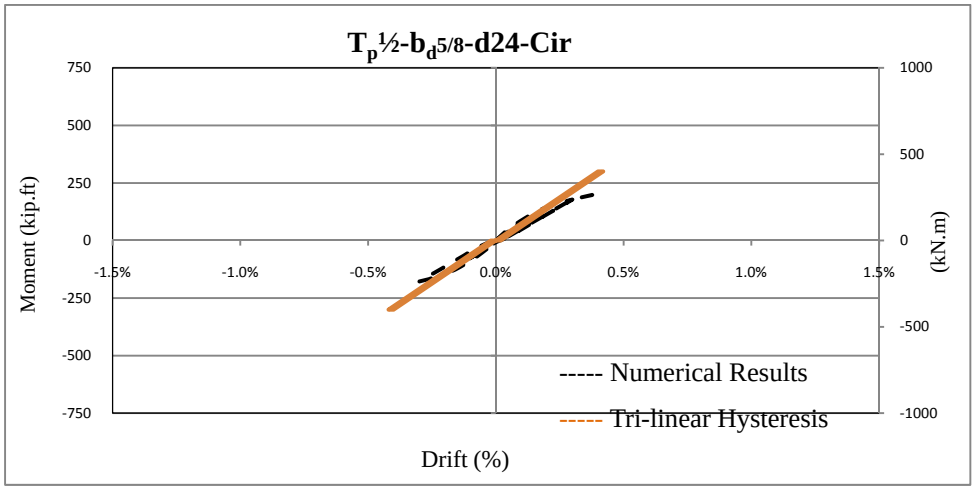

Figure D-66 Comparison Of The Numerical And Simulated Tri-Linear Hysteresis Of The T_p½-b_d5/8-d24-Cir Connection

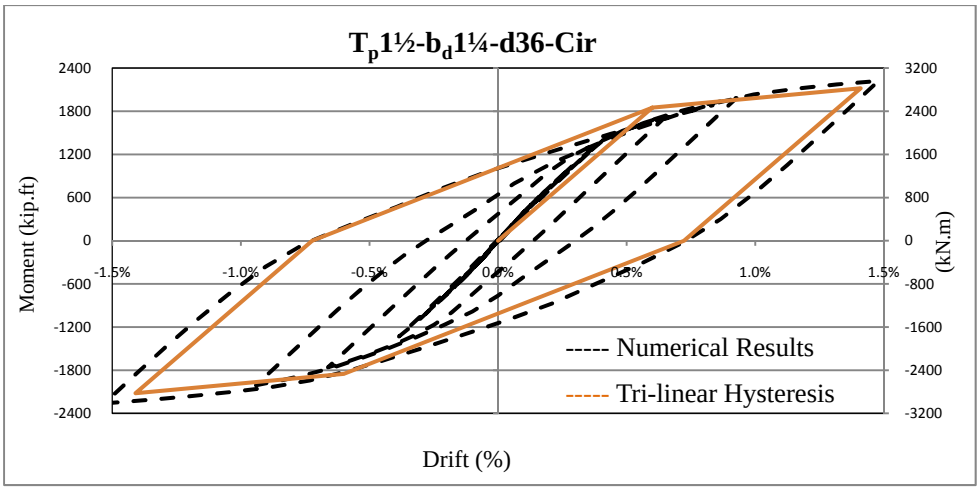

Figure D-67 Comparison Of The Numerical And Simulated Tri-Linear Hysteresis Of The $T_p1½\text{-}b_d1¼$-d36-Cir Connection

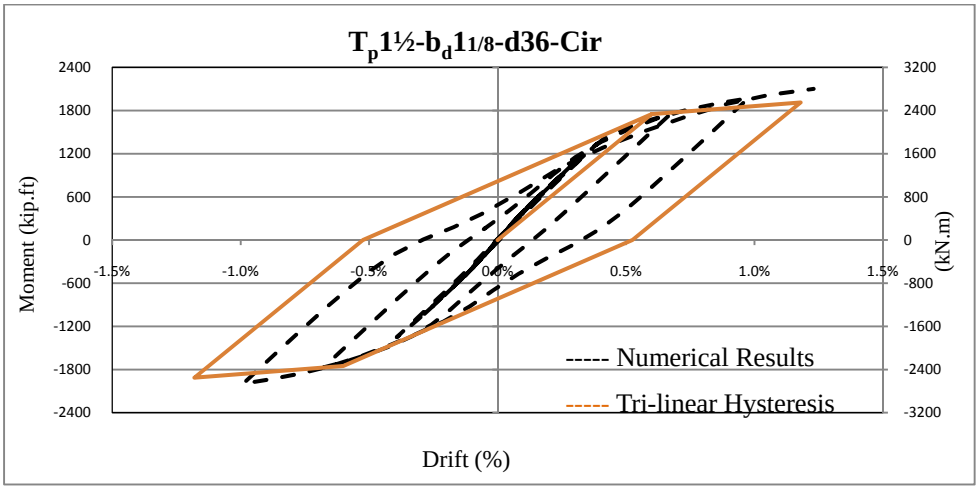

Figure D-68 Comparison Of The Numerical And Simulated Tri-Linear Hysteresis Of The $T_p1½\text{-}b_d11/8$-d36-Cir Connection

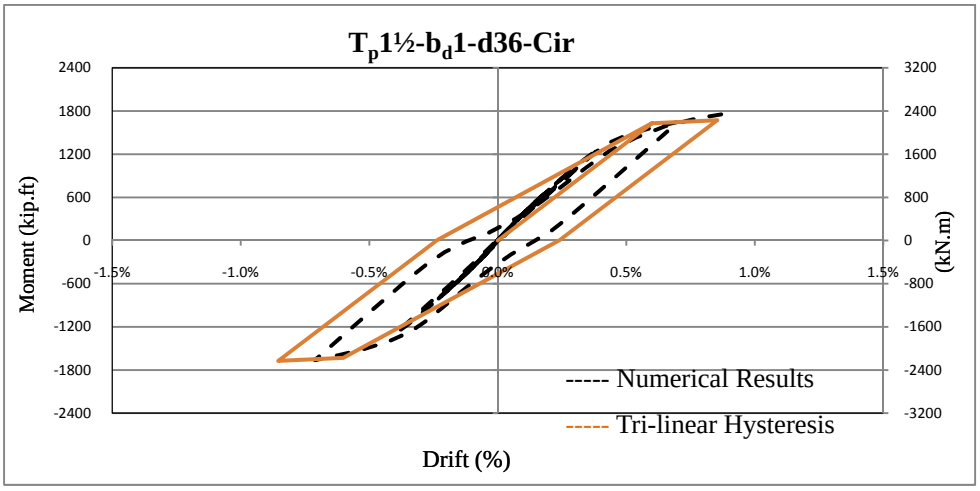

Figure D-69 Comparison Of The Numerical And Simulated Tri-Linear Hysteresis Of The $T_p1½\text{-}b_d1$-d36-Cir Connection

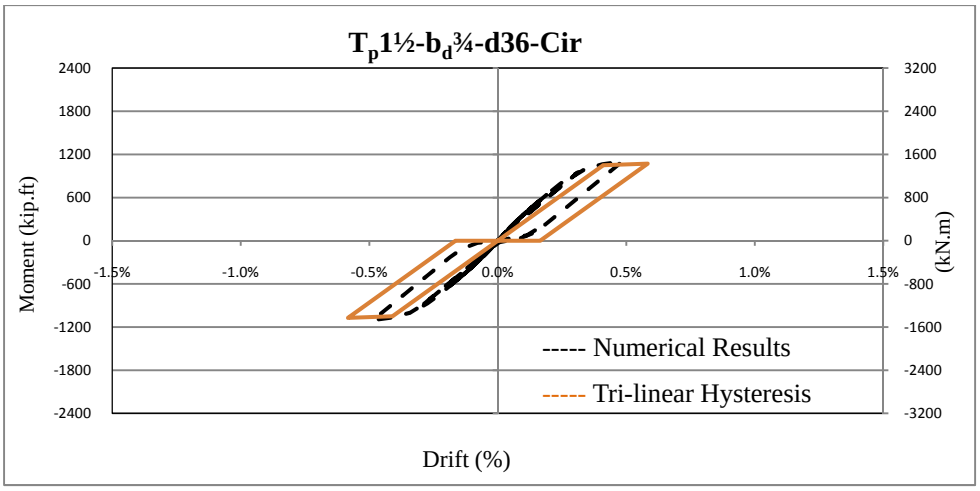

Figure D-70 Comparison Of The Numerical And Simulated Tri-Linear Hysteresis Of The $T_p1½-b_d¾$-d36-Cir Connection

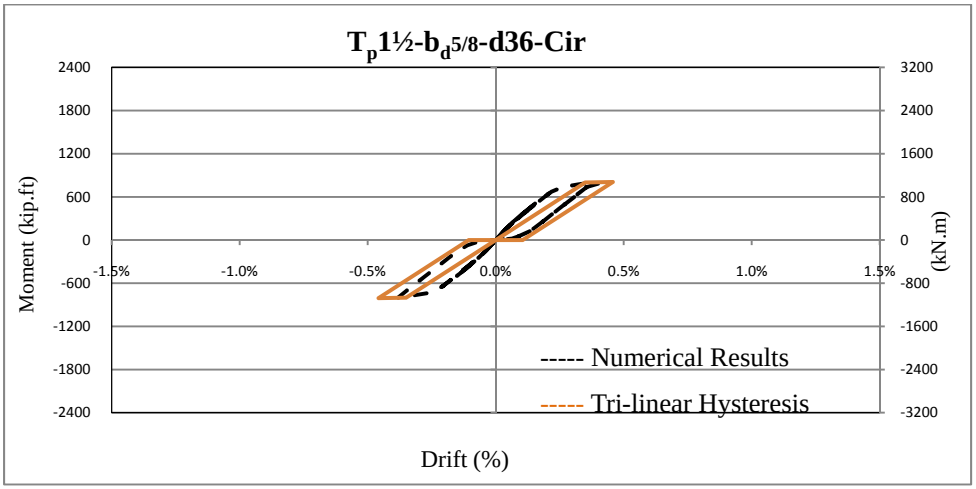

Figure D-71 Comparison Of The Numerical And Simulated Tri-Linear Hysteresis Of The $T_p1½-b_d5/8$-d36-Cir Connection

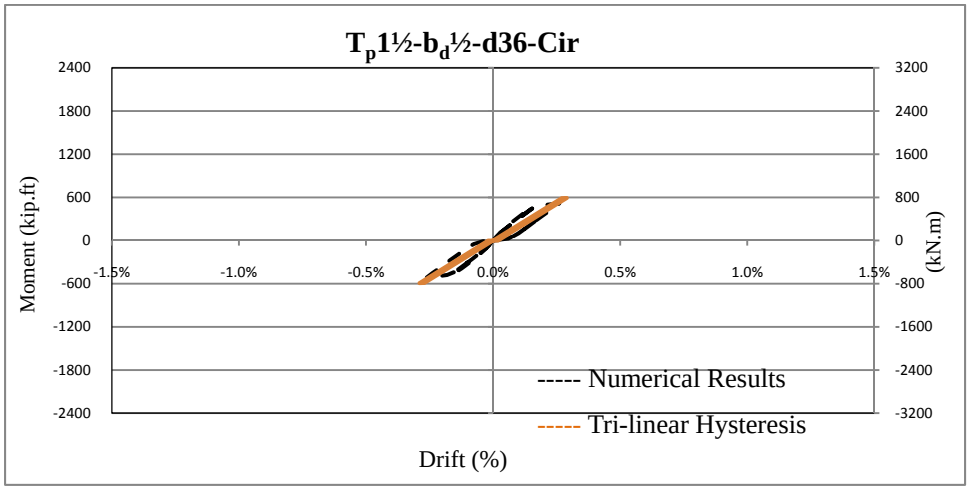

Figure D-72 Comparison Of The Numerical And Simulated Tri-Linear Hysteresis Of The $T_p1½-b_d½$-d36-Cir Connection

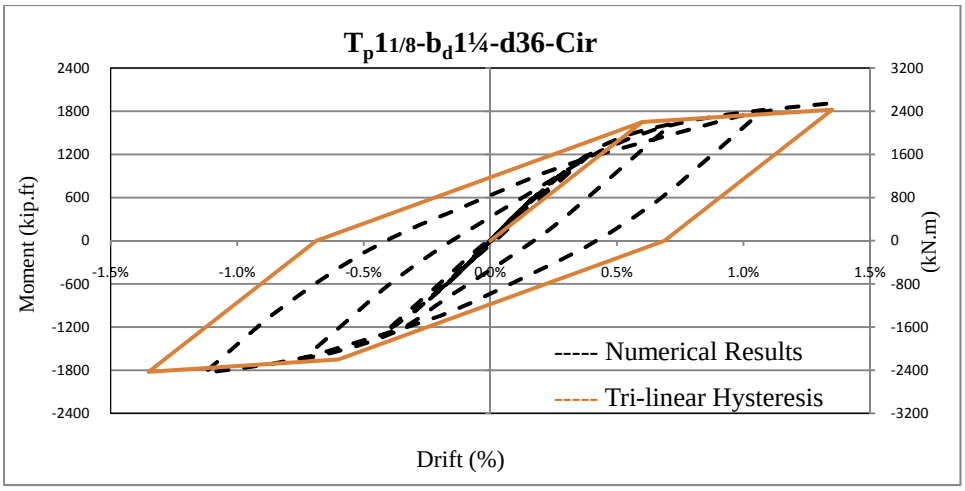

Figure D-73 Comparison Of The Numerical And Simulated Tri-Linear Hysteresis Of The T_p11/8-b_d1¼-d36-Cir Connection

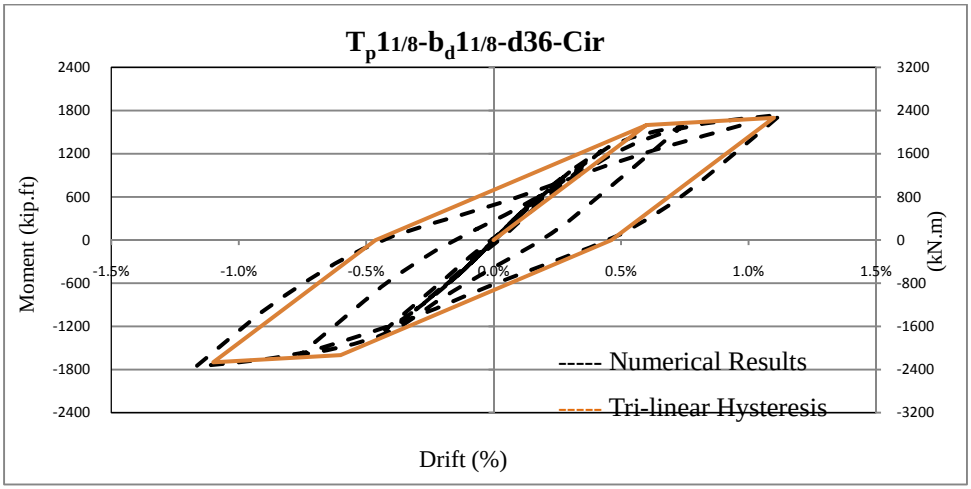

Figure D-74 Comparison Of The Numerical And Simulated Tri-Linear Hysteresis Of The T_p11/8-b_d11/8-d36-Cir Connection

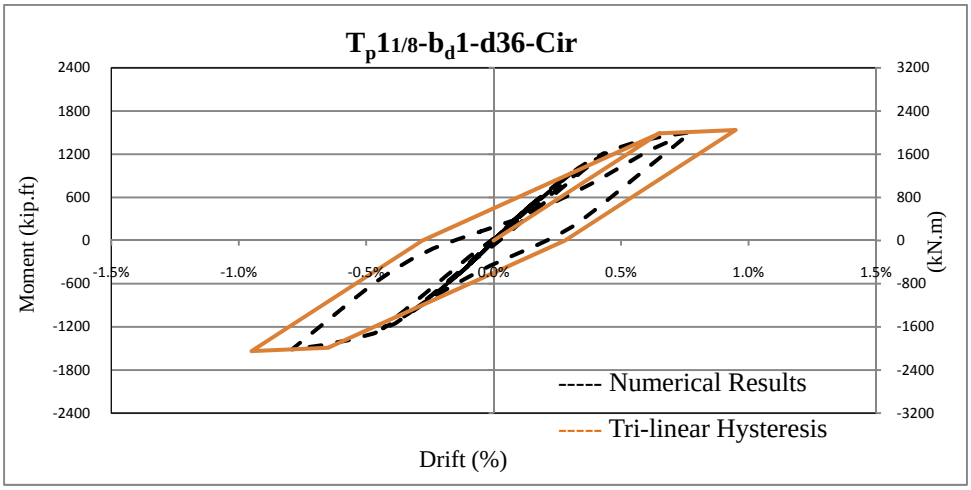

Figure D-75 Comparison Of The Numerical And Simulated Tri-Linear Hysteresis Of The T_p11/8-b_d1-d36-Cir Connection

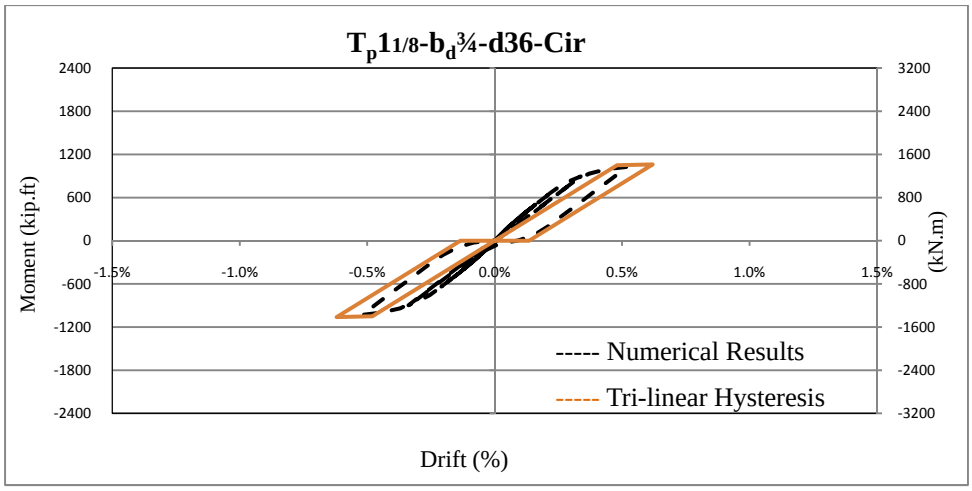

Figure D-76 Comparison Of The Numerical And Simulated Tri-Linear Hysteresis Of The T_p11/8-b_d¾-d36-Cir Connection

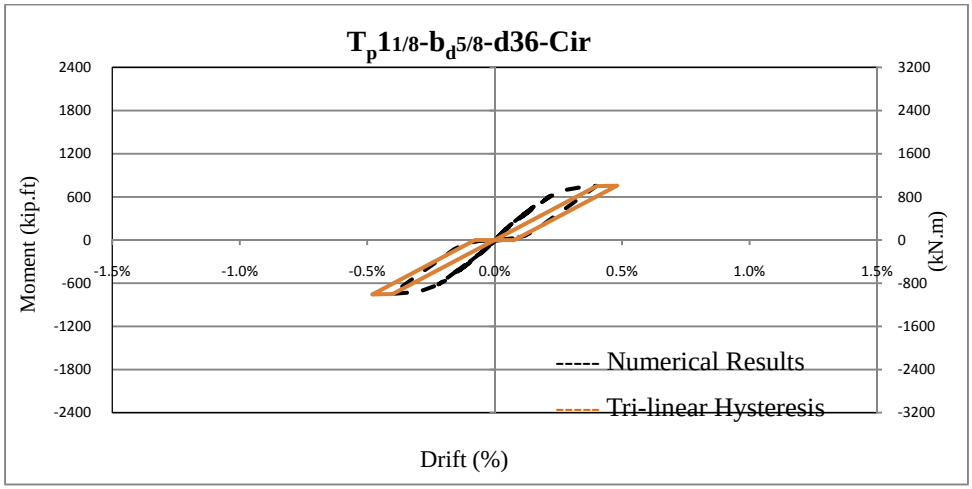

Figure D-77 Comparison Of The Numerical And Simulated Tri-Linear Hysteresis Of The T_p11/8-b_d5/8-d36-Cir Connection

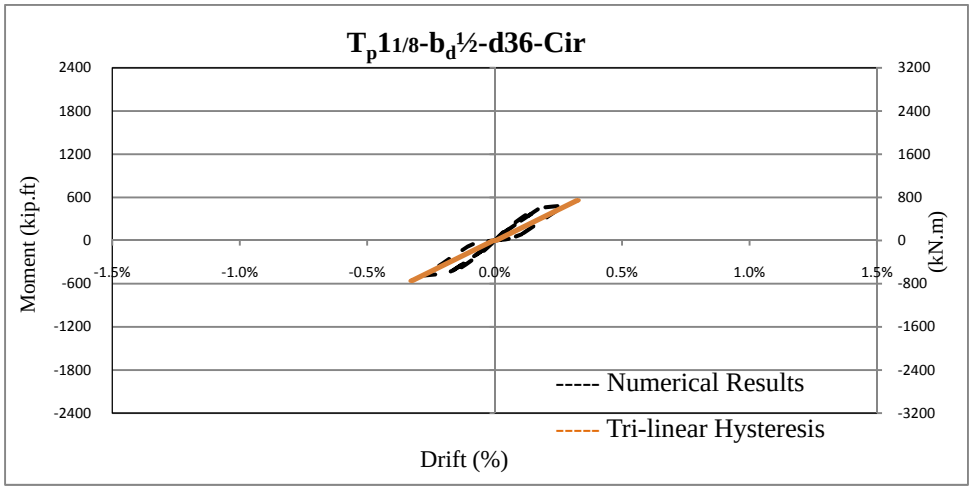

Figure D-78 Comparison Of The Numerical And Simulated Tri-Linear Hysteresis Of The T_p11/8-b_d½-d36-Cir Connection

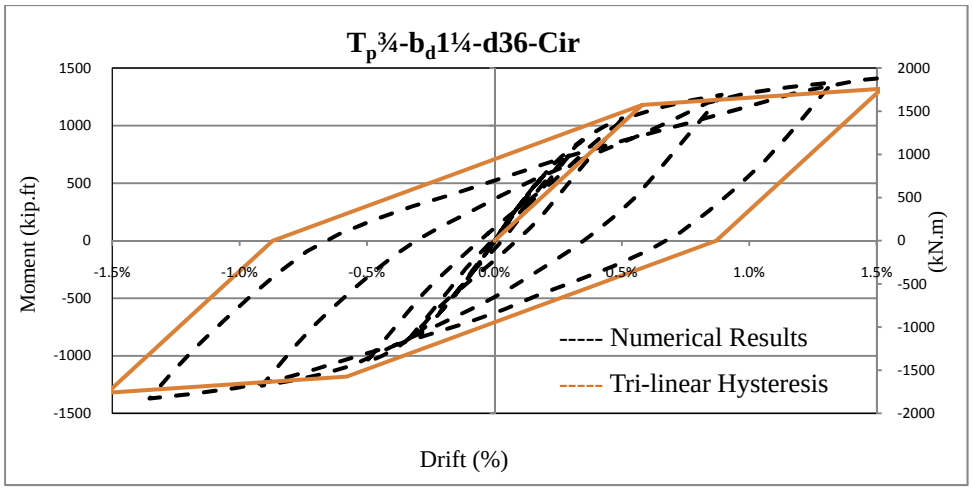

Figure D-79 Comparison Of The Numerical And Simulated Tri-Linear Hysteresis Of The T_p¾-b_d1¼-d36-Cir Connection

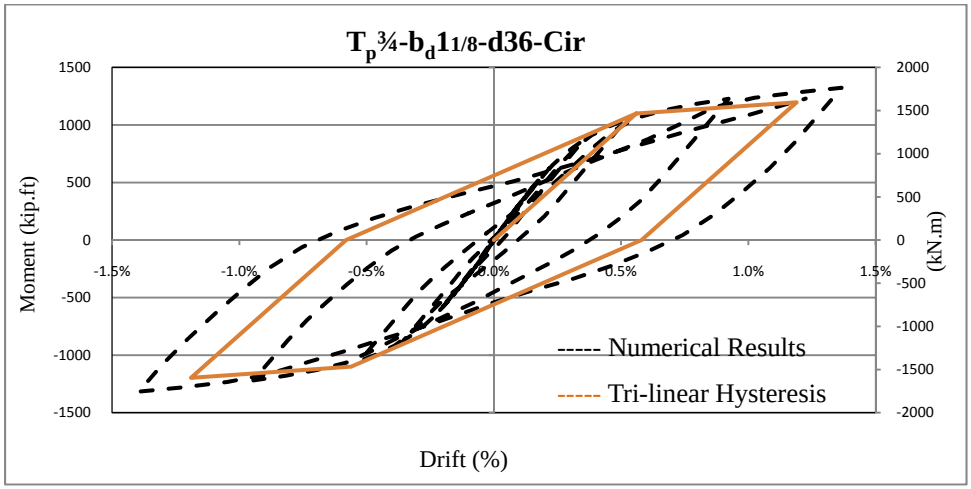

Figure D-80 Comparison Of The Numerical And Simulated Tri-Linear Hysteresis Of The T_p¾-b_d11/8-d36-Cir Connection

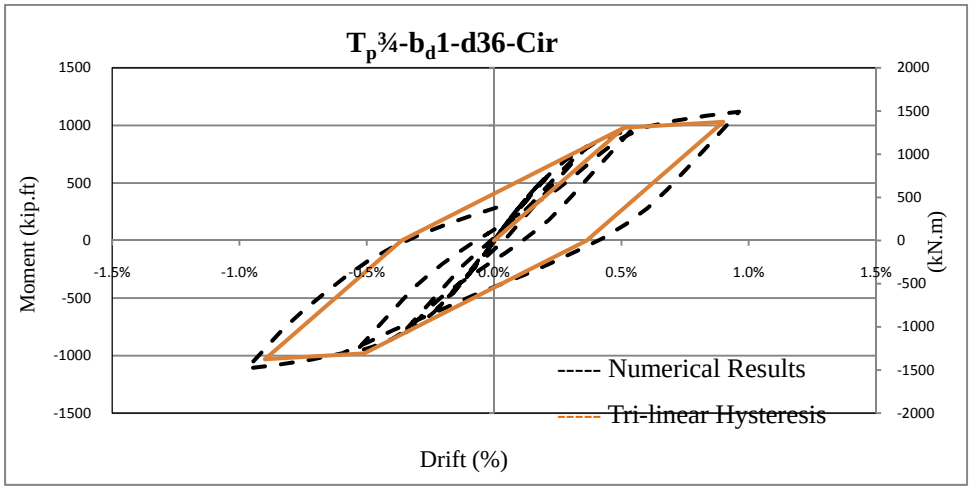

Figure D-81 Comparison Of The Numerical And Simulated Tri-Linear Hysteresis Of The T_p¾-b_d1-d36-Cir Connection

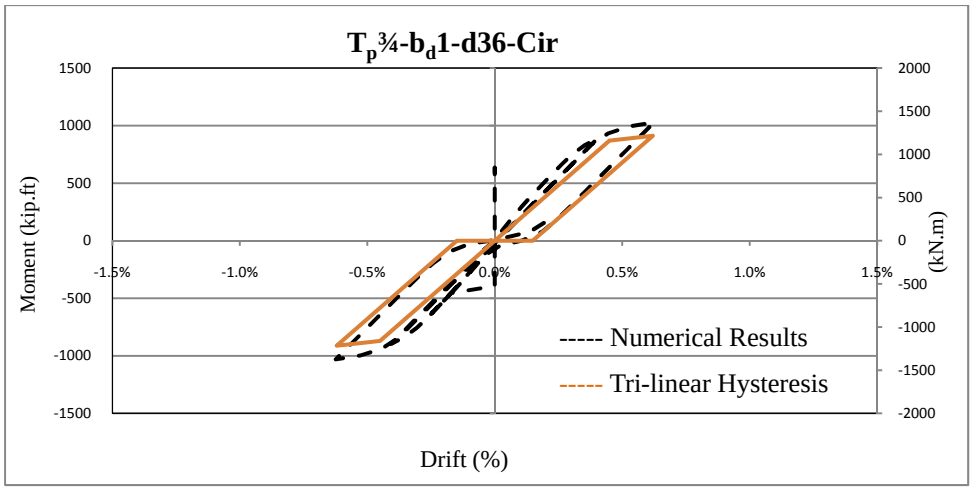

Figure D-82 Comparison Of The Numerical And Simulated Tri-Linear Hysteresis Of The T_p¾-b_d1-d36-Cir Connection

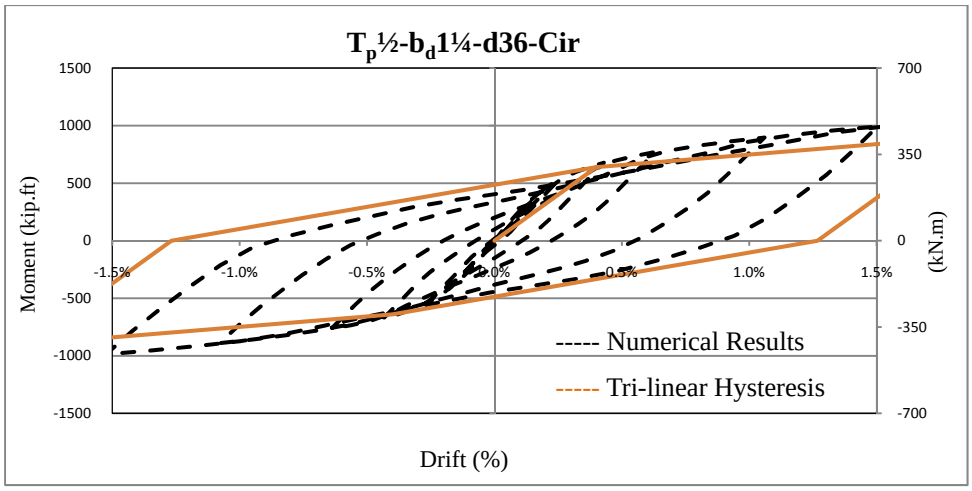

Figure D-83 Comparison Of The Numerical And Simulated Tri-Linear Hysteresis Of The T_p½-b_d1¼-d36-Cir Connection

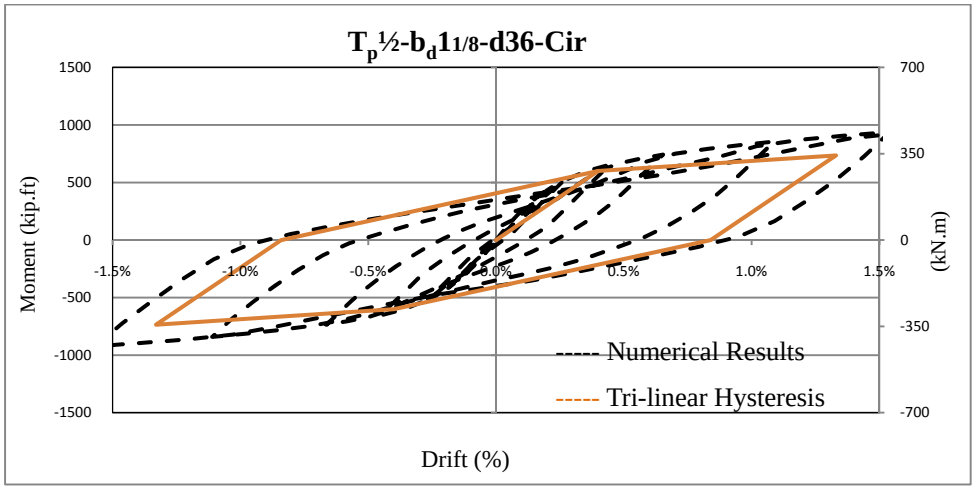

Figure D-84 Comparison Of The Numerical And Simulated Tri-Linear Hysteresis Of The T_p½-b_d11/8-d36-Cir Connection

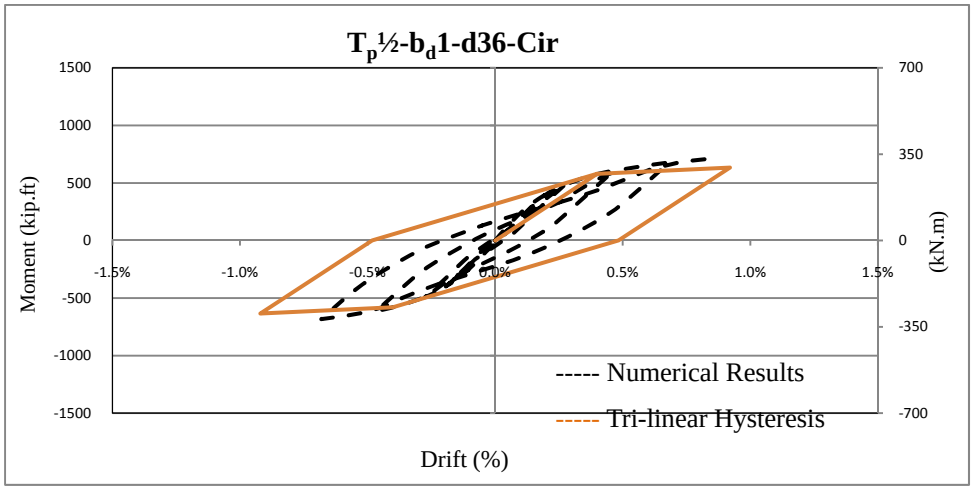

Figure D-85 Comparison Of The Numerical And Simulated Tri-Linear Hysteresis Of The T_p½-b_d1-d36-Cir Connection

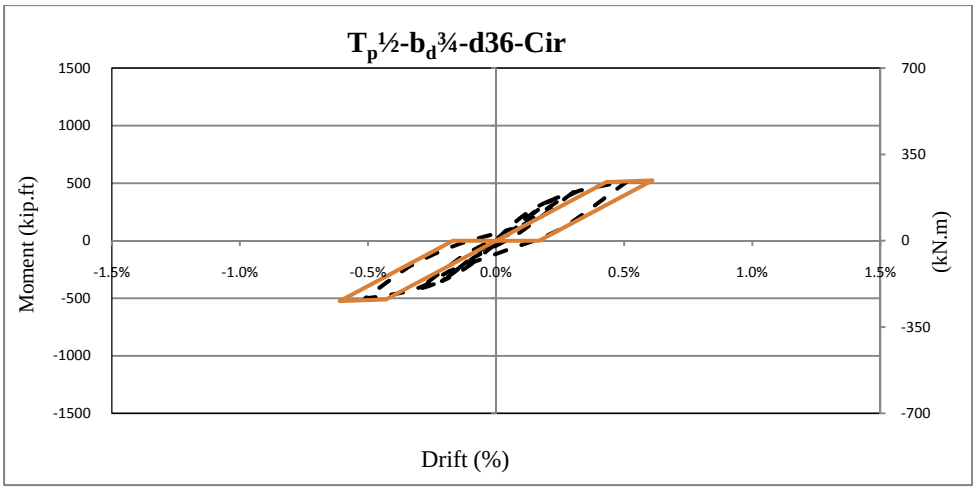

Figure D-86 Comparison Of The Numerical And Simulated Tri-Linear Hysteresis Of The T_p½-b_d¾-d36-Cir Connection

APPENDIX E

COMPARISSON OF THE MODELS WITH CIRCULAR AND SQUARE BOLT PATTERN

The simulated tri-linear hysteresis characteristics of the models with circular and square bolt pattern are presented in pair in this section. Close examination of the results presented reveal that in majority of the cases, using the circular bolt pattern may improve the moment capacity, stiffness, ductility, and eventually the overall energy dissipation of the connection.

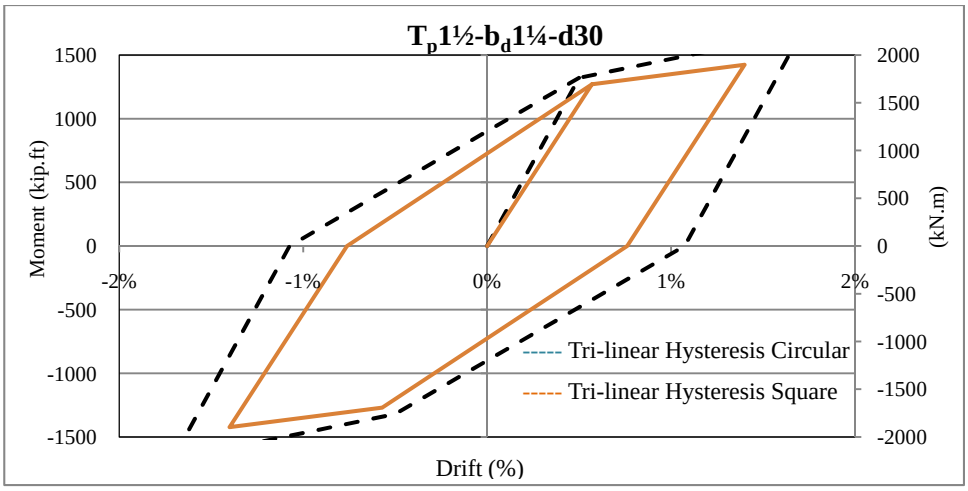

Figure E-1 Comparison Of Tri-Linear Hysteresis Of The Model $T_p1½\text{-}b_d1¼\text{-}d30$ With Circular And Square Bolt Pattern

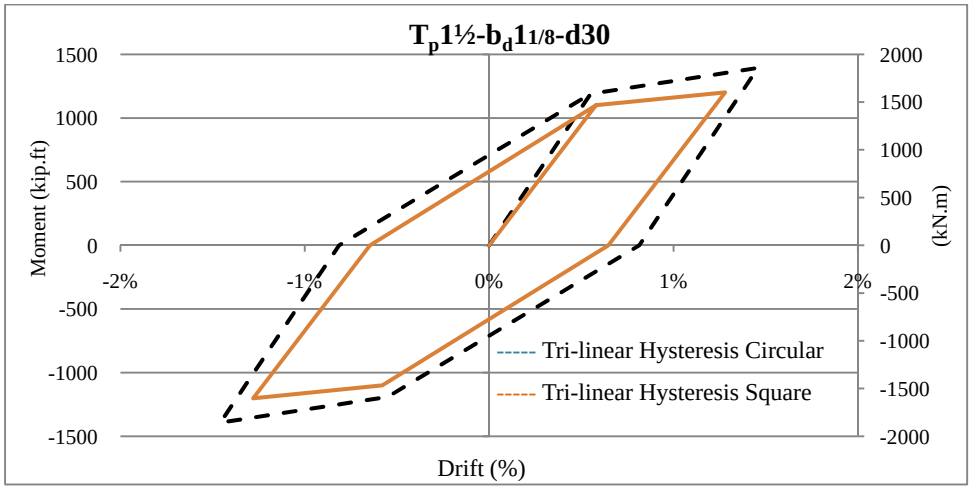

Figure E-2 Comparison Of Tri-Linear Hysteresis Of The Model $T_p1½\text{-}b_d11/8\text{-}d30$ With Circular And Square Bolt Pattern

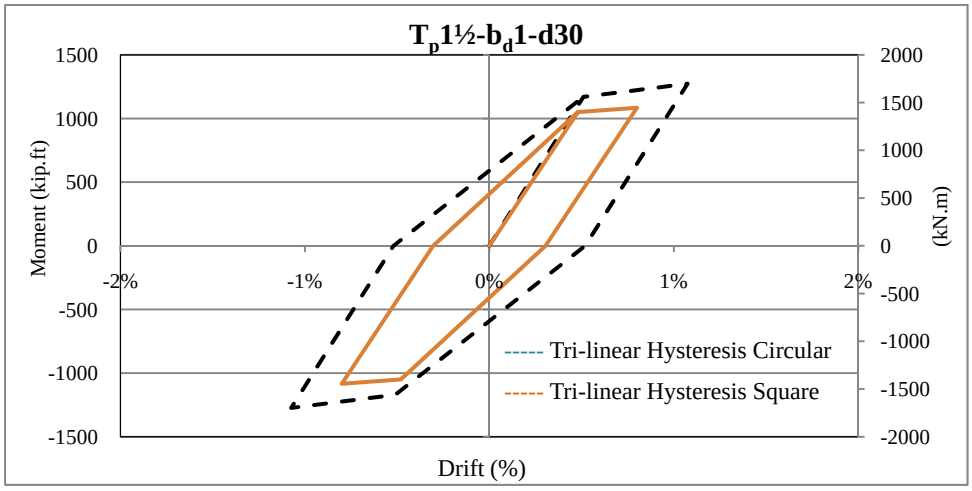

Figure E-3 Comparison Of Tri-Linear Hysteresis Of The Model $T_p1½\text{-}b_d1\text{-}d30$ With Circular And Square Bolt Pattern

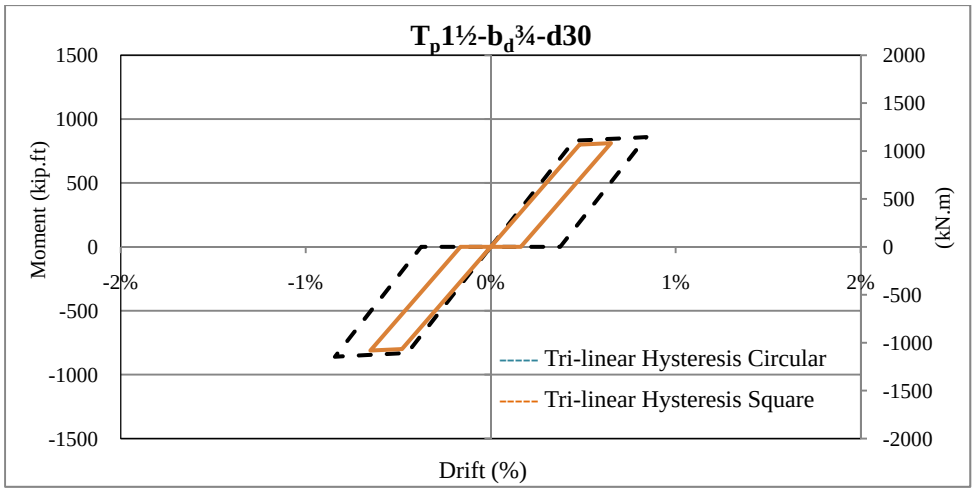

Figure E-4 Comparison Of Tri-Linear Hysteresis Of The Model $T_p1½\text{-}b_d¾\text{-}d30$ With Circular And Square Bolt Pattern

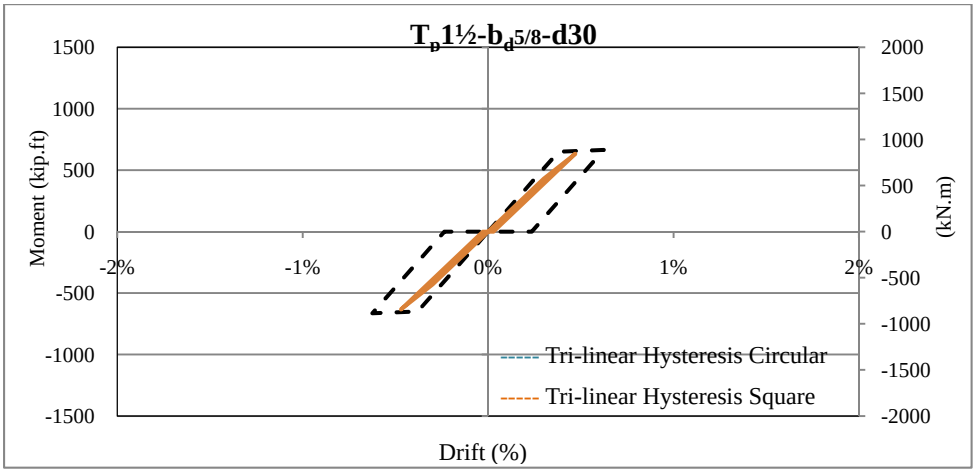

Figure E-5 Comparison Of Tri-Linear Hysteresis Of The Model $T_p1½\text{-}b_d5/8\text{-}d30$ With Circular And Square Bolt Pattern

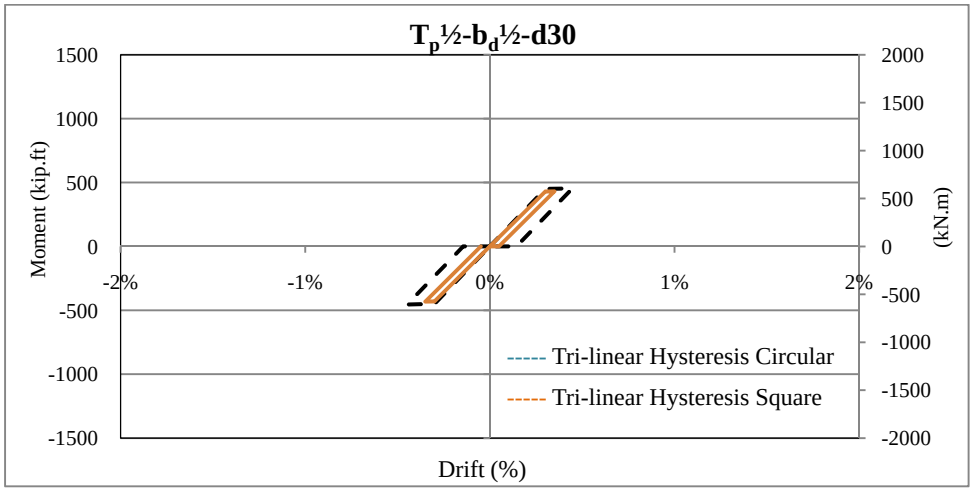

Figure E-6 Comparison Of Tri-Linear Hysteresis Of The Model $T_p½\text{-}b_d½\text{-}d30$ With Circular And Square Bolt Pattern

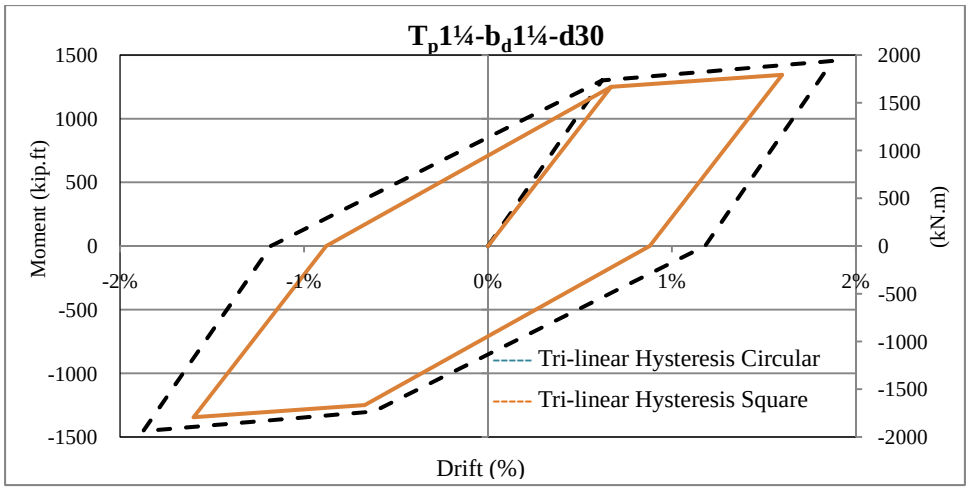

Figure E-7 Comparison Of Tri-Linear Hysteresis Of The Model $T_p1¼\text{-}b_d1¼\text{-}d30$ With Circular And Square Bolt Pattern

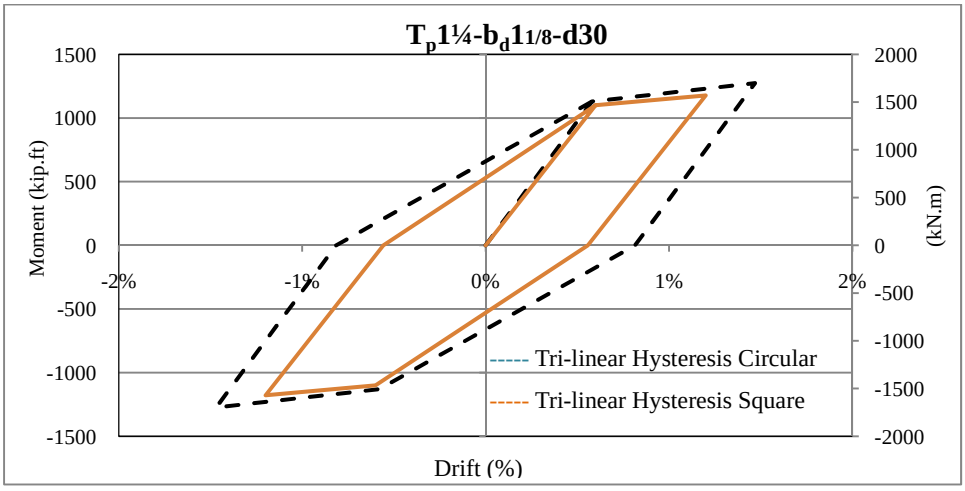

Figure E-8 Comparison Of Tri-Linear Hysteresis Of The Model $T_p1¼\text{-}b_d11/8\text{-}d30$ With Circular And Square Bolt Pattern

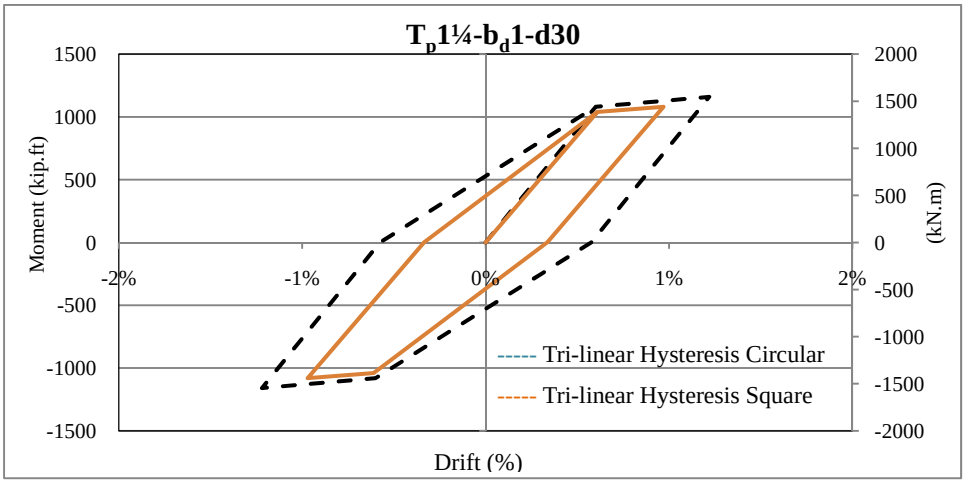

Figure E-9 Comparison Of Tri-Linear Hysteresis Of The Model Tp1¼-bd1-d30 With Circular And Square Bolt Pattern

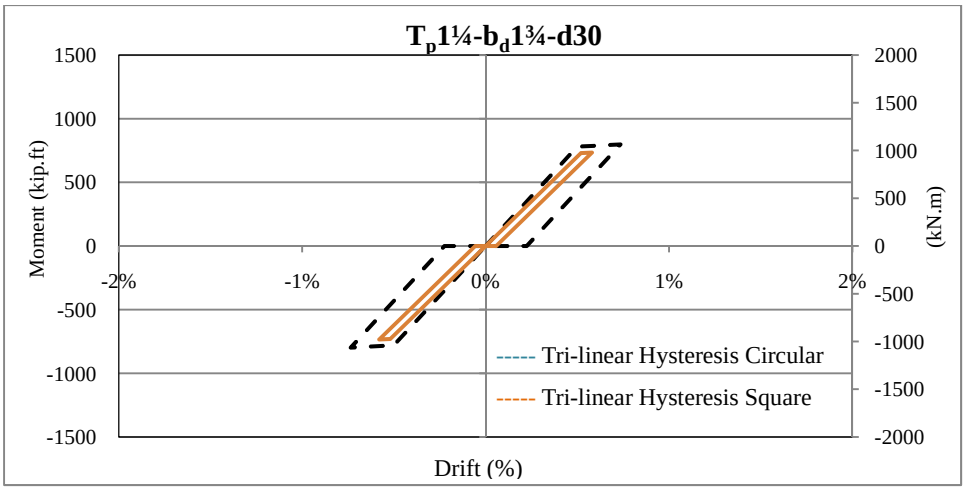

Figure E-10 Comparison Of Tri-Linear Hysteresis Of The Model $T_p1¼\text{-}b_d1¾\text{-}d30$ With Circular And Square Bolt Pattern

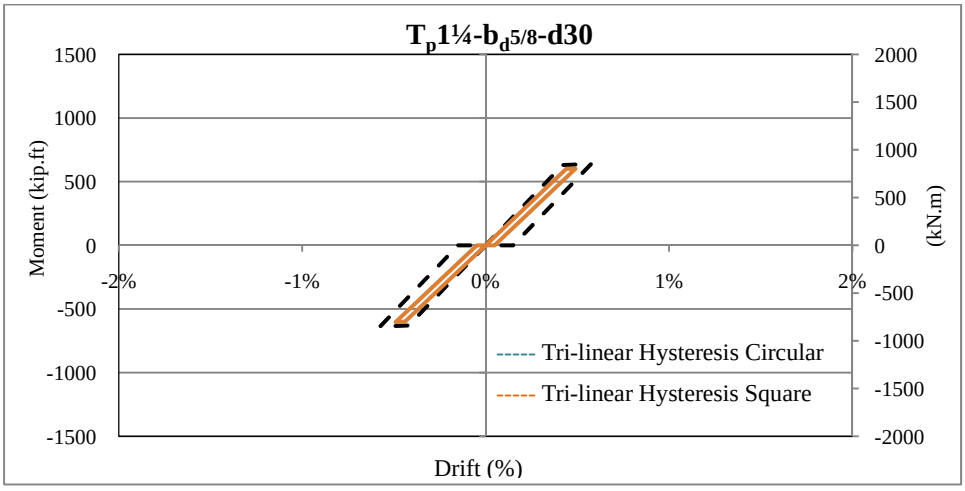

Figure E-11 Comparison Of Tri-Linear Hysteresis Of The Model $T_p1¼\text{-}b_d5/8\text{-}d30$ With Circular And Square Bolt Pattern

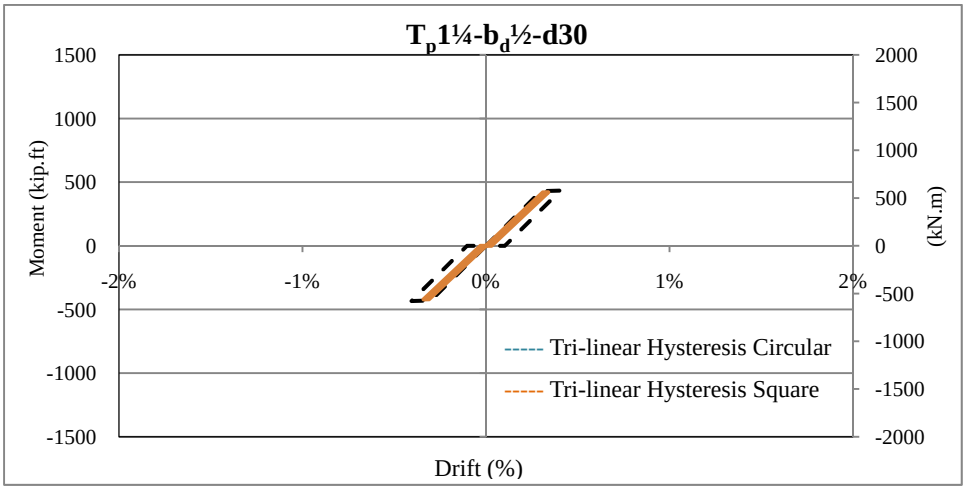

Figure E-12 Comparison Of Tri-Linear Hysteresis Of The Model $T_p1¼\text{-}b_d½\text{-}d30$ With Circular And Square Bolt Pattern

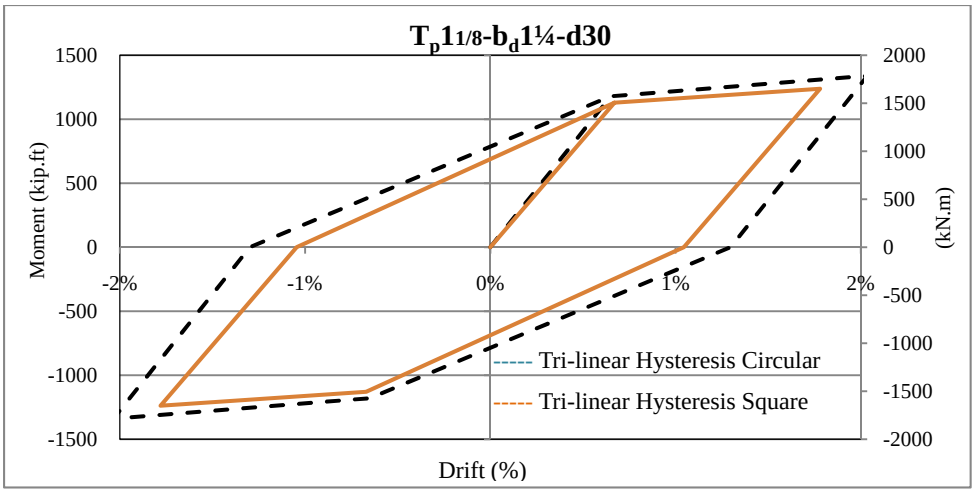

Figure E-13 Comparison Of Tri-Linear Hysteresis Of The Model $T_p11/8$-$b_d1¼$-d30 With Circular And Square Bolt Pattern

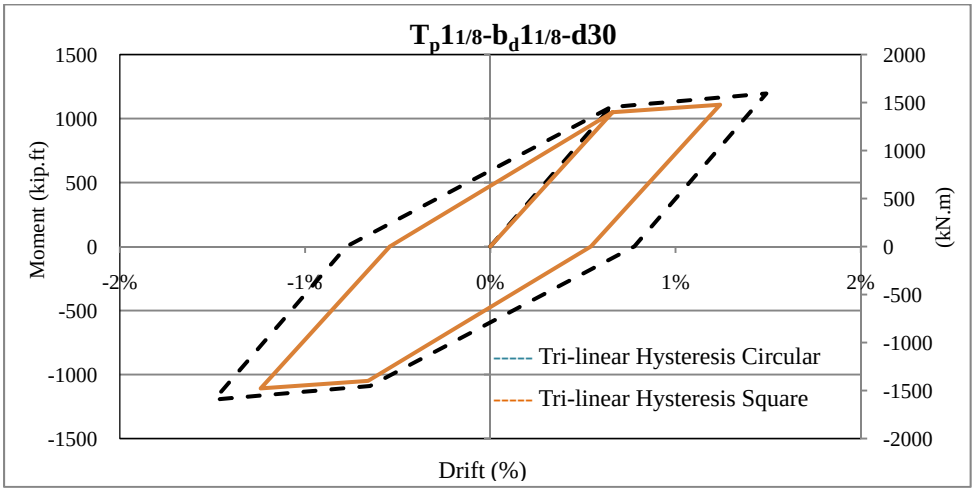

Figure E-14 Comparison Of Tri-Linear Hysteresis Of The Model $T_p11/8$-$b_d11/8$-d30 With Circular And Square Bolt Pattern

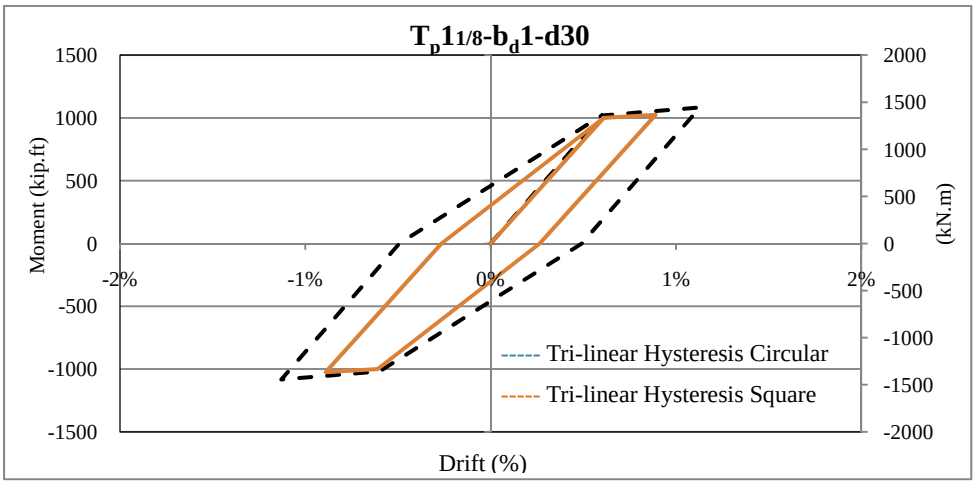

Figure E-15 Comparison Of Tri-Linear Hysteresis Of The Model $T_p11/8$-b_d1-d30 With Circular And Square Bolt Pattern

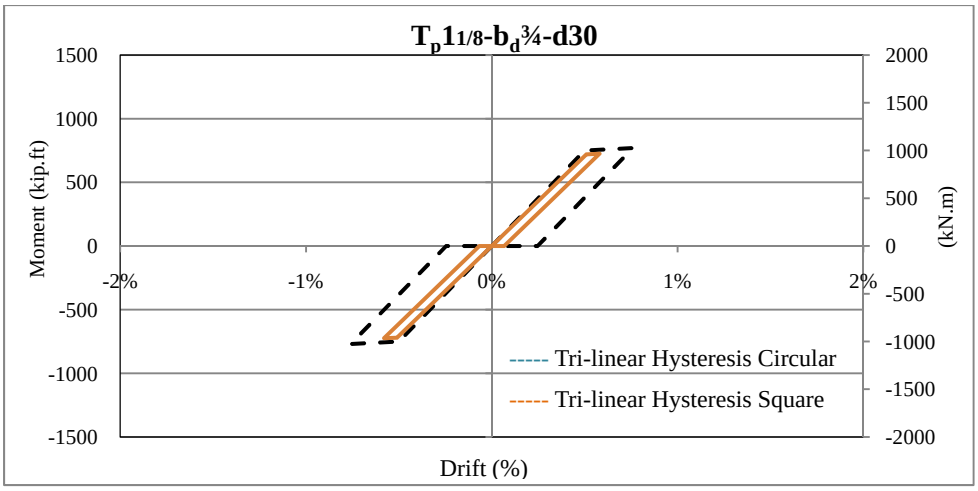

Figure E-16 Comparison Of Tri-Linear Hysteresis Of The Model T_p11/8-b_d¾-d30 With Circular And Square Bolt Pattern

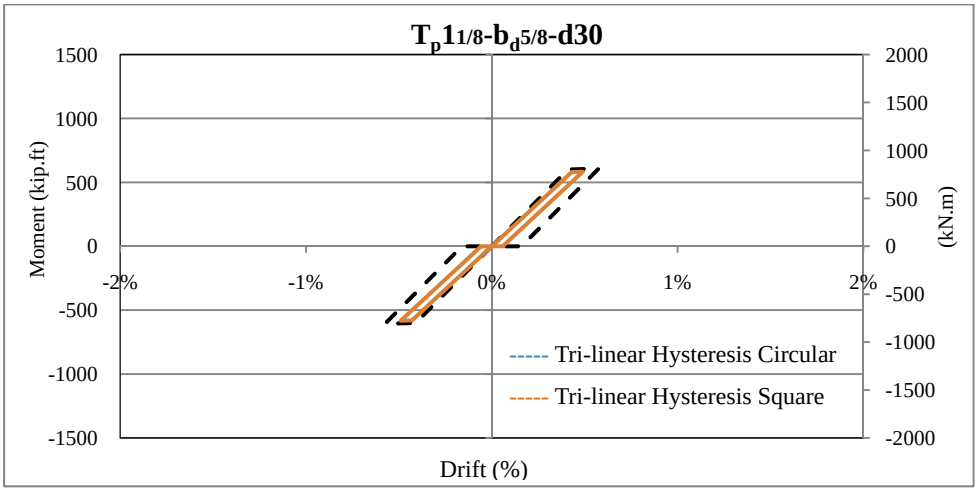

Figure E-17 Comparison Of Tri-Linear Hysteresis Of The Model T_p11/8-b_d5/8-d30 With Circular And Square Bolt Pattern

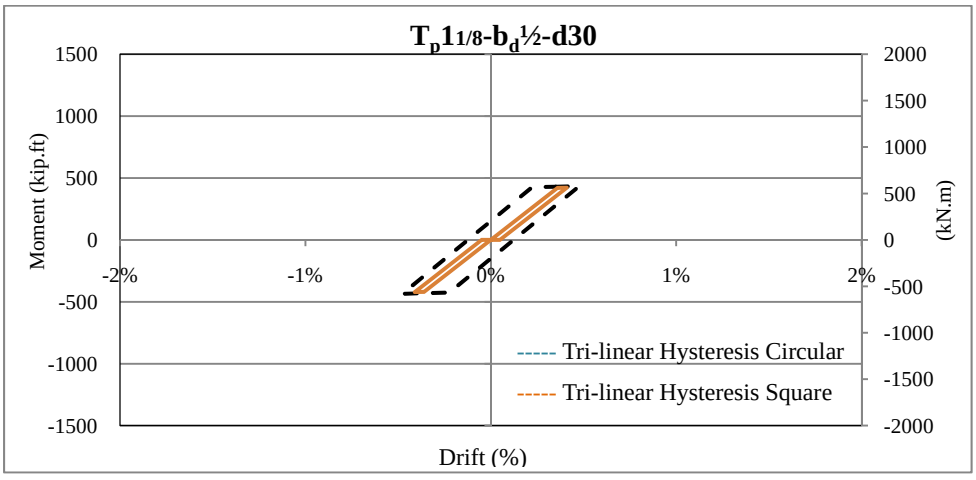

Figure E-18 Comparison Of Tri-Linear Hysteresis Of The Model T_p11/8-b_d½-d30 With Circular And Square Bolt Pattern

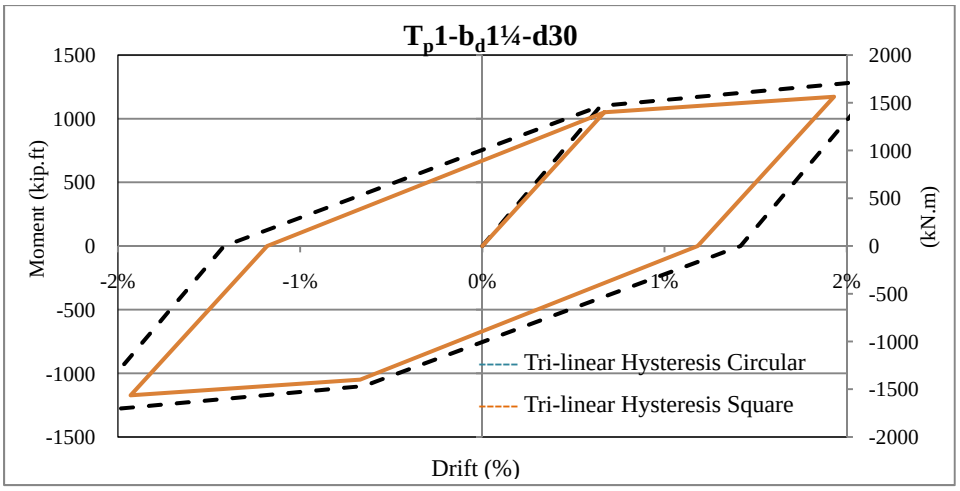

Figure E-19 Comparison Of Tri-Linear Hysteresis Of The Model T_p1-$b_d1¼$-d30 With Circular And Square Bolt Pattern

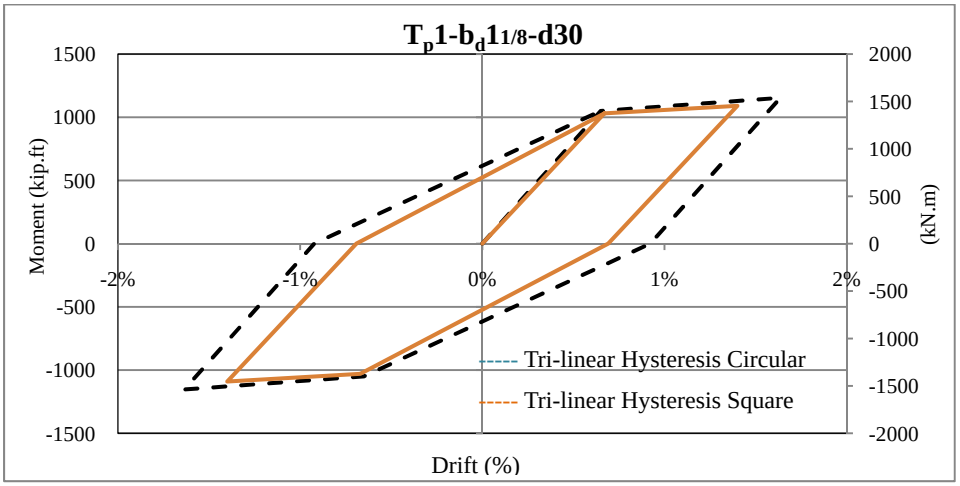

Figure E-20 Comparison Of Tri-Linear Hysteresis Of The Model T_p1-$b_d11/8$-d30 With Circular And Square Bolt Pattern

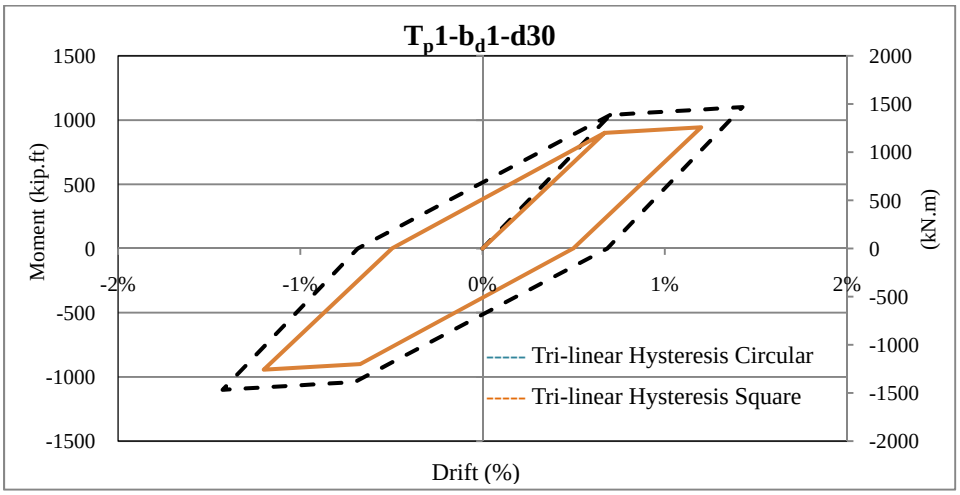

Figure E-21 Comparison Of Tri-Linear Hysteresis Of The Model T_p1-b_d1-d30 With Circular And Square Bolt Pattern

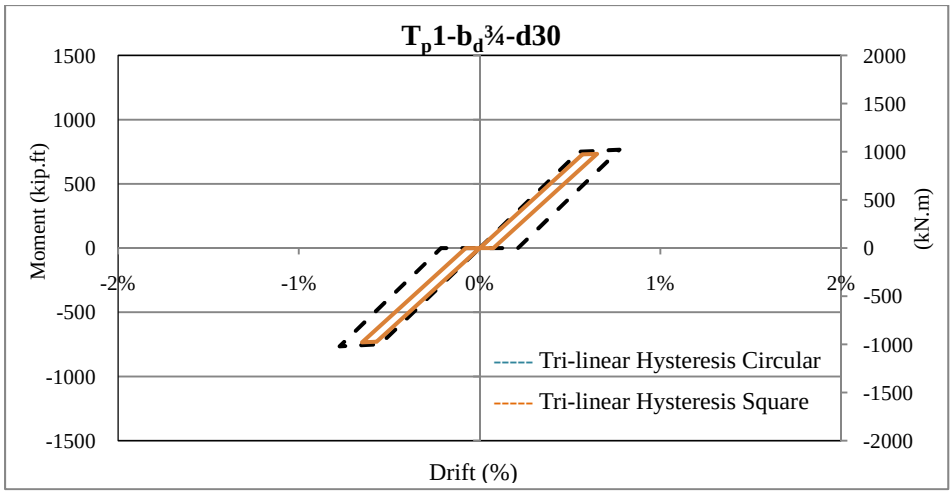

Figure E-22 Comparison Of Tri-Linear Hysteresis Of The Model T_p1-b_d¾-d30 With Circular And Square Bolt Pattern

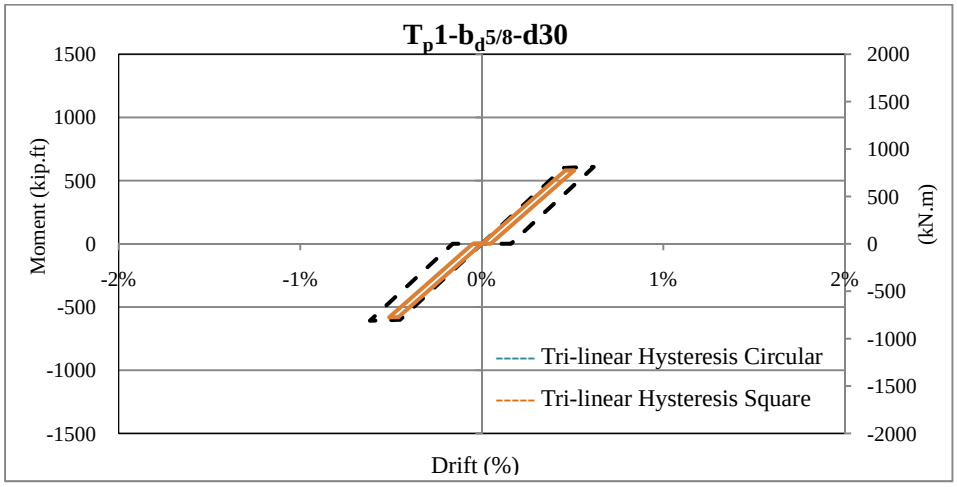

Figure E-23 Comparison Of Tri-Linear Hysteresis Of The Model T_p1-b_d5/8-d30 With Circular And Square Bolt Pattern

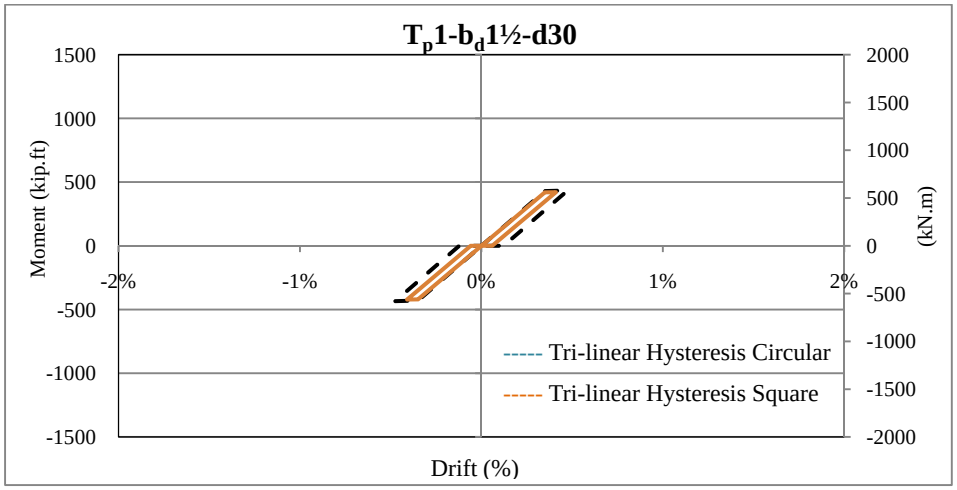

Figure E-24 Comparison Of Tri-Linear Hysteresis Of The Model T_p1-b_d1½-d30 With Circular And Square Bolt Pattern

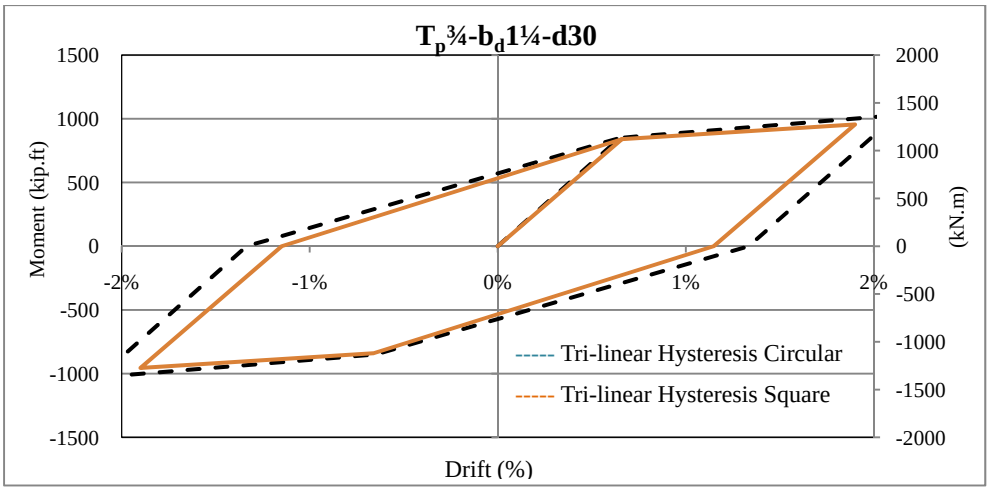

Figure E-25 Comparison Of Tri-Linear Hysteresis Of The Model T_p¾-b_d1¼-d30 With Circular And Square Bolt Pattern

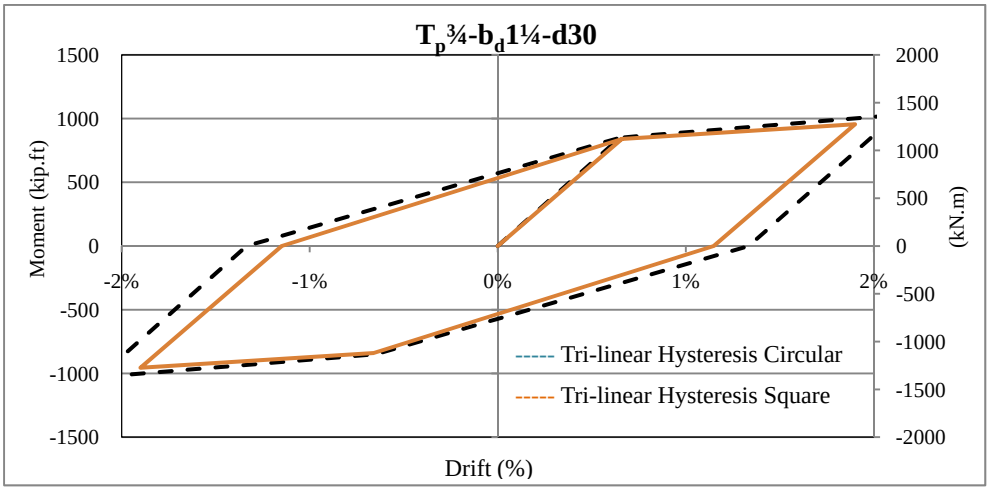

Figure E-26 Comparison Of Tri-Linear Hysteresis Of The Model T_p¾-b_d1¼-d30 With Circular And Square Bolt Pattern

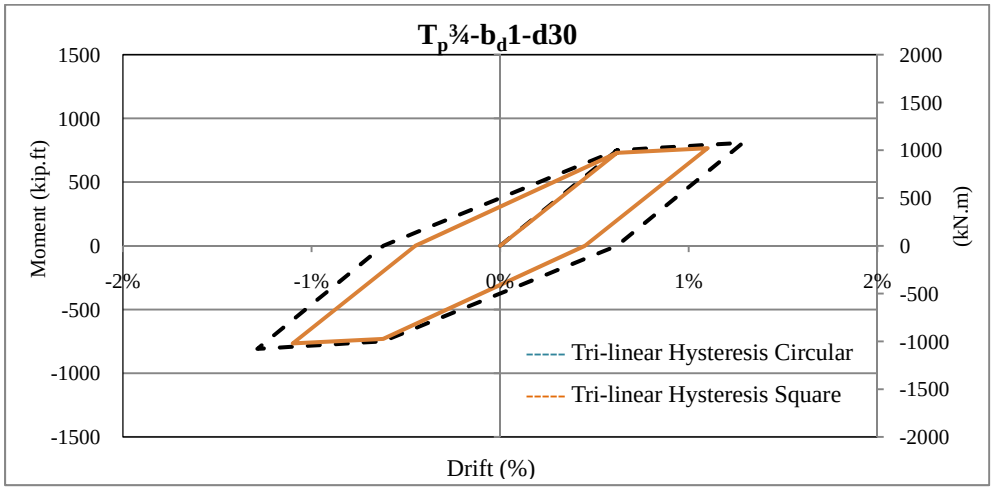

Figure E-27 Comparison Of Tri-Linear Hysteresis Of The Model T_p¾-b_d1-d30 With Circular And Square Bolt Pattern

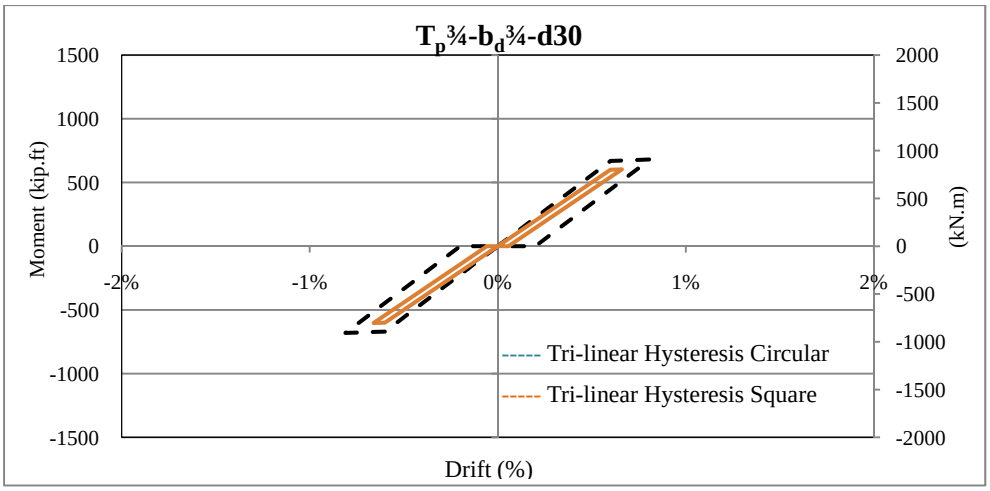

Figure E-28 Comparison Of Tri-Linear Hysteresis Of The Model T_p¾-b_d¾-d30 With Circular And Square Bolt Pattern

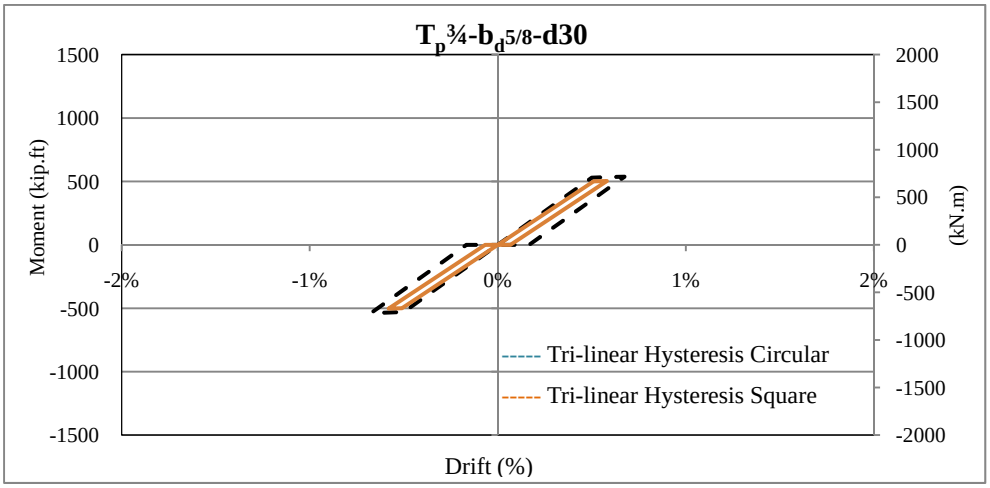

Figure E-29 Comparison Of Tri-Linear Hysteresis Of The Model T_p¾-b_d5/8-d30 With Circular And Square Bolt Pattern

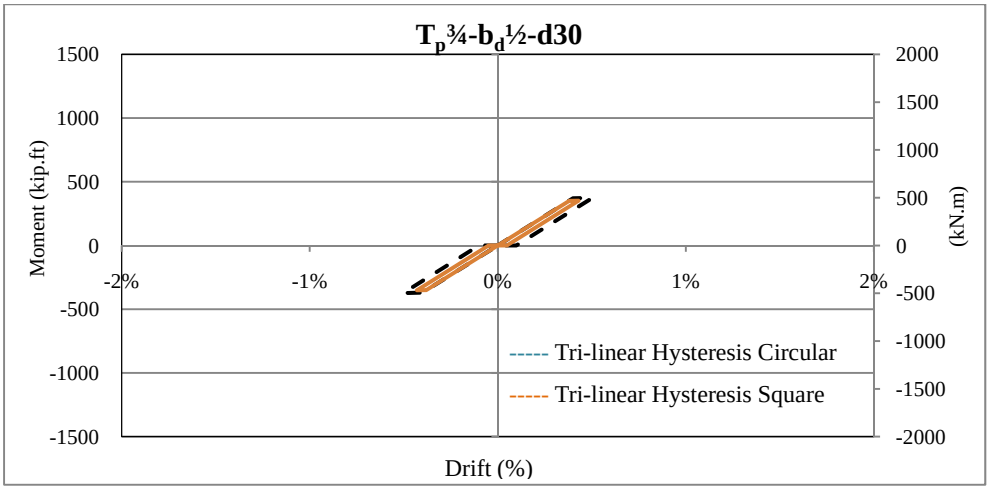

Figure E-30 Comparison Of Tri-Linear Hysteresis Of The Model T_p¾-b_d½-d30 With Circular And Square Bolt Pattern

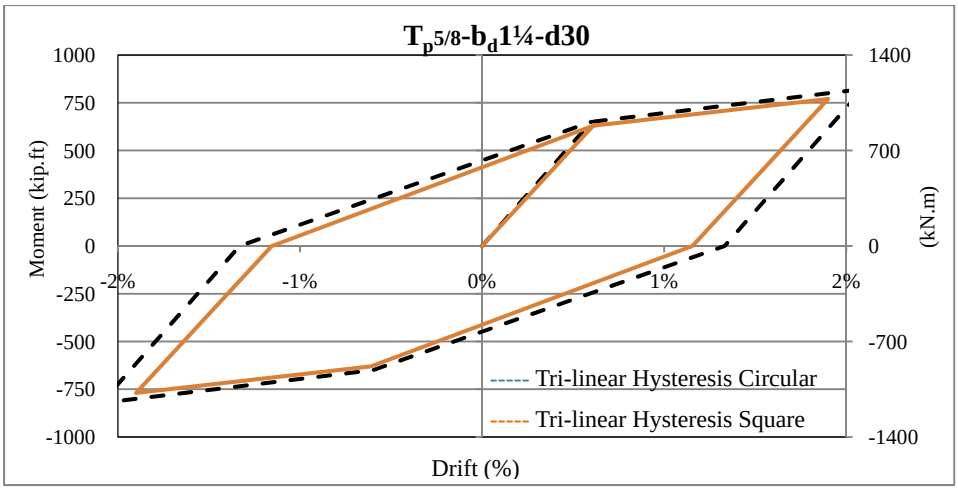

Figure E-31 Comparison Of Tri-Linear Hysteresis Of The Model T_p5/8-b_d1¼-d30 With Circular And Square Bolt Pattern

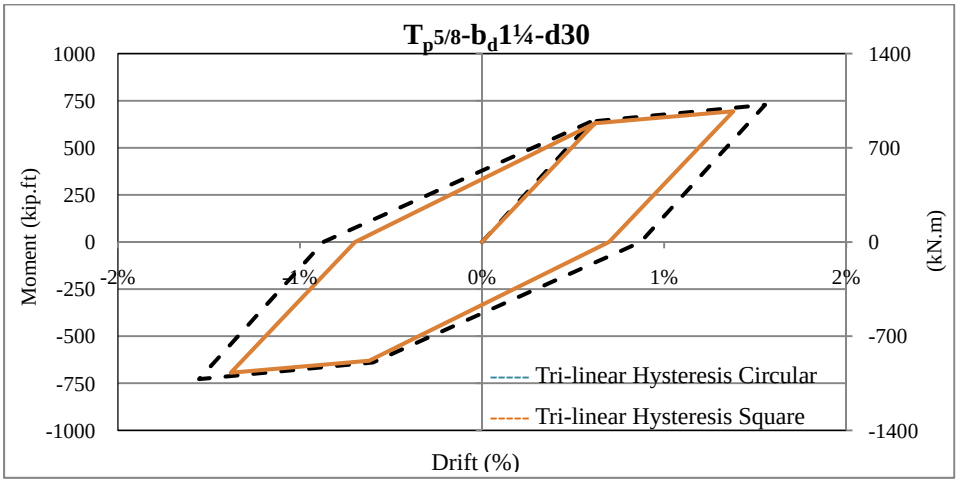

Figure E-32 Comparison Of Tri-Linear Hysteresis Of The Model T_p5/8-b_d1¼-d30 With Circular And Square Bolt Pattern

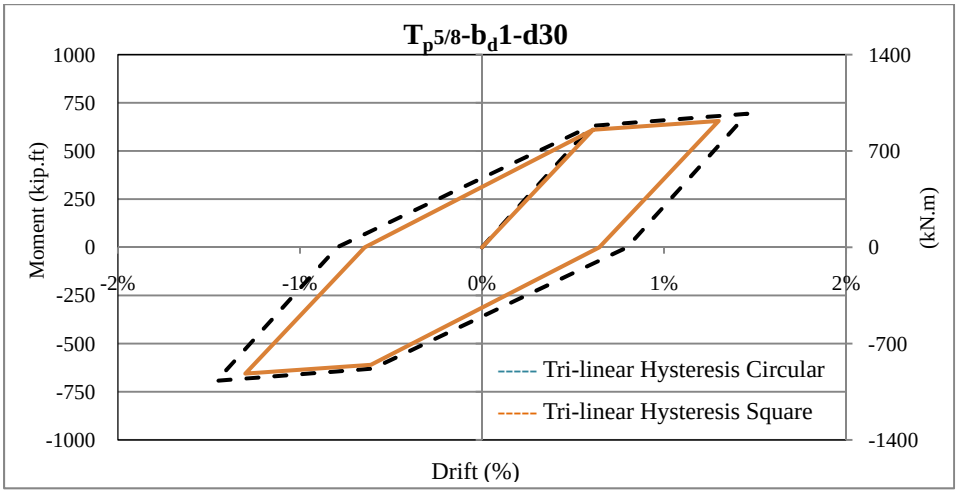

Figure E-33 Comparison Of Tri-Linear Hysteresis Of The Model T_p5/8-b_d1-d30 With Circular And Square Bolt Pattern

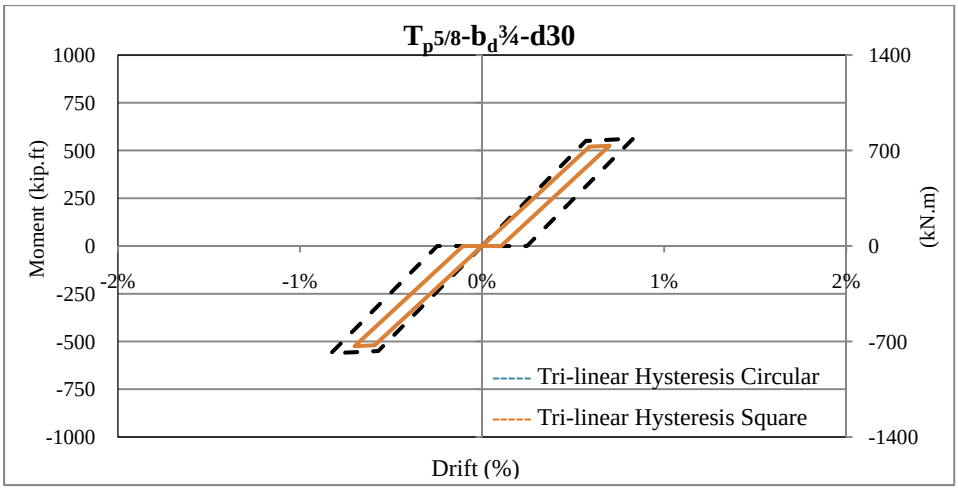

Figure E-34 Comparison Of Tri-Linear Hysteresis Of The Model T_p5/8-b_d¾-d30 With Circular And Square Bolt Pattern

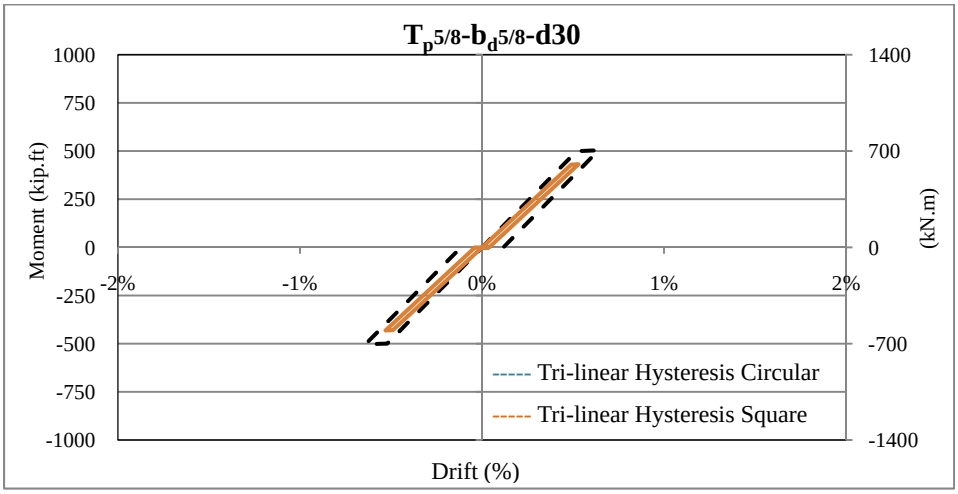

Figure E-35 Comparison Of Tri-Linear Hysteresis Of The Model T_p5/8-b_d5/8-d30 With Circular And Square Bolt Pattern

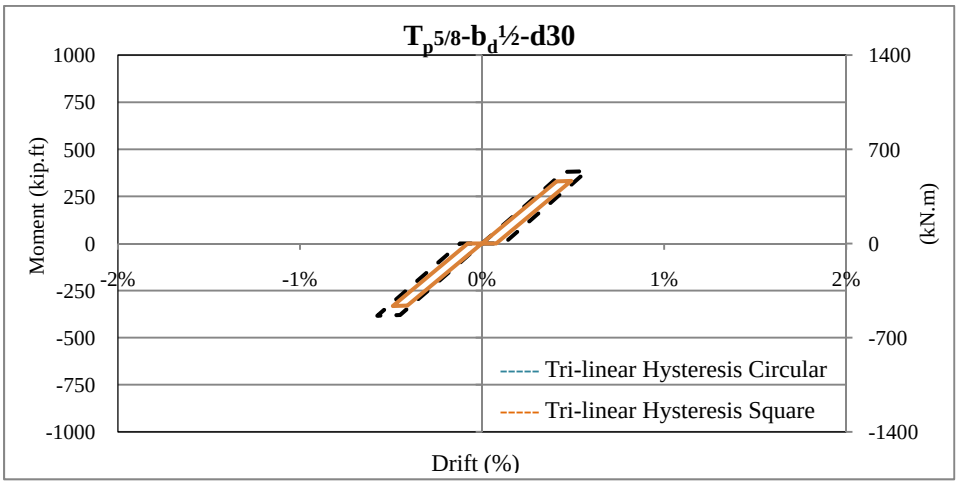

Figure E-36 Comparison Of Tri-Linear Hysteresis Of The Model T_p5/8-b_d½-d30 With Circular And Square Bolt Pattern

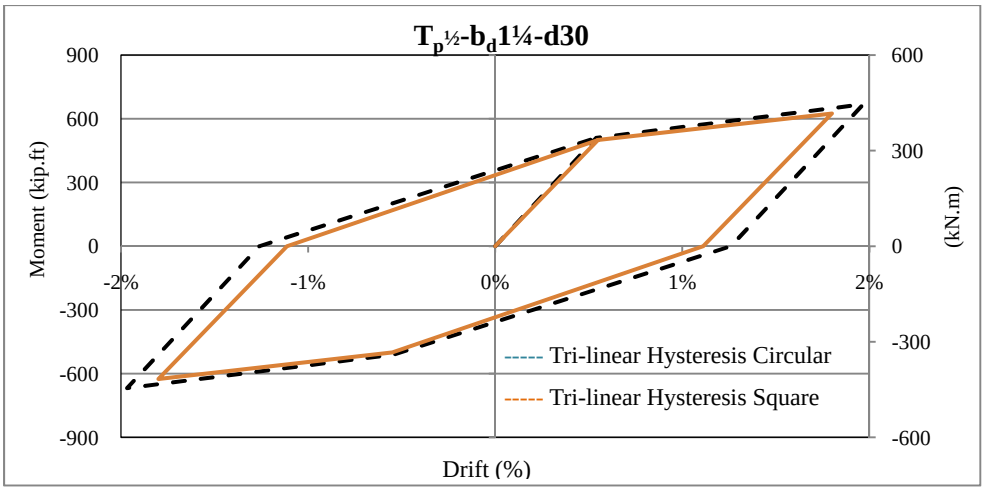

Figure E-37 Comparison Of Tri-Linear Hysteresis Of The Model T_p½-b_d1¼-d30 With Circular And Square Bolt Pattern

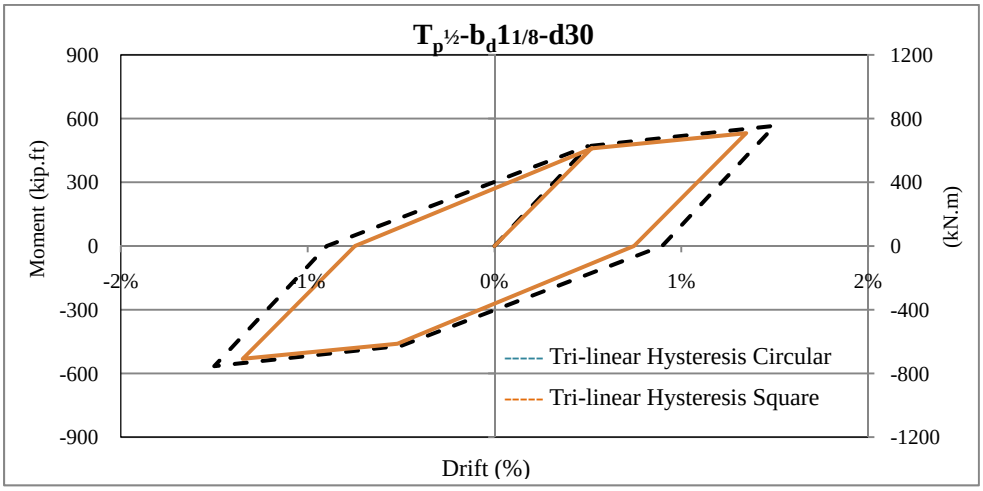

Figure E-38 Comparison Of Tri-Linear Hysteresis Of The Model T_p½-b_d11/8-d30 With Circular And Square Bolt Pattern

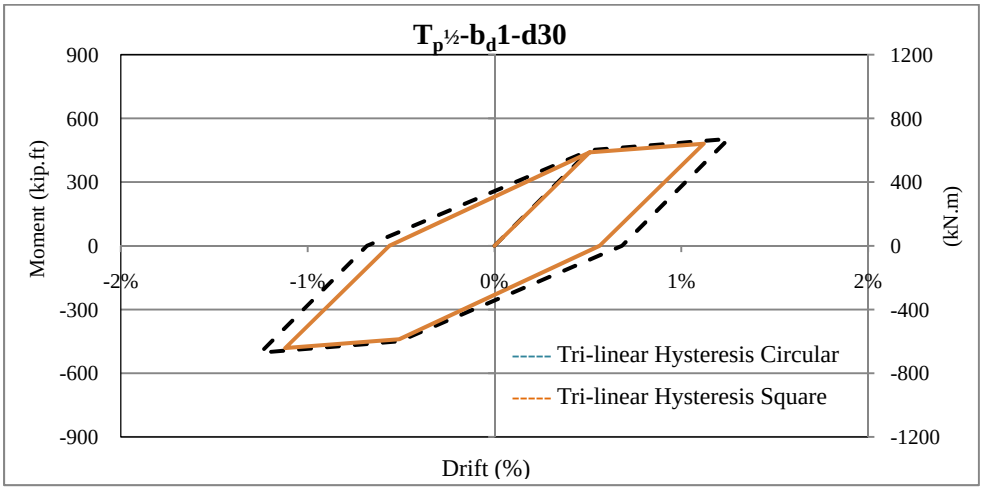

Figure E-39 Comparison Of Tri-Linear Hysteresis Of The Model T_p½-b_d1-d30 With Circular And Square Bolt Pattern

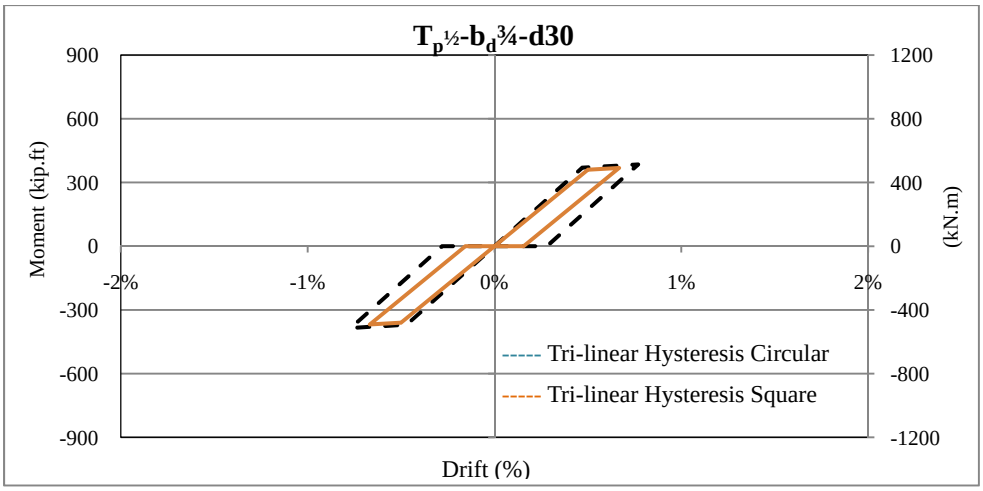

Figure E-40 Comparison Of Tri-Linear Hysteresis Of The Model T_p½-b_d¾-d30 With Circular And Square Bolt Pattern

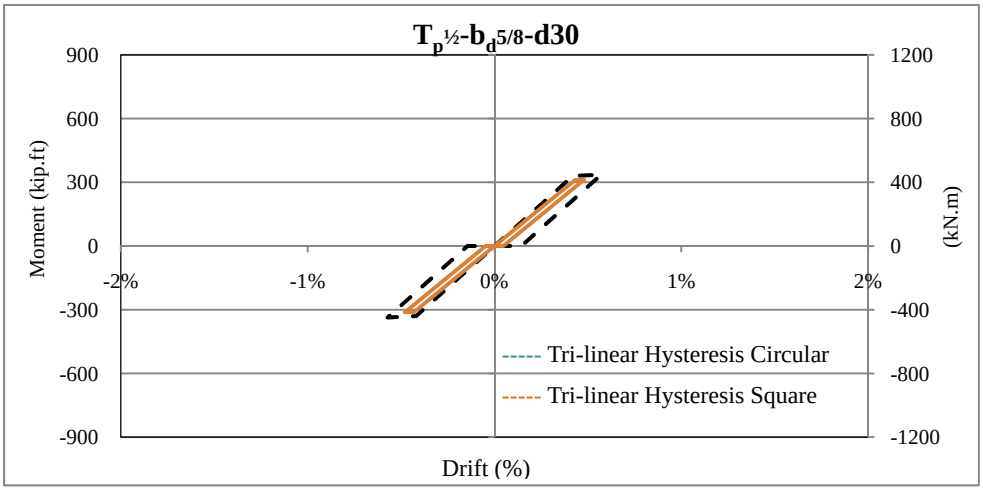

Figure E-41 Comparison Of Tri-Linear Hysteresis Of The Model T_p½-b_d5/8-d30 With Circular And Square Bolt Pattern

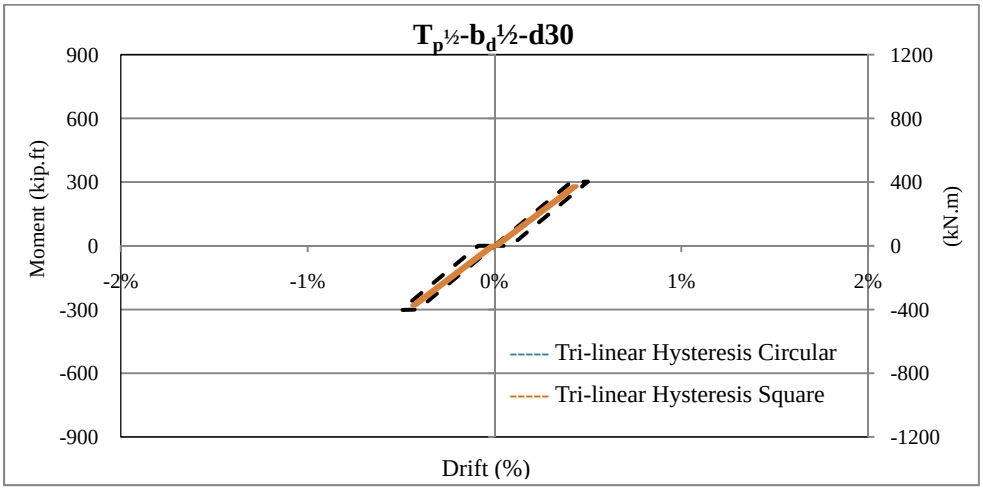

Figure E-42 Comparison Of Tri-Linear Hysteresis Of The Model T_p½-b_d½-d30 With Circular And Square Bolt Pattern

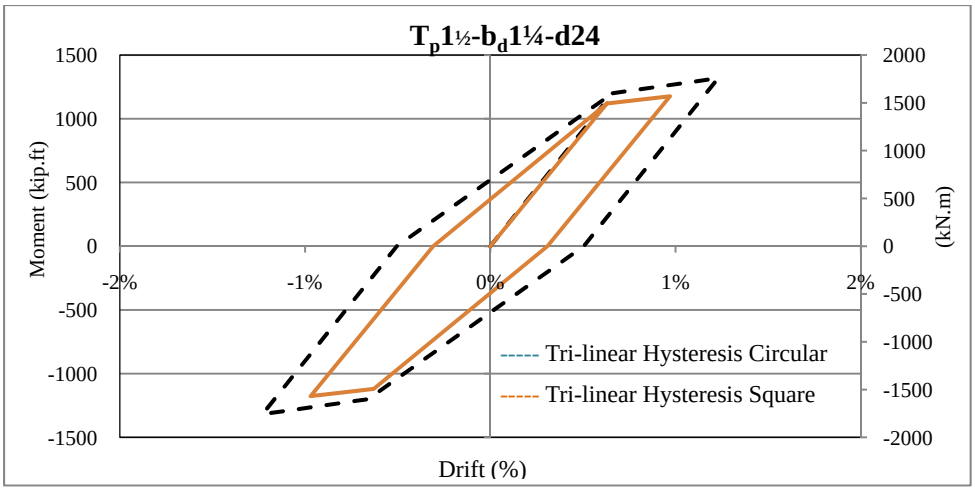

Figure E-43 Comparison Of Tri-Linear Hysteresis Of The Model $T_p1½\text{-}b_d1¼\text{-}d24$ With Circular And Square Bolt Pattern

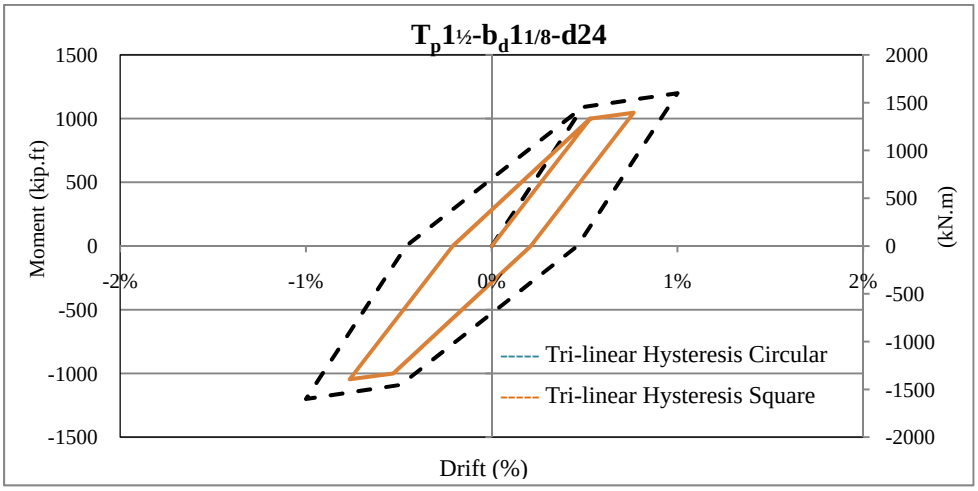

Figure E-44 Comparison Of Tri-Linear Hysteresis Of The Model $T_p1½\text{-}b_d11/8\text{-}d24$ With Circular And Square Bolt Pattern

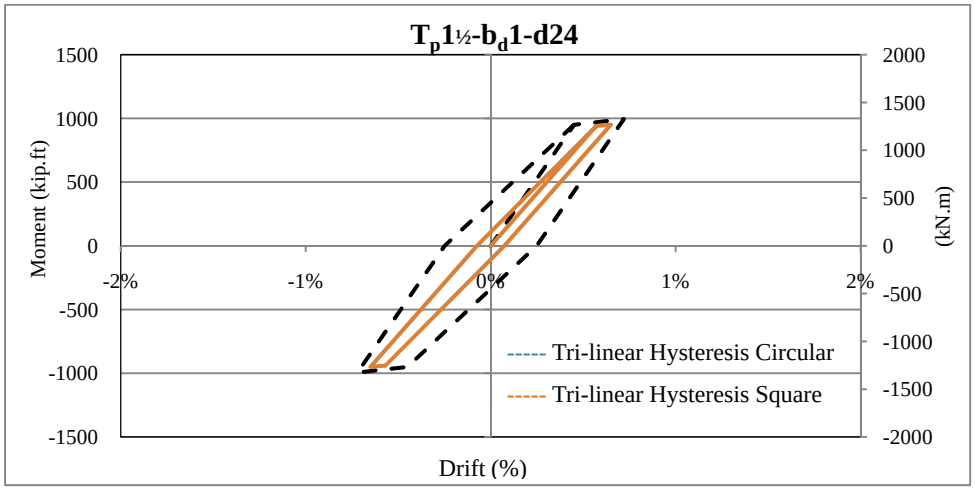

Figure E-45 Comparison Of Tri-Linear Hysteresis Of The Model $T_p1½\text{-}b_d1\text{-}d24$ With Circular And Square Bolt Pattern

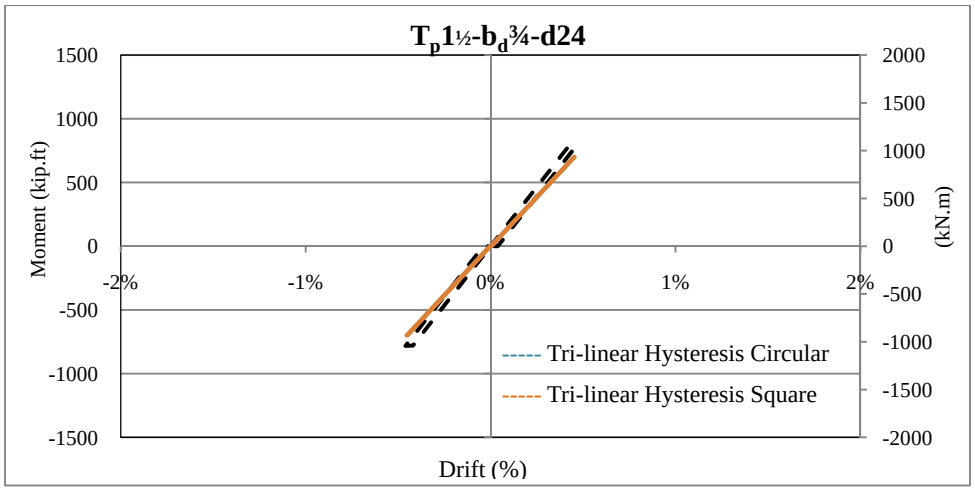

Figure E-46 Comparison Of Tri-Linear Hysteresis Of The Model $T_p1½\text{-}b_d¾\text{-}d24$ With Circular And Square Bolt Pattern

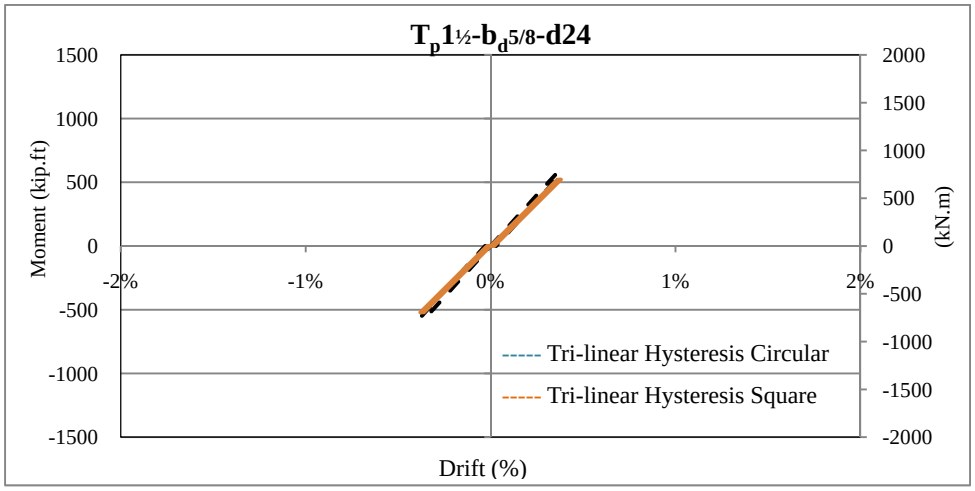

Figure E-47 Comparison Of Tri-Linear Hysteresis Of The Model $T_p1½\text{-}b_d5/8\text{-}d24$ With Circular And Square Bolt Pattern

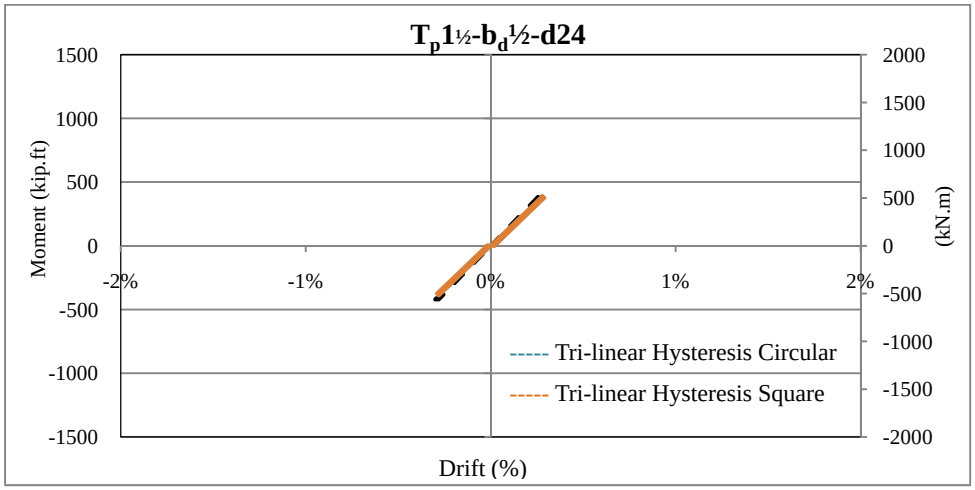

Figure E-48 Comparison Of Tri-Linear Hysteresis Of The Model $T_p1½\text{-}b_d½\text{-}d24$ With Circular And Square Bolt Pattern

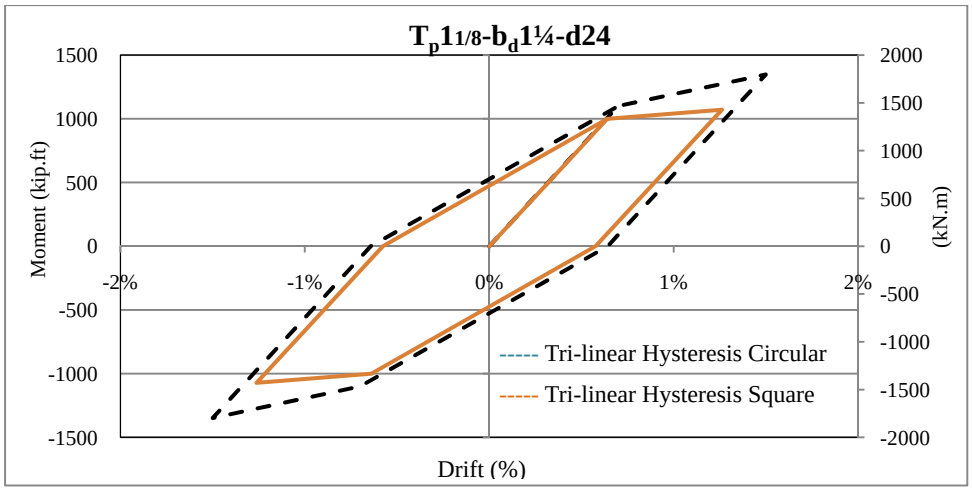

Figure E-49 Comparison Of Tri-Linear Hysteresis Of The Model T_p11/8-b_d1¼-d24 With Circular And Square Bolt Pattern

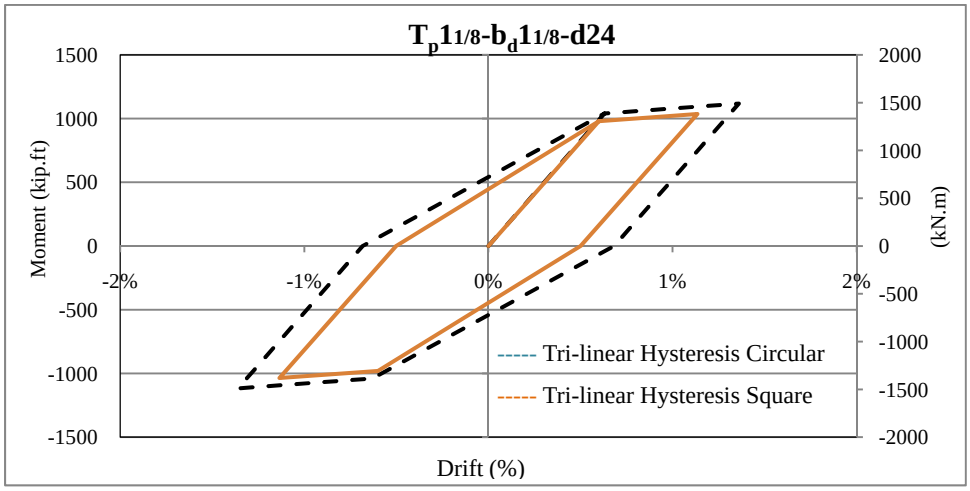

Figure E-50 Comparison Of Tri-Linear Hysteresis Of The Model T_p11/8-b_d11/8-d24 With Circular And Square Bolt Pattern

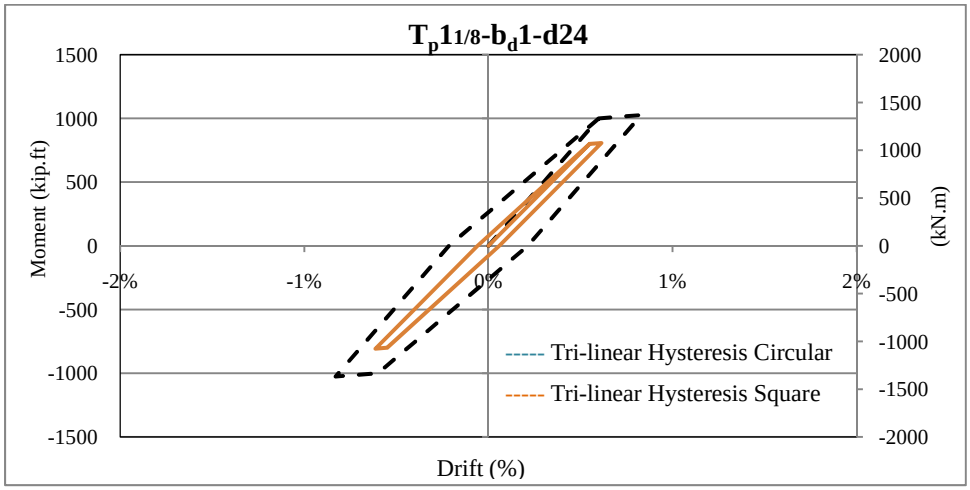

Figure E-51 Comparison Of Tri-Linear Hysteresis Of The Model T_p11/8-b_d1-d24 With Circular And Square Bolt Pattern

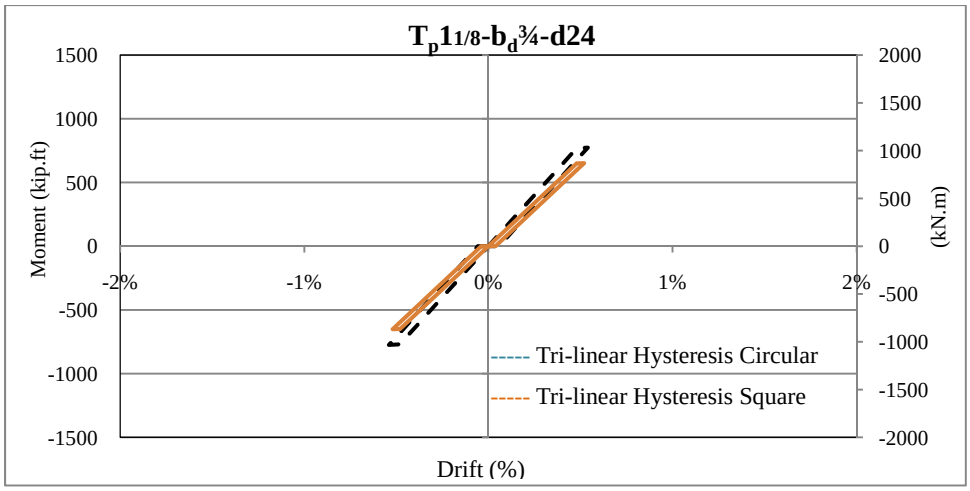

Figure E-52 Comparison Of Tri-Linear Hysteresis Of The Model $T_p11/8$-$b_d¾$-d24 With Circular And Square Bolt Pattern

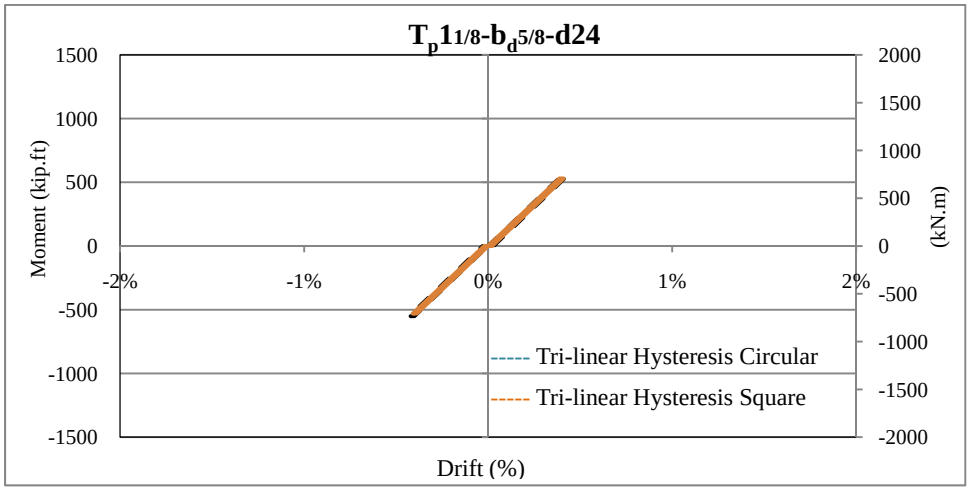

Figure E-53 Comparison Of Tri-Linear Hysteresis Of The Model $T_p11/8$-$b_d5/8$-d24 With Circular And Square Bolt Pattern

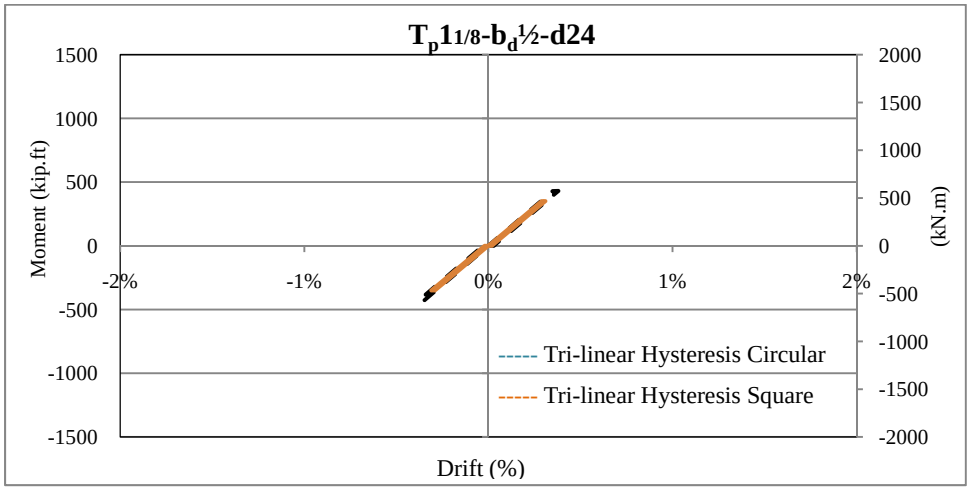

Figure E-54 Comparison Of Tri-Linear Hysteresis Of The Model $T_p11/8$-$b_d½$-d24 With Circular And Square Bolt Pattern

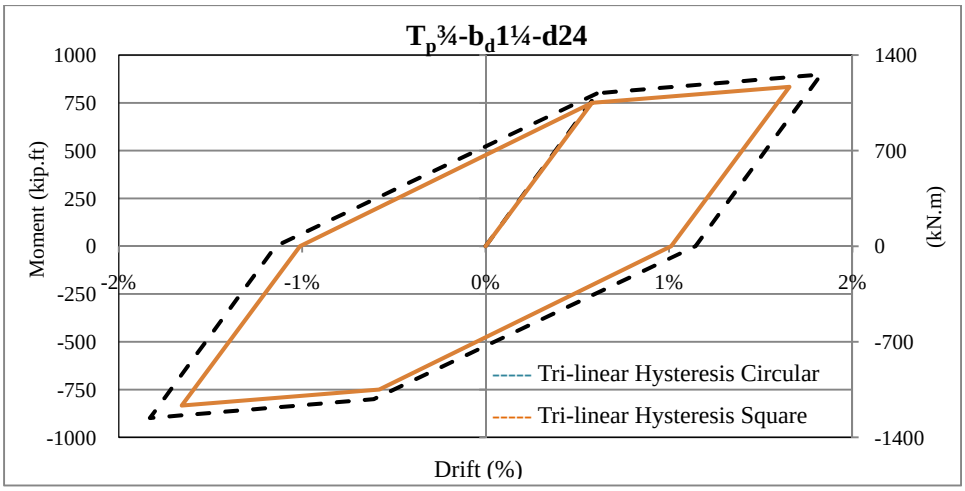

Figure E-55 Comparison Of Tri-Linear Hysteresis Of The Model T_p¾-b_d1¼-d24 With Circular And Square Bolt Pattern

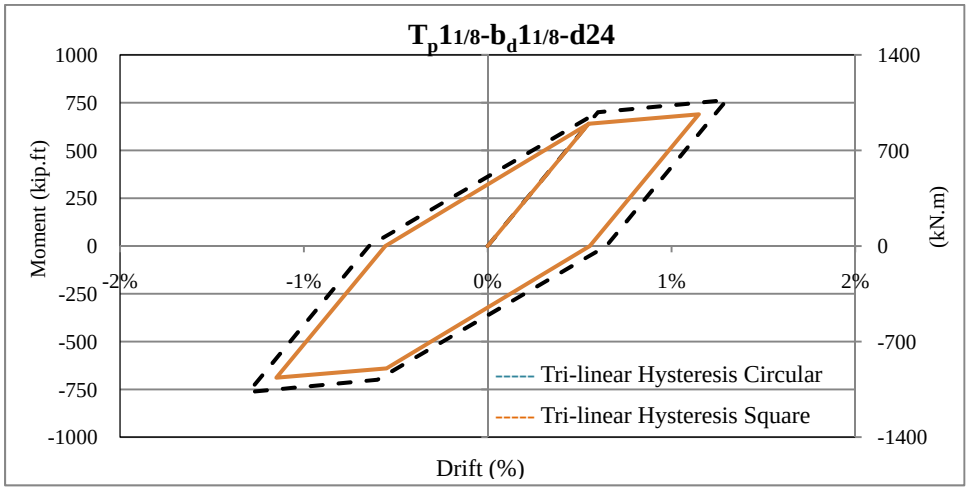

Figure E-56 Comparison Of Tri-Linear Hysteresis Of The Model T_p11/8-b_d11/8-d24 With Circular And Square Bolt Pattern

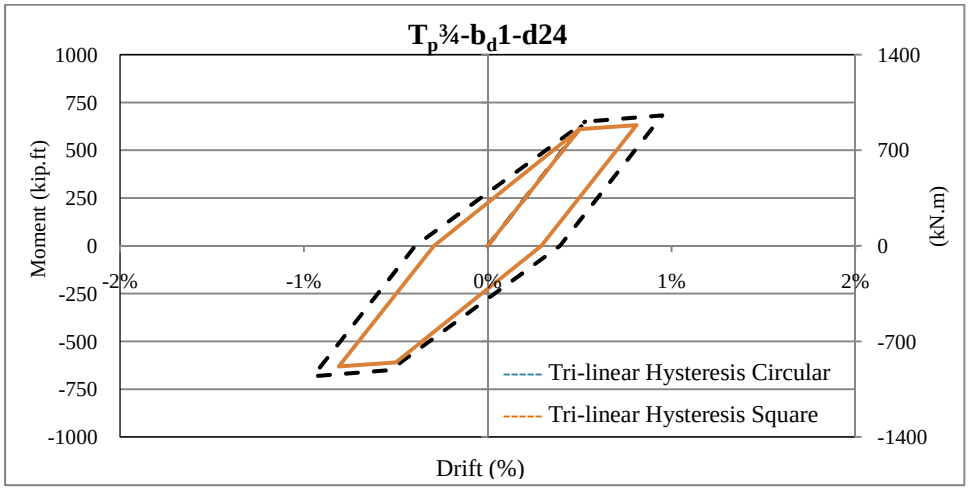

Figure E-57 Comparison Of Tri-Linear Hysteresis Of The Model T_p¾-b_d1-d24 With Circular And Square Bolt Pattern

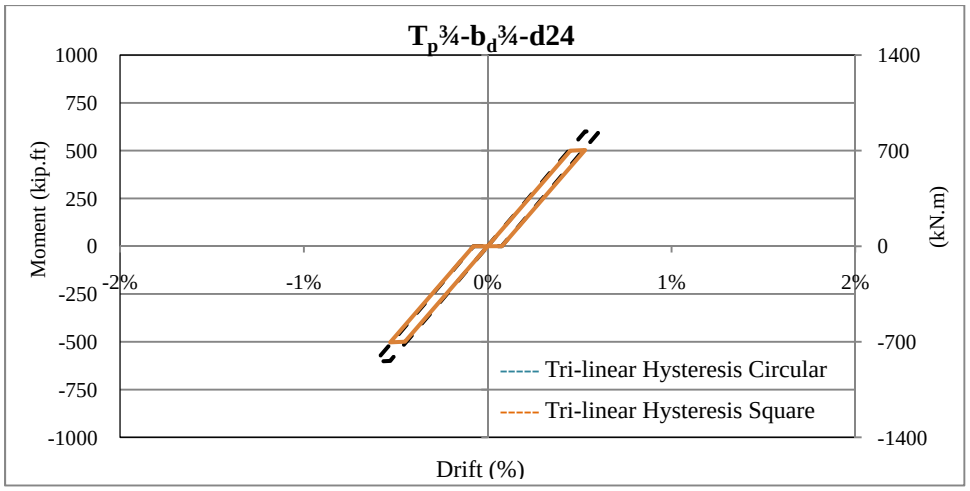

Figure E-58 Comparison Of Tri-Linear Hysteresis Of The Model T_p¾-b_d¾-d24 With Circular And Square Bolt Pattern

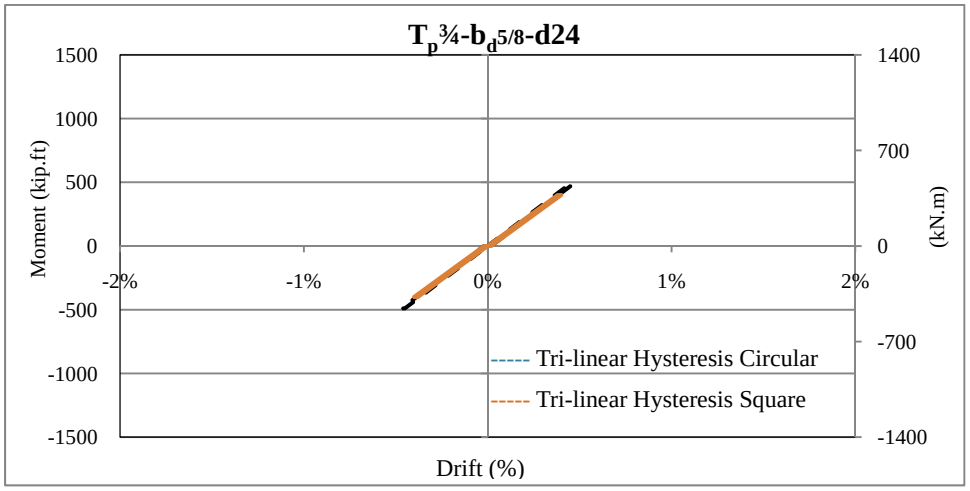

Figure E-59 Comparison Of Tri-Linear Hysteresis Of The Model T_p¾-b_d5/8-d24 With Circular And Square Bolt Pattern

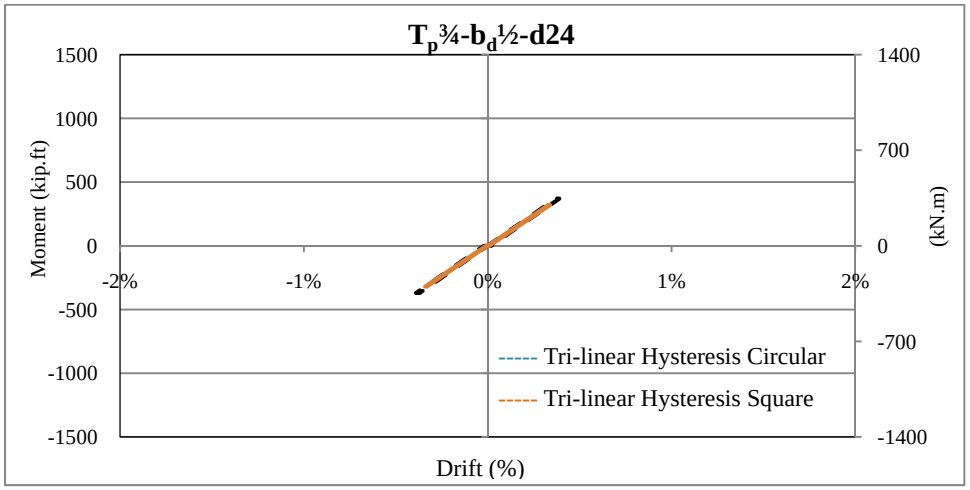

Figure E-60 Comparison Of Tri-Linear Hysteresis Of The Model T_p¾-b_d½-d24 With Circular And Square Bolt Pattern

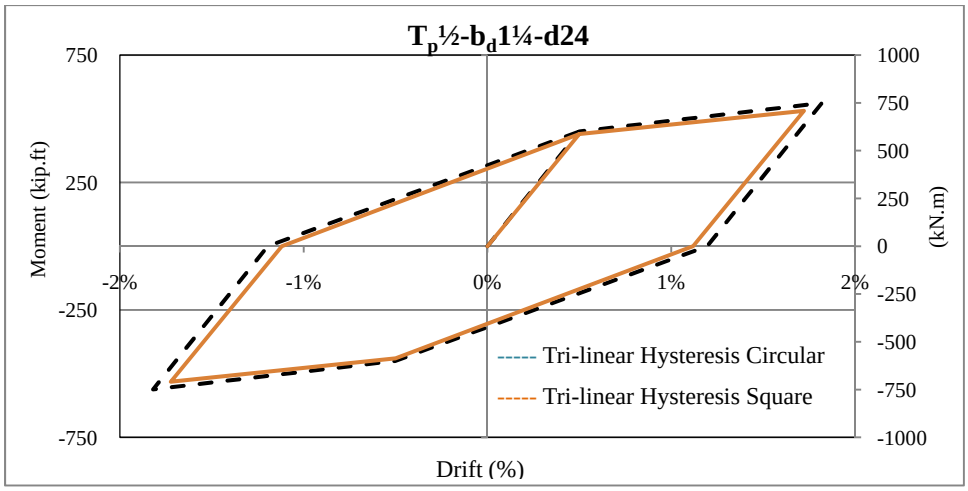

Figure E-61Comparison Of Tri-Linear Hysteresis Of The Model T_p½-b_d1¼-d24 With Circular And Square Bolt Pattern

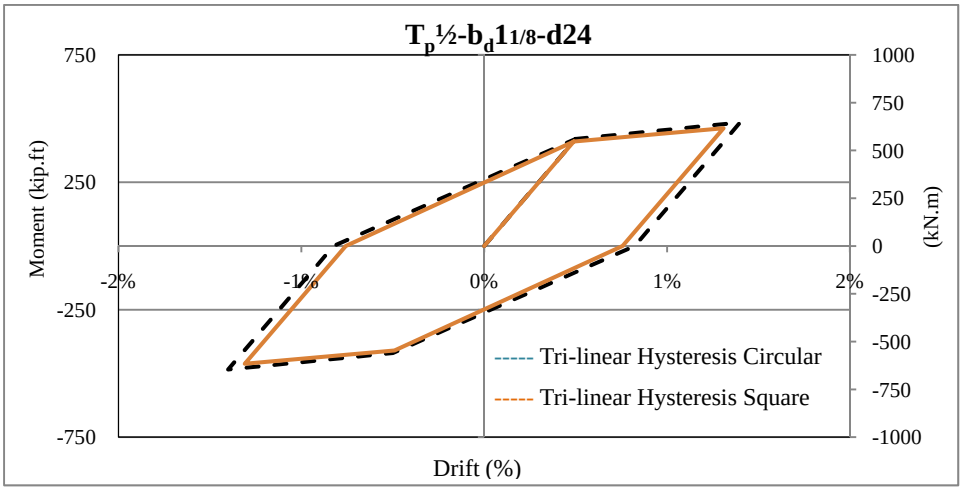

Figure E-62 Comparison Of Tri-Linear Hysteresis Of The Model T_p½-b_d11/8-d24 With Circular And Square Bolt Pattern

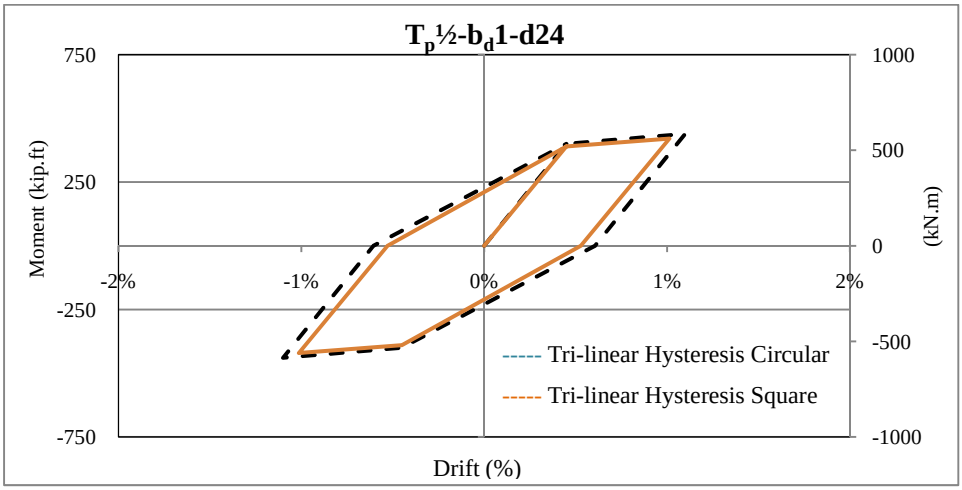

Figure E-63 Comparison Of Tri-Linear Hysteresis Of The Model T_p½-b_d1-d24 With Circular And Square Bolt Pattern

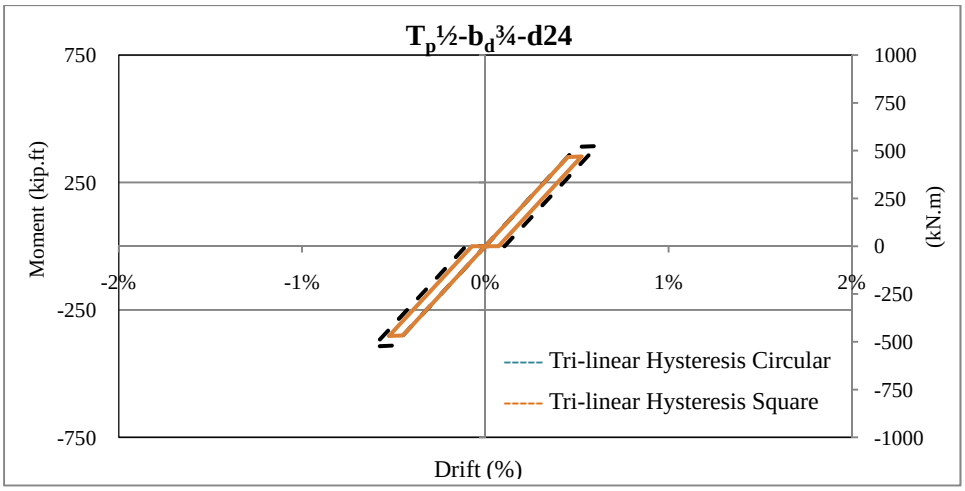

Figure E-64 Comparison Of Tri-Linear Hysteresis Of The Model T_p½-b_d¾-d24 With Circular And Square Bolt Pattern

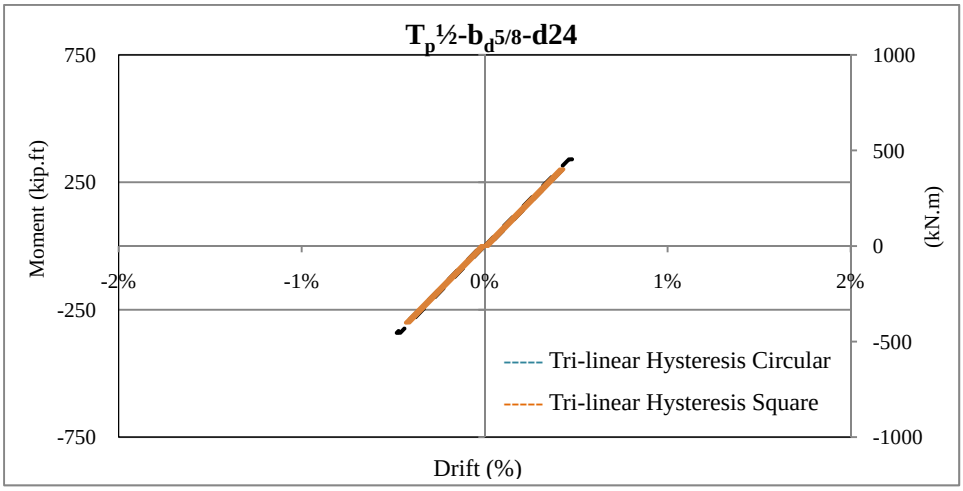

Figure E-65 Comparison Of Tri-Linear Hysteresis Of The Model T_p½-b_d5/8-d24 With Circular And Square Bolt Pattern

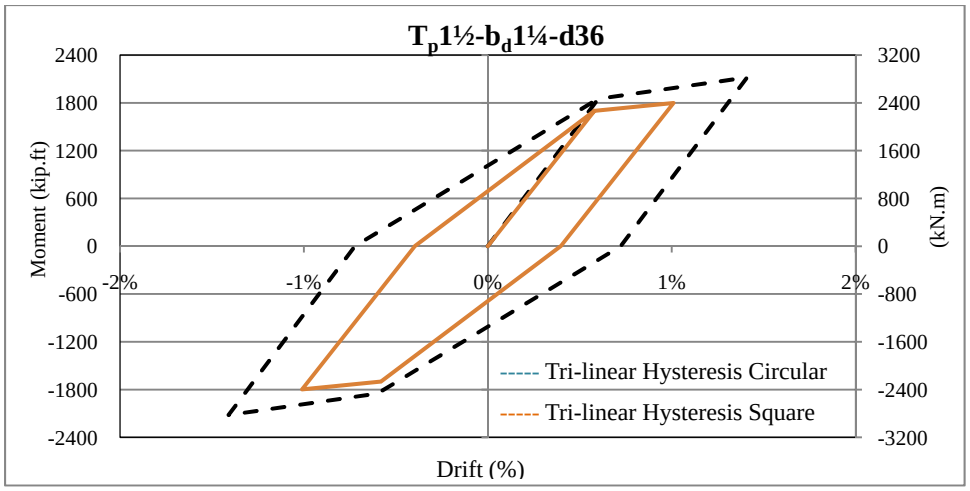

Figure E-66 Comparison Of Tri-Linear Hysteresis Of The Model $T_p1½\text{-}b_d1¼\text{-}d36$ With Circular And Square Bolt Pattern

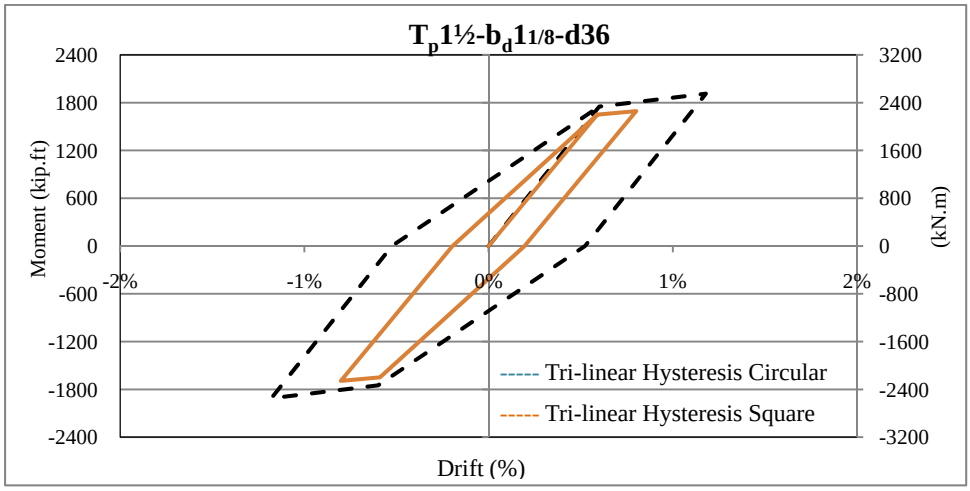

Figure E-67 Comparison Of Tri-Linear Hysteresis Of The Model $T_p1½\text{-}b_d11/8\text{-}d36$ With Circular And Square Bolt Pattern

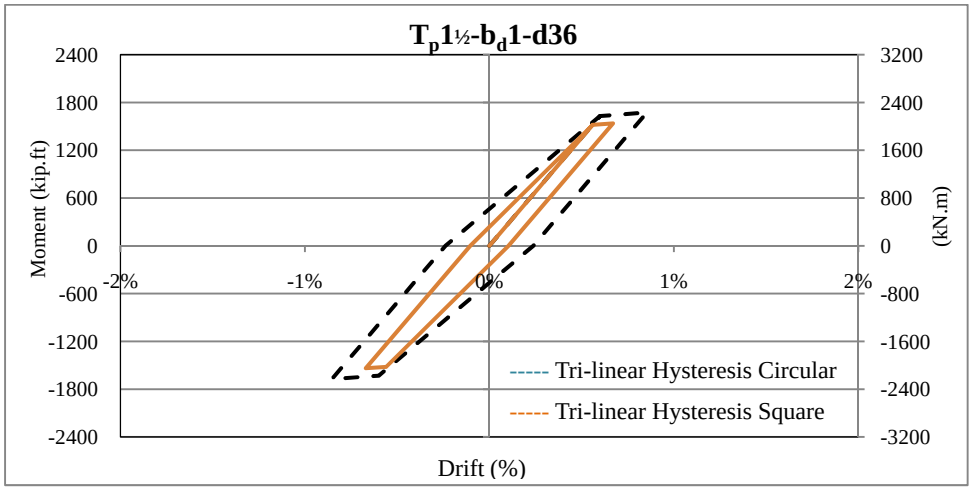

Figure E-68 Comparison Of Tri-Linear Hysteresis Of The Model $T_p1½\text{-}b_d1\text{-}d36$ With Circular And Square Bolt Pattern

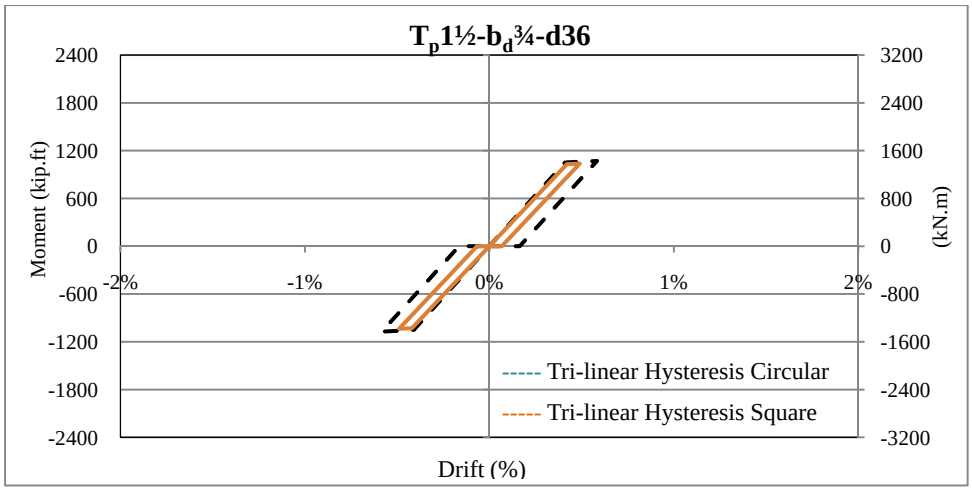

Figure E-69 Comparison Of Tri-Linear Hysteresis Of The Model $T_p1½\text{-}b_d¾\text{-}d36$ With Circular And Square Bolt Pattern

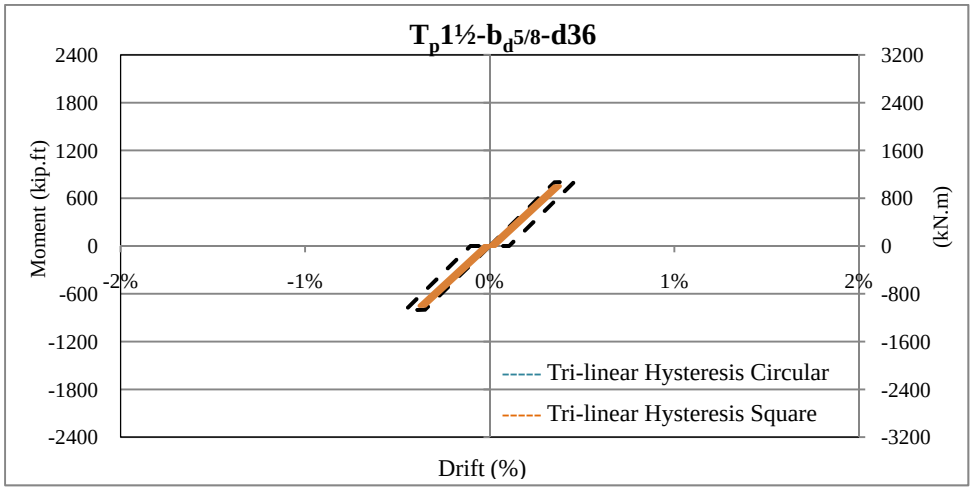

Figure E-70 Comparison Of Tri-Linear Hysteresis Of The Model $T_p1½\text{-}b_d5/8\text{-}d36$ With Circular And Square Bolt Pattern

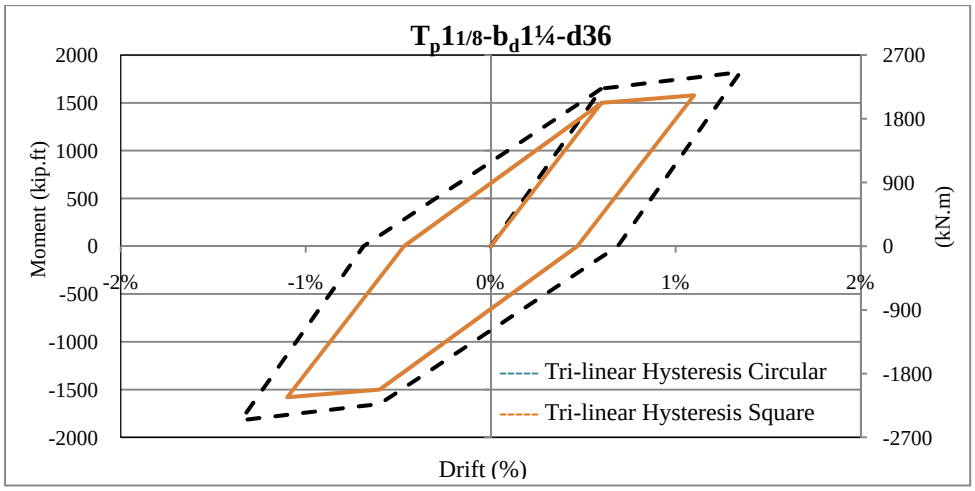

Figure E-71 Comparison Of Tri-Linear Hysteresis Of The Model T_p11/8-b_d1¼-d36 With Circular And Square Bolt Pattern

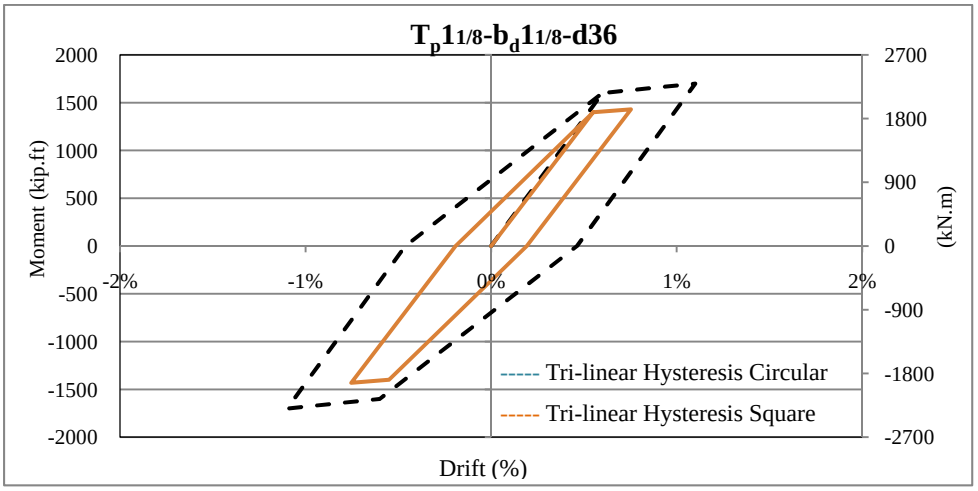

Figure E-72 Comparison Of Tri-Linear Hysteresis Of The Model T_p11/8-b_d11/8-d36 With Circular And Square Bolt Pattern

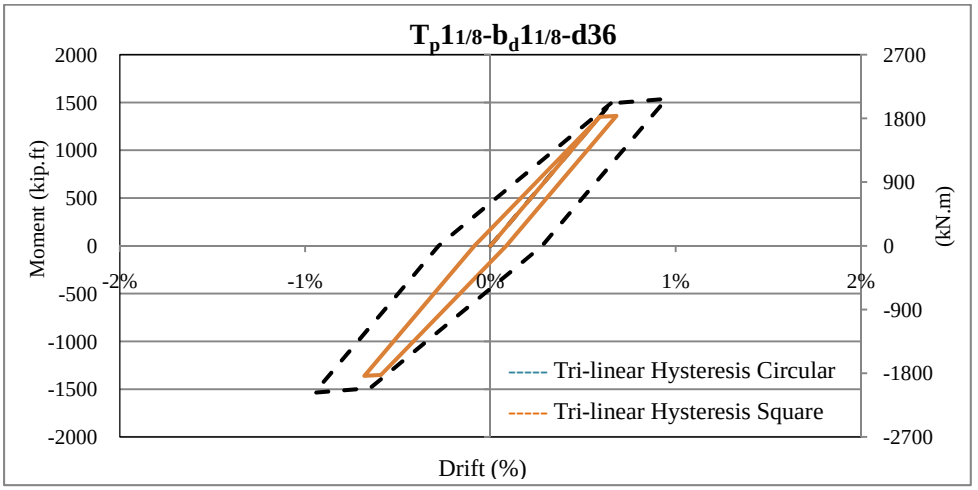

Figure E-73 Comparison Of Tri-Linear Hysteresis Of The Model T_p11/8-b_d11/8-d36 With Circular And Square Bolt Pattern

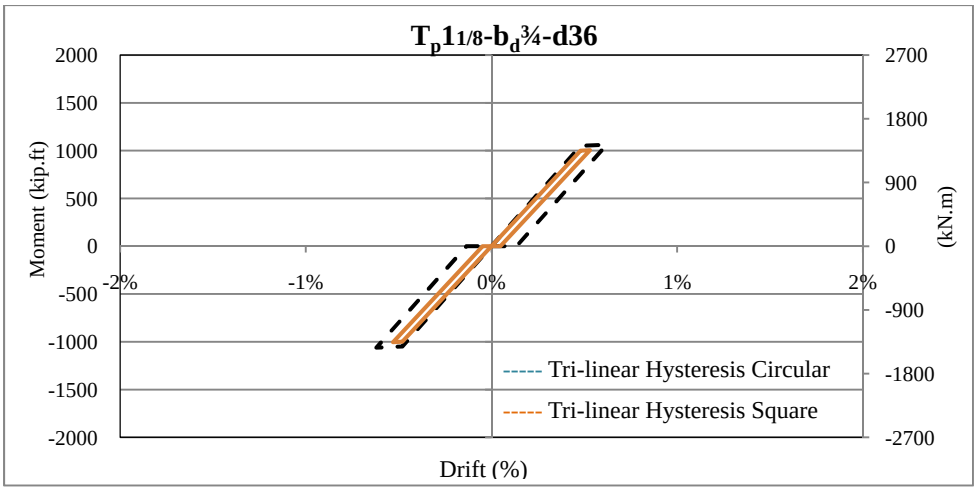

Figure E-74 Comparison Of Tri-Linear Hysteresis Of The Model T_p11/8-b_d¾-d36 With Circular And Square Bolt Pattern

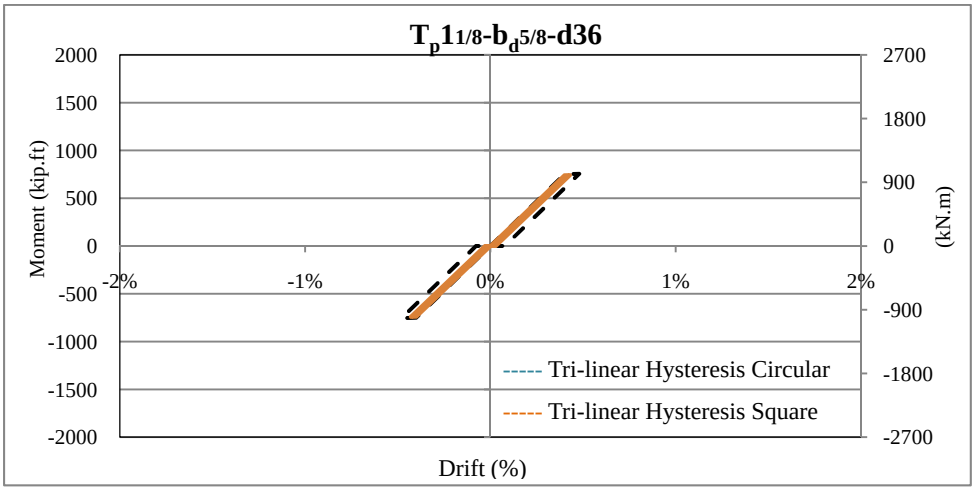

Figure E-75 Comparison Of Tri-Linear Hysteresis Of The Model T_p11/8-b_d5/8-d36 With Circular And Square Bolt Pattern

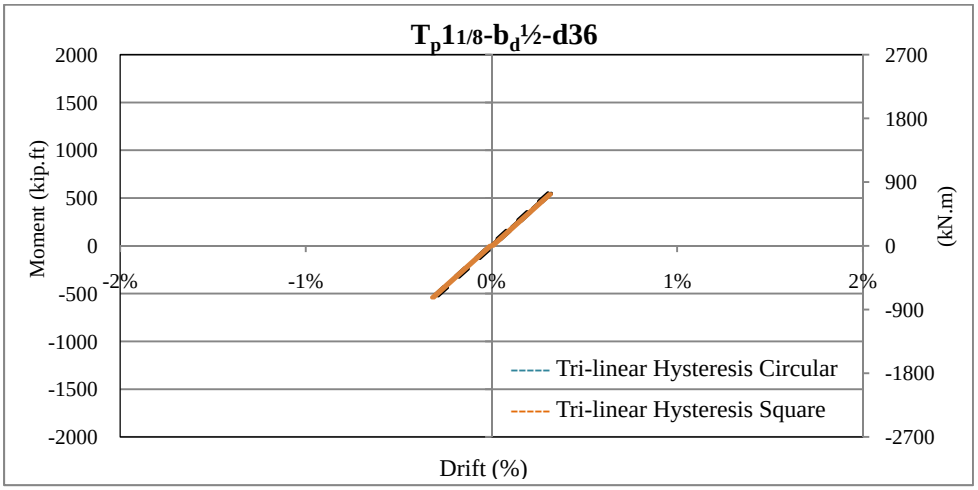

Figure E-76 Comparison Of Tri-Linear Hysteresis Of The Model T_p11/8-b_d½-d30 With Circular And Square Bolt Pattern

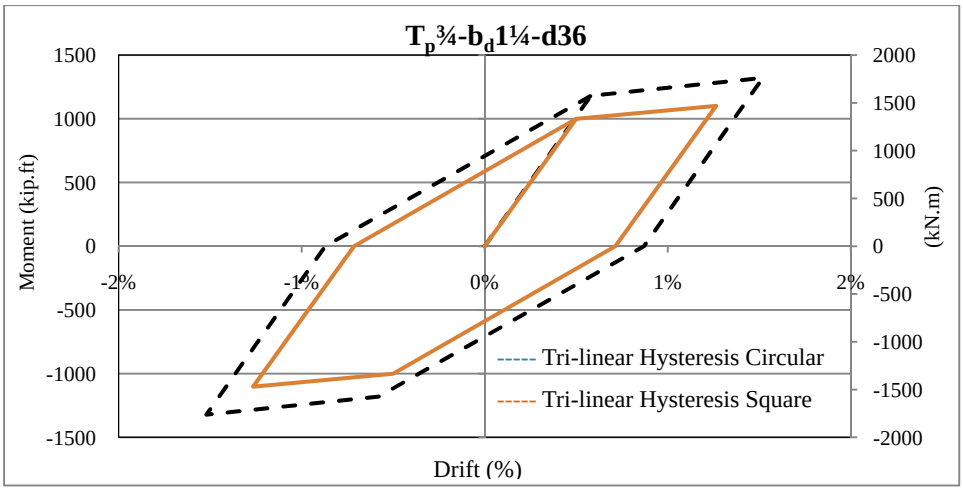

Figure E-77 Comparison Of Tri-Linear Hysteresis Of The Model T_p¾-b_d1¼-d36 With Circular And Square Bolt Pattern

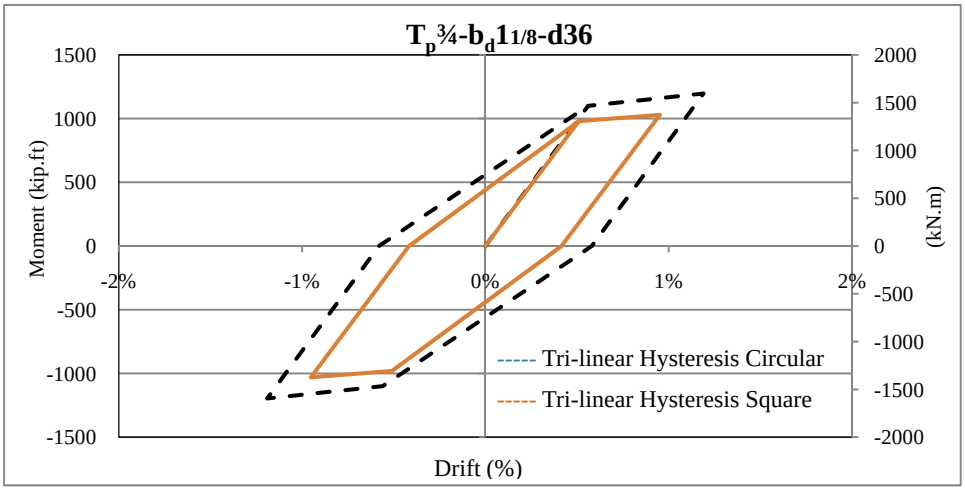

Figure E-78 Comparison Of Tri-Linear Hysteresis Of The Model T_p¾-b_d11/8-d36 With Circular And Square Bolt Pattern

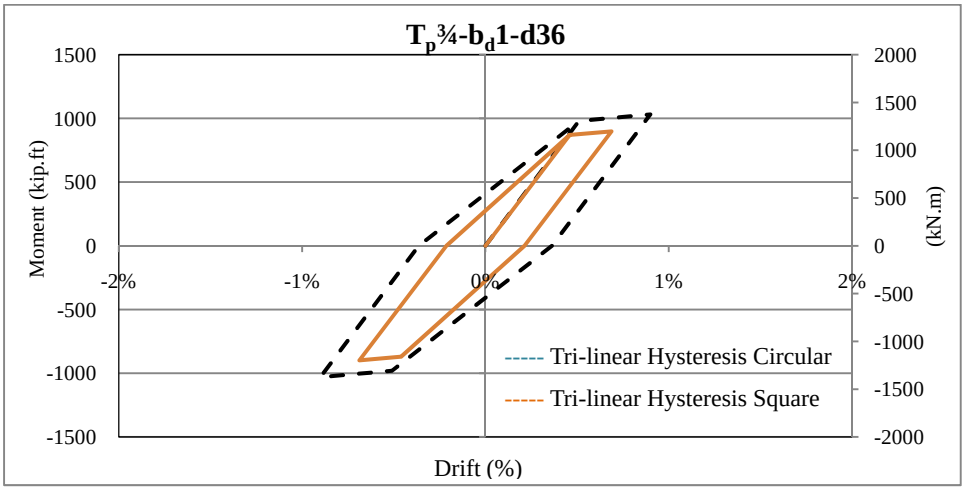

Figure E-79 Comparison Of Tri-Linear Hysteresis Of The Model T_p¾-b_d1-d36 With Circular And Square Bolt Pattern

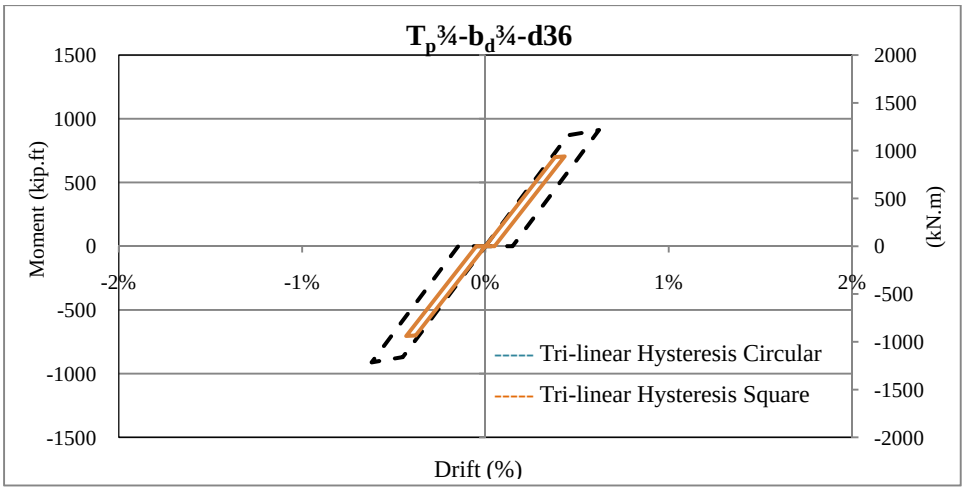

Figure E-80 Comparison Of Tri-Linear Hysteresis Of The Model T_p¾-b_d¾-d36 With Circular And Square Bolt Pattern

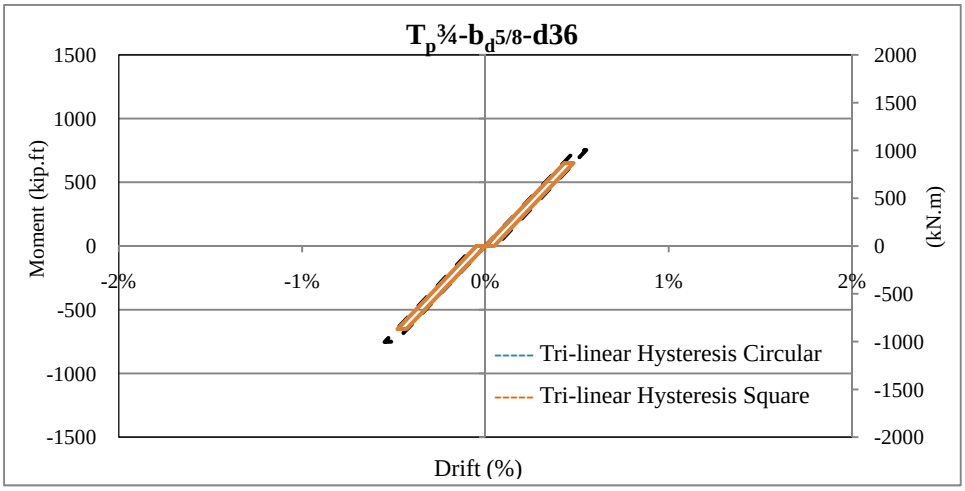

Figure E-81 Comparison Of Tri-Linear Hysteresis Of The Model T_p¾-b_d5/8-d36 With Circular And Square Bolt Pattern

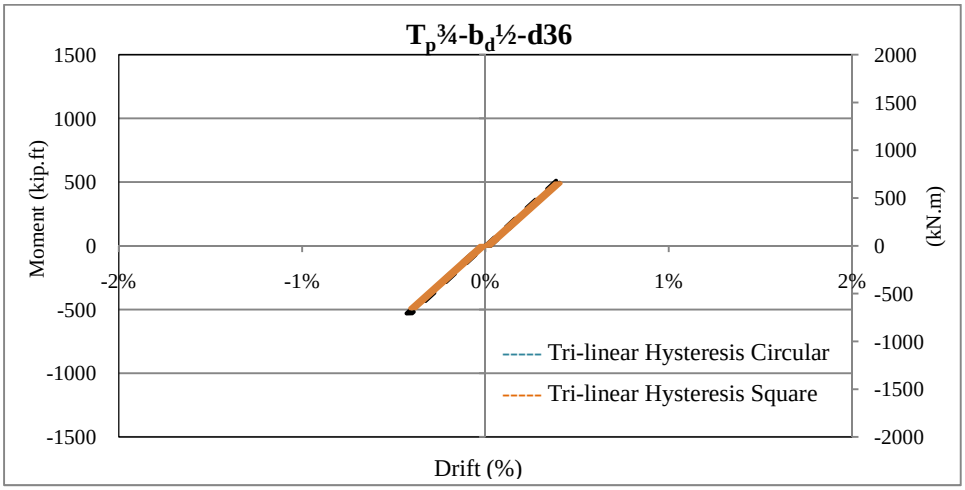

Figure E-82 Comparison Of Tri-Linear Hysteresis Of The Model T_p¾-b_d½-d36 With Circular And Square Bolt Pattern

APPENDIX F

NON-LINIEAR REGRESSION ANALYSIS

The statistical parameters used during non-linear regression analysis are presented in this section.

Table F-1 Non-Linear Regression Parameters To Predict The M_y of Category-1 Connections With Circular Bolt Pattern

SUMMARY OUTPUT

Regression Statistics	
Multiple R	0.990058088
R Square	0.980215018
Adjusted R Square	0.978767337
Standard Error	0.064671143
Observations	45

ANOVA

	df	*SS*	*MS*	*F*	*Significance F*
Regression	3	8.495533	2.831844	677.093	6.12E-35
Residual	41	0.171477	0.004182		
Total	44	8.66701			

	Coefficients	*Standard Error*	*t Stat*	*P-value*	*Lower 95%*	*Upper 99%*	*Lower 95.0%*	*Upper 95.0%*
Intercept	3.380126374	0.247026	13.68329	7.06E-17	2.881247	3.879005	2.881247	3.879005
X Variable 1	0.190410183	0.044057	4.321905	9.61E-05	0.101435	0.279385	0.101435	0.279385
X Variable 2	0.612549537	0.01771	34.58735	5.84E-32	0.576783	0.648316	0.576783	0.648316
X Variable 3	0.656100182	0.043104	15.22143	1.81E-18	0.56905	0.74315	0.56905	0.74315

Table F-2 Non-Linear Regression Parameters To Predict The E_y Of Category-1 Connections With Circular Bolt Pattern

SUMMARY OUTPUT

Regression Statistics	
Multiple R	0.987612
R Square	0.975378
Adjusted R Square	0.973576
Standard Error	0.049522
Observations	45

ANOVA

	df	*SS*	*MS*	*F*	*Significance F*
Regression	3	3.988158	1.327719	541.3881	5.41E-33
Residual	41	0.10055	0.002452		
Total	44	4.088708			

	Coefficients	*Standard Error*	*t Stat*	*P-value*	*Lower 95%*	*Upper 95%*	*Lower 95.0%*	*Upper 95.0%*
Intercept	8.569298	0.187909	45.60333	9.25E-37	8.189807	8.948789	8.189807	8.948789
X Variable 1	0.667076	0.03373	19.77708	1.4E-22	0.598957	0.735194	0.598957	0.735194
X Variable 2	0.212732	0.013562	15.68629	6.29E-19	0.185344	0.24012	0.185344	0.24012
X Variable 3	0.604488	0.032004	18.88772	7.68E-22	0.539854	0.669122	0.539854	0.669122

Table F-3 Non-Linear Regression Parameters To Predict The E_t Of Category-1 Connections With Circular Bolt Pattern

SUMMARY OUTPUT

Regression Statistics	
Multiple R	0.985401
R Square	0.971015
Adjusted R Square	0.968841
Standard Error	0.127959
Observations	44

ANOVA

	df	*SS*	*MS*	*F*	*Significance F*
Regression	3	21.94124	7.313746	446.6784	8.88E-31
Residual	40	0.654945	0.016374		
Total	43	22.59618			

	Coefficients	*Standard Error*	*t Stat*	*P-value*	*Lower 95%*	*Upper 95%*	*Lower 95.0%*	*Upper 95.0%*
Intercept	6.859392	0.488725	14.03529	4.82E-17	5.871643	7.847141	5.871643	7.847141
X Variable 1	0.269632	0.087353	3.086694	0.003667	0.093085	0.44618	0.093085	0.44618
X Variable 2	1.071141	0.03567	30.02941	4.67E-29	0.99905	1.143232	0.99905	1.143232
X Variable 3	0.504534	0.083323	6.055143	3.95E-07	0.336131	0.672936	0.336131	0.672936

Table F-4 Non-Linear Regression Parameters To Predict The θ_f Of Category-1 Connections With Circular Bolt Pattern

SUMMARY OUTPUT

Regression Statistics	
Multiple R	0.987248
R Square	0.974658
Adjusted R Square	0.972124
Standard Error	0.07716
Observations	45

ANOVA

	df	*SS*	*MS*	*F*	*Significance F*
Regression	4	9.159312	2.289828	384.6044	2.45E-31
Residual	40	0.238149	0.005954		
Total	44	9.397461			

	Coefficients	*Standard Error*	*t Stat*	*P-value*	*Lower 95%*	*Upper 95%*	*Lower 95.0%*	*Upper 95.0%*
Intercept	-2.99938	0.295695	-10.1435	1.28E-12	-3.597	-2.40176	-3.597	-2.40176
X Variable 1	-0.2706	0.05273	-5.13171	7.77E-06	-0.37717	-0.16402	-0.37717	-0.16402
X Variable 2	0.736995	0.02113	34.87834	1.45E-31	0.694289	0.779701	0.694289	0.779701
X Variable 3	-11.509	0.857912	-13.4151	2.16E-16	-13.2429	-9.77511	-13.2429	-9.77511
X Variable 4	11.00693	0.831856	13.23178	3.39E-16	9.325685	12.68817	9.325685	12.68817

Table F-5 Non-Linear Regression Parameters To Predict The M_y Of Category-2 Connections With Circular Bolt Pattern

SUMMARY OUTPUT

Regression Statistics	
Multiple R	0.990804401
R Square	0.981698362
Adjusted R Square	0.980353851
Standard Error	0.063108974
Observations	45

ANOVA

	df	*SS*	*MS*	*F*	*Significance F*
Regression	3	8.756556	2.918852	732.8749	1.25E-35
Residual	41	0.163292	0.003983		
Total	44	8.919849			

	Coefficients	*Standard Error*	*t Stat*	*P-value*	*Lower 95%*	*Upper 95%*	*Lower 95.0%*	*Upper 95.0%*
Intercept	3.190375151	0.240238	13.28005	1.93E-16	2.705204	3.675546	2.705204	3.675546
X Variable 1	1.146436709	0.035219	32.55127	6.45E-31	1.07531	1.217564	1.07531	1.217564
X Variable 2	0.221067927	0.018984	11.64499	1.4E-14	0.182729	0.259407	0.182729	0.259407
X Variable 3	0.669636649	0.042095	15.90788	3.83E-19	0.584625	0.754649	0.584625	0.754649

Table F-6 Non-Linear Regression Parameters To Predict The E_y Of Category-2 Connections With Circular Bolt Pattern

SUMMARY OUTPUT

Regression Statistics	
Multiple R	0.993291
R Square	0.986627
Adjusted R Square	0.985649
Standard Error	0.041732
Observations	45

ANOVA

	df	*SS*	*MS*	*F*	*Significance F*
Regression	3	5.267992	1.755997	1008.302	2E-38
Residual	41	0.071403	0.001742		
Total	44	5.339395			

	Coefficients	*Standard Error*	*t Stat*	*P-value*	*Lower 95%*	*Upper 95%*	*Lower 95.0%*	*Upper 95.0%*
Intercept	6.713411	0.157812	42.54057	1.51E-35	6.394703	7.032118	6.394708	7.032118
X Variable 1	0.782005	0.023281	33.58946	1.86E-31	0.734987	0.829022	0.734987	0.829022
X Variable 2	0.128526	0.012553	10.23831	7.32E-13	0.103174	0.153878	0.103174	0.153878
X Variable 3	0.917232	0.026986	33.98904	1.17E-31	0.862733	0.971732	0.862733	0.971732

Table F-7 Non-Linear Regression Parameters To Predict The E_t Of Category-2 Connections With Circular Bolt Pattern

SUMMARY OUTPUT

Regression Statistics	
Multiple R	0.983701
R Square	0.967667
Adjusted R Square	0.964434
Standard Error	0.10758
Observations	34

ANOVA

	df	*SS*	*MS*	*F*	*Significance F*
Regression	3	10.39124	3.463747	299.2844	1.95E-22
Residual	30	0.347203	0.011573		
Total	33	10.73844			

	Coefficients	*Standard Error*	*t Stat*	*P-value*	*Lower 95%*	*Upper 95%*	*Lower 95.0%*	*Upper 95.0%*
Intercept	1.674556	0.934333	1.792247	0.083185	-0.23361	3.582719	-0.23361	3.582719
X Variable 1	0.291487	0.073235	3.980146	0.000403	0.141921	0.441053	0.141921	0.441053
X Variable 2	0.785677	0.038358	20.48296	3.46E-19	0.70734	0.864013	0.70734	0.864013
X Variable 3	1.321459	0.160803	8.217881	3.57E-09	0.993056	1.649862	0.993056	1.649862

Table F-8 Non-Linear Regression Parameters To Predict The θ_i Of Category-2 Connections With Circular Bolt Pattern

SUMMARY OUTPUT

Regression Statistics	
Multiple R	0.988768
R Square	0.977663
Adjusted R Square	0.975181
Standard Error	0.070177
Observations	41

ANOVA

	df	*SS*	*MS*	*F*	*Significance F*
Regression	4	7.759925	1.939981	393.9194	3.56E-29
Residual	36	0.177293	0.004925		
Total	40	7.937218			

	Coefficients	*Standard Error*	*t Stat*	*P-value*	*Lower 95%*	*Upper 95%*	*Lower 95.0%*	*Upper 95.0%*
Intercept	-1.51032	0.288825	-5.22919	7.45E-06	-2.09609	-0.92456	-2.09609	-0.92456
X Variable 1	-0.05009	0.040708	-1.23036	0.226542	-0.13264	0.032474	-0.13264	0.032474
X Variable 2	0.892516	0.026601	33.5523	9.3E-29	0.838567	0.946465	0.838567	0.946465
X Variable 3	-7.62079	0.809951	-9.40895	3.08E-11	-9.26344	-5.97813	-9.26344	-5.97813
X Variable 4	6.970838	0.785595	8.87332	1.37E-10	5.377577	8.564098	5.377577	8.564098

Table F-9 Non-Linear Regression Parameters To Predict The M_y Of Category-1 Connections With Square Bolt Pattern

SUMMARY OUTPUT

Regression Statistics	
Multiple R	0.983133494
R Square	0.966551466
Adjusted R Square	0.964217847
Standard Error	0.087206991
Observations	47

ANOVA

	df	*SS*	*MS*	*F*	*Significance F*
Regression	3	9.44972	3.149907	414.1857	9.84E-32
Residual	43	0.327018	0.007605		
Total	46	9.776738			

	Coefficients	*Standard Error*	*t Stat*	*P-value*	*Lower 95%*	*Upper 95%*	*Lower 95.0%*	*Upper 95.0%*
Intercept	2.978558135	0.366825	8.119844	3.21E-10	2.238786	3.71833	2.238786	3.71833
X Variable 1	0.254997384	0.065331	3.903175	0.00033	0.123245	0.386749	0.123245	0.386749
X Variable 2	0.606808323	0.023392	25.94069	6.85E-28	0.559634	0.653983	0.559634	0.653983
X Variable 3	0.709120585	0.064495	10.99505	4.49E-14	0.579055	0.839186	0.579055	0.839186

Table F-10 Non-Linear Regression Parameters To Predict The E_v Of Category-1 Connections With Square Bolt Pattern

SUMMARY OUTPUT

Regression Statistics	
Multiple R	**0.986431667**
R Square	**0.973047434**
Adjusted R Square	**0.971167023**
Standard Error	**0.048666048**
Observations	**47**

ANOVA

	df	*SS*	*MS*	*F*	*Significance F*
Regression	**3**	**3.676669**	**1.225556**	**517.4651**	**9.51E-34**
Residual	**43**	**0.101841**	**0.002368**		
Total	**46**	**3.778509**			

	Coefficients	*Standard Error*	*t Stat*	*P-value*	*Lower 95%*	*Upper 95%*	*Lower 95.0%*	*Upper 95.0%*
Intercept	**7.605847102**	**0.204707**	**37.15476**	**2.58E-34**	**7.193016**	**8.018679**	**7.193016**	**8.018679**
X Variable 1	**0.55080143**	**0.036458**	**15.10785**	**8.33E-19**	**0.477277**	**0.624326**	**0.477277**	**0.624326**
X Variable 2	**0.189939319**	**0.013054**	**14.55024**	**3.24E-18**	**0.163613**	**0.216265**	**0.163613**	**0.216265**
X Variable 3	**0.774050473**	**0.035991**	**21.5066**	**1.23E-24**	**0.701467**	**0.846634**	**0.701467**	**0.846634**

Table F-11 Non-Linear Regression Parameters To Predict The E_t Of Category-1 Connections With Square Bolt Pattern

SUMMARY OUTPUT

Regression Statistics	
Multiple R	0.989805039
R Square	0.979714016
Adjusted R Square	0.978298715
Standard Error	0.042257518
Observations	47

ANOVA

	df	*SS*	*MS*	*F*	*Significance F*
Regression	3	3.708341	1.236114	692.23	2.12E-36
Residual	43	0.076785	0.001786		
Total	46	3.785126			

	Coefficients	*Standard Error*	*t Stat*	*P-value*	*Lower 95%*	*Upper 95%*	*Lower 95.0%*	*Upper 95.0%*
Intercept	7.764668252	0.174784	44.42442	1.44E-37	7.412183	8.117153	7.412183	8.117153
X Variable 1	0.578497371	0.031621	18.29474	6.59E-22	0.514728	0.642267	0.514728	0.642267
X Variable 2	0.190096875	0.011334	16.77227	1.76E-20	0.16724	0.212954	0.16724	0.212954
X Variable 3	0.728488092	0.030003	24.28076	9.85E-27	0.667982	0.788994	0.667982	0.788994

Table F-12 Non-Linear Regression Parameters To Predict The θ_f Of Category-1 Connections With Square Bolt Pattern

SUMMARY OUTPUT

Regression Statistics	
Multiple R	0.981658182
R Square	0.963652787
Adjusted R Square	0.960191148
Standard Error	0.080497461
Observations	47

ANOVA

	df	*SS*	*MS*	*F*	*Significance F*
Regression	4	7.215445	1.803861	278.3805	1.25E-29
Residual	42	0.272153	0.00648		
Total	46	7.487598			

	Coefficients	*Standard Error*	*t Stat*	*P-value*	*Lower 95%*	*Upper 95%*	*Lower 95.0%*	*Upper 95.0%*
Intercept	-2.769313404	0.345092	-8.02485	5.17E-10	-3.46574	-2.07289	-3.46574	-2.07289
X Variable 1	-0.232690985	0.060739	-3.83101	0.00042	-0.35527	-0.11012	-0.35527	-0.11012
X Variable 2	0.657546039	0.021596	30.44797	2.96E-30	0.613964	0.701128	0.613964	0.701128
X Variable 3	-8.544075061	0.826903	-10.3326	4.19E-13	-10.2128	-6.87532	-10.2128	-6.87532
X Variable 4	8.029032465	0.793852	10.11402	7.99E-13	6.426974	9.631091	6.426974	9.631091

Table F-13 Non-Linear Regression Parameters To Predict The M_y Of Category-2 Connections With Square Bolt Pattern

SUMMARY OUTPUT

Regression Statistics	
Multiple R	0.987203499
R Square	0.974570748
Adjusted R Square	0.972614651
Standard Error	0.072932763
Observations	43

ANOVA

	df	*SS*	*MS*	*F*	*Significance F*
Regression	3	7.950414	2.650138	498.2223	4.02E-31
Residual	39	0.207448	0.005319		
Total	42	8.157862			

	Coefficients	*Standard Error*	*t Stat*	*P-value*	*Lower 95%*	*Upper 95%*	*Lower 95.0%*	*Upper 95.0%*
Intercept	3.735326686	0.298306	12.52181	3.05E-15	3.131946	4.338707	3.131946	4.338707
X Variable 1	1.047538957	0.039545	26.4896	1.52E-26	0.967551	1.127527	0.967551	1.127527
X Variable 2	0.29760369	0.025561	11.64274	2.91E-14	0.245901	0.349306	0.245901	0.349306
X Variable 3	0.557031901	0.052351	10.64041	4.29E-13	0.451143	0.662921	0.451143	0.662921

Table F-14 Non-Linear Regression Parameters To Predict The E_y Of Category-2 Connections With Square Bolt Pattern

SUMMARY OUTPUT

Regression Statistics	
Multiple R	0.992171619
R Square	0.984404522
Adjusted R Square	0.98320487
Standard Error	0.045400678
Observations	43

ANOVA

	df	*SS*	*MS*	*F*	*Significance F*
Regression	3	5.07416	1.691387	820.575	2.92E-35
Residual	39	0.080388	0.002061		
Total	42	5.154548			

	Coefficients	*Standard Error*	*t Stat*	*P-value*	*Lower 95%*	*Upper 95%*	*Lower 95.0%*	*Upper 95.0%*
Intercept	6.613017316	0.185695	35.61217	2.33E-31	6.237413	6.988622	6.237413	6.988622
X Variable 1	0.748725052	0.024617	30.41501	8.87E-29	0.698933	0.798518	0.698933	0.798518
X Variable 2	0.160260947	0.015912	10.07175	2.09E-12	0.128076	0.192446	0.128076	0.192446
X Variable 3	0.947876953	0.032588	29.08644	4.71E-28	0.881961	1.013793	0.881961	1.013793

Table F-15 Non-Linear Regression Parameters To Predict The E_t Of Category-2 Connections With Square Bolt Pattern

SUMMARY OUTPUT

Regression Statistics	
Multiple R	0.976426652
R Square	0.953409008
Adjusted R Square	0.949526425
Standard Error	0.100860644
Observations	40

ANOVA

	df	*SS*	*MS*	*F*	*Significance F*
Regression	3	7.494165	2.498055	245.5605	5.11E-24
Residual	36	0.366223	0.010173		
Total	39	7.860389			

	Coefficients	*Standard Error*	*t Stat*	*P-value*	*Lower 95%*	*Upper 95%*	*Lower 95.0%*	*Upper 95.0%*
Intercept	4.228770683	0.433087	9.764263	1.17E-11	3.350431	5.107111	3.350431	5.107111
X Variable 1	0.293223303	0.059968	4.889673	2.1E-05	0.171603	0.414844	0.171603	0.414844
X Variable 2	0.666557847	0.036236	18.39492	6.85E-20	0.593068	0.740048	0.593068	0.740048
X Variable 3	0.85181998	0.073827	11.53813	1.19E-13	0.702093	1.001547	0.702093	1.001547

Table F-16 Non-Linear Regression Parameters To Predict The θ_f Of Category-2 Connections With Square Bolt Pattern

SUMMARY OUTPUT

Regression Statistics	
Multiple R	**0.980396805**
R Square	**0.961177895**
Adjusted R Square	**0.956741083**
Standard Error	**0.099291176**
Observations	**40**

ANOVA

	df	*SS*	*MS*	*F*	*Significance F*
Regression	**4**	**8.543072**	**2.135768**	**216.6371**	**3.63E-24**
Residual	**35**	**0.345056**	**0.009859**		
Total	**39**	**8.888127**			

	Coefficients	*Standard Error*	*t Stat*	*P-value*	*Lower 95%*	*Upper 95%*	*Lower 95.0%*	*Upper 95.0%*
Intercept	**-0.584700681**	**0.428086**	**-1.36585**	**0.180699**	**-1.45376**	**0.284359**	**-1.45376**	**0.284359**
X Variable 1	**-0.203098741**	**0.05991**	**-3.39009**	**0.001745**	**-0.32472**	**-0.08148**	**-0.32472**	**-0.08148**
X Variable 2	**0.947849958**	**0.035876**	**26.42001**	**1.04E-24**	**0.875017**	**1.020683**	**0.875017**	**1.020683**
X Variable 3	**-8.748249343**	**1.179154**	**-7.41909**	**1.11E-08**	**-11.1421**	**-6.35444**	**-11.1421**	**-6.35444**
X Variable 4	**7.878933997**	**1.14619**	**6.87402**	**5.56E-08**	**5.552044**	**10.20582**	**5.552044**	**10.20582**

REFERENCES

[1] AISC (2005). *Load and Resistance Factor Design Specification for Structural Steel Building*, 13th Edition, American Institute of Steel Construction, Chicago.

[2] Douty, R. T., and McGuire, W. (1963). "Research on Bolted Connections – A Progress Report," *Proceeding of the 1963 AISC National Engineering Conference*, Tulsa, OK, April 24-26, 1963, AISC, 48-55

[3] Douty, R. T., and McGuire, W. (1965). "High Strength Bolted Moment Connection," *Journal of the Structural Division*, ASCE, 91(2), 101-128.

[4] Nair, R. S., Birkemore, P. C., and Munse, W. H. (1974). "High Strength Bolts Subjected to Tension and Prying," *Journal of Structural Division*, ASCE, 100(2), 351-372.

[5] Kennedy, N. A., Vinnakota, S., Sherbourne, A. (1981). "The Split-Tee Analogy in Bolted Splices and Beam-Column Connections", *Journal in Structural Steelwork*, John Willey and Sons, New York, pp. 2.138-2.157.

[6] Kennedy, D.J. and Hafez, M.A. (1984). "A Study of End-Plate Connections for Steel Beams," Canadian *Journal of Civil Engineering*, 11(2), 139-149

[7] European committee for standardization, Eurocode 3: Part 1.1 Revised Annex J: Joint in building Frame, Env 1993-1-1: 1992/A2: 1998

[8] Murray, T.M., and Shoemaker, W.L. (2002) Steel Design Guide Series 16, Flush and Extended Multiple-Row Moment End-Plate Connections, American Institute of Steel Construction, Chicago, IL.

[9] Srouji, R., Kukreti, A., and Murray, T. M. (1983). "Yield-Line Analysis of End-Plate Connections with Bolt Force Predictions", Report No. FESL/MBMA 83-05, University of Oklahoma, Norman, Oklahom

[10] Hendrick, D. M., Kukreti, A. R., and Murray, T. M. (1985). " Unification of the Flush End-Plate Design Procedure, "Report No. FESL/MBMA 85-01, Fears Structural Engineering Laboratory, University of Oklahoma, Norman, Oklahom

[11] Morrison, S. J., Astaneh-Asl, A., and Murray, T. M. (1985). ”Analytical and Experimental Investigation of the Extended Stiffened Moment End-Plate Connection with Four Bolts at the Beam Tension Flanges,” Report No. FSEL/MBMA 86-01, University of Oklahoma, Norman, Oklahoma.

[12] Morrison, S. J., Astaneh-Asl, A., and Murray, T. M. (1986). “Analytical and Experimental Investigation of the Multiple Row Extended 1/3 Moment End-Plate Connection with Eight Bolts at the Beam Tension Flange,” Report No. FSEL/MBMA 86-01, University of Oklahoma, Norman, Oklahoma.

[13] Borgsmiller, J.T. (1995), “Simplified Method for Design of Moment End-Plate Connections,” M.S. Thesis, Department of Civil Engineering, Virginia Polytechnic Institute and State University, Blacksburg, Virginia.

[14] Astaneh, A., Nader, M.N., and Malik, L., (1989), “Cyclic Behavior of Double Web Angle Connections.” *Journal of Structural Engineering*, ASCE, Vol. 115, No. 5, pp. 1101-1118

[15] Adey, B.T., Grondin, G. Y., and Cheng, J.J.R. (2000). “Cyclic Loading of End Plate Moment Connections,” *Canadian Journal of Civil Engineering*, National Research Council of Canada, 27(4), 683-701

[16] Meng, R. L., and Murray, T. M. (1996). “Moment End-Plate Connections for Seismic Loading”, Research Report No. CE/VPI-ST-96/04, submitted to National Science Foundation, Arlington, Virginia, May 1996.

[17] Meng, R. L., and Murray, T. M. (1997).”Seismic Performance of Bolted End-Plate Moment Connection,” *Proceeding of the 1997 National Steel Construction Conference, Chicago, Illinois*, AISC, May 7-9, 1997, 30-1-30-14.

[18] Boorse, M. R. (1999) “Evaluation of the Inelastic Rotation Capacity of Flush End-Plate Moment Connection,” M.S Thesis, Department of Civil Engineering, Virginia Polytechnic Institute and State University, Blacksburg, Virginia.

[19] Bursi, O. S., Jaspart, J. P., (1997). “Benchmark for Finite Element Modeling of Bolted Steel Connections,” *Construction Steel Research*, 43, 17-42

[20] Bursi, O. S., Jaspart, J. P., (1998). “Basic Issues in the Finite Element Simulation of Extended End-Plate Connections,” *Computers and Structure*s, 69, 361-382

[21] Mays, T. W., (2000). Application of the Finite Element Method to the Siesmic Design and Analysis of Large Moment End-Plate Connection, Ph.D. Dissertation, Department of Civil Engineering, Virginia Polytechnic Institute and State University, Blacksburg, Virginia.

[22] Murray, T.M. (1988). “Recent Development for the design of Moment End-Plate Connections,” *Steel Beam-to-Column Building Connections*, W.F. Chen, ed., Elsevier Applied Science, New York, 133-162.

[23] AISC (1999). *Load and Resistance Factor Design Specification for Structural Steel Building*, American Institute of Steel Construction, Chicago.

[24] Grundy, P., Thomas, I.R. and Bennetts, I.D. (1980). “Beam-to-Column Moment connection,” *Journal of the Structural Division*, ASCE, 106(1), 313-330

[25] Krishnamurthy, N. (1978). “A Fresh Look at Bolted End-Plate Behavior and Design,” *Engineering Journal*, AISC, 15(2), 39-49.

[26] Aggarwal, A.K. and Coates, R.C. (1987). “Strength Criteria for Bolted Beam-Column Connections,” *Journal of Constructional Steel Research*, Elsevier Applied Science, 7(3), 213-22

[27] AISC (1989). *Manual of Steel Construction, Allowable Stress Design*, American Institute of Steel Construction, Chicago.

[28] Murray T. M., (1990). *AISC Design Guide Series 4, Extended End-Plate Moment Connections*, American Institute of Steel Construction, Chicago.

[29] Ghassemieh, M., Kukreti, A.R. and Murray, T.M. (1983). “Inelastic Finite Element Analysis of Stiffened End-Plate Moment Connections,” *Research Report No. FSEL/MBMA 83-02*, Fears Structural Engineering Laboratory, School of Civil Engineering and Environmental Science, University of Oklahoma, Norman, Oklahoma.

[30] Murray, T.M., Kurkreti, A.R. (1988). “Design of 8-Bolt Stiffened Moment End-Plates,” *Engineering Journal*, AISC, Second Quarter, 1988, 74-78.

[31] Ghobareh A, Osman A, Korol RM. (1990), “Behavior of Extended End-Plate Connections under Cyclic Loading,” *Engineering Structure*, 12(1), 15-27.

[32] Ghobarah A, Korol RM, Osman A. (1992), “Cyclic Behavior of Extended End-Plate Joints,” *Journal of Structural Engineering*, 118(5), 1333-53.

[33] Tsai K. C., Popov E. P. (1990), “Cyclic Behavior of End-Plate Moment Connections,” *Journal of Structural Engineering*, 116(11), 2917-30

[34] Chasten, C.P., Lu, L.W. and Driscoll, G.C. (1992). “Prying and Shear in End-Plate Connection Design,” *Journal of Structural Engineering*, ASCE, 122(11), 1307-1316

[35] Graham, J. (1993). “Observation from the Behavior of Bolted Beam to Unstiffened Column Rigid Connections,” *The Structural Engineering*, Institution of Structural Engineers, 71(6), 99-105

[36] Yorgun, C., Bayramoglu, G., (2001). “Cyclic Test for Welded-Plate Sections with End-Plate Connections,” *Journal of Constructional Steel Research*, 57(12), 1309-20.

[37] Broderick, B. M., and Thomson, A.W. (2002). “The response of flush end-plate joints under earthquake loading,” Journal of Constructional Steel Research, 58(9), 1161–75.

[38] Sumner, E. A., and Murray, T. M. (2001), Experimental investigation of the MRE ½ End-Plate Connection, Research Report No. CE/VPI-ST-00/03, SAC Report No. SAC/BD-00/21, submitted to the SAC Joint Venture, May 2000, 327 Pages.

[39] Sumner, E.A., and Murray, T.M. (2001), *Experimental Investigation of Four Bolts Wide Extended End-plate Moment Connections*, Research Report No. CE/VPI-ST-01/15, submitted to Star Building System, Inc., Oklahoma City, Oklahoma, December 2001, 114 pages.

[40] Sumner, E.A., (2003), “Unified Design of Extended End-Plate Moment Connections Subjected to Cyclic Loading,” Ph*.D. Dissertation*, Virginia Polytechnic Institute and State University, Blacksburg, Virginia.

[41] Shi, G., Shi, Y., and Wang, Y. (2007). “Behavior of End-Plate Moment Connections under Earthquake Loading,” *Engineering Structure*, 29, 703-716.

[42] Shi, Y., Shi, G., Wang, Y. (2007). “Experimental and Theoretical Analysis of the Moment-Rotation Behavior of Stiffened Extended End-Plate Connections,” *Journal of Constructional Steel Research*, 63, 1279-1293.

[43] Kato, B., and McGuire, W. (1973). “Analysis of T-stub Flange-to-Column Connection,” *Journal of the Structural Division*, ASCE, 99(5), 865-888.

[44] Agerskov, H., (1976). “High-Strength Bolted Connections Subjected to Prying,” *Journal of the Structural Division*, ASCE, 102(1), 161-175.

[45] Agerskov, H., (1977). “Analysis of Bolted Connections Subjected to Prying,” *Journal of the Structural Division*, ASCE, 103(11), 2145-2163.

[46] Fisher, J. W., and Struik, J. H. A. (1974). “Guide to Design Criteria for Bolted and Riveted Joints,” John Wiley and Sons, New York.

[47] Fleischman, R. B., Chasten C. P., Lu, L. W., and Driscoll, G. C. (1991). “Top-and-Seat-Angle Connections and End-Plate Connections: Snug vs. Fully Pretensioned Bolts,” AISC, Engineering Journal, 1st Qtr., 28, 18-28.

[48] Bahaari, M. R., Sherbourne A. N., (1999). “Behavior of Eight-Bolt Large Capacity Endplate Connection,” *Computer and Structure*, 77, 315-325.

[49] Murray, T. M., Kline, D. P., and Rojiani, K. B. (1992). “Use of Snug-Tightened Bolts in End-Plate Connections,” *Connections is Steel Structure II: Behavior, Strength and Design: Proceeding of the second international Workshop*, Pittsburgh, PA, April 10-12, 1991, Bjorhovde, Colson, Haaijer and Stark, ed., Pergamon, 1991, 27-34.

[50] Krishnamurthy, N., and Graddy, D.E. (1976). “Correlation between 2- and 3- Dimensional Finite Element Analysis of Steel Bolted End-Plate Connections,” *Computer and Structures*, Pergamon, 6(4-5/6), 381-389.

[51] Krishnamurthy, N., Huang H. T., Jefferey P. K., and Avery L. K., 1979. “Analytical *M-θ* Curve for End-Plate Connections,” *Journal of Structural Division*, 105(ST1), 133-145.

[52] Krishnamurthy, N., (1980). “Modeling and Prediction of Steel Bolted Connection Behavior,” *Computer and Structure*, 11, 75-82

[53] American Institute of Steel Construction. Manual of Steel Construction Load and Resistance factor Design, 3rd ed. Chicago, IL, 2001.

[54] Kukreti, A. R., Murray, T. M., and Ahuja, V. (1982). “Analysis of Stiffened End-Plate Connections with Multiple Bolt Rows at the Beam Flanges,” presented at Sino-American Symposium on Bridge and Structural Engineering, Beijing, China, September, 13-19, (1982)

[55] Kukreti, A. R., Ghassemieh, M., and Murry, T. M. (1990). “Behavior ad Design of Large-Capacity Moment End Plates,” *Journal of Structural Engineering*, ASCE, 116(3), 809-828.

[56] Gebbeken, N., Rothert, H., and Binder, B. (1994). “On The Numerical Analysis of Stiffened Endplate Connection,” *Journal of Constructional Steel Research*, Elsevier Applied Science, 30(1), 177-196.

[57] Bahhari, M. R., and Sherbourne, A. N. (1994). “Computer Modeling of an Extended End-Plate Bolted Connection,” *Computer and Structures*, 52, 879-893.

[58] Bahhari, M R., Sherbourne, A N. (1996). “Structural Behavior of End-Plate Bolted Connections to Stiffened Columns,” *Journal of Structural Engineering*, ASCE, 122(8), 926-935.

[59] Bahaari, M. R., Sherbourne, A. N. (1996). “3D Simulation of Bolted Connection to Un-stiffened Column-II. Extended Endplate Connections,” *Journal of Constructional Steel Research*, Elsevier Applied Science, 40(3), 189-223.

[60] Maggi, Y. I., Goncalves, R. M., Leon, R. T., and Ribeiro, L. F. L. (2005). “Parametric analysis of steel bolted end plate connections using finite element modeling,” *Journal of Constructional Steel Research,* **61**(5), 689–708

[61] Fleischman, R. B., Chasten, C. P., Lu, Lu, L. W. and Driscoll, G. C. (1991). “Top-and-Seat Angles Connection and End-Plate Connection: Snug vs. Fully Pre-Tensioned Bolts,” AISC Engineering Journal, 1st Qrt., 28, 18-28.

[62] Kulak, G. L., Fisher, J. W., Struik, J. H. A, “Guise to design Criteria for Bolted and Rivered Joints”, 2nd Ed, (New York: John Wiley & Sons, 1987).

[63] Piluso, V., and Rizzano, G. (2007). “Experimental Analysis and Modelling of Bolted T-stubs Under Cyclic Loads,” *Journal of Constructional Steel Research*, 64, 655-69.

[64] Abolmaali, A., Kukreti, A., Motahari, A., Ghsemieh, M, “Energy Dissipation Characteristics of Semi-Rigid Connections,” *Journal of Constructional Steel Research*, Volume 65, Issue 5, May 2009, Pages 1187-1197

[65] A. Abolmaali, A.R. Kukreti and H. Razavi, “Hysteresis behavior of semi-rigid double web angle steel connections”, *Journal of Constructional Steel Research* 59 (2003), pp. 1057–1082

[66] Vishay Measurement Group INC, (1992) “Student Manual for Strain Gage Technology”,

[67] Zienkiewics, O., Taylor, R. L., “The Finite Element Mothods,” 4th ed., Maidenhead: McGraw-Hill, 1989.

[68] Kiamanesh R., Abolmaali A., and Ghammemieh M., “The Effect of Stiffeners on the Strain Patterns of the Welded Connection Zone”, *Journal of Constructional Steel Research, (2010), 66(1), 19-27.*

[69] Ghobadi M. S., Mazroi A., Ghassemieh M.. “Cyclic Response Characteristics of Retrofitted Moment Resisting Connection”*, Journal of Constructional Steel Research* (2008); 65(3):

[70] ABAQUS Version 6.8-2 User’s Manual, Hibbit, Carlson &Sorensen Inc., Michigan; 2008.

[71] Doghri I., Benallal A., Billardon r., “An Integration Algorithm and the Corresponding Consistent Tangent Operator for Fully Coupled Elastoplastic and Damage Equations”, *Communications in Applied Numerical Methods,* (1988); (4):731-40

[72] American Institute of Steel Construction. “Prequalified Connections for Special and Intermediate Steel Moment Frames for Seismic Applications” Chicago, IL, December-2005.

[73] AISC (2002), Load and resistance factor design specification for structural steel building, American Institute of Steel Construction, Chicago, IL.

[74] FEMA recommended seismic design criteria new steel moment frame building, Report no. FEMA-350. *Federal Emergency Management Agency*; 2000.

BIOGRAGHICAL INFORMATION

Roozbeh Kiamanesh earned his first B.S in 2001 in Construction Engineering from University of Tehran Science and Technology. He pursued his second B.S in Civil Engineering in 2005 and M.S in Structural Engineering both from University of Oklahoma (OU). Then he was admitted in Ph.D. program of the University of Texas at Arlington in fall 2007 and got his Ph.D. in summer 2011 in Applied Mechanics in Structural Engineering.

During his undergraduate and graduate studies he published three papers in journals and international conferences in different fields of his study.

He has years of teaching experience in almost all of the structural engineering courses in undergraduate and graduate level.

Currently, he has accepted an offer from Bell Helicopter as a senior design engineer and he will join the aerospace industry prior to his graduation.